V. 120, NO. 6
NOVEMBER 2023

ACI STRUCTURAL JOURNAL

A JOURNAL OF THE AMERICAN CONCRETE INSTITUTE

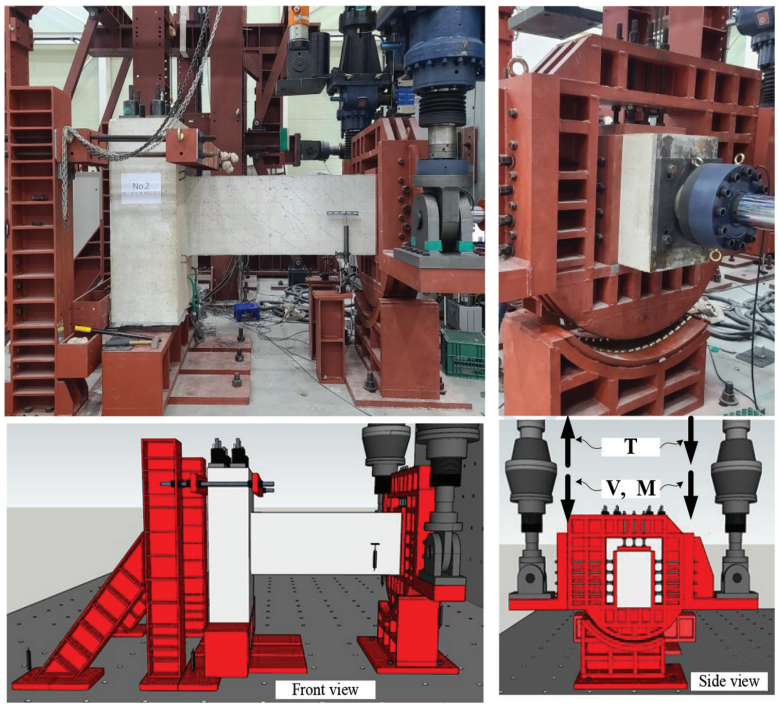

American Concrete Institute

CONTENTS

ACI Structural Journal

November 2023, V. 120, No. 6

A JOURNAL OF THE AMERICAN CONCRETE INSTITUTE
AN INTERNATIONAL TECHNICAL SOCIETY

Contents continued on next page

Discussion is welcomed for all materials published in this issue and will appear ten months from this journal's date if the discussion is received within four months of the paper's print publication. Discussion of material received after specified dates will be considered individually for publication or private response. ACI Standards published in ACI Journals for public comment have discussion due dates printed with the Standard.

The *ACI Structural Journal* (ISSN 0889-3241) is published bimonthly by the American Concrete Institute. Publication office: 38800 Country Club Drive, Farmington Hills, MI 48331. Periodicals postage paid at Farmington, MI, and at additional mailing offices. Subscription rates: $192 per year, payable in advance. POSTMASTER: Send address changes to: *ACI Structural Journal*, 38800 Country Club Drive, Farmington Hills, MI 48331.

Canadian GST: R 1226213149.

Direct correspondence to 38800 Country Club Drive, Farmington Hills, MI 48331. Telephone: +1.248.848.3700. Facsimile (FAX): +1.248.848.3701. **Website: http://www.concrete.org.**

CONTENTS

MEETINGS

JANUARY

7-11—TRB 103rd Annual Meeting, Washington, DC, https://www.trb.org/AnnualMeeting/AnnualMeeting.aspx

16-18—AED Summit, Las Vegas, NV, https://aedsummit2024.mapyourshow.com/8_0/#

22-25—World of Concrete, Las Vegas, NV, www.worldofconcrete.com

23-25—National Pavement Expo and Conference, Tampa, FL, https://nationalpavementexpo.com

FEBRUARY

6-9—2024 PCI Convention at The Precast Show, Denver, CO, www.pci.org/PCI/News-Events/Event-Category?type=conv

8-10—The Precast Show, Denver, CO, https://precast.org/theprecastshow

11-13—Geo Week, Denver, CO, www.geo-week.com

24-25—Advanced Materials for Sustainable Infrastructure Development - Exploring Emerging Technologies for Reducing Carbon Emissions, Ventura, CA, www.grc.org/advanced-materials-for-sustainable-infrastructure-development-grs-conference/2024

ACI CONCRETE CONVENTION: FUTURE DATES

2024—March 24-28, Hyatt Regency New Orleans, New Orleans, LA
2024—November 3-7, Philadelphia Marriott Downtown, Philadelphia, PA
2025—Mar. 30-Apr. 3, Sheraton Centre Toronto Hotel, Toronto, ON, Canada

For additional information, contact:
Event Services, ACI
38800 Country Club Drive
Farmington Hills, MI 48331
Telephone: +1.248.848.3795
email: conventions@concrete.org

ON COVER: 120-S101, p. 155, Fig. 4—Loading system.

Contributions to *ACI Structural Journal*

The *ACI Structural Journal* is an open forum on concrete technology and papers related to this field are always welcome. All material submitted for possible publication must meet the requirements of the "American Concrete Institute Publication Policy" and "Author Guidelines and Submission Procedures." Prospective authors should request a copy of the Policy and Guidelines from ACI or visit ACI's website at **www.concrete.org** prior to submitting contributions.

Papers reporting research must include a statement indicating the significance of the research.

The Institute reserves the right to return, without review, contributions not meeting the requirements of the Publication Policy.

All materials conforming to the Policy requirements will be reviewed for editorial quality and technical content, and every effort will be made to put all acceptable papers into the information channel. However, potentially good papers may be returned to authors when it is not possible to publish them in a reasonable time.

Discussion

All technical material appearing in the *ACI Structural Journal* may be discussed. If the deadline indicated on the contents page is observed, discussion can appear in the designated issue. Discussion should be complete and ready for publication, including finished, reproducible illustrations. Discussion must be confined to the scope of the paper and meet the ACI Publication Policy.

Follow the style of the current issue. Be brief—1800 words of double spaced, typewritten copy, including illustrations and tables, is maximum. Count illustrations and tables as 300 words each and submit them on individual sheets. As an approximation, 1 page of text is about 300 words. Submit one original typescript on 8-1/2 x 11 plain white paper, use 1 in. margins, and include two good quality copies of the entire discussion. References should be complete. Do not repeat references cited in original paper; cite them by original number. Closures responding to a single discussion should not exceed 1800-word equivalents in length, and to multiple discussions, approximately one half of the combined lengths of all discussions. Closures are published together with the discussions.

Discuss the paper, not some new or outside work on the same subject. Use references wherever possible instead of repeating available information.

Discussion offered for publication should offer some benefit to the general reader. Discussion which does not meet this requirement will be returned or referred to the author for private reply.

Send manuscripts to:
http://mc.manuscriptcentral.com/aci

Send discussions to:
Journals.Manuscripts@concrete.org

STATEMENT OF OWNERSHIP

UNITED STATES POSTAL SERVICE®

Statement of Ownership, Management, and Circulation (All Periodicals Publications Except Requester Publications)

1. Publication Title	2. Publication Number	3. Filing Date
ACI Structural Journal	0 8 8 9 _ 3 2 4 1	Sept. 26, 2023
4. Issue Frequency	**5. Number of Issues Published Annually**	**6. Annual Subscription Price**
bi-monthly	6	$192

7. Complete Mailing Address of Known Office of Publication *(Not printer) (Street, city, county, state, and ZIP+4®)*

American Concrete Institute
38800 Country Club Drive
Farmington Hills, MI 48331

Contact Person: Tiesha Elam

Telephone *(Include area code)*: 248-848-3753

8. Complete Mailing Address of Headquarters or General Business Office of Publisher *(Not printer)*

American Concrete Institute, 38800 Country Club Drive, Farmington Hills, MI 48331

9. Full Names and Complete Mailing Addresses of Publisher, Editor, and Managing Editor *(Do not leave blank)*

Publisher *(Name and complete mailing address)*

John C. Glumb, 38800 Country Club Drive, Farmington Hills, MI 48331

Editor *(Name and complete mailing address)*

Tiesha Elam, 38800 Country Club Drive, Farmington Hills, MI 48331

Managing Editor *(Name and complete mailing address)*

Lauren E. Mentz, 38800 Country Club Drive, Farmington Hills, MI 48331

10. Owner *(Do not leave blank. If the publication is owned by a corporation, give the name and address of the corporation immediately followed by the names and addresses of all stockholders owning or holding 1 percent or more of the total amount of stock. If not owned by a corporation, give the names and addresses of the individual owners. If owned by a partnership or other unincorporated firm, give its name and address as well as those of each individual owner. If the publication is published by a nonprofit organization, give its name and address.)*

Full Name	Complete Mailing Address
American Concrete Institute	38800 Country Club Drive
	Farmington Hills, MI 48331

11. Known Bondholders, Mortgagees, and Other Security Holders Owning or Holding 1 Percent or More of Total Amount of Bonds, Mortgages, or Other Securities. If none, check box → ▣ None

Full Name	Complete Mailing Address

12. Tax Status *(For completion by nonprofit organizations authorized to mail at nonprofit rates) (Check one)*

The purpose, function, and nonprofit status of this organization and the exempt status for federal income tax purposes:

▣ Has Not Changed During Preceding 12 Months

☐ Has Changed During Preceding 12 Months *(Publisher must submit explanation of change with this statement)*

PS Form **3526,** July 2014 *[Page 1 of 4 (see instructions page 4)]* PSN: 7530-01-000-9931 **PRIVACY NOTICE:** See our privacy policy on *www.usps.com.*

STATEMENT OF OWNERSHIP

13. Publication Title	14. Issue Date for Circulation Data Below
ACI Structural Journal	September 2023

15. **Extent and Nature of Circulation**			**Average No. Copies Each Issue During Preceding 12 Months**	**No. Copies of Single Issue Published Nearest to Filing Date**
a. Total Number of Copies *(Net press run)*			1820	1764
b. Paid Circulation *(By Mail and Outside the Mail)*	(1)	Mailed Outside-County Paid Subscriptions Stated on PS Form 3541 (Include paid distribution above nominal rate, advertiser's proof copies, and exchange copies)	1078	1063
	(2)	Mailed In-County Paid Subscriptions Stated on PS Form 3541 *(Include paid distribution above nominal rate, advertiser's proof copies, and exchange copies)*		
	(3)	Paid Distribution Outside the Mails Including Sales Through Dealers and Carriers, Street Vendors, Counter Sales, and Other Paid Distribution Outside USPS®	404	401
	(4)	Paid Distribution by Other Classes of Mail Through the USPS (e.g., First-Class Mail®)		
c. Total Paid Distribution *[Sum of 15b (1), (2), (3), and (4)]* ▶			1482	1464
d. Free or Nominal Rate Distribution *(By Mail and Outside the Mail)*	(1)	Free or Nominal Rate Outside-County Copies included on PS Form 3541		
	(2)	Free or Nominal Rate In-County Copies Included on PS Form 3541		
	(3)	Free or Nominal Rate Copies Mailed at Other Classes Through the USPS (e.g., First-Class Mail)		
	(4)	Free or Nominal Rate Distribution Outside the Mail *(Carriers or other means)*		
e. Total Free or Nominal Rate Distribution *(Sum of 15d (1), (2), (3) and (4))*				
f. Total Distribution *(Sum of 15c and 15e)* ▶			1482	1464
g. Copies not Distributed *(See Instructions to Publishers #4 (page #3))* ▶			338	300
h. Total *(Sum of 15f and g)*			1820	1764
i. Percent Paid *(15c divided by 15f times 100)* ▶			100%	100%

* If you are claiming electronic copies, go to line 16 on page 3. If you are not claiming electronic copies, skip to line 17 on page 3.

PS Form **3526,** July 2014 *(Page 2 of 4)*

UNITED STATES POSTAL SERVICE®

Statement of Ownership, Management, and Circulation (All Periodicals Publications Except Requester Publications)

16. Electronic Copy Circulation	Average No. Copies Each Issue During Preceding 12 Months	No. Copies of Single Issue Published Nearest to Filing Date
a. Paid Electronic Copies ▶	146	146
b. Total Paid Print Copies (Line 15c) + Paid Electronic Copies (Line 16a) ▶	1628	1610
c. Total Print Distribution (Line 15f) + Paid Electronic Copies (Line 16a) ▶	1628	1610
d. Percent Paid (Both Print & Electronic Copies) (16b divided by 16c × 100) ▶	100%	100%

■ **I certify that 50% of all my distributed copies (electronic and print) are paid above a nominal price.**

17. Publication of Statement of Ownership

■ If the publication is a general publication, publication of this statement is required. Will be printed in the November 2023 issue of this publication. ☐ Publication not required.

18. Signature and Title of Editor, Publisher, Business Manager, or Owner	Date
Lauren Mentz	9/26/2023

I certify that all information furnished on this form is true and complete. I understand that anyone who furnishes false or misleading information on this form or who omits material or information requested on the form may be subject to criminal sanctions (including fines and imprisonment) and/or civil sanctions (including civil penalties).

PRIVACY NOTICE: See our privacy policy on *www.usps.com.*

ACI STRUCTURAL JOURNAL TECHNICAL PAPER

Title No. 120-S90

Strut-and-Tie Models Using Multi-Material and Multi-Volume Topology Optimization: Load Path Approach

by Tuo Zhao, Ammar A. Alshannaq, David W. Scott, and Glaucio H. Paulino

The development of strut-and-tie models (STMs) for the design of reinforced concrete (RC) deep beams considering a general multi-material and multi-volume topology optimization framework is presented. The general framework provides flexibility to control the location/inclination/length scale of the ties according to practical design requirements. Optimality conditions are applied to evaluate the performance of the optimized STM layouts. Specifically, the Michell number Z (or load path) is used as a simple and effective criterion to quantify the STMs. The experimental results confirm that the layout with the lowest load path Z achieves the highest ultimate load. Moreover, significantly reduced cracking is observed in the optimized layouts compared to the traditional layout. This observation implies that the optimized layouts may require less crack-control reinforcement, which would lower the total volume of steel required for the deep beams.

Keywords: load path; Michell number; multi-material topology optimization; reinforced concrete (RC) deep beam; strut and tie.

INTRODUCTION

In 1904, Michell wrote the revolutionary paper "The Limits of Economy of Material in Frame-Structures," which is a landmark in the field of optimization in general and topology optimization in particular. He derived the well-known Michell's optimality conditions (Michell 1904), that provide analytical ways to find optimal truss structures. The definition of the optimal structure is the least-weight truss with given allowable stresses, which is also known as the minimal total load path theory. The load path has been quantified using the Michell number, Z, defined as follows

$$Z = \sum_e |F_e| L_e = \sum_{e \in G^T} |F_e| L_e + \sum_{e \in G^C} |F_e| L_e \tag{1}$$

where L_e and F_e denote the length and internal axial force of the e-th truss member in the structure, respectively; and G^T and G^C are the sets of tension and compression members, respectively. For any statically determinate truss that is fully stressed (to the tensile stress limit σ^T and compressive stress limit σ^C), the volume of the truss can be calculated as follows

$$V = \frac{\sum_{e \in G^T} |F_e| L_e}{\sigma^T} + \frac{\sum_{e \in G^C} |F_e| L_e}{\sigma^C} = \frac{(\sigma^C + \sigma^T) Z + (\sigma^C - \sigma^T) C}{2 \sigma^C \sigma^T} \tag{2}$$

where $C = \sum_{e \in G^T} |F_e| L_e - \sum_{e \in G^C} |F_e| L_e$, which is known as the Maxwell number. Maxwell (1864) states that C is a constant value for given boundary and loading conditions—that is, C is independent of the structural layout. As a result, minimizing the load path Z for a given design problem is equivalent to minimizing the volume V if the structure is fully stressed.

A pioneering work by Kumar (1978) applies the load path theory of truss frameworks to design reinforced concrete (RC) deep beams by navigating optimal load transmission. Following and building upon Kumar's study, this work extends Michell's optimality conditions to understand the optimal load path for STMs and uses the load path Z (or the Michell number) as a criterion to quantify the efficiency of the STM. Compared to existing criteria (Schlaich et al. 1987; Xia et al. 2020; He et al. 2020), the present criterion is simpler. The experimental results in the "Load-deflection curves" section in this paper verify that the STM layout with the lowest load path Z (or Michell number) achieves the highest ultimate load.

The STMs are powerful tools for analyzing and designing RC structures. However, traditional STMs dramatically simplify the complex stress state found in deep concrete elements in compression, which greatly limits their efficiency in many practical design applications. More recently, topology optimization has been used to automatically generate STMs, including the works of Liang et al. (2000, 2001), Leu et al. (2006), Bruggi (2010), Mozaffari et al. (2020), and Zhou and Wan (2021), which is just a small sample of references in the field. The optimized STM layouts provide deeper insight into the load paths in RC members and, ultimately, aid in more efficient structural designs. However, most topology optimization formulations for STMs use only a single material, assuming the struts and ties have the same linear behavior. Victoria et al. (2011) extend the single material optimization using a bilinear material model with different behaviors in compression and tension to represent the struts and ties, respectively. Gaynor et al. (2013) and Jewett and Carstensen (2019) consider different materials for the struts and ties, but most are typically restricted to a single volume constraint for both materials (that is, each material volume cannot be constrained separately). Thus, these models are limited in practical application. In many real-world RC structure design cases, restricting the location of reinforcement (ties) to certain regions while controlling

ACI Structural Journal, V. 120, No. 6, November 2023.
MS No. S-2020-408.R3, doi: 10.14359/51739089, received March 21, 2023, and reviewed under Institute publication policies.

the allowable angle of inclination or length scale of ties according to design requirements is essential.

The aforementioned limitations can be addressed by a general multi-material topology optimization approach, which efficiently accommodates an arbitrary number of materials and constraints (Zhang et al. 2018; Sanders et al. 2018). This general approach is applied to a novel STM framework using multi-material topology optimization with multiple volume constraints. The present framework allows the designer to adjust the ties' locations, inclinations, and scales based on practical design specifications.

RESEARCH SIGNIFICANCE

This work proposes a simple and efficient criterion (the Michell number Z in Eq. (1)) to quantify the efficiency of the topologically optimized STMs. It is shown that the optimized STM layouts with lower Z outperformed the traditional layout in terms of improving load-bearing capacity and ductility. The framework developed in this paper can form the benchmark of an efficient, general, and practical STM design method for RC structures.

MULTI-MATERIAL AND MULTI-VOLUME TOPOLOGY OPTIMIZATION FORMULATION FOR STRUT-AND-TIE MODELS

The design for an optimal STM layout consists of determining the cross-sectional areas of the truss members using the ground structure method (GSM) (for example, Dorn et al. [1964]). In this method, the design domain is discretized using a set of nodes that are interconnected by truss members to form an initial ground (that is, reference) structure (GS). Based on a tailored design update scheme, unnecessary members are gradually removed from the initial GS; the optimal STM design is then obtained. The topology optimization formulation for STMs using the GSM is given as

$$\min_{\boldsymbol{x}_1,\boldsymbol{x}_2} J(\boldsymbol{x}_1,\boldsymbol{x}_2) = \min_{\boldsymbol{x}_1,\boldsymbol{x}_2} -\Pi(\boldsymbol{x}_1,\boldsymbol{x}_2,\boldsymbol{u}(\boldsymbol{x}_1,\boldsymbol{x}_2))$$

$$\text{s.t.} \sum_{i\in G^j} \boldsymbol{L}_i^T \boldsymbol{x}_i - V_{max}^j \le 0, j = 1,\ldots, n, \text{ and } i = 1, 2 \quad (3)$$

$$\text{with } \boldsymbol{u}(\boldsymbol{x}_1, \boldsymbol{x}_2) = \arg\min_{\boldsymbol{u}} \Pi(\boldsymbol{x}_1, \boldsymbol{x}_2, \boldsymbol{u})$$

where $\boldsymbol{x}_1$ and $\boldsymbol{x}_2$ are the vectors of design variables (cross-sectional areas of the truss members) for struts (concrete) and ties (reinforcement), respectively, which can be constrained separately, and s.t. is subject to. The objective function J is the negative total potential energy of the system in equilibrium, and $\boldsymbol{u}$ is the displacement vector (state variable), which is obtained as the minimizer of the potential energy Π; thus, general nonlinear constitutive behavior can be incorporated (Sanders et al. 2020). The formulation (Eq. (3)) considers a total of n independent volume constraints and denotes G^j as the set of material indexes for the j-th volume constraint. The term $\boldsymbol{L}_i^T\boldsymbol{x}_1$ indicates the total volume associated with the design variable $\boldsymbol{x}_1$, with $\boldsymbol{L}_i$ being the length vector for the i-th material, and V_{max}^j is the allowable volume for the j-th volume constraint. The main feature of Eq. (3) is that it can efficiently handle a general setting of volume constraints. In particular, defining material subregions will allow the control of locations/inclination/length scale of the ties according to practical design requirements.

Design-variable update scheme to general volume constraints for STMs

An essential component of any topology optimization framework is a reliable and efficient design-variable update scheme. Zhang et al. (2018) formulated a general design-variable update scheme tailored for the multi-material topology optimization formulation that does not require a predefined candidate material sequence and can efficiently and effectively handle an arbitrary number of candidate materials and volume constraints. Inspired by this work, the current study derives a design-variable update scheme for the present strut-and-tie optimization formulation (Eq. (3)).

The derivation of the design-variable update scheme is based on sequential explicit, convex approximations. The objective function in the formulation (Eq. (3)) is approximated at optimization step k as a convex function constructed based on the objective function gradient (Christensen and Klarbring 2008; Groenwold and Etman 2008). Introducing a set of intervening variable vectors $\boldsymbol{y}_i(\boldsymbol{x}_i)$, the approximation of the objective function at the k-th optimization step is

$$J^k(\boldsymbol{x}_1,\boldsymbol{x}_2) = J(\boldsymbol{x}_1^k,\boldsymbol{x}_2^k) + \sum_{i=1}^{2}\left[\frac{\partial J}{\partial \boldsymbol{y}_i}(\boldsymbol{x}_1^k,\boldsymbol{x}_2^k)\right]^T\left[\boldsymbol{y}_i(\boldsymbol{x}_i) - \boldsymbol{y}_i(\boldsymbol{x}_i^k)\right] \quad (4)$$

where $\boldsymbol{x}_1^k, \boldsymbol{x}_2^k$ are the values of the design variables at optimization step k; and $\partial J/\partial \boldsymbol{y}_i$ is the gradient of J with respect to the intervening variable $\boldsymbol{y}_i$, which depends on the gradient of J with respect to $\boldsymbol{x}_i$. In the following, to simplify the notation, $\boldsymbol{b}_i$ denotes this gradient $\partial J/\partial \boldsymbol{y}_i$. Having defined the approximated objective J^k, a subproblem (by neglecting the constant terms in J^k) is formulated as

$$\min_{\boldsymbol{x}_1,\boldsymbol{x}_2} \sum_{i=1}^{2}[\boldsymbol{b}_i(\boldsymbol{x}_1^k,\boldsymbol{x}_2^k)]^T\boldsymbol{y}_i(\boldsymbol{x}_i)$$

$$\text{s.t.} \sum_{i\in G^j} \boldsymbol{L}_i^T\boldsymbol{x}_i - V_{max}^j \le 0, j = 1, \ldots, nc \quad (5)$$

$$x_{i,L}^{(e),k} \le x_i^{(e)} \le x_{i,U}^{(e),k}, \forall i \text{ and } e$$

where $x_{i,L}^{(e),k}$ and $x_{i,U}^{(e),k}$ are the lower and upper bounds for the design variable $x_i^{(e)}$ determined through a user-prescribed move limit. Introducing a set of Lagrange multipliers λ_j for each volume constraint, the Lagrangian of the previous subproblem is expressed as

$$L(\boldsymbol{x}_1, \boldsymbol{x}_2, \lambda_1,\ldots, \lambda_{nc}) = \sum_{j=1}^{nc}\left\{\sum_{i\in G^j}\left[\left[\boldsymbol{b}_i(\boldsymbol{x}_1^k,\boldsymbol{x}_2^k)\right]^T\boldsymbol{y}_i(\boldsymbol{x}_i) + \lambda_j\boldsymbol{L}_i^T\boldsymbol{x}_i\right] - \lambda_j V_{max}^j\right\} \quad (6)$$

The previous Lagrangian function has a clearly separable structure with respect to each volume constraint. This means that the minimizer of the Lagrangian with respect to $\boldsymbol{x}_i$, denoted as $\boldsymbol{x}_i^*$, can be expressed in the following form

$$x_i^{(e)*} = Q_i^{(e)}\left(\boldsymbol{x}_1^k, \boldsymbol{x}_2^k, \lambda_j\right), \forall i \in G^j \tag{7}$$

In other words, $\boldsymbol{x}_i^*$ only depends on the Lagrange multiplier of the volume constraint associated with $\boldsymbol{x}_i$. Plugging $\boldsymbol{x}_i^*$ back into the Lagrangian gives the dual objective function

$$D(\lambda_1, \ldots, \lambda_{nc}) = L(\boldsymbol{x}_1^*, \boldsymbol{x}_2^*, \lambda_1, \ldots, \lambda_{nc}) = \sum_{j=1}^{nc}\left\{\sum_{i \in G^j}\left[\left[\boldsymbol{b}_i\left(\boldsymbol{x}_1^k, \boldsymbol{x}_2^k\right)\right]^T \boldsymbol{y}_i\left(\boldsymbol{x}_i^*\right) + \lambda_j \boldsymbol{V}_i^T \boldsymbol{x}_i^*\right] - \lambda_j V_{max}^j\right\} \tag{8}$$

Because $\boldsymbol{x}_i^*$ only depends on λ_j if $i \in G^j$, it concludes that the dual objective function D also has a separable structure with respect to λ_j—namely, $D(\lambda_1, \ldots, \lambda_{nc}) = \sum_{j=1}^{nc} D^j(\lambda_j)$. As a result, the set of maximizing Lagrange multipliers $\lambda_1^*, \ldots, \lambda_{nc}^*$ can be computed by sequentially calculating the maximizing Lagrange multiplier λ_j^* for each $D^j(\lambda_j)$. The general formula of the updated design variable is then obtained

$$x_i^{(e),\,k+1} = Q_i^{(e)}\left(\boldsymbol{x}_1^k, \boldsymbol{x}_2^k, \lambda_j^*\right), \forall i \in G^j \tag{9}$$

Based on the previous formula, because the update of the design variable depends only on the Lagrange multiplier of its corresponding volume constraint, the design variables associated with each volume constraint can be updated independently. The present design-variable update scheme has been applied to the STM design example shown in the next section.

NUMERICAL EXAMPLES

A practical computational tool for STMs is developed to assist engineers in better understanding and designing RC structures using the present multi-material topology optimization framework. The new STM framework will provide engineers with the flexibility to specify the inclination/length scale of reinforcement and to control the tensile (tie) regions where reinforcement needs to be placed depending on design requirements through the use of multiple volume constraints.

A numerical study is conducted on the STMs for the two-dimensional (2-D) RC deep beam, as shown in Fig. 1(a). In this example, both struts and ties are modeled using truss elements with bilinear material models, as shown in Fig. 1(b). Five design scenarios are considered in this numerical example. In the first scenario, two materials share the entire domain (refer to Fig. 1(c)), and each material is associated with an individual volume constraint—that is, $V_{max}^j = 0.5V_{max}$, $j = 1, 2$. In the second and third scenarios, two materials share and split the domain (Fig. 1(e) and (g)), and the tie region is constrained within two-thirds and half of the entire domain, respectively. In the last two scenarios, struts and ties share and split the domain (Fig. 1(i) and (k)), and the allowable angle of inclination of ties is restricted to 90 degrees and 45 degrees, respectively. The optimized results for the five scenarios are shown in Fig. 1(d), (f), (h), (j), and (l). From the comparison of the results, varying specified tie regions/inclinations can significantly affect the STM and, in turn, the behavior of the resulting RC beam.

Besides specifying the tie regions/inclinations, the present STM design framework allows engineers to control the length scale of struts and ties either together or independently. Considering the length scale of STM designs is important from a practical point of view because the difficulties in the construction of the deep beam highly depend on the design of reinforcing bars in the STM. The length control approach in the present STM design framework is demonstrated using the deep beam example shown in Fig. 1. Without any restrictions on the length scale, the layouts of the initial ground structure for both struts and ties are shown in Fig. 1(c). The corresponding optimized STM design is shown in Fig. 1(d) (which is the same plot as the one in Fig. 2(a)). This design can be simplified by restricting the length of members in the initial ground structures for both the struts and ties. For instance, assuming that the minimum length scale is $\sqrt{2}$, the optimized design is obtained, as shown in Fig. 2(b), which has a simpler topology than the design shown in Fig. 2(a). Two alternative designs in Fig. 2(c) and (e) are obtained considering different minimum length scales of $\sqrt{5}$ and $\sqrt{10}$, respectively. Moreover, the length scale control can be applied to ties independently. For example, assuming that only ties are restricted to the minimum length scales, the optimized designs are achieved in Fig. 2(d) and (f). These two designs have different topologies than the ones in Fig. 2(c) and (e) accounting for length scale control for both struts and ties together. In summary, the flexible length control approach provides a variety of alternative STM configurations with different levels of complexity on the final topology.

The present STM framework generates a variety of optimized STM designs considering the specified tie regions, proper angles of inclination, and minimum length scale of the reinforcement. Furthermore, the efficiency of those alternative designs is investigated using the unified load path criterion in Eq. (1).

The design library in Fig. 3 collects alternative STM designs for a deep beam structure. Among those designs, Fig. 3(a) and (b) present conventional STM design layouts suggested by ACI 318-19 (ACI Committee 318 2019). The optimized designs with the present framework are shown in Fig. 3(a) to (l). As all the designs in Fig. 3 are statically determinate for the given boundary conditions, the internal forces in struts and ties can be easily calculated using static equilibrium conditions. Consequently, the load path Z for each design is determined using Eq. (1). As the load path Z decreases, the efficiency of the STM increases. For example, the standard ACI layout in Fig. 3(a) has a larger load path Z than the optimized layout in Fig. 3(k). The test results in the "Load-deflection curves" section demonstrate that the specimen with an optimized STM layout (Fig. 3(k)) can achieve a greater ultimate load than the specimen with the standard ACI layout for a given volume of tension reinforcement (Fig. 3(a)).

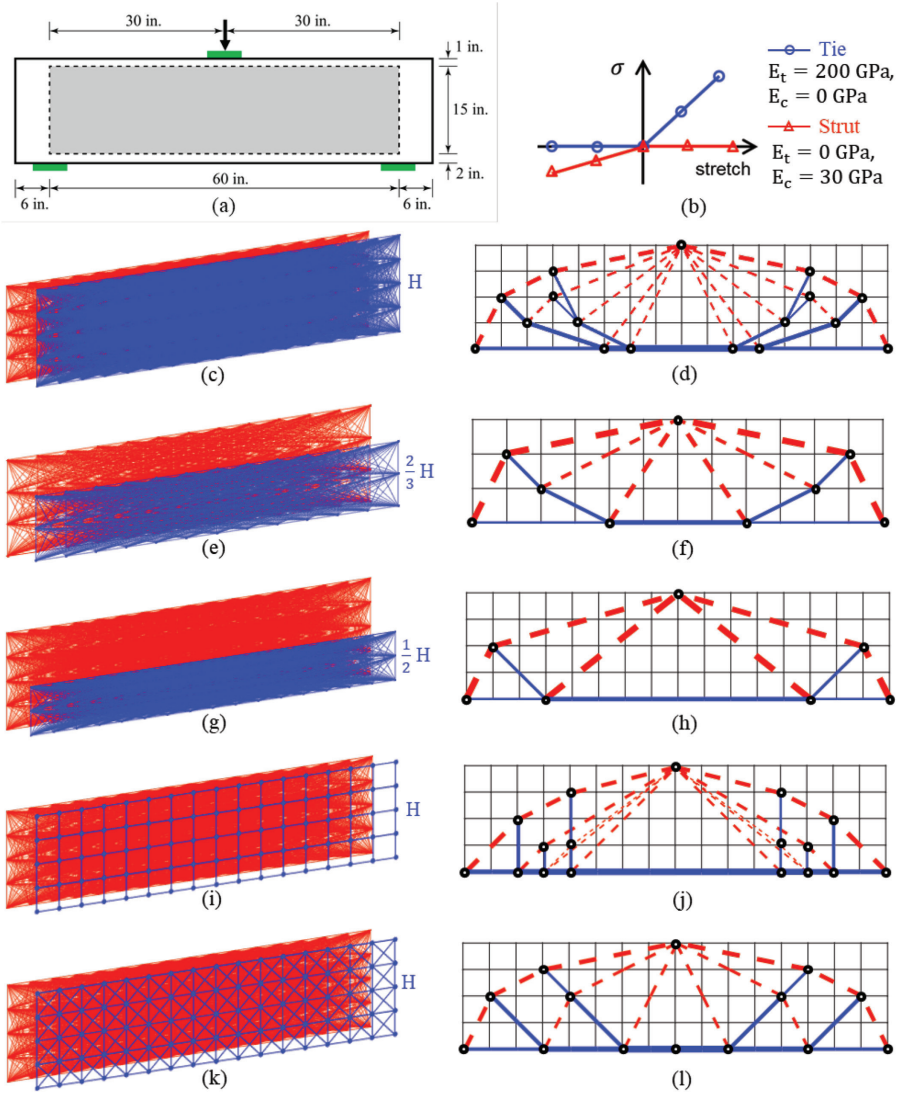

Fig. 1—Optimized strut-and-tie models for reinforced deep beam considering various design scenarios: (a) geometry of beam with highlighted design domain (that is, gray region); (b) simplified bilinear material model for both struts and ties; (c) scenario 1: strut (red) and tie (blue) regions share design domain; (d), (f), (h), (j), and (l) corresponding optimized STM designs for scenarios 1 to 5; (e) and (g) scenarios 2 and 3: tie region can only occupy two-thirds and half of entire domain, respectively; and (i) and (k) scenarios 4 and 5: allowable angle of inclination of tie is 90 degrees and 45 degrees, respectively. (Note: Full-color PDF of this paper can be accessed at www.concrete.org.)

EXPERIMENTAL EVALUATION OF OPTIMIZED STRUT-AND-TIE MODELS

The experimental research on RC deep beams presented in the literature focuses on the conventional STMs suggested by ACI 318 (Schlaich et al. 1987; MacGregor 1997; Breña and Roy 2009; Birrcher et al. 2009; Panjehpour et al. 2015; Ismail 2016; Ismail et al. 2018; Martinez et al. 2017; Rezaei et al. 2019; Kondalraj and Appa Rao 2021). The present work selects two optimized STMs (Fig. 4(b) and (c)) and compares their behavior with the most common STM (Fig. 4(a)) of ACI 318-19. The designs employed contained one significant deviation from ACI 318 guidelines: crack-control reinforcement (ACI 318-19, Section 23.5) was omitted from the beam designs to allow an evaluation of the relative crack pattern development in the various beams. Five RC deep beam specimens were constructed: two for the standard ACI model, one for optimized layout I, and two for optimized layout II. All five specimens have the same geometry as shown in Fig. 5. Regarding the reinforcement arrangements of the specimens, a longitudinal reinforcement ratio $\rho = 2\%$ was used for each specimen. To visualize the reinforcement layouts in a formwork, a three-dimensional (3-D) rendering of the reinforcement design was generated, as shown in Fig. 6(a) to (i), with more reinforcement details for the specimens given in Appendix A. Figures 6(h) and (i) show the designs involving multiple layers of reinforcing bars. Positioning those reinforcing bars inside formwork can be challenging from a construction perspective. To overcome this issue, customized reinforcing bar chairs were created using 3-D printing. Using this method, the geometry of the reinforcing bar chairs can be specified for a given reinforcement design. For example, the two customized reinforcing bar chairs in Fig. 7 facilitated the accurate positioning of the reinforcing bars.

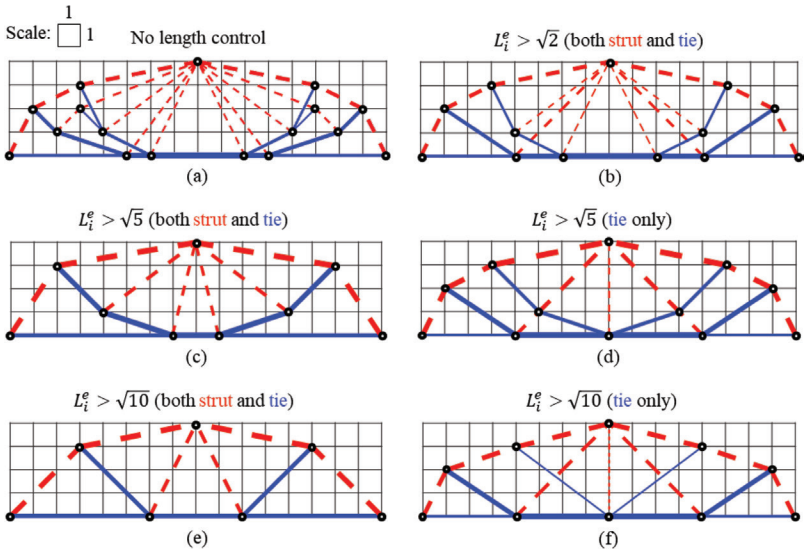

Fig. 2—Flexible length control for optimized STM (assuming that dimension of unit square in background grid for each design is 1): (a) optimized design without length constraints for both struts and ties; (b), (c), and (e) optimized designs with length constraints for both struts and ties, where upper bound of length is defined as √2, √5, and √10, respectively; and (d) and (f) optimized designs with length constraints on ties only, with allowable length defined as √5 and √10, respectively.

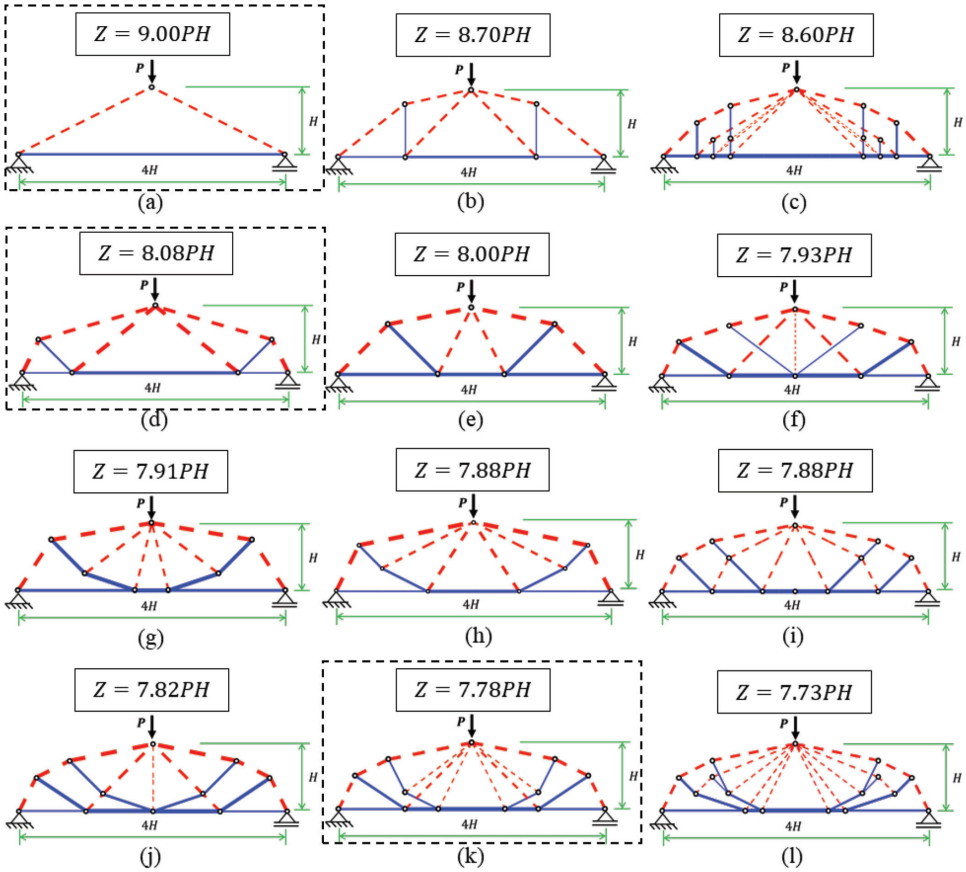

Fig. 3—Deep beam STM design library. Load path Z (that is, Eq. (1)) indicates efficiency of alternative designs in this library. As load path Z decreases through (a) to (l), efficiency of corresponding design improves. Three highlighted layouts (that is, (a), (d), and (k)) are selected for experimental validation in "Experimental Evaluation of Optimized Strut-and-Tie Models" section.

Experimental setup and procedure

The beams were cast with concrete having a compressive strength of 8.5 ksi (58.6 MPa) at the time of testing and reinforced with Grade 60 steel reinforcing bars (nominal yield strength of 60 ksi [414 MPa]). Reinforcing bar development was checked according to ACI 318-19; refer to Fig. 5 for visualizations of beam and support locations and Appendix A for reinforcement layouts. The steel reinforcing bars of the five RC deep beams were instrumented with 350 Ω strain gauges prior to concrete casting. The locations of the strain

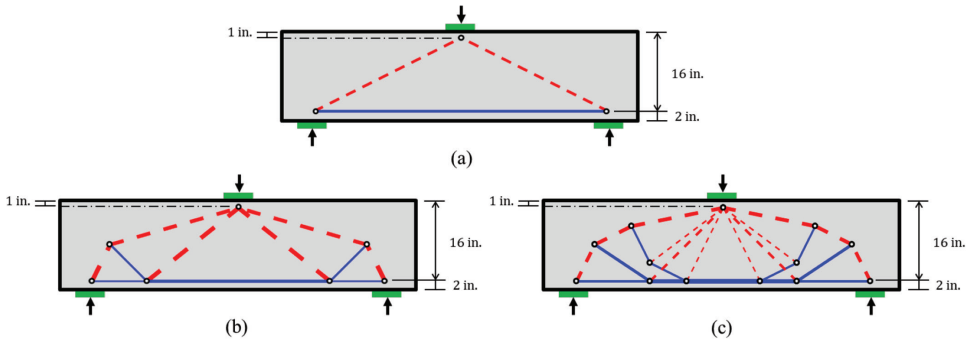

Fig. 4—Three layouts of strut-and-tie models for experimental evaluation: (a) conventional model in ACI 318-19; and (b) and (c) two optimized strut-and-tie models. (Note: 1 in. = 25.4 mm.)

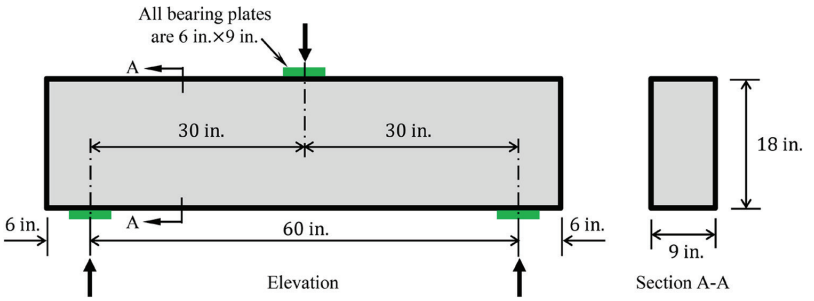

Fig. 5—Deep beam specimen geometry for evaluating optimized strut-and-tie models. (Note: 1 in. = 25.4 mm.)

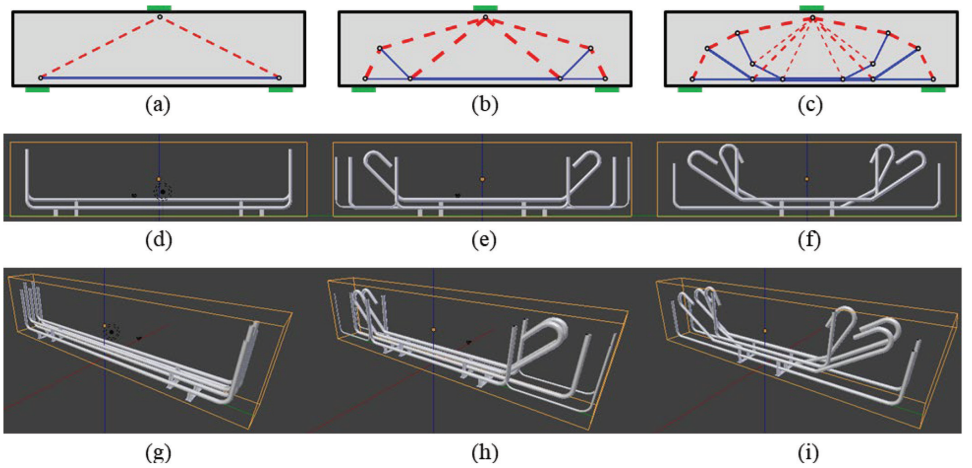

Fig. 6—Schematics of STM reinforcement layouts: (a) to (c) three selected STM layouts designated as standard ACI layout, optimized layout I, and optimized layout II, respectively; (d) to (f) front view of reinforcement designs; and (g) to (i) perspective view of reinforcement designs.

gauges were selected to monitor the role of key reinforcing bars in the optimized layouts; these locations are labeled in the three figures of Appendix A. Figures 8(a) to (c) show the steel reinforcement used for the tested beams of the ACI layout, optimized layout I, and optimized layout II, respectively. Also, the lead wires for the strain gauges are presented in Fig. 8. Moreover, two linear variable differential transformers (LVDTs) were used to estimate the effective strain in the concrete struts. For the midspan deflection, a string potentiometer was used. A 200 kip (890 kN) load cell connected to a hydraulic load ram was used to record load values. The test setup and instrumentation are shown in Fig. 9.

The program of testing consisted of applying an increasing load while monitoring crack initiation on the beam. Once a crack was visually observed, the hydraulic jack valve was closed to hold the load constant, and the cracks and their corresponding load values were highlighted on the beam. Additional load was then applied; this process was repeated until extensive cracks were observed, which prevented further safe monitoring. At that point, continuous loading to complete failure was carried out, and the failure load was recorded.

Load-deflection curves

An increasing load was applied to the specimen until it eventually failed. The load-deflection behavior of the

specimens is shown in Fig. 10 as solid/dashed curves. Each curve represents the applied load versus the midspan deflection of the deep beam. The ultimate loads (that is, maximum loads measured in the specimens) considering the three different STM layouts are given in Table 1. It is observed that the optimized STM layout II (Specimen No. 5), which has the lowest load path Z, reaches the highest ultimate load; and the standard ACI STM layout (Specimens No. 1 and 2), which has the largest load path Z, achieves the lowest ultimate load. This indicates that the load path Z can serve as an effective criterion to evaluate the efficiency of the STM.

Moreover, the initial stiffness values are observed to decrease with the optimization in the reinforcement design. This can be attributed to the fact that the optimized designs have more reinforcement closer to the cross section's neutral axis, which results in a smaller moment of area for transformed cross sections when determining the overall transformed cross-sectional stiffness.

Furthermore, deflection values are increased with optimized layouts I and II (Specimens No. 3 to 5) compared to the standard ACI layout (Specimens No. 1 and 2). This demonstrates the improved behavior of the optimized designs in which more tension cracks in the central region, more steel yielding, and, thus, more efficient load paths (Z) were observed.

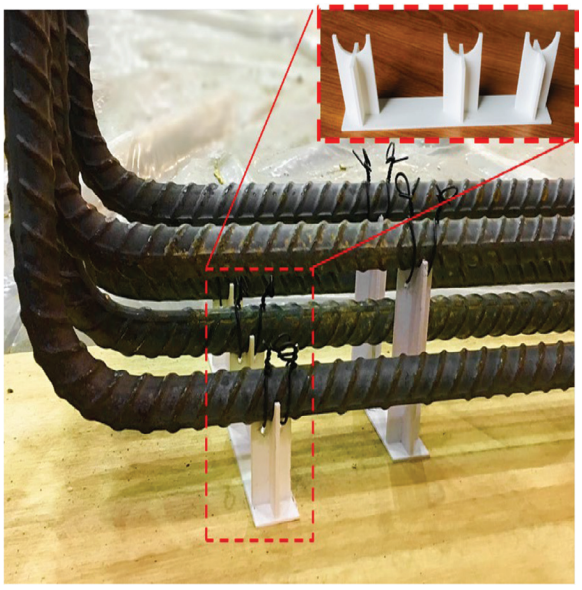

Fig. 7—Positioning reinforcement using 3-D-printed reinforcing bar chairs (fused filament fabrication, with polylactic acid [PLA] plastic material).

Observed failure modes

The failure modes of the specimens, considering the standard ACI STM layout (Specimens No. 1 and 2) and optimized layout I (Specimen No. 3), were characterized by strut

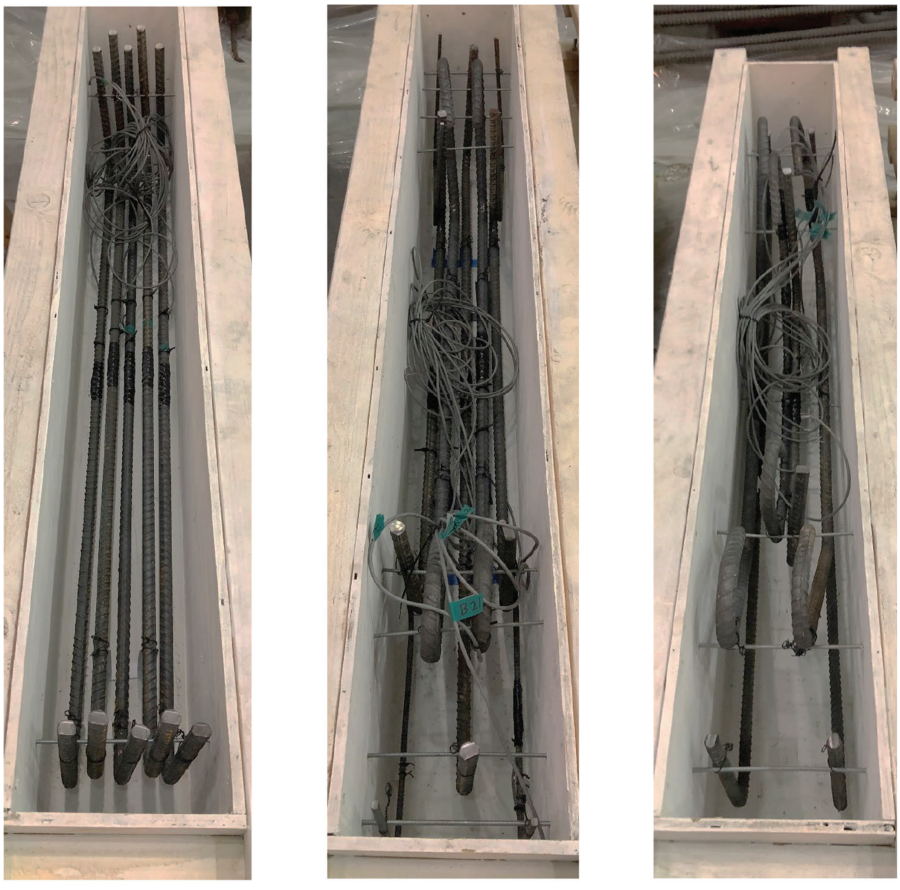

Fig. 8—Steel reinforcement cages used for: (a) ACI layout; (b) optimized layout I; and (c) optimized layout II.

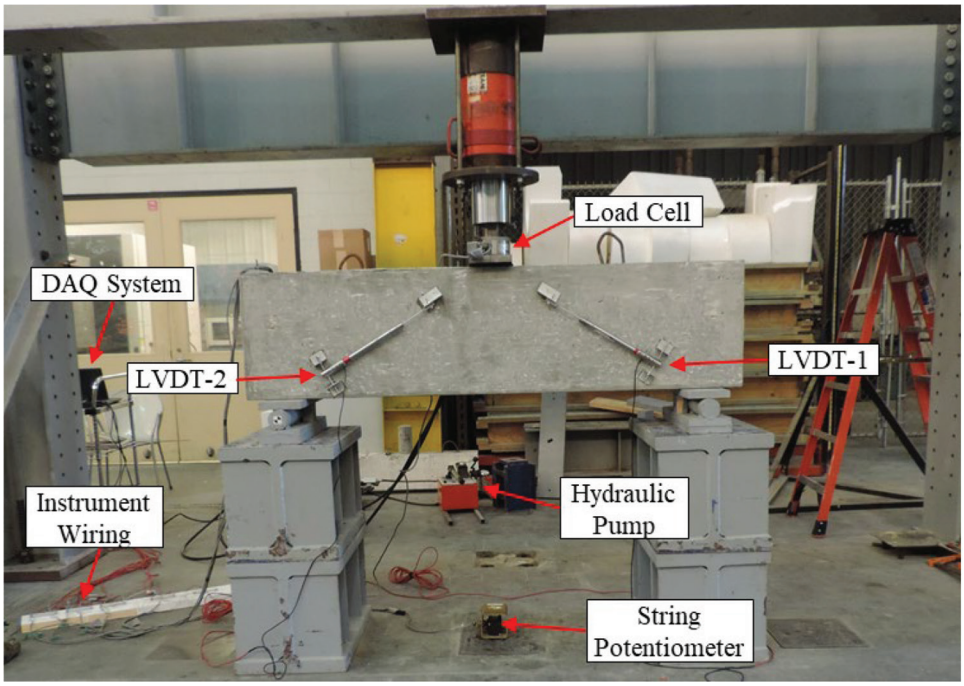

Fig. 9—Experimental setup and testing station.

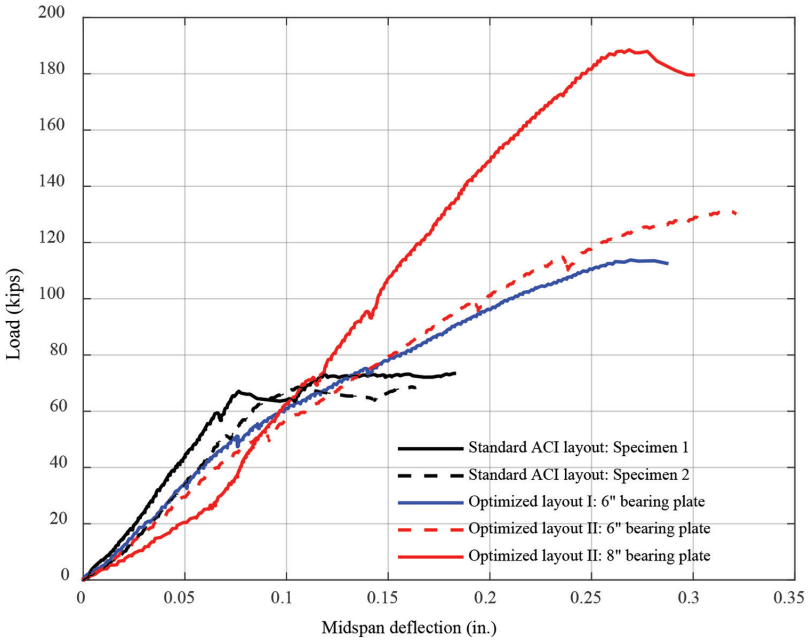

Fig. 10—Test results of deep beams considering different STM layouts. (Note: 1.0 in. = 25.4 mm; 1.0 kip = 4.45 kN.)

crushing. However, the ACI layout had larger crack widths compared to optimized layout I, which can be attributed to the more efficient load path *Z* introduced by more inclined steel reinforcing bars to mitigate large crack widths. On the other hand, the specimens with optimized STM layout II (Specimens No. 4 and 5) had a different failure mode characterized by bearing failure instead of strut failure, as shown in Fig. 11(f) and (h). When optimized layout II was tested with a 6 in. (0.15 m) bearing support plate (Specimen No. 4), the failure mode was characterized by bearing failure, showing the improved design obtained with more inclined steel reinforcing bars and a more optimal load path *Z*, which mitigates the inclined strut failure mode of the tested specimen. To attempt to avoid an undesirable experimental failure mode in the optimized layout II specimens, the bearing plate width was increased from 6 to 8 in. (0.15 to 0.20 m) for the load test of Specimen No. 5. A higher load capacity was observed using the 8 in. (0.20 m) bearing plates, even though the section still failed in bearing. This shift of the controlling failure mode (for optimized layout II) demonstrates the effectiveness of the novel STM layout. Future testing can incorporate more robust bearing layouts, which are expected to result in further optimization of the proposed STM.

Figure 11 shows how the total number of observed tension cracks (cracks in the midspan region of the beam) increased for optimized layouts I (Specimen No. 3) and II

with 6 in. (0.15 m) (Specimen No. 4) and 8 in. (0.20 m) (Specimen No. 5) bearing schemes. Moreover, shear cracks were observed to reduce in optimized layout I compared to the standard ACI design. No shear cracks were observed in optimized layout II (both 6 and 8 in. [0.15 and 0.20 m] bearing schemes). In terms of first crack loads in the struts, crack initiation was observed in the ACI layout (Specimens No. 1 and 2) at 66 kip (294 kN). Crack initiation for optimized layout I (Specimen No. 3) was observed at 75 kip (334 kN), and crack initiation for optimized layout II with a 6 in. (0.15 m) bearing (Specimen No. 4) was observed at 114 kip (507 kN). The strut crack initiation for optimized layout II with an 8 in. (0.20 m) bearing (Specimen No. 5) is not included in this discussion because the test was not halted for crack inspection after 94 kip (418 kN) for safety reasons; however, it can be reported that no cracks were observed up to the 94 kip (418 kN) load. These observations indicate a definable improvement in the load-carrying behavior for the optimized designs.

Table 1—Comparison of load path *Z* and ultimate load for three strut-and-tie layouts

STM layout	Load path (Eq. (1))	Specimen	Ultimate load, kip (kN)
Standard ACI	9.00*PH*	No. 1 (6 in. [0.15 m] bearing plate)	73.5 (327)
		No. 2 (6 in. [0.15 m] bearing plate)	68.7 (305)
Optimized I	8.08*PH*	No. 3 (6 in. [0.15 m] bearing plate)	114 (506)
Optimized II	7.78*PH*	No. 4 (6 in. [0.15 m] bearing plate)	131 (583)
		No. 5 (8 in. [0.20 m] bearing plate)	189 (839)

Observed strain gauge values

As discussed previously, strain gauges were used in specific locations on the internal reinforcement of the test specimens to attempt to compare the strain progression of the various reinforcement layouts under loading. Figure 12

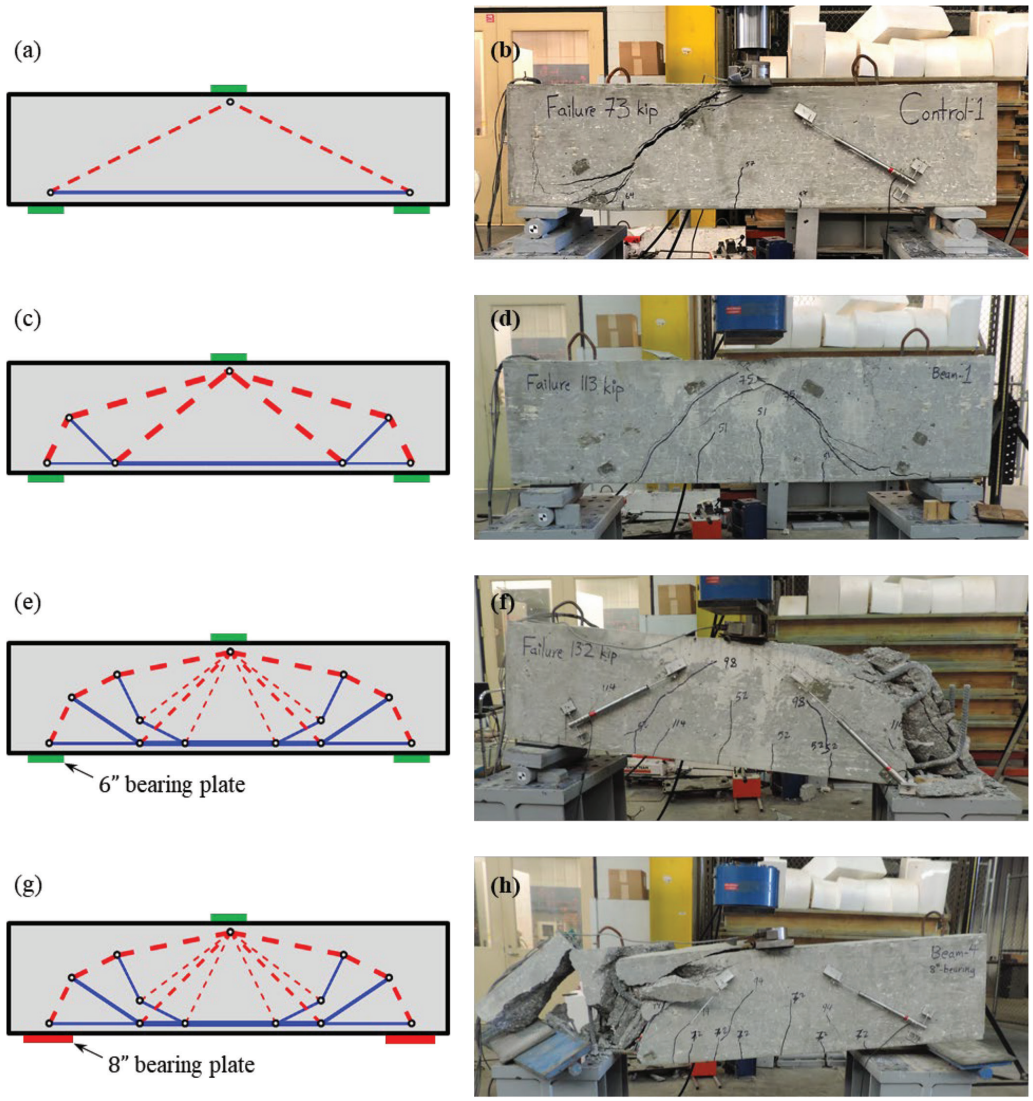

Fig. 11—Failure modes of deep beams considering standard ACI layout with 6 in. (0.15 m) bearing plate, optimized layout I with 6 in. bearing plate, optimized layout II with 6 in. bearing plate, and optimized layout II with 8 in. (0.20 m) bearing plate, respectively.

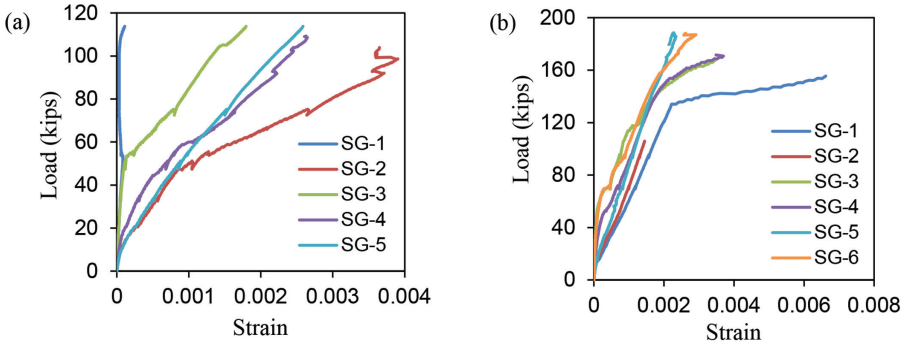

Fig. 12—Strain gauge values with loading for: (a) optimized layout I; and (b) optimized layout II (with 8 in. [0.20 m] bearing plate).

shows the measured strain gauge values of optimized layouts I (Specimen No. 3) and II (Specimen No. 5). As shown in Fig. 12(a), for optimized layout I, yielding was attained in the central region of the reinforcing bars (SG-2, 4, and 5), while SG-1 did not exhibit significant strain in the reinforcing bar because it was near the support. However, for the case of SG-3, it is interesting to note the sudden increase in strain values after the first tension crack and the increasing strain to eventual yielding with the progression of the strut crack. Figure 12(b) presents the load-strain behavior for optimized layout II with an 8 in. (0.20 m) bearing plate. Some key observations can be summarized as follows:

1. SG-1 and SG-5 located in the middle region demonstrated different behaviors due to the shape of the steel reinforcing bars they are attached to. Note that any gauges that appeared to fail early in the loading process are omitted from the reporting of data.

2. SG-3 and SG-4 were attached to the same steel reinforcing bar at two different inclinations; the steel in these regions has yielded, indicating that the inclined regions of the steel reinforcing bar participated in resisting transverse loading in the strut.

3. SG-6 behaved similarly to SG-3 and SG-4 but was on a different reinforcing bar, indicating similar behavior among all inclined reinforcing bars for optimized layout II.

EVALUATION OF STM USING ACI 318 DESIGN CONCEPTS

Table 1 gives the ultimate experimental load attained for each specimen tested. As noted, the beams reinforced with optimized layout II (Specimens No. 4 and 5) supported a larger applied load than the others. In addition, the controlling failure mode of the optimized II design shifted from compression to bearing; a more robust bearing detail would be expected to result in an even greater ultimate load for a beam with optimized layout II. Thus, as expected, the STM layout has a substantial impact on the load-deflection behavior of deep beams. To provide a basis for comparison between the various beam layouts, the ultimate experimental loads are compared to a novel analysis procedure inspired by design guidelines in ACI 318-19. However, it is important to note that the analysis presented herein does not directly follow the ACI design procedures (for optimized layouts). Rather, the analysis procedure is intended to give an insight into the effect of these layouts on the stress fields of the deep beams tested herein. The failure modes checked are the capacity of the nodes, the capacity of the ties, and the capacity of the struts. Based on the failure modes observed in the testing, it has been assumed that the nominal strength of the strut controls the ultimate load of the beam for all layouts to simplify the comparison.

A sketch of the STMs with the standard ACI layout, optimized layout I, and optimized layout II visualizing the force flow in the beam are shown in Fig. 13(a) to (c), respectively. The dashed lines, solid lines, and dimensionless round circles represent the compression elements, tension elements, and nodes (that is, the intersection of struts and ties), respectively. The results of static analysis including the relative internal force magnitudes for the ACI layout, optimized layout I, and optimized layout II are shown in Table 2. This table also summarizes the assumed reinforcement inclination angles for each of the three layouts.

For all the beams, the concrete compressive strength f_c' = 8.5 ksi (58.6 MPa), and the dimensions of the beams are as follows:

- Length of the truss L = 60 in. (1.52 m)
- Height of the truss H = 15 in. (0.38 m)
- Width of the beam b_w = 9 in. (0.23 m)
- Width of the bearing plates $b_1 = b_2$ = 6.0 in. (0.15 m) (Note that Specimen No. 5 with optimized layout II has a different bearing plate at the supports—that is, b_1 = 8 in. [0.2 m].)
- Effective height of the tie w_{T1} = 4 in. (0.1 m)
- Effective height of the node at the applied load w_{T2} = 2 in. (0.05 m)

Standard ACI layout

For the standard ACI STM layout, the standard ACI analysis procedure is followed in a backward fashion in which the load is known and β_s (the strut coefficient) is determined by calibrating the experimental results (that is, the stress in the compression strut at the ultimate load) from testing to the analytical capacity of the strut in compression.

First, calculate the width of the strut at Nodes 1 and 2 using Eq. (10) and (11), and then take the lowest value corresponding to the highest stress (in this case, w_c^2).

$$w_c^1 = b_1 \sin\alpha_1 + w_{T1} \cos\alpha_1 = 6.26 \text{ in. } (0.16 \text{ m}) \quad (10)$$

$$w_c^2 = (b_2/2)\sin\alpha_1 + w_{T2}\cos\alpha_1 = 3.13 \text{ in. } (0.08 \text{ m}) \quad (11)$$

Then, determine the compressive force in the strut from the known ultimate load $P = 71.1$ kip (316 kN), which is the average of Specimens No. 1 and 2 (refer to Table 1)

$$C_{2n} = 1.118P = 1.118 \times 71.1 \text{ kip } (316 \text{ kN}) = 79.5 \text{ kip } (354 \text{ kN}) \quad (12)$$

The next step is the calculation of the effective compressive stress in the strut at Node 2 using Eq. (13)

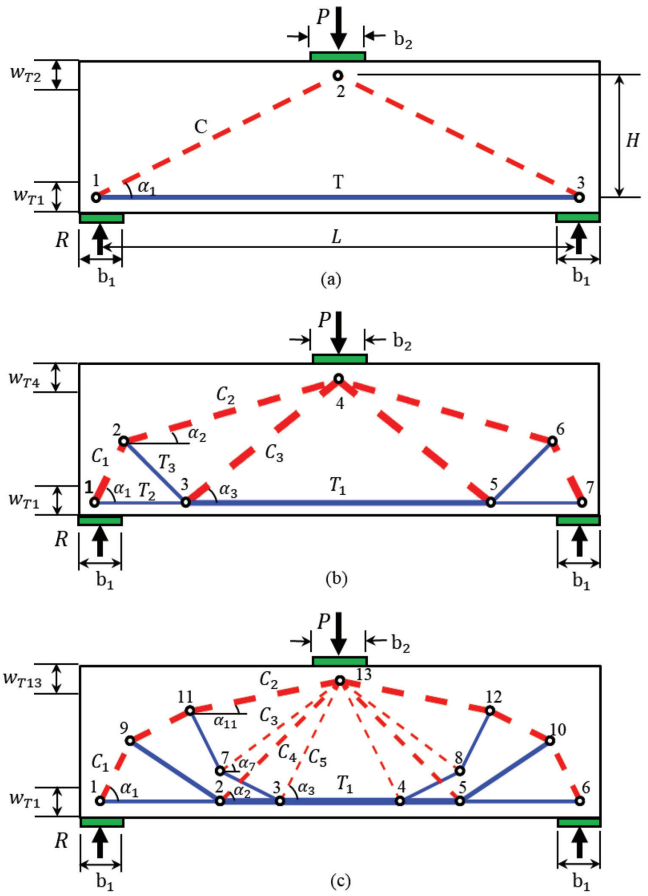

Fig. 13—Deep beam strut-and-tie models: (a) standard ACI STM layout; (b) optimized STM layout I; and (c) optimized STM layout II.

$$f_{ce}^s = \frac{C_{2n}}{w_c^2 b_w} = 2.82 \text{ ksi } (19.4 \text{ MPa}) \quad (13)$$

Using Eq. (14), the value of β_s is obtained, assuming that the strut and node confinement modification factor is equal to 1.0 ($\beta_c = 1.0$)

$$\beta_s = \frac{f_{ce}^s}{0.85\beta_c f_c'} = 0.39 \quad (14)$$

It is noteworthy that this value is very similar to the value found in ACI 318-19 ($\beta_s = 0.4$) for the case of no minimum reinforcement for crack control. The omission of minimum reinforcement was intended to allow a better evaluation of the performance of the novel layouts on the overall performance of the deep beams relative to one another. For this reason, significant transverse cracks were observed.

Optimized layout I

For optimized layout I, the analysis procedure is the same as that given in the previous section, except that the resultant of the forces (C_R) acting at Node 4 (refer to Fig. 13(b)) and the corresponding α_R are calculated with Eq. (15) and (16), respectively. This resolution of forces is intended to simplify the analytical procedure.

$$C_R = \sqrt{(C_2\sin\alpha_2 + C_3\sin\alpha_3)^2 + (C_2\cos\alpha_2 + C_3\cos\alpha_3)^2} = 1.118P \quad (15)$$

$$\alpha_R = \tan^{-1}\left(\frac{C_2\sin\alpha_2 + C_3\sin\alpha_3}{C_2\cos\alpha_2 + C_3\cos\alpha_3}\right) = 0.464 \quad (16)$$

Then, the width of the strut at Nodes 1 and 4 is calculated as

$$w_c^1 = b_1\sin\alpha_1 + w_{T1}\cos\alpha_1 = 7.16 \text{ in. } (0.18 \text{ m}) \quad (17)$$

$$w_c^4 = (b_2/2)\sin\alpha_R + w_{T2}\cos\alpha_R = 3.13 \text{ in. } (0.08 \text{ m}) \quad (18)$$

As $w_c^4 < w_c^1$, then w_c^4 is used for the calculation of the effective compressive stress in the strut at Node 4. Given the ultimate load $P = 114$ kip (507 kN) reached during the

Table 2—Relative magnitudes of internal forces (as fraction of applied load *P*) and angles (in radians) for ACI layout, optimized layout I, and optimized layout II, as shown in Fig. 13(a) to (c), respectively

ACI	T		C		α_1	
	1		1.118		$\tan^{-1}(1/2)$	
Optimized I	T_1	T_2	T_3	C_1	C_2	C_3
	1	0.2500	0.4714	0.5590	0.6067	0.5336
	α_1		α_2		α_3	
	$\tan^{-1}(2)$		$\tan^{-1}(2/7)$		$\tan^{-1}(4/5)$	
Optimized II	T_1	C_1	C_2	C_3	C_4	C_5
	1	0.5590	0.6622	0.1169	0.3030	0.0958
	α_1	α_2	α_3	α_7	α_{11}	
	$\tan^{-1}(2)$	$\tan^{-1}(1)$	$\tan^{-1}(2)$	$\tan^{-1}(3/4)$	$\tan^{-1}(1/5)$	

corresponding experimental test (refer to Table 1), the effective compressive stress is obtained as

$$f_{ce}^{s} = \frac{C_R}{w_c^4 b_w} = \frac{1.118P}{w_c^4 b_w} = 4.52 \text{ ksi (31.2 MPa)} \quad (19)$$

In turn, the value of β_s is calculated, assuming that the strut and node confinement modification factor is equal to 1.0 ($\beta_c = 1.0$)

$$\beta_s = \frac{f_{ce}^{s}}{0.85\beta_c f_c'} = 0.625 \quad (20)$$

The larger value of $\beta_s = 0.625$ calculated for optimized layout I compared to that calculated for the standard ACI layout indicates a more efficient load path in the optimized layout. It should be noted that the β_s value calculated for optimized layout I is less than the value $\beta_s = 0.75$, which assumes the inclusion of minimum distributed reinforcement for crack control.

Optimized layout II

Similar to the procedure shown in the previous section, the resultant of the forces acting at Node 13 (refer to Fig. 13(c)) is determined (C_R) for optimized layout II with its corresponding α_R as shown in Eq. (21) and (22).

$$\begin{aligned} C_{Rx} &= C_2\sin\alpha_{11} + C_3\sin\alpha_7 + C_4\sin\alpha_2 + C_5\sin\alpha_3 = 0.5P \\ C_{Ry} &= C_2\cos\alpha_{11} + C_3\cos\alpha_7 + C_4\cos\alpha_2 + C_5\cos\alpha_3 = P \end{aligned} \quad (21)$$

$$\begin{aligned} C_R &= \sqrt{(C_{Rx})^2 + (C_{Ry})^2} = 1.118P \\ \alpha_R &= \tan^{-1}\left(\frac{C_{Rx}}{C_{Ry}}\right) = 0.464 \end{aligned} \quad (22)$$

For the optimized layout II with a 6 in. bearing plate (that is, $b_1 = 6$ in. [0.15 m]), the width of the strut at Nodes 1 and 13 is calculated as

$$w_c^1 = b_1\sin\alpha_1 + w_{T1}\cos\alpha_1 = 7.16 \text{ in. (0.18 m)} \quad (23)$$

$$w_c^{13} = (b_2/2)\sin\alpha_R + w_{T2}\cos\alpha_R = 3.13 \text{ in. (0.08 m)} \quad (24)$$

where the smaller value w_c^{13} is selected for calculating the effective compressive stress in the strut at Node 13. It is also known that the ultimate load $P = 131$ kip (583 kN) from the experiment (refer to Table 1). Following the same procedure presented in the previous section, the value of β_s is calculated, assuming that the strut and node confinement modification factor is equal to 1.0 ($\beta_c = 1.0$)

$$\beta_s = \frac{f_{ce}^{s}}{0.85\beta_c f_c'} = \left(\frac{C_R}{w_c^{13} b_w}\right)/(0.85\beta_c f_c') = \left(\frac{1.118P}{w_c^{13} b_w}\right)/(0.85\beta_c f_c') = 0.719 \quad (25)$$

For the optimized layout II with an 8 in. bearing plate (that is, $b_1 = 8$ in. [0.2 m]), the width of the strut at Nodes 1 and 13 is obtained as

$$w_c^1 = b_1\sin\alpha_1 + w_{T1}\cos\alpha_1 = 8.94 \text{ in. (0.23 m)} \quad (26)$$

$$w_c^{13} = (b_2/2)\sin\alpha_R + w_{T2}\cos\alpha_R = 3.13 \text{ in. (0.08 m)} \quad (27)$$

Given the ultimate load $P = 189$ kip (841 kN) from the experiment (refer to Table 1), the value of β_s is obtained, assuming that the strut and node confinement modification factor is equal to 1.0 ($\beta_c = 1.0$)

$$\beta_s = \left(\frac{1.118P}{w_c^{13} b_w}\right)/(0.85\beta_c f_c') = 1.038 \quad (28)$$

All the results are summarized in Table 3. The resulting β_s for the optimized layout II with a 6 in. (0.15 m) bearing plate (Specimen No. 4) shows a slightly improved performance because of the premature bearing failure, but with even more improvement in the ultimate load. However, β_s for optimized layout II with an 8 in. (0.20 m) bearing plate (Specimen No. 5) shows that a more desirable load path is used when premature bearing failure is suppressed. It is important to note that the calculations for both optimized layout II with 6 and 8 in. (0.15 and 0.20 m) bearing plates are based on the assumption that the nominal strength of the strut controls the ultimate failure. Nonetheless, for the specific case of optimized layout II, a bearing failure was observed rather than a strut failure, so the actual values of β_s will be higher than the calculated value herein.

CONCLUSIONS

This work presents a multi-material/multi-volume topology optimization framework to design practical strut-and-tie model (STM) layouts for reinforced concrete (RC) structures. Inspired by Michell's optimality conditions, the efficiency of optimized STM layouts is quantified by the load path Z (or the Michell number), which serves as a simple and efficient criterion for evaluating any STM. An experimental testing program indicated that the optimized STM layouts possess significantly improved behavior compared to the traditional layout using the same overall reinforcement ratio. As such, it is expected that designs with optimized layouts could result in smaller total volume of reinforcing steel needed to resist a given set of design loads, resulting in a more economical design. It is acknowledged that, at present, the more complex reinforcement layouts may increase fabrication costs. However, given advancements in reinforcement layout construction using computer-aided reinforcement fabrication, it is anticipated that reducing the total volume of steel needed in a given deep beam design will eventually

Table 3—Summary of analysis results for all layouts (refer to Fig. 13 for node numbering)

Standard ACI layout	w_c^1	w_c^2	C_{2n}	f_{ce}^s	β_s
	6.26 in. (0.16 m)	3.13 in. (0.08 m)	79.5 kip (354 kN)	2.82 ksi (19.4 MPa)	0.390
Optimized layout I	w_c^1	w_c^4	C_R (equal to C_{4n})	f_{ce}^s	β_s
	7.16 in. (0.18 m)	3.13 in. (0.08 m)	128 kip (569 kN)	4.52 ksi (35.2 MPa)	0.625
Optimized layout II with 6 in. bearing plate	w_c^1	w_c^{13}	C_R (equal to C_{13n})	f_{ce}^s	β_s
	7.16 in. (0.18 m)	3.13 in. (0.08 m)	146 kip (649 kN)	5.20 ksi (35.9 MPa)	0.719
Optimized layout II with 8 in. bearing plate	w_c^1	w_c^{13}	C_R (equal to C_{13n})	f_{ce}^s	β_s
	8.94 in. (0.23 m)	3.13 in. (0.08 m)	211 kip (939 kN)	7.49 ksi (51.6 MPa)	1.038

Note: 1.0 in. = 25.4 mm; 1.0 kip = 4.45 kN; 1.0 ksi = 6.89 MPa.

result in a more efficient and cost-effective design. Given the significantly reduced cracking observed in the optimized layouts compared to the traditional STM layout, it is possible that the optimized layouts would require less crack-control reinforcement, potentially further reducing the total volume of steel needed in the deep beams.

In addition, to extend the present framework as a practical RC structures design tool, further research could be conducted in the following aspects: 1) a three-dimensional (3-D) design domain with a complex stress state; 2) incorporating realistic plasticity material models in the optimization framework for concrete and steel; 3) achieving higher structural ductility through transverse reinforcement optimization; and 4) the application of the design and analysis procedures presented herein to a database of known reliable experimental results for deep beams available in the established literature.

ACKNOWLEDGMENTS

The authors acknowledge the support from the U.S. National Science Foundation (NSF) under grant No. 2105811.

AUTHOR BIOS

Tuo Zhao *is a Postdoctoral Research Associate in the Department of Civil and Environmental Engineering at Princeton University, Princeton, NJ. He was the winner of the ACI Georgia Chapter LaGrit F. "Sam" Morris Student Scholarship. His research interests include multi-material topology optimization and nonlinear analysis of reinforced concrete (RC) structures.*

Ammar A. Alshannaq *is an Assistant Professor in the Department of Civil Engineering at Yarmouk University, Irbid, Jordan. His research interests include repairing and strengthening existing RC structures, characterization and testing of fiber-reinforced polymer (FRP) materials, and optimization and novel design of deep RC beams.*

David W. Scott *is a Professor in the Department of Civil Engineering and Construction at Georgia Southern University, Statesboro, GA. He is a member of ACI Committees E706, Concrete Repair Education; 364, Rehabilitation; 440, Fiber-Reinforced Polymer Reinforcement; and 546, Repair of Concrete. His research interests include novel materials and systems for civil infrastructure, evaluation of highway safety structures, and repair of concrete structures.*

Glaucio H. Paulino *is the Margareta Engman Augustine Professor at Princeton University. He is a Professor of the Civil and Environmental Engineering Department, and the Princeton Materials Institute (PMI). His research interests include the development of methodologies to characterize the deformation and fracture behavior of existing and emerging materials and structural systems, and topology optimization for multiscale/multiphysics problems.*

REFERENCES

ACI Committee 318, 2019, "Building Code Requirements for Structural Concrete (ACI 318-19) and Commentary (ACI 318R-19) (Reapproved 2022)," American Concrete Institute, Farmington Hills, MI, 624 pp.

Birrcher, D.; Tuchscherer, R.; Huizinga, M.; Bayrak, O.; Wood, S.; and Jirsa, J., 2009, "Strength and Serviceability Design of Reinforced Concrete Deep Beams," Report No. FHWA/TX-09/0-5253-1, Center for Transportation Research, The University of Texas at Austin, Austin, TX, 400 pp.

Breña, S. F., and Roy, N. C., 2009, "Evaluation of Load Transfer and Strut Strength of Deep Beams with Short Longitudinal Bar Anchorages," *ACI Structural Journal*, V. 106, No. 5, Sept.-Oct., pp. 678-689.

Bruggi, M., 2010, "On the Automatic Generation of Strut and Tie Patterns under Multiple Load Cases with Application to the Aseismic Design of Concrete Structures," *Advances in Structural Engineering*, V. 13, No. 6, Dec., pp. 1167-1181. doi: 10.1260/1369-4332.13.6.1167

Christensen, P. W., and Klarbring, A., 2008, *An Introduction to Structural Optimization*, Springer Science+Business Media B.V., Dordrecht, the Netherlands.

Dorn, W. S.; Gomory, R. E.; and Greenberg, H. J., 1964, "Automatic Design of Optimal Structures," *Journal de Mécanique*, V. 3, No. 1, pp. 25-52.

Gaynor, A. T.; Guest, J. K.; and Moen, C. D., 2013, "Reinforced Concrete Force Visualization and Design Using Bilinear Truss-Continuum Topology Optimization," *Journal of Structural Engineering*, ASCE, V. 139, No. 4, Apr., pp. 607-618. doi: 10.1061/(ASCE)ST.1943-541X.0000692

Groenwold, A. A., and Etman, L. F. P., 2008, "On the Equivalence of Optimality Criterion and Sequential Approximate Optimization Methods in the Classical Topology Layout Problem," *International Journal for Numerical Methods in Engineering*, V. 73, No. 3, Jan., pp. 297-316. doi: 10.1002/nme.2071

He, Z.-Q.; Liu, Z.; Wang, J.; and Ma, Z. J., 2020, "Development of Strut-and-Tie Models Using Load Path in Structural Concrete," *Journal of Structural Engineering*, ASCE, V. 146, No. 5, May, p. 06020004. doi: 10.1061/(ASCE)ST.1943-541X.0002631

Ismail, K. S., 2016, "Shear Behaviour of Reinforced Concrete Deep Beams," PhD thesis, University of Sheffield, Sheffield, UK, 312 pp.

Ismail, K. S.; Guadagnini, M.; and Pilakoutas, K., 2018, "Strut-and-Tie Modeling of Reinforced Concrete Deep Beams," *Journal of Structural Engineering*, ASCE, V. 144, No. 2, Feb., p. 04017216. doi: 10.1061/(ASCE)ST.1943-541X.0001974

Jewett, J. L., and Carstensen, J. V., 2019, "Experimental Investigation of Strut-and-Tie Layouts in Deep RC Beams Designed with Hybrid Bi-linear Topology Optimization," *Engineering Structures*, V. 197, Oct., Article No. 109322. doi: 10.1016/j.engstruct.2019.109322

Kondalraj, R., and Appa Rao, G., 2021, "Experimental Verification of ACI 318 Strut-and-Tie Method for Design of Deep Beams without Web Reinforcement," *ACI Structural Journal*, V. 118, No. 1, Jan., pp. 139-152.

Kumar, P., 1978, "Optimal Force Transmission in Reinforced Concrete Deep Beams," *Computers & Structures*, V. 8, No. 2, Apr., pp. 223-229. doi: 10.1016/0045-7949(78)90026-3

Leu, L.-J.; Huang, C.-W.; Chen, C.-S.; and Liao, Y.-P., 2006, "Strut-and-Tie Design Methodology for Three-Dimensional Reinforced Concrete Structures," *Journal of Structural Engineering*, ASCE, V. 132, No. 6, June, pp. 929-938. doi: 10.1061/(ASCE)0733-9445(2006)132:6(929)

Liang, Q. Q.; Xie, Y. M.; and Steven, G. P., 2000, "Topology Optimization of Strut-and-Tie Models in Reinforced Concrete Structures Using an

Evolutionary Procedure," *ACI Structural Journal*, V. 97, No. 2, Mar.-Apr., pp. 322-331.

Liang, Q. Q.; Xie, Y. M.; and Steven, G. P., 2001, "Generating Optimal Strut-and-Tie Models in Prestressed Concrete Beams by Performance-Based Optimization," *ACI Structural Journal*, V. 98, No. 2, Mar.-Apr., pp. 226-232.

MacGregor, J. G., 1997, *Reinforced Concrete: Mechanics and Design*, Prentice Hall, Upper Saddle River, NJ.

Martinez, G. A.; Beiter, K. S.; Ghiami Azad, A. R.; Polo, G. E.; Shinn, R. L.; Hrynyk, T. D.; and Bayrak, O., 2017, "Testing and Analysis of Two Deep Beams Designed Using Strut-and-Tie Method," *ACI Structural Journal*, V. 114, No. 6, Nov.-Dec., pp. 1531-1542. doi: 10.14359/51689504

Maxwell, J. C., 1864, "XLV. On Reciprocal Figures and Diagrams of Forces," *The London, Edinburgh, and Dublin Philosophical Magazine and Journal of Science*, V. 27, No. 182, Series 4, pp. 250-261. doi: 10.1080/14786446408643663

Michell, A. G. M., 1904, "LVIII. The Limits of Economy of Material in Frame-Structures," *The London, Edinburgh, and Dublin Philosophical Magazine and Journal of Science*, V. 8, No. 47, Series 6, pp. 589-597. doi: 10.1080/14786440409463229

Mozaffari, S.; Akbarzadeh, M.; and Vogel, T., 2020, "Graphic Statics in a Continuum: Strut-and-Tie Models for Reinforced Concrete," *Computers & Structures*, V. 240, Nov., Article No. 106335. doi: 10.1016/j.compstruc.2020.106335

Panjehpour, M.; Chai, H. K.; and Voo, Y. L., 2015, "Refinement of Strut-and-Tie Model for Reinforced Concrete Deep Beams," *PLOS ONE*, V. 10, No. 6, June, Article No. e0130734. doi: 10.1371/journal.pone.0130734

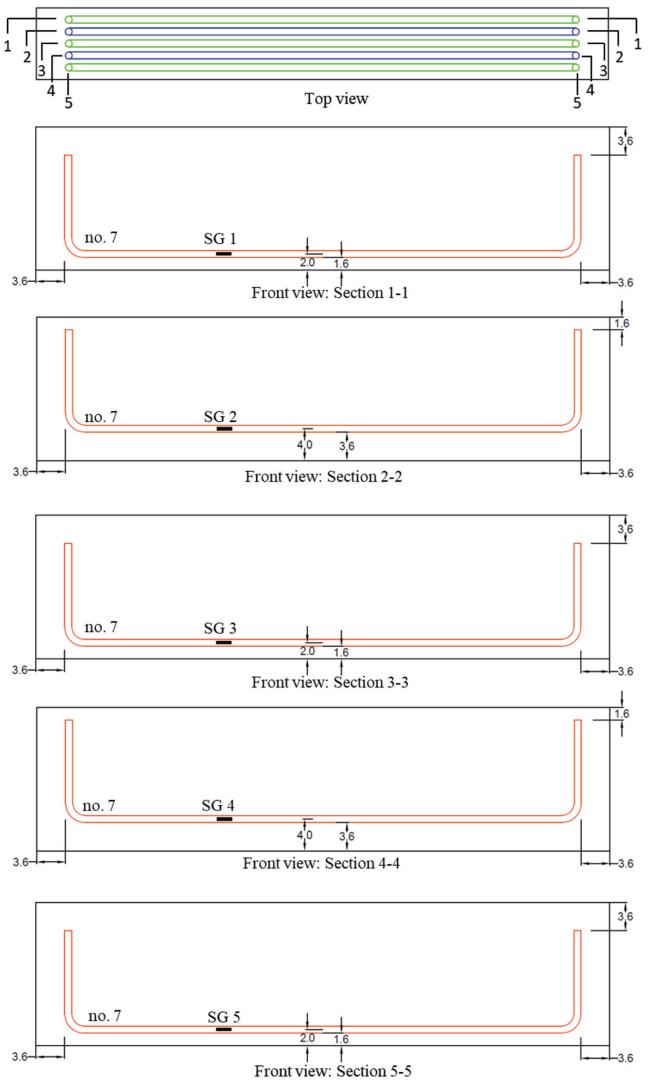

Fig. A1—Reinforcement details of specimen with standard ACI STM layout. (Note: Labeled dimensions are in inches; 1.0 in. = 25.4 mm.)

Rezaei, N.; Klein, G.; and Garber, D. B., 2019, "Strut Strength and Failure in Full-Scale Concrete Deep Beams," *ACI Structural Journal*, V. 116, No. 3, May, pp. 65-74. doi: 10.14359/51713306

Sanders, E. D.; Aguiló, M. A.; and Paulino, G. H., 2018, "Multi-Material Continuum Topology Optimization with Arbitrary Volume and Mass Constraints," *Computer Methods in Applied Mechanics and Engineering*, V. 340, Oct., pp. 798-823. doi: 10.1016/j.cma.2018.01.032

Sanders, E. D.; Ramos, A. S. Jr.; and Paulino, G. H., 2020, "Topology Optimization of Tension-Only Cable Nets under Finite Deformations," *Structural and Multidisciplinary Optimization*, V. 62, No. 2, Aug., pp. 559-579. doi: 10.1007/s00158-020-02513-7

Schlaich, J.; Schäfer, K.; and Jennewein, M., 1987, "Toward a Consistent Design of Structural Concrete," *PCI Journal*, V. 32, No. 3, May-June, pp. 74-150. doi: 10.15554/pcij.05011987.74.150

Victoria, M.; Querin, O. M.; and Martí, P., 2011, "Generation of Strut-and-Tie Models by Topology Design Using Different Material Properties in Tension and Compression," *Structural and Multidisciplinary Optimization*, V. 44, No. 2, Aug., pp. 247-258. doi: 10.1007/s00158-011-0633-z

Xia, Y.; Langelaar, M.; and Hendriks, M. A. N., 2020, "A Critical Evaluation of Topology Optimization Results for Strut-and-Tie Modeling of Reinforced Concrete," *Computer-Aided Civil and Infrastructure Engineering*, V. 35, No. 8, Aug., pp. 850-869. doi: 10.1111/mice.12537

Zhang, X. S.; Paulino, G. H.; and Ramos, A. S. Jr., 2018, "Multi-Material Topology Optimization with Multiple Volume Constraints: A General Approach Applied to Ground Structures with Material Nonlinearity," *Structural and Multidisciplinary Optimization*, V. 57, No. 1, Jan., pp. 161-182. doi: 10.1007/s00158-017-1768-3

Zhou, L., and Wan, S., 2021, "Development of Strut-and-Tie Models Using Topology Optimization Based on Modified Optimal Criterion," *Structural Concrete*, V. 22, No. 6, Dec., pp. 3304-3314. doi: 10.1002/suco.202100123

APPENDIX A

This Appendix details the reinforcement design including the location of strain gauges for the standard ACI STM layout (Fig. A1), optimized layout I (Fig. A2), and optimized layout II (Fig. A3), respectively.

APPENDIX B

Appendix B includes an example to show the calculation of the Michell number Z for the STM layout in Fig. 3(d). Because this truss system is statically determinate, the internal axial force of the members can be calculated using the equilibrium conditions—that is, $N_{12} = N_{67} = -0.56P$, $N_{24} = N_{46} = -0.61P$, $N_{34} = N_{45} = -0.53P$, $N_{13} = N_{57} = 0.25P$, $N_{23} = N_{56} = 0.47P$, and $N_{35} = P$ (refer to the labeled node numbers in Fig. B1). Moreover, the length of each truss member is given as $L_{12} = L_{67} = 0.56H$, $L_{24} = L_{46} = 1.82H$, $L_{34} = L_{45} = 1.6H$, $L_{13} = L_{57} = 0.75H$, $L_{23} = L_{56} = 0.71H$, and $L_{35} = 2.5H$. Therefore, the Michell number Z can be obtained using Eq. (1) as $Z = \Sigma_e|F_e|L_e = 2|F_{12}|L_{12} + 2|F_{24}|L_{24} + 2|F_{34}|L_{34} + 2|F_{13}|L_{13} + 2|F_{23}|L_{23} + F_{35}|L_{35} = 8.08PH$.

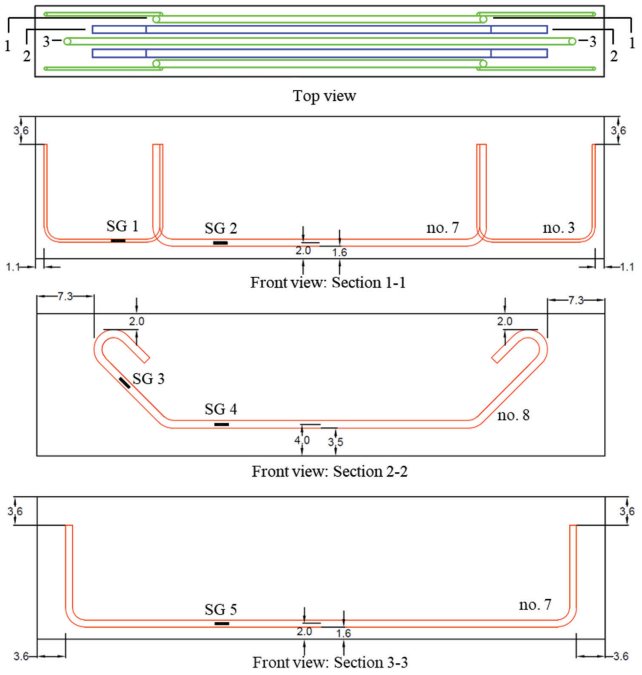

Fig. A2—Reinforcement details of specimen with the optimized STM layout I. (Note: Labeled dimensions are in inches; 1.0 in. = 25.4 mm.)

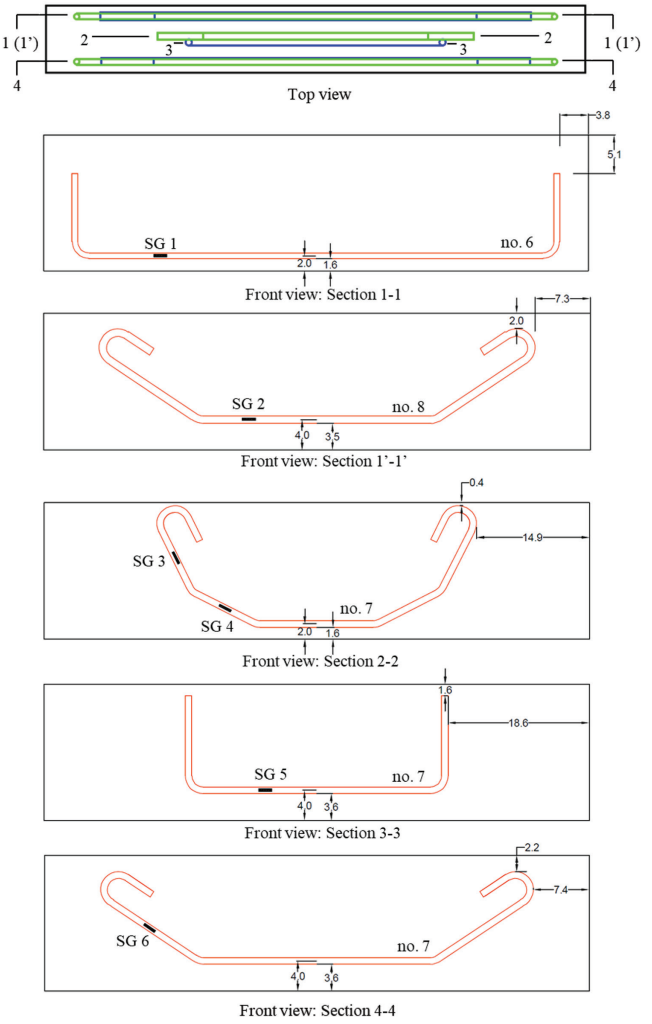

Fig. A3—Reinforcement details of specimen with optimized STM layout II. (Note: Labeled dimensions are in inches; 1.0 in. = 25.4 mm.)

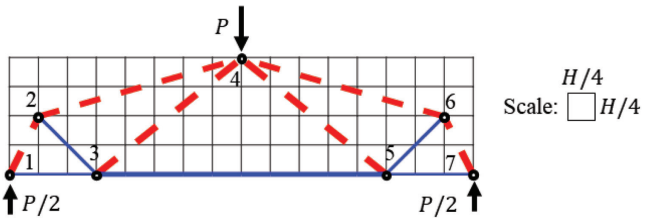

Fig. B1—Labeled node numbers for truss system in Fig. 3(d).

JOIN AN ACI Chapter!

The American Concrete Institute has Chapters and Student Chapters located throughout the world. Participation in a local chapter can be extremely rewarding in terms of gaining greater technical knowledge and networking with leaders in the concrete community.

Because chapters are distinct and independent legal entities, membership includes both ACI members and non-ACI members and is made up of a diverse blend of architects, engineers, consultants, contractors, educators, material suppliers, equipment suppliers, owners, and students—basically anyone interested in concrete. Many active ACI members initially became involved in ACI through their local chapter. In addition to technical programs and publications, many chapters sponsor ACI Certification programs, ACI educational seminars, project award recognition programs, and social events with the goal of advancing concrete knowledge.

Check out the Chapters Special Section from the November 2020 *Concrete International*: www.concrete.org/publications/concreteinternational.aspx

---

Student Chapters

Join or form an ACI Student Chapter to maximize your influence, knowledge sharing, and camaraderie! ACI has 240+ student chapters located throughout the world, each providing opportunities for students to:

- Connect with their peers and participate in concrete-related activities such as: student competitions, ACI Conventions, ACI Certification Programs, ACI Educational Seminars, local chapter meetings, social events, and community service projects;
- Network with members of local chapters, many of whom have been in the industry for decades and can help to develop professional relationships and offer career advice;
- Win recognition for their universities through the University Award; and
- Learn about the many scholarships and fellowships offered by the ACI Foundation and by ACI's local chapters.

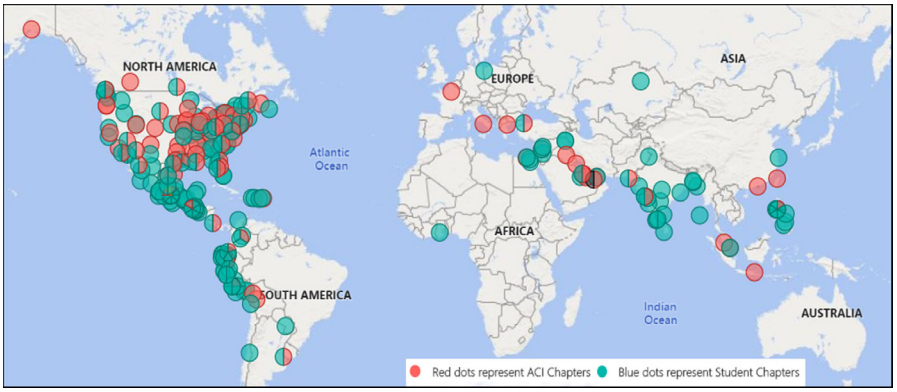

American Concrete Institute

www.concrete.org/chapters

ACI STRUCTURAL JOURNAL TECHNICAL PAPER

Title No. 120-S91

Validation of ACI 369.1 Code Nonlinear Modeling Parameters Using Non-Ductile Reinforced Concrete Building

by Hamid Khodadadi Koodiani, Anil Suwal, Adolfo B. Matamoros, and Andrés Lepage

This study evaluates the accuracy of building performance metrics calculated with nonlinear numerical models created based on the provisions in the ASCE 41 and ACI 369.1 standards. The evaluation was based on a seven-story non-ductile reinforced concrete building located in Van Nuys, CA, instrumented and severely damaged during the 1994 Northridge Earthquake. The purpose of the evaluation is to validate the computed system-level response of nonlinear models created with modeling parameters in ASCE 41/ACI 369.1. The study also evaluates the effect of Rayleigh damping parameters and joint modeling approach on the accuracy of building performance metrics. It was found that ASCE 41/ACI 369.1 models provided a reasonable representation of building response, with error indexes for displacement signals ranging between 0.28 and 0.40, although the error range was higher than those achieved by other researchers by optimizing modeling parameters outside the provisions in the ASCE 41/ACI 369.1 standards.

Keywords: ACI 369.1; ASCE 41; beam-column joint; damping; frequency domain error (FDE) index; modeling parameter; nonlinear response; slab-column connection; structural models.

INTRODUCTION

Historically, the main design objective for proportioning building structures for natural hazards such as earthquakes has been to protect human life. With the publication of the 1967 UBC Code and Appendix A of the 1971 ACI 318 Building Code, largely in response to the 1966 Caracas and 1971 San Fernando earthquakes, there was a marked improvement in design provisions and detailing requirements for reinforced concrete (RC) buildings that drastically reduced the risk to human life in new construction. In light of the success of improved detailing requirements, it is no longer considered sufficient to protect human life, and the objective has been expanded to minimize financial losses caused by severe earthquakes through the use of performance-based design methodologies.

Older RC building structures, designed prior to the introduction of modern seismic detailing requirements in 1967, are more vulnerable to both loss of human life and financial losses. The need to lower the seismic risk at an optimal cost requires the development of effective evaluation methods and standards that allow engineers and owners to make well-informed decisions about optimal retrofit measures, or the need to replace a building if the retrofit cost is too high. Seismic evaluation standards with uniform evaluation criteria have been introduced with the goal of addressing those public safety concerns in a scientifically objective manner. The most widely adopted seismic evaluation standard in the United States is ASCE 41, which has modeling parameters and acceptance criteria to evaluate the structural performance of RC building components. Provisions for RC structures in ASCE 41-17[1] are based on the ACI 369.1-17[2] standard, which will be adopted by reference in ASCE 41-23 and future editions of ASCE 41.

Modeling parameters provided in the ASCE 41 standard constitute the basis of nonlinear models used to calculate deformation demands up to the stage of collapse. These parameters were developed and calibrated based on engineering judgment and results from structural component tests. Differences between element data sets, calibration confidence levels, and level of conservatism have produced inherent differences across modeling parameters of different element types that introduce bias in numerical analysis. For example, deformations at the capping point (deformation corresponding to loss of lateral load capacity) of beams are typically lower than columns because the former are based on engineering judgement while the latter are based on 50% probability of exceedance of an experimental data set. This causes nonlinear deformations to concentrate in beams after the caping deformation is exceeded in numerical analyses, underestimating the expected damage to columns.

Although the ASCE 41 standard allows the use of linear elastic models, the focus of this study is on the nonlinear dynamic analysis procedure, which is the most complex among the evaluation methods permitted in ASCE 41 and is intended to be the most accurate. The nonlinear dynamic procedure in the ASCE 41 is a two-step process. It requires creating numerical models to calculate lateral deformations in the structure and inelastic rotation demands in elements as a first step, followed by a comparison between inelastic deformations demands and acceptance criteria associated with specific performance levels at each element. The main objective of this paper is to evaluate the accuracy of nonlinear models created with ASCE 41 modeling parameters to reproduce global response metrics. The accuracy of the models to estimate inelastic deformations at the element level requires a separate lengthy evaluation outside the scope of this paper and presented elsewere.[3] The main premise of this paper is that, to estimate element deformations accurately, numerical models must be able to reproduce global response metrics such as story lateral deformations accurately.

ACI Structural Journal, V. 120, No. 6, November 2023.

MS No. S-2022-120.R3, doi: 10.14359/51739083, received January 18, 2023, and reviewed under Institute publication policies.

RESEARCH SIGNIFICANCE

Accurate modeling parameters and estimates of deformations are critical to the successful implementation of performance-based standards because the expected magnitude of the damage, its distribution, and the building performance level are established on the basis those metrics. The benchmark study presented in this paper validates the performance-based methodology and component modeling parameters in the ASCE 41 and ACI 369.1 standards by comparing computed and measured metrics of a nonductile instrumented RC frame building that was subjected to a strong earthquake and experienced severe damage. Comparisons are performed using an objective measure of cumulative error over the entire duration of response, and not just at the peaks. This type of validation is of utmost importance to determine if estimates of damage produced with these standards are accurate or distorted due to modeling bias introduced by the standard modeling provisions.

Case study building

The building modeled in this study is a seven-story reinforced concrete frame structure located in Van Nuys, CA,[4] designed in 1965 and constructed in 1966. It is rectangular in plan with overall dimensions of approximately 150 ft (46 m) in the east-west (longitudinal) direction and approximately 60 ft (18 m) in north-south (transverse) direction. The building has eight bays in the east-west (E-W) direction and three bays in the north-south (N-S) direction. The structural system of the building consisted of exterior beam-column frames and interior slab-column frames. The plan and elevation view of the building are presented in Fig. 1 and 2.

Reinforcement detailing for beams, columns and slabs of the building are reported by Suwal.[3] Four bays of the exterior north frame had infill masonry walls in the first story.[5] The building structure had normal weight aggregate concrete with specified concrete compressive strength values shown in Table 1. Expected concrete compressive strength and expected yield strength of reinforcing bars were calculated following the provisions in ASCE 41-17 Section 10.2.2.1.3, with a factor to translate lower-bound material properties to expected strength material properties of 1.5 for concrete and 1.25 for reinforcing steel. This building recently has been studied in different studies.[6-8]

Recorded earthquakes and observed damage

The building suffered severe structural damage during the 1994 Northridge earthquake. During the Northridge earthquake, the building was instrumented with an array of 16 accelerometers.[3,9] A detailed damage survey is presented by Trifunac et al.[9] The Northridge earthquake had a magnitude of 6.7 (M_w) and the epicenter was located approximately 4.3 miles (7 km) west of the building. Structural damage concentrated in the E-W perimeter frames and damage in the N-S frames was limited to minor flexural cracks in the end-bay beams. Severe damage was observed at different column locations of the E-W perimeter.[5] The most severe structural damage consisted of column shear failure in the fourth and fifth floor levels of the south perimeter frame.[9] In addition, many beam-column joints below the fifth floor level also sustained minor to moderate shear cracks. Concrete spalling and hairline flexural cracks were observed in several spandrel beams. Nonstructural damage was not very extensive and was mostly observed in the fourth story.[9] Although records from several earthquakes exist,[3] this study focuses on the 1994 Northridge Earthquake because it produced the largest inelastic deformations and most severe damage.[3,9]

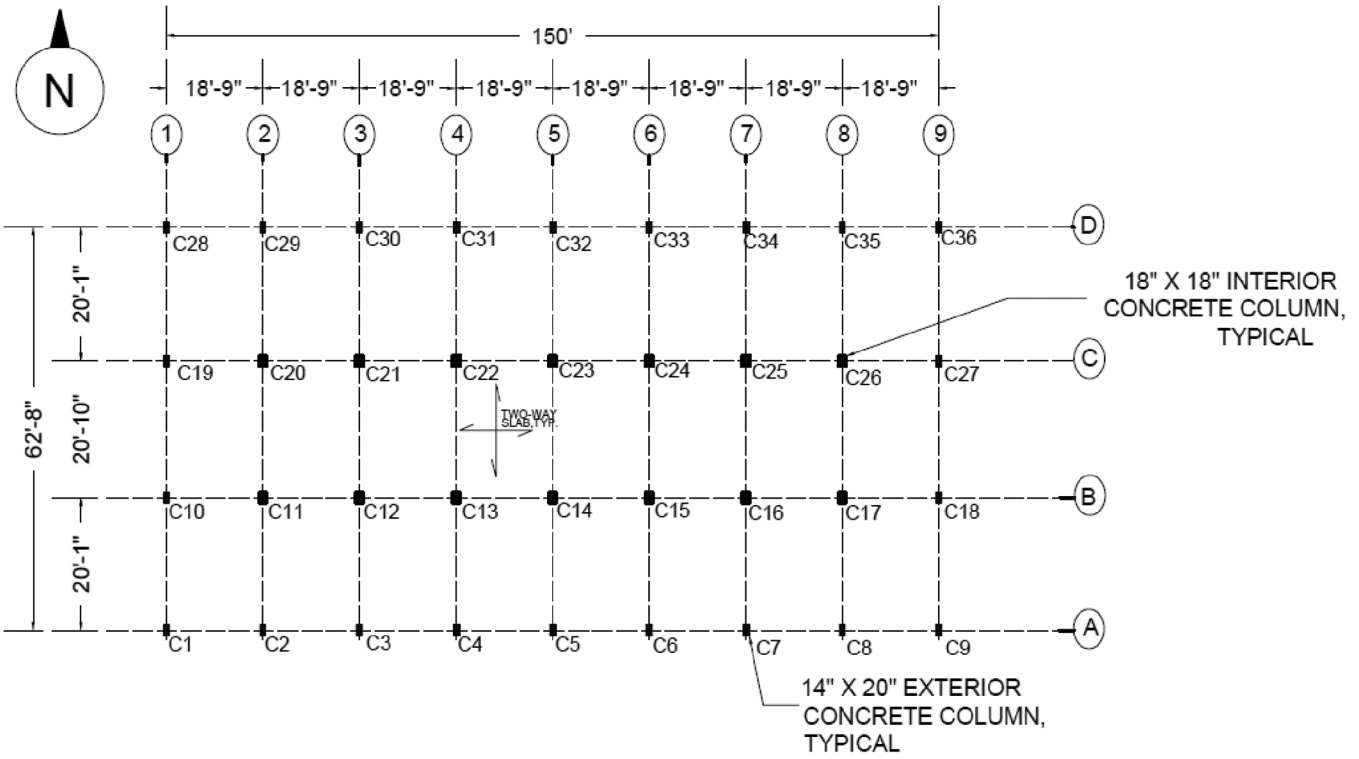

Fig. 1—Typical floor plan. (Note: 1 ft = 0.3048 m; 1 in. = 25.4 mm.)

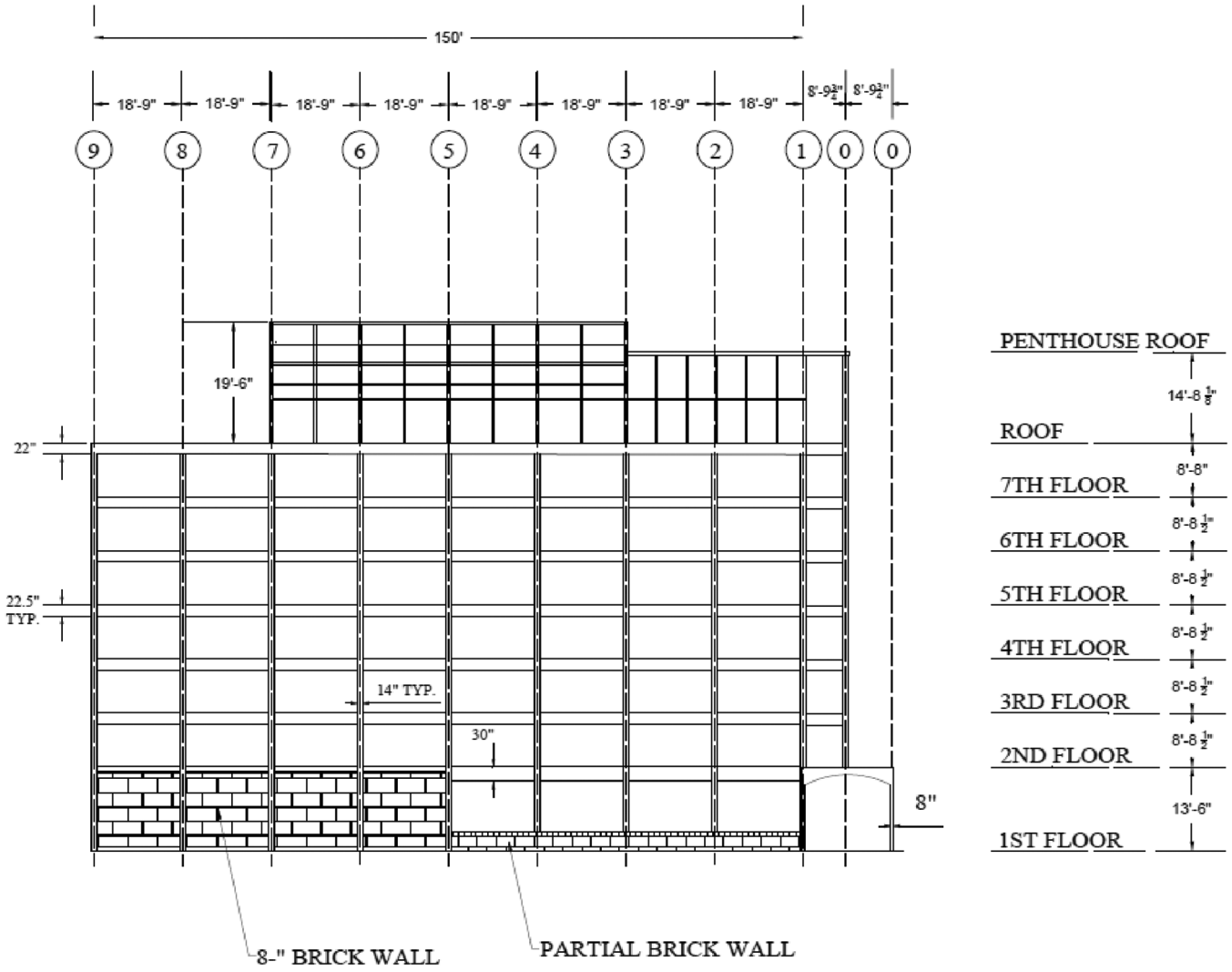

Fig. 2—North frame elevation of study building. (Note: 1 ft = 0.3048 m; 1 in. = 25.4 mm.)

Table 1—Material properties

Component	Property	Based on specified values, ksi	
		Lower-bound (Specified)	Mean (Expected)
Column reinforcement	Yield stress, f_y	60	75
Beam and slab reinforcement	Yield stress, f_y	40	50
Column concrete, ground to second floor	Peak strength, f_c'	5	7.5
Column concrete, second to third floor	Peak strength, f_c'	4	6
Beam and slab concrete, second floor	Peak strength, f_c'	4	6
All other concrete, third floor to roof	Peak strength, f_c'	3	4.5

Numerical models of case-study building

This paper evaluates the accuracy of global (in contrast to element-level) response metrics calculated with nonlinear models of a moment frame building created in accordance with the provisions of the ASCE 41/ACI 369.1 standards. Results presented in this paper describe findings from two-dimensional models of the E-W and N-S frames of the building structure, which were the simplest and most computationally efficient of all models evaluated in the study (nonlinear three-dimensional [3-D] models of the building were created for comparison purposes). The reduced computational cost of two-dimensional (2-D) models is also beneficial for more complex studies that require many simulations such as incremental dynamic or FEMA P695 fragility analyses. Although the presence of infill masonry walls in four first-story bays of the north perimeter frame introduces eccentricity between the center of stiffness and center of mass at that level, simulations with 3-D computer models conducted as part of this study showed that their effect on the displacement response did not affect the accuracy of the 2-D modeling approach. All nonlinear models in the study were created in the OpenSees[10] software platform.

Numerical models included a perimeter beam-column and interior slab-column frames connected by rigid links to simulate a rigid diaphragm constraint. Each beam and column face location in the building model included a zero-length rotational spring element that simulated the inelastic moment-rotation relationship of the respective beam or column plastic hinge. A simple analysis, based on criteria in NIST GCR12-917-21[11] for the ratio of building height to the product of shear wave velocity and building period, indicated that the effects of soil-foundation-structure interaction would not be significant. For this reason, foundation flexibility was not considered in this study and the building model was assumed to be fixed at the ground floor level. The computed building weight included self-weight of columns, beams, slabs, partition loads, roofing, flooring, ceiling, mechanical, electrical, plumbing, and other miscellaneous loads acting on the building. The total weight of the building structure was calculated to be 10,740 kip (47,780 kN). Taking advantage of the symmetry of the structure and to reduce computational cost, only half of the building was modeled. The structural system of the building consisted of two exterior moment frames and two interior slab-column frames in the E-W direction, and two exterior moment frames and seven interior slab-column frames in the N-S direction. Both E-W and N-S models had one exterior and one interior frame, so the stiffness and strength of all interior frame elements of the N-S model were adjusted by a factor of 3.5. The total mass of the E-W and N-S two-frame models was half of the mass of the building. The total mass of each model was evenly distributed between nodes at beam-column joint locations. Slab and beam dead loads were calculated and assigned as uniformly distributed loads at each floor beam. The difference between gravity loads applied directly to the elements and the total weight of the floor was applied to a gravity column built with truss elements. Detailed load calculations of the building structure are provided elsewhere.[3]

For calculating element stiffness and strength, spandrel beams of the exterior frames were modeled as L-shaped beams including a compression flange consisting of the portion of the slab adjacent to the spandrel beam. The compression flange width was calculated according to the provisions in ACI 318-19.[12]

Material models

Moment-rotation relationships for the springs were defined based on ASCE 41 modeling parameters. Flexural capacities (yield moments) were calculated using moment-curvature analysis. The concrete material model by Kent and Park[13] was used for the moment-curvature analysis, and the reinforcing steel was modeled using a stress-strain relationship that included strain hardening. Yield stress of the longitudinal reinforcement used in the calculations was consistent with expected yield stress values calculated with material factors in ASCE 41. Reinforcing bar stress at loss of lateral load capacity (capping point) was assumed to be 20% higher than the yield strength This value was chosen based on research by Mander and Matamoros,[14] who performed a statistical analysis of more than 500,000 tensile tests of reinforcing bars. They showed that for ASTM A615 Grade 60 reinforcement the static increase factors corresponding to yield, 2% strain and 5% strain were 1.2, 1.35, and 1.6, respectively.[14] The 20% increase with respect to yield corresponds approximately to the average of the static increase factors at 2 and 5% strain.

Lumped plasticity model

Structural members were modeled using a lumped plasticity approach with each structural member simulated as an elastic beam-column element having zero-length rotational springs at each end. The zero-length rotational springs, where all inelastic rotations were concentrated, had nonlinear moment-rotation relationships simulating the response of the elements up to deformations at loss of gravity load carrying capacity. The moment-rotation relationship for the nonlinear rotational springs was defined using the envelope curve and hysteresis rules in the peak-oriented Ibarra-Medina-Krawinkler (IMK) material model,[15-17] which simulates monotonic and cyclic stiffness and strength deterioration. The envelope moment-rotation curve was implemented using the modified version of the IMK model, represented in Fig. 3(a). The ASCE 41 standard provides modeling parameters a, b, and c needed to define the generalized envelope curve shown in Fig. 4. Figure 3(b) shows a calculated hysteretic response of a nonlinear rotational spring for a typical exterior frame column at the fifth story (between floor levels 5 and 6). The dashed line in Fig. 3(b) corresponds to the ASCE 41 envelope curve used to define the moment-rotation relationship in the IMK model. The parameters that define the moment-rotation curve are initial stiffness (K_e), yield moment (M_y), capping moment (M_c), capping deformation (θ_p), post-capping deformation (θ_{pc}), residual moment (M_r), and ultimate deformation (θ_u).

In the IMK model, the rate of cyclic deterioration of the parameters that control the envelope curve uses an energy-based rule that has two parameters: normalized energy dissipation capacity, λ, and an exponent term to describe how the rate of cyclic deterioration changes with accumulation of damage, c. Values assigned to cyclic deterioration parameters followed recommendations by Haselton and Liel.[18]

Slab-column connections

Flat-slab moment frames in the 1960s were typically designed for gravity loads only, without any detailing requirements to resist earthquake loads. Several techniques to model the nonlinear response of slab-column connections have been proposed. One of the most important technical questions regarding building response is estimation of frame stiffness to lateral loads. Experimental research by Hwang and Moehle[19] showed that flat slabs usually have lower lateral stiffness than theoretically estimated based on full width. Hwang and Moehle[19] also observed steady stiffness degradation with increasing story drifts due to the propagation of cracks. To account for these behaviors, several researchers have proposed the use of an effective slab width factor α and a stiffness factor β. For example, Kang et al.[20] proposed an effective slab width factor α of 0.75 and stiffness factor β of 1/3. Hwang and Moehle[19] found that the effective width factor mainly depends on the span of the slab l_1 as well as the

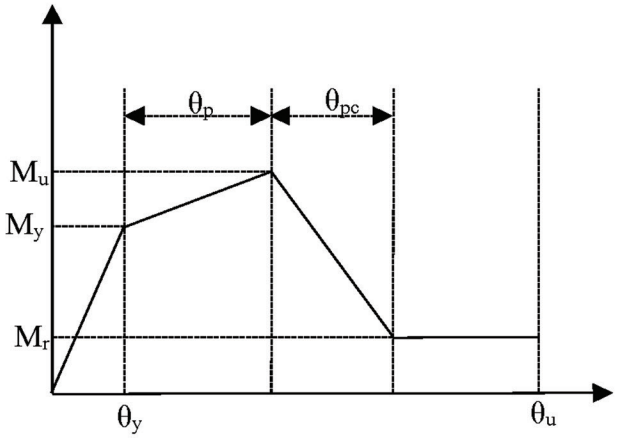

a) Monotonic envelope curve

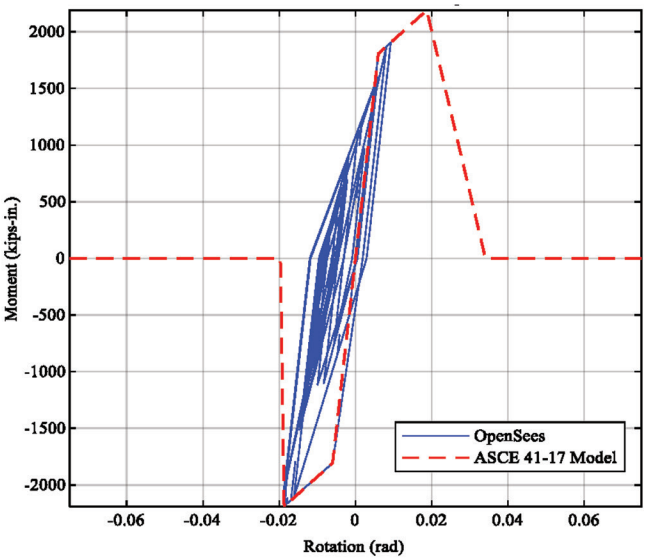

b) Calculated hysteretic response

Fig. 3—Modified IMK model. (Note: 1 kip-in. = 112.98 N-m.)

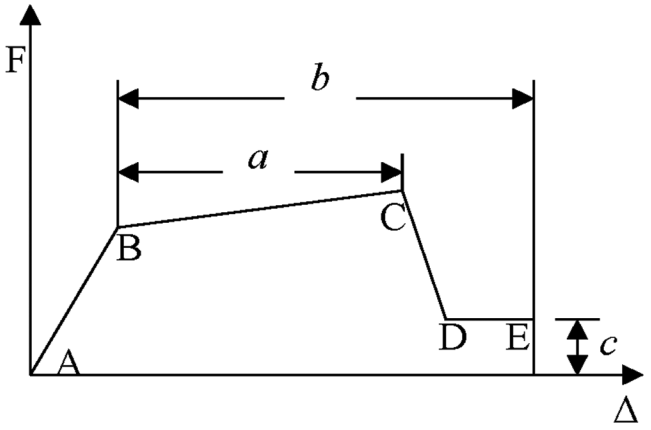

Fig. 4—Idealized envelope curve defined in ASCE 41.

column dimension in the direction of the applied lateral load c_1. Several other researchers including Pecknold,[21] Durrani et al.,[22] Allen and Darvall,[23] Grossman,[24] and Vanderbilt and Corley[25] also proposed equations to estimate the effective slab width and stiffness factors.

The effective beam width model described in Section C10.4.4.2.1 of the ASCE 41 standard was adopted in this study. The effective width of interior and exterior connections was calculated using Eq. C-10-2a and C10-2b of ASCE 41 by Huang and Moehle,[19] and stiffness factor β was calculated using Eq. C10-3 of ASCE 41, also by Huang and Moehle.[19]

Beam-column joint model

Section 10.4.2.2.2 of ASCE 41-17 stipulates that modeling parameters for joints shall be derived from test data or from rational analyses. Joint strengths calculated in accordance with ASCE 41 were higher than joint shear demands, so simple models were used to simulate joint flexibility because this approach would be most useful to practitioners. Several different beam-column joint idealizations were evaluated in this study. One of the models followed recommendations in ASCE 41 for modeling of beam-column joints in the linear analysis procedure (Table 2). The remaining models evaluated simple approaches for modeling the joint region using combinations of elastic and rigid offsets. Elastic offsets were modeled using beam column elements with the elastic properties of the slab, beam, or column element framing into the joint. The length of horizontal offsets was taken as half the column depth, whereas the length of vertical offsets was taken equal to the beam/slab depth.

ASCE 41-13 and ASCE 41-17 models

This study included a comparison between nonlinear models created using modeling parameters in the ASCE 41-13 and ASCE 41-17 standards. The main difference between the two consists of changes to column modeling parameters implemented in ACI 369.1-17 and adopted into the ASCE 41-17 provisions, where the probability of exceedance of modeling parameters for flexure-shear critical columns changed from 35% to 50%.[26,27] This difference is illustrated in Fig. 5, which shows envelope curves for the exterior fourth-story column (E-W exterior frame) of the building generated with modeling parameters in the ASCE 41-17 and ASCE 41-13 standards.

Frequency domain error (FDE) index evaluation

Goodness of fit of the calculated versus recorded response was evaluated objectively using the frequency domain error (FDE) index.[27] The FDE index was used to identify the models that had the best correlation with measured roof displacements. All evaluations were performed using the response of the models to the 1994 Northridge earthquake recorded at the base of the building because it had the highest intensity at the site of all recorded earthquakes, and because the instrumentation provided measurements of strong motion at the building base and the roof. Displacement records inferred from acceleration records at these two locations were used to obtain the relative displacement at

Table 2—Description of different numerical models

Exterior frame	Interior frame	Model
Rigid beam offsets Flexible column offsets	Rigid column offsets Flexible slab offsets	M-1
Rigid column and beam offsets	Rigid column and slab offsets	M-2
Flexible column and beam offsets	Flexible column and slab offsets	M-3
Flexible column and beam offsets	Rigid column and slab offsets	M-4

Table 3—Comparison of FDE index for different numerical models

	FDE index							
	E-W, longitudinal direction				N-S, transverse direction			
	2% damping		5% damping		2% damping		5% damping	
Models	30 sec	60 sec	30 sec	60 sec	30 sec	60 sec	30 sec	60 sec
13 M-1	33.8%	30.3%	37.3%	36.1%	38.4%	37.2%	31.5%	36.1%
13 M-2	37.4%	33.4%	38.8%	34.3%	29.0%	32.3%	28.1%	31.3%
13 M-3	34.0%	30.8%	32.9%	28.9%	40.2%	39.5%	Did not converge	
13 M-4	35.6%	30.6%	34.7%	30.3%	35.6%	30.6%	34.7%	30.3%
17 M-1	38.3%	34.9%	36.8%	35.4%	37.7%	38.6%	33.2%	35.1%
17 M-2	37.5%	33.4%	36.2%	34.7%	28.9%	32.0%	33.5%	36.1%
17 M-3	34.0%	30.8%	32.1%	35.2%	28.9%	32.0%	30.4%	32.5%
17 M-4	35.6%	30.6%	34.7%	30.3%	30.5%	32.0%	28.2%	29.7%

the roof. Table 3 shows the FDE index value for dynamic analyses with modeling parameters based on ASCE 41-13 and ASCE 41-17, for each of the joint modeling assumptions, and mass- and stiffness-proportional damping ratios of 2 and 5%. As shown in Table 3, the FDE index was calculated for durations of 30 seconds (strong shaking) and 60 seconds (totality of the record, including strong shaking and free vibration response). Models with ASCE 41-13 modeling parameters had inconsistent results, with model 13 M-3 providing the lowest FDE index for the E-W direction and model 13 M-2 for the N-S direction. In both directions, models 13 M-4 and 17 M-4, with flexible offsets in beams and columns of the moment frames and rigid offsets in the beams and columns of slab-column frames, had the lowest FDE indexes overall, so these joint modeling assumptions were adopted for all remaining simulations in the study. Dragovich and Lepage[28] stated that an FDE index of 0.75 signifies very poor correlation whereas FDE indexes below 0.25 represent a very good correlation. A study performed by Lepage et al.[29] for case-study building, in which modeling parameters were varied outside the provisions in ASCE 41 including hysteresis loop parameters for the Takeda model, found a range of the FDE indexes for calculated roof displacement between 19 and 60%. A comparison with the results of the study by Lepage et al.[29] shows that the best ASCE 41 models had good accuracy, without an effort to optimize hysteresis parameters, which are not prescribed in ASCE 41. In 2023, Khodadadi Koodiani et al. used machine learning techniques to propose new equations to calculate the nonlinear modeling parameters for new construction[30] and also existing concrete columns.[31]

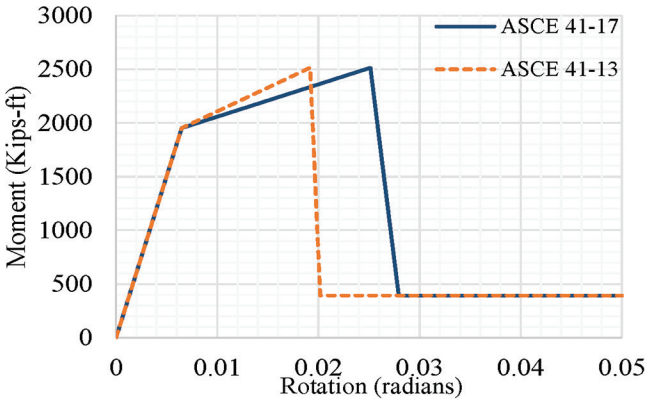

Fig. 5—Moment-rotation envelope curves for exterior column (fourth story). (Note: 1 kip-ft = 1355.8 N-m.)

Damping ratio

ASCE 41-17 Section 7.2.3.6 stipulates that for nonlinear dynamic analyses 3% or lower, viscous damping should be used, and that higher damping ratios shall be permitted if substantiated through analyses or test data. Two types of Rayleigh damping were considered in this study, mass-proportional and stiffness-proportional damping.[32] The effect of mass-proportional damping decreases asymptotically with increasing modal frequency (decreasing modal period), while the effect of stiffness-proportional damping increases linearly with increasing modal frequency. Consequently, mass-proportional damping has a greater effect on lower frequency modes while the effect of stiffness-proportional damping is higher for higher modes. Rayleigh damping coefficients α and β in the building models were calculated for 2 and 5% viscous damping ratios, based on the frequencies of the first and fourth modes. Models with

Table 4—Comparison of FDE index for 17 M-4 model with different damping types

	FDE for model 17 M-4			
	E-W direction		N-S direction	
	2% damping			
Damping type	30 sec	60 sec	30 sec	60 sec
Proportional to mass only	36.1%	31.4%	31.1%	33.1%
Proportional to mass and initial stiffness	35.7%	30.6%	30.4%	32.0%
Proportional to mass and updated stiffness	35.6%	30.6%	30.4%	32.1%
	5% damping			
Proportional to mass and initial stiffness	34.7%	30.3%	28.2%	29.6%
Proportional to mass and updated stiffness	34.7%	30.3%	28.2%	29.7%

Rayleigh damping coefficients based on the frequencies of the second and fourth modes were also evaluated, but calculated FDE indexes were significantly lower using the frequencies of the first and fourth modes.

Calculated FDE indexes, summarized in Tables 3 and 4, were similar but slightly lower for models with a damping ratio of 5% than for models with a damping ratio of 2%. Different types of stiffness-proportional damping were evaluated, depending on the state of the stiffness matrix used to calculate the damping matrix. The lowest FDE indexes (best fit) corresponded to the models with a 5% damping ratio and damping matrix proportional to mass and the initial stiffness or proportional to mass and updated stiffness. Rayleigh damping proportional to mass and initial stiffness was adopted because it provided the lowest FDE indexes.

Period of building models

Another important metric is the calculated period of vibration. Table 5 provides a summary of calculated building periods and those reported in earlier studies by different researchers, along with building periods calculated for the models analyzed in this study. Ambient measurement results are presented for reference as well. Because the main difference between models based on the ASCE 41-13 and ASCE 41-17 standards were column modeling parameters that only affect the nonlinear response, calculated periods were the same for the two standards and a single value is reported for both models. It is important to point out that the periods reported by Blume[4] and Barin and Pincheira[35] correspond to the initial period of the building at the start of the nonlinear simulation, and that the period reported by Lepage[34] is based on uncracked section properties. The period reported by Paspuleti[36] was calculated using a nonlinear fiber model in which gravity and lateral loads were applied prior to the eigenvalue analysis of the structure. Effective stiffness coefficients in ASCE 41 are based on measured deflections at yield from component tests and resulted in effective periods significantly larger than reported by most researchers. This difference is caused by the element stiffness used to calculate the period of the building. Researchers including Lepage[34] defined stiffness based on uncracked section properties, resulting in much lower calculated periods that are closer to values measured through ambient vibration experiments reported by Todorovska and Trifunac.[37]

Table 5—Calculated and measured building periods

	E-W direction		N-S direction	
Models	T_1, sec	T_2, sec	T_1, sec	T_2, sec
M-1 (13 and 17)	1.78	0.58	—	—
M-2 (13 and 17)	1.54	0.52	1.66	0.55
M-3 (13 and 17)	1.81	0.61	1.87	0.61
M-4 (13 and 17)	1.73	0.58	1.76	0.58
Islam[33]	1.39	0.46	—	—
Blume[4]	0.86	0.79	—	—
Lepage[34]	0.89	—	0.97	—
Barin and Pincheira[35]	0.81	—	—	—
Paspuleti[36]	1.93	0.64	—	—
Measurements[37]				
1967	0.53	—	0.48	—
1971 after San Fernando earthquake	0.72	—	0.68	—
1971 after San Fernando earthquake repairs	0.64	—	0.58	—
1994, 2 weeks after Northridge earthquake	1.00	—	0.71	—
1994, 3 months after Northridge earthquake (with temporary steel braces)	0.91	—	0.71	—

Nonlinear static analyses

Calculated base shear strengths in the E-W and N-S directions were approximately 18% and 15% of the building weight, respectively (Fig. 6 and 7). Pushover analysis results displayed in Fig. 6 and 7 showed that the change in modeling parameters *a* and *b* between the 2013 and 2017 editions of the ASCE 41 Standard caused model 17 M-4 to have larger deformations at collapse than model 13 M-4. The difference was smaller in the E-W direction (Fig. 6), where the maximum story drift ratios were 3.5% for model 13 M-4 and 3.75% for model 17 M-4. The largest drift ratios in both models occurred at the second and third stories. Mean drift ratios for models 13 M-4 and 17 M-4 were 2% and 2.25%, respectively. In the N-S direction, the difference between the two models was larger. Maximum interstory drift ratios

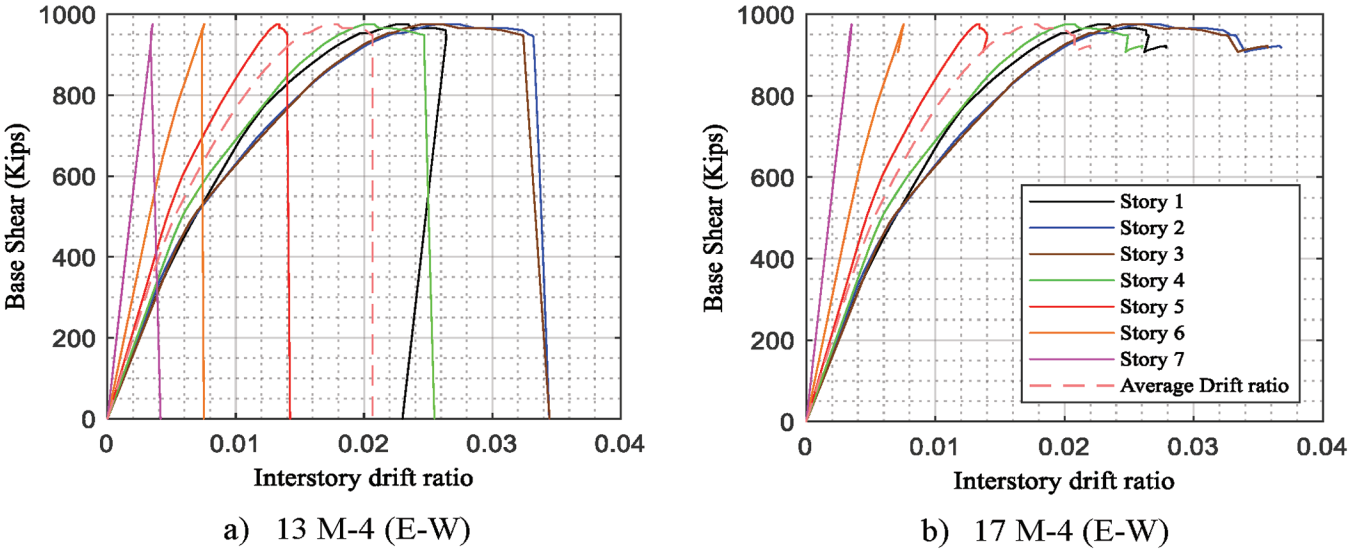

Fig. 6—Pushover curves for E-W models. (Note: 1 kip = 4.45 kN.)

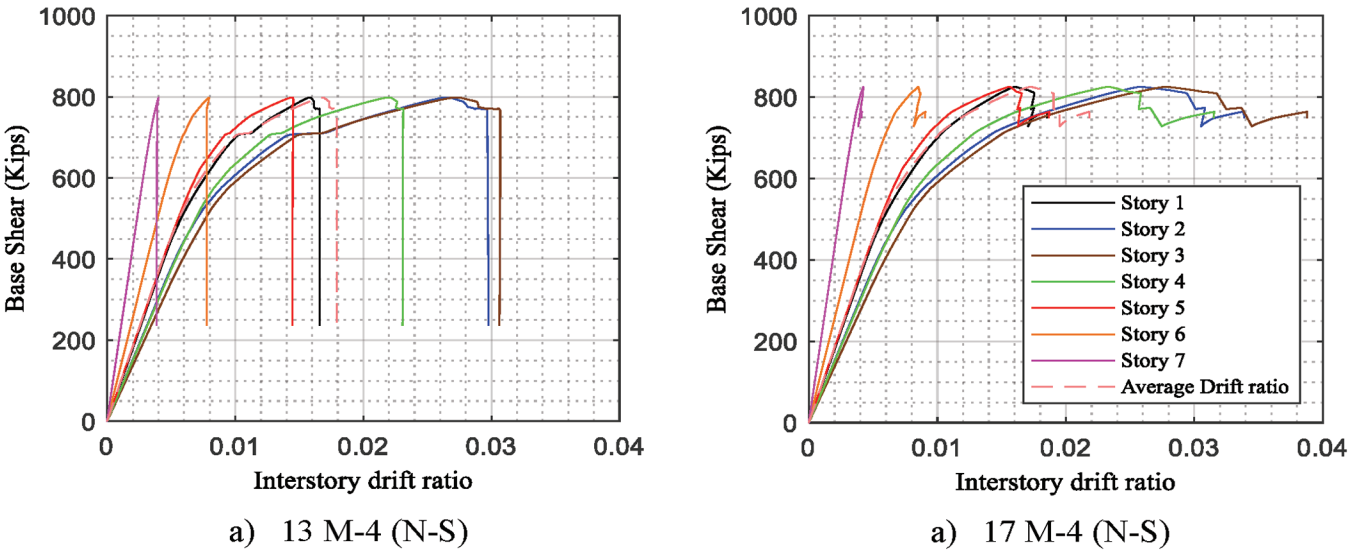

Fig. 7—Pushover curves for N-S models. (Note: 1 kip = 4.45 kN.)

were 3.2% and 3.9% for models 13 M-4 and 17 M-4, respectively. Calculated demands were largest at stories 2, 3, and 4 for both models. Mean drift ratios for models 13 M-4 and 17 M-4 were 1.8% and 2.2%, respectively (Fig. 7). The jagged shape of the curves in Fig. 6 and 7 and the sudden drop in strength past the point of maximum shear demand are indicative of brittle failure.

Nonlinear dynamic analyses

Assumptions about damping affected the magnitude of the peak displacements during the strong shaking phase and the attenuation during the free vibration phase. Increasing the damping ratio had the effect of decreasing displacement at the largest peak and changing the permanent displacement. The accuracy of the match between the two signals (calculated versus recorded) in the free vibration phase was affected by the effective stiffness, which influences the periods of vibration of the structure. Figure 8 shows the comparison between the recorded roof displacement and the calculated response for models 17 M-4 and 13 M-4, for damping ratios of 5 and 2% in both E-W and N-S directions. Recorded and calculated roof displacements of models 13 M-4 with 5 and 2% damping had very similar response until $t = 25$ seconds, with the exception of the peak point at approximately 8 seconds, where the recorded displacement was slightly higher than calculated. The latter portion of the calculated response (after 25 seconds) had similar behavior to the recorded displacement, although the recorded displacement attenuated at a faster rate.

In the strong vibration phase, before t = 25 seconds, models with 2% damping ratio matched positive peaks more closely than models with 5% damping ratio, and the opposite was true for negative peaks. This trend was more noticeable for the N-S direction than in the E-W direction. For both damping ratios in the E-W direction, the response had a closer match during strong shaking, before 25 sec, than it did during the free-vibration phase. In the N-S direction both 13 M-4 and 17 M-4 models with 5% damping matched the recorded response very closely.

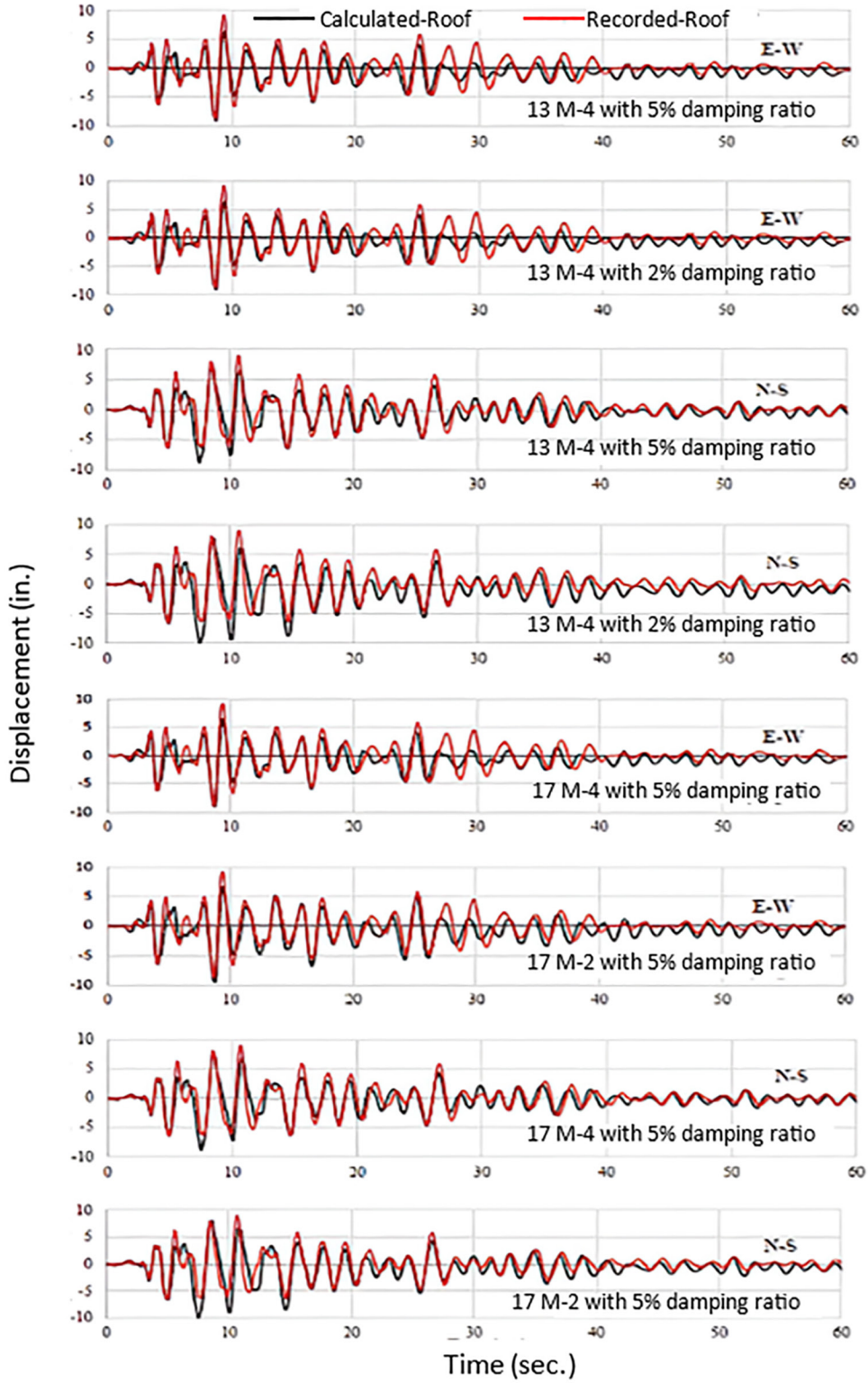

Fig. 8—Comparison between calculated and recorded relative roof displacement for E-W and N-S directions, Northridge earthquake, and models 13 M-4 and 17 M-4 with 5 and 2% damping ratio. (Note: 1 in. = 25.4 mm.)

Spatial distribution of displacements and accelerations

The spatial distribution of peak accelerations, lateral displacements, and drift ratios are presented in Fig. 9. Each figure shows a comparison between the peak metric calculated with the 17 M-4 model and values recorded or inferred from acceleration records from the building instrumentation array for the 1994 Northridge Earthquake. In general, the 2-D models were able to closely reproduce the distribution of these parameters over the height of the building. The 2-D models nearly matched recorded accelerations in both directions, and most accurately at the lower stories (Fig. 9(a)).

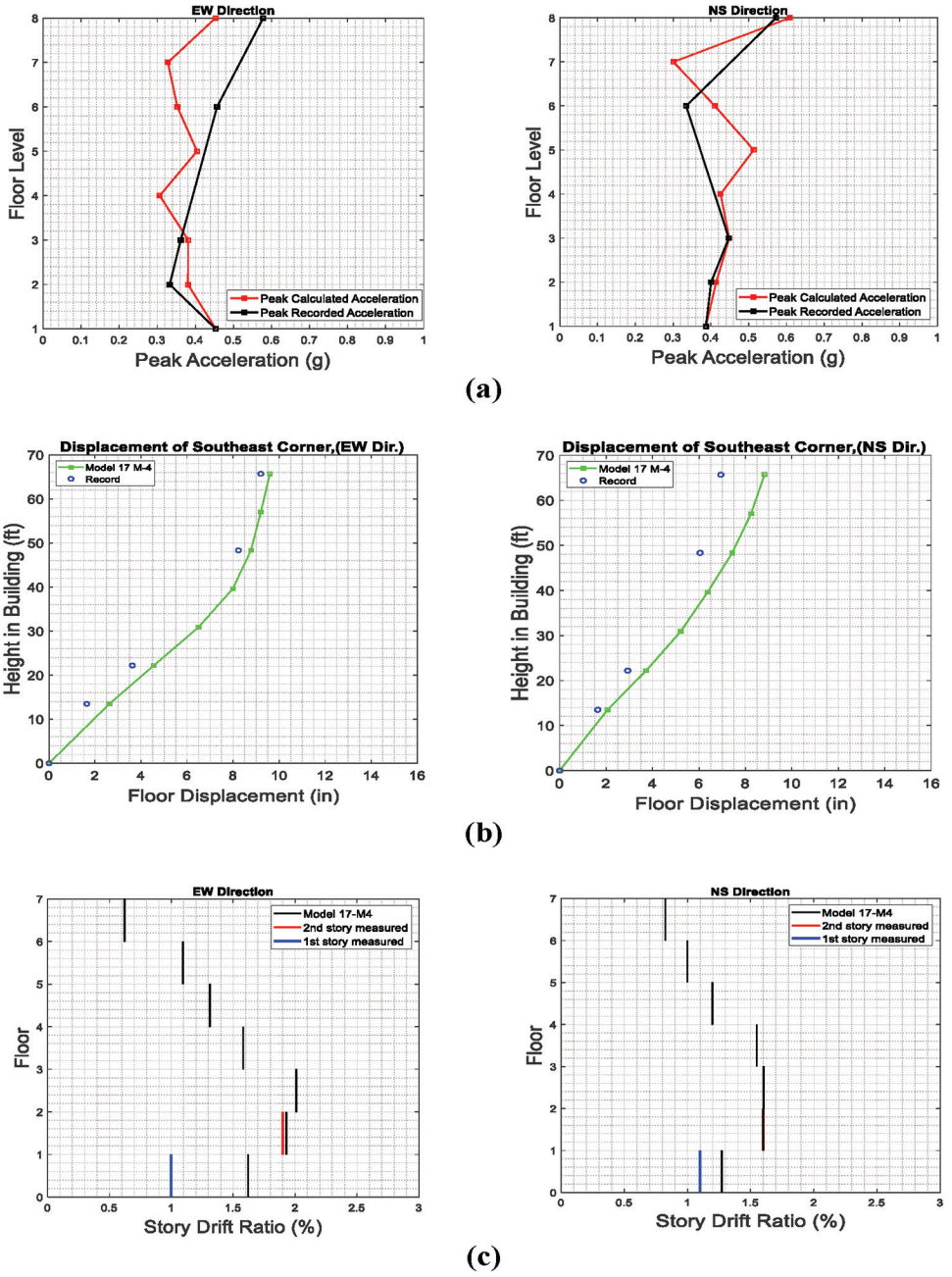

Fig. 9—(a) Peak acceleration profile in E-W and N-S directions; (b) floor displacement profile in E-W and N-S directions; and (c) story drift ratio profile in E-W and N-S directions. (Note: 1 in. = 25.4 mm; 1 ft = 0.3048 m.)

In the E-W direction, the error in calculated accelerations ranged between 5% at the third level and 28% at the roof. In the N-S direction, the errors were smaller, ranging between zero at the third level and 18% at the sixth level.

Lateral displacements (Fig. 9(b)) were overestimated by the model, with differences ranging from 4 to 38% in the E-W direction and 19 to 21% in the N-S direction. This is likely the result of modeling bare frames, neglecting the stiffness of nonstructural partition elements. The density of the instrumentation array only permitted reporting of recorded drift ratios in the lower two stories (Fig. 9(c)). In both directions, calculated drift ratios were very close for the second level. The largest difference between calculated and recorded drift ratios (inferred from instrument data) was at the first level of the E-W direction, likely due to the omission of the first-story masonry walls in the model. The results indicate that this simplification affected calculated displacements at the top of the first level but had a small effect on calculated displacements and accelerations at higher levels of the building.

CONCLUSIONS

The model developed in the study based on the ASCE 41 modeling parameters and guidelines provided a reasonable representation of building response as quantified by the frequency domain error (FDE) index, with FDE indexes ranging between 0.28 and 0.40. Other researchers have been able to obtain estimates as low as 0.20,[26] by optimizing parameters outside the ranges provided in the ASCE 41 standard. This difference may be partially caused by the lack

of guidance in ASCE 41/ACI 369.1 about the shape of the hysteresis curve of building components.

FDE indexes for models based on the ASCE 41-13 and ASCE 41-17 standards had similar values. This similarity indicates that the nonlinear dynamic response of the system for the 1994 Northridge earthquake ground motion recorded at the building was not affected by changes in modeling parameters introduced in the ASCE 41-17 provisions. This observation may differ for stronger levels of shaking and for nonlinear static analyses because there was a significant increase in plastic rotations corresponding to nonlinear modeling parameters *a* and *b* that define the idealized moment-rotation curves between the two versions of the standard.

Assumptions about the flexibility of beam and column joint offsets had a small effect on the accuracy of the numerical models. Models with flexible beam and column offsets in the exterior moment-resisting frames, and rigid beam and column offsets in the interior slab-column frames had the lowest FDE indexes.

Different combinations of mass-proportional and stiffness-proportional Rayleigh damping were evaluated in the study, for viscous damping ratios of 2 and 5%. The lowest FDE indexes were obtained using mass-proportional and initial stiffness-proportional damping and a 5% damping ratio.

The two-dimensional (2-D) models were able to accurately capture the spatial distribution of displacements and accelerations over the height of the building, in both directions, although they consistently overestimated displacements in both directions. This pattern was expected considering that the stiffness of nonstructural partition elements was neglected in the models.

The periods of vibration of the building were in close agreement with the periods calculated by other researchers. The periods of the models with flexible joint offsets in the exterior frame and rigid joint offsets in the interior frame were in better agreement with values reported by other researchers than models with rigid joint offsets in both frames (exterior and interior).

Results from nonlinear static analyses show that in both directions model 17 M-4 had slightly higher story drift ratio and mean drift ratio at collapse than model 13 M-4. The difference between the deformation capacity at collapse of ASCE 41-13 and ASCE 41-17 in the nonlinear static analyses is attributed to changes in the modeling parameters for columns introduced in ASCE 41-17, extending the deformation at loss of lateral load capacity of columns. In nonlinear analyses the difference was not significant because most building components remained below the deformation corresponding to loss of lateral load capacity (capping point).

AUTHOR BIOS

ACI member **Hamid Khodadadi Koodiani** *is a PhD Student at The University of Texas at San Antonio, San Antonio, TX. He received his BS and MS from the University of Shiraz, Shiraz, Iran. He is a member of ACI Committees 369, Seismic Repair and Rehabilitation and 374, Performance-Based Seismic Design of Concrete Buildings.*

Anil Suwal *is a Structural Engineer at Transystems Corporation, Kansas City, MO. He received his PhD in civil engineering from The University of Texas at San Antonio.*

Adolfo B. Matamoros, *FACI, is Peter T. Flawn Professor in the Department of Civil Engineering at The University of Texas at San Antonio. He received his licentiate from the University of Costa Rica, San José, Costa Rica, and his MS and PhD from the University of Illinois at Urbana-Champaign, Champaign, IL. He is past Chair of ACI Committee 369, Seismic Repair and Rehabilitation, and a member of ACI 374, Performance-Based Seismic Design of Concrete Buildings; ACI Subcommittee 318-H, Seismic Provisions; and Joint ACI-ASCE Committee 408, Bond and Development of Reinforcement.*

Andrés Lepage, *FACI, is a Professor at The University of Kansas, Lawrence, KS. He received his PhD in civil engineering from the University of Illinois at Urbana-Champaign. He is a member of ACI Committees 318, Structural Concrete Building Code; 335, Composite and Hybrid Structures; 374, Performance-Based Seismic Design of Concrete Buildings; and 375, Performance-Based Design of Concrete Buildings for Wind Loads.*

NOTATION

a	=	modeling parameter representing plastic rotation at incipient lateral-strength degradation
b	=	modeling parameter representing plastic rotation at incipient axial degradation
c	=	cyclic deterioration calibration term: exponent term to describe how rate of cyclic deterioration changes with accumulation of damage
K_e	=	initial stiffness
M_c	=	capping moment
M_r	=	residual moment
M_y	=	yield moment
α	=	effective slab width factor
β	=	stiffness factor
λ	=	normalized energy dissipation capacity
θ_p	=	capping deformation
θ_{pc}	=	post-capping deformation
θ_u	=	ultimate deformation

REFERENCES

1. ASCE/SEI 41-17, "Seismic Evaluation and Retrofit of Existing Buildings," American Society of Civil Engineers, Reston, VA, 2017, 576 pp.

2. ACI Committee 369, "Standard Requirements for Seismic Evaluation and Retrofit of Existing Concrete Buildings (ACI 369.1-17) and Commentary," American Concrete Institute, Farmington Hills, MI, 2017, 110 pp.

3. Suwal, A., "Performance Evaluation of a Non-Ductile Reinforced Concrete Moment Frame Building," PhD dissertation, The University of Texas at San Antonio, San Antonio, TX, 2018.

4. Blume. J. A., and Assoc., "Chapter 29: Holiday Inn," *San Fernando, California Earthquake of February 9, 1971, Volume I, Part A*, U. S. Department of Commerce, National Oceanic and Atmospheric Administration, Washington, DC, 1973.

5. Krawinkler, H., "Van Nuys Hotel Building Testbed Report: Exercising Seismic Performance Assessment," Pacific Earthquake Engineering Research Center, University of California, Berkeley, Berkeley, CA, 2005.

6. Suwal, A.; Khodadadi Koodiani, H.; Matamoros, A.; and Lepage, A., *Probabilistic Evaluation of Modeling Parameters for Reinforced Concrete Moment Frame Building*, Springer Nature Switzerland, 2023, pp. 80-89.

7. Sen, A.; Cook, D.; Liel, A.; Basnet, T.; Creagh, A.; Khodadadi Koodiani, H.; Berkowitz, R.; Ghannoum, W.; Hortacsu, A.; Kim, I.; Lehman, D.; Lowes, L.; Matamoros, A.; Naeim, F.; Sattar, S.; and Smith, R., "ASCE/SEI 41 Assessment of Reinforced Concrete Buildings: Benchmarking Linear Procedures and FEMA P-2018 with Empirical Damage Observations," *Earthquake Spectra*, V. 39, No. 3, 2023, pp. 1658-1682. doi: 10.1177/87552930231173454

8. Sen, A.; Cook, D.; Liel, A.; Basnet, T.; Creagh, A.; Khodadadi Koodiani, H.; Berkowitz, R.; Ghannoum, W.; Hortacsu, A.; Kim, I.; Lehman, D.; Lowes, L.; Matamoros, A.; Naeim, F.; Sattar, S.; and Smith, R., "ASCE/SEI 41 Assessment of Reinforced Concrete Buildings: Benchmarking Nonlinear Dynamic Procedures with Empirical Damage Observations," *Earthquake Spectra*, V. 39, No. 3, 2023, pp. 1721-1754. doi: 10.1177/87552930231173453

9. Trifunac, M.; Ivanovic, S.; and Todorovska, M., "Instrumented 7-Story Reinforced Concrete Building in Van Nuys, California: Description of the Damage from the 1994 Northridge Earthquake and Strong Motion Data," Report CE, V. 99, No. 2. 1999.

10. McKenna, F.; Fenves, G. L.; and Scott, M. H., "Open System for Earthquake Engineering Simulation," University of California, Berkeley, Berkeley, CA, 2000.

11. NIST GCR 12-917-21, "Soil-Structure Interaction for Building Structures," National Institute of Standards and Technology, Gaithersburg, MD, 2012, 292 pp.

12. ACI Committee 318, "Building Code Requirements for Structural Concrete (ACI 318-19) and Commentary (ACI 318R-19) (Reapproved 2022)," American Concrete Institute, Farmington Hills, MI, 625 pp.

13. Kent, D. C., and Park, R., "Flexural Members with Confined Concrete," *Journal of the Structural Division*, ASCE, V. 97, No. 7, 1971, pp. 1969-1990. doi: 10.1061/JSDEAG.0002957

14. Mander, T. J., and Matamoros, A. B., "Constitutive Modeling and Overstrength Factors for Reinforcing Steel," *ACI Structural Journal*, V. 116, No. 3, May 2019, pp. 219-232. doi: 10.14359/51713320

15. Ibarra, L. F.; Medina, R. A.; and Krawinkler, H., "Hysteretic Models that Incorporate Strength and Stiffness Deterioration," *Earthquake Engineering & Structural Dynamics*, V. 34, No. 12, 2005, pp. 1489-1511. doi: 10.1002/eqe.495

16. Altoontash, A., "Simulation and Damage Models for Performance Assessment of Reinforced Concrete Beam-Column Joints," PhD dissertation, Stanford University, Stanford, CA, 2004, 232 pp.

17. Lignos, D., "Sidesway Collapse of Deteriorating Structural Systems Under Seismic Excitations," PhD dissertation, Stanford University, Stanford, CA, 2008, 457 pp.

18. Haselton, C. B., and Liel, A. B., "Beam-Column Element Model Calibrated for Predicting Flexural Response Leading to Global Collapse of RC Frame Buildings," Pacific Earthquake Engineering Research Center, Berkeley, CA, 2008, 136 pp.

19. Hwang, S.-J., and Moehle, J. P., "Models for Laterally Loaded Slab-Column Frames," *ACI Structural Journal*, V. 97, No. 2, Mar.-Apr. 2000, pp. 345-352.

20. Kang, T. H.-K.; Wallace, J. W.; and Elwood, K. J., "Nonlinear Modeling of Flat-Plate Systems," *Journal of Structural Engineering*, ASCE, V. 135, No. 2, 2009, pp. 147-158. doi: 10.1061/(ASCE)0733-9445(2009)135:2(147)

21. Pecknold, D. A., "Slab Effective Width for Equivalent Frame Analysis," *ACI Journal Proceedings*, V. 72, No. 4, Apr. 1975, pp. 135-137.

22. Durrani, A.; Du, Y.; and Luo, Y., "Seismic Resistance of Nonductile Slab-Column Connections in Existing Flat-Slab Buildings," *ACI Structural Journal*, V. 92, No. 4, July-Aug. 1995, pp. 479-487.

23. Allen, F., and Darvall, P., "Lateral Load Equivalent Frame," *ACI Journal Proceedings*, V. 74, No. 7, July 1977, pp. 294-299.

24. Grossman, J. S., "Verification of Proposed Design Methodologies for Effective Width of Slabs in Slab-Column Frames," *ACI Structural Journal*, V. 94, No. 2, Mar.-Apr. 1997, pp. 181-196.

25. Vanderbilt, M. D., and Corley, W. G., "Frame Analysis of Concrete Buildings," *Concrete International*, V. 5, No. 12, Dec. 1983, pp. 33-43.

26. Elwood, K. J.; Matamoros, A. B.; Wallace, J. W.; Lehman, D. E.; Heintz, J. A.; Mitchell, A. D.; Moore, M. A.; Valley, M. T.; Lowes, L. N.; Comartin, C. D.; and Moehle, J. P., "Update to ASCE/SEI 41 Concrete Provisions," *Earthquake Spectra*, V. 23, No. 3, 2007, pp. 493-523. doi: 10.1193/1.2757714

27. Ghannoum, W. M., and Matamoros, A. B., "Nonlinear Modeling Parameters and Acceptance Criteria for Concrete Columns," *Seismic Assessment of Existing Reinforced Concrete Buildings*, SP-297, K. J. Elwood, J. Dragovich, and I. Kim, eds., American Concrete Institute, Farmington Hills, MI, 2014, pp. 1-24.

28. Dragovich, J. J., and Lepage, A., "FDE Index for Goodness-Of-Fit Between Measured and Calculated Response Signals," *Earthquake Engineering & Structural Dynamics*, V. 38, No. 15, 2009, pp. 1751-1758. doi: 10.1002/eqe.951

29. Lepage, A.; Hopper, M. W.; Delgado, S. A.; and Dragovich, J. J., "Best-Fit Models for Nonlinear Seismic Response of Reinforced Concrete Frames," *Engineering Structures*, V. 32, No. 9, 2010, pp. 2931-2939. doi: 10.1016/j.engstruct.2010.05.012

30. Khodadadi Koodiani, H.; Majlesi, A.; Shahriar, A.; and Matamoros, A., "Non-Linear Modeling Parameters for New Construction RC Columns," *Frontiers in Built Environment*, V. 9, 2023. doi: 10.3389/fbuil.2023.1108319

31. Khodadadi Koodiani, H.; Jafari, E.; Majlesi, A.; Shahin, M.; Matamoros, A.; and Alaeddini, A., "Machine Learning Tools to Improve Nonlinear Modeling Parameters of RC Columns," arXiv preprint, 2023. doi: 10.48550/arXiv.2303.16140

32. Charney, F. A., "Unintended Consequences of Modeling Damping in Structures," *Journal of Structural Engineering*, ASCE, V. 134, No. 4, 2008, pp. 581-592. doi: 10.1061/(ASCE)0733-9445(2008)134:4(581)

33. Islam, M. S., "Analysis of the Northridge Earthquake Response of a Damaged Non-Ductile Concrete Frame Building," *Structural Design of Tall Buildings*, V. 5, No. 3, 1996, pp. 151-182. doi: 10.1002/(SICI)1099-1794(199609)5:3<151::AID-TAL76>3.0.CO;2-4

34. Lepage, A., "A Method for Drift-Control in Earthquake-Resistant Design of Reinforced Concrete Building Structures," PhD thesis, University of Illinois, Urbana, IL, 1997.

35. Barin, B., and Pincheira, J. A., "Influence of Modeling Parameters and Assumptions on the Seismic Response of an Existing RC Building," Department of Civil and Environmental Engineering, University of Wisconsin–Madison, Madison, WI, 2002.

36. Paspuleti, C., "Seismic Analysis of an Older Reinforced Concrete Frame Structure," master's thesis, University of Washington, Seattle, WA, 2002.

37. Todorovska, M., and Trifunac, M., "Impulse Response Analysis of the Van Nuys 7-Story Hotel During 11 Earthquakes (1971-1994): One-Dimensional Wave Propagation and Inferences on Global and Local Reduction of Stiffness Due to Earthquake Damage," Report CE 06-01, Department of Civil Engineering, University of Southern California, Los Angeles, CA, 2006, 61 pp.

ACI STRUCTURAL JOURNAL TECHNICAL PAPER

Title No. 120-S92

Shear Strength Model for Steel Fiber-Reinforced Concrete Columns

by Wisena Perceka and Wen-Cheng Liao

This paper aims to propose shear strength prediction equations for steel fiber-reinforced concrete (SFRC) columns by observing mechanisms known from the test results of SFRC columns subjected to lateral cyclic and different axial loading levels. The experimental results are first compared to the shear strength models previously proposed. The comparison is emphasized on the concrete contribution because the experimental results showed that the axial loading level significantly affected the internal redistribution from concrete to shear reinforcing bars. The proposed equations are examined using experimental results of 25 SFRC columns. The average measured-to-proposed shear strength ratio is 1.02, with a standard deviation of 0.18 and a coefficient of variation (COV) of 17%. By setting the equivalent bond strength value for all cases, the accuracy drops by 11 and 17% for standard deviation and COV, respectively, with an average measured-to-proposed shear strength ratio of 1.00. The proposed equations predict the actual test data with higher accuracy compared to other equations.

Keywords: axial loading; concrete shear strength; high-strength concrete; shear strength equation; steel fiber; strength redistribution.

INTRODUCTION

The use of high-strength concrete and steel reinforcing bars can lead to the reduction of the cross-section size of a reinforced concrete (RC) member and the elimination of several reinforcing bars in the plastic hinge region.[1-3] Concrete, however, turns more brittle as its compressive strength increases[1,2,4,5]; more transverse reinforcement may be required accordingly. Nevertheless, lower-story columns with large cross-section sizes may still be required in tall buildings due to the presence of high axial compression load.[1,6,7] Meanwhile, the brittleness increases with the increase of an axial compression loading level.[1,6,7] With the limitation of the column cross-section size, adding more transverse reinforcement is the only way to improve column ductility, particularly for high-strength RC columns under high axial loading levels. The presence of more transverse reinforcement leads to the possibility of the occurrence of steel congestion. Other than that, the ACI 318 code limits the maximum shear strength provided by shear reinforcing bars against the extreme widths of the crack.[8,9] An alternative material, therefore, needs to be applied so that high-strength RC columns with a low amount of transverse reinforcement can achieve the ductility required.

Previous research studies showed that short and discontinuous steel fibers were able to be used in concrete.[1,2,4,5,10-17] The presence of steel fibers can affect concrete characteristics in improving their post-peak behavior and toughness, and RC members in improving their shear resistance, bending, and bond strength between the steel reinforcing bars and concrete.[1,2,4,5,10-17] These are caused by steel fibers' bridging action, crossing microcracks in the matrix that redistributes stress and resists crack opening.[1,2,4,5] These advantages influenced researchers to perform research on the application of steel fibers to RC members in an RC building structure located in a moderate-to-high seismic region.[15] In an RC building structure, RC members such as beam ends and bottom columns on the ground floor function as "fuses" during earthquakes. Those members shall be designed as ductile members with flexure failure governing the failure mode, for which the shear capacity shall exceed the shear demand. For shear capacity, a comprehensive study of shear behavior and design methodology is necessary. Many shear design equations for steel fiber-reinforced concrete (SFRC) beams are available in the literature.[4] By contrast, information regarding shear design equations for SFRC columns is still limited. Hence, the shear behavior of SFRC columns shall be fully understood prior to evaluating or deriving the new shear strength model.

According to the literature, only Lee[16] and Bae et al.[17] performed comprehensive experimental and analytical studies of the shear behavior of SFRC columns under lateral cyclic and axial compression loading. Lee[16] performed tests on normal-strength SFRC, while Bae et al.[17] conducted tests on high-strength SFRC columns. Their specimens were subjected to lateral displacement reversal and axial compression load with an axial ratio of 0.1. However, as the behavior of normal-strength concrete columns is different from that of high-strength concrete columns, particularly columns under high axial loading levels,[1,6,7] the applicability of the current shear strength equations needs to be further examined by using test results of high-strength SFRC columns under different axial loading level. A modification to those equations is conducted if necessary.

RESEARCH SIGNIFICANCE

The accuracy of the previous equations is unsure because those equations were proposed based on very limited test data, particularly the lack of the test results of SFRC columns made of high-strength materials. First, the results of the previous experimental study[1] are reviewed. Once the shear

ACI Structural Journal, V. 120, No. 6, November 2023.

MS No. S-2022-134.R3, doi: 10.14359/51739084, received December 13, 2022, and reviewed under Institute publication policies.

failure mechanism can be figured out, the new equations can be proposed accordingly. The new equations are compared with test data collected from previous studies.

REVIEW OF EXPERIMENTAL PROGRAM

The proposed model is developed based on experimental evidence from the tests of eight large-scale double-curvature columns under lateral cyclic and axial compression loads.[1] A brief description of the experimental program is presented, and the detail testing program and the results can be found in the literature.[1]

Specimen design and test setup

Eight large-scale double-curvature columns made of high strength concrete with steel fibers and high strength steel for longitudinal and transverse reinforcements were tested to failure on a multi-axial testing system (MATS) in the National Center Research on Earthquake Engineering (NCREE) laboratory. The detailed test setup is available in the literatures.[1,3] Figure 1 presents specimen design,[1] while detailed information on each specimen design is listed in Table 1. The steel fibers were only applied to the middle part of the specimen, while the concrete foundations (rigid blocks) were constructed using normal concrete. All the specimens were constructed with transverse reinforcement spacing exceeding code compliance for maximum spacing of transverse reinforcement to ensure the effectiveness of steel fibers in affecting the shear behavior of high-strength concrete columns.[1] Two groups of tests were defined depending on their volume content. Each group was prepared to evaluate the shear behavior of SFRC columns under axial compression load ratio ranging from 0.1 to 0.4. An investigation was extended to the evaluation of the effect of a 100% increase in fiber volume fraction (from 0.75 to 1.5%) on the shear strength and behavior of SFRC columns under the same axial compression load ratio.

The steel fiber used was a hooked-end steel fiber (Fig. 2) with a ratio of fiber length-to-fiber diameter (aspect ratio) of 79 and tensile strength of 2300 MPa (328,571 psi). The design concrete compressive strength of the middle part of the specimen was 70 MPa (10,000 psi). For both concrete foundations, the design concrete compressive strength was 40 MPa (5714 psi). All the columns (the middle part of a specimen) were longitudinally reinforced using high-strength deformed bars (SD685) with a diameter of 32 mm (1.26 in.) and were transversally reinforced using high-strength deformed bars (SD785) with a diameter of 13 mm (0.5 in.). The development length of longitudinal bars into a concrete foundation was 70 cm (27.56 in.).

Test results

Figures 3 and 4, respectively, present the lateral force-drift relationships and cracking patterns at peak lateral force for all specimens tested.[1] The measured nominal drift, the stress of shear reinforcing bar, crack angle, and shear strength components at diagonal cracking and at the maximum strength of each specimen, tested by Perceka and Liao,[1] are summarized in Table 2. The cracking stage was the stage when the appearance of first diagonal crack passing transverse reinforcement.[1] It can be seen from Table 2 that the peak strengths of columns under low axial loading levels (axial loading ratio of 0.1 and 0.2) were greater than their cracking strengths. This mechanism existed as the strength redistribution from concrete to transverse reinforcing bars occurred. After cracking, the concrete shear strength still increased up to peak lateral force. This mechanism proved that the steel fibers served as bridging action across the micro-cracks to redistribute strength after the first cracking occurred while preventing crack opening. Therefore, no premature failure occurred. The specimens under high axial loading level (axial load ratios of 0.3 and 0.4, except S3-500-0.75-0.3), on the other hand, showed that there was no difference between cracking strength and peak strength because the first diagonal crack and the specimen reached peak strength simultaneously. Only a few or no cracks appeared before specimens reached their maximum strength, where no cracks passed

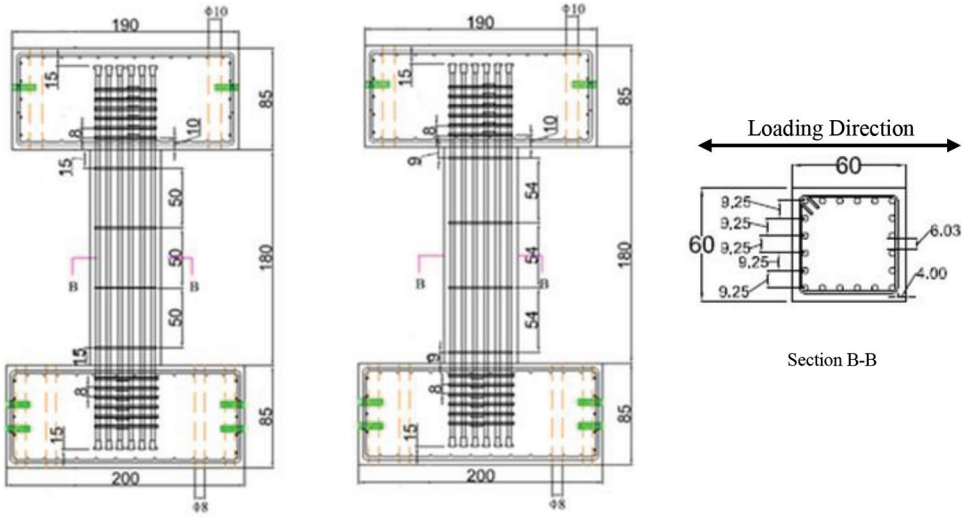

Fig. 1—(a) Specimens with fiber volume fractions of 0.75%; (b) specimens with fiber volume fractions of 1.5%; and (c) column cross section.[1] (Note: Units in cm; 1 cm = 0.39 in.)

Table 1—Details of specimen design[1]

Specimen ID	$b_c = h_c$, mm	Concrete strength	Longitudinal reinforcing bar		Transverse reinforcing bar		Steel fibers		Axial compression force, kN (Axial load ratio, $P_u/A_g f_c'$)
		$f_{c,spec}' = 70$ MPa $f_{c,test}'$, MPa	$f_{yl,spec}$ ($f_{yl,test}$), MPa	ρ_l, %	$f_{yh,spec}$ ($f_{yh,test}$), MPa	ρ_s, %	L_f/D_f	V_f, %	
S1-500-0.75-0.10	600	80.66	685 (701)	4.52 (20D32)	785 (859)	0.10 (D13-500)	79	0.75	2903.76 (0.1)
S2-500-0.75-0.20		80.07							5765.04 (0.2)
S3-500-0.75-0.30		74.43							8038.44 (0.3)
S4-500-0.75-0.40		76.79							11,057.8 (0.4)
S5-540-1.50-0.10		84.82				0.09 (D13-540)		1.50	3053.52 (0.1)
S6-540-1.50-0.20		84.76							6102.72 (0.2)
S7-540-1.50-0.30		87.48							9447.84 (0.3)
S8-540-1.50-0.40		83.51							12,025.4 (0.4)

Note: *S* is specimen; number following specimen (1 to 8) is specimen number; numbers of 500 and 540 are transverse reinforcement spacing, in mm; numbers of 0.75 and 1.50 are fiber volume fractions (0.75% and 1.50%); numbers of 0.1, 0.2, 0.3, and 0.4 denote axial load ratio; 1 MPa = 145 psi; 1 mm = 0.039 in.

Fig. 2—Presence of hooked-end steel fibers.

transverse reinforcement.[1] No strength redistribution from concrete to transverse reinforcing bars occurred because the concrete experiencing damages lost the ability to perform strength redistribution.[1]

Another mechanism observed was the increase of concrete shear strength associated with increasing axial loading level.[1] However, it can be seen from Table 2 that the increased shear strength rate decreased as the axial loading level increased. Furthermore, the test results showed that improving fiber volume fraction up to 100% (from 0.75 to 1.50%) did not result in a proportional improvement of concrete shear strength (Table 2). Besides the effect of fiber volume fraction and axial loading level on the concrete shear strength at cracking and peak strengths, the improvement of fiber volume fractions showed little effect on the stress of shear reinforcing bars. With increasing axial compression load, the stress in the shear reinforcement decreased. This also proved that little or no strength redistribution from concrete to shear reinforcement occurred for specimens under high axial loading levels.

EXAMINATION OF SHEAR STRENGTH EQUATIONS

The previous shear strength prediction equations for an SFRC member, including the equations for SFRC beams without shear reinforcement, are selected and examined herein.

Review of shear strength equations proposed by previous researchers

Lee—Lee[16] proposed shear strength prediction equations for computing the SFRC column shear strength by correlating the normalized shear strength of SFRC columns-to-normalized shear strength of RC column ratio (RSCR) and fiber volume fraction, as shown in Eq. (1a).

$$RSCR = \frac{V_{n,SFRC}}{V_{n,RC}} = 1 + 0.146\,V_f \tag{1a}$$

For columns without steel fibers, Lee[16] adopted the following equation

$$V_{RC} = V_c + V_s + V_P \tag{1b}$$

In which

$$V_c = k\sqrt{f_c'}A_e \tag{1c}$$

$$V_s = \frac{A_v f_{yh} d}{s}\cot 30° \tag{1d}$$

$$V_P = \frac{D-c}{2a}P_u \tag{1e}$$

By substituting Eq. (1c), (1d), and (1e) into Eq. (1b), and correlating between Eq. (1b) and Eq. (1a), the shear strength equation of SFRC column proposed by Lee[16] is

$$V_{n,SFRC} = \left(k\sqrt{f_c'}A_e + \frac{A_v f_{yh} d}{s}\cot 30° + \frac{D-c}{2a}P_u\right)(1 + 0.146\,V_f) \tag{1f}$$

Bae et al.—Bae et al.[17] performed tests on normal- and high-strength SFRC columns under low axial loading levels and modified the model provided in ASCE 41-13 to predict the SFRC column shear strength. The equations proposed by Bae et al.[17] are shown in Eq. (2)

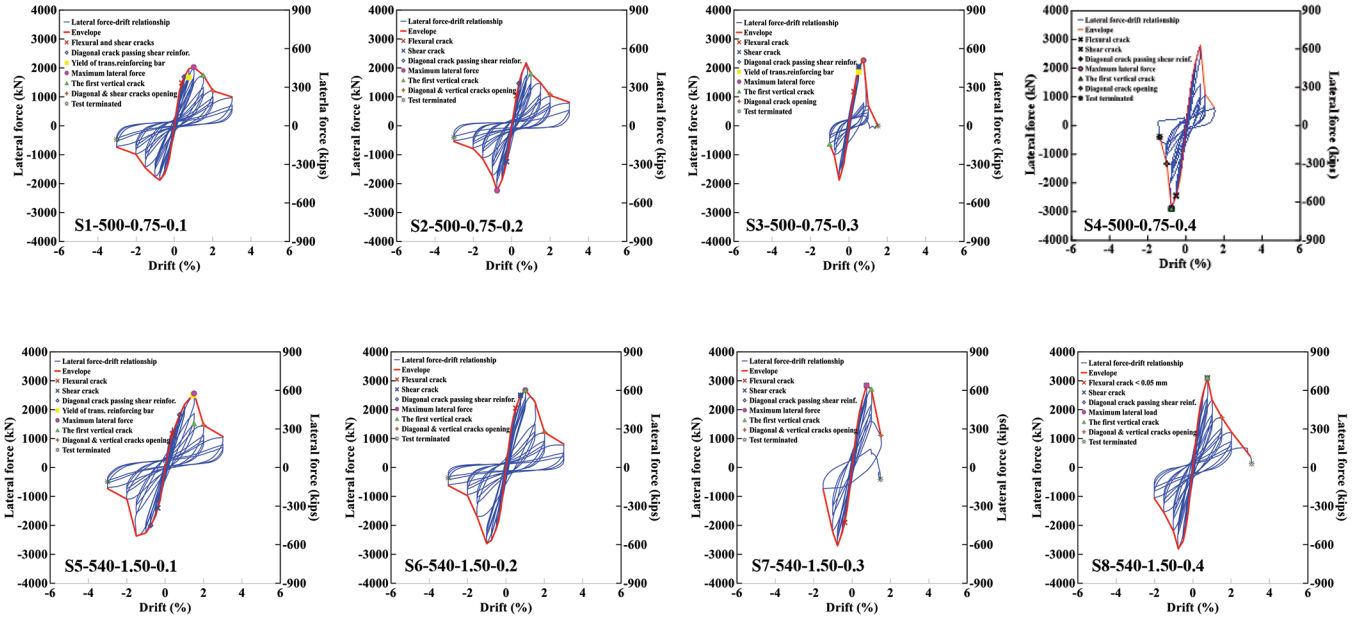

Fig. 3—Lateral force-drift relationship of specimens tested.[1]

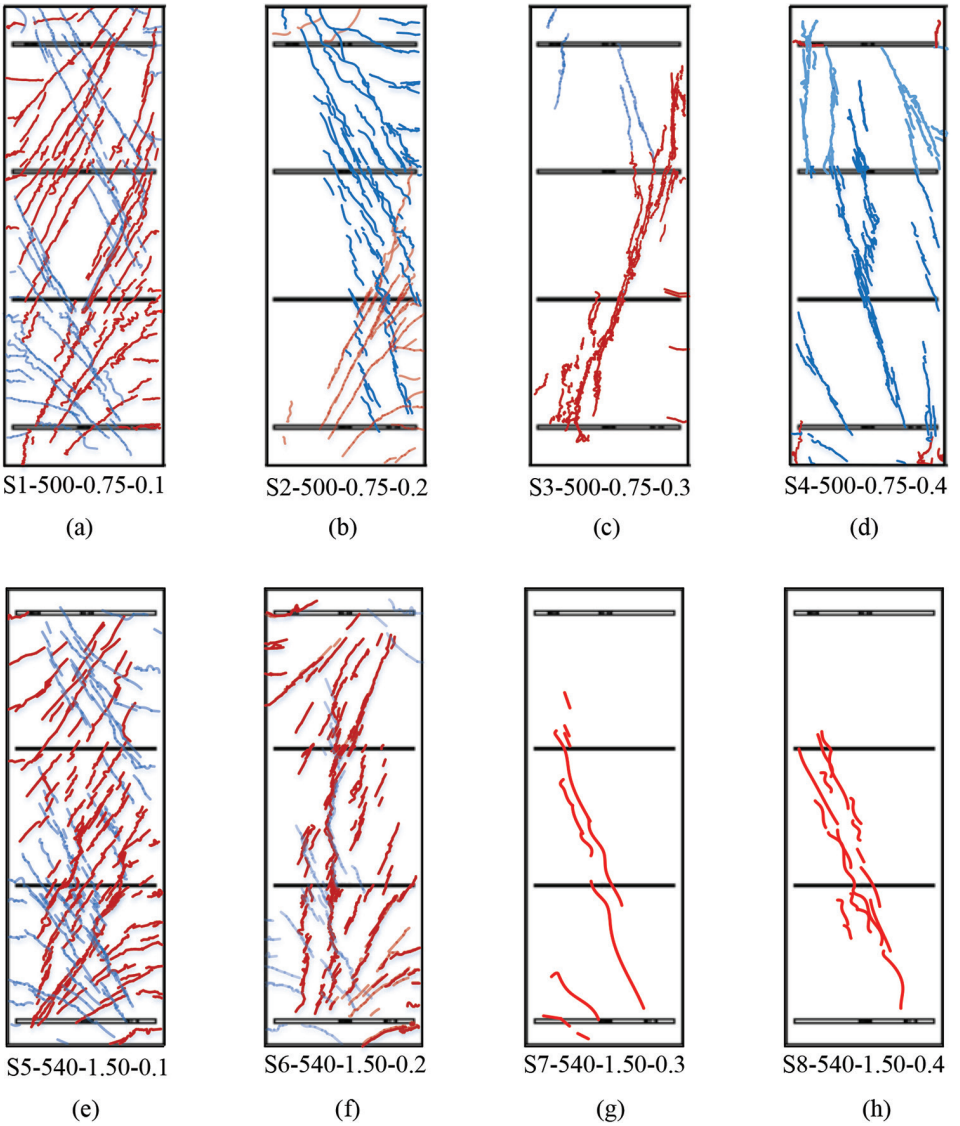

Fig. 4—Crack patterns at peak lateral force for specimens with fiber volume fraction of 0.75% (a to d) and specimens with fiber volume fraction of 1.50% (e to h).

Table 2—Nominal drift, stress of shear reinforcing bar, crack angle, and shear strength components[1]

Specimen ID	Drift, %		σ_{st}, MPa		θ, deg		$V_{s,test}$, kN		$V_{n,test}$, kN		$V_{c,test}$, kN	
	At cracking strength	At peak strength	At cracking strength	At peak strength	At cracking strength	At peak strength	At cracking strength	At peak strength	At cracking strength	At peak strength	At cracking strength	At peak strength
S1-500-0.75-0.1	0.50	1.00	82.45	859	41	32	25.53	370.01	1482.12	2027.42	1456.59	1657.41
S2-500-0.75-0.2	0.375	0.75	43.58	600.23	40	27	13.98	317.08	1465.36	2239.43	1451.38	1922.35
S3-500-0.75-0.3	0.50	0.75	141.31	302.66	20	19	104.50	236.59	2042.21	2261.99	1937.71	2025.40
S4-500-0.75-0.4	0.75	0.75	75.52	75.52	19	19	59.03	59.03	2889.27	2889.27	2830.24	2830.24
S5-540-1.50-0.1	0.75	1.50	27.19	859	45	33	7.32	329.66	1398.15	2561.86	1390.83	2232.20
S6-540-1.50-0.2	0.75	1.00	23.70	645.66	28	27	12.00	315.81	2113.61	2673.18	2101.61	2357.37
S7-540-1.50-0.3	0.75	0.75	127.89	127.89	22	22	38.90	36.02	2836.30	2836.30	2797.40	2800.28
S8-540-1.50-0.4	0.75	0.75	470.50	475.50	21	21	5.42	5.02	3099.06	3099.06	3093.64	3094.04

Note: $V_{c,SFRC,test} = V_{n,test} - V_{s,test}$, where $V_{s,test} = (A_v \cdot \sigma_{st} \cdot d/s)\cot\theta$; 1 MPa = 145 psi; 1 kN = 0.225 kip.

$$V_{c,SFRC} = (0.068 f_{sp} + 0.56)\left(\frac{f_{sp}}{M/Vd}\sqrt{1 + \frac{P_u}{f_{sp}A_g}}\right)0.8A_g \text{ (MPa)} \quad (2a)$$

$$V_{c,SFRC} = (0.068 f_{sp} + 80)\left(\frac{f_{sp}}{M/Vd}\sqrt{1 + \frac{P_u}{f_{sp}A_g}}\right)0.8A_g \text{ (psi)}$$

where the prediction equation for the splitting strength of a concrete cylinder containing steel fibers, f_{sp}, is

$$f_{sp} = \frac{f_{cuf}}{20 - \sqrt{\alpha V_f \frac{L_f}{D_f}}} + 0.7 + \sqrt{\alpha V_f \frac{L_f}{D_f}} \text{ (MPa)} \quad (2b)$$

$$f_{sp} = \frac{f_{cuf}}{20 - \sqrt{\alpha V_f \frac{L_f}{D_f}}} + 100 + 156\sqrt{\alpha V_f \frac{L_f}{D_f}} \text{ (psi)}$$

The parameter α is the bond factor determined by the shape of steel fiber that corresponds to numbers 0.5, 0.75, and 1.0 for straight, crimped, and hooked, respectively. Bae et al.[17] also used the shear strength of the shear reinforcement equation proposed by Lee.[16]

Perceka et al.—Perceka et al.[4] proposed shear strength equations for SFRC beams (not including deep beams) based on the evaluation and regression analysis of 236 beams with and without steel fibers. The concrete and steel fiber parameters were expressed in one term. That assumption was consistent with the preliminary definition in mixture design proportion for SFRC, where steel fibers were treated as aggregates in concrete material.[2,4,5] Separating concrete and steel fiber parameters may lead to a misconduct basic mechanism concept. This is because the steel fibers are assumed to be able to provide strength independently when the contribution of concrete strength drops due to damage. Hence, Perceka et al.[4] proposed an equation by expressing the multiplication between the original RC beam shear strength equation and fiber effectiveness factor. The detailed equation of ACI 318-14 was adopted by Perceka et al.[4] According to Joint ACI-ASCE Committee 326, the ACI 318-14 detailed equations were developed by involving RC beams failing in shear and diagonal tension.[4,8] The proposed equation is presented in Eq. (3a).

Figure 5 presents the comparison between beam test data and calculated shear strength using Eq. (3a). The inclined lines represent the left-hand side of Eq. (3a), while the right-hand side of Eq. (3a) presents the horizontal lines. The horizontal line was proposed to set the upper bound of the shear strength of a SFRC beam due to the limitation of beam test data.[4] Furthermore, the fiber volume fraction shall be limited to not greater than 1.5%. According to the literature, the tensile strain hardening mechanism can be achieved with a fiber volume fraction of less than 2%.[15] The fiber effectiveness factor was derived based on the regression analysis presented in Fig. 6, where the maximum value was set as 2.6. The equivalent bond strength, τ_{eq}, process calculation can be found in the literatures.[5,18]

$$V_{c,SFRC} = \left(0.16\sqrt{f_c'} + 17.2\rho_w \frac{V_u d}{M_u}\right)F_{eff} b_w d \le 0.29\sqrt{f_c'} F_{eff} b_w d \text{ (MPa)} \quad (3a)$$

$$V_{c,SFRC} = \left(1.9\sqrt{f_c'} + 2500\rho_w \frac{V_u d}{M_u}\right)F_{eff} b_w d \le 3.5\sqrt{f_c'} F_{eff} b_w d \text{ (psi)}$$

$$F_{eff} = 1 + \frac{\tau_{eq} V_f \frac{L_f}{D_f}}{0.75\sqrt{f_c'}} \text{ (MPa)} \quad (3b)$$

$$F_{eff} = 1 + \frac{\tau_{eq} V_f \frac{L_f}{D_f}}{0.11\sqrt{f_c'}} \text{ (psi)}$$

To evaluate SFRC column shear strength in this study, the equations shown in Eq. (3a) are modified by adding the original axial load parameters of the ACI 318-14 equation for concrete shear strength.[6-8] The parameter, M_u, of the left-hand side of Eq. (3a) is replaced by M_m, where M_m is shown in Eq. (3c).

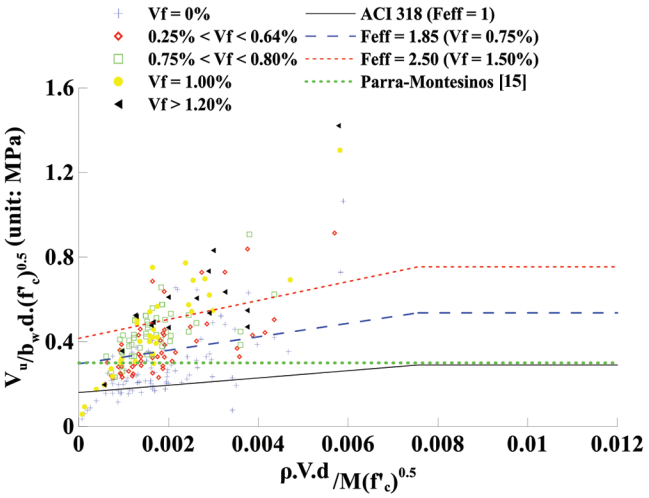

Fig. 5—Comparison between beam test data and calculated shear strength using Eq. (3a).[4]

$$M_m = M_u - P_u[(4h - d)/8] \tag{3c}$$

Meanwhile, the right-hand side of Eq. (3a) can be rewritten by including the axial load parameters for the upper limit of the ACI 318 equation for concrete shear strength.[6-8] Hence, Eq. (3a) can be rewritten as follows

$$V_{c,SFRC} = \left(0.16\sqrt{f_c'} + 17.2\rho_w \frac{V_u d}{M_u - P_u \frac{(4h-d)}{8}}\right) F_{eff} b_w d \quad \text{(MPa)}$$
$$\le 0.29\sqrt{f_c'} F_{eff} b_w d \sqrt{1 + \frac{0.29 P_u}{A_g}}$$

$$V_{c,SFRC} = \left(1.9\sqrt{f_c'} + 2500\rho_w \frac{V_u d}{M_u - P_u \frac{(4h-d)}{8}}\right) F_{eff} b_w d \quad \text{(psi)}$$
$$\le 3.5\sqrt{f_c'} F_{eff} b_w d \sqrt{1 + \frac{P_u}{500 A_g}}$$

(3d)

For an alternative, Perceka et al.[4] proposed equations by multiplying the shear strength equations for non-prestressed concrete provided in ACI 318-19[9] and fiber effectiveness factors. The following are alternative equations

For $A_v \ge A_{v,min}$

$$V_{c,SFRC} = \left(0.17\sqrt{f_c'} + \frac{P_u}{6A_g}\right) F_{eff} b_w d \quad \text{(MPa)}$$
$$V_{c,SFRC} = \left(2\sqrt{f_c'} + \frac{P_u}{6A_g}\right) F_{eff} b_w d \quad \text{(psi)} \tag{4a}$$

$$V_{c,SFRC} = \left(0.66(\rho_w)^{1/3}\sqrt{f_c'} + \frac{P_u}{6A_g}\right) F_{eff} b_w d \quad \text{(MPa)}$$
$$V_{c,SFRC} = \left(8(\rho_w)^{1/3}\sqrt{f_c'} + \frac{P_u}{6A_g}\right) F_{eff} b_w d \quad \text{(psi)} \tag{4b}$$

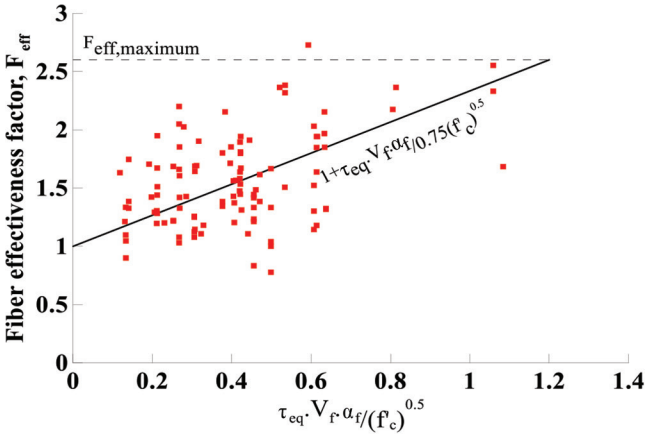

Fig. 6—Relationship between fiber effectiveness factor and normalized steel fiber parameters.[4]

For $A_v < A_{v,min}$

$$V_{c,SFRC} = \left(0.66\lambda_s(\rho_w)^{1/3}\sqrt{f_c'} + \frac{P_u}{6A_g}\right) F_{eff} b_w d \quad \text{(MPa)}$$
$$V_{c,SFRC} = \left(8\lambda_s(\rho_w)^{1/3}\sqrt{f_c'} + \frac{P_u}{6A_g}\right) F_{eff} b_w d \quad \text{(psi)} \tag{4c}$$

where

$$\lambda_s = \sqrt{\frac{2}{1 + \frac{d}{10}}} \text{ (psi)} \tag{4d}$$

Comparison between existing models of shear strength and test results

The ratio of measured-to-calculated concrete shear strength of each column specimen is presented in Table 3. The comparison is emphasized on concrete shear strength due to the presence of axial load affecting the shear strength provided by concrete instead of the shear strength provided by shear reinforcing bars. Based on the summation of concrete strength, axial load effect, and steel fibers parameters, Eq. (1f) presents the calculated strengths as less than the measured strengths with the average of measured strength-to-calculated strength ratio of 1.59. Meanwhile, the equation proposed by Bae et al. (Eq. (2a))[17] presents conservative results, where all measured concrete strength-to-calculated strength ratios are greater than 1 with an average value of 1.22. Compared to Eq. (1f), Eq. (2a) shows more precise results. The left-hand side of Eq. (3d) is not applicable to predict the concrete shear strength. The negative values of M_M indicate the small normal tensile stress caused by the moment effect. In contrast, the strengths calculated using the right-hand side of Eq. (3d) are greater than those calculated using Eq. (1f) and Eq. (2a). Hence, by using the right-hand side of Eq. (3d), the ratio of measured-to-predicted strengths is less than 1. In the calculation using modified ACI 318-19 shear strength for concrete (Eq. (4)), the results are not conservative for seven specimens, except specimen S1-500-0.75-0.1. These results demonstrate that Eq. (4) overestimates the concrete shear strength. The results

Table 3—Ratio of measured concrete shear strength-to-calculated concrete shear strength ratio of each specimen

Specimen				Concrete	Longitudinal reinforcing bar			Transverse reinforcing bar		Steel fibers			Axial load ratio	$V_{c,SFRC,test}$	$V_{c,SFRC,test}/V_{c,SFRC,1}$	$V_{c,SFRC,test}/V_{c,SFRC,2}$	$V_{c,SFRC,test}/V_{c,SFRC,3}$	$V_{c,SFRC,test}/V_{c,SFRC,4}$
ID	$b_c = h_c$, mm	d, mm	a/d	f_c', MPa	f_y, MPa	ρ_l, %	ρ_t, %	f_{yt}, MPa	ρ_s, %	L_f/d_f	V_f, %	T_{eq}, MPa						
1	2	3	4	5	6	7	8	9	10	11	12	13	14	15	16	17	18	19
S1-500-0.75-0.1[1]	600	531.2	1.69	80.71	700	4.52	3.03	859	0.100	79	0.75	8.78	0.1	1657.41	1.22	1.17	0.70	1.02
S2-500-0.75-0.2[1]	600	531.2	1.69	80.07	700	4.52	2.52	859	0.100	79	0.75	8.75	0.2	1922.35	1.21	1.09	0.64	0.81
S3-500-0.75-0.3[1]	600	531.2	1.69	74.43	700	4.52	2.52	859	0.100	79	0.75	8.54	0.3	2025.40	1.38	1.07	0.60	0.69
S4-500-0.75-0.4[1]	600	531.2	1.69	76.79	700	4.52	2.52	859	0.100	79	0.75	8.63	0.4	2830.24	2.38	1.28	0.73	0.76
S5-540-1.50-0.1[1]	600	531.2	1.69	84.82	700	4.52	3.03	859	0.092	79	1.5	8.93	0.1	2232.20	1.45	1.47	0.63	0.93
S6-540-1.50-0.2[1]	600	531.2	1.69	84.76	700	4.52	2.52	859	0.092	79	1.5	8.93	0.2	2357.37	1.30	1.23	0.53	0.67
S7-540-1.50-0.3[1]	600	531.2	1.69	87.48	700	4.52	2.52	859	0.092	79	1.5	9.03	0.3	2800.28	1.55	1.20	0.52	0.58
S8-540-1.50-0.4[1]	600	531.2	1.69	83.51	700	4.52	2.52	859	0.092	79	1.5	8.88	0.4	3094.04	2.24	1.25	0.52	0.54

Note: $V_{c,SFRC,1}$ was calculated using Eq. (1f) ($[V_c + V_p] \times [1+0.146V_f]$); $V_{c,SFRC,2}$ was calculated using Eq. (2a); $V_{c,SFRC,3}$ was calculated using Eq. (3d); $V_{c,SFRC,4}$ was calculated using Eq. (4); 1 MPa = 145 psi; 1 kN = 0.225 kip.

obtained using the right-hand side of Eq. (3d) and Eq. (4) contradict the comparison results for SFRC beams reported by Perceka et al.,[4] showing that the ratio of measured-to-calculated strengths was greater than 1. This indicates that both the axial load parameters used in the right-hand side of Eq. (3d) and axial load parameters in ACI 318-19 concrete shear strength overestimate the contribution of axial load in increasing concrete shear strength.

To observe the sensitivity of previous shear strength equations in predicting concrete shear strength, the parameters affecting shear strength are examined, where the considered parameters affecting shear strength are axial loading level and fiber volume fraction. The comparison between the previous concrete shear strength equations reviewed in this study is performed by plotting the relationship between the normalized concrete shear strength and axial load ratio, as shown in Fig. 7. The shear strength of shear reinforcement is not included. The parameters varied are concrete compressive strength with concrete strengths of 70 MPa (10,000 psi) and 100 MPa (14,286 psi) and fiber volume fraction with a volume of 0.75 and 1.5%.

Figure 7 shows that the summation of concrete and axial load parameters with the presence of steel fibers, as obtained by using Eq. (1f), decreases as the axial load ratio increases. The trend disagrees with the fact that the concrete shear strength increases as the axial load increases. Despite conservative results mathematically, separating concrete and axial load parameters can lead to a misconduct basic mechanism concept. This may define that the degradation of concrete strength and the presence of axial load is independent. The curves plotted using the equation proposed by Lee[16] also show that the proposed equation is insensitive to the improvement of fiber volume fraction and concrete compressive strength. Moreover, the effect of the improvement of fiber volume fraction on the equation proposed by Bae et al.[17] (Eq. (2a)) is negligible. On the other hand, the concrete shear strength calculated using Eq. (2a) is affected by the increase in concrete compressive strength. Furthermore, Eq. (2a) shows that the concrete shear strength increases with the increasing axial load ratio. The trend of the curve plotted using Eq. (2a) is more reasonable compared to Eq. (1f). However, Eq. (2) is too conservative because the presence of steel fibers slightly influences the concrete shear strength.

Unlike the two equations previously mentioned, the effect of the increase of fiber volume fraction on the right-hand

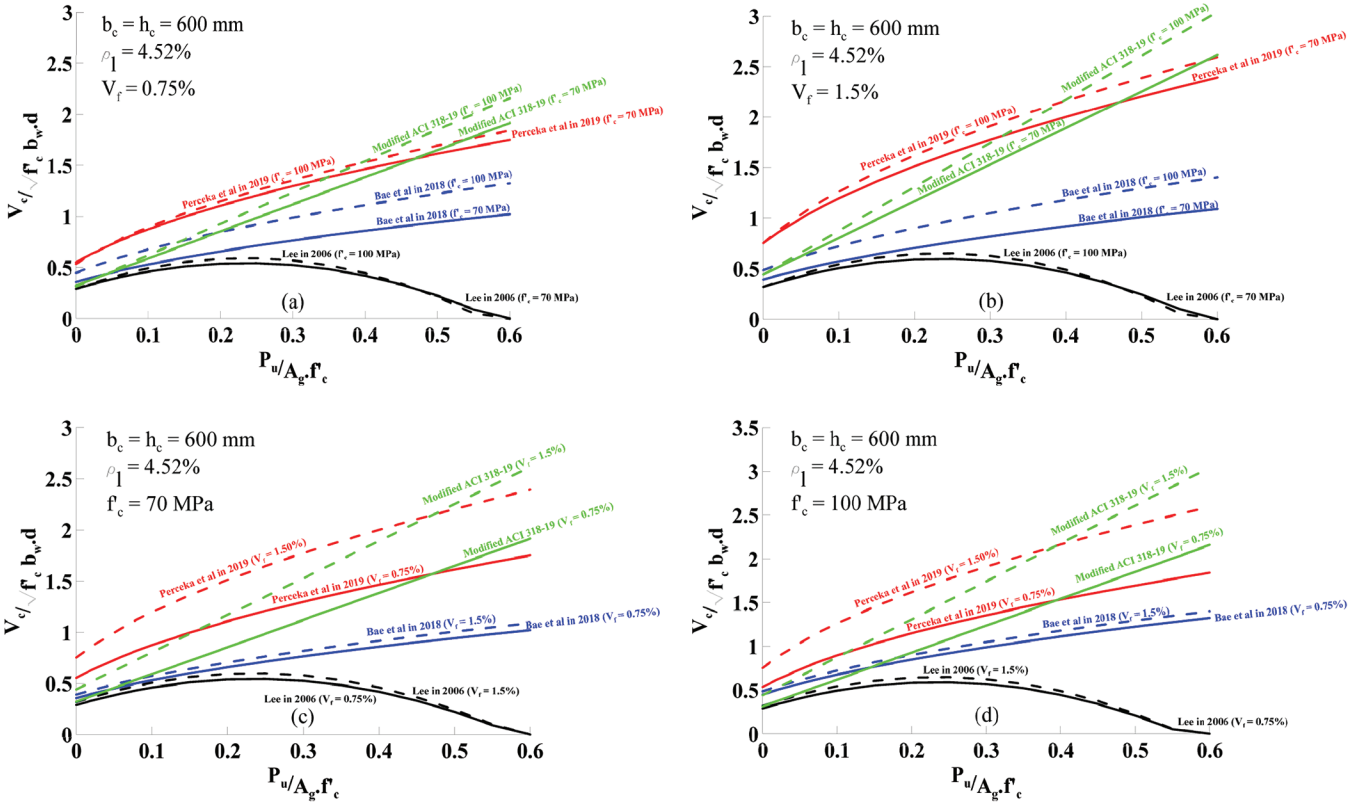

Fig. 7—Relationship between concrete shear strength prediction equations and axial load ratios for presenting: (a) and (b) effect of concrete compressive strength with constant fiber volume fraction; and (c) and (d) effect of fiber volume fraction with constant concrete compressive strength.

side of Eq. (3d) and modified ACI 318-19[9] (Eq. (4)) is clearly seen. This is caused by expressing the steel fiber and concrete parameters in one term. Also, the fiber effectiveness factor involves the bond strength between steel fiber and the surrounding cement matrix in concrete. As reported by Liao et al.,[5] the bond strength shall be considered in every SFRC calculation. Besides the effect of steel fiber volume fraction improvement, the increase of concrete compressive strength effect is shown by Eq. (3d) and Eq. (4) as well. Both the right-hand side of Eq. (3d) and modified ACI 318-19[4] show similar percentage strength improvement as proved by using Eq. (2a). Based on the examination, a new equation shall be proposed such that the results are not as conservative as the equations proposed by Lee[16] and Bae et al.,[17] while it shall not overestimate the shear strength either.

PROPOSED SHEAR STRENGTH MODEL

A new equation is proposed considering the steel fiber parameters, particularly the bond strength. Moreover, the axial load parameters are modified such that the rate of increase of concrete shear strength decreases as the axial load increases.

Force transfer mechanism

After observing damage occurring at peak strength, the force transfer mechanism of specimens under low and high axial loads differed. Figure 8 shows the free body of the fixed-fixed column. The general force transfer mechanism of specimens under low axial load tends to be similar to the force transfer mechanism in slender columns reported by Shen et al.[19] (Fig. 8(a)). The diagonal cracks of SFRC columns tended to spread from the compression zone to the specimen side that underwent tension force. The diagonal cracks in the tension side occurred due to insufficient internal support at the node; however, despite the specimen being constructed with wide shear reinforcement spacing, the cracks spread from the compression zone to the region between adjacent shear reinforcing bars in a vertical direction (internal support). This mechanism seemed to describe the presence of other shear reinforcing bars in the middle of adjacent shear reinforcing bars. These other shear reinforcing bars were actually steel fibers. This mechanism indicates that steel fibers could substitute shear reinforcement. No mechanism tended to present a compression strut between the compression zone from one column ends to another compression zone at the opposite end. Moreover, Perceka and Liao[1] reported that no concrete crushing was found in the compression zone at peak lateral force. The failure type of SFRC columns under low axial loading level was shear-tension failure.

For SFRC columns under a high axial loading level, as shown in Fig. 8(b), the force transfer mechanism can be approached using the force transfer mechanism described by Priestley et al.[20] It was reported that diagonal cracks appeared suddenly on the surface of the web of a column, in which little or no flexural or flexural shear cracks were seen.[1] That diagonal crack can be analogized and simplified as a compression strut connecting two compression

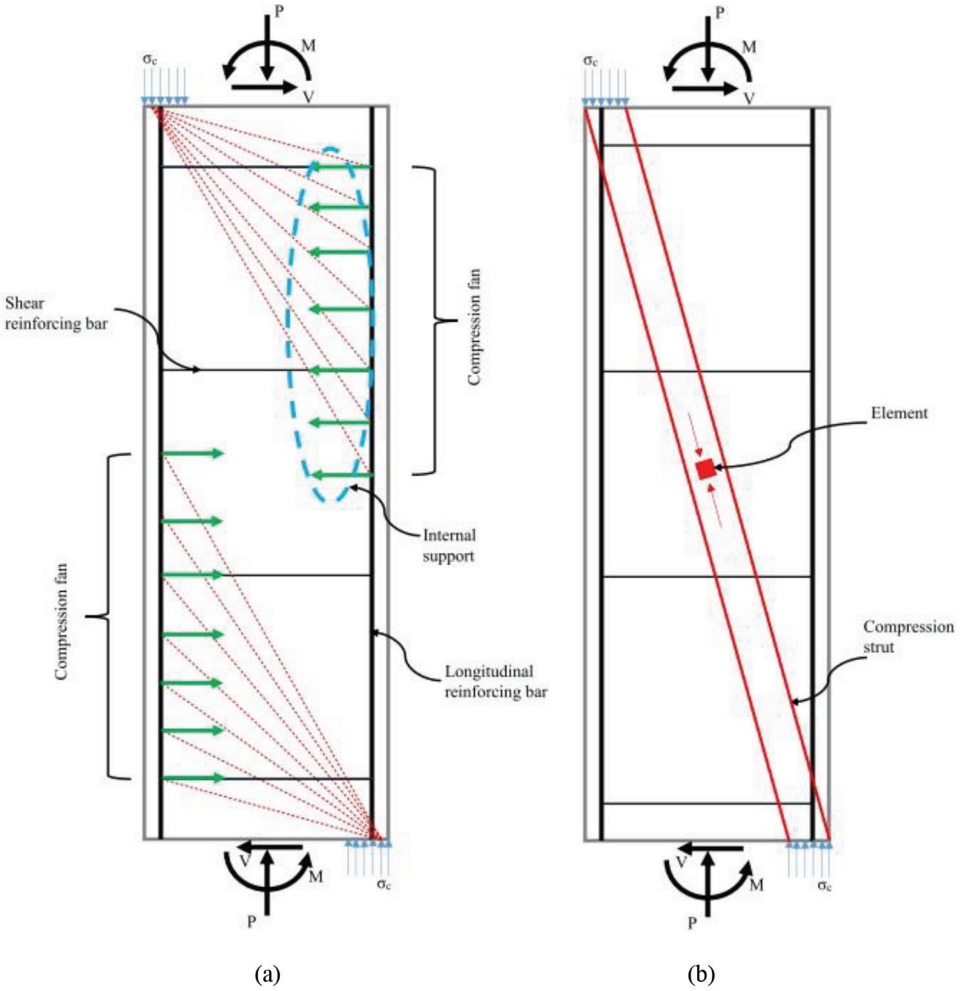

Fig. 8—Force transfer mechanism in SFRC column: (a) under low axial loading level; and (b) under high axial loading level.

zones, namely a compression zone on the top and bottom of the column. The axial compression loads operating on the column improve shear strength by generating an inclined compression strut. No concrete crushing was found in the compression zone.

Proposed shear strength equation

For shear and diagonal tension, the shear strength equation can be derived based on the shear strength equation for an RC member with shear-tension failure mode, as reported in the ACI-ASCE Committee 326 document adopted by ACI 318-14.[8] The derivation process is based on the principal stress at the point of diagonal cracking, as shown in Eq. (5a).[6,7] The axial and shear without moment were considered since the effect of the moment was assumed to be small.[6,7]

$$V_c = \frac{f_t(max)}{F_2} b_w d \sqrt{1 + \frac{P_u}{f_t(max) b_w d}} \tag{5a}$$

Because the steel fiber and concrete parameters are expressed in one term, the ratio $f_t(max)/F_2$ is set as $0.29\sqrt{f_c'}\,F_{eff}$ (MPa) or $3.5\sqrt{f_c'}\,F_{eff}$ (psi) (Fig. 5). Meanwhile, the parameter $f_t(max)$ is set to be equal to the modulus of rupture of SFRC material. It is worth mentioning that the presence of steel fibers increased the concrete modulus of rupture.[21,22] The modulus of rupture of SFRC material expressed in Eq. (5b) was derived by using regression analysis on test data shown in Fig. 9.[22] It shall be noted that if $f_t(max)$ remains $0.50\sqrt{f_c'}$ (MPa) or $6\sqrt{f_c'}$ (psi), as proposed by Ou and Kurniawan,[7] the ratio $P_u/f_t(max)b_w d$ may lead the concrete shear strength to increase significantly.

$$\frac{f_{r,SFRC}}{\sqrt{f_c'}} = \left(0.5 + 1.03\frac{\tau_{eq} V_f \frac{L_f}{D_f}}{\sqrt{f_c'}}\right) \text{(MPa)}$$
$$\frac{f_{r,SFRC}}{\sqrt{f_c'}} = \left(6 + 1.03\frac{\tau_{eq} V_f \frac{L_f}{D_f}}{\sqrt{f_c'}}\right) \text{(psi)} \tag{5b}$$

The test data used in the derivation process of Eq. (5b) is limited to a fiber volume fraction of 1.5%, while the maximum value of Eq. (5b) shall not be greater than 1.7 due to the limitation of test data. By substituting Eq. (5b) into Eq. (5a) and setting $f_t(max)/F_2$ as $0.29\sqrt{f_c'}F_{eff}$ (MPa) or $3.5\sqrt{f_c'}F_{eff}$ (psi), Eq. (5a) turns Eq. (5c) as follows

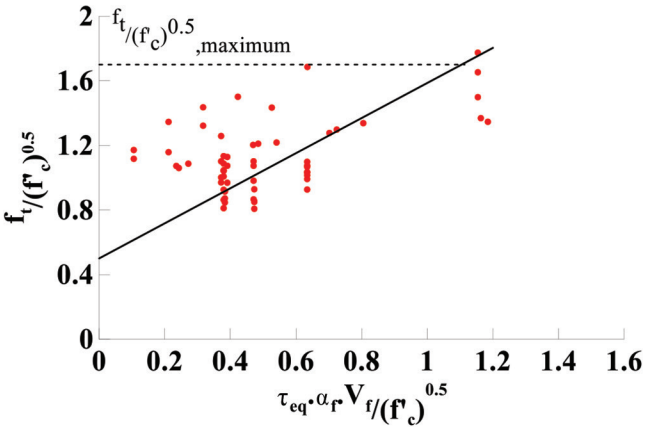

Fig. 9—Relationship between normalized modulus of rupture and normalized steel fiber parameters.[22]

$$V_{c,SFRC} = 0.29\sqrt{f'_c}F_{eff}b_w d\sqrt{1+\frac{P_u}{\left(0.5+1.03\dfrac{\tau_{eq}V_f\dfrac{L_f}{D_f}}{\sqrt{f'_c}}\right)\sqrt{f'_c}b_w d}}\ \text{(MPa)}$$

$$V_{c,SFRC} = 3.5\sqrt{f'_c}F_{eff}b_w d\sqrt{1+\frac{P_u}{\left(6+1.03\dfrac{\tau_{eq}V_f\dfrac{L_f}{D_f}}{\sqrt{f'_c}}\right)\sqrt{f'_c}b_w d}}\ \text{(psi)} \quad (5c)$$

Similar to high-strength RC columns without steel fibers,[6,7] even though the strength of concrete in the SFRC column increased with increasing axial compression load, the rate of increase of shear strength tends to decrease.[1] In this study, a reduction factor (Eq. (5d)) to reduce the principal tensile strength caused by the presence of compressive stress acting in the other principal direction[7] is adopted.

$$\sigma_t = \alpha f_t \quad (5d)$$

The reduction factor for principal tensile strength was limited up to 0.6 because the largest axial compression load ratio in the column test data collected was 0.6. Equation (5e) shows the reduction factor α

$$\alpha = \left(1 - 0.85\sqrt{\frac{P_u}{f_c' A_g}}\right) \text{ for } 0 \le \frac{P_u}{f_c' A_g} \le 0.6 \quad (5e)$$

Because of the limitation of test data, it is assumed that the behavior of ordinary high-strength concrete and high-strength concrete with steel fibers under biaxial loading conditions remains the same. This assumption is based on the fact that the rate of increase of both normal concrete and SFRC shear strength tends to decrease with increasing axial compression load. Therefore, the use of the reduction factor shown in Eq. (5e) is acceptable to be applied in the SFRC column. The final equation of concrete shear strength with steel fibers shown in Eq. (5f) is provided by substituting Eq. (5e) into Eq. (5d) and setting σ_t to be equal to $f_t(max)$.

$$V_{c,SFRC} = 0.29\alpha\sqrt{f'_c}F_{eff}b_w d\sqrt{1+\frac{P_u}{\alpha\left(0.5+1.03\dfrac{\tau_{eq}V_f\dfrac{L_f}{D_f}}{\sqrt{f'_c}}\right)\sqrt{f'_c}b_w d}}\ \text{(MPa)}$$

$$V_{c,SFRC} = 3.5\alpha\sqrt{f'_c}F_{eff}b_w d\sqrt{1+\frac{P_u}{\alpha\left(6+1.03\dfrac{\tau_{eq}V_f\dfrac{L_f}{D_f}}{\sqrt{f'_c}}\right)\sqrt{f'_c}b_w d}}\ \text{(psi)} \quad (5f)$$

To calculate the SFRC column shear strength, the shear strength provided by concrete is taken as the smaller of the left-hand side of Eq. (3d) and (5f). To simplify the calculation process, the equivalent bond strength originally derived based on micromechanical modeling for hooked-end steel fiber in a cement-based matrix[5,18] is set as 8 MPa (1143 psi) regardless of the length, diameter, and tensile strength of hooked-end steel fiber. This value is taken based on the average value of the bond strength of steel fiber in concrete with f'_c of 40 MPa (5714 psi).[4] Thus, Eq. (5f) can be rewritten and shown in Eq. (5g). When the calculation is performed using the left-hand side of Eq. (3d), the bond strength of 8 MPa (1143 psi) can be substituted into Eq. (3b).

$$V_{c,SFRC} = 0.29\alpha\sqrt{f'_c}\left(1+\frac{11V_f\dfrac{L_f}{D_f}}{\sqrt{f'_c}}\right)b_w d\sqrt{1+\frac{P_u}{\alpha\left(0.5+8.24\dfrac{V_f\dfrac{L_f}{D_f}}{\sqrt{f'_c}}\right)\sqrt{f'_c}b_w d}}\ \text{(MPa)}$$

$$V_{c,SFRC} = 3.5\alpha\sqrt{f'_c}\left(1+\frac{10,391V_f\dfrac{L_f}{D_f}}{\sqrt{f'_c}}\right)b_w d\sqrt{1+\frac{P_u}{\alpha\left(6+1,177\dfrac{V_f\dfrac{L_f}{D_f}}{\sqrt{f'_c}}\right)\sqrt{f'_c}b_w d}}\ \text{(psi)} \quad (5g)$$

For the shear strength provided by shear reinforcing bars, the equation provided in ACI 318 for the shear strength of shear reinforcement with a crack angle degree of 45 is used. By considering the stress of shear reinforcement tending to decrease with increasing axial loading level, using steel stress equal to the specified or actual yield stress of shear reinforcing bars (SD685 or SD785) can overestimate the shear strength provided by shear reinforcement. Hence, Liao et al.[3] used the stress in a shear reinforcing bar not greater than 600 MPa (85,714 psi) and a crack angle of 45 degrees for computing the shear strength provided by shear reinforcement in a high-strength RC column. The equation is presented in Eq. (6).

$$V_s = (A_v f_{sh} d)/s \quad (6)$$

Table 4—Ratio of measured-to-calculated shear strengths of collected database

Specimen				Concrete	Longitudinal reinforcing bar			Transverse reinforcing bar		Steel fibers			Axial load ratio					
ID	$b_c = h_c$, mm	d, mm	a/d	f_c', MPa	f_{yl}, MPa	ρ_l, %	ρ_w, %	f_{yt}, MPa	ρ_s, %	L_f/d_f	V_f, %	τ_{eq}, MPa		$V_{n,test}$	$V_{n,test}/V_{n1}$	$V_{n,test}/V_{n2}$	$V_{n,test}/V_{n3}$	$V_{n,test}/V_{n4}$
1	2	3	4	5	6	7	8	9	10	11	12	13	14	15	16	17	18	19
S1-500-0.75-0.1[1]	600	531.2	1.69	80.71	700	4.52	3.03	859	0.100	79	0.75	8.78	0.1	2027.42	1.22	1.20	1.14	1.16
S2-500-0.75-0.2[1]	600	531.2	1.69	80.07	700	4.52	2.52	859	0.100	79	0.75	8.75	0.2	2239.43	1.18	1.09	1.14	1.15
S3-500-0.75-0.3[1]	600	531.2	1.69	74.43	700	4.52	2.52	859	0.100	79	0.75	8.54	0.3	2261.99	1.23	1.04	1.12	1.13
S4-500-0.75-0.4[1]	600	531.2	1.69	76.79	700	4.52	2.52	859	0.100	79	0.75	8.63	0.4	2889.27	1.93	1.16	1.35	1.36
S5-540-1.50-0.1[1]	600	531.2	1.69	84.82	700	4.52	3.03	859	0.092	79	1.5	8.93	0.1	2561.86	1.38	1.44	1.12	1.16
S6-540-1.50-0.2[1]	600	531.2	1.69	84.76	700	4.52	2.52	859	0.092	79	1.5	8.93	0.2	2673.18	1.26	1.23	1.09	1.12
S7-540-1.50-0.3[1]	600	531.2	1.69	87.48	700	4.52	2.52	859	0.092	79	1.5	9.03	0.3	2836.295	1.34	1.10	1.08	1.11
S8-540-1.50-0.4[1]	600	531.2	1.69	83.51	700	4.52	2.52	859	0.092	79	1.5	8.88	0.4	3099.06	1.83	1.13	1.18	1.20
HSC-V1[17]	400	332	2.41	64.80	593.7	3.97	2.98	570.6	0.120	60	1	7.69	0.1	608.00	0.89	1.19	1.01	0.98
HSC-V2[17]	400	332	2.41	67.60	593.7	3.97	2.98	570.6	0.120	60	2	7.81	0.1	632.00	0.80	1.19	0.76	0.74
HSC-TV1[17]	400	332	2.41	64.80	593.7	3.97	2.98	570.6	0.49	60	1	7.69	0.1	782.99	0.83	1.07	1.14	1.12
NSC-V1[17]	400	332	2.41	35.60	593.7	3.97	2.98	570.6	0.12	60	1	6.41	0.1	398.09	0.73	1.14	0.78	0.71
NSC-TV1[17]	400	332	2.41	35.60	593.7	3.97	2.98	570.6	0.49	60	1	6.41	0.1	587.58	0.73	1.03	0.98	0.91
Specimen				Concrete	Longitudinal reinforcing bar			Transverse reinforcing bar		Steel fibers			Axial load ratio					
ID	$b_c = h_c$, mm	d, mm	a/d	f_c', MPa	f_{yl}, MPa	ρ_l, %	ρ_t, %	f_{yt}, MPa	ρ_s, %	L_f/d_f	V_f, %	τ_{eq}, MPa		$V_{n,test}$	$V_{n,test}/V_{n1}$	$V_{n,test}/V_{n2}$	$V_{n,test}/V_{n3}$	$V_{n,test}/V_{n4}$
1	2	3	4	5	6	7	8	9	10	11	12	13	14	15	16	17	18	19
[16]	300	240.5	1.50	61	420	3.14	2.36	420	0.26	60	1	7.19	0.1	419.00	0.75	0.80	1.22	1.18
	300	240.5	1.50	61	420	3.14	2.36	420	0.26	60	1.5	7.19	0.1	444.00	0.75	0.85	1.15	1.10
	300	240.5	1.50	68	420	3.14	2.36	420	0.26	60	2	7.47	0.1	450.00	0.69	0.80	1.02	0.98
	300	240.5	1.50	61	420	3.14	2.36	420	0.21	60	1	7.19	0.1	427.00	0.84	0.90	1.35	1.30
	300	240.5	1.50	61	420	3.14	2.36	420	0.21	60	1.5	7.19	0.1	403.00	0.75	0.84	1.11	1.05
	300	240.5	1.50	68	420	3.14	2.36	420	0.21	60	2	7.47	0.1	410.00	0.69	0.79	0.97	0.93
	300	240.5	1.50	27	420	3.14	2.36	420	0.26	60	1	5.62	0.1	228.00	0.51	0.64	0.77	0.69
	300	240.5	1.50	28	420	3.14	2.36	420	0.26	60	1.5	5.67	0.1	270.00	0.56	0.74	0.81	0.75
	300	240.5	1.50	25	420	3.14	2.36	420	0.26	60	2	5.51	0.1	322.00	0.64	0.92	0.93	0.93
	300	240.5	1.50	27	420	3.14	2.36	420	0.21	60	1	5.62	0.1	218.00	0.55	0.70	0.80	0.71
	300	240.5	1.50	28	420	3.14	2.36	420	0.21	60	1.5	5.67	0.1	239.00	0.56	0.75	0.77	0.71
	300	240.5	1.50	25	420	3.14	2.36	420	0.21	60	2	5.51	0.1	262.00	0.60	0.86	0.81	0.81

Note: V_{n1} calculated using Eq. (1f); V_{n2}: V_c (Eq. (2a)) + V_s (from Eq. (1f)); V_{n3}: min ($V_{c,SFRC}$ [left-hand side of Eq. (3d)]) $V_{c,SFRC}$ (Eq. (5f)) + V_s(Eq.6); V_{n4}: Min ($V_{c,SFRC}$ [left-hand side of Eq. (3d)]) $V_{c,SFRC}$ (Eq. (5g)) + V_s (Eq.6); 1 MPa = 145 psi; 1 kN = 0.225 kip.

ASSESSMENT OF PROPOSED EQUATIONS USING COLUMN TEST DATA

To observe the accuracy of the proposed equations, the ratio of measured-to-predicted strengths of the collected database is summarized in Table 4. The average of measured-to-proposed shear strength ratios is 1.02, with a standard deviation of 0.18 and a coefficient of variation (COV) of 17%. With the use of the equivalent bond strength of 8 MPa (1143 psi) for all cases, the accuracy drops by 11% and 17% for standard deviation and COV, respectively, where the average of measured-to-proposed shear strength ratios is 1.00. Despite the loss of accuracy compared to the comparison results

using the equations previously proposed, the new equation still tends to be more accurate. A low standard deviation value indicates that the data do not spread out and are clustered around the mean value. A similar meaning is proved by the value of COV, in which the low value of COV means the proposed equations predict the actual test data with high accuracy. Moreover, it is known that the proposed equation is applicable to normal-strength SFRC columns. An illustrative example of the application of proposed equations to calculate the shear strength of the SFRC column is presented in Appendix A,* in which, the cross section designed is shown in Fig. 10 of Appendix A.

CONCLUSIONS

The shear behavior of steel fiber-reinforced concrete (SFRC) columns was reviewed to understand the failure mechanism. Previous shear strength models are examined and evaluated using experimental results prior to proposing the shear strength model as well. Therefore, the following conclusions can be drawn.

1. The observation has empathized with the concrete contribution because the presence of axial load affected the concrete shear strength instead of the shear strength of shear reinforcement. This is supported by the fact that the internal force in the shear reinforcing bar decreased as the axial load increased.

2. The comparison between measured and calculated concrete shear strength shows that the equation proposed by Lee[16] and Bae et al.[17] is conservative, with the average measured strength-to-calculated strength ratio of 1.59 and 1.40, respectively. The latter shows more reasonable results. On the other hand, involving axial load parameters from ACI 318 code for equations proposed by Perceka et al.[4] can overestimate the measured concrete strength.

3. Prior to proposing a shear strength model, the effect of concrete compressive strength and fiber volume fraction on each previous equation is examined. This study shows that the trend of curved plotted using the equation provided by Lee[16] contradicts the fact that the concrete shear strength increases as the axial load increases since the term containing axial load turns smaller as the axial load increases higher. In addition, the curves plotted using the equation proposed by Lee[16] tend to prove that the equation is not sensitive to the improvement of fiber volume fraction and concrete compressive strength.

4. The concrete shear strength calculated using the equation proposed by Bae et al.[17] is affected by the increase in concrete compressive strength. Furthermore, the proposed equations agree with the fact that the concrete shear strength increases with the increasing axial load. However, the trend of the curve tends to indicate that the improvement of fiber volume fraction has little effect on the concrete shear strength.

5. By expressing the steel fiber and concrete parameters in one term, the detailed equation (the right-hand side of Eq. (3d)) and the modified ACI 318-19 (Eq. (4)) are not only affected by the axial load parameters but also are affected by the increase of fiber volume fraction. The results show that involving the fiber effectiveness factor is reasonable because all steel fiber parameters, particularly the bond strength between steel fiber and concrete matrix, have been considered.

6. The new equation is proposed based on the principal stress at the point of diagonal cracking by considering axial and shear without moment since the effect of the moment can be neglected as the axial compression load increases. To address the decrease of the rate of concrete shear strength with the increasing of axial load, an equation to reduce the principal tensile strength caused by the presence of compressive stress acting in the other principal direction is used. In addition, the equation for predicting the modulus of rupture of SFRC shall be substituted to not overestimate the effect of axial load.

7. To observe the accuracy of the proposed equations, 25 test specimens are compared to the results obtained using the proposed equation. The average of measured-to-proposed nominal shear strength ratios is 1.02, with a standard deviation of 0.18 and a coefficient of variation (COV) of 17%. Using constant equivalent bond strength value for all cases leads the accuracy to drop by 11% and 17% for standard deviation and COV, respectively, while the average of measured-to-proposed shear strength ratios is 1.00. Therefore, the proposed equations predict the actual test data with higher accuracy compared to other equations.

AUTHOR BIOS

Wisena Perceka *is an Assistant Professor in the Department of Civil Engineering at Parahyangan Catholic University, Bandung, Indonesia. He received his BS from Parahyangan Catholic University; his MS from Bandung Institute of Technology, Bandung, Indonesia; and his PhD from National Taiwan University, Taipei, Taiwan. His research interests include high-performance concrete, fiber-reinforced concrete, reinforced concrete structures, prestressed concrete, bridge engineering, and earthquake-resistant design of steel and reinforced concrete structures.*

ACI member **Wen-Cheng Liao** *is a Professor in the Department of Civil Engineering at National Taiwan University, Taiwan, where he received his BS and MS. He received his PhD from the University of Michigan, Ann Arbor, MI. He is the Director of the Taiwan Concrete Institute (TCI) and the Secretary/Treasurer of the American Concrete Institute (ACI) Taiwan Chapter. His research interests include high-performance concrete, fiber-reinforced concrete, and seismic-resistant reinforced concrete structure design.*

ACKNOWLEDGMENTS

This research was sponsored by the Ministry of Science and Technology (MOST), Taiwan, under Grant No. 110-2224-E-002 -009. The authors would like to thank the National Center for Research on Earthquake Engineering (NCREE) and S.-J. Hwang from the Department of Civil Engineering at National Taiwan University. The opinions expressed in this paper are those of the authors and do not necessarily reflect the views of the sponsor.

NOTATION

A_e = effective shear area (Eq. (1c), (1f))
A_g = gross section area (Eq. (2a))
A_v = total area of transverse reinforcing bars parallel to loading direction (Eq. (1d), (1f))
$A_{v,min}$ = minimum transverse reinforcement area that should be provided in RC column (Eq. (4))
a = shear span (Eq. (1e-f))
b_c = column specimen section width (Table 1)
b_w = section width (Eq. (3a), (3d), (4a-c), (5a), (5c), (5f-g))

*The Appendix is available at **www.concrete.org/publications** in PDF format, appended to the online version of the published paper. It is also available in hard copy from ACI headquarters for a fee equal to the cost of reproduction plus handling at the time of the request.

c = depth of compression zone on column section (Eq. (1e-f))
D = depth of column section (Eq. (1e-f))
D_f = steel fiber diameter (Eq. (2b), (3b), (5b-c), (5f-g))
d = effective depth of column section (Eq. (1d), (1f), (3a), (3d), (4a-d), (5a), (5c), (5f-g))
F_{eff} = fiber effectiveness factor (Eq. (3a-b))
F_2 = shear stress at cracking point-to-average shear stress of effective cross section ratio (Eq. (5a))
f_c' = specified concrete compressive strength (Eq. (1c), (1f), (3a-b), (3d), (4a-c), (5b-c), (5d), (5e), (5f-g))
f_{cuf} = cube compressive strength of fiber-reinforced concrete material (Eq. (2b))
$f_{r,SFRC}$ = modulus of rupture of SFRC (Eq. (5b))
f_{sh} = stress of transverse reinforcement for analysis and design (Eq. (6)), (limited to 600 MPa [86 ksi])
f_{sp} = modified cube compressive strength after considering fiber parameters (Eq. (2a-b))
f_t = principal tensile strength of concrete (Eq. (5a), (5d))
f_{yh} = specified yield stress of transverse reinforcement (Eq. (1d), (1f))
h = column section height (Eq. (3c-d))
h_c = column specimen section height (Table 1)
k = factor of flexural ductility on concrete shear capacity ($\sqrt{0.29}$ (MPa) [$\sqrt{3.5}$ (psi)]) (Eq. (1c), (1f))
L_f = steel fiber length (Eq. (2b), (3b), (5b-c), (5f-g))
M_m = modified factored moment after considering axial compression force (Eq. (3c))
M_u = moment corresponding to applied axial compression force (Eq. (3c-d))
M/Vd = shear span-to-effective depth ratio (= a/d) (Eq. (2a))
P_u = axial compression force (Eq. (1e-f), (2a), (3d))
s = transverse reinforcement spacing (Eq. (1d), (1f))
V_c = shear strength provided by concrete (Eq. (1b-c))
$V_{c,SFRC}$ = concrete shear strength of SFRC column (Eq. (2a), (3a), (3d), (5f-g))
Vd/M = inverse of shear span-to-effective depth ratio (= d/a) (Eq. (3b))
V_f = fiber volume fraction (Eq. (1a) [in percent], (1f) [in percent], (2b), (3b), (5b))
$V_{n,RC}$ = nominal shear strength of RC column (Eq. (1a-b))
$V_{n,SFRC}$ = nominal shear strength of SFRC column (Eq. (1a), (1f))
V_p = shear strength improvement by axial compression force (Eq. (1e))
V_s = shear strength provided by transverse reinforcement (Eq. (1d), (6))
α = bond factor determined by shape of steel fiber (Eq. (2b)); reduction factor for principal tensile strength due to presence of compressive stress acting in other principal direction (Eq. (5d-e))
λ_s = factor used to modify shear strength based on effect of member depth (Eq. (4d))
θ = shear crack angle to column longitudinal axis (Table 2)
ρ_l = longitudinal reinforcement ratio (Tables 1, 3, and 4)
ρ_s = transverse reinforcement ratio (Eq. (3a))
ρ_w = tensile longitudinal reinforcement ratio (Eq. (3a))
σ_{st} = measured stress of shear reinforcing bar (Table 2)
σ_t = reduced concrete principal tensile strength due to presence of compressive stress acting in other principal direction (Eq. (5d))
τ_{eq} = equivalent bond strength (Eq. (3b), (5b-c), (5f))

REFERENCES

1. Perceka, W., and Liao, W.-C., "Experimental Study of Shear Behavior of High Strength Steel Fiber Reinforced Concrete Columns," *Engineering Structures*, V. 240, 2021, pp. 1-16. doi: 10.1016/j.engstruct.2021.112329

2. Perceka, W.; Liao, W. C.; and Wang, Y. D., "High Strength Concrete Columns under Axial Compression Load: Hybrid Confinement Efficiency of High Strength Transverse Reinforcement and Steel Fibers," *Materials (Basel)*, V. 9, No. 4, 2016, p. 264. doi: 10.3390/ma9040264

3. Liao, W.-C.; Perceka, W.; and Wang, M., "Experimental Study of Cyclic Behavior of High- Strength Reinforced Concrete Columns with Different Transverse Reinforcement Detailing Configurations," *Engineering Structures*, V. 153, 2017, pp. 290-301. doi: 10.1016/j.engstruct.2017.10.011

4. Perceka, W.; Liao, W.-C.; and Wu, Y.-F., "Shear Strength Prediction Equations and Experimental Study of High Strength Steel Fiber-Reinforced Concrete Beams with Different Shear Span-to-Depth Ratios," *Applied Sciences (Basel, Switzerland)*, V. 9, No. 22, 2019, p. 4790. doi: 10.3390/app9224790

5. Liao, W. C.; Perceka, W.; and Liu, E. J., "Compressive Stress-Strain Relationship of High Strength Steel Fiber Reinforced Concrete," *Journal of Advanced Concrete Technology*, V. 13, No. 8, 2015, pp. 379-392. doi: 10.3151/jact.13.379

6. Ou, Y.-C., and Kurniawan, D. P., "Shear Behavior of Reinforced Concrete Columns with High-Strength Steel and Concrete," *ACI Structural Journal*, V. 112, No. 1, Jan.-Feb. 2015, pp. 35-46. doi: 10.14359/51686822

7. Ou, Y.-C., and Kurniawan, D. P., "Effect of Axial Compression on Shear Behavior of High-Strength Reinforced Concrete Columns," *ACI Structural Journal*, V. 112, No. 2, Mar.-Apr. 2015, pp. 209-220. doi: 10.14359/51687300

8. ACI Committee 318, "Building Code Requirements for Structural Concrete (ACI 318-14) and Commentary (318R-14)," American Concrete Institute, Farmington Hills, MI, 2014, 520 pp.

9. ACI Committee 318, "Building Code Requirements for Structural Concrete (ACI 318-19) and Commentary (318R-19)," American Concrete Institute, Farmington Hills, MI, 2019, 520 pp.

10. Ezeldin, A. S., and Balaguru, P. N., "Normal and High Strength Fiber Reinforced Concrete under Compression," *Journal of Materials in Civil Engineering*, ASCE, V. 4, No. 4, 1992, pp. 415-429. doi: 10.1061/(ASCE)0899-1561(1992)4:4(415)

11. Hsu, L. S., and Hsu, C. T., "Stress-Strain Behavior of Steel-Fiber High-Strength Concrete under Compression," *ACI Structural Journal*, V. 91, No. 4, July-Aug. 1994, pp. 448-457. doi: 10.14359/4152

12. Mansur, M. A.; Chin, M. S.; and Wee, T. H., "Stress-Strain Relationship of High Strength Fiber Concrete in Compression," *Journal of Materials in Civil Engineering*, ASCE, V. 11, No. 1, 1999, pp. 21-29. doi: 10.1061/(ASCE)0899-1561(1999)11:1(21)

13. Ou, Y. C.; Tsai, M. S.; Liu, K. Y.; and Chang, K. C., "Compressive Behavior of Steel Fiber Reinforced Concrete with a High Reinforcing Index," *Journal of Materials in Civil Engineering*, ASCE, V. 24, No. 2, 2012, pp. 207-215. doi: 10.1061/(ASCE)MT.1943-5533.0000372

14. Thomas, J., and Ramaswamy, A., "Mechanical Properties of Steel Fiber-Reinforced Concrete," *Journal of Materials in Civil Engineering*, ASCE, V. 19, No. 5, 2007, pp. 385-392. doi: 10.1061/(ASCE)0899-1561(2007)19:5(385)

15. Parra-Montesinos, G. J., "High-Performance Fiber-Reinforced Cement Composites: An Alternative for Seismic Design of Structures," *ACI Structural Journal*, V.102, No. 5, Sept.-Oct. 2005, pp. 668-675. doi: 10.14359/14662

16. Lee, H. H., "Shear Strength and Behavior of Steel Fiber Reinforced Concrete Columns under Seismic Loading," *Engineering Structures*, V. 29, No. 7, 2007, pp. 1253-1262. doi: 10.1016/j.engstruct.2006.08.016

17. Bae, B. I.; Chung, J. H.; Choi, H. K.; Jung, H. S.; and Choi, C. S., "Experimental Study on the Cyclic Behavior of Steel Fiber Reinforced High Strength Concrete Columns and Evaluation of Shear Strength," *Engineering Structures*, V. 157, 2018, pp. 250-267. doi: 10.1016/j.engstruct.2017.11.072

18. Xu, B. W.; Ju, J. W.; and Shi, H. S., "Progressive Micromechanical Modeling for Pullout Energy of Hooked-end Steel Fiber in Cement-based Composites," *International Journal of Damage Mechanics*, V. 20, No. 6, 2011, pp. 922-938. doi: 10.1177/1056789510385260

19. Shen, W. C.; Hwang, S. J.; Li, Y. A.; Weng, P. W.; and Moehle, J. P., "Force-Displacement Model for Shear-Critical Reinforced Concrete Columns," *ACI Structural Journal*, V. 118, No. 1, Jan. 2021, pp. 241-249. doi: 10.14359/51728092

20. Priestley, M. J. N.; Verma, R.; and Xiao, Y., "Seismic Shear Strength of Reinforced Concrete Columns," *Journal of Structural Engineering*, ASCE, V. 120, No. 8, 1994, pp. 2310-2329. doi: 10.1061/(ASCE)0733-9445(1994)120:8(2310)

21. Parra-Montesinos, G. J., "Shear Strength of Beams with Deformed Steel Fibers," *Concrete International*, V. 28, No. 11, Nov. 2006, pp. 57-66.

22. Perceka, W., "Shear Behavior of High Strength Steel Fiber Reinforced Concrete Columns," doctoral dissertation, Department of Civil Engineering, National Taiwan University, Taipei, Taiwan, 2019.

We're Building the Future

Mission: We make strategic investments in ideas, research, and people to create the future of the concrete industry

Through its councils and programs, the ACI Foundation helps to keep the concrete industry at the forefront of advances in material composition, design, and construction. Our focus:

Our Concrete Innovation Council identifies technologies and innovation that are aligned with ACI and industry strategies and helps facilitate their use when appropriate

Our Concrete Research Council advances the knowledge and sustainable aspects of concrete materials, construction, and structures by soliciting, selecting, financing, and publishing research

Our Scholarship Council supports our future concrete innovators and leaders by administering fellowships and scholarships to help bridge the financial gap for students

Our Veterans Rebate for ACI Certification program helps honorably discharged veterans and increases skills in the industry's workforce. ACICertification.org/veteranrebate

aci Foundation

Building the Future

ACI STRUCTURAL JOURNAL TECHNICAL PAPER

Title No. 120-S93

Seismic Behavior of Monolithic Exterior Beam-Column Connections with Unbonded Post-Tensioning

by Sanghee Kim, Thomas H.-K. Kang, Donghyuk Jung, Byung Un Kwon, and Dong Joo Lee

This paper presents experimental results on seismic behaviors of post-tensioned (PT) monolithic exterior beam-column connections. Lateral cyclic loading tests were carried out for six full-scale exterior beam-column joint subassemblies fabricated with normal- and high-strength materials. Despite substantial joint cover spalling, the normal-strength specimens exhibited satisfactory lateral strengths and hysteretic behaviors up to ±5% drift ratios by virtue of the confinement effect of post-tensioning. The high-strength PT specimens also showed stable hysteretic behaviors with significantly reduced joint damages. It was found that the post-tensioning can increase the joint shear strength by more than 60% in both types of specimens. Furthermore, the post-tensioning was effective in retaining the lateral stiffness of the beam-column joints under the repeated loads, especially in high-strength specimens, enabling them to maintain at least 90% of their first-cycle stiffnesses throughout the testing.

Keywords: cyclic test; exterior beam-column connection; high-strength concrete (HSC); joint shear demand; joint shear strength; monolithic connection; tendons; unbonded post-tensioning.

INTRODUCTION

In reinforced concrete (RC) frame structures, beam-column joints transfer forces from a beam to a column, and are required to possess sufficient stiffness, strength, and deformation capabilities. In structural engineering practice, the beam-column joints are often assumed as rigid parts, but in reality, they experience complex force interactions that may lead to considerable shear distortions. Therefore, the deformation capability of the beam-column joints is quite significant in their structural performance (Gao et al. 2020). In seismic design of buildings, the strong-column/weak-beam concept is widely adopted to avoid the failure of the vertical element or joint panel in the column. ACI 318-19 (ACI Committee 318 2019) and ACI 352R-02 (Joint ACI-ASCE Committee 352 2002) provide the minimum requirements and recommendations for the design of RC beam-column connections, respectively. The design recommendations in ACI 352R-02, which were revised in 2002 and reapproved in 2010, have not been updated for approximately 20 years without reflecting important advancements in concrete technologies such as fiber reinforcement, high-strength materials, prestressing, and more. Although ACI 352R-02 covers the use of high-strength concrete (HSC) as high as 100 MPa (14.5 ksi), it does not seem to properly include design features for HSC distinguished from normal-strength concrete (NSC) and still lacks an experimental basis supporting the current provisions.

Over the past years, numerous pioneering efforts have been made on employing high-strength materials in RC beam-column connections. Kang et al. (2019) carried out quasi-static cyclic tests for three full-scale RC beam-column joint subassemblies (two roof-exterior joints and one exterior joint) to investigate the seismic performance of special moment frames fabricated with high-strength materials and steel fiber reinforcement. The experimental results showed that HSC reinforced with 600 MPa (87 ksi) steel bars can be applied to special moment frames. Ehsani and Alameddine (1991) studied the shear strength of exterior beam-column joints constructed with HSC (55 to 97 MPa [8 to 14 ksi]) and the joint confinement effect of lateral reinforcement. Ehsani et al. (1987) experimentally compared the behaviors of beam-column joints constructed with NSC and HSC and proposed a modified shear stress model for HSC beam-column joints. Hwang et al. (2014) carried out cyclic loading tests for exterior beam-column joints reinforced with high-strength steel. Although the joint specimens showed unsatisfactory behaviors in terms of both deformation and energy-dissipation capabilities due to insufficient development length of the 600 MPa (87 ksi) steel bars, the authors explored the use of high-strength reinforcement in special moment frames through the pioneering study. The previous studies on high-strength materials demonstrated that the upper limits on the material strengths in the current design standards and guides fall far behind the recent developments of construction material technology.

The prestressing technique is known to be very effective in controlling deflection and crack of concrete members, enabling long-span structures through the application of compressive stress to concrete prior to loading. Furthermore, prestressing can enhance the seismic performance of beam-column connections by reducing residual deformation and increasing the shear capacity of the joint panel. Park and Thompson (1977) conducted an experimental study on prestressed and partially prestressed interior beam-column connections subjected to cyclic loading. The prestressed connections exhibited ductile behavior with no diagonal tension failure at the joint area. The prestressing tendons greatly contributed to increasing the shear capacity of the joint, and more improved joint performance was observed

ACI Structural Journal, V. 120, No. 6, November 2023.

MS No. S-2022-156.R2, doi: 10.14359/51739085, received January 2, 2023, and reviewed under Institute publication policies.

from the prestressed specimens compared to the partially prestressed ones. Kam and Pampanin (2009, 2010) conducted cyclic loading tests for externally prestressed RC beam-column joints. In the tests, exterior beam-column joints with non-ductile details were seismically retrofitted through the "selective weakening" technique, in which the beam was weakened by cutting its bottom bars and prestressed with external rods in its longitudinal direction. The retrofitting scheme increased the flexural capacity of the beam by 80%, preventing the joint shear failure. Shiohara et al. (2002) also tested six half-scale exterior beam-column joints (three RC and three post-tensioned [PT] specimens) under quasi-static cyclic loading. The PT specimens showed higher joint shear force and column bar stress than those of the RC specimens. As such, several research efforts have been made to evaluate the seismic performance of prestressed beam-column connections from decades ago. However, the number of studies on this topic is still limited, and it is not well addressed in the current seismic design provisions and guidelines. In addition, structural/seismic responses of full-scale exterior beam-column connections with internal post-tensioning have not been studied before.

Therefore, this study aims to grasp further the seismic behavior of exterior beam-column connections with a high focus on the effects of: 1) high-strength materials; and/or 2) prestressing. Herein, the high strength is defined as a compressive strength greater than 80 MPa (11.6 ksi) for concrete and a yield strength greater than 600 MPa (87 ksi) for steel reinforcement. A series of quasi-static cyclic loading tests were conducted for two groups of full-scale exterior beam-column joint assemblies. First, the specimens fabricated with normal-strength materials were tested with and without unbonded post-tensioning. In addition, the specimens with HSC and steel were also considered along with the application of post-tensioning.

RESEARCH SIGNIFICANCE

PT special moment frames with longer spans than in practice with ordinary RC are typically used for office and residential buildings and parking structures. However, research on the seismic behavior of PT exterior beam-column connections in monolithic concrete structures is relatively rare. To the authors' knowledge, monolithic PT exterior connections as part of special moment frames with seismic detailing and unbonded tendons in accordance with ACI 318 and ACI 352R have not been researched in both experimental and analytical contexts. In this study, a total of five full-scale PT exterior beam-column joint subassemblies and full-scale RC counterparts were built and tested under reversed cyclic loading. Experimental assessment included the joint shear strength of the PT exterior connections and the unbonded tendon contribution in the calculation of joint shear demand, as well as the joint shear behavior with HSC and steel reinforcing bars under inelastic deformation reversals.

EXPERIMENTAL PROGRAM

The current experimental study was carried out in two phases. Phase 1 was intended to assess the prestressing effect of unbonded tendons on the shear strength and failure mechanism of beam-column joints fabricated with the normal-strength materials. As a follow-up study, Phase 2 explored the effectiveness of applying prestressing to beam-column joints constructed with high-strength steel and concrete.

For this study, a special RC moment frame with a floor height and a span length of 3500 and 8100 mm (138 and 319 in.), respectively, was considered. Accordingly, full-scale beam-column joint subassemblies with a column height and a beam length of 3500 and 4050 mm (138 and 159 in.), respectively, were designed with each end of the beam and column assumed as inflection points where bending moment is zero. At the time, the specimen design was initiated before ACI 318-19 was published. Therefore, a total of six beam-column joints (three for each phase) were designed in accordance with ACI 318-14 (ACI Committee 318 2014) and ACI 352R-02. The probable moment strength (M_{pr}) of the beam, which included the contribution of unbonded tendons, was calculated using Eq. (1) and (2). To estimate tensile stress (f_{ps}) of the tendons at M_{pr}, Eq. (3) and (4) provided in Section 20.3.2.4.1 of ACI 318-14 and ACI 318-19 were used. Joint shear force demand (V_u) on a plane at midheight of the joint at M_{pr} was computed by combining all force components (that is, a tensile force resultant from the beam's longitudinal bars and tendons, and column's shear force) within the joint panel as shown in Eq. (5). It is worth noting that the PT forces acting at the center of the joint were expected to affect V_u considerably; therefore, the tensile forces of all PT tendons were considered in Eq. (5) in this study. In the calculation of M_{pr} and V_u, a stress multiplier ($\alpha = 1.25$) was applied to the nonprestressed reinforcement of the beam. For the calculation of nominal shear strength (V_n) of the joint, Eq. (6) provided in ACI 352R-02 was used

$$M_{pr} = \sum A_p f_{ps}\left(d_p - \frac{a}{2}\right) + \sum \alpha A_s f_y\left(d_s - \frac{a}{2}\right) \quad (1)$$

$$a = \frac{\sum A_p f_{ps} + \sum \alpha A_s f_y}{0.85 f_c' b} \quad (2)$$

$$f_{ps} = f_{se} + 70 + \frac{f_c'}{100\rho_p}\ (\text{MPa})$$
$$[f_{ps} = f_{se} + 10{,}000 + \frac{f_c'}{100\rho_p}\ (\text{psi})] \quad (3)$$

$$\rho_p = \sum A_p / b d_p \quad (4)$$

$$V_u = \sum T_u - V_c = \sum \alpha A_s f_y + \sum f_{ps} A_p - \frac{M_{pr}}{l_c} \quad (5)$$

$$V_n = 0.083\gamma\sqrt{f_c'} b_j h_c (\text{MPa})\ [V_n = \gamma\sqrt{f_c'} b_j h_c\ (\text{psi})] \quad (6)$$

where M_{pr} is the probable moment strength; A_p is the sectional area of individual seven-wire strand contributing to the maximum moment transferred between the beam and column or nominal moment of beam as per Section 15.4.1.1 of ACI 318-19 (that is, all strands); f_{ps} is the tensile stress of tendons corresponding to nominal moment of beam; d_p is the distance of centroid of prestressing reinforcement

Table 1—Test specimen details

Phase	ID	f_c', MPa	f_y, MPa	Beam							Column			Joint
				Size, mm	Bar	s_{beam}, mm	Tendons	w_1	w_2	M_{pr}, kN·m	Size, mm	s_{col}, mm	m	V_u/V_n
Phase 1	RCN	35	400	400 x 650	8-D22	100	None	1.25	0.84	786	500 x 500	125	1.22	0.99
	PTN-1	35	400	400 x 650	5-D22	100	5	1.25	0.84	712	500 x 500	125	1.22	1.23
	PTN-2	35	400	400 x 650	5-D22	100	8	1.25	0.84	786	500 x 500	125	1.22	1.58
Phase 2	PTH-1	80	600	400 x 650	5-D29	145	6	1	0.55	1562	500 x 500	148	1	1.45
	PTH-2	100	600	400 x 650	6-D29	145	6	1.12	0.61	1768	500 x 500	115	1.02	1.56
	PTH-3	120	600	400 x 650	8-D29	145	6	1.23	0.67	2203	500 x 500	115	1.04	1.77

Note: f_c' is specified compressive strength of concrete; f_y is specified tensile stress of flexural reinforcement; s_{beam} is spacing of stirrups; w_1 and w_2 are ratio of provided to required development length of headed longitudinal bar as per ACI 318-14 and ACI 318-19, respectively, calculated using specified material properties; M_{pr} is probable moment strength based on specified material's properties with application of $\alpha = 1.25$; s_{col} is spacing of column confinement; m is ratio of provided to required column transverse reinforcement amounts calculated using specified material properties; and V_u and V_n are shear force acting on joint and nominal shear strength of joint according to ACI 352R, calculated using specified material's properties, respectively. 1 MPa = 0.145 ksi; 1 mm = 0.039 in.; 1 kN·m = 0.7375 kip·ft.

from beam's compression face; a is the depth of compression block; α is the stress multiplier (herein 1.25); A_s is the sectional area of individual nonprestressed reinforcing bars subjected to tension; f_y is the specified yield strength of reinforcing bars; d_s is the centroid of longitudinal reinforcement from the beam's compression face; f_c' is the specified concrete strength; b is the width of the beam; f_{se} is the effective stress in prestressing reinforcement after allowance for all prestress loss (measured values are used for any case); ρ_p is the ratio of total area of prestressing reinforcement to bd_p; V_u is the joint shear demand; T_u is the tension force; V_c is the horizontal shear force of the column acting on the joint panel; l_c is the length of the column; V_n is the nominal shear strength of the joint; γ is the shear strength factor (herein 12); b_j is the effective joint width; and h_c is the depth of the column.

Phase 1 specimen design

For Phase 1 testing, three full-scale beam-column joint specimens with normal-strength materials were constructed. All specimens had the identical beam and column sizes of 400 x 650 mm (15.8 x 25.6 in.) and 500 x 500 mm (19.7 x 19.7 in.), respectively, but they had different reinforcements to achieve varying joint shear demand to capacity ratios (V_u/V_n). The specified compressive strength of concrete was 35 MPa (5.1 ksi), and the specified yield strength of all steel reinforcing bars was 400 MPa (58 ksi). Table 1 and Fig. 1 provide details of the test specimens.

The specimen denoted as RCN was a conventional RC beam-column joint without post-tensioning. As a control specimen, RCN was designed to have V_u/V_n close to 1, intended to have joint shear failure at relatively high drift ratios. The beam of RCN was reinforced with eight D22 (d_b = 22.2 mm [0.88 in.]) longitudinal bars at the top and bottom of the section, respectively, and D10 (d_b = 9.5 mm [0.38 in.]) stirrups at 100 mm (3.9 in.) spacing. For anchorage, the D22 bar had a circular head with a diameter and a thickness of 48 and 22 mm (1.9 and 0.9 in.), respectively. Regarding the headed bar, ACI 318-14 specifies the minimum clear spacing of $4d_b$ (Section 25.4.4.1). Furthermore, the net bearing area (A_{brg}) of the head should be at least four times the bar area (that is, $A_{brg} \geq 4A_b$) (Section 25.4.4.1 of ACI 318-14 and ACI 318-19). For closely spaced headed bars, it is also recommended to use the development length greater than $d/1.5$ to prevent concrete breakout failure, where d is the depth of the beam (R25.4.4.2 of ACI 318-14). According to previous studies (Kang et al. 2009; Shao et al. 2016), however, the $4d_b$ clear spacing requirement in ACI 318-14 seemed to be overly strict, and it was experimentally proven that the clear spacing can be reduced to $2d_b$ (even possibly as low as $1.2d_b$ in the test) without compromising the lateral resistance of the beam-column joint. Therefore, it was decided to use the clear spacing of at least $2d_b$ for the Phase 1 specimens. Furthermore, ACI 318-19, which was published later, also specifies the minimum clear bar spacing of $2d_b$—that is, a center-to-center spacing of $3d_b$ (Section 25.4.4.1 of ACI 318-19). A_{brg} of the head was determined as 3.76 times the bar area (that is, $A_{brg} = 3.76A_b$). For the location of the bar head, ACI 352R-02 recommends that the heads are located within 50 mm (2 in.) from the internal hoops (that is, near the boundary of confined core) to make sure the heads are located within the diagonal compression strut of the joint. For all the specimens in Phase 1, including RCN, however, the heads were placed at 100 mm (3.9 in.) from the internal hoops, meaning that the heads were shifted inside by 50 mm (2 in.). This design was intended to locate the bar heads within the region confined by the tendons in the PT specimens (PTN-1 and PTN-2), and the same location was applied to RCN for consistency (refer to Fig. 1). The corresponding development length of the headed bars calculated according to Section 25.4.4.2 of ACI 318-14 was 353 mm (13.9 in.), and the heads were still located within the compression zone of the joint. Considering the minimum development length of 283 mm (11.1 in.) calculated using the nominal material strengths (Section 25.4.4.2 of ACI 318-14), the provided length was found to be sufficient, having a provided to required development length ratio (w_1) of 1.25. When the provided to required development length ratio (w_2) was calculated as per the current ACI 318 (Section 25.4.4.2 of ACI 318-19), it significantly reduced to 0.84 due to the inclusion of the stress multiplier (that is, $1.25f_y$) specified in Section 18.8.5.2 of ACI 318-19, indicating the stricter requirement of the current Code. Column RCN was provided with ten D25 bars in the longitudinal direction.

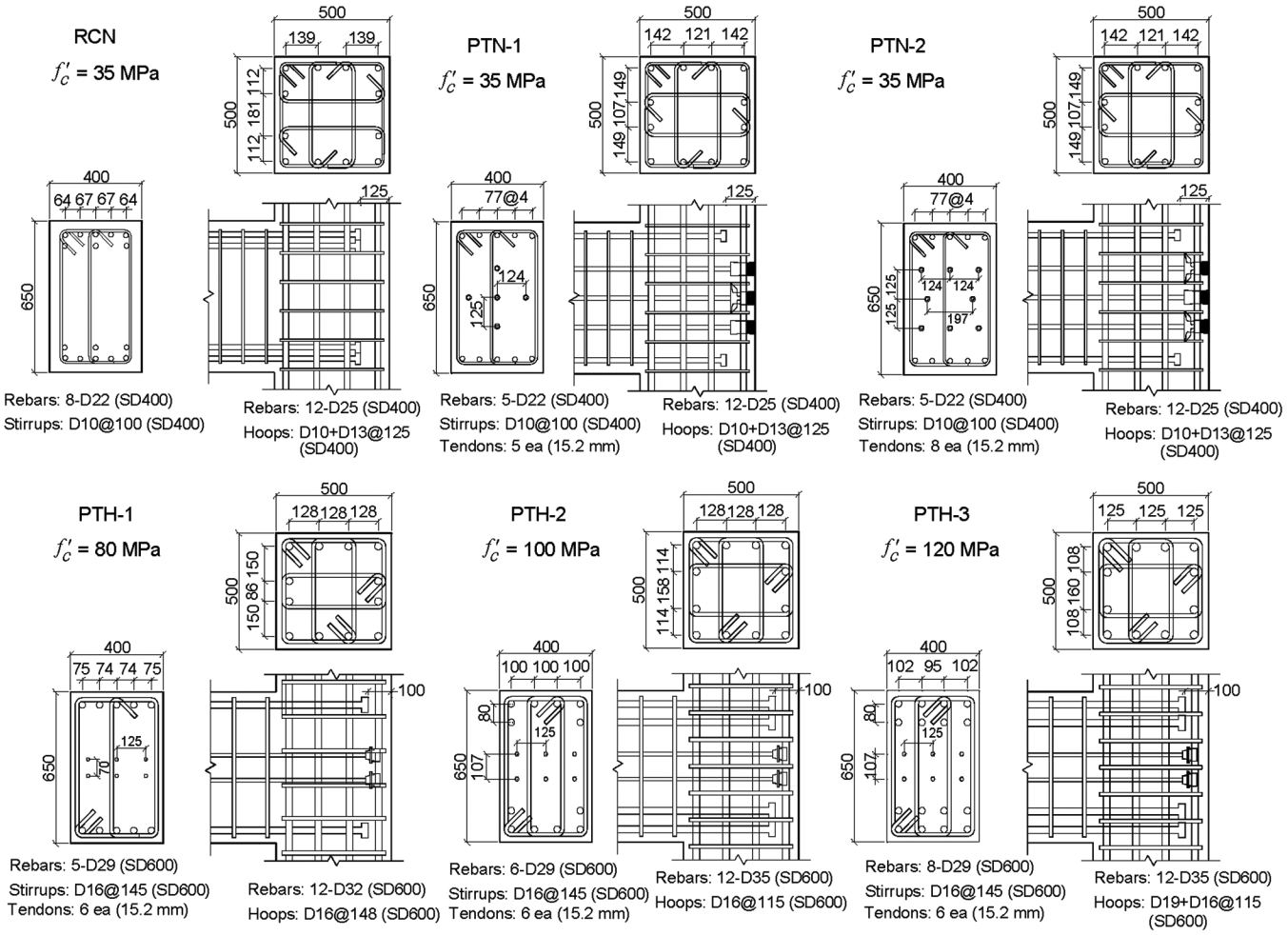

Fig. 1—Details of specimens. (Note: Units in mm; 1 mm = 0.039 in.; 1 MPa = 0.145 ksi.)

For transverse reinforcement, D10 and D13 (d_b = 12.7 mm [0.5 in.]) bars were provided as internal hoops and crossties, respectively, at 125 mm (4.9 in.) spacing, assuming that the column is a part of the special moment frame. The ratio (m) of provided to required transverse reinforcements (Section 18.7.5.4 of ACI 318-14) was 1.22.

PTN-1 and PTN-2 were the RC beam-column joint specimens prestressed with unbonded tendons. With a presumption that the prestressing would increase the shear capacity of the joint, PTN-1 was designed to have a target V_u/V_n of 1.23, approximately 20% higher than that of RCN. To achieve this ratio, the beam of PTN-1 was reinforced with ten D22 headed bars and post-tensioned with four SWPC-7B tendons arranged in a cruciform. Just as PTN-1, PTN-2 was also provided with the same headed bars and unbonded tendons but for a higher V_u/V_n, 1.58. In the beam of PTN-2, ten D22 headed bars were placed along with eight unbonded tendons (SWPC-7B). For the headed bars in both PTN-1 and PTN-2, the same head size (48 and 22 mm [1.9 and 0.9 in.] in diameter and thickness, respectively), location (100 mm [3.9 in.] from the internal hoops), net bearing area (A_{brg} = 3.76A_b), and development length (353 mm) used in RCN were applied. Each provided tendon had a nominal cross-sectional area of 138.7 mm^2 (0.21 in.^{2}) and a nominal ultimate stress of 1860 MPa (267 ksi). The tendons were prestressed to have a target effective stress (f_{se}) corresponding to 60% of their specified tensile strength, and anchored with live end on the joint side without supplementary reinforcement. As transverse reinforcement in the beam for both PTN-1 and PTN-2, D10 stirrups were placed every 100 mm (3.9 in.). The column design of the PT specimens was identical to that of RCN. All Phase 1 specimens (including Phase 2 specimens) were designed to have a column-to-beam moment ratio of 1.42 to 1.76 (that is, strong-column/weak-beam). They satisfied Section 18.7.3.2 of ACI 318-14, which requires that the summation of the nominal flexural strength of the columns framing into the joint shall be equal to or larger than 1.2 times that of the beams framing into the joint.

Phase 2 specimen design

After the Phase 1 testing, Phase 2 proceeded with the aim to evaluate the structural responses of the PT beam-column joints constructed with high-strength materials. For Phase 2, three full-scale PT beam-column joints were constructed. As in the case of Phase 1, all specimens had the identical beam and column sizes of 400 x 650 mm (15.8 x 25.6 in.) and 500 x 500 mm (19.7 x 19.7 in.), respectively, but with varying target V_u/V_n. The nominal compressive strength of concrete ranged between 80 and 120 MPa (11.6 and 17.4 ksi), and the nominal yield strength of all steel reinforcing bars was 600 MPa (87 ksi). Details of the test specimens are shown in Table 1 and Fig. 1.

PTH-1 was designed to have V_u/V_n of 1.45 with 80 MPa (11.6 ksi) concrete. The beam of PTH-1 was longitudinally reinforced with ten D29 (d_b = 28.7 mm [1.13 in.]) headed bars. For the beam's transverse reinforcement of all Phase 2 specimens, including PTH-1, D16 (d_b = 15.9 mm [0.625 in.]) stirrups were placed at every 145 mm (5.7 in.). The heads of D29 bars had a thickness of 29 mm (1.1 in.) and a diameter of 65 mm (2.6 in.), which satisfied $A_{brg} = 4.0A_b$ (Section 25.4.4.1 of ACI 318-14). The clear spacing and the center-to-center spacing between the D29 bars were 45 mm (1.8 in.) ($1.62d_b$) and 74 mm (2.9 in.) ($2.58d_b$), respectively, which were less than the Code's spacing requirements (Section 25.4.4.1 of ACI 318-14 and ACI 318-19). As was the case of Phase 1 specimens, the authors decided to have a more practical layout of headed reinforcements based on the prior experimental results (Kang et al. 2009) that the clear spacing between $1.2d_b$ and $7.6d_b$ had no marked influence on the lateral resistance of the well-confined exterior beam-column joint. The heads of the D29 bars were placed at 75 mm (3 in.) from the internal hoops, again, to take advantage of the confinement effect by the post-tensioning. The provided development length was 370 mm (14.6 in.), and the resultant ratios (w_1 and w_2) of the provided to required development length were 1.06 and 0.73, respectively. For prestressing of the joint, six SWPC-7B tendons were used with a target f_{se} of approximately 60% of their specified tensile strength. Unlike the case of Phase 1 specimens, the tendons were anchored with the dead end 50 mm (2 in.) away from the outer column face. For the column of PTH-1, 12 D32 bars were provided in the longitudinal direction with D16 hoops spaced every 148 mm (5.8 in.) ($m \approx 1$).

PTH-2 was designed with 100 MPa (14.5 ksi) concrete for V_u/V_n of 1.56. The beam was reinforced with 12 D29 headed bars (center-to-center spacing of $3.48d_b$). The head size, location, and development length of the D29 bars were the same as those used in PTH-1. The beam also had six SWPC-7B tendons prestressed at the same level of f_{se} used in PTH-1 with dead-end anchors in the joint. The column was provided with 12 D35 longitudinal bars and D16 hoops spaced at every 115 mm (4.5 in.) ($m \approx 1$). The different amount of transverse reinforcement, compared to PTH-1, was due to the different specified strength of concrete.

PTH-3 was targeted at V_u/V_n of 1.69 by using 120 MPa (17.4 ksi) concrete, which exceeded the strength limit specified in ACI 352R-02. A total of 16 D29 headed bars (center-to-center spacing of $3.31d_b$) were used as longitudinal beam reinforcement with the same head size, location, and development length. For prestressing, six SWPC-7B tendons were used as well. The column was reinforced with 12 D35 longitudinal bars, and D16 and D19 (d_b = 19.1 mm [0.75 in.]) hoops spaced every 115 mm (4.5 in.) ($m \approx 1$).

Measured material properties

As mentioned earlier, the concrete with different target compressive strengths was used for Phase 1 (35 MPa [5 ksi]) and Phase 2 (80 to 120 MPa [11.6 to 17.4 ksi]). For Phase 1, the concrete strengths measured on the day of testing were 29.1 MPa (4.2 ksi) for RCN and 35.1 MPa (5.1 ksi) for PTN-1 and PTN-2. For the HSC in Phase 2, zirconia silica fume was used to secure long-term strength and to control hydration heat during curing. To prevent water evaporation, the specimens were sealed cured at room temperature for 4 months. Table 2 shows the concrete mixture proportions used in this study. Measured strengths of concrete used in PTH-1, PTH-2, and PTH-3 were 103.4, 80.6, and 96 MPa (15, 11.7, and 13.9 ksi), respectively, which was different from each target value.

Table 2—Concrete mixture proportions

Material	Strength or quantity			
f_c', MPa	35	80	100	120
$f_{c\,meas}'$, MPa	29.1, 35.1	103.4	80.6	96
w/b, %	—	18.8	14.9	13.5
S/a, %	—	40	36	35
Water, kg/m^3	—	150	140	130
Cement, kg/m^3	—	400	470	432
Fine aggregate, kg/m^3	—	578	484	473
Coarse aggregate, kg/m^3	—	882	876	892
ZrSF, kg/m^3	—	120	141	144
Slag, kg/m^3	—	280	329	384
HRWR, kg/m^3	—	10	11.75	—

Note: f_c' is specified compressive concrete strength; $f_{c\,meas}'$ is measured compressive concrete strength; w/b is water-binder ratio; S/a is fine aggregate ratio; ZrSF is zirconia silica fume; HRWR is high-range water reducer; and all values are averages of three samples. 1 MPa = 0.145 ksi; 1 kg/m^3 = 0.0624 lb/ft^3.

For a variety of reinforcing steel bars, tensile tests were also conducted in accordance with ASTM E8/E8M (2016). The measured yield strength of the D22 and D29 bars, used as longitudinal reinforcement of the beams in Phases 1 and 2, were 555 and 642 MPa (80 and 93 ksi), respectively. The transverse reinforcement of D10, D13, and D16 bars had measured yield strengths of 488, 499, and 688 MPa (70.8, 72.4, and 96.9 ksi), respectively. Measured strengths of the other reinforcement are summarized in Table 3.

Post-tensioning

For prestressing of both Phase 1 and Phase 2 specimens, the SWPC-7B tendons were commonly used but with slightly different anchoring methods. For Phase 1, the tendons on the beam end were dead-end anchored, while those on the other end (that is, joint side) were live-end anchored. The prestressing force reached initially to 70% of their measured tensile strength (1860 MPa [270 ksi]) as per Section 20.3.2.5 of ACI 318-14 and ACI 318-19, and reduced instantaneously after relative movement of the tendons (6 mm [0.24 in.]), presumably caused by anchorage seating. The effective stress of the tendons (f_{se}) was 1206 MPa (175 ksi), approximately 64% of the tensile strength, at the time of testing. On the other hand, the tendons used in the Phase 2 specimens were dead-end anchored in the beam-column joint. The tendons were also initially prestressed to 70% of their measured tensile strength (1776 MPa [258 ksi]). Due to excessive anchorage seating, however, actual f_{se} reduced to 710 MPa (103 ksi), eventually reaching 40% of the tensile strength.

Testing

Figure 2 shows the test setup for a T-shaped beam-column joint subassembly with a loading protocol. The column of the specimens was set horizontally with pinned supports at each end. To apply reversed lateral cyclic loading, a hydraulic actuator with a force capacity of 2000 kN (450 kip) was installed at the end of the vertical beam, having a distance of 4050 mm (159 mm) from the center of the joint. Out-of-plane deformation of the specimens was prevented by installing ball jigs on each face of the beam at the midspan. The displacement-controlled loading protocol was determined based on Chapter 5.2 of ACI 374.1-05 (ACI Committee 374 2005). The loading was quasi-statically applied with a rate of 0.2 to 1.3 mm/s (0.0079 to 0.051 in./s) until each target inter-story drift ratio was reached. The target drift ratio, which started from 0.5%, varied with increments of 0.25 and 0.5% up to the drift ratio of 2%, and then had a constant increment of 1% up to the drift ratio of 5%. At each target drift ratio, the loading was repeated three times, as illustrated in Fig. 2. In the testing, axial load was not applied to the column. It was expected that the absence of axial load would enable a more conservative performance assessment of the connection under an engineering judgment that a certain degree of axial compression (less than 30% of column's axial load capacity) is advantageous in delaying concrete cracking and securing the headed bars.

Figure 2 also shows locations and types of sensors used for experimental measurements. Lateral displacement of the beam was measured by a wire potentiometer. Shear deformation of the joint panel was measured by two pairs of linear variable differential transformers (LVDTs) installed on each face. At the end of the tendons, a load cell was installed to estimate compressive force induced by post-tensioning. Strain gauges were also attached to longitudinal and transverse reinforcement of the beam (refer to Fig. 2). More detailed information on the location of strain gauges can be found from Kwon (2016).

Table 3—Mechanical properties of steel bars and concrete

Reinforcing bars	f_y, MPa	Measured values, MPa		
		f_{y_meas}	f_{u_meas}	E_{s_meas}
D10	400	488	625	—
D13	400	499	641	—
D22	400	555	677	—
D25	400	484	652	—
D16	600	668	791	198,100
D19	600	645	775	187,700
D29	600	642	739	184,900
Tendons for Phase 1	1860	—	1893	—
Tendons for Phase 2	1860	—	1776	—
Concrete		f'_{c_meas}	f_{ct_meas}	E_{c_meas}
35 MPa for RCN		29.1	—	19,100
35 MPa for PTN-1, PTN-2		35.1	—	20,100
80 MPa for PTH-1		103.4	7.1	45,600
100 MPa for PTH-2		80.6	5.7	35,200
120 MPa for PTH-3		96	4.4	43,500

Note: f_y is specified yield strength of steel; $f_{y,meas}$, $f_{u,meas}$, and $E_{c,meas}$ are measured yield strength, measured ultimate strength, and elastic modulus of steel, respectively; and $f'_{c,meas}$ and $f_{ct,meas}$ are measured ultimate strength and measured splitting tensile strength of concrete, respectively. 1 MPa = 0.145 ksi.

EXPERIMENTAL RESULTS

Damage observation

At the drift ratio of 0.5%, RCN started to have 400 mm (15.7 in.) long diagonal cracking in the joint panel. The diagonal cracks increased further by 120 mm (4.7 in.), and a new vertical crack (150 mm [5.9 in.] length) developed in the beam at the 0.75% drift ratio. As the drift ratio increased to 2%, more cracks formed in the beam and the joint panel. At the 3% drift ratio, the joint panel experienced spalling of cover concrete, and the diagonal cracking extended further in the longitudinal direction of the column. When the test was terminated at the 4% drift ratio, more concrete spalling

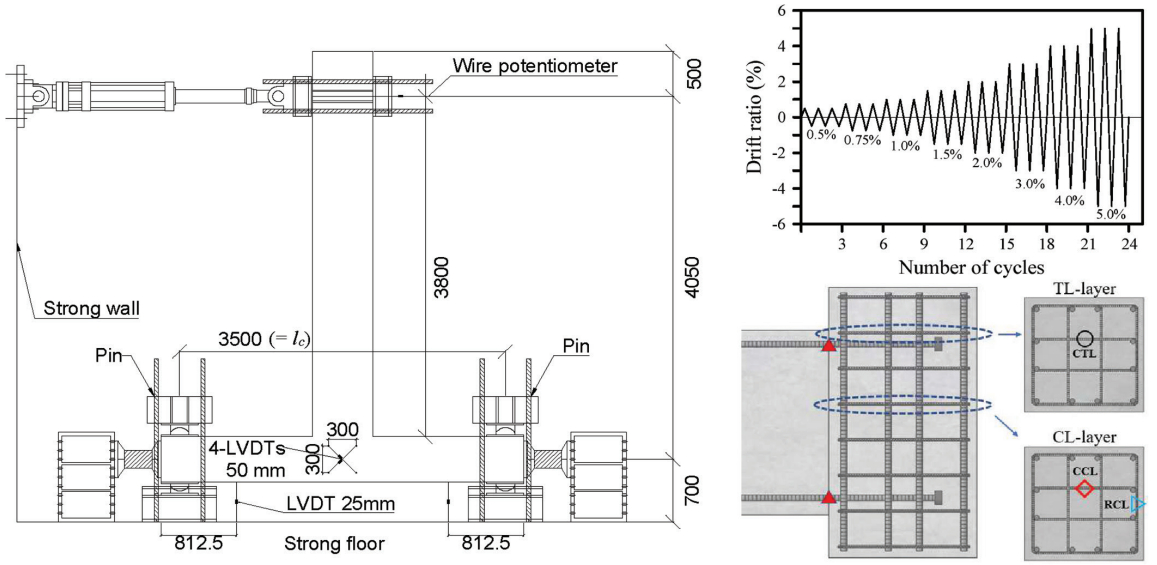

Fig. 2—Test setup and load plan. (Note: Units in mm; 1 mm = 0.039 in.).

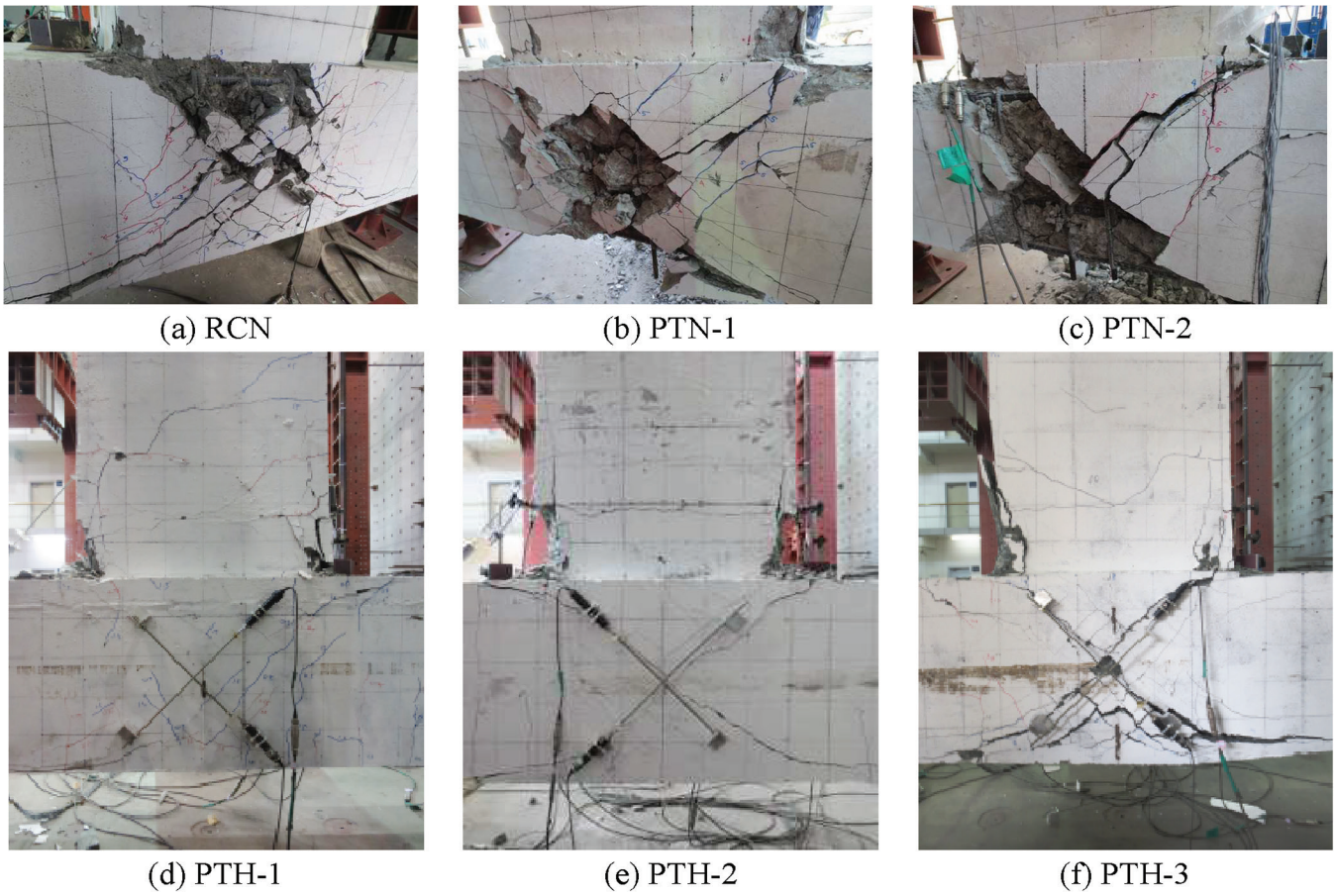

Fig. 3—Damage status of joint panels after tests.

occurred, exposing the internal reinforcement in the joint panel.

Unlike RCN, PTN-1 showed no sign of damages until it reached the drift ratio of 0.75%. At the 1% drift ratio, the joint panel experienced diagonal cracks longer than 400 mm (15.7 in.) with several cracks in the beam as well. While being loaded up to the 3% drift ratio, PTN-1 had more cracking, which caused spalling of concrete at the beam-column interface. At the 4 to 5% drift ratios, both the joint panel and the outer face of the column experienced a significant loss of concrete, as shown in Fig. 3.

The damage pattern of PTN-2 was quite analogous to that of PTN-1. The first crack of PTN-2 appeared in the joint panel, at a drift ratio of 1%, with a length of 100 mm (3.9 in.). More diagonal cracks developed on both sides of the joint at the 2% drift ratio. When PTN-1 reached the 3% drift ratio, the joint cracks opened further with the formation of additional cracks at the top and bottom of the beam. As was the case for PTN-1, PTN-2 also lost a massive amount of cover concrete in the joint panel and the outer face of the column at the 4 to 5% drift ratio, as illustrated in Fig. 3.

The first damage reported from PTH-1 was fine diagonal cracking in the joint panel that appeared during the 0.5 to 1% drift ratios. At a drift ratio of 1.5%, several flexural cracks were generated in the beam and the column as well adjacent to the joint. From the 3% drift ratio, spalling of the cover concrete began to occur at the top and bottom of the beam. With the increase in the drift ratios, the existing cracks widened further and became more noticeable, including the diagonal cracks across the joint panel.

In PTH-2, the drift ratios of 0.5 to 0.75% induced fine flexural cracks in the beam and column along with 300 mm (11.8 in.) long diagonal cracks in the joint panel. With the increment of drift ratios up to 4%, additional cracking occurred with a higher concentration in the beam. Finally, at the drift ratio of 5%, the stirrups in the beam were seen due to spalling of concrete at the top and bottom sections of the beam. The X-shaped diagonal cracks in the joint panel became larger and clearer.

PTH-3 had minor cracks only in the beam when it reached the 0.75% drift ratio. While the drift ratios increased to 3%, PTH-3 also experienced diagonal cracks on both faces of the joint panel with additional cracking in the beam. At drift ratios of 4 to 5%, the joint panel cracks widened and extended further to the outer face of the column. At the same time, concrete at the top and bottom sections of the beam spalled off significantly.

Flexural and shear responses of joints

Based on the lateral cyclic loading tests, global responses of the specimens were obtained. Figure 4 presents the moment-drift ratio responses of all the specimens. Figure 5 shows joint shear force-distortion relationships of the joint panels. In Table 4, primary experimental results of all the specimens are summarized and compared with corresponding expected values that accounted for the measured material strengths.

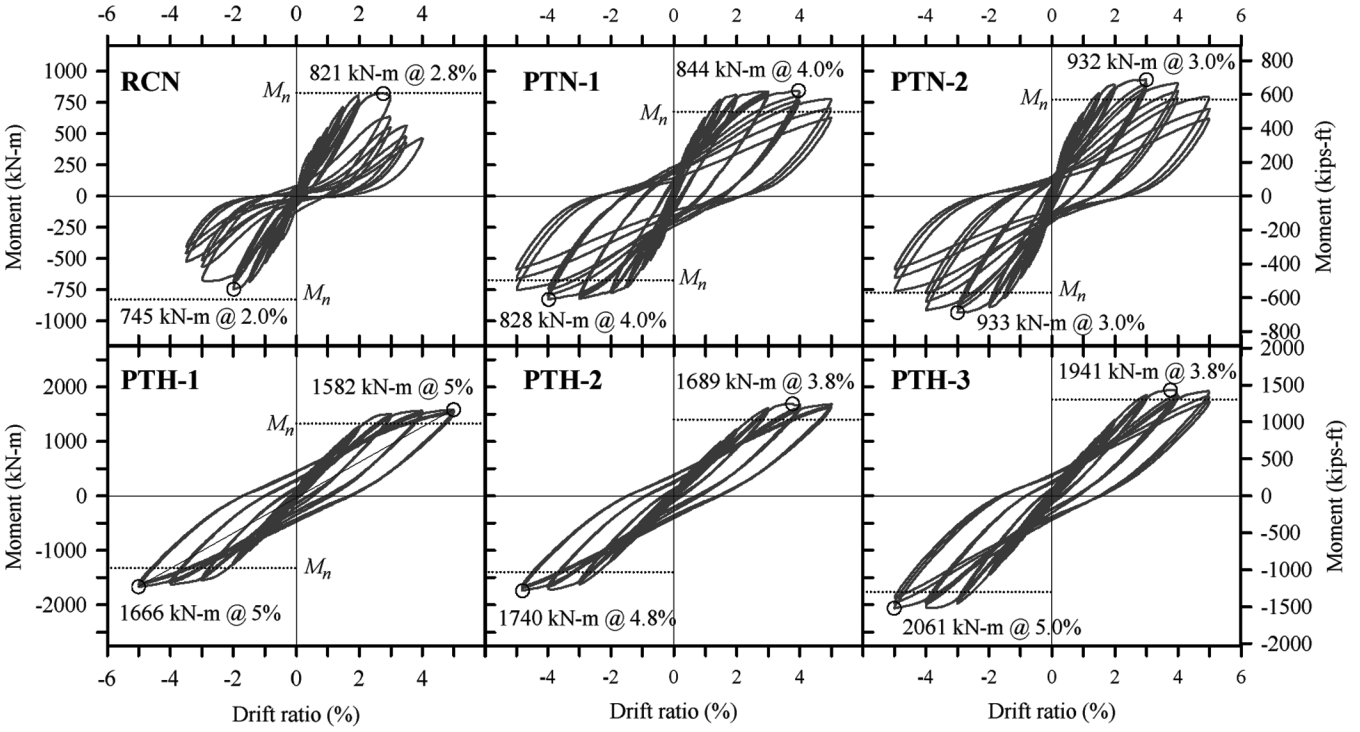

Fig. 4—Moment-drift relationships.

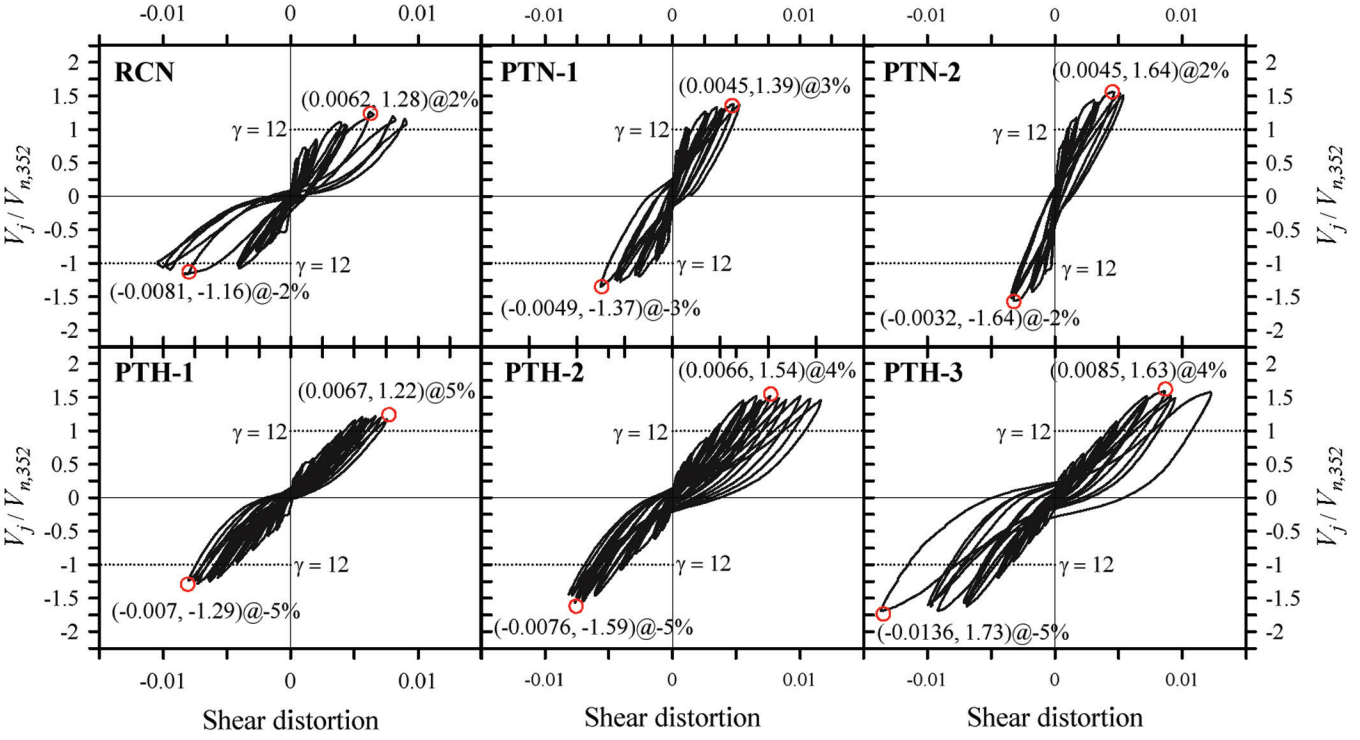

Fig. 5—Joint shear distortion (values for Phase 1 specimens were not measured at V_{j_peak} *except for negative* V_{j_peak} *of RCN).*

Moment-related values were estimated from the moment at the beam-column interface calculated by multiplying the measured actuator force by the distance between the loading point and the column face. By using the measured material strengths provided in Table 3, the expected joint shear force (V_u*) and strength (V_n*) were also recalculated using Eq. (5) and (6), respectively. The peak joint shear force (V_{j_peak}) was estimated from the peak measured moment (M_{peak}) using Eq. (7). Herein, the effective flexural depth of the beam, d, was computed using Eq. (8), and lever-arm depth factor, $j = (d - a/2)/d$, was estimated by substituting the measured material strengths into Eq. (2). For estimation of d in Eq. (8), the prestressing force measured at Δ_{peak} was used for PTH-2 and PTH-3. In the case of PTN-1, PTN-2, and PTH-1, however, f_{ps} was used instead due to the unavailability of the measured force. The values of j were calculated as 0.78 to 0.85 for the

Table 4—Summary of test results

ID	Direction	w_1*	w_2*	m*	j	M_n*, kN·m	V_u*/ V_n*	M_y, kN·m	M_{peak}, kN·m	M_{peak}/M_n*	V_{j_peak}, kN	V_{j_peak} /V_n*	Δ_y, %	Δ_{peak}, %	$\Delta_{0.8}$, %	μ
RCN	+	0.82	0.73	1.82	0.85	836	1.22	730	821	0.98	1556	1.28	1.58	2.8	3.25	2.06
	–					836	1.22	665	745	0.89	1412	1.16	1.42	2.0	3.2	2.25
	Avg.					836	1.22	698	783	0.94	1484	1.22	1.5	2.4	3.23	2.16
PTN-1	+	0.90	0.75	1.51	0.83	767	1.35	720	844	1.09	1856	1.39	1.33	3.95	4.95	3.72
	–					767	1.35	730	828	1.07	1821	1.37	1.48	3.97	4.97	3.36
	Avg.					767	1.35	725	836	1.08	1839	1.38	1.41	3.96	4.96	3.54
PTN-2	+	0.90	0.75	1.51	0.78	839	1.74	815	932	1.10	2186	1.64	1.45	2.99	4.96	3.42
	–					839	1.74	815	933	1.11	2189	1.64	1.52	3.00	4.99	3.28
	Avg.					839	1.74	815	933	1.10	2188	1.64	1.49	3.00	4.98	3.35
PTH-1	+	1.06	0.73	0.86	0.93	1365	1.08	1375	1582	1.16	2797	1.22	2.4	4.99	4.99	2.08
	–					1365	1.08	1450	1666	1.22	2946	1.29	2.65	5.00	5.00	1.89
	Avg.					1365	1.08	1413	1624	1.19	2871	1.25	2.53	5.00	5	1.99
PTH-2	+	0.94	0.64	1.41	0.88	1460	1.46	1530	1689	1.14	3119	1.54	2.8	3.77	5.00	1.79
	–					1460	1.46	1600	1740	1.17	3214	1.59	2.93	4.81	5.00	1.71
	Avg.					1460	1.46	1565	1715	1.15	3167	1.57	2.87	4.29	5	1.75
PTH-3	+	1.02	0.70	1.42	0.88	1827	1.67	1780	1941	1.05	3601	1.63	2.82	3.75	5.00	1.77
	–					1827	1.67	1920	2061	1.11	3823	1.73	2.9	5.01	5.01	1.73
	Avg.					1827	1.67	1850	2001	1.08	3712	1.68	2.86	4.38	5.00	1.75

Note: w_1* and w_2* are ratio of provided to required development length of headed longitudinal bar as per ACI 318-14 and ACI 318-19, respectively, calculated using material properties (f_{y_meas} and f_{c_meas}); m* is ratio of provided to required column transverse reinforcement amounts, calculated using measured material properties; M_n* and V_u* are calculated peak moment and input shear force based on measured material properties; M_{peak} is measured peak moment; V_n* is calculated joint shear strength according to ACI 352R-02 based on $f_c'_{meas}$; V_{j_peak} is measured peak shear strength of joint ($M_{peak}/jd - V_{col}$), where jd is moment arm's length and V_{col} is column shear; M_y and Δ_y are yield moment and drift at yield point estimated based on ACI 374.2R-13, respectively; Δ_{peak} is drift ratio at peak moment; $\Delta_{0.8}$ is post-peak drift ratio corresponding to $0.8M_{peak}$; and μ is ductile ratio (= Δ_y divided by $\Delta_{0.8}$).

Phase 1 specimens and 0.88 to 0.93 for the Phase 2 specimens. For simplicity, j = 0.8 (Phase 1) and j = 0.9 (Phase 2) were used in the calculation of V_{j_peak}.

$$V_{j\_peak} = \frac{M_{peak}}{jd} - \frac{M_{peak}}{l_c} \tag{7}$$

$$d = \frac{\sum A_p f_{ps} d_p + \sum A_s f_{y,meas} d_s}{A_p f_{ps} + A_s f_{y,meas}} \tag{8}$$

The results presented in Table 4 revealed that there existed a certain degree of discrepancies between the design-level expectations and the experimentally obtained values. For the Phase 1 specimens, the expected joint shear demand to capacity ratios (V_u*/V_n*) exceeded those (V_u/V_n) determined during the design process. This is mainly attributed to the high measured strength of D22 steel bars. For the Phase 2 specimens, V_u*/V_n* were less than V_u/V_n due to the unexpectedly varying concrete strengths and the excessive prestress loss in the tendons. The values of V_u*/V_n* for RCN (1.22), PTN-1 (1.35), and PTN-2 (1.74) are all greater than 1, which imply that those specimens may have joint shear failure modes. The values of V_u*/V_n* for PTH-1 (1.08), PTH-2 (1.46), and PTH-3 (1.67) also present high chances of joint shear failures triggered during the tests. The updated material strengths also affected the ratio (w_1* and w_2*) of provided to required development length of the headed bar presented in Table 4. Herein, w_1* indicates the provided to required ratio calculated as per ACI 318-14, while w_2* is the corresponding value for the ACI 318-19 requirement. As shown in Table 4, w_1* (0.82 to 1.06) and w_2* (0.64 to 0.75) for both Phase 1 and Phase 2 specimens decreased considerably compared to w_1 and w_2, respectively, presented in Table 1. The newly updated values of w_1* and w_2* imply that all the headed bars in the specimens may not be completely anchored, and thus experience undesirable slips during the tests. In Table 4, the ratio (m*) of provided to required transverse reinforcements changed as well with the updated material strengths. It is found that m* for PTH-1 reduced to 0.86, whereas those for PTH-2 and PTH-3 increased above 1.4, although they were all designed with the target $m \approx 1$. The large variations of m* for the PTH-series specimens were attributable again to the unexpected variation in measured concrete strengths.

In the moment-drift ratio responses in Fig. 4, RCN recorded M_{peak} as high as 821 kN·m (606 kip·ft) at 2 to 3% drift ratios. M_{peak} did not fully reach the expected capacities (M_n*), as indicated by M_{peak}/M_n* of 0.98 and 0.89 in the positive and negative directions, respectively, in Table 4. After the peak strengths, RCN rapidly lost its lateral resistance in both directions as it was deformed to a drift ratio of 4%. Such a brittle response of RCN was expected by its V_{j_peak}/V_n* (= 1.22) and partially by the insufficient development length of the headed bars (that is, w_2* < 1), which caused the high stress concentration in the joint region. As a result, the unconfined

(cover) concrete in the joint experienced the severe diagonal cracking. In the case of the PTN-series specimens, PTN-1 recorded M_{peak} of 836 kN·m (617 kip·ft) on average at the 4% drift ratio, achieving M_{peak}/M_n* of 1.08. PTN-2 attained 933 kN·m (687 kip·ft) at a drift ratio of 3% with M_{peak}/M_n* of 1.10. In contrast to RCN, both PTN-1 and PTN-2 maintained the moments above 80% of the peak values until the tests were terminated. Moreover, the PTN-series specimens attained M_n* at the 1 to 1.5% drift ratios, developing the early lateral resistance. Even though all the Phase 1 specimens experienced the severe joint panel deterioration (refer to Fig. 3) associated with the high V_{j_peak}/V_n*, the PT specimens exhibited much more stable hysteretic responses and appeared to have only the concrete cover damage outside the joint hoops. It is considered that the restraining force provided by the post-tensioning counteracted the undesirable damaging effect associated with the high shear demand and the inadequately anchored headed bars, preventing the crack propagation toward the joint core.

Figure 4 also provides the moment-drift ratio relationships of the PTH-series specimens in Phase 2. All three specimens exhibited the peak moments exceeding the expected values calculated based on the measured material properties. The testing of Phase 2 specimens was terminated at ±5% drift ratios, where the stroke limit of the horizontal actuator was reached. PTH-1 recorded M_{peak} of 1624 kN·m (120 kip·ft) on average at the drift ratio of 5% with M_{peak}/M_n* of 1.19. The global responses of PTH-2 and PTH-3 were quite similar to those of PTH-1 in that they all showed stable hysteretic relationships and that no significant strength drop was seen. M_{peak}/M_n* of PTH-2 and PTH-3 were 1.17 and 1.08, respectively. Above all, it is worth noticing that, despite their high joint shear demands (that is, V_{j_peak}/V_n* = 1.25 to 1.68), the PTH-series specimens did not even exhibit the extensive joint cover damages observed in the Phase 1 specimens. The alleviated damages of the PTH-series specimens seemed to be attributable to the prestressing effect of post-tensioning, which provided additional strength for HSC and restrained crack opening.

As stated earlier, in all PT beam-column specimens used in this study, the headed bars did not meet the current design recommendation regarding the location of the heads (that is, 50 mm [2 in.] from the internal hoops) specified by ACI 352R-02, as well as ACI 318-19's development length for headed bars (that is, $w_2 \approx 0.64$ to 0.75). However, the headed bars properly carried the forces and did not adversely affect the structural performance. This test result implies that additional compression struts developed by the post-tensioning toward the beam played a crucial role in securing the headed bars, which had the relatively shorter development lengths.

In Fig. 5, hysteretic shear distortion of the joint panels is shown with respect to the experiment-based joint shear force normalized by the shear strength computed using measured material properties (that is, V_{j_peak}/V_n*). The shear distortion was estimated from the measurements of two LVDTs diagonally installed in the joint panel. V_{j_peak}/V_n*, provided in Table 4, indicates the peak of V_{j_peak}/V_n* curves and quantitatively estimates the peak shear demand presumably imposed

	RCN	PTN-1	PTN-2	PTH-1	PTH-2	PTH-3
K_y (kN/mm)	2.82	3.30	3.43	3.49	3.33	3.85
K_p (kN/mm)	1.91	1.39	2.03	2.06	2.91	3.36

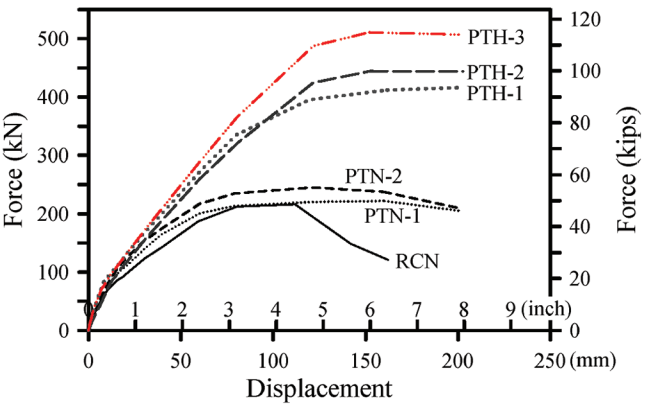

Fig. 6—Force-displacement envelope curves and secant stiffnesses at yield and peak points.

on the joint panels with the joint shear capacity. RCN exhibited the shear distortions of ±0.01 rad at a 2% drift ratio. The joint shear failure occurred at a 3% drift ratio, for which no joint shear distortion data were obtained. The average V_{j_peak}/V_n* (= 1.22) was the same as V_u*/V_n*, showing a good agreement between the expected and actual shear forces. PTN-1 and PTN-2 showed narrow shear distortion ranges (±0.005 rad) at 3% and 2% drift ratios, respectively, beyond which the measurements were terminated prior to reaching V_{j_peak} at concrete spalling. Only slight differences were seen between V_{j_peak}/V_n* and V_u*/V_n* in the two PT specimens. Compared to the Phase 1 specimens, the Phase 2 specimens showed much wider shear distortion ranges as high as 0.0136 rad, and had a tendency that V_{j_peak}/V_n* values were all greater than V_u*/V_n*. Furthermore, unlike the Phase 1 specimens, which sustained the significant joint deterioration, the PTH-series specimens did not suffer from such heavy damages, although their V_{j_peak}/V_n* exceeded V_u*/V_n* and were far greater than 1. It is presumed that the confining pressure from the post-tensioning tendons enabled the joint panels to accommodate the higher shear force and deformation than were expected, and those effects were more effective in the high-strength specimens.

Lateral stiffness

Figure 6 compares the lateral force-displacement envelope curves of the specimens in the positive direction. Secant stiffness values at yield and peak points (K_y and K_p) estimated from the envelope curves were compared as well. Except for RCN, all the PT specimens exhibited overall stable post-peak responses, but the force reduction after the peak was more noticeable in the Phase 1 specimens. The lateral strengths of the Phase 2 specimens were almost twice as high as those of the Phase 1 specimens. The lateral stiffness values, K_y and K_p, showed some variations, and also tended to be higher in the high-strength specimens (Phase 2), but not as high as the variation in lateral strength.

Figure 7 depicts the degradation of the lateral stiffnesses under the incrementally increasing cyclic loading. First, Fig. 7(a) describes how the secant stiffnesses recorded in the

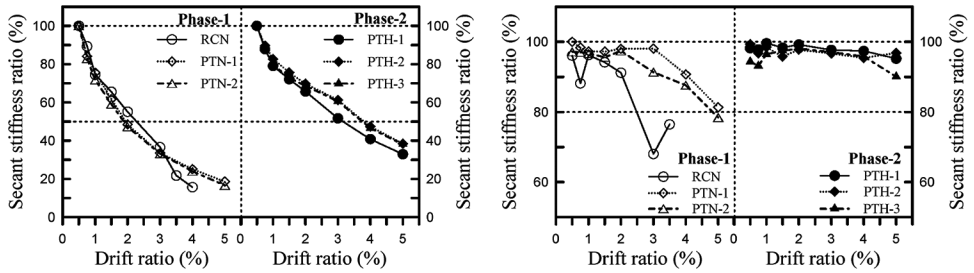

(a) Secant stiffness ratio with respect to initial secant stiffness

(b) Secant stiffness ratio (K_3/K_1) between third and first cycles

Fig. 7—Lateral stiffness variations under repeated loading.

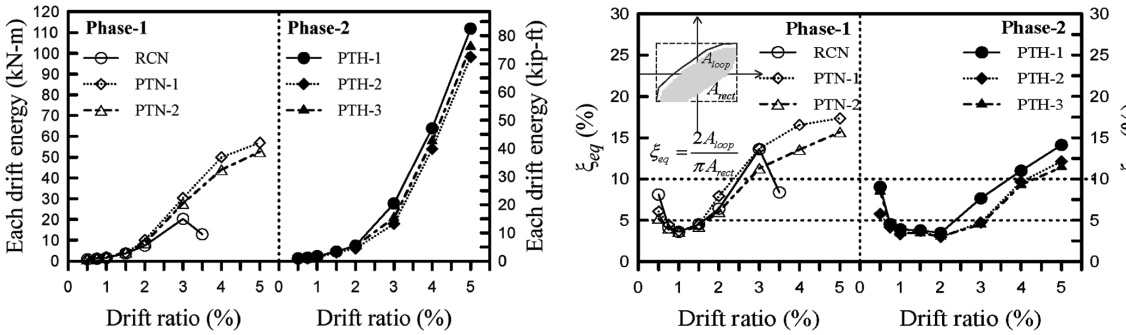

(a) Dissipated energy of each specimen

(b) Equivalent viscous damping ratios.

Fig. 8—Dissipated energy of each specimen and equivalent viscous damping ratios.

first cycle of each target drift ratio reduced with respect to the initial secant stiffness at the 0.5% drift ratio. In the case of the Phase 1 specimens, RCN initially maintained higher stiffness than the PT specimens up to a drift ratio of 3%, but the stiffness dropped more rapidly after that. Eventually, the stiffness of the Phase 1 specimens dropped below 20% of the initial stiffness. Compared to their counterparts, the stiffness reduction of the Phase 2 specimens was much alleviated, and proceeded on a slower pace, recording as low as 33% of the initial stiffness. It seems that the stiffness variations reasonably reflect the damage status shown in Fig. 3, and the impacts of using post-tensioning and high-strength materials. On the other hand, Fig. 7(b) compares the ratios (K_3/K_1) of the secant stiffness in the third cycle (K_3) to that in the first cycle (K_1) at the same target drift ratio (positive direction only) to evaluate how the lateral stiffness degraded under the repeated loading. The stiffness ratios, maintained above approximately 95%, started to deviate at the drift ratio of 2%. RCN rapidly lost its K_3/K_1 below 70% after reaching the peak strength at the 3% drift ratio. The PTN-series specimens showed much gradual stiffness reduction than RCN with final K_3/K_1 of approximately 80%. Meanwhile, the PTH-series specimens hardly lost their stiffnesses in response to the repeated loading, maintaining K_3/K_1 above 90% to the end of testing. The combination of the post-tensioning and high-strength materials proved to be very effective in retaining the lateral stiffness in the high drift ratios.

Energy dissipation and damping

To assess the seismic energy absorption and damping capacities of the specimens, energy dissipations and equivalent viscous damping ratios obtained from the tests are compared in Fig. 8. The energy dissipations in Fig. 8(a) were estimated by calculating the area within the hysteresis loop of each target drift ratio. The energies dissipated by the Phase 1 specimens were similar up to the drift ratio of 2%. At the 3% drift ratio, PTN-1 began to dissipate more energy, approximately 10% and 40% greater than those of PTN-2 and RCN, respectively. PTN-1 and PTN-2 showed continuously increasing energy dissipation up to above 50 kN·m (36.9 kip·ft) until the end of testing. Among the Phase 2 specimens, PTH-1 showed the higher energy dissipation capacity from the 3% drift ratio, followed by PTH-3 and PTH-2. All three specimens maintained a high-growing trend in the energy dissipation up to above 95 kN·m (70 kip·ft).

Figure 8(b) compares the equivalent viscous damping ratios, $\xi_{eq} = (2A_{loop}/\pi A_{rec})$, where A_{loop} is the area enclosed by the hysteresis loop in the first loading cycle and A_{rec} is the area of circumscribed rectangle of the loop. Up to a drift ratio of 1.5%, all six specimens had comparable damping ratios below 5%. At the 3% drift ratio, the Phase 1 specimens showed a much higher level of damping ratios above 10%, whereas the Phase 2 specimens still remained between 4.5 and 7.7%. The damping ratios of PTN-1 and PTN-2 at the 5% drift ratio were 17.3% and 15.7%, respectively. Relatively lower damping ratios (11.4 to 14.1%) were reported from the PTH-series specimens at the same drift ratio. The specimens in Phase 1 seemed to have inevitably wider shapes of hysteresis loops compared to those in Phase 2, as a result of the earlier yielding and much lower flexural capacities.

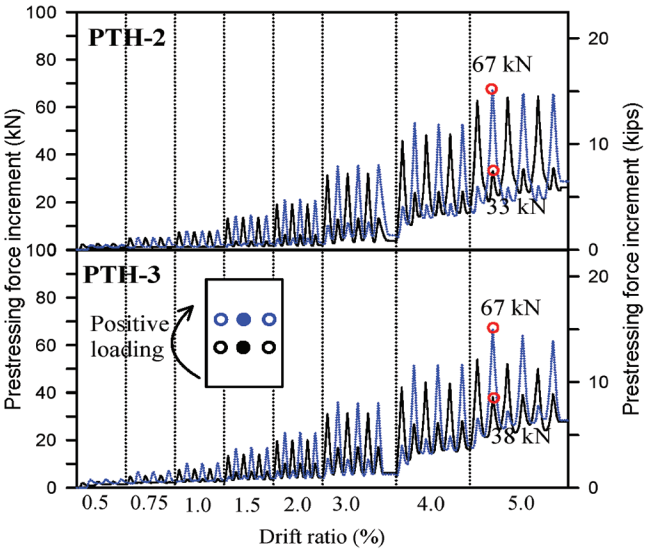

Fig. 9—Variation of PT force of two tendons.

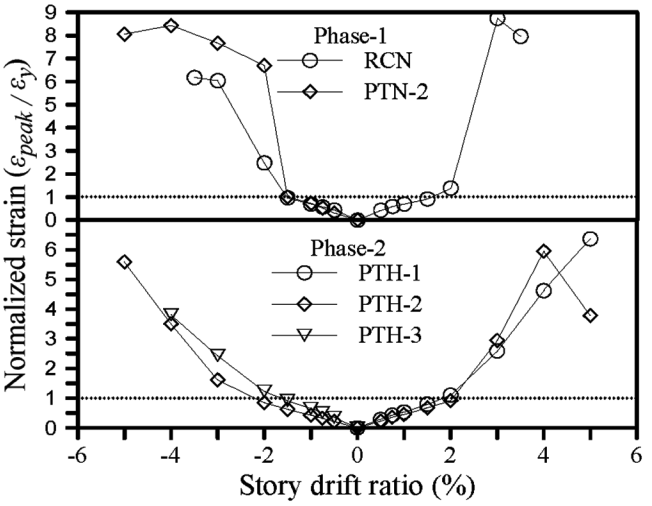

Fig. 10—Strain values of longitudinal reinforcing bars at each target drift ratio.

Behaviors of PT tendons

Figure 9 shows the amount of PT forces of the tendons changed from the initial values in PTH-2 and PTH-3. As illustrated in Fig. 9, the center tendons from each upper and lower layer (blue and black solid circles) were selected, and the vertical axis indicates the amount of forces varied from the beginning of the testing. In Fig. 9, the forces of the blue and black tendons alternately changed depending on the loading direction and continuously increased with the drift ratio. Both specimens recorded the highest force variations in the blue tendons as high as 67 kN (15.1 kip) in the first loading cycle at the –5% drift ratio, where the maximum flexural capacities (M_{peak}) were reported. At the same time, the black tendons still had the force variations of 33 to 38 kN (7.4 to 8.5 kip). At their highest forces, it was calculated that the tendons were responsible for 25.7% and 24% of the flexural strength of the beam in PTH-2 and PTH-3, respectively. In terms of the flexural contribution, the tendons seemed to reach almost the upper limit of Section 18.6.3.5(c) of ACI 318-14, which restricts the contribution of prestressing steel below 25% of the flexural strength at the joint section, though this provision may not need to apply to monolithic prestressed beam-column connections. Based on Eq. (3) and (4), each tendon was expected to have 27.3 kN (6.1 kip) additional force at M_{peak}. The actual force variations of the black tendons were close to or slightly higher than the expectation. On the other hand, the variations in the blue tendons were much greater than the expected value by a factor of 2.45.

Behaviors of longitudinal and transverse reinforcements

Tensile strains of the longitudinal steel bars in the beam were measured by the strain gauges installed at the beam-column interface (refer to Fig. 2). Figure 10 shows the peak strains reported from the first loading cycle of each target drift ratio. The strain values were normalized by the measured yield strain of the bars (that is, $\varepsilon_{peak}/\varepsilon_y$). Strain data for PTN-1 and PTN-2 are partially unavailable due to early loss of the strain gauges. In Fig. 10, it is seen that all the steel bars yielded within the drift ratios of ±2% regardless of the specimen types. This is consistent with results of the authors' previous study done with the same test setup, reinforcing bars, and concrete batch plant (Kang et al. 2019) in which longitudinal bars yielded at the drift ratio of 2% in the beam-column joint specimen reinforced with steel fibers (the specimen denoted as E-HPFRC). After the yielding, the normalized strain values of the nonprestressed specimens (that is, RCN and E-HPFRC) rose close to 9. In contrast, the normalized strains of the post-tensioned specimens were relatively low, approximately or below 6. Based on the previous and current experimental results, the existence of PT tendons appears to have little effect on the yielding of the longitudinal bars, but they indeed contributed to carrying tensile stresses and reducing the excessive demands on the steel bars in the highly nonlinear responses.

Strains of the internal hoops confining the joint panel were also measured (refer to Fig. 2). In the top layer (TL), one strain gauge was placed parallel with the beam (CTL). In the center layer (CL), two strain gauges were placed parallel and perpendicular to the beam (CCL and RCL), respectively. Figure 11 displays the maximum values of available strains normalized by the yield strain at each target drift ratio with the locations of the strain gauges. In Phase 1, despite some variations, yielding of CTL was not seen in any specimens. CCL in RCN yielded at the drift ratio of 1.5%, but CCL in PTN-2 reached close to yielding with the normalized strain of 0.97. Compared with the substantial joint shear cover spalling of the Phase 1 specimens, the strains of the transverse reinforcements in the joint were relatively small. In Phase 2, yielding of CTL and RCL was not shown, and CCL sustained higher strains than them in all specimens. In PTH-1 and PTH-3, CCL yielded at the 3 to 4% drift ratios. CCL in PTH-2 almost yielded with the normalized strain of 0.96.

Discussion on γ-value for shear strength of monolithic PT beam-column connection

In both Phase 1 and Phase 2 testing, the monolithic PT beam-column joints exhibited the satisfactory joint shear

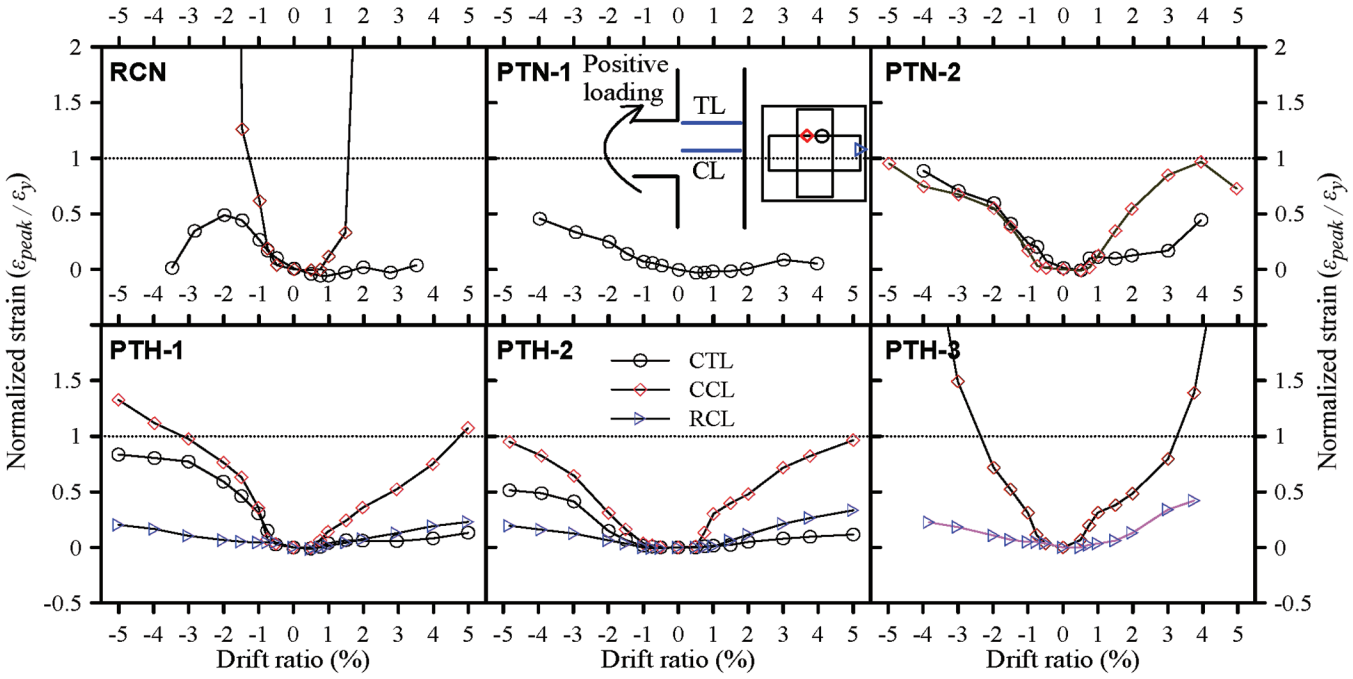

Fig. 11—Strain values of internal hoops at each target drift ratio.

strengths, recording V_{j_peak}/V_n* greater than 1. In spite of the severe spalling of concrete, PTN-1 and PTN-2 had V_{j_peak}/V_n* of 1.38 and 1.64, respectively. The PTH-series specimens showed even greater V_{j_peak}/V_n* values as high as 1.68 in PTH-3. In the calculation of shear strength (V_n*) using Eq. (6), the shear strength factor (γ) of 12 was applied as recommended by ACI 352R-02 for the exterior beam-column connection. However, if the previous V_{j_peak}/V_n* values are reflected, the γ value becomes almost 20 for both the normal-strength joint (PTN-3; 12 × 1.63 = 19.6) and high-strength joint (PTH-3; 12 × 1.73 = 20.8). Based on the current experimental results, therefore, it seems reasonable to adjust the shear strength factor up to γ = 20 for exterior beam-column connection with unbonded post-tensioning. It is estimated that the prestressed beam section had compressive stress (based on f_{se}) of 3.2 and 2.3 MPa (465 and 335 psi) for the PTN- and PTH-series specimens, respectively. Although more extensive research with various parameters is needed to update the current ACI 352R-02 guide, this experimental study suggests that a minimum compressive stress of 2.3 MPa (335 psi) can achieve γ = 20.

SUMMARY AND CONCLUSIONS

The current study experimentally investigates the seismic behavior of monolithic exterior beam-column connections with unbonded post-tensioning. Six full-scale beam-column connection subassemblies, fabricated with normal- and high-strength materials, were tested under quasi-static lateral cyclic loading. Important findings of the experiments are summarized as follows:

1. In the testing of normal-strength specimens, the conventional reinforced concrete (RC) beam-column connection (RCN) sustained the severe joint shear damage with the rapid strength deterioration, associated with the high joint shear demand and the inadequate development length of the headed bars. Under such unfavorable (similar or worse) conditions, the post-tensioned (PT) specimens (PTN-1 and PTN-2) showed quite stable hysteretic responses up to ±5% drift ratios along with the apparent joint cover damages. The post-tensioning effectively prestressed the joint core in the in-plane direction, delaying the crack development and helping the embedment of the headed bars.

2. The high-strength (PTH-series) specimens equipped with post-tensioning achieved their expected flexural strengths with the excellent deformation capacities up to the ±5% drift ratios. Despite the insufficient development length of the headed bars, they far exceeded the expected joint shear strengths by approximately 26 to 67% with no substantial joint damages, demonstrating a great potential of combining the high-strength materials with post-tensioning.

3. The high-strength PT beam-column connections were found to be more effective in maintaining their lateral stiffnesses. The average stiffness reduction ratio of the PTH-series specimens was almost half of that of the PTN-series specimens. Up until the 5% drift ratio, the PTH-series specimens were able to retain the first-cycle stiffnesses above 90% under the load repetitions.

4. As anticipated, the absolute energy dissipations of the PTH-series specimens, with much larger beam moment strength, were almost twice as high as those of the PTN-series specimens. Compared to RCN, the PTN-series specimens exhibited superior energy dissipation capability at the drift ratios of 3 to 5%. The PTN-series specimens recorded the high equivalent viscous damping ratios (15 to 17%) due to the earlier yielding and more plastic behavior. The damping ratios of the PTH-series specimens increased at relatively slower paces up to 11 to 14%.

5. The PT beam-column connections demonstrated the joint shear strengths greater than the expected estimates by as high as 63% and 67% in the normal and high material strength specimens, respectively. The current results imply that the joint shear strength can be better estimated when the

shear strength factor (γ) in ACI 352R-02 is raised from 12 up to 20 for monolithic exterior beam-column connections post-tensioned with unbonded tendons (and with a minimum compressive stress of 2.3 MPa [334 psi] in the beam section).

AUTHOR BIOS

ACI member **Sanghee Kim** *is an Assistant Professor at Kyonggi University, Suwon, South Korea. Before that, he was a Postdoctoral Researcher at Seoul National University, Seoul, South Korea. He received his BS from Jeonbuk National University, Jeonju, South Korea, and his MS and PhD from Seoul National University. His research interests include the structural behavior and impact resistance of reinforced and steel fiber-reinforced concrete structures.*

Thomas H.-K. Kang, *FACI, is a Professor of structural engineering and the Interdisciplinary Program in Artificial Intelligence at Seoul National University. He is a member of ACI Subcommittee 318-T, Post-Tensioned Concrete; and Joint ACI-PTI Committee 320, Post-Tensioned Concrete Building Code; Joint ACI-ASCE Committees 352, Joints and Connections in Monolithic Concrete Structures, and 423, Prestressed Concrete; and Joint ACI-ASME Committee 359, Concrete Containments for Nuclear Reactors. He received the ACI Wason Medal for Most Meritorious Paper in 2009. His research interests include the design and behavior of reinforced, prestressed, and post-tensioned concrete structures.*

ACI member **Donghyuk Jung** *is an Assistant Professor at Korea University, Seoul, South Korea, where he received his BS. He received his MS and PhD from the University of Illinois Urbana-Champaign, Urbana, IL. He was also a Postdoctoral Researcher at Seoul National University. His research interests include the design of reinforced concrete structures using advanced materials such as shape memory alloys.*

Byung Un Kwon *is a Structural Engineer at CNP Dongyang, Seoul, South Korea. He received his BS from Hanyang University, Seoul, South Korea, and his MS from Seoul National University. His research interests include the seismic design and construction of reinforced and post-tensioned concrete beam-column connections.*

Dong Joo Lee *is a Designer/Engineer at Hanssem Co., Ltd., Seoul, South-Korea. She received her BArch from Hongik University, Seoul, South Korea, and her MS from Seoul National University. Her research interests include the design and behavior of precast and prestressed concrete structures.*

ACKNOWLEDGMENTS

The work presented in this paper was funded by the Korea Foundation of Nuclear Safety grant (No. 220324-0122-SB110) and by the Institute of Engineering Research at Seoul National University. The views expressed are those of authors, and do not necessarily represent those of the sponsors.

REFERENCES

ACI Committee 318, 2014, "Building Code Requirements for Structural Concrete (ACI 318-14) and Commentary (ACI 318R-14)," American Concrete Institute, Farmington Hills, MI, 520 pp.

ACI Committee 318, 2019, "Building Code Requirements for Structural Concrete (ACI 318-19) and Commentary (ACI 318R-19) (Reapproved 2022)," American Concrete Institute, Farmington Hills, MI, 624 pp.

ACI Committee 374, 2005, "Acceptance Criteria for Moment Frames Based on Structural Testing and Commentary (ACI 374.1-05) (Reapproved 2019)," American Concrete Institute, Farmington Hills, MI, 9 pp.

ASTM E8/E8M-16, 2016, "Standard Test Methods for Tension Testing of Metallic Materials," ASTM International, West Conshohocken, PA.

Ehsani, M. R., and Alameddine, F., 1991, "Design Recommendations for Type 2 High-Strength Reinforced Concrete Connections," *ACI Structural Journal*, V. 88, No. 3, May-June, pp. 277-291.

Ehsani, M. R.; Moussa, A. E.; and Vallenilla, C. R., 1987, "Comparison of Inelastic Behavior of Reinforced Ordinary- and High-Strength Concrete Frames," *ACI Structural Journal*, V. 84, No. 2, Mar.-Apr., pp. 161-169.

Gao, X.; Xiang, D.; He, Y.; and Li, J., 2020, "Shear Deformation and Force Transfer of Exterior Beam-Column Joints," *ACI Structural Journal*, V. 117, No. 6, Nov., pp. 253-263.

Hwang, H.-J.; Park, H.-G.; Choi, W.-S.; Chung, L.; and Kim, J.-K., 2014, "Cyclic Loading Test for Beam-Column Connections with 600 MPa (87 ksi) Beam Flexural Reinforcing Bars," *ACI Structural Journal*, V. 111, No. 4, July-Aug., pp. 913-921. doi: 10.14359/51686920

Joint ACI-ASCE Committee 352, 2002, "Recommendations for Design of Beam-Column Connections in Monolithic Reinforced Concrete Structures (ACI 352R-02) (Reapproved 2010)," American Concrete Institute, Farmington Hills, MI, 37 pp.

Kam, W. Y., and Pampanin, S., 2009, "Experimental and Numerical Validation of Selective Weakening Retrofit for Existing Non-Ductile R.C. Frames," *Proceedings, ATC & SEI 2009 Conference on Improving the Seismic Performance of Existing Buildings and Other Structures,* B. Goodno, ed., San Francisco, CA, pp. 706-720.

Kam, W. Y., and Pampanin, S., 2010, "Selective Weakening and Post-Tensioning for Retrofit of Non-Ductile R.C. Exterior Beam-Column Joints," *Proceedings of 14th European Conference on Earthquake Engineering 2010*, Republic of Macedonia, pp. 923-930.

Kang, T. H.-K.; Kim, S.; Shin, J. H.; and LaFave, J. M., 2019, "Seismic Behavior of Exterior Beam-Column Connections with High-Strength Materials and Steel Fibers," *ACI Structural Journal*, V. 116, No. 4, July, pp. 31-43. doi: 10.14359/51715568

Kang, T. H.-K.; Shin, M.; Mitra, N.; and Bonacci, J. F., 2009, "Seismic Design of Reinforced Concrete Beam-Column Joints with Headed Bars," *ACI Structural Journal*, V. 106, No. 6, Nov.-Dec., pp. 868-877.

Kwon, B., 2016, "Seismic Tests of RC Exterior Beam-Column Joints with High-Strength Materials and Unbonded Tendons," master's thesis, Seoul National University, Seoul, South Korea.

Park, R., and Thompson, K., 1977, "Cyclic Load Tests on Prestressed and Partially Prestressed Beam-Column Joints," *PCI Journal*, V. 22, No. 5, pp. 84-110. doi: 10.15554/pcij.09011977.84.110

Shao, Y.; Darwin, D.; O'Reilly, M.; Lequesne, R. D.; Ghimire, K. P.; and Hano, M., 2016, "Anchorage of Conventional and High-Strength Headed Reinforcing Bars," University of Kansas Center for Research, Inc., Lawrence, KS.

Shiohara, H.; Sato, A. T.; Otani, S.; and Matsumori, T., 2002, "Effects of Beam-Prestressing Force on the Strength and Failure Mode of R/C Exterior Beam-Column Joints," *Proceedings of 1st* fib *Congress*, Osaka, Japan, pp. 133-140.

ACI STRUCTURAL JOURNAL TECHNICAL PAPER

Title No. 120-S94

Experimental Fatigue Analysis of Stresses Caused by Superloads on Concrete Pavements

by Nathanial Buettner and Julie Vandenbossche

Superloads, defined as vehicles with a gross vehicle weight of over 890 kN, are believed to overload jointed plain concrete pavements (JPCPs) and have the potential to cause significantly more fatigue damage than typical truck traffic. It is anticipated that the fatigue damage is greater when the superload is applied later in the life of the JPCP. In this study, the stress pulses generated by superloads on JPCPs were characterized using finite element modeling and related to fatigue damage through the fatigue testing of concrete beams. Concrete beams subjected to loading profiles that simulate those of a superload were observed to accumulate fatigue damage at an accelerated rate when applied after 70% of the fatigue life of the concrete was consumed. Moreover, through the collection of fatigue life and beam response data, the effects of stress ratio, stress range, flexural strength, and damage state at the time of loading on the fatigue damage imposed by a superload movement were elucidated.

Keywords: damage; fatigue; nonlinear; overload; pavement; superload.

INTRODUCTION

Superloads, defined as vehicles that carry loads over 890 kN,[1] are increasingly used in the United States to move heavy freight and construction equipment. Superloads commonly consist of a tractor and trailer, span two lanes, and have axle loads that are greater than the state law allows. The trailers on these vehicles have unique axle configurations consisting of repeating single, tandem, or tridem axles. Given that superloads have the potential to overload pavements and bridges and cause significantly more damage than typical truck traffic, a permit must be obtained from the Department of Transportation (DOT) or similar government agency in the state(s) of travel.

Currently, the damaging effects of superloads on the fatigue performance of jointed plain concrete pavements (JPCPs) are unestablished. For this reason, government agencies do not completely consider the potential fatigue damage caused by a superload movement before issuing a permit. Instead, permits are typically issued as a function of weight-distance or infrastructure use.[1] Based on current practices in the design of JPCPs, superloads with single and tandem axle trailers are hypothesized to generate fatigue damage that can lead to bottom-up and top-down cracking, respectively.[2]

The quantification of the fatigue damage at a given location in a JPCP requires an accurate characterization of the stress pulse generated. Current pavement design methodologies, such as pavement mechanistic-empirical (pavement ME) and the 1993 American Association of State Highway and Transportation Officials (AASHTO) pavement design guide, cannot predict the stresses from the unique axle configurations of superloads for concrete pavements.[2,3] These design methodologies also do not consider the damage state in the concrete at the time of loading when predicting fatigue damage accumulation, as fatigue damage is assumed to accumulate linearly in accordance to Miner's Rule.[4] Concrete has been observed to accumulate damage nonlinearly,[5-7] with damage accumulating rapidly later in the fatigue life of the concrete. Thus, there is a critical need to characterize the stress pulses generated by superloads and to relate these stress pulses to fatigue damage with consideration to the existing damage state in the concrete. A computational and laboratory research strategy was used for that purpose, with the results of the computational component (that is, stress characterization) being documented in greater detail in other works.[8,9] The primary emphasis of this paper is on the laboratory investigation.

RESEARCH SIGNIFICANCE

The significance of superload movements on JPCPs is evaluated by considering the unique characteristics of the stress pulses and the damage state of the concrete at the time of loading. These parameters, which have yet to be considered in the context of superloads, are critical to examine to quantify the actual impact of superloads on pavement life. Furthermore, this analysis provides guidance for government agencies to more accurately predict the fatigue damage caused by a superload so that the adequacy of current permitting procedures can be evaluated.

SUPERLOAD STRESS CHARACTERIZATION

The first step in determining the stresses generated by superloads was to identify the characteristics of the loads and axles configurations typical of superloads. Ten superload vehicle profiles were obtained from the Pennsylvania Department of Transportation (PennDOT), of which five unique superload configurations were identified. These superloads have axle configurations hypothesized to be critical to the development of bottom-up and top-down midslab transverse cracking.

The maximum stresses and stress pulses generated by the heaviest of each of the five superloads (trailers detailed in Table 1) on JPCPs were evaluated using finite element software.[10] The structural models of JPCPs consisted of specific combinations of slab thickness (203, 254, and 330 mm),

ACI Structural Journal, V. 120, No. 6, November 2023.
MS No. S-2022-177.R2, doi: 10.14359/51739086, received March 3, 2023, and reviewed under Institute publication policies.

shoulder type (asphalt and concrete), and dowel diameter (32 and 38 mm). The JPCPs were designed to have two 3.7 m lanes consisting of 13 slabs each with a joint spacing of 4.6 m and longitudinal joint load-transfer efficiency of 0.9. The concrete was assumed to have an elastic modulus of 32 GPa, Poisson's ratio of 0.18, coefficient of thermal expansion of 8.1×10^{-6} mm/mm/°C, and unit weight of 24 kN/m^3. The modulus of subgrade reaction was assumed to be 54 kPa/mm to represent a medium-stiff support.

Superload movements were evaluated in combination with two different linear temperature gradients (–0.05 and 0.07°C/mm) present throughout the depth of the slab. These values were selected because they were identified as the larger positive and negative temperature gradients that develop in pavements in Pennsylvania.[8] The analysis was also performed when a temperature gradient was not present. Full details on the incremental finite element analysis (for example, meshing, analysis procedure, and so on) can be found in other works.[8,9] The pertinent results of the stress characterization in regard to the laboratory investigation are discussed as follows.

Table 1—Characteristics of Pennsylvania superloads

Superload	SL1	SL2	SL3	SL4	SL5
Gross vehicle weight, kN	2298	3850	2580	2360	2360
Axle type on trailer	Single	Single	Tandem	Tandem	Tandem
Number of axle type on trailer	20	24	12	8	8
Axle load, kN	102	80	166	206	198
Spacing between axles, m	2.8	1.5	3.7 to 3.8	4.3	4.4
Tandem axle spacing, m	—	—	1.8	1.6	1.8

Results

Table 2 lists the maximum stress generated by the superloads for each pavement structure under each of the temperature gradient conditions. High stresses developed in the 203 and 254 mm thick JPCPs with asphalt shoulders when the superload was applied with a 0.07°C/mm temperature gradient. The stresses were much lower when the superload was applied with the –0.05°C/mm temperature gradient or no temperature gradient. The environmental conditions at the time of superload movement are observed to have a significant impact on the magnitude of the maximum stress. The largest axle loads were those associated with SL1 and

Table 2—Maximum stresses caused by superloads on JPCP structural models

Superload	Concrete slab thickness, mm	Shoulder type	Maximum stress when temperature gradient = 0.07°C/mm, MPa	Maximum stress when temperature gradient = –0.05°C/mm, MPa	Maximum stress when no temperature gradient, MPa
SL1	203	Asphalt	4.18	2.66	2.88
SL1	254	Asphalt	3.30	2.19	1.99
SL1	203	Concrete	3.40	2.06	2.01
SL1	254	Concrete	2.74	1.76	1.43
SL1	330	Concrete	1.98	1.32	0.94
SL2	203	Asphalt	3.46	2.10	2.14
SL2	254	Asphalt	2.92	1.92	1.57
SL2	203	Concrete	3.17	2.00	1.84
SL2	254	Concrete	2.71	1.83	1.36
SL2	330	Concrete	2.11	1.22	0.94
SL3	203	Asphalt	3.57	2.37	2.21
SL3	254	Asphalt	2.97	2.20	1.63
SL3	203	Concrete	3.05	1.96	1.64
SL3	254	Concrete	2.55	1.92	1.22
SL3	330	Concrete	1.92	1.46	0.86
SL4	203	Asphalt	4.08	2.56	2.75
SL4	254	Asphalt	3.42	2.54	2.09
SL4	203	Concrete	3.34	2.17	1.96
SL4	254	Concrete	2.80	2.15	1.48
SL4	330	Concrete	2.14	1.82	1.06
SL5	203	Asphalt	3.77	2.36	2.44
SL5	254	Asphalt	3.16	2.35	1.81
SL5	203	Concrete	3.11	2.01	1.73
SL5	254	Concrete	2.61	1.99	1.29
SL5	330	Concrete	1.97	1.68	0.92

SL4 (Table 1), and these consequently resulted in the highest maximum stresses.

The maximum stresses listed in Table 2 were examined in the context of stress ratio, which is used as a predictor of the number of cycles to failure in current JPCP design. Stress ratio is defined as

$$SR = \sigma/f_r \quad (1)$$

where SR is the stress ratio; σ is the maximum stress at the slab edge (MPa); and f_r is the modulus of rupture (MOR) (MPa).

The maximum stresses generated from a superload and a 0.07°C/mm temperature gradient can correspond to stress ratios approaching or even greater than 1 depending on the structural features and material properties of the JPCP. For instance, thinner slabs with asphalt shoulders and lower-strength concrete (that is, concrete with an MOR of 3.5 to 4.1 MPa) are found to be particularly susceptible to high stress ratios. JPCPs with a slab thickness greater than 254 mm, concrete shoulders, and higher-strength concrete (that is, concrete with an MOR of 4.8 to 5.5 MPa) tend to have stress ratios that are significantly lower. High stress ratios are also unlikely to occur when there is a –0.05°C/mm temperature gradient or no temperature gradient.

The maximum stresses caused by the five superloads on JPCPs with asphalt shoulders developed adjacent to the lane/shoulder joint regardless of the temperature gradient condition. These stresses developed at midslab on JPCPs subjected to the peak temperature gradients and approximately a meter laterally from midslab on JPCPs when no temperature gradient was present. The location of the maximum stress on JPCPs with concrete shoulders varied for each combination of superload, slab thickness, and temperature gradient. For these JPCPs, the maximum stress caused by the superload and a 0.07°C/mm or –0.05°C/mm temperature gradient occurred at midslab, but not always directly adjacent to the lane/shoulder joint. If there was not a temperature gradient in the slab at the time of loading, the maximum stress occurred from between 0 and 4 m from the longitudinal joint.

Figure 1 shows the effects of slab thickness, shoulder type, and temperature gradient on the stress pulses generated at midslab adjacent to the lane/shoulder joint. The maximum stress and the stress range were the features of interest for these stress pulses. Stress range is defined as the difference in the maximum and minimum stresses of a given stress pulse. The highest maximum stresses and stress ranges were generated in the 203 mm thick JPCP with asphalt shoulders from a superload and a 0.07°C/mm temperature gradient. Stress ranges of approximately 3.5, 2, and 4 MPa were generated as a result of superloads SL1, SL2, and SL4, respectively, with a minimum stress range of 2 MPa between the tandem axle peaks of SL4. The maximum stress and stress range are shown to decrease by approximately 2 MPa for SL1 and SL4 and by less than 0.4 MPa for SL2 if the slab thickness is increased from 203 to 254 mm. The maximum stresses and stress ranges also decrease if the JPCP has concrete shoulders instead of asphalt shoulders. The stress pulses generated by superload movement in the presence of a –0.05 °C/mm temperature gradient are inverted forms of the other pulses

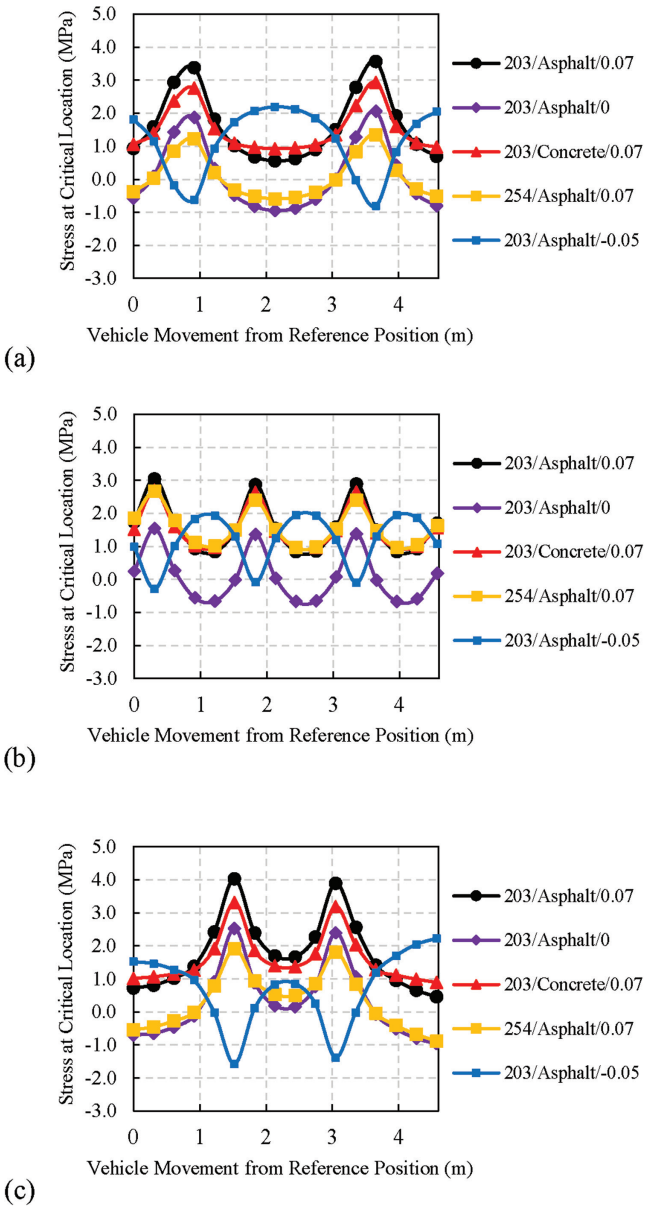

Fig. 1—Examples of stress pulses generated by: (a) SL1; (b) SL2; and (c) SL4 at critical location of JPCPs with various combinations of slab thickness/shoulder type/temperature gradient.

because the tension occurred at the top of the slab instead of the bottom. The stress pulses generated by superload movement in the presence of: 1) a 0.07°C mm temperature gradient; and 2) no temperature gradient have a similar pulse shape and stress range. However, the maximum stresses in the JPCPs with no temperature gradient are found to be significantly smaller because the slab was not curled and thus fully supported when loaded. In these instances, stress reversals from tension to compression were present between the two axle loads. Stress reversals have been shown in the literature to decrease the fatigue life of concrete.[11,12] However, based on the results of Zhang et al.,[12] the stress reversals caused by superloads are not anticipated to significantly impact the fatigue damage because the magnitude of the stress is low.

It is important to note that these results apply to JPCPs with a medium-stiff support. However, the stresses generated by

superloads are not anticipated to be very sensitive to changes in the modulus of subgrade reaction.

DEVELOPMENT OF EXPERIMENTAL INVESTIGATION

Using the results of the superload stress characterization, an experimental investigation was developed to quantify the fatigue damage in concrete imposed by a superload. The fatigue test programs of this investigation, the constant amplitude and damaged concrete testing, were developed using the same parameters of interest and performed using the same test setup, data acquisition, materials, and specimen preparation.

Loading profiles

Three of the single-axle stress pulses and one tandem-axle stress pulse from the superloads were incorporated into the fatigue test investigation. The details of the loading profiles are provided in Fig. 2. The maximum stress ratios correspond to the maximum stresses identified through the finite element analysis of the superloads. The loading profiles shown in Fig. 2(a) through (c) were generated using a sinusoidal wave function. A seating load of 0.7 MPa (that is, 15 to 20% of the maximum load) was adopted for each of these loading profiles to represent the curling stress caused by a high positive-temperature gradient. The loading frequency depicted in Fig. 2(a) and (b) corresponds to the SL1 superload traveling at a speed of 24 km/h (15 mph). The loading frequency exhibited in Fig. 2(c) was increased to 8 Hz to decrease the testing time. This was deemed acceptable because the number of cycles to failure for a maximum stress ratio of 0.7 has been observed to be less sensitive to loading frequency.[13]

The tandem-axle loading profile with a maximum stress ratio of 0.9 was programmed as a custom waveform that ramped directly to the target values (Fig. 2(d)) given the constraints of the test program. Tandem-axle loading profiles with a maximum stress ratio below 0.9 were not evaluated in the fatigue testing because these pulses had similar stress ranges to the single-axle stress pulses shown in Fig. 2(a) through (c). A seating load of 0.7 MPa (that is, 15 to 20% of the maximum load) was adopted in between tandem-axle fatigue cycles to represent the curling stress caused by a high positive-temperature gradient. The load that corresponds to a stress of 1.4 MPa was specified in between the maximum stresses of an individual tandem axle. This characteristic of the tandem axle loading profile was observed to be present when the JPCP has a high positive-temperature gradient. The loading frequency depicted in Fig. 2(d) represents the movement of a SL4 superload traveling at a speed of 24 km/h (15 mph).

Test setup

A four-point bending load configuration was used for loading the beams. A beam size of 102 x 102 x 610 mm was chosen to fatigue the concrete beams in flexural tension only.[14] The support span was designed to be 533 mm with three 178 mm loading spans. The loading was applied using a load frame equipped with a 24.5 kN, 152 mm stroke actuator, 2.5 metric ton load cell, and 164 cm^3/s hydraulic supply.

To establish the target loads to generate the fatigue stresses, 102 x 102 x 610 mm concrete beams were tested in four-point bending and the average flexural strength was calculated.[15] Then, the load input required to reach the target applied stress was calculated with Eq. (2)

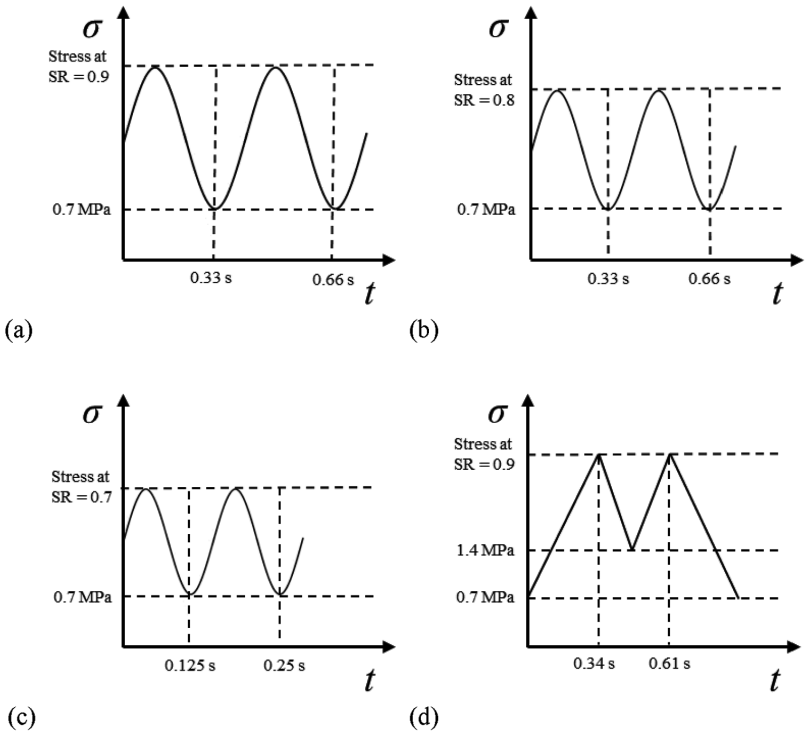

Fig. 2—Loading profiles for: (a) single axle at SR *= 0.9; (b) single axle at* SR *= 0.8; (c) single axle at* SR *= 0.7; and (d) tandem axle at* SR *= 0.9.*

$$\sigma_{app} = SRf_r = \frac{P_{app}L}{bh^2} \quad (2)$$

where σ_{app} is the applied stress (MPa); SR is the stress ratio; f_r is the average flexural strength of the concrete (MPa); P_{app} is the load corresponding to the applied stress (N); L is the support span length (mm); b is the width of the beam (mm); and h is the depth of the beam (mm).

Instrumentation and data acquisition

The beams that were tested in fatigue were instrumented with linear variable differential transformers (LVDTs) and strain gauges, as shown in Fig. 3. The LVDTs measured neutral axis deflection and were positioned on the neutral axis of each concrete beam with a harness. The harness was fixed to the beam at middepth directly over the supports, allowing the LVDTs to stay in position as the load was applied. Three LVDTs were located on both sides of the concrete beam: one at midspan and one at each end of the middle third of the support span. Strain gauges with a 102 mm gauge length were mounted at the center of the top and bottom face on each concrete beam to measure bending strain. A "half-bridge" bridge circuit was configured with the two resistors having a resistance of 120 ohms.

The high-speed, closed-loop, modular controller used to operate the test setup sampled the deflection from the LVDTs at a frequency of 1024 Hz and recorded the maximum and minimum deflection for every cycle. A data logger sampled and recorded the bending strain at a frequency of 250 Hz, which sufficiently captured the strain peaks.[9]

Strengths

To examine the influence of strength on the fatigue behavior of concrete beams, two target levels of concrete strength were identified: "lower strength" and "higher strength." The lower-strength and higher-strength conditions were defined as having an MOR between 3.4 and 4.1 MPa and between 4.8 and 5.5 MPa, respectively.

These strengths were defined assuming an ASTM standard beam size.[15] Instead of casting 152 x 152 x 533 mm concrete beams for flexural strength testing, 102 x 203 mm concrete cylinders were cast and the compressive strength results were correlated to MOR. The cylinders were tested in accordance to ASTM C39/C39M-21 on a loading machine.[16] The following relationship, which is recommended by the American Concrete Pavement Association (ACPA),[17] was used

$$\text{MOR} = 2.3f_c'^{2/3} \quad (3)$$

where MOR is the modulus of rupture of the concrete for the ASTM standard beam size (MPa); and f_c' is the compressive strength of the concrete (MPa).

Materials

The concrete mixture design used to achieve the target strengths, consisting of AASHTO No. 67 and No. 8 limestone, ordinary sand, and Type I/II cement, is presented in Table 3. This mixture meets the specifications for a PennDOT Class AA paving mixture.[18] The specific gravities of the No. 67 limestone, No. 8 limestone, and ordinary sand are 2.60, 2.70, and 2.62, respectively. An air entrainer and a high-range water-reducing admixture were incorporated during mixing to achieve a slump of 51 mm and an air content of 5%. In each cast, concrete beams were cast for flexural strength testing and fatigue testing, and concrete cylinders were cast for weekly compressive strength and elastic modulus testing. All concrete specimens were cast and cured in accordance with ASTM C192/C192M-19.[19]

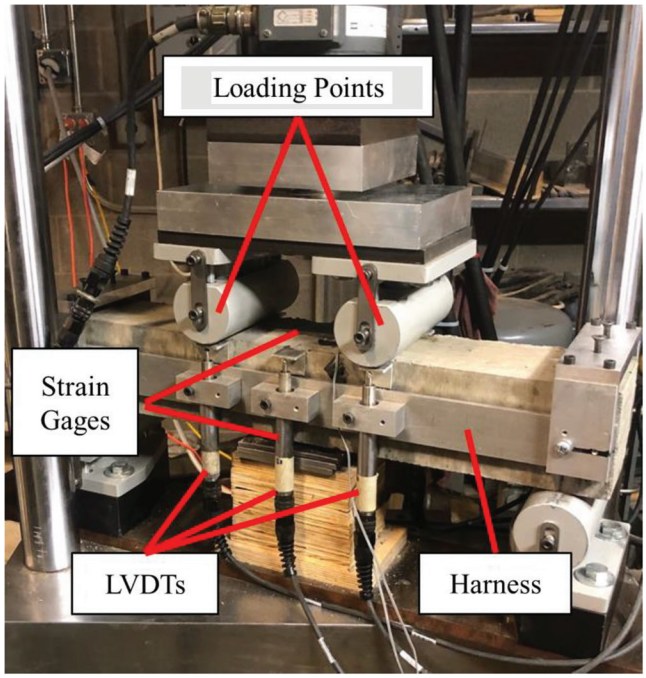

Fig. 3—Test setup for fatigue testing.

Table 3—Concrete mixture design developed for fatigue testing

Water-cement ratio (w/c)	0.44
No. 67 coarse aggregate, kg/m^3	860
No. 8 coarse aggregate, kg/m^3	178
Fine aggregate, kg/m^3	799
Cement, kg/m^3	341
Water, kg/m^3	151
Air entrainer, mL/m^3 cement	330
High-range water-reducing admixture, mL/m^3 cement	710
Target air content, %	5
Target slump, cm	5.0 ± 1.3

EXPERIMENTAL INVESTIGATION

Constant-amplitude testing

The goal of the constant-amplitude testing was to quantify the number of cycles to failure and nonlinear responses of the concrete beams subjected to superload loading profiles. In the constant-amplitude fatigue test, one of the four loading profiles in Fig. 2 was applied cyclically to the concrete beam until failure (that is, complete fracture of the beam). Three concrete beams were tested for each combination of loading profile (Fig. 2(a) through (d)) and strength level (lower or higher). Two additional beams were tested at stress ratios

of 0.8 and 0.9 to reduce scatter in the lower-strength data, resulting in a total of 20 fatigue tests.

Constant-amplitude fatigue tests were conducted on lower-strength concrete beams at 3 to 6 days after casting. This was when the concrete had an average compressive strength of 22 to 29 MPa, corresponding to an MOR of 3.4 to 4.1 MPa for the standard ASTM beam size. For lower-strength concrete, at least two concrete beams were prepared and tested on each test day to establish the load input required to reach the target applied stress. Three beams, instead of two, were tested to establish the load input if the difference in the flexural strengths of the first two beams was greater than 0.5 MPa. The higher-strength concrete beams were tested at 14 to 28 days after casting. This was when the concrete had an average compressive strength of 37 to 45 MPa, which correlates to an MOR of 4.8 to 5.5 MPa. Flexural strength gain occurs more slowly when the concrete has higher strength (that is, 14 days after casting), so at least two to three beams were tested within 2 days of the fatigue testing to establish the strength needed for defining the load input. The flexural strengths measured for the 102 x 102 x 610 mm concrete beams were approximately 20% higher than the predicted moduli of rupture for the standard ASTM beam size, indicating a size effect.

Fatigue life results

S-N curves, which relate stress ratio to the number of cycles to failure, were developed to examine the effects of stress ratio on the fatigue life of concrete beams subjected to the single-axle loading profiles. The *S-N* curves were first fit separately for lower-strength and higher-strength concrete beams, as shown in Fig. 4. Lower- and higher-strength concrete beams were observed to exhibit a similar number of cycles to failure at stress ratios of 0.8 and 0.9. The average number of cycles to failure caused by a stress ratio of 0.7 for lower- and higher-strength concrete was found to be statistically different at a 90% confidence level (but not at 95%) based on a paired *t*-test. This possible difference in fatigue life based on strength level is hypothesized to be a consequence of the stress range and not because of the concrete strength. Stress range has been observed to influence the fatigue life of concrete.[20,21] While the minimum stress was 0.7 MPa for all loading profiles, the maximum stress applied to the concrete beams varied based on the strength level. Consequently, the lower-strength beams experienced a smaller stress range in each fatigue cycle than the higher-strength beams. If all the fatigue life data for both strength levels was combined into one *S-N* curve (Fig. 5(a)), the coefficient of determination was observed to decrease compared to the *S-N* curves in Fig. 4. However, if stress ratio range, defined as the difference in the maximum and minimum stress ratios of a given stress pulse, was plotted against the number of cycles to failure, the resulting fit (Fig. 5(b)) was more comparable to the *S-N* curves in Fig. 4. This finding indicates that stress range may have affected the fatigue damage caused by a stress ratio of 0.7, but more research is necessary to confirm this effect. However, there is no clear influence of strength level observed on the fatigue life and so additional testing is required.

The *S-N* curves shown in Fig. 4 were compared to others in the literature that were developed based on data from beam fatigue testing, as presented in Fig. 6. In general, the *S-N* curves predict a comparable number of cycles to failure for each stress ratio. The *S-N* curve for lower-strength concrete has a similar slope to the zero-maintenance *S-N* curve,[22] and the *S-N* curve for higher-strength concrete has a similar slope to the curves from the Portland Cement Association (PCA)[23] and Chatti et al.[14] The zero-maintenance and PCA *S-N* curves were developed with fatigue data gathered from multiple studies with several combinations of testing

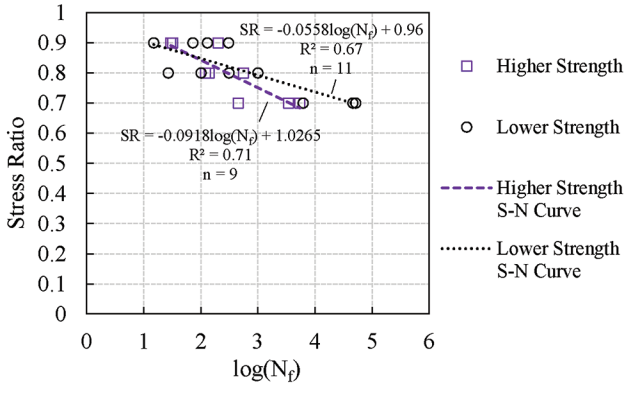

Fig. 4—Stress ratio versus log(N_f) for concrete beams subjected to single-axle loading profiles (separated by strength).

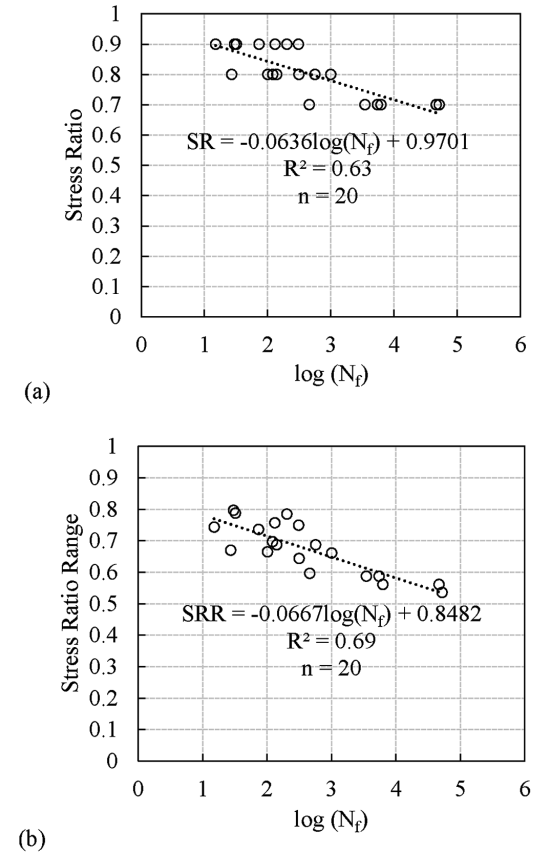

Fig. 5—(a) Stress ratio versus log(N_f); and (b) stress ratio range versus log(N_f) for concrete beams subjected to single-axle loading profiles (all data).

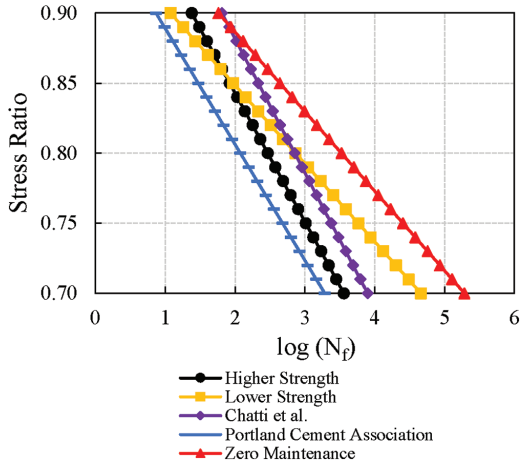

Fig. 6—Comparison of higher-strength and lower-strength S-N *curves to others in literature.*[14,22,23]

factors that resulted in the slopes shown in Fig. 6. The Chatti et al. *S-N* curve was developed from the fatigue testing of 102 x 102 x 610 mm beams with flexural strengths of 4.1 to 5.5 MPa for a beam size of 102 x 102 x 305 mm. These beams were also subjected to single-axle loading profiles. This combination of factors is similar to those included in this study and yields a curve similar to the *S-N* curve for higher-strength concrete of this study.

The fatigue lives of concrete beams subjected to the tandem-axle loading profile (Fig. 2(d)) are shown in Table 4. Each fatigue cycle for this stress pulse represents two applications of the maximum stress. The average number of applications to failure were compared for concrete beams subjected to the single- and tandem-axle loading profiles at a stress ratio of 0.9 using a *t*-test. At a 95% level of confidence, the averages were not statistically different, indicating that these two loading profiles may generate similar fatigue lives.

Nonlinear response

The beam response data was used to evaluate the nonlinear progression of damage in the concrete. The midspan deflection data was used to calculate compliance, which is an indicator of the stiffness of the concrete. For each constant-amplitude fatigue test, the compliance for every fatigue cycle was calculated using Eq. (4)

$$C_i = \frac{\delta_{i,max} - \delta_{i,min}}{P_{i,max} - P_{i,min}} \quad (4)$$

where C_i is compliance for cycle i (mm/N); $\delta_{i,max}$ is the maximum average midspan deflection for cycle i (mm); $\delta_{i,min}$ is the minimum average midspan deflection for cycle i (mm); $P_{i,max}$ is the maximum load for cycle i (N); and $P_{i,min}$ is the minimum load for cycle i (N).

The compliance for every fatigue cycle was normalized to the initial compliance to account for inherent differences between specimens, as shown in Eq. (5)

$$C_i^{norm} = C_i/C_0 \quad (5)$$

Table 4–Number of cycles to failure for concrete beams subjected to tandem-axle loading profile (*SR* = 0.9)

	Cycles to failure		
Strength level	Sample 1	Sample 2	Sample 3
Lower	12	110	137
Higher	7	11	51

where C_i^{norm} is the normalized compliance for cycle i; and C_0 is the initial compliance (mm/N).

Figure 7 shows the progression of normalized compliance during cyclic loading for several concrete beams. The trends depicted in Fig. 7 generally represent those found in each test. Normalized compliance was observed to increase in three phases. In the first 10 to 15% of the fatigue life, normalized compliance was observed to increase at a slightly decelerating rate. Then, up to approximately 70 to 80% of the fatigue life, the normalized compliance was observed to increase linearly. Lastly, in the final portion of the fatigue life, normalized compliance was found to increase at an accelerating rate. In each test, the majority of normalized compliance gain (that is, stiffness loss) was observed to occur after 70 to 80% of the fatigue life was consumed. This finding indicates that the application of the superload may be more damaging when applied later in the fatigue life and less damaging when applied earlier in the fatigue life.

The bending strain during cyclic loading was used to corroborate the findings in the normalized compliance data. For each constant amplitude fatigue test, the maximum bending strain and difference between maximum and minimum bending strain were plotted as a function of the number of cycles. The nonlinear progression of bending strain during cyclic loading was observed in the strain readings when the beam failed at or near the strain gauges. Figure 8 shows data for when this was the case. The bending strain data for this specimen indicates the same nonlinear damage development observed in the normalized compliance data (*SR* = 0.8 and N_f = 101 in Fig. 7(a)).

Damaged concrete testing

The damaged concrete testing was conducted to further investigate the nonlinear behavior of concrete beams subjected to the stresses imposed by superloads. In a damaged concrete fatigue test, the single-axle loading profile with a maximum stress ratio of 0.7 (Fig. 2(c)) was applied cyclically until the beam exhibited a target normalized compliance (that is, damage level [*D*]). The damaged beam was then overloaded for 10 fatigue cycles using either the loading profile in Fig. 2(a) or (b), representing a superload movement. After the overload, the loading profile was reverted back to that depicted in Fig. 2(c) and applied cyclically to failure.

Normalized compliances representing 15, 50, and 85% life consumed were chosen as the damage levels when the overload was applied. To identify these values, the normalized compliance was evaluated at 15, 50, and 85% life consumed for each constant-amplitude test involving a single-axle loading profile. A second-order polynomial relationship was

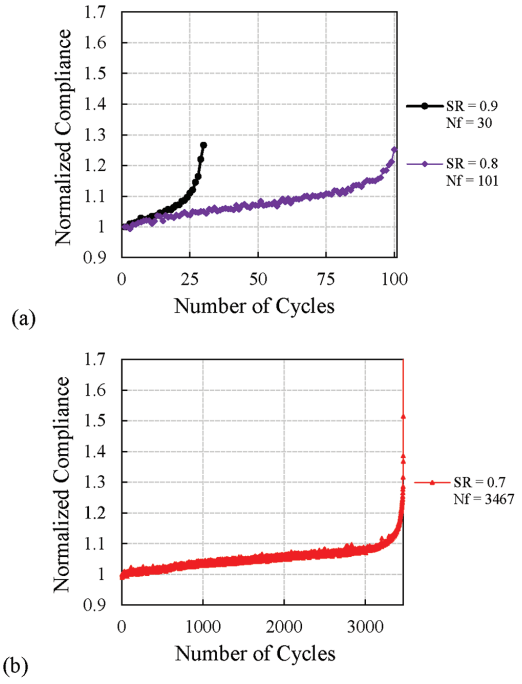

Fig. 7—Normalized compliance versus number of cycles for concrete beams subjected to: (a) SR = *0.9,* SR = *0.8; and (b)* SR = *0.7.*

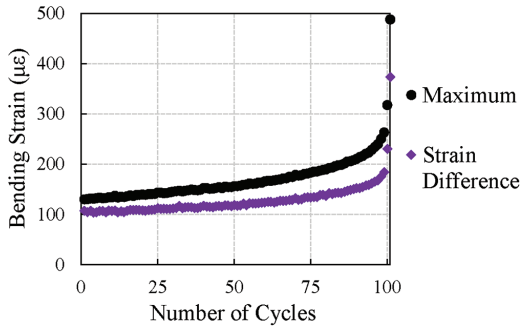

Fig. 8—Bending strain versus number of cycles for concrete beam subjected to SR = *0.8 (*N_f = *101).*

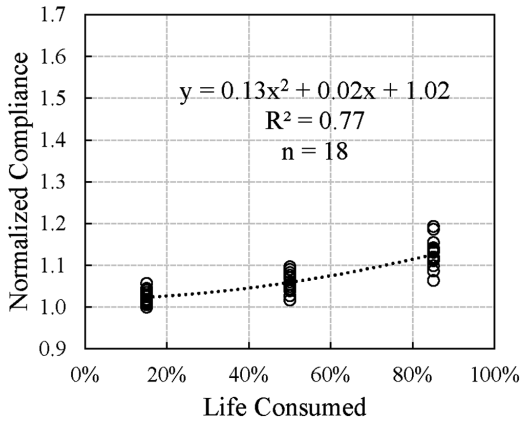

Fig. 9—Normalized compliance evaluated at 15, 50, and 85% life consumed of constant-amplitude fatigue tests.

developed (Fig. 9). Two tests were excluded from the relationship due to instrumentation error. From this relationship, the target normalized compliances were chosen to be 1.03, 1.06, and 1.13 for 15%, 50%, and 85% life consumed, respectively.

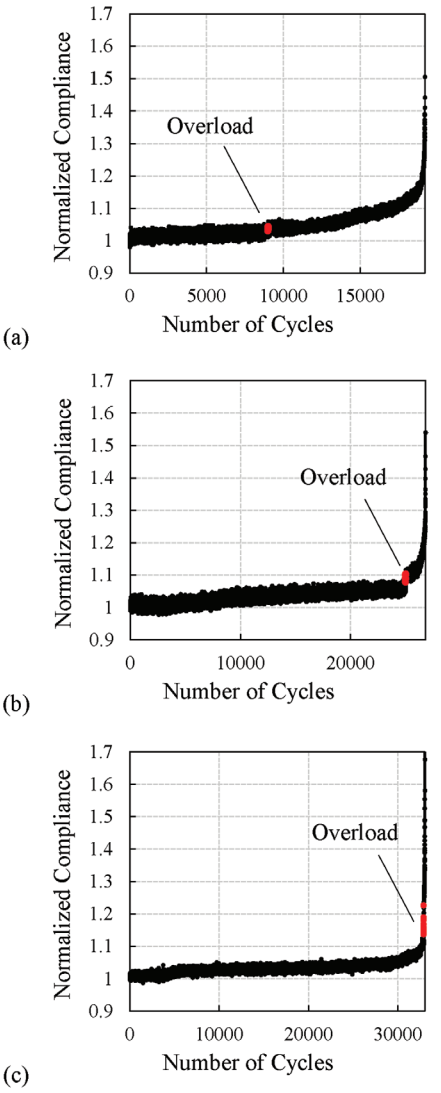

Fig. 10—Normalized compliance versus number of cycles for higher-strength concrete beams subjected to overload of SR = *0.9 at: (a)* D = *15%; (b) 50%; and (c) 85%.*

To account for cyclic variation inherent to a loading frequency of 8 Hz, the average normalized compliance over 2 seconds was compared to these targets during testing instead of point values. When the target normalized compliance was approximately reached (that is, at target $C_i^{norm} \pm 0.01$ for percent life consumed = 15%, 50% and $C_i^{norm} \pm 0.02$ for percent life consumed = 85%), the beam was overloaded.

Three concrete beams were tested for each combination of overload (Fig. 2(a) and (b)), strength level (lower or higher), and damage level (D = 15%, 50%, or 85% life consumed). Damaged concrete tests were conducted within the same testing windows as the constant-amplitude tests.

Results

Lower-strength beams tended to require more fatigue cycles to reach the target normalized compliances than higher-strength beams, further indicating the effect of stress range. Complete details on the fatigue cycle data for the damaged concrete testing can be found in work by Buettner.[9]

Figure 10 demonstrates the effect of percent life consumed on the impact of an overload. At D = 15%, an overload at

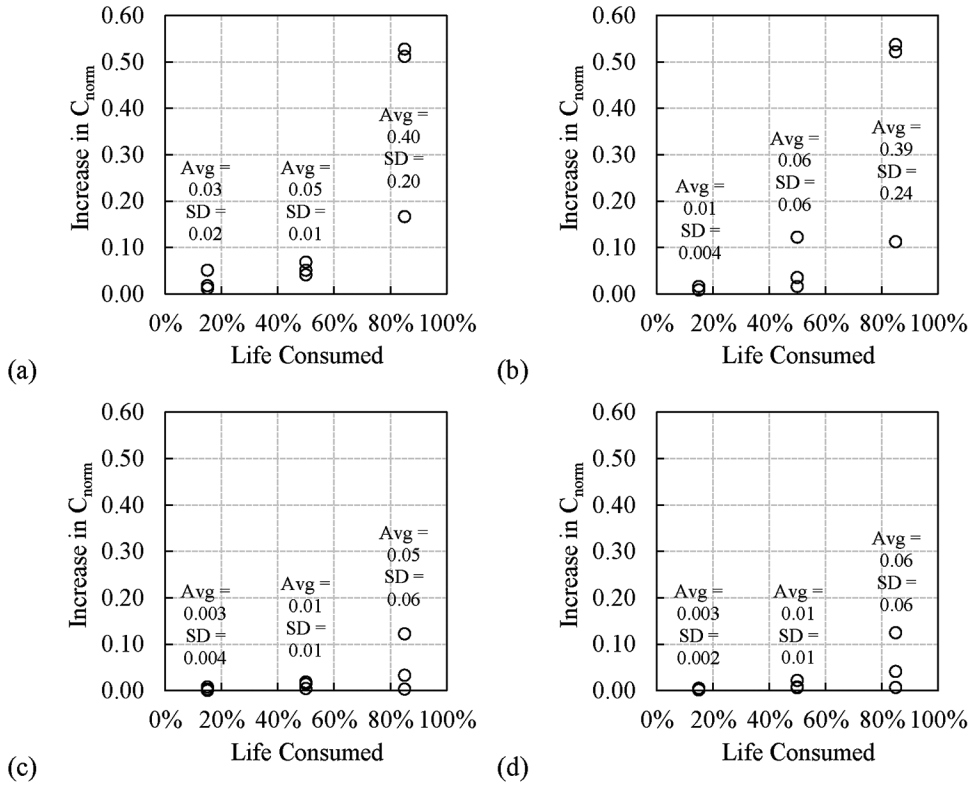

Fig. 11—Increase in average normalized compliance due to: (a) overload of SR *= 0.9 on lower-strength concrete; (b) overload of* SR *= 0.9 on higher-strength concrete; (c) overload of* SR *= 0.8 on lower-strength concrete; and (d) overload of* SR *= 0.8 on higher-strength concrete.*

a stress ratio of 0.9 caused a slight but noticeable increase in normalized compliance. At D = 50%, the increase was observed to be greater, accelerating during cyclic loading after its application. At D = 85%, the normalized compliance increased to at or near failure of the beam. This trend was investigated for all damaged concrete tests by comparing the average normalized compliance before the overload to the average normalized compliance immediately after the overload, as shown in Fig. 11. If the specimen failed during the overload, the average normalized compliance after the overload was assumed to be 1.65 (that is, the average of the normalized compliances at failure for all other damaged concrete tests). Figure 11 also shows the average (Avg) and standard deviation (SD) for each set of three tests. The increase in normalized compliance caused by an overload was found to be greater for higher stress ratios and greater percent life consumed. The results also became more variable as the percent life consumed increased, as indicated by the increase in standard deviation. In general, overloads at a stress ratio of 0.8 were not found to be significantly impactful to the stiffness of the concrete until later in the fatigue life. Overloads at a stress ratio of 0.9 were impactful throughout the fatigue life and especially critical at D = 85%. The flexural strength was not observed to impact the effects of percent life consumed or overload stress ratio. Specimens that failed at or near the strain gauges exhibited bending strain data that corroborates these findings, as detailed in work by Buettner.[9]

CONCLUSIONS

In this study, the stress pulses caused by superloads were characterized and related to fatigue damage in the experimental investigation. Moreover, through the collection of fatigue life and beam response data, the effects of stress ratio, stress range, flexural strength, and damage state at the time of loading on the fatigue damage caused by a superload movement were examined. The following conclusions are drawn based on this study:

1. The environmental conditions at the time of superload movement have a significant impact on the maximum stress.

2. There is not a discernable influence of strength level on the fatigue life or nonlinear fatigue behavior of concrete subjected to superload stress pulses.

3. The stress range of a given superload stress pulse does not appear to impact the fatigue life of concrete if the stress ratio is 0.8 or 0.9. However, the fatigue life may be impacted if the stress ratio is 0.7.

4. The existing damage state in the concrete has an increasingly significant impact on the fatigue damage imposed by a superload as percent life consumed increases.

5. The traditional *S-N* curve and linear damage hypothesis approach for fatigue damage prediction in jointed plain concrete pavements (JPCPs) have limitations when being used to assess the damage due to a superload. Specifically, this approach may overpredict the damage caused by the superload early in pavement life and underpredict the damage caused by a superload later in pavement life.

The results of this study provide government agencies with pertinent information on permitting superloads on

JPCPs with 4.6 m joint spacings. Specifically, the results of the stress analysis suggest that the time of year and time of day are important factors to evaluate given the dependence of the maximum stress on the temperature gradient present in the JPCP. Further research on the effects of seasonal variations in field conditions (for example, modulus of subgrade reaction) would elucidate how to adjust permitting fees (that is, damage costs) as a function of the time of the year.

The results of the experimental investigation suggest that the structural state of the JPCP is also an important consideration, as the stresses generated by superloads may be less damaging than anticipated early in pavement life and more damaging than anticipated later in pavement life. Further research is necessary so that the number of cycles to failure and nonlinear fatigue behavior observed in laboratory tests can be linked to the fatigue behavior of JPCPs with different structural sizes under varying field conditions.

AUTHOR BIOS

ACI member **Nathanial Buettner** *is a PhD Student at Northwestern University, Evanston, IL. He received his BS and MS in civil and environmental engineering from the University of Pittsburgh, Pittsburgh, PA, in 2019 and 2021, respectively. He received the ACI Pittsburgh Chapter Founders Award in 2019. His research interests include the analysis of concrete pavements and the characterization of cementitious materials.*

ACI member **Julie Vandenbossche** *is a Professor at the University of Pittsburgh. She received her BS and MS in civil engineering from Michigan State University, East Lansing, MI, in 1991 and 1995, respectively, and her PhD from the University of Minnesota, Minneapolis, MN, in 2003. Her research interests include the design, analysis, and rehabilitation of concrete pavements and the characterization of cementitious materials.*

ACKNOWLEDGMENTS

This material is based upon work supported by the Pennsylvania Department of Transportation and the National Science Foundation Graduate Research Fellowship Program under Grant No. 1747452. Any opinions, findings, and conclusions or recommendations expressed in this material are those of the authors and do not necessarily reflect the views of the National Science Foundation. Specifically, the authors would like to thank Bryan Materials Group for providing aggregates and admixtures, Kosmos Cement Company for providing cement, and Z. Brody and M. Oleson of the University of Pittsburgh for their contributions to the project.

REFERENCES

1. Papagiannakis, A., "Practices for Permitting Superheavy Load Movements on Highway Pavements," *NCHRP Synthesis 476*, The National Academies Press, Washington, DC, 2015, 253 pp.

2. ARA, Inc., "Guide for Mechanistic–Empirical Design of New and Rehabilitated Pavement Structures," *Final Report NCHRP 1-37A*, Transportation Research Board of the National Academies, Washington, DC, 2004.

3. AASHTO, "AASHTO Guide for the Design of Pavement Structures," American Association of State Highway and Transportation Officials, Washington, DC, 1993.

4. Miner, M. A., "Cumulative Damage in Fatigue," *Journal of Applied Mechanics*, V. 12, No. 3, 1945, pp. 159-169. doi: 10.1115/1.4009458

5. Holmen, J. O., "Fatigue of Concrete by Constant and Variable Amplitude Loading," *Fatigue of Concrete Structures*, SP-75, American Concrete Institute, Farmington Hills, MI, 1982, pp. 71-110.

6. Oh, B. H., "Cumulative Damage Theory of Concrete under Variable-Amplitude Fatigue Loadings," *ACI Materials Journal*, V. 88, No. 1, Jan.-Feb. 1991, pp. 41-48.

7. Grzybowski, M., and Meyer, C., "Damage Accumulation in Concrete with and without Fiber Reinforcement," *ACI Materials Journal*, V. 90, No. 6, Nov.-Dec. 1993, pp. 594-604.

8. Buettner, N.; Zhang, Q.; Vandenbossche, J. M.; and Oswalt, J., "Investigating the Effects of Superloads on Fatigue Performance in Jointed Plain Concrete Pavements," *12th International Conference on Concrete Pavements*, Sept. 27-Oct. 1, 2021.

9. Buettner, N., "Investigation of the Fatigue Damage Imposed by Superloads on Damaged Jointed Plain Concrete Pavements," MS thesis, University of Pittsburgh, Pittsburgh, PA, 2022.

10. Khazanovich, L.; Yu, T.; Rao, S.; Galasova, E.; Shats, E.; and Jones, R., "ISLAB2000 – Finite Element Analysis Program for Rigid and Composite Pavements User's Guide," ERES Consultants, Champaign, IL, 2000.

11. Cornelissen, H. A. W., "Fatigue Failure of Concrete in Tension," *HERON*, V. 29, No. 4, 1984, pp. 1-68.

12. Zhang, B.; Phillips, D. V.; and Wu, K., "Effects of Loading Frequency and Stress Reversal on Fatigue Life of Plain Concrete," *Magazine of Concrete Research*, V. 48, No. 177, 1996, pp. 361-375. doi: 10.1680/macr.1996.48.177.361

13. Hsu, T. T., "Fatigue of Plain Concrete," *ACI Journal Proceedings*, V. 78, No. 4, July-Aug. 1981, pp. 292-305.

14. Chatti, K.; Manik, A.; Salama, H.; Brake, N.; Haider, S. W.; Mohtar, C. E.; and Lee, H. S., "Effect of Michigan Multi-Axle Trucks on Pavement Distress (Volume III)," Report No. RC-1504, Michigan Department of Transportation, Lansing, MI, 2009, 121 pp.

15. ASTM C78/C78M-21, "Standard Test Method for Flexural Strength of Concrete (Using Simple Beam with Third-Point Loading)," ASTM International, West Conshohocken, PA, 2021.

16. ASTM C39/C39M-21, "Standard Test Method for Compressive Strength of Cylindrical Concrete Specimens," ASTM International, West Conshohocken, PA, 2021.

17. ACI Committee 330, "Guide for the Design and Construction of Concrete Parking Lots (ACI 330R-08)," American Concrete Institute, Farmington Hills, MI, 2008, 36 pp.

18. PennDOT, "Materials Specifications (Publication 408/2020)," Pennsylvania Department of Transportation, Harrisburg, PA, 2020.

19. ASTM C192/C192M-19, "Standard Practice for Making and Curing Concrete Test Specimens in the Laboratory," ASTM International, West Conshohocken, PA, 2019.

20. Murdock, J. W., and Kesler, C. E., "Effect of Range of Stress on Fatigue Strength of Plain Concrete Beams," *ACI Journal Proceedings*, V. 55, No. 8, Aug. 1958, pp. 221-231.

21. Tepfers, R., "Tensile Fatigue Strength of Plain Concrete," *ACI Journal Proceedings*, V. 76, No. 8, Aug. 1979, pp. 919-934.

22. Darter, M. I., "Design of a Zero-Maintenance Plain Jointed Concrete Pavement, Volume One—Development of Design Procedures," *Report* No. FHWA-RD-77-111, Federal Highway Administration, Washington, DC, 1977, 261 pp.

23. Packard, R. G., and Tayabji, S. D., "New PCA Thickness Design Procedure for Concrete Highway and Street Pavements," *Proceedings of the 3rd International Conference on Concrete Pavement Design and Rehabilitation*, Purdue University, West Lafayette, IN, 1985, pp. 225-236.

ACI STRUCTURAL JOURNAL TECHNICAL PAPER

Title No. 120-S95

Normal- and High-Strength Continuously Wound Ties

by Malory R. Gooding, Elizabeth A. Mosier, and Bahram M. Shahrooz

Advancements in steel reinforcement bending machines have allowed for the fabrication of continuously wound ties (CWTs). CWTs are being used in place of conventional transverse reinforcement to reduce waste and construction time and to alleviate congestion. A total of 20 reduced-scale special boundary elements (SBEs), using Grade 60 and Grade 80 conventional hoops and CWTs, were tested under uniaxial compression to evaluate the performance of members with CWTs. All the specimens exceeded ACI nominal axial strength capacity at zero eccentricity calculated using the measured material properties and ignoring reduction factors. The CWT specimens exhibited improved post-peak ductility compared to conventional hoops when all the current ACI requirements for SBE transverse reinforcement were satisfied. Post-peak ductility was further enhanced by using Grade 80 CWTs in conjunction with 10 ksi (69 MPa) concrete. Confined concrete strengths from three well-established models were reasonably close to the measured values; however, all the models were found to overestimate post-peak ductility regardless of the type of transverse reinforcement.

Keywords: ACI 318; axial loading; confined concrete; ductility; high-strength reinforcement; hoops; seismic detailing; special boundary elements (SBEs); transverse reinforcement.

INTRODUCTION

A large body of past research on columns and boundary elements[1-13] has demonstrated the importance of support for the longitudinal bars, distribution of transverse reinforcement, vertical tie spacing, and tie volumetric ratio. Supporting every longitudinal bar has been found to enhance ductility and strength. Well-distributed transverse reinforcement and a higher tie volumetric ratio improve strength and ductility. Decreasing vertical tie spacing is a key factor to enhance strength capacity by delaying or preventing buckling of longitudinal bars. Transverse reinforcement is especially critical for special boundary elements (SBEs). The use of 135- or 180-degree hooks in crossties has generally been found to improve post-peak ductility, although some studies[1,7] have reported little enhancement compared to alternating 135- and 90-degree hooks. Using crossties rather than rectilinear hoops to support longitudinal reinforcement in boundary elements has been found to reduce strength and deformation capacity as crossties did not adequately restrain longitudinal bars from buckling.[12,13] The importance of confinement becomes even more pronounced for high-strength concrete (HSC). Increased confinement is required for HSC to achieve similar behavior and strength and ductility enhancements as normal-strength concrete. Some studies[10] have concluded that increasing tie yield strength did not have a large effect on HSC behavior because ties only yielded for well-confined specimens at the second peak strength.

The aforementioned past research indicates the performance of columns and boundary elements is improved if large quantities of transverse reinforcement are provided; however, the cost is expected to increase, and constructability issues may arise due to congestion of large quantities of transverse reinforcement. One option to achieve enhanced performance while at the same time mitigating constructability/congestion issues is to use continuously wound ties (CWTs). CWTs are also expected to improve construction speed, cut material waste, and reduce the overall project cost. Additionally, high-strength reinforcing bars (HSS) may be used to alleviate congestion and reduce the total amount of reinforcement. The term CWTs can refer to either: 1) a circular or rectangular helical made of a single piece of reinforcing bar (Fig. 1(a)); or 2) a single hoop set with multiple legs made of a single piece of reinforcing steel (Fig. 1(b)). The performance of members using the first type was reported previously.[14] Members and connections reinforced with the first type were found to have better post-peak behavior and generally higher strength and stiffness than their counterparts with conventional transverse steel. This paper focuses on the second type.

Very large axial loads cause appreciable transverse expansion that could straighten hooks, leading to loss of confinement and post-peak ductility of confined core concrete. In contrast to conventional hoops, CWTs do not have separate components and have fewer hooks. Because fewer hooks could straighten, members reinforced with CWTs are anticipated to have enhanced ductility. Due to the paucity of experimental and/or field data, the current version of ACI 318[15] (referred to as "Code" hereinafter) considers CWTs to be equivalent to a conventional hoop set made up of individual pieces of reinforcement. To remedy the lack of data on the performance of members using CWTs, the reported research was conducted. The influence of the grade of reinforcement, concrete compressive strength, shape of the cross section, tie spacing, and lateral support of longitudinal reinforcement was investigated in addition to the type of transverse reinforcement (conventional or CWTs). Furthermore, stress-strain diagrams from three well-established confined concrete models were compared against their experimental counterparts.

ACI Structural Journal, V. 120, No. 6, November 2023.

MS No. S-2022-205.R3, doi: 10.14359/51739017, received January 20, 2023, and reviewed under Institute publication policies.

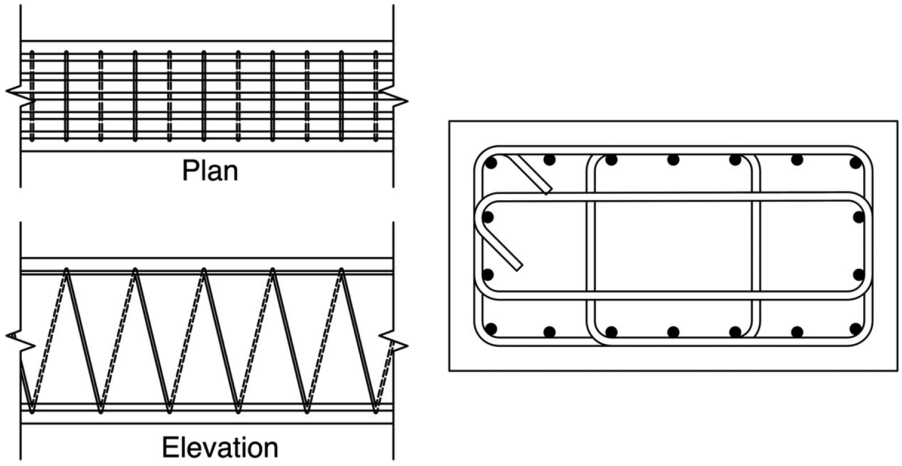

(a) rectangular helical (b) continuously wound tie

Fig. 1—Unconventional types of transverse reinforcement.

RESEARCH SIGNIFICANCE

Conventional hoops consist of an outside tie and crossties with or without seismic hooks. The crossties and hooks increase congestion in already heavily reinforced members and regions such as columns in special moment frames or SBEs. With the increasing use of CWTs aimed at alleviating congestion and accelerating the construction process, it is important to examine the strength, ductility, and performance of axially loaded members reinforced with CWTs as well as model the constitutive relationship of concrete confined by CWTs. These issues are addressed through the presented research.

EXPERIMENTAL PROGRAM

A total of twenty 6 ft (1.83 m) tall specimens representing the confined core of SBEs were fabricated and subjected to uniaxial, monotonically increasing axial compression in a universal testing machine. The top and bottom surfaces of the test specimens were in full contact with the machine's floor and compression platen. Full contact and uniform distribution of the applied load were achieved by applying high-strength self-leveling grout on the contact surfaces.[16,17] The research program was completed in two phases. The results and observations from the first phase informed the selection of the test variables for the second-phase specimens. The test variables were the type of transverse reinforcement, the grade of reinforcement, concrete strength, shape of the cross section, lateral support of longitudinal bars, and whether the specimen complies with ACI 318-19 (compliant or noncompliant).

In Phase 1, each specimen using CWTs had an identical counterpart with conventional hoops, resulting in five groups of two specimens. The transverse and longitudinal reinforcement were either Grade 60 or Grade 80 with a design yield strength of 60 or 80 ksi (414 or 552 MPa), respectively. Concrete with a specified compressive strength of 6 or 10 ksi (41 or 69 MPa) was used. Square and rectangular cross sections were used in four and six specimens, respectively. The primary focus of Phase 1 was identifying the differences between using conventional hoops and CWTs.

All 10 specimens in Phase 2 were rectangular; eight were reinforced with CWTs, and the remaining two had conventional hoops. Grades 60 and 80 steel reinforcement and 6 or 10 ksi (41 or 69 MPa) concrete strength were also used in this phase. In addition to comparing CWTs versus conventional hoops, which was achieved through four specimens, the second-phase specimens provided data to evaluate: a) the effect of meeting or not meeting all the applicable transverse reinforcement spacing Code requirements for SBEs; and b) the impact of laterally supporting all or every other longitudinal bar.

Specimen details

The number and size of reinforcing bars and overall dimensions were selected in consultation with professional engineers while ensuring the expected capacity would not exceed the maximum load that the universal testing machine capacity (3900 kip [17.4 MN]) could apply. The test specimens were designed as 0.6-scale of the confined core of an actual SBE.

For the rectangular specimens, two configurations were used: 1) every other long-direction longitudinal bar was supported; and 2) all the longitudinal bars in the long direction were supported (refer to Fig. 2). Because of congestion issues, the same number of longitudinal bars could not be achieved for the second configuration. To maintain nearly equal longitudinal reinforcement ratios between the two configurations, fewer but larger-diameter reinforcing bars (12 No. 6) were used in the second configuration. The first configuration had a total of 18 No. 5 longitudinal reinforcing bars. Transverse reinforcement in all the specimens consisted of No. 4 hoops or CWTs. Six specimens in Phase 2 did not comply with the transverse reinforcement spacing in the Code for SBEs. Noncompliance in these cases was achieved by assuming No. 5 hoops in design calculations but using No. 4 hoops in the test specimen. This approach allowed consistency throughout the noncompliant specimens and a realistic concept on how the Code could be altered. The specimen details and the applicable Code design equations are summarized in Table 1.

Two measures were followed to induce failure in the central test region. First, the ends were heavily reinforced with hoops spaced at 2 in. (50.8 mm) on center (refer to Fig. 3). Second, the central test region was made to be smaller in the cross section than the ends. The central test region was detailed with no cover to focus on the core confined by CWTs or conventional hoops to evaluate the effectiveness of the transverse reinforcement without the influence of the amount of concrete cover. Due to imperfect tie dimensions, the actual specimens had covers ranging from 3/8 to 5/8 in. (9.5 to 16 mm). The actual dimensions are provided in Table 1. The presence of a small amount of cover did not impact the specimen design, as transverse reinforcement spacing was controlled by $0.09(f_c'/f_y)$ (refer to Table 1), which does not depend on the cross-sectional area. The axial load strength, which was used to compare the performance of various specimens, was determined based on the actual dimensions. Moreover, other comparison metrics, such as buckling of longitudinal bars, straightening of hooks, or fracture of transverse reinforcement, would not be impacted by the small covers in the test specimens.

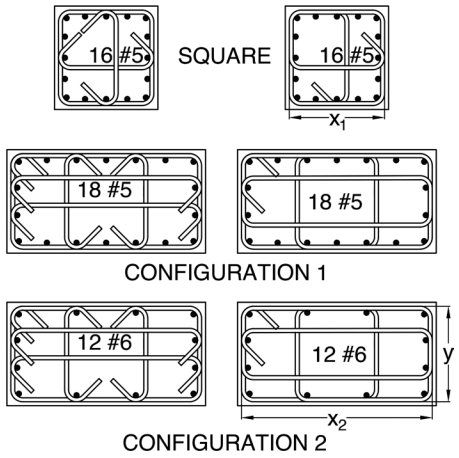

Fig. 2—Cross sections of test specimens. (Note: Design dimensions: x_1 = 12 in. [305 mm], x_2 = 24 in. [610 mm], and y = 12 in. [305 mm]. Standard hook dimensions were used for conventional ties and CWTs.)

Average concrete compressive strengths at various ages are summarized in Table 2. The reported strengths are from field-cured 6 x 12 in. (152 x 305 mm) cylinders tested according to ASTM C39/C39M-21.[18] Reinforcing bars were obtained from several different sources due to availability

Table 1—Specimen details

Hoop configuration	Specimen ID	*h*, in.	*b*, in.	ρ	Required tie spacing, in.	Minimum A_{sh}/sb_c	Tie volume ratio	s/d_b	Governing Code provision	Actual tie spacing, in.	Actual outside dimensions, in.
1	CON-RT-Y-60-6-#5	24	12	0.0194	3.70	0.009	0.026	5.8	18.10.6.4	3-5/8	24-3/4 x 13-1/8
1	CWT-RT-Y-60-6-#5	24	12	0.0194	3.70	0.009	0.030	5.8	18.10.6.4	3-5/8	24-3/4 x 13-1/8
1	CON-RT-Y-60-10-#5	24	12	0.0194	2.22	0.016	0.044	3.4	18.10.6.4	2-1/8	24-3/4 x 13-1/8
1	CWT-RT-Y-60-10-#5	24	12	0.0194	2.22	0.016	0.052	3.4	18.10.6.4	2-1/8	24-3/4 x 13-1/8
1	CON-RT-Y-80-10-#5	24	12	0.0194	2.96	0.012	0.033	4.6	18.10.6.4	2-7/8	24-3/4 x 13-1/8
1	CWT-RT-Y-80-10-#5	24	12	0.0194	2.96	0.012	0.038	4.6	18.10.6.4	2-7/8	24-3/4 x 13-1/8
Square	CON-SQ-Y-60-10-#5	12	12	0.0344	3.33	0.015	0.028	5.2	18.10.6.4	3-1/4	13 x 13-1/8
Square	CWT-SQ-Y-60-10-#5	12	12	0.0344	3.33	0.015	0.032	5.2	18.10.6.4	3-1/4	13 x 13-1/8
Square	CON-SQ-Y-80-10-#5	12	12	0.0344	3.13	0.016	0.029	5.0	18.10.6.5b	3-1/8	13 x 13-1/8
Square	CWT-SQ-Y-80-10-#5	12	12	0.0344	3.13	0.016	0.034	5.0	18.10.6.5b	3-1/8	13 x 13-1/8
2	CON-RT-Y-60-10-#6	24	12	0.0183	2.22	0.016	0.044	2.8	18.10.6.4	2-1/8	24-7/8 x 12-7/8
2	CWT-RT-Y-60-10-#6	24	12	0.0183	2.22	0.016	0.052	2.8	18.10.6.4	2-1/8	25 x 13
2	CON-RT-Y-80-10-#6	24	12	0.0183	2.96	0.012	0.033	3.8	18.10.6.4	2-7/8	25-1/4 x 13-1/4
2	CWT-RT-Y-80-10-#6	24	12	0.0183	2.96	0.012	0.038	3.8	18.10.6.4	2-7/8	25 x 13
1	CWT-RT-N-60-6-#5	24	12	0.0194	3.70	0.009	0.029	6.0	18.10.6.4	3-3/4	25 x 13-1/8
1	CWT-RT-N-60-10-#5	24	12	0.0194	2.22	0.010	0.032	5.4	18.10.6.4	3-3/8	25 x 13
1	CWT-RT-N-80-10-#5	24	12	0.0194	2.96	0.011	0.035	5.0	18.10.6.4	3-1/8	25 x 13
2	CWT-RT-N-60-6-#6	24	12	0.0183	3.70	0.008	0.027	5.3	18.10.6.4	4-0	25 x 13
2	CWT-RT-N-60-10-#6	24	12	0.0183	2.22	0.010	0.032	4.5	18.10.6.4	3-3/8	25 x 13
2	CWT-RT-N-80-10-#6	24	12	0.0183	2.96	0.009	0.029	5.0	18.10.6.4	3-3/4	24-7/8 x 13-1/8

Note: CON/CWT is conventional hoops/continuously wound ties; RT/SQ is rectangular/square; Y/N is meets Code/does not meet Code; 60/80 is Grade 60/Grade 80; 6/10 is concrete strength in ksi; #5/#6 is size of longitudinal bars; 1 in. = 25.4 mm; 1 ksi = 6.895 MPa; diameter of No. 5 = 15.9 mm; diameter of No. 6 = 19.1 mm. In Section 18.10.6.4, A_{sh}/sb_c is the greater of $0.03([A_g/A_{ch}] - 1)(f_c'/f_{yt})$ and $0.09(f_c'/f_{yt})$. In Section 18.10.6.5(b), maximum vertical spacing of transverse reinforcement for Grade 60 is the lesser of $6d_b$ and 6 in., and for Grade 80 is the lesser of $8d_b$ and 5 in. Consistent with ACI 318-19, these equations are in in.-lb units. A_{ch} is cross-sectional area of member measured to outside edges of transverse reinforcement; A_g is gross area of concrete section; A_{sh} *is* total cross-sectional area of transverse reinforcement, including crossties, within spacing *s* and perpendicular to dimension b_c; b_c is cross-sectional dimensions of member core measured to outside edges of transverse reinforcement composing area A_{sh}; d_b is nominal diameter of transverse reinforcement; f_c' is specified compressive strength of concrete; f_{yt} is specified yield strength of transverse reinforcement; *s* is spacing of transverse reinforcement in longitudinal direction.

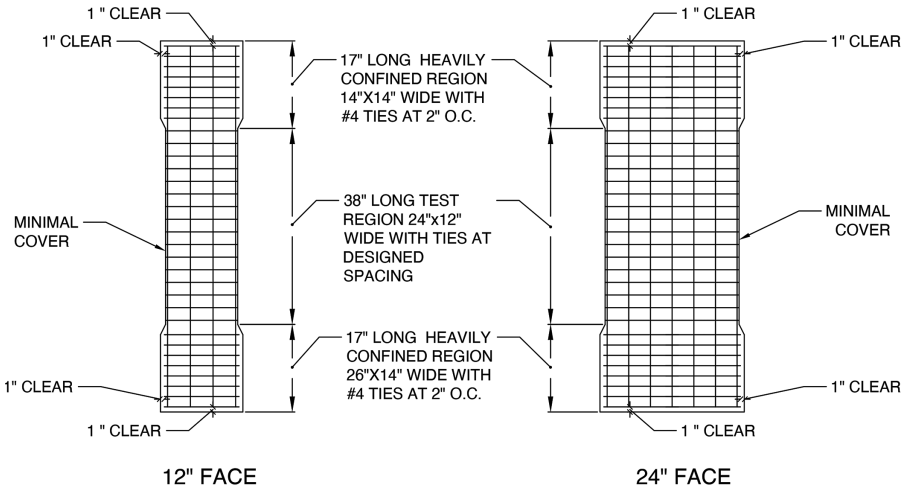

Fig. 3—Elevation views of 12 x 24 in. (305 x 610 mm) specimens.

Table 2—Measured concrete compressive strength

Phase	Age, days	6000 psi mixture	10,000 psi mixture
		psi (MPa)	
1	10	5010 (34.5)	7700 (53.1)
	28	6610 (45.6)	8710 (60.1)
	47	6380 (44)	Not applicable
	49	6830 (47.1)	Not applicable
	54	Not applicable	8750 (60.3)
	60	Not applicable	9400 (64.8)
	63	Not applicable	8640 (59.6)
2	7	4760 (32.8)	8190 (56.5)
	28	5400 (37.2)	9380 (64.7)
	33	5190 (35.8)	9400 (64.8)
	57	5350 (36.9)	9400 (64.8)

and logistical constraints. The measured material properties are provided in Table 3, and the reinforcing bars used for each specimen are identified in Table 4.

Instrumentation

The specimens were instrumented with linear variable displacement transducers (LVDTs) on all four faces of the specimen to measure the overall axial deformation. Axial shortening was measured over approximately a 26 in. (660 mm) gauge length vertically centered in the test region. Additionally, strain gauges were used to record strains in the longitudinal bars and transverse reinforcement at the midheight. Using the measured strains, stresses in the longitudinal and transverse reinforcement were inferred from the experimentally obtained stress-strain relationships.

Synthesis and discussion of test results

The specimens were grouped such that they were identical, except for one variable. The following grouping was selected: a) type of confinement—conventional versus CWTs; b) grade of reinforcement—Grade 60 versus Grade 80; c) lateral support of longitudinal reinforcement—all bars are supported or some bars are not supported while meeting ACI 318-19, Section 18.10.6.4(f)—that is, "Transverse reinforcement shall be configured such that the spacing h_x between laterally supported longitudinal bars around the perimeter of the boundary element shall not exceed the lesser of 14 in. and two-thirds of the boundary element thickness."; d) whether the specimen is compliant with all the Code transverse reinforcement requirements or not; e) concrete compressive strength—6 versus 10 ksi (41 versus 69 MPa); and f) shape of the test specimen—rectangular versus square.

The following metrics were used to compare similar specimens:

1. P_{max}/P_o, where P_{max} is the maximum measured axial load and P_o is the calculated axial load capacity using the measured material properties and without any reduction factors—that is, $P_o = 0.85f_c'(A_g - A_{st}) + f_yA_{st}$, where A_g is the gross area of the concrete section; A_{st} is the total area of longitudinal reinforcement; and f_y is the yield strength of longitudinal reinforcement.
2. f_{tie}/f_{yt}, where f_{tie} is the maximum experimentally inferred stress in transverse reinforcement and f_{yt} is the measured yield strength of transverse reinforcement.
3. f_{cc}'/f_c', where f_{cc}' is the maximum value of experimentally obtained confined concrete stress and f_c' is the measured concrete strength.
4. ε_{85}, which is the strain corresponding to experimentally obtained $0.85f_{cc}'$—that is, post-peak strain corresponding to 85% of the peak stress.

Conventional versus continuously wound ties

The specimens with CWTs exhibited better post-peak ductility, which is evident from Table 5, which indicates ε_{85} is larger for all the cases using CWTs than those with conventional hoops. The average, maximum, and minimum values of ε_{85} for the specimens with CWTs are larger than those using conventional hoops. The average value of ε_{85} is increased by 75% by using CWTs (12.3 με for CWTs versus 7.03 με for conventional hoops). The 95% confidence range of ε_{85} is 5.02 to 9.04 με for the specimens reinforced with conventional hoops in comparison to 10.9 to 13.7 με for those with CWTs. Out of seven cases with CWTs, the values

Table 3—Measured material properties of reinforcement

Size	Grade	Bar ID	f_y, ksi (MPa)	f_u, ksi (MPa)	Elongation, %
No. 4	ASTM A706 Grade 60	1	63.7 (439)	87 (600)	15.7
No. 4	ASTM A706 Grade 60	2	62.5 (431)	92.7 (639)	10.6
No. 4	ASTM A706 Grade 80	2	89.7 (618)	122 (841)	8.90
No. 4	ASTM A706 Grade 80	3	79.1 (545)	113 (779)	7.63
No. 5	ASTM A706 Grade 60	1	67.7 (467)	92.4 (637)	9.93
No. 5	ASTM A706 Grade 80	4	86.9 (599)	114 (786)	8.47
No. 4	ASTM A706 Grade 60	5	70.6 (487)	97.6 (673)	21.6
No. 4	ASTM A706 Grade 80	5	85.3 (588)	118 (814)	8.32
No. 5	ASTM A706 Grade 60	5	66.8 (461)	95.1 (656)	19.0
No. 5	ASTM A706 Grade 80	5	82.1 (566)	107 (738)	16.5
No. 6	ASTM A706 Grade 60	5	70.7 (487)	96.4 (665)	19.1
No. 6	ASTM A706 Grade 80	5	84.3 (581)	111 (765)	15.6

Table 4—Reinforcing bar IDs for each specimen

Specimen ID	Bar ID*		
	No. 4	No. 5	No. 6
CON-RT-Y-60-6-#5	1	1	N/A
CWT-RT-Y-60-6-#5	2	1	N/A
CON-RT-Y-60-10-#5	1	1	N/A
CWT-RT-Y-60-10-#5	2	1	N/A
CON-RT-Y-80-10-#5	3	4	N/A
CWT-RT-Y-80-10-#5	2	4	N/A
CON-SQ-Y-60-10-#5	1	1	N/A
CWT-SQ-Y-60-10-#5	2	1	N/A
CON-SQ-Y-80-10-#5	3	4	N/A
CWT-SQ-Y-80-10-#5	2	4	N/A
CWT-RT-Y-60-10-#6	5	5	5
CON-RT-Y-60-10-#6	5	5	5
CWT-RT-Y-80-10-#6	5	5	5
CON-RT-Y-80-10-#6	5	5	5
CWT-RT-N-60-6-#5	5	5	5
CWT-RT-N-60-10-#5	5	5	5
CWT-RT-N-80-10-#5	5	5	5
CWT-RT-N-60-6-#6	5	5	5
CWT-RT-N-60-10-#6	5	5	5
CWT-RT-N-80-10-#6	5	5	5

*Refer to Table 3 for material properties for different bar IDs.

of P_{max}/P_o and f_{tie}/f_{yt} in four and six specimens are larger than their counterparts with conventional hoops, respectively. On average, P_{max}/P_o is slightly larger for the CWT specimens, and the 95% confidence range is nearly the same: 1.08 to 1.18 for conventional hoops versus 1.09 to 1.18 for CWTs. The normalized tie stress (f_{tie}/f_{yt}) in CWTs is higher than conventional hoops: the average is 0.84 versus 0.71, and the 95% confidence range is 0.64 to 1.03 versus 0.49 to 0.93. The larger normalized tie stresses indicate CWTs could be engaged more than conventional hoops before reaching the peak load-carrying capacity. The average value of f_{cc}'/f_c' for conventional hoops (1.21) is slightly larger than its counterpart for CWTs (1.19). The same trend is seen for the 95% confidence range—1.15 to 1.27 for conventional hoops versus 1.14 to 1.24 for CWTs. Hence, the type of transverse reinforcement did not impact the level of confinement.

Damage patterns for comparable specimens with conventional hoops and CWTs are shown in Fig. 4. The small cover spalled primarily in the test region, with some spalling extending into the top and bottom heavily reinforced segments. Several longitudinal bars buckled and fractured in the specimen with CWTs (Fig. 5). The transverse reinforcement either bulged outward or fractured. The number of buckled longitudinal bars, straightened hooks, and fractured transverse reinforcement is compared in Fig. 6 for the specimens that were identical in all aspects except for the type of transverse reinforcement. A larger number of longitudinal bars in specimens with CWTs buckled in comparison to those using conventional hoops. A similar trend is observed in terms of the number of fractured CWTs, which is consistent with the larger values of f_{tie}/f_{yt} and ε_{85} in these specimens. The hooks in four specimens reinforced with conventional hoops had straightened, whereas the hooks in the comparable specimens using CWTs had not. A reverse trend is observed for two specimens with CWTs.

Grade of reinforcement

A total of 16 specimens could be compared to examine the influence of the grade of reinforcement (eight with Grade 60 and eight with Grade 80); a clear trend could not be identified. As seen from Table 6, axial strength (P_{max}/P_o) and post-peak ductility quantified by ε_{85} did not appreciably change between the two grades; for example, the average value of P_{max}/P_o is 1.13 for Grade 60 versus 1.10 or Grade 80, and with 95% confidence, the average value of ε_{85} ranges from 6.5 to 12.4 με for Grade 60 and 8.9 to 12.8 με for Grade 80. Confined concrete stress (f_{cc}'/f_c') was nearly the same for the two grades—the average for Grade 60 is 1.19 versus 1.20 for Grade 80. The average tie stress normalized with respect to the measured yield strength (f_{tie}/f_{yt}) was 8% larger for Grade 80 in comparison to Grade 60. The higher-grade

Table 5—Effect of transverse reinforcement type

	ID	P_{max}/P_o	f_{tie}/f_{yt}	$\varepsilon_{85} \times 10^3$	f_{cc}/f_c'	ID	P_{max}/P_o	f_{tie}/f_{yt}	$\varepsilon_{85} \times 10^3$	f_{cc}/f_c'
	Conventional					Continuously wound ties				
	CON-RT-Y-60-6-#5	1.19	0.67	5.40	1.20	CWT-RT-Y-60-6-#5	1.14	0.72	12.2	1.12
	CON-RT-Y-60-10-#5	1.23	0.49	5.30	1.30	CWT-RT-Y-60-10-#5	1.25	0.96	12.4	1.30
	CON-RT-Y-80-10-#5	1.14	0.65	7.90	1.25	CWT-RT-Y-80-10-#5	1.17	0.87	14.9	1.24
	CON-SQ-Y-60-10-#5	1.07	0.35	2.90	1.21	CWT-SQ-Y-60-10-#5	1.11	1.14	13.0	1.24
	CON-SQ-Y-80-10-#5	1.12	1.22	10.2	1.30	CWT-SQ-Y-80-10-#5	1.06	0.36	12.5	1.19
	CON-RT-Y-60-10-#6	1.15	0.61	7.19	1.16	CWT-RT-Y-60-10-#6	1.13	0.76	8.60	1.15
	CON-RT-Y-80-10-#6	1.01	0.97	10.3	1.06	CWT-RT-Y-80-10-#6	1.09	1.05	12.7	1.12
Average		1.13	0.71	7.03	1.21		1.14	0.84	12.3	1.19
Maximum		1.23	1.22	10.3	1.30		1.25	1.14	14.9	1.30
Minimum		1.01	0.35	2.90	1.06		1.06	0.36	8.60	1.12
Coefficient of variation (COV)		0.064	0.415	0.387	0.070		0.055	0.309	0.152	0.057
95% confidence range		1.08 to 1.18	0.49 to 0.93	5.02 to 9.04	1.15 to 1.27		1.09 to 1.18	0.64 to 1.03	10.9 to 13.7	1.14 to 1.24

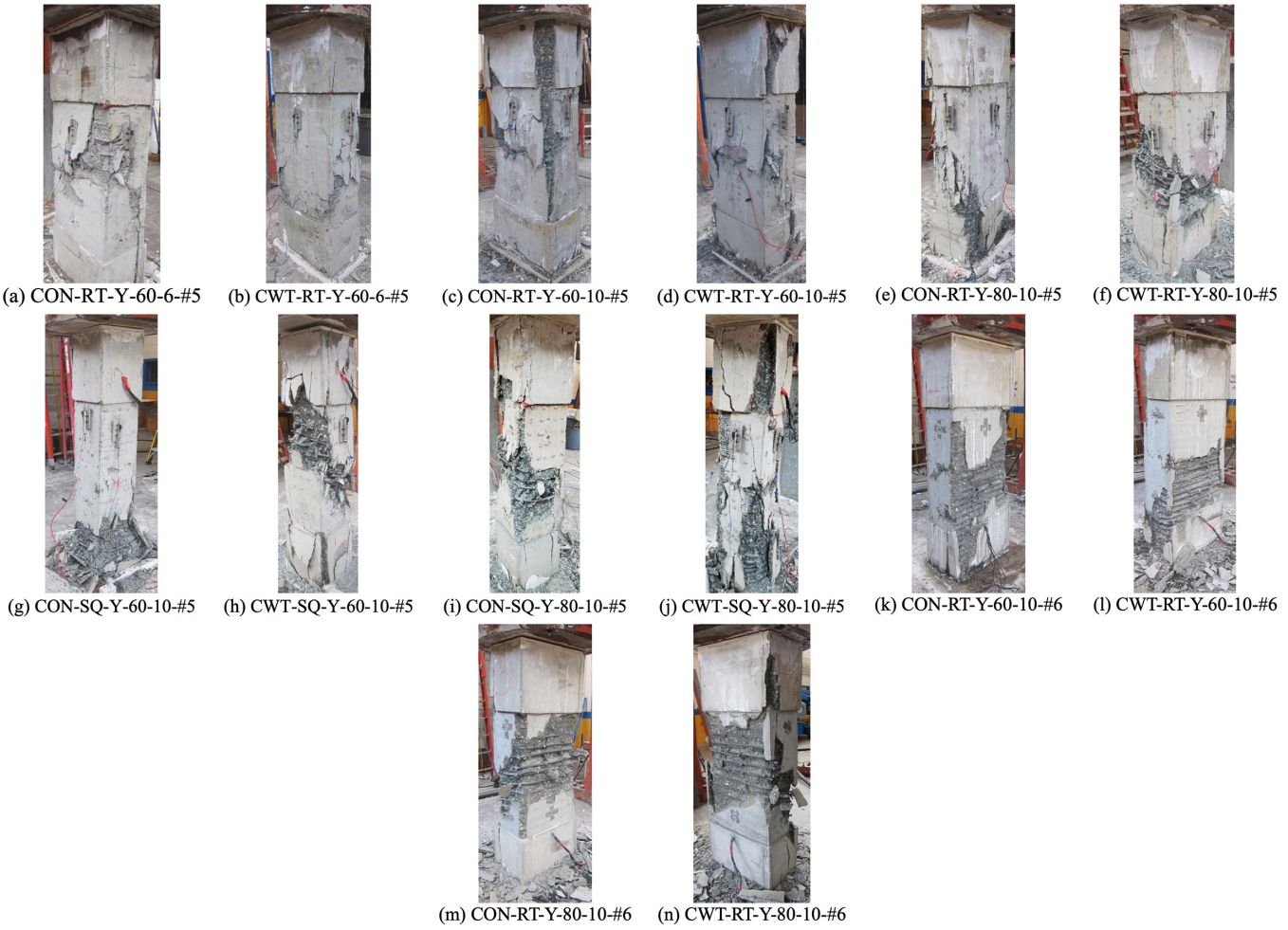

Fig. 4—Damage patterns in specimens with conventional hoops and continuously wound ties.

reinforcement maintained the integrity of the confined core, allowing more lateral expansion, which resulted in higher stress in comparison to what Grade 60 transverse reinforcement could provide.

Lateral support of longitudinal bars

The results from 14 comparable specimens were evaluated to examine the impact of lateral support of longitudinal bars. However, the value of ε_{85} could not be determined for

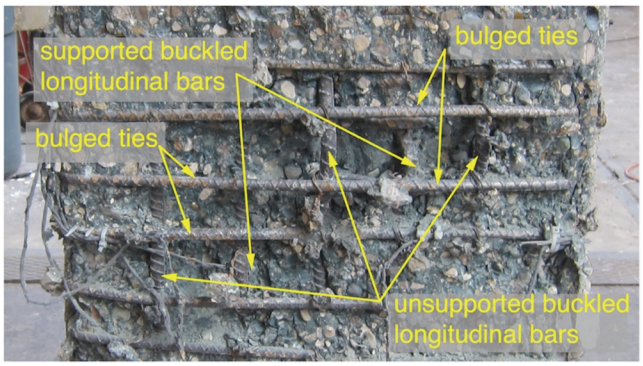

(a) CON-RT-Y-80-10-#5

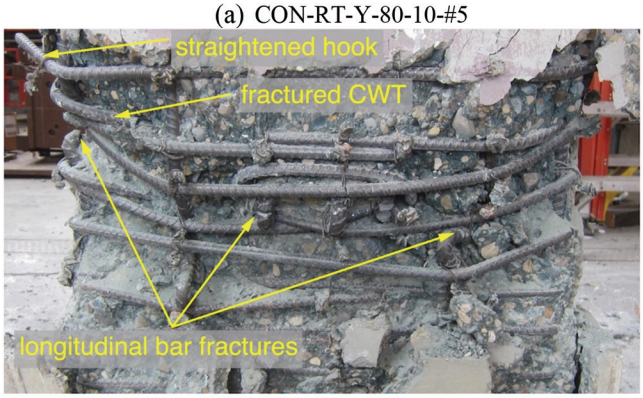

(b) CWT-RT-Y-80-10-#5

Fig. 5—Representative damage patterns.

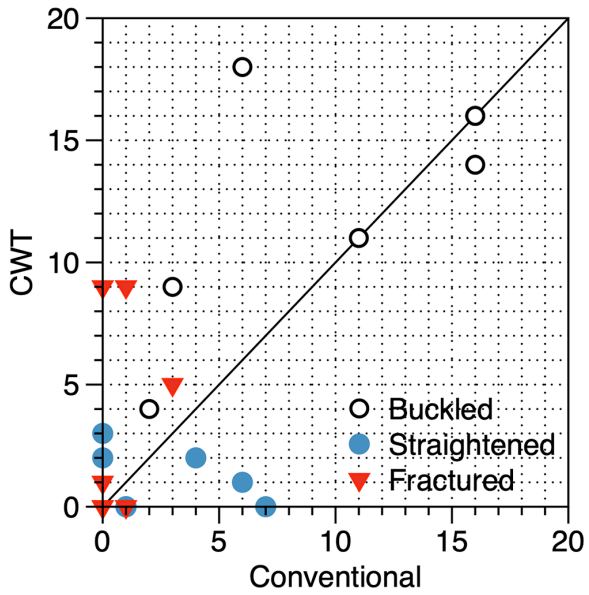

Fig. 6—Comparison of number of damaged longitudinal and transverse bars.

CWT-RT-N-80-10-#5 due to issues with the data acquisition system. The specimens using Configuration 2 (Fig. 2), that is, those in which every other longitudinal bar was supported, could resist higher axial forces—on average, P_{max}/P_o is 6% larger than their counterparts with all the longitudinal bars laterally supported. This trend is partially because Configuration 2 specimens had a slightly larger longitudinal reinforcement ratio (0.019 versus 0.018). However, the difference is primarily attributed to a better distribution of longitudinal bars in Configuration 2 specimens. The spacing between longitudinal bars met the Code requirements regardless of whether all the bars on the long face were laterally supported (Configuration 2 [refer to Fig. 2]) or not (Configuration 1, with four out of seven bars being supported). Both cases had the same number of longitudinal bars on the short faces. The larger number of longitudinal bars for Configuration 1 resulted in a more uniform confining pressure, leading to larger confined concrete strength than what could be achieved for those using Configuration 2. Normalized peak confined concrete stress (f_{cc}'/f_c') also supports this trend. The average f_{cc}'/f_c' is 9.4% larger for Configuration 1 specimens compared to those having Configuration 2; and with 95% confidence, the average value is between 1.19 and 1.31 compared to 1.08 and 1.20 for Configuration 1 (refer to Table 7). The influence of distributing the longitudinal bars around the perimeter is well established.[11] The same bar size was used for both configurations, so their lateral stiffness is directly impacted by the spacing between the longitudinal bars. The larger spacing between the longitudinal bars in Configuration 2 reduced the stiffness, resulting in larger lateral deformation of ties, as seen from larger stress in the transverse reinforcement for Configuration 1 specimens. For example, on average, the value of f_{tie}/f_{yt} is 22% larger than that for the specimens using Configuration 2 (0.09 for Configuration 2 versus 0.74 for Configuration 1—refer to Table 7). The more uniform confining pressure in Configuration 1 is expected to also enhance post-peak ductility. However, Table 7 indicates that the average ε_{85} is nearly the same for both configurations (9.95 με versus 10.4 με); and with 95% confidence, the average ε_{85} ranges between 7.22 and 12.7 με for Configuration 1, which is close to the 95% confidence range of 8.19 and 12.6 με for Configuration 2. The reason for this discrepancy from the expected trend is unclear.

Compliance with ACI transverse reinforcement requirements

All the specimens for this comparison used CWTs. The measured data (Table 8) indicate a better performance was achieved by satisfying the Code requirements for transverse reinforcement in terms of axial load strength (the average P_{max}/P_o is 1.16 for those meeting the Code requirements versus 1.09 if the requirements are not met) and post-peak ductility (the average ε_{85} is nearly 14% larger for the compliant specimens in comparison to the noncompliant ones), and the average normalized tie stress (f_{tie}/f_{yt}) for the specimens satisfying the Code provisions is 7.4% larger than those that did not. The difference between the two details is less pronounced for f_{cc}'/f_c'; with 95% confidence, the average for the compliant specimens is from 1.11 to 1.25 versus 1.07 to 1.27 for the noncompliant specimens.

Concrete compressive strength

The results in Table 9 do not show a clear trend in terms of the effect of concrete compressive strength. The normalized axial load strength (P_{max}/P_o) and confined concrete strength (f_{cc}'/f_c') are larger for the specimens using 6 ksi (41 MPa) than those with 10 ksi (69 MPa) (1.19 versus 1.15 and 1.22 versus 1.18, respectively). On the other hand, a reverse trend

Table 6—Effect of grade of reinforcement

	ID	P_{max}/P_o	f_{tie}/f_{yt}	$\varepsilon_{85} \times 10^3$	f_{cc}/f_c'	ID	P_{max}/P_o	f_{tie}/f_{yt}	$\varepsilon_{85} \times 10^3$	f_{cc}/f_c'
	Grade 60					Grade 80				
	CON-RT-Y-60-10-#5	1.23	0.49	5.30	1.30	CON-RT-Y-80-10-#5	1.14	0.65	7.90	1.25
	CWT-RT-Y-60-10-#5	1.25	0.96	12.4	1.30	CWT-RT-Y-80-10-#5	1.17	0.87	14.9	1.24
	CON-SQ-Y-60-10-#5	1.07	0.35	2.90	1.21	CON-SQ-Y-80-10-#5	1.12	1.22	10.2	1.30
	CWT-SQ-Y-60-10-#5	1.11	1.14	13.0	1.24	CWT-SQ-Y-80-10-#5	1.06	0.36	12.5	1.19
	CON-RT-Y-60-10-#6	1.15	0.61	7.19	1.16	CON-RT-Y-80-10-#6	1.01	0.97	10.3	1.06
	CWT-RT-Y-60-10-#6	1.13	0.76	8.60	1.15	CWT-RT-Y-80-10-#6	1.09	1.05	12.7	1.12
	CWT-RT-N-60-10-#5	1.05	0.84	10.4*	1.07	CWT-RT-N-80-10-#5	1.11	0.66	N/A	1.31
	CWT-RT-N-60-10-#6	1.05	1.01	15.6	1.06	CWT-RT-N-80-10-#6	1.05	0.88	7.77	1.15
Average		1.13	0.77	9.42	1.19		1.10	0.83	10.9	1.20
Maximum		1.25	1.14	15.56	1.30		1.17	1.22	14.9	1.31
Minimum		1.05	0.35	2.90	1.06		1.01	0.36	7.77	1.06
COV		0.068	0.352	0.450	0.078		0.048	0.323	0.241	0.075
95% confidence range		1.08 to 1.18	0.58 to 0.96	6.49 to 12.4	1.12 to 1.25		1.06 to 1.13	0.65 to 1.02	8.95 to 12.8	1.14 to 1.26

*Last reading before losing instrumentation.

Table 7—Effect of lateral support for longitudinal bars

	ID	P_{max}/P_o	f_{tie}/f_{yt}	$\varepsilon_{85} \times 10^3$	f_{cc}/f_c'	ID	P_{max}/P_o	f_{tie}/f_{yt}	$\varepsilon_{85} \times 10^3$	f_{cc}/f_c'
	Not all longitudinal bars are supported (Configuration 1*)					All longitudinal bars are supported (Configuration 2*)				
	CON-RT-Y-60-10-#5	1.23	0.49	5.30	1.30	CON-RT-Y-60-10-#6	1.15	0.61	7.19	1.16
	CWT-RT-Y-60-10-#5	1.25	0.96	12.4	1.30	CWT-RT-Y-60-10-#6	1.13	0.76	8.60	1.15
	CON-RT-Y-80-10-#5	1.14	0.65	7.90	1.25	CON-RT-Y-80-10-#6	1.01	0.97	10.3	1.06
	CWT-RT-Y-80-10-#5	1.17	0.87	14.9	1.24	CWT-RT-Y-80-10-#6	1.09	1.05	12.7	1.12
	CWT-RT-N-60-6-#5	1.20	0.67	8.76	1.26	CWT-RT-N-60-6-#6	1.22	1.00	10.5	1.29
	CWT-RT-N-60-10-#5	1.05	0.84	10.4†	1.07	CWT-RT-N-60-10-#6	1.05	1.01	15.6	1.06
	CWT-RT-N-80-10-#5	1.11	0.66	N/A	1.31	CWT-RT-N-80-10-#6	1.05	0.88	7.77	1.15
Average		1.17	0.74	9.95	1.25		1.10	0.90	10.4	1.14
Maximum		1.25	0.96	14.90	1.31		1.22	1.05	15.6	1.29
Minimum		1.05	0.49	5.30	1.07		1.01	0.61	7.19	1.06
COV		0.059	0.219	0.342	0.067		0.065	0.180	0.285	0.067
95% confidence range		1.11 to 1.22	0.62 to 0.85	7.22 to 12.7	1.19 to 1.31		1.05 to 1.15	0.78 to 1.02	8.19 to 12.6	1.08 to 1.2

*Refer to Fig. 2.

†Last reading before losing instrumentation.

is seen for the other two comparison metrics—the average f_{tie}/f_{yt} is 8%, and ε_{85} is 20% higher for the specimens with the higher concrete strength.

Shape of boundary element

Out of four comparable specimens, two rectangular specimens exhibited larger post-peak ductility (that is, larger ε_{85}) than their square counterparts, and two square specimens showed opposite trends (Table 10). However, the difference between the two shapes in terms of ε_{85} is not appreciable—with 95% confidence, the average value is between 5.88 and 14.4 με for rectangular specimens compared to 5.08 and 14.2 με for square specimens. All four rectangular specimens developed a larger capacity than their square counterparts—the average value of P_{max}/P_o was 1.20 and 1.09 (10% difference) for rectangular and square specimens, respectively. Normalized confined concrete strength (f_{cc}'/f_c') is larger in three rectangular specimens, but on average, it is only 2.9% larger than that for the square specimens. The larger value of f_{tie}/f_{yt} is evenly divided between the two shapes, but the average value of square specimens is larger by 2.8% (0.765 versus 0.744).

Evaluation of confined concrete models

Using the measured material properties and as-built dimensions, confined concrete stress-strain relationships were determined using studies by Saatcioglu and Razvi,[19] Razvi and Saatcioglu,[20] and Mander et al.[6] The results

Table 8—Effect of compliance with ACI transverse reinforcement requirements

	ID	P_{max}/P_o	f_{tie}/f_{yt}	$\varepsilon_{85} \times 10^3$	f_{cc}/f_c'	ID	P_{max}/P_o	f_{tie}/f_{yt}	$\varepsilon_{85} \times 10^3$	f_{cc}/f_c'
	ACI-compliant					Not ACI-compliant				
	CWT-RT-Y-60-6-#5	1.14	0.72	12.2	1.12	CWT-RT-N-60-6-#5	1.20	0.67	8.76	1.26
	CWT-RT-Y-60-10-#5	1.25	0.96	12.4	1.30	CWT-RT-N-60-10-#5	1.05	0.84	10.4*	1.07
	CWT-RT-Y-80-10-#5	1.17	0.87	14.9	1.24	CWT-RT-N-80-10-#5	1.11	0.66	N/A	1.31
	CWT-RT-Y-60-10-#6	1.13	0.76	8.60	1.15	CWT-RT-N-60-10-#6	1.05	1.01	15.6	1.06
	CWT-RT-Y-80-10-#6	1.09	1.05	12.7	1.12	CWT-RT-N-80-10-#6	1.05	0.88	7.77	1.15
Average		1.16	0.87	12.2	1.18		1.09	0.81	10.6	1.17
Maximum		1.25	1.05	14.9	1.30		1.20	1.01	15.6	1.31
Minimum		1.09	0.72	8.60	1.12		1.05	0.66	7.77	1.06
COV		0.052	0.157	0.186	0.067		0.058	0.183	0.326	0.097
95% confidence range		1.11 to 1.21	0.75 to 0.99	10.2 to 14.1	1.11 to 1.25		1.04 to 1.15	0.68 to 0.94	7.23 to 14.0	1.07 to 1.27

*Last reading before losing instrumentation.

Table 9—Effect of concrete compressive strength

	ID	P_{max}/P_o	f_{tie}/f_{yt}	$\varepsilon_{85} \times 10^3$	f_{cc}/f_c'	ID	P_{max}/P_o	f_{tie}/f_{yt}	$\varepsilon_{85} \times 10^3$	f_{cc}/f_c'
	f_c' = 6000 psi (41.4 MPa)					f_c' = 10,000 psi (69 MPa)				
	CON-RT-Y-60-6-#5	1.19	0.67	5.40	1.20	CON-RT-Y-60-10-#5	1.23	0.49	5.30	1.30
	CWT-RT-Y-60-6-#5	1.14	0.72	12.2	1.12	CWT-RT-Y-60-10-#5	1.25	0.96	12.4	1.30
	CWT-RT-N-60-6-#5	1.20	0.67	8.76	1.26	CWT-RT-N-60-10-#5	1.05	0.84	N/A	1.07
	CWT-RT-N-60-6-#6	1.22	1.00	10.5	1.29	CWT-RT-N-60-10-#6	1.05	1.01	15.6	1.06
Average		1.19	0.76	9.22	1.22		1.15	0.83	11.1	1.18
Maximum		1.22	1.00	12.2	1.29		1.25	1.01	15.6	1.30
Minimum		1.14	0.67	5.40	1.12		1.05	0.49	5.30	1.06
COV		0.028	0.207	0.315	0.062		0.095	0.281	0.474	0.114
95% confidence range		1.15 to 1.22	0.61 to 0.92	6.37 to 12.1	1.14 to 1.29		1.04 to 1.25	0.6 to 1.05	5.14 to 17	1.05 to 1.31

Table 10—Effect of shape of boundary elements

	ID	P_{max}/P_o	f_{tie}/f_{yt}	$\varepsilon_{85} \times 10^3$	f_{cc}/f_c'	ID	P_{max}/P_o	f_{tie}/f_{yt}	$\varepsilon_{85} \times 10^3$	f_{cc}/f_c'
	Square					Rectangular				
	CON-SQ-Y-60-10-#5	1.07	0.35	2.90	1.21	CON-RT-Y-60-10-#5	1.23	0.49	5.30	1.30
	CWT-SQ-Y-60-10-#5	1.11	1.14	13.0	1.24	CWT-RT-Y-60-10-#5	1.25	0.96	12.4	1.30
	CON-SQ-Y-80-10-#5	1.12	1.22	10.2	1.30	CON-RT-Y-80-10-#5	1.14	0.65	7.90	1.25
	CWT-SQ-Y-80-10-#5	1.06	0.36	12.5	1.19	CWT-RT-Y-80-10-#5	1.17	0.87	14.9	1.24
Average		1.09	0.76	9.65	1.24		1.20	0.74	10.1	1.27
Maximum		1.12	1.22	13.00	1.30		1.25	0.96	14.9	1.30
Minimum		1.06	0.35	2.90	1.19		1.14	0.49	5.30	1.24
COV		0.026	0.623	0.483	0.040		0.041	0.283	0.428	0.026
95% confidence range		1.06 to 1.12	0.3 to 1.23	5.08 to 14.2	1.19 to 1.28		1.15 to 1.25	0.54 to 0.95	5.88 to 14.4	1.24 to 1.3

from these models are plotted against their experimentally obtained counterparts in Fig. 7 for 14 specimens in which the type of transverse reinforcement (conventional or CWTs) was the only variable. Similar trends were observed for the other specimens.[16,17] It should be noted that the models do not distinguish between conventional hoops or CWTs; hence, two experimental results are shown for each set of analytically generated stress-strain relationships. Furthermore, Fig. 8 compares the experimentally obtained peak concrete compressive strength (f_{cc}') and strain at 85% of peak compressive strength (ε_{85}) against the values from the three selected models.

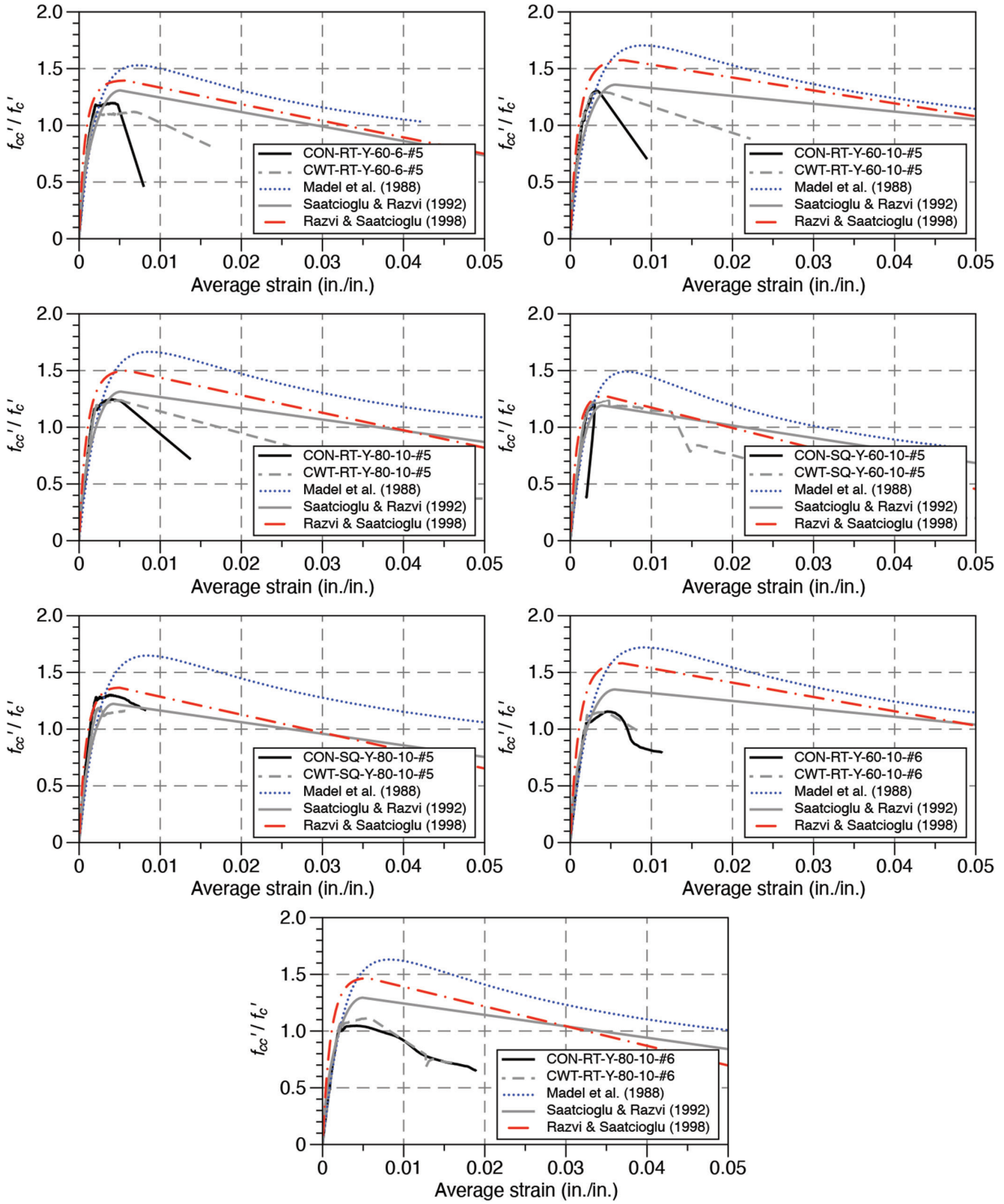

Fig. 7—Representative comparison of measured and calculated stress-strain relationships for comparable specimens with conventional hoops and continuously wound ties.

All the models tend to overestimate ε_{85}, although Razvi and Saatcioglu[20] is slightly more accurate, particularly for CWT specimens. The measured ε_{85} for the specimens with CWTs is on average 0.601 times the calculated value, and the corresponding ratio is 0.346 for conventional hoops (refer to Table 11). The same trend is observed for the other two models, but these two models tend to overestimate ε_{85} to a greater extent, that is, the ratios shown in Table 11 are smaller. If all the specimens are considered, the differences between the three models in terms of predicting post-peak stiffness (ε_{85}) are slightly less, though all still overestimate the experimentally obtained value.

The models predict f_{cc}' better than ε_{85}. On average, f_{cc}' (normalized with respect to f_c') is 0.985 and 1.014 times the values from Saatcioglu and Razvi[19] for the specimens using conventional hoops and CWTs, respectively. With 95% confidence, the mean measured f_{cc}' for the specimens with conventional hoops is 0.948 to 1.023 times the value

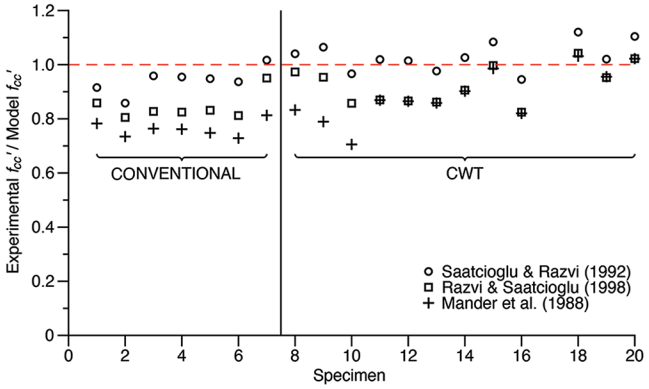

(a) Peak compressive strength (f_{cc}')

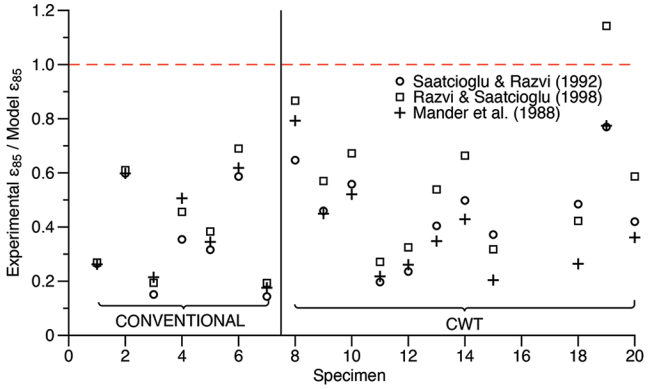

(b) Strain at 85% of peak stress (ε_{85})

Fig. 8—Experimental values of f_{cc}' *and* ε_{85} *versus values from various models.*

determined by Saatcioglu and Razvi.[19] The corresponding values are 0.971 to 1.058 for CWT specimens. If all the specimens are considered, with 95% confidence, the mean measured f_{cc}'/f_c' is between 0.973 and 1.035 times what Saatcioglu and Razvi[19] predict. The other two models overestimate f_{cc}'/f_c' more. Considering all the specimens, the measured/calculated magnitude of f_{cc}'/f_c' is on average 0.898 and 0.844 for Razvi and Saatcioglu[20] and Mander et al.,[6] respectively, versus 1.004 for Saatcioglu and Razvi.[19]

A clear explanation for the noticeable differences between the measured post-peak behavior (ε_{85}) and those from the models could not be identified. A plausible reason could be the models have been developed mostly based on the experimental data from specimens that were shorter (18 to 47 in. [0.457 to 1.19 m]) than the test specimens (72 in. [1.83 m]). The uniformity of concrete strength is reduced as the specimen height increases. Another reason could be due to the differences in the aggregates used in the test specimens versus those in the specimens that are basis of the models. Aggregate surface roughness affects tension stiffening.

SUMMARY AND CONCLUSIONS

Continuously wound ties (CWTs) offer advantages over conventional transverse reinforcement in terms of construction speed, reducing material waste, and alleviating congestion. ACI 318-19 considers CWTs the same as conventional transverse reinforcement. The main goal of this project was to compare the performance of CWTs to conventional hoops.

Based on the presented data, the following conclusions are drawn:

Table 11—Comparison of key experimental and analytical parameters of confined concrete

	ε_{85} (measured/calculated)			f_{cc}'/f_c' (measured/calculated)		
	Saatcioglu and Razvi[19]	Razvi and Saatcioglu[20]	Mander et al.[6]	Saatcioglu and Razvi[19]	Razvi and Saatcioglu[20]	Mander et al.[6]
Conventional hoops						
Average	0.277	0.346	0.288	0.985	0.879	0.803
Maximum	0.459	0.570	0.449	1.064	0.954	0.869
Minimum	0.144	0.193	0.176	0.915	0.827	0.748
COV	0.446	0.452	0.337	0.051	0.059	0.057
95% confidence range	0.185 to 0.368	0.23 to 0.461	0.216 to 0.359	0.948 to 1.023	0.84 to 0.918	0.769 to 0.837
CWTs						
Average	0.487	0.601	0.479	1.014	0.908	0.867
Maximum	0.770	1.143	0.793	1.120	1.042	1.031
Minimum	0.236	0.318	0.204	0.858	0.805	0.705
COV	0.314	0.392	0.403	0.079	0.092	0.131
95% confidence range	0.401 to 0.574	0.468 to 0.735	0.37 to 0.588	0.971 to 1.058	0.863 to 0.954	0.805 to 0.928
All specimens						
Average	0.410	0.507	0.409	1.004	0.898	0.844
Maximum	0.770	1.143	0.793	1.120	1.042	1.031
Minimum	0.144	0.193	0.176	0.858	0.805	0.705
COV	0.425	0.475	0.458	0.071	0.082	0.117
95% confidence range	0.332 to 0.488	0.399 to 0.615	0.324 to 0.493	0.973 to 1.035	0.866 to 0.931	0.801 to 0.888

1. As expected, the type of confinement did not noticeably affect the compressive strength. On the other hand, the specimens confined with CWTs exhibited improved post-peak ductility in comparison to those employing conventional hoops. The influence of CWTs is less noticeable in terms of the maximum tie stress and confined concrete stress.

2. The test results did not identify a clear trend in terms of the influence of the grade of reinforcement.

3. Compliance with current ACI transverse reinforcement requirements could only be evaluated with reference to CWTs. The values of maximum axial load, transverse reinforcement stress, strain at 85% peak concrete stress, and peak compressive strength are reduced if the CWTs do not meet ACI transverse reinforcement requirements.

4. The values of ε_{85} and f_{tie}/f_{yt} are larger for high-strength (10 ksi [69 MPa]) concrete. However, a reverse trend is observed for P_{max}/P_o and f_{cc}'/f_c' if 6 ksi (41.4 MPa) is used.

5. Regardless of the type of transverse reinforcement, Saatcioglu and Razvi[19] predict the confined concrete compressive strength reasonably well and better than the two other models considered in this study. All the models overpredict the post-peak ductility of confined concrete, although Razvi and Saatcioglu[20] is slightly better, particularly for CWT specimens.

RECOMMENDATIONS

1. All the current ACI requirements for transverse reinforcement ought to be satisfied to take full advantage of the enhanced post-peak ductility offered by CWTs. Moreover, it is recommended to use Grade 80 CWTs in conjunction with high-strength concrete (10 ksi [69 MPa]) to further enhance ductility.

2. The use of Saatcioglu and Razvi's[19] model is recommended to obtain the expected compressive strength confined by CWTs or conventional hoops. The likely value of ε_{85} for either type of transverse reinforcement should be taken as one-half of the value computed from Razvi and Saatcioglu.[20]

AUTHOR BIOS

Malory R. Gooding *recently joined Julie Cromwell & Associates, LLC, in Cincinnati, OH, where she has been involved in the design and evaluation of new and existing structures. She received her BS and MS in civil engineering from the University of Cincinnati, Cincinnati, OH. Her graduate research is a part of the research reported in this paper. Her research was based on work supported by the National Science Foundation Graduate Research Fellowship Program.*

Elizabeth A. Mosier *recently joined San Engineering LLC in Denver, CO, as a project engineer. She received her BS in architectural engineering from the University of Cincinnati in 2020. She is currently completing her MS in civil engineering from the University of Cincinnati. Her graduate research is a part of the research reported in this paper.*

Bahram M. Shahrooz, *FACI, is a Professor of structural engineering at the University of Cincinnati and a licensed professional engineer in Ohio. He is an active member of several ACI committees. His research interests include prestressed concrete bridges, concrete and hybrid buildings, and high-strength reinforcement.*

ACKNOWLEDGMENTS

The Charles Pankow Foundation, ACI Foundation, and CRSI Foundation provided the funding for this project. The project was guided by the Industry Advisory Panel consisting of R. Klemencic, Chairman and CEO of MKA; J. Moehle from the University of California, Berkeley; N. Anderson from SGH; and R. Bayat from Englekirk. Janell Concrete and Masonry Equipment, Inc.; Dayton Superior; Contractors Materials Company; Alamillo; Nucor; Commercial Metals Company; and Pacific Steel Group donated the materials used to fabricate the test specimens. Their donations are gratefully acknowledged. The assistance of the laboratory staff at the Pacific Earthquake Engineering Research Center at the University of California, Berkeley, where the tests were conducted, was crucial to completing the testing program. Danis Construction facilitated and assisted with the fabrication of Phase 1 specimens.

REFERENCES

1. Arteta, C. A.; To, D. V.; and Moehle, J. P., "Experimental Response of Boundary Elements of Code-Compliant Reinforced Concrete Shear Walls," *Proceedings of the 10th U.S. National Conference in Earthquake Engineering (10NCEE)*, Anchorage, AK, 2014, 11 pp.

2. Arteta, C. A., "Seismic Response Assessment of Thin Boundary Elements of Special Concrete Shear Walls," PhD dissertation, University of California, Berkeley, Berkeley, CA, 2015, 222 pp.

3. Behrouzi, A.; Welt, T.; Lehman, D.; Lowes, L.; LaFave, J.; and Kuchma, D., "Experimental and Numerical Investigation of Flexural Concrete Wall Design Details," *Structures Congress 2017: Buildings and Special Structures*, J. G. Soules, ed., Denver, CO, 2017, pp. 418-433.

4. Cusson, D., and Paultre, P. "High-Strength Concrete Columns Confined by Rectangular Ties," *Journal of Structural Engineering*, ASCE, V. 120, No. 3, 1994, pp. 783-804.

5. Moehle, J. P., and Bavanagh, T., "Confinement Effectiveness of Crossties in RC," *Journal of Structural Engineering*, ASCE, V. 111, No. 10, 1985, pp. 2105-2120.

6. Mander, J. B.; Priestley, M. J. N.; and Park, R., "Observed Stress-Strain Behavior of Confined Concrete," *Journal of Structural Engineering*, ASCE, V. 114, No. 8, 1988, pp. 1827-1849.

7. Massone, L. M.; Polanco, P.; and Herrera, P., "Experimental and Analytical Response of RC Wall Boundary Elements," *Proceedings of the 10th U.S. National Conference in Earthquake Engineering (10NCEE)*, Anchorage, AK, 2014, 11 pp.

8. Saatcioglu, M., and Razvi, S. R., "High-Strength Concrete Columns with Square Sections under Concentric Compression," *Journal of Structural Engineering*, ASCE, V. 124, No. 12, 1998, pp. 1438-1447.

9. Scott, B. D.; Park, R.; and Priestley, M. J. N., "Stress-Strain Behavior of Concrete Confined by Overlapping Hoops at Low and High Strain Rates," *ACI Journal Proceedings*, V. 79, No. 1, Jan.-Feb. 1982, pp. 13-27.

10. Sharma, U. K.; Bhargava, P.; and Kaushik, S. K., "Behavior of Confined High Strength Concrete Columns under Axial Compression," *Journal of Advanced Concrete Technology*, V. 3, No. 2, 2005, pp. 267-281.

11. Sheikh, S. A., and Uzumeri, S. M., "Strength and Ductility of Tied Concrete Columns," *Journal of the Structural Division*, ASCE, V. 106, No. 5, 1980, pp. 1079-1102.

12. Welt, T. S., "Detailing for Compression in Reinforced Concrete Wall Boundary Elements: Experiments, Simulations, and Design Recommendations," PhD dissertation, University of Illinois Urbana-Champaign, Urbana, IL, 2015, 566 pp.

13. Welt, T. S.; Massone, L. M.; LaFave, J. M.; Lehman, D. E.; McCabe S. L.; and Polanco P., "Confinement Behavior of Rectangular Reinforced Concrete Prisms Simulating Wall Boundary Elements," *Journal of Structural Engineering*, ASCE, V. 143, No. 4, 2017, p. 04016204.

14. Shahrooz, B. M.; Forry, M. L.; Anderson, N. S.; Bill, H. L.; and Doellman, A. M., "Continuous Transverse Reinforcement—Behavior and Design Implications," *ACI Structural Journal*, V. 113, No. 5, Sept.-Oct. 2016, pp. 1085-1094.

15. ACI Committee 318, "Building Code Requirements for Structural Concrete (ACI 318-19) and Commentary (ACI 318R-19) (Reapproved 2022)," American Concrete Institute, Farmington Hills, MI, 2019, 624 pp.

16. Gooding, M. R.; Mosier, E. A.; and Shahrooz, B. M., "Normal and High-Strength Continuously Wound Ties," Final Report, Charles Pankow Foundation, Haymarket, VA, 2022, 82 pp.

17. Gooding, M. R., "Normal and High-Strength Continuously Wound Ties," MSc thesis, University of Cincinnati, Cincinnati, OH, 2020, 208 pp.

18. ASTM C39/C39M-21, "Standard Test Method for Compressive Strength of Cylindrical Concrete Specimens," ASTM International, West Conshohocken, PA, 2021, 8 pp.

19. Saatcioglu, M., and Razvi, S. R., "Strength and Ductility of Confined Concrete," *Journal of Structural Engineering*, ASCE, V. 118, No. 6, 1992, pp. 1590-1607. doi: 10.1061/(ASCE)0733-9445(1992)118:6(1590)

20. Razvi, S., and Saatcioglu, M., "Confinement Model for High-Strength Concrete," *Journal of Structural Engineering*, ASCE, V. 125, No. 3, 1999, pp. 281-289. doi: 10.1061/(ASCE)0733-9445(1999)125:3(281)

ACI STRUCTURAL JOURNAL TECHNICAL PAPER

Title No. 120-S96

Hysteresis Evaluation of Discrete Damper with Adaptive Shear Links for Extensively Damaged Reinforced Concrete Frame

by Naveen Kumar Kothapalli, R. Siva Chidambaram, and Pankaj Agarwal

The global seismic capacity of an extensively damaged reinforced concrete (RC) portal frame is enhanced by the addition of a discrete damper with adaptive shear link elements. Cyclic tests are performed to evaluate the hysteresis behavior of the proposed damper device with two different sets of shear link elements. Hysteresis performance of the damper-fit RC frame is also evaluated under a displacement-controlled reversed cyclic test. Moreover, a specially designed interlinked coupler-box assembly is used as a local retrofitting technique for restoring the buckled or ruptured longitudinal reinforcing bars of damaged columns in the RC frame. The competency and efficacy of the proposed retrofit techniques are established by comparing the hysteretic behavior, failure mechanism, energy dissipation, strength, and stiffness degradations with the initial tested conventional bare frame. The lateral strength efficiency of the damper-fit model frame is relatively enhanced by 2.5 times with a higher rate of energy dissipation capacity. The proposed damper device functions as a safeguarding element, which protects the principal structural members against lateral-induced damages, and the independent load-transfer mechanism allows for gravity load transfer of the frame despite its nullified lateral strength.

Keywords: coupler-box assembly; discrete damper; load-bearing pedestals; seismic retrofitting; shear link elements; styrene-butadiene rubber (SBR).

INTRODUCTION

The principal structural members of reinforced concrete (RC) frame buildings undergo inelastic rotations or deformations on the incidence of a strong earthquake, which causes local distress or damage. These damages progress as a hinge mechanism in multi-storied structures, which leads to a catastrophic failure with heavy loss. In particular, the damages are more substantial in soft-story buildings, where the ground-story columns are subjected to enormous deformations that form the plastic hinges, leading to a failure mechanism. It is a challenging task for a structural engineer to provide an efficient and well-tested retrofitting solution for such failures. The passive response control technique in the form of dampers or dampening devices is one solution, where the input seismic energy is dissipated through various operating mechanisms. Metallic-yield dampers are frequently used dampening systems that work on the principle of inelastic yielding. The constituent metallic elements of these dampers undergo inelastic deformations to dissipate the enforced energy, which prominently improves the initial strength and stiffness of connected RC frames. Many forms of metallic dampening systems are studied in the literature, such as a dual-function metallic damper by Li and Li (2007); an aluminium shear-yield damper by Sahoo and Rai (2009); single and dual steel pipe seismic dampers by Maleki and Bagheri (2010) and Maleki and Mahjoubi (2013), respectively; infilled pipe dampers as introduced by Maleki and Mahjoubi (2014); a low-yield strength shear panel damper by Zhang et al. (2013); steel strip prismatic slit dampers by Lee et al. (2015); a metallic flexure and shear yield mechanism damper by Sahoo et al. (2015); a dual-performance hybrid structural damper proposed by Hosseini Hashemi and Moaddab (2017); a box-shaped steel slit damper by Lee and Kim (2017); and a honeycomb-shaped steel damper as recommended by Lee et al. (2017). The use of added damping and stiffness (ADAS) and triangular added damping and stiffness (TADAS) yield dampers to retrofit moment resisting frames is considered by TahamouliRoudsari et al. (2018); an innovative shear-bending metallic damper with K-shaped bending components by Li et al. (2019); and combined metallic-yield dampers to strengthen soft-story RC frames were studied by Oinam and Sahoo (2019).

The point of major concern in adopting metallic dampers is that the post-yield behavior is depreciative due to buckling or yielding of metal components, which induces damage to the corresponding RC structural member. As reviewed from the literature and also evident from the experimental tests on metallic dampers, the components undergo damage by crushing or crumbling, which makes them incompetent to endure the vertical gravity loads of the associated frame structure. Thus, the RC frames equipped with metallic dampers experience a concurrent loss in gravitational and lateral load capacities, making them more vulnerable to impending damage. The proposed invention deals with a low-cost hysteretic-yield discrete damper with independent load-transfer mechanisms for gravity and earthquake-induced lateral loads, as shown in Fig. 1. This ensures the frame's vertical load capacity, despite its reduced or annulled lateral resistance. The suggested load-transfer mechanism of slide-rubber bearings assists in maintaining the integrity of the frame structure despite its loss in lateral strength. The

ACI Structural Journal, V. 120, No. 6, November 2023.

MS No. S-2022-252.R1, doi: 10.14359/51739087, received February 13, 2023, and reviewed under Institute publication policies.

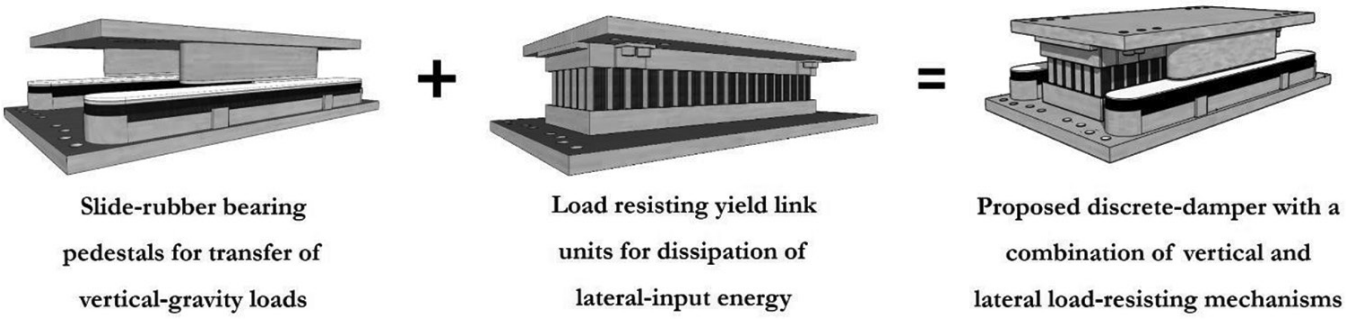

Fig. 1—Operating mechanism of proposed discrete yield damper.

recommended damper adopts adaptive yield link elements to dissipate the input lateral energy by experiencing inelastic deformations. The deformable links preferred in this current study are composite link units made with the inner ply of radial rubber tires sandwiched between thin metal sheets. The ideology of adopting these link units is stimulated by the experimental investigation on their energy dissipation potential by Goyal and Agarwal (2017). The link units exclusively deform under the application of lateral drifts and remain serene under existing gravity loads. Thus, the gravity load-carrying capability of the damper-fit model frame remains persistent through the slide-rubber bearings, even after the failure of the link unit. Restoration of the proposed damper requires replacement of yielded links post-damage. The threaded bolting arrangement of the grid to the upper base plate makes it simpler to replace the yield links. The damper device is associated with the RC frame through high-strength threaded Allen bolts at the top and bottom base plates. Thus, the process of repair and reinstallation of the damper becomes an uncomplicated task with minimal cost and workforce.

RESEARCH SIGNIFICANCE

The adoption of metallic-yield dampers in retrofitting or strengthening RC frame structures is a common practice, where the inelastic deformations of metal elements dissipate the input seismic energy. The post-yield behavior of the dampers degrades or deteriorates due to inelastic rotations, which eventually leads to a failure by buckling or rupture. This comprehensive damper failure disintegrates the vertical load-carrying capacity of frames along with its lateral load resistance. The proposed damper device provides a feasible solution to overcome this consequence by providing independent load-transfer mechanisms. The recommended damper uses slide-rubber bearings to transfer the vertical loads and adaptive yield link units for dissipation of input lateral energy, where the post-yield damage of link units does not affect the structural integrity of connected RC frames. The proposed damper is quantified by component-level and structural-level cyclic tests, which manifests the competency of damper in retrofitting and strengthening RC frame structures.

STRUCTURAL CONFIGURATION AND CYCLIC PERFORMANCE OF PROPOSED DAMPER COMPONENT

The proposed damper device consists of flexible rubber bearing pedestals for vertical load transmission and a square-grid framework fabricated with mild-steel plates to grip the lateral-load-resisting adaptive yield link units. The element used in the fabrication of pedestals and the viscoelastic yield link unit is prepared from the inner-ply part of the radial rubber tires. The ply part is a category of synthetic rubber polymer—styrene-butadiene rubber (SBR)—with intrinsic steel wires. The SBR element is generally compounded with better abrasion and heat resistance than natural rubber. The mechanical aging behavior of SBRs by an abrasion test was evaluated by Nakazono and Matsumoto in 2011, where minor changes were noticed in the mechanical properties and the crosslinking points were barely broken by mechanical forces. These rubbers have high abrasion resistance and good aging stability, which are adhered to each other using synthetic rubber adhesives. This rubber-ply part is fixed with corresponding sections of stainless steel (SS) and polytetrafluoroethylene (PTFE) sheets over which the upper bearing of mirror-textured SS surface slides smoothly. The structural configuration of bearings allows for consistent vertical load transfer with minimal lateral load resistance. Contrarily, the adaptive yield link units are independent of gravity loads and exclusively resist the lateral load by experiencing inelastic deformations. The adaptive link units are made by encapsulating rubber links (made by adhering individual ply units) within thin mild-steel sheets. The end parts of the link unit are implanted in the slotted grid framework, which leads to double-curvature shear yielding at the midcenter to dissipate input energy. The link units are arranged with their metal sheets oriented perpendicular to the direction of applied lateral force. A preliminary investigation of the proposed damping technique is performed with 36 yield link units, and the structural configuration of the damper device is shown in Fig. 2. Displacement-controlled reversed cyclic testing of increasing amplitudes until failure of the link unit is executed on the damper component, and the hysteresis behavior is shown in Fig. 3(a). The amount of hysteresis energy dissipated by the links is plotted against corresponding lateral displacements, as shown in Fig. 3(b).

A gradual increase in lateral strength with lower initial stiffness is observed in the damper component. A progressive increase in energy dissipation manifests the potentiality

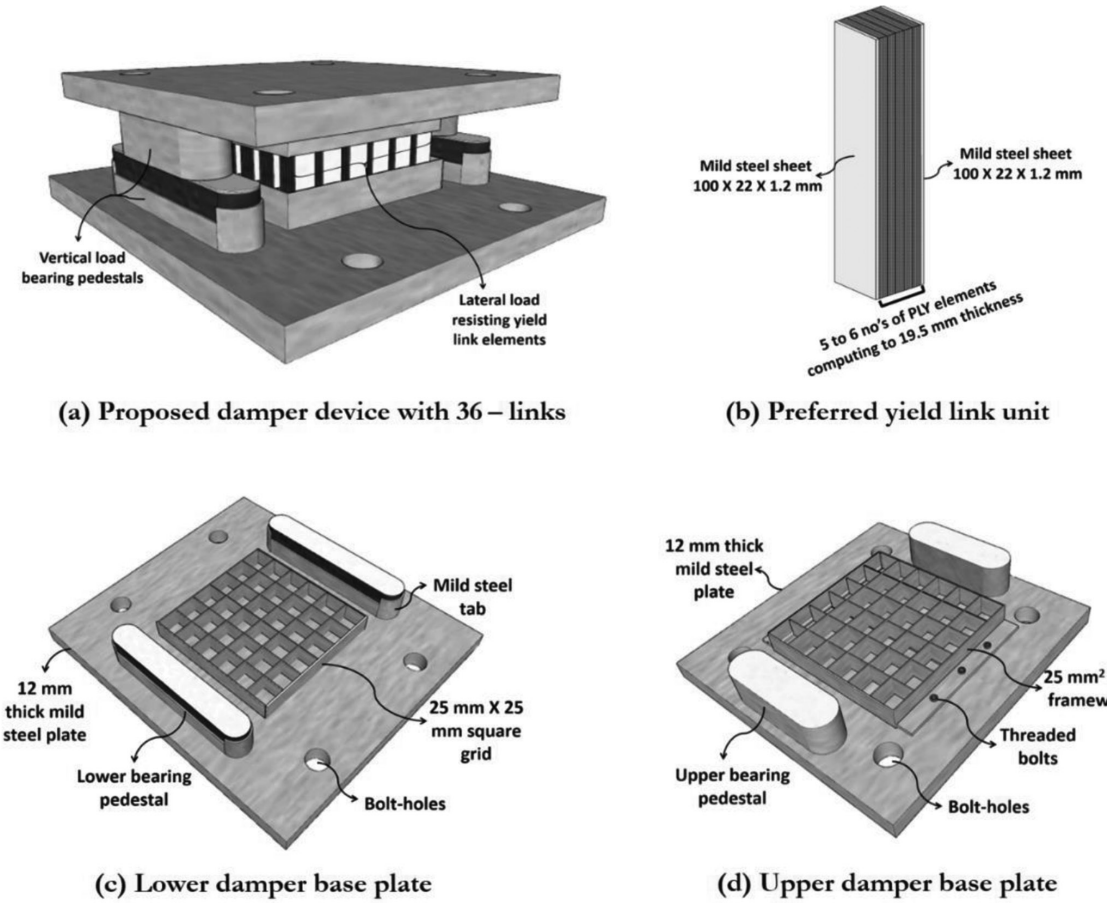

Fig. 2—Structural configuration of damper with 36 numbered yield link units.

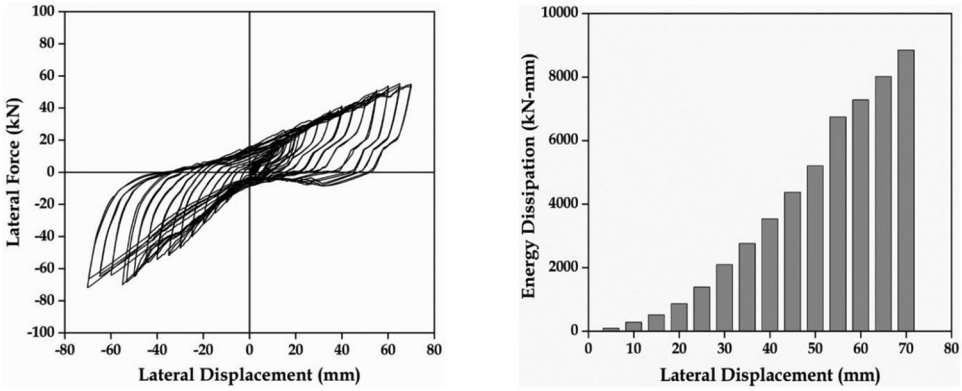

Fig. 3—Hysteresis performance of 36-link damper.

of link unit in absorbing the lateral input energy. The sequential arrangement of links in the square-grid framework allows synchronous yielding with higher energy dissipation until failure. This further assists in improving the lateral strength of damper until the failure of a major number of link units. The lateral deflection behavior varies in the mild-steel and rubber-ply element of a link, due to which the failure initiates by steel debonding. The link units deform and distort under applied lateral force, which leads to failure by buckling or rupturing of steel sheets and debonding in rubber-ply elements. Subsequently, the distorted link units eject out from their respective slots and get jammed between the grids of upper and lower base plates. This leads to an increase in lateral strength of the damper post-failure of the link unit. Thus, the exhaustive failure of link unit—that is, detachment of rubber plies and buckling or rupture of steel sheet, is considered as the end of damper efficiency and the test is stopped at 70 mm (2.76 in.) lateral displacement. The damaged or yielded links post-failure are shown in Fig. 4, where the outer-grid units are relatively more disfigured. However, the vertical load-transfer component of slide-rubber bearings remains intact without any damage.

The damper device preferred in retrofitting the full-scale RC model frame is designed with 114 yield link units, with

Damaged damper with yielded links

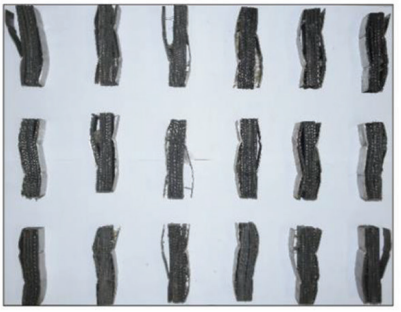

Severely damaged exterior grid links

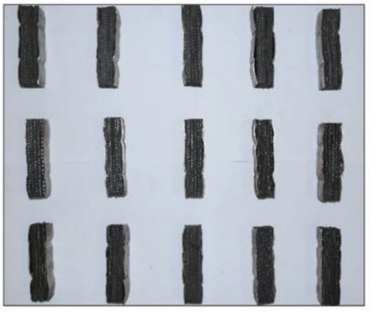

Moderately yielded interior grid links

Fig. 4—Failure pattern in 36-link damper.

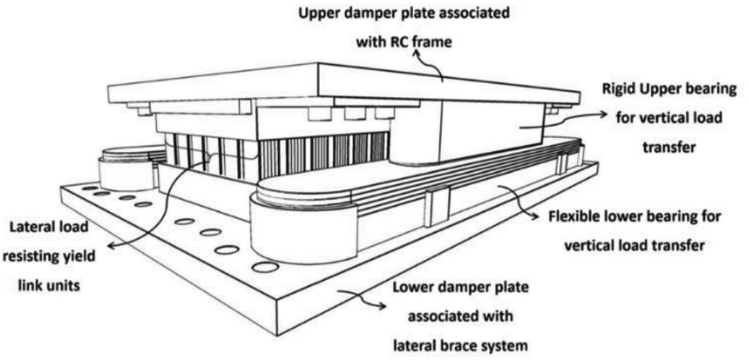

(a) Proposed damper with 114 – yield link units

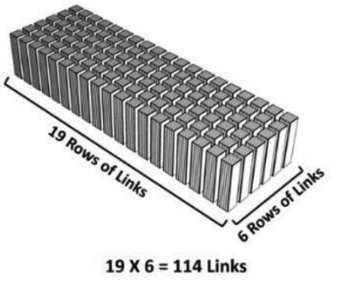

(b) Orientation of link units

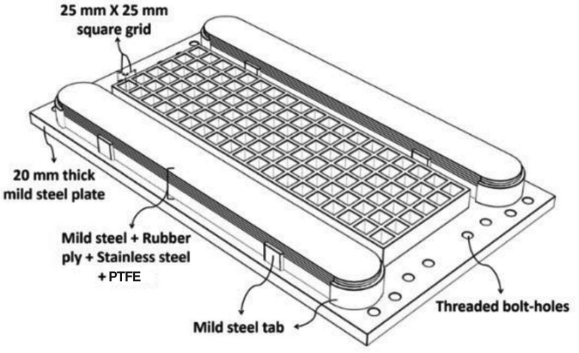

(c) Lower damper base plate

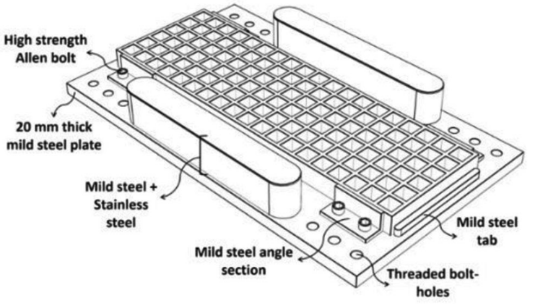

(d) Upper damper base plate

Fig. 5—Structural configuration of damper with 114 numbered yield link units.

its structural configuration shown in Fig. 5. It is composed of two square-grid frameworks of 25 mm (0.038 in.) grid size, which is firmly gripped with the corresponding upper and lower base plates. The bottom grid is welded, while the top grid is bolted to allow ease of link installation. These grids are laterally surrounded by oval-shaped slide-rubber bearings. The lower bearing pedestals of mild-steel plates plus rubber pads made from ply elements, SS sheets, and PTFE

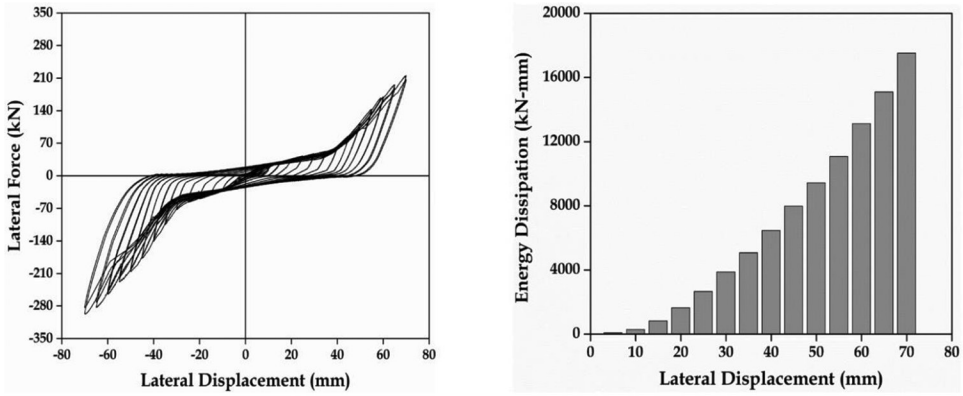

(a) Hysteretic behaviour

(b) Energy dissipated vs drift ratio plot

Fig. 6—Hysteresis performance of 114-link damper.

sheets are fixed to the lower base plate, while mild-steel plates with SS sheets of mirror-finished texture constitute the upper bearings that are fixed with the upper base plate. Synthetic rubber adhesives are used to glue the individual ply elements, while cyanoacrylate adhesives are used for bonding PTFE and SS sheets. The lower bearing pedestals are additionally confined along their length using mild-steel tabs to prevent any possible slip failure. The proportional length of upper bearing is kept half of the lower one with their midcenters converged. Dimensions of the grid framework and bearings depend on the damper capacity and may decrease or increase with the required number of link units. Threaded bolt holes are drilled on the base plates to associate the damper with the RC frame system. The damper device is assembled by inverting the upper square grid over the lower grid and installing the link units in the potential direction of lateral force, as seen in Fig. 5(b). The upper bearing pedestals, along with the base plate, are then inverted over the lower one with the convergence of midcenters, and the upper square grid is meticulously bolted with the upper base plate. After damper installation, the lateral free-play of load-bearing pedestals is verified along with the vertical free-play of link units in their respective slotted grids. High-strength threaded Allen bolts of 12.9 material grade are used to connect the damper with the secondary plates of test setup or with the structural RC frame system.

The proposed damper component with 114 yield link units is tested under reversed cyclic lateral displacements, and the obtained hysteresis response is plotted as shown in Fig. 6(a). The energy dissipation plot against corresponding lateral displacements is shown in Fig. 6(b). The lateral strength of damper component relies on the hysteretic behavior of link unit. The link elements undergo bending in double curvature with their corresponding edges pinned by the square-grid frameworks. The initial strength and stiffness of the damper are relatively low in the elastic phase of link deformation. However, a sudden increase in lateral strength is noticed post 35 mm (1.38 in.) lateral displacement by virtue of the cumulative inelastic deformation of link units. Eventually, the metal sheets of the link units experience plastic strain, which causes debonding with separation of the ply elements. The mid-portion of the link unit experiences inelastic deformations, which leads to the generation of local plastic hinges on either side of the link. These generated hinges allow the local rotation of the link unit in its respective slotted grid, which reduces the lateral strength of the damper in its mean displacement range. Thus, a constant width of the hysteresis loops is noticed within the mean lateral displacement range of ±30 mm (1.18 in.), where the strength of the damper becomes relatively constant. The energy dissipating potential of the damper improves gradually with the increase in lateral displacement. The link units undergo a continuous reversal of stresses until failure, where the adhesive bonding fails internally within the plies or with the metal sheets. The collective deformation of link units absorbs the lateral input energy until failure, which occurs by debonding or buckling/rupturing of the metal sheet. An identical post-failure behavior is noticed in the links, where the distorted link units get blocked between the grids, leading to a rise in lateral strength of the damper device. The damaged link units post-testing are shown in Fig. 7, where the double-curvature shear in the link unit along with the generated plastic hinges are evident. The outer-grid link units are relatively more distorted or disfigured. The vertical load-transfer pedestals of slide-rubber bearings remain undisturbed post-testing. A linear incremental pattern is noticed in the cumulative energy dissipation of the damper device with the adopted number of viscoelastic yield link elements, as seen in Fig. 8.

EXPERIMENTAL INVESTIGATION ON RC PORTAL FRAME RETROFITTED WITH PROPOSED DAMPER DEVICE

Experimental investigation on the adoption of the proposed damper device in retrofitting frame structures is studied by a cyclic test on a full-scale RC portal frame in the structural test facility at the Department of Earthquake Engineering, Indian Institute of Technology Roorkee. The initial tested conventional bare frame (hereby referred to as the ICB frame) is designed and detailed as per the current codal provisions IS 1893:2016 (2016) and IS 13920:2016 (2016), respectively. The structural configuration of model frame, along with its reinforcement detailing, is shown in Fig. 9. Thermomechanical treated (TMT) processed reinforcing bars with an average yield strength of 500 MPa (72.5 ksi) are used for reinforcing the frame sections. Construction of the frame is accomplished using ordinary

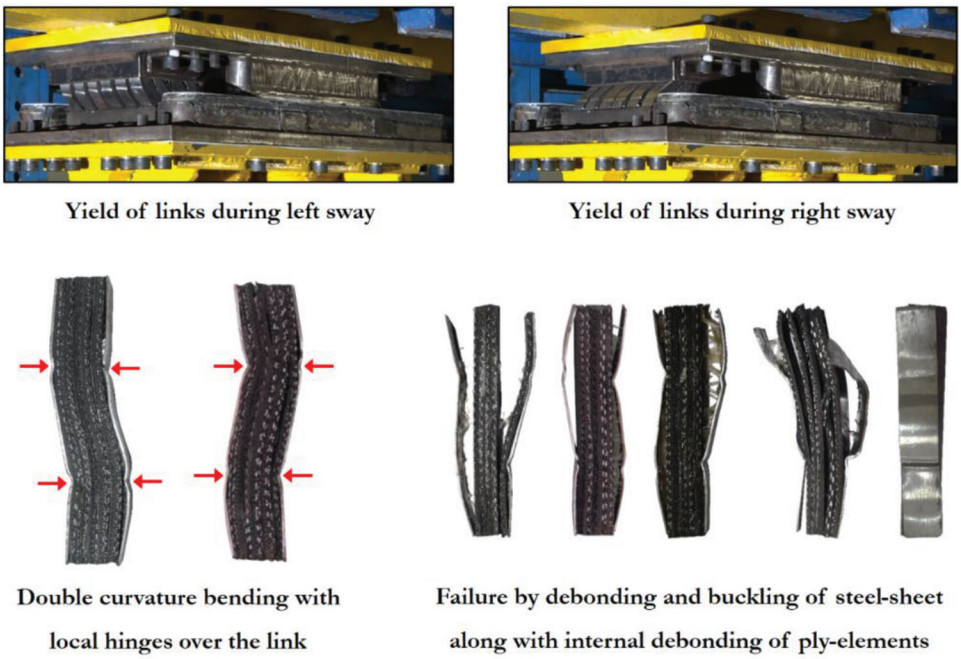

Fig. 7—Failure pattern in 114-link damper.

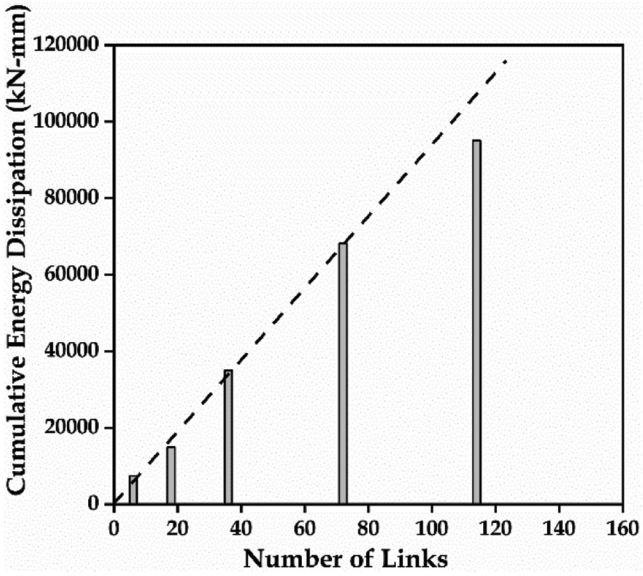

Fig. 8—Incremental pattern in cumulative energy dissipation with adopted number of yield link units.

portland cement (OPC) of Grade 43 (C), regionally available river sand as fine aggregate (FA), and appropriately crushed granite stone as coarse aggregate (CA), which are mixed in a nominal proportion of 1.00 (C):1.50 (FA):3.00 (CA) with a water-cement ratio (w/c) of 0.50. The constructed frame is tested under displacement-controlled reversed cyclic loads as per the interim testing protocol mentioned in the FEMA 461 (2007) standard recommendations. A combination of constant vertical gravity load of 100 kN (22.48 kip) and increasing lateral displacements until failure of the portal frame is enforced using three servo-controlled hydraulic actuators. The actuators—one horizontal: 500 kN (112.4 kip), ±250 mm (9.84 in.); and two vertical: 250 kN (56.2 kip), ±250 mm (9.84 in.), are integrally connected to the loading beam, which is bracketed to the frame through tie-rod assemblies, as shown in Fig. 10. Testing is carried out at a constant loading frequency of 0.01 Hz, with an initial loading rate of 0.1 mm/s (0.0039 in./s), which is augmented at a rate of 0.2 mm (0.0079 in.) until 4 mm/s (0.16 in./s) at the end of the test sequence. The horizontal actuator exercises lateral displacements in an incremental sinusoidal wave pattern until failure, and the acquired response data are used in plotting hysteresis curves.

The hysteresis loop response of the ICB frame is shown in Fig. 11, where a well-distributed balanced behavior is noticed with a gradual peak and post-peak performance until 6% lateral drift. The increase in applied lateral drift intensifies the bending moment at the column base of the ICB frame, where the closely spaced stirrups enhance the ductile performance of the potential plastic hinge region with an eventual failure by longitudinal reinforcing bar yielding. Thus, the cover concrete at column base of the ICB frame crumbles with rupture or buckling failure in the longitudinal reinforcing bars. The local rotation of beam-column joints leads to the formation of distinct width shear cracks at 6% lateral drift. These inclined shear cracks propagate as crushing in cover concrete and deformation in the adjacent stirrups. The damaged ICB frame post the preliminary test is shown in Fig. 12, where the longitudinal reinforcing bars buckle/rupture at column base along with crumbling of cover concrete at beam-column joints.

Restoration of buckled longitudinal reinforcing bars of columns in model frame using proposed local retrofitting approach of coupler-box assembly

The damaged plastic hinge locations at the column base of the ICB frame are locally restored using the proposed retrofitting technique of interlinked coupler-box assembly. Specially designed coupler sleeves are adopted to reconnect

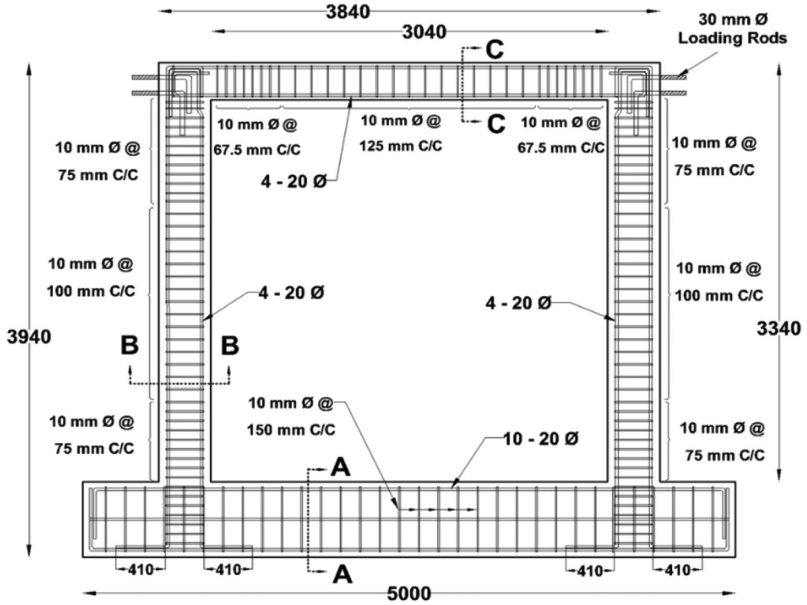

(a) Reinforcement detailing

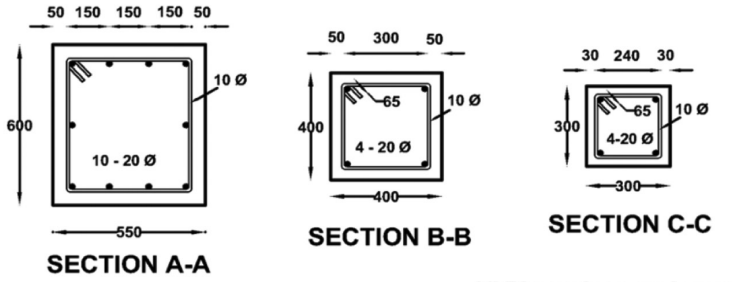

(b) Dimensions of the frame sections

Fig. 9—Structural detailing of tested RC portal frames.

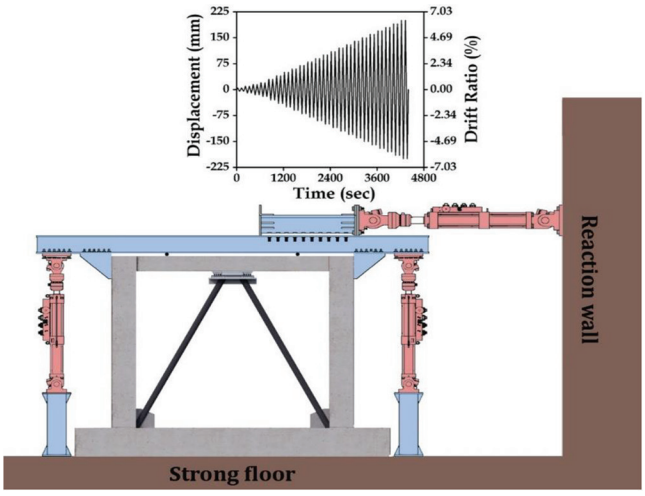

Fig. 10—Illustrative diagram of test setup for RC model frames.

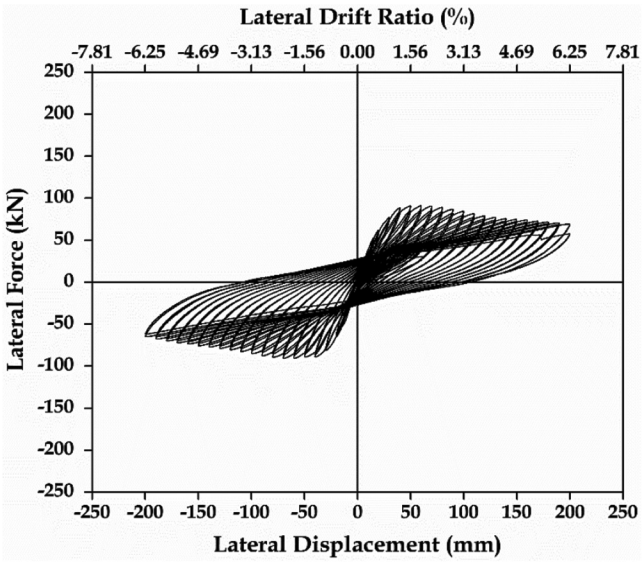

Fig. 11—Hysteresis behavior of ICB frame.

the buckled or ruptured longitudinal reinforcing bars of the columns, where the reinforcing bar devising processes of swaging or threading are impractical. The recommended coupler sleeve grips the connected reinforcing bar elements through external bolting, high-strength epoxy mortar grout, and frictional gripping from the internal grooved surface. Interlinking or interconnecting the coupler sleeves of a column member prevents the bond-slip failure of connected reinforcing bars from their respective sleeves, which can occur at regions of high rotations and moment—that is, at

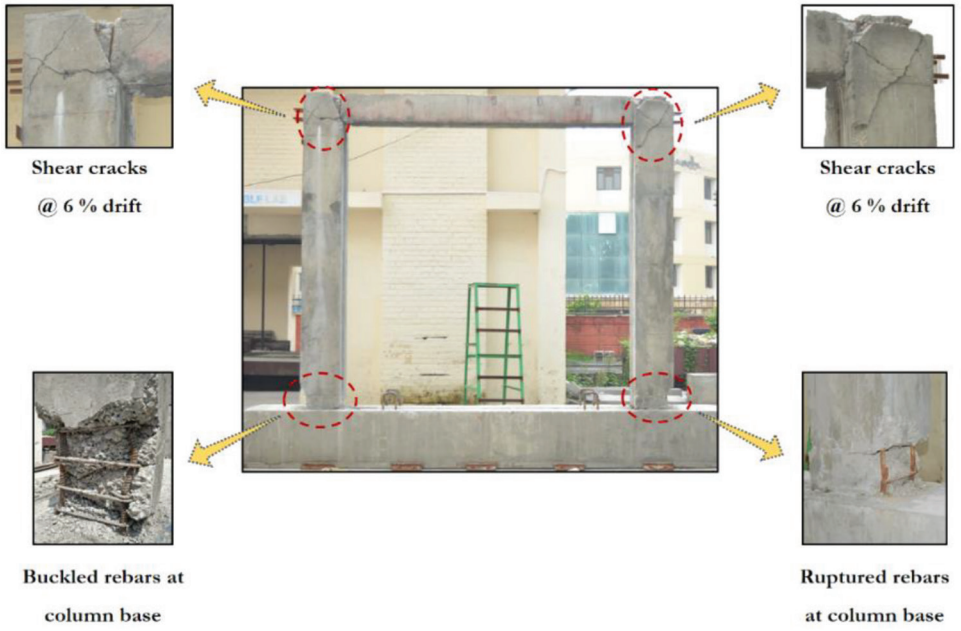

Fig. 12—Damaged ICB frame post-primary test.

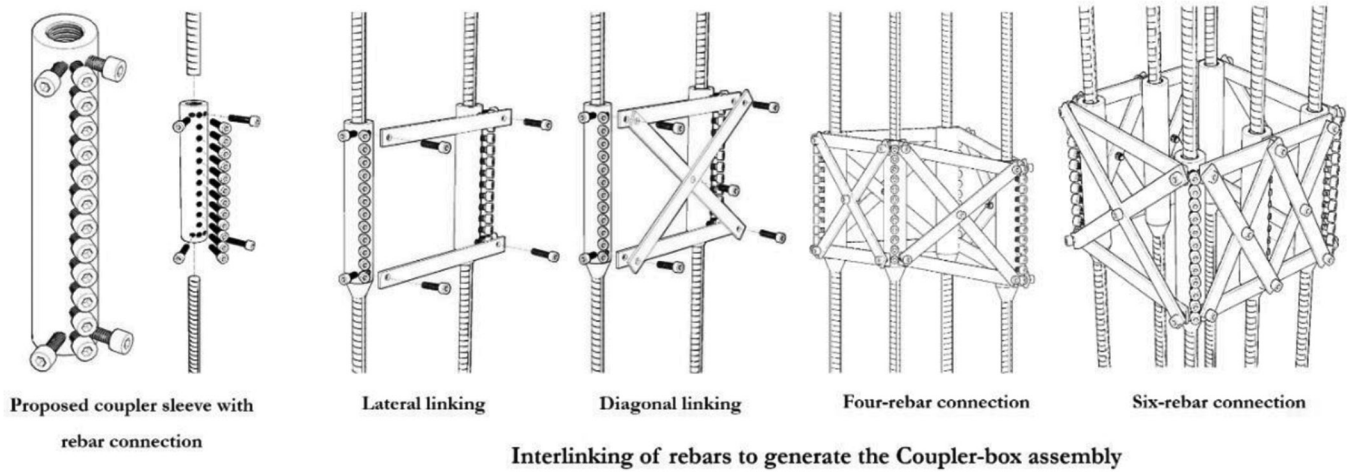

Fig. 13—Descriptive diagrams of reinforcing bar coupler sleeve along with interlinking technique of coupler-box assembly.

the plastic hinge locations. The interconnecting mechanism allows for the combined participation of sleeve-connected reinforcing bars against lateral loading and additionally confines the core concrete. The inserted coupler sleeves of the column member are interlinked using flat steel bars in lateral and diagonal directions. High-strength bolts of 8 mm (0.32 in.) diameter are adopted for the interlinking procedure, and the detailed process is shown in Fig. 13. A detailed explanation of the interlinking technique is presented in Kothapalli et al. (2022).

The sequence of plastic hinge restoration in the damaged columns of the tested frame with the recommended technique of coupler-box assembly is shown in Fig. 14. Gusset-base plates of 20 mm (0.79 in.) thickness and predetermined dimensions are clamped with the coupler-box assemblies at column base, shown in Fig. 15, and with the bottom longitudinal reinforcement at the midsection of the RC beam to support the circular lateral brace pipes. Post-installation of base plates, regeneration of the frame section is executed using concrete of mixture ratio proportion 1.00 (C):1.40 (FA):2.20 (CA) with a *w*/*c* of 0.45. The damaged stirrups at the beam-column joints are restored or reorganized prior to the casting process.

Global retrofitting of local-restored RC frame with proposed damper device

The proposed discrete damper device assembled with adaptive yield link units of composite rubber-ply elements is associated with the model frame at its midsection. Additional plates of 16 mm (0.63 in.) thickness, with threaded bolt holes for damper connection, are welded with the upper base plate of the model frame and at the top section of the lateral brace pipes. The lateral bracing system of hollow circular steel pipes is designed to be elastic, which operates as a force-transferring component between the damper and the foundation beam. Circular steel pipe of gross area A_g, external diameter D, thickness t, effective length L_c, and radius of gyration r is verified for the limiting values

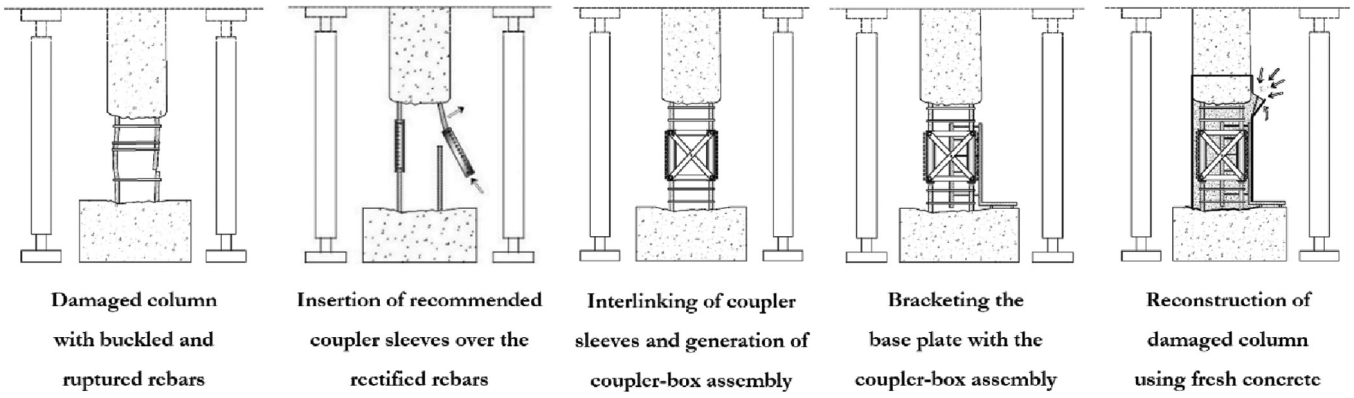

Fig. 14—Illustrative figures depicting sequence of restoration in column plastic hinge.

(a) Base plate connection with the coupler-box assembly at column base

(b) Embedding the base plate at the mid-centre of the RC beam

Fig. 15—Implanted base plates for supporting lateral brace system.

of slenderness ratio (L_c/r) and width-thickness ratio (D/t) as specified by the ANSI/AISC 341-16 (2016) codal provisions. The gusset plate for the association of brace pipes with the model frame is designed using the elliptical clearance model recommended by Kotulka (2007), and the plate thickness is computed with block shear, Whitmore yielding, and Whitmore fracture criteria. Circular steel pipes with 114.3 mm (4.5 in.) external diameter, 3.6 mm (0.14 in.) thickness, and a gusset plate with 8 mm (0.32 in.) thickness are preferred for the model frame. The damper device with installed link units is connected to the frame using high-strength threaded Allen bolts of 16 mm (0.63 in.) diameter. The vertical free-play of link units in their respective slotted square grids under existing gravity loads of the model frame is verified post-installation of the damper device.

The discrete yield damper-equipped model frame (hereby referred to as the DYD frame) is tested under similar load conditions as the ICB frame, and the hysteresis behavior is shown in Fig. 16. The initial strength and stiffness of the DYD frame are high until a considerable increase in the inelastic deformation of the link unit. The 1.2 mm (0.05 in.) thick mild-steel sheets on either side of the link unit induce stiffness, which improves the cumulative response of the model frame. A gradual increase in lateral strength of the model frame is noticed until a drift of 2.5%. The adaptive yield link unit is retained on its edges within the slots of the square-grid framework, which compels the link to deform

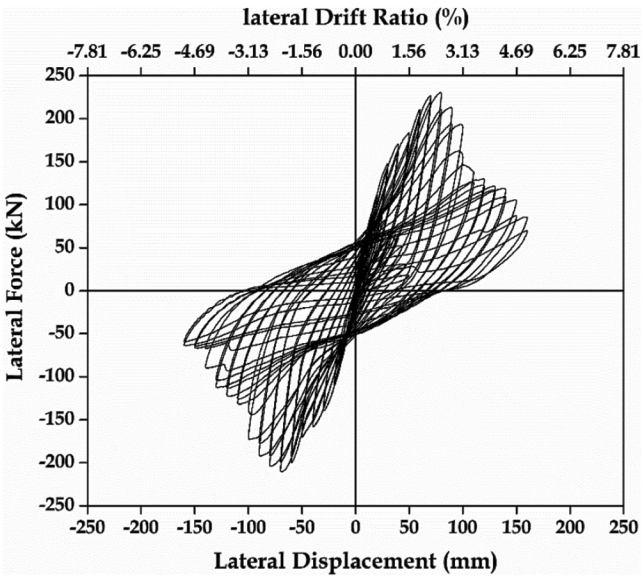

Fig. 16—Hysteresis behavior of damper-equipped DYD frame.

in double curvature under reversed cyclic lateral loads. The intermediate fragment of the SBR ply element deforms on the application of lateral displacement and dissipates a higher amount of energy until failure by debonding. The variation in lateral stiffness of the composite link unit causes detachment of the metal sheet from the rubber-ply element,

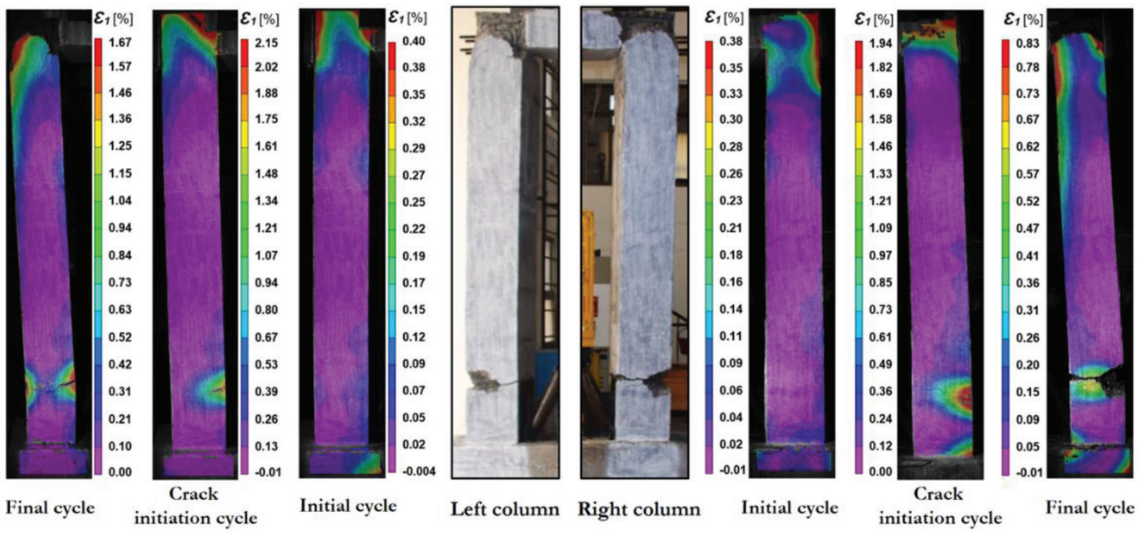

(a) Principal strain (ε_1) variation during left sway of frame: Negative half - cycle

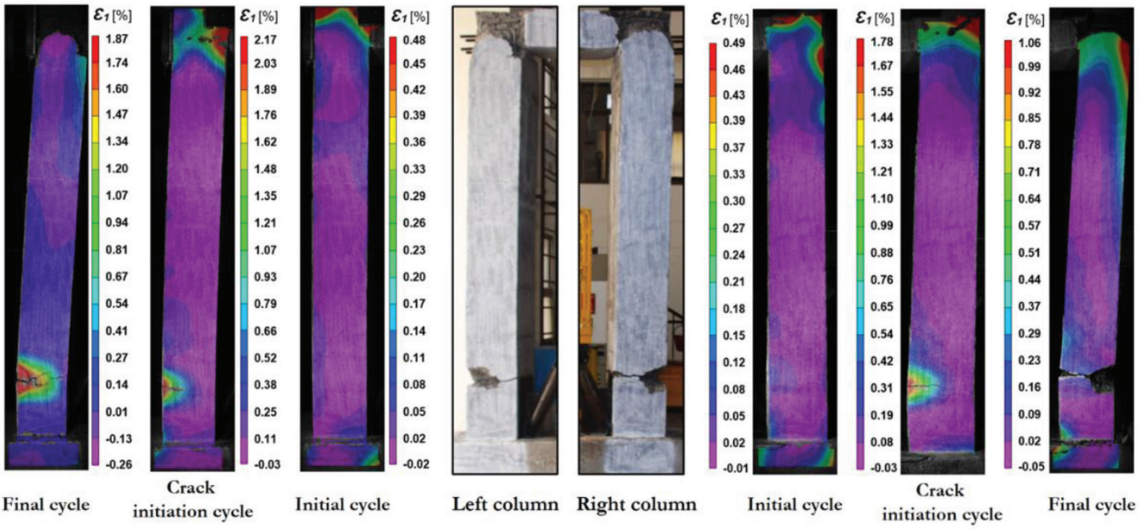

(b) Principal strain (ε_1) variation during right sway of frame: Positive half - cycle

Fig. 17—Superficial strain variations in columns of DYD frame monitored using DIC technique. (Note: Full-color PDF of this paper can be accessed at www.concrete.org.)

which leads to a complete distortion failure. Thus, a drop in the lateral strength capacity of the model frame is noticed post 3.2% drift, where a significant number of yield links are exhausted. Subsequent to this drift ratio, most of the distorted link units snap out from their respective square grids and get blocked between the frameworks. However, the residual capacity of damper along with the RC model frame leads to a gradual decrease in lateral strength efficiency of DYD specimen until 5% drift ratio.

Superficial crack propagations along with the principal strain ε_1 variations in columns of the DYD frame are monitored using the digital image correlation (DIC) technique. Complementary metal-oxide semiconductor (CMOS) camera sensors of 8.9-megapixel quality, equipped with 10 mm (0.39 in.) lenses, are employed for the DIC technique. A calibration plank of 40 mm (1.57 in.) grid size is adopted along the column height, which is spray-painted and prespeckled with a 0.20 in.-sized (5.08 mm) roller. Images are captured at a rate of two frames per second using VIC-Snap software and post-processing is performed using VIC-3D software. The selected subset size is 45 pixels, step size is 11, and the strain computation filter size is 29 pixels. Strain variations in lateral direction are presented at three distinct phases of testing—that is, at the initial, crack induction, and final displacement cycles of the model frame, as seen in Fig. 17. Damaged columns of the DYD frame post-cyclic testing are seen in Fig. 17, where the plastic hinges are shifted above the coupler-box assemblies, and inclined shear cracks are generated near the beam-column joints. The relocation in plastic hinges is evident from the higher principal strain variations above the coupler-box, as inferred from the DIC processed images. The induced rigidity of coupler-box assembly along with the base plate shifts the plastic hinge above the restored column section of the DYD frame. Limited shear confinement along with the local-induced frame rotations generate inclined shear cracks

Table 1—Cyclic test results of tested RC portal frames

Specimen ID	Compressive strength on testing day, MPa (ksi)	Yield stage				Maximum stage				Ultimate stage				Ductility factor, μ	Energy dissipation, kN·mm (kip·in.)
		Positive		Negative		Positive		Negative		Positive		Negative			
		P_y, kN (kip)	Δ_y, mm (in.)	P_y, kN (kip)	Δ_y, mm (in.)	P_m, kN (kip)	Δ_m, mm (in.)	P_m, kN (kip)	Δ_m, mm (in.)	P_u, kN (kip)	Δ_u, mm (in.)	P_u, kN (kip)	Δ_u, mm (in.)	Δ_u/Δ_y	
Conventional frame	26.28 (3.81)	60.1 (13.5)	18.5 (0.73)	60.6 (13.6)	18 (0.71)	91.2 (20.5)	59.49 (2.34)	90.8 (20.4)	69.42 (2.73)	72.9 (16.4)	166.9 (6.57)	72.7 (16.3)	166.2 (6.54)	9.12	312,629.33 (2766.89)
Damper-fit frame	32.73 (4.75)	140.9 (31.7)	28 (1.1)	127.9 (28.8)	26 (1.02)	230.4 (51.8)	78.95 (3.11)	210.3 (47.3)	69.37 (2.73)	184.3 (41.4)	98.17 (3.87)	168.3 (37.8)	99.97 (3.94)	3.68	385,962.17 (3416.05)

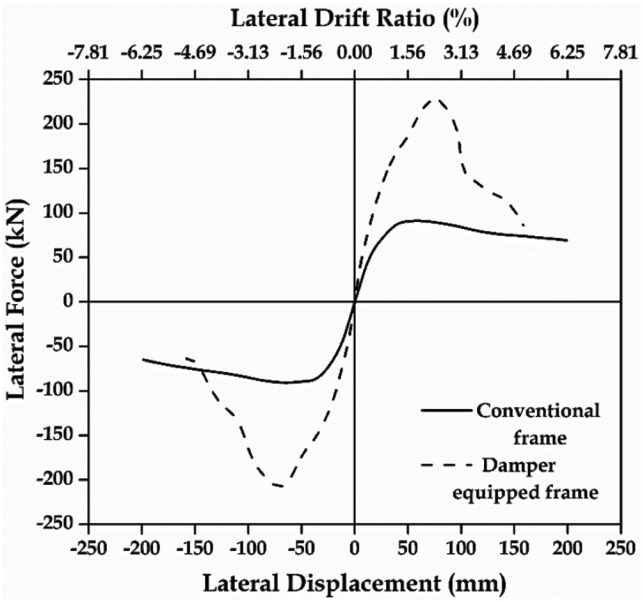

Fig. 18—Comparative hysteresis envelope of tested model frames.

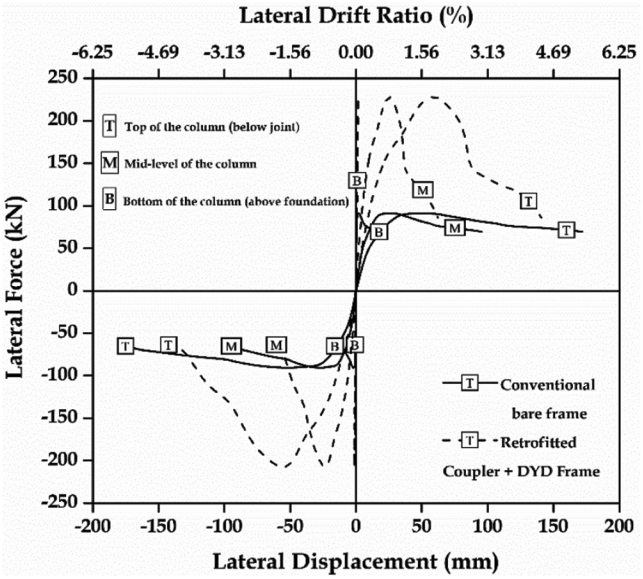

Fig. 19—Lateral deflection profiles of tested model frames.

of distinct width near the beam-column joints. The vertical load-transferring element of slide-rubber bearings remains undisturbed with the retention in gravitational load capacity of the RC frame. The lateral damping units are extensively damaged with the links erupting out from their respective square grids. The lateral displacement of damper beyond 3% frame drift compels the link unit to deform beyond its permissible range, which causes eruption with total distortion. The disfigured link units get clogged and hinder the movement of the damper device, which causes local rotations in the supporting brace pipe and bottom damper base plate. This provokes the discharge of a few link units away from the damper. The metal sheets, along with the individual ply elements, undergo debonding failure, which leads to crushing or rupturing failure in link units.

COMPARATIVE PERFORMANCE EVALUATION OF RETROFITTED RC FRAME WITH DISCRETE DAMPER DEVICE

Comparative performance of the original ICB frame and the retrofitted DYD frame is established by a backbone curve derived from the hysteretic loop behavior, as seen in Fig. 18, and the cyclic test results are presented in Table 1. A two-fold increase in initial strength and stiffness is noticed in the DYD frame. The peak lateral strength of the DYD frame is relatively enhanced by 2.5 times. The post-peak behavior varies in the model frames, where a gradual rate of degradation in ICB and a faster rate of deterioration in DYD frames are noticed. Damage to the damper at peak lateral strength transfers the applied load to the principal structural members, which undergo inelastic rotations until failure by plastic hinge formation. This causes a sudden decrement in lateral strength capacity of the DYD frame post-peak load. Contrarily, the closely spaced shear reinforcement in columns of the ICB frame improves its ductility, by which a gradual degradation is noticed until failure. The lateral deflection profile of columns in the tested model frames are plotted with their corresponding LVDT and DIC data, as shown in Fig. 19. The profile of DYD frame column at its base (above the foundation) shows minimal deflection by virtue of the rigidity induced by coupler-box assembly and gusset base plate.

The damage pattern is identical in the tested model frames with plastic hinge formation in columns and shear cracks at the beam-column joints. However, the location of plastic hinge in the column varies in the DYD frame with a shift above the coupler-box assembly. The induced rigidity of coupler-box assembly along with the embedded base plate generates this shift of plastic hinge. The intensity of damage in the DYD frame increases post-failure of the yield links. The link units of the damper confine the damage locally and dissipate the lateral input energy of the model frame. Thus,

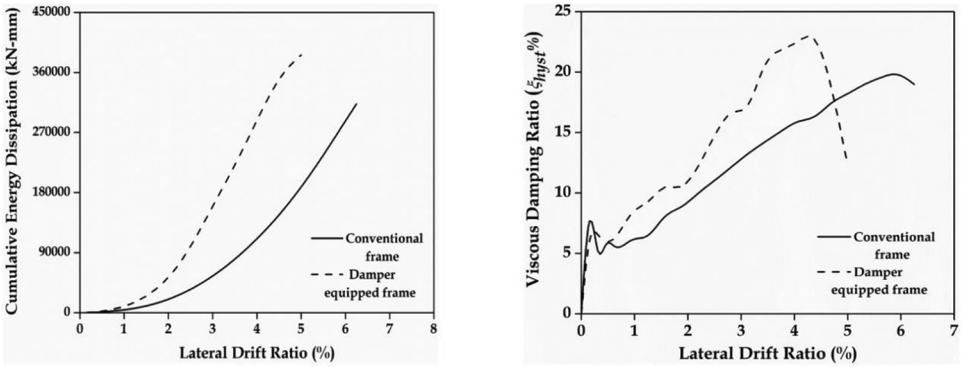

(a) Cumulative energy dissipated vs drift ratio plot

(b) Equivalent Viscous Damping (EVD) ratio vs drift ratio plot

Fig. 20—Energy-based parametric comparison in tested model frames.

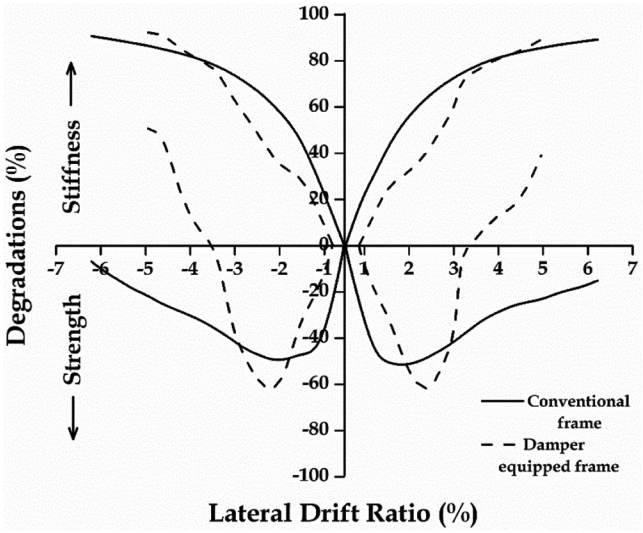

Fig. 21—Degradation plots of strength and stiffness in tested model frames.

the debonding failure in link units, along with their segregation, transfers the impending load onto the model frame and causes damage to the structural members.

The cumulative amount of energy dissipated by the model frames and the equivalent viscous damping (EVD) ratio ξ_{hyst}, computed using the elastic strain energy approach, are plotted against corresponding lateral drifts, as seen in Fig. 20. The DYD frame maintains a higher energy dispersion rate, with an average increase of 2 to 2.5 times over the ICB frame. The adopted yield link units of the damper device in the DYD frame undergo inelastic deformations to dissipate energy, which improves the frame's energy absorption capacity without any significant damage to the principal structural members. Contrarily, the columns of the ICB frame undergo flexural deformations to dissipate the input energy, which is relatively low with critical damage to the principal structural members. However, a reduction in the dispersion rate is noticed in the DYD frame post-4.5% lateral drift. The failure of yield link units post-4% drift nullifies the effect of damper in energy dissipation, which reduces the overall dissipating efficiency of model frame. This is also evident from the EVD ratio plot, where a sudden declination in rate is noticed post-4.5% drift. The estimated value of viscous damping ratio is directly proportional to the amount of energy dissipated in each cyclic displacement. Thus, a similar variation trend to that of the energy dissipation is noticed, where the DYD frame accomplishes a higher damping percentage.

The variations in strength and stiffness degradations post the elastic state of the model frames are plotted against corresponding lateral drifts, as seen in Fig. 21. Degradations in the DYD frame are initiated at a relatively high drift ratio, owing to its higher lateral yield drift. The ICB frame experiences a gradual degradation in stiffness by virtue of the generated flexural plastic hinges at the column base. The stiffness degradation rate in the DYD frame varies with the stiffness variation in damper component, where an enhanced rate is noticed until 2% drift. The damage in link units post-2% drift causes a shift in the degradation rate with a reduced pace until 3.5% drift. The extensive damage to the damper component post-3.5% drift leads to the inelastic rotations in RC columns, which increases the degradation rate further. The strength degradation rate of the model frame follows a trend similar to that of the backbone curve of the hysteresis loops, where a gradual degradation until failure is noticed in the ICB frame. The degradation rate varies with the model frame's yield strength, where the decrease in strength below the yield point of DYD frame causes a curve transition below the horizontal axis post-3.5% drift. The addition of the damper component assists in improving the initial yield strength of the model frame, and the failure in link units leads to an abrupt loss in strength below the yield point.

Damage resistance capacities of the tested model frames are determined using the modified damage index (DI) proposed by Park and Ang (1985). The computed values of DI are plotted against corresponding drifts, as shown in Fig. 22. A higher rate of variation in DI values is noticed in the DYD frame owing to its improved yield point. The DYD frame reaches its collapse stage at 2.7% drift, whereas the ICB frame achieves it at 4% lateral drift.

CONCLUSIONS

As inferred from the past earthquake damage reports, open ground stories or soft stories in multi-storied reinforced concrete (RC) frame buildings are more vulnerable to damage by virtue of their deficiency in lateral strength and stiffness. The present research focuses on retrofitting and strengthening such damaged frames with buckled reinforcing bars using the local confinement technique of coupler-box assembly and the addition of a discrete damper with adaptive yield link units. Composite units of rubber plies enclosed within thin metal sheets are adopted as yield links, and the efficiency of the proposed damper is evaluated by reversed cyclic tests on model components with 36 and 114 yield link units. The performance of the proposed damper as a strengthening measure is assessed by reversed cyclic test on a damper-fit full-scale RC portal frame, and parametric-based conclusions are drawn from the derived computational qualitative parameters, which are detailed as follows:

1. The cumulative effect of adopted yield link units made from low-cost materials such as thin metal sheets and inner plies of worn-out radial rubber tires in resisting lateral loads is evident from the proportional gain in strength with an increase in the lateral displacement. The concurrent inelastic yielding in link units under applied lateral drift of the damper improves the energy dissipation potentiality. The inelastic deformations at the midsection of the link unit generate local plastic hinges on either side of the link, further improving the hysteretic behavior with higher energy dissipation.

2. The lateral strength of the damper component is proportional to the number of link units associated. The strength of a damper with 114 link units is approximately four times that of a damper with 36 links. The energy dissipation capacity is also doubled in the higher-numbered link damper. The efficiency of vertical load transmission remains consistent in the damper devices, with the bearing pedestals remaining intact.

3. Global efficiency of the portal frame is enhanced by the addition of the proposed damper device (114 yield link units), where lateral strength is relatively improved by 2.5 times, and a two-fold increase is noticed in the initial stiffness and post-yield behavior. The post-peak behavior depreciates in the damper-fit model frame due to debonding failure of yield link units.

4. The link elements operate as a safeguarding mechanism and deform to dissipate the lateral input energy, which improves the global dissipation efficiency of the discrete yield damper-equipped model (DYD) frame by 150%. The calculated performance parameters of energy dissipations, damping, and degradations in strength and stiffness for retrofitted DYD frame establish the capability of proposed strengthening technique in improving the global behavior of the damaged initial conventional bare (ICB) frame. Additionally, the gravity load-transfer capacity of the frame remains persistent, despite its ineffective lateral strength, which is not the general case with other metallic-yield damping systems.

5. Experimental verification of the proposed strengthening technique, with a conveniently operated damper device and adaptive yield link units, develops assurance in enhancing the pre- and post-yield behavior of damaged RC frame structures and may also be applicable in the field of retrofitting.

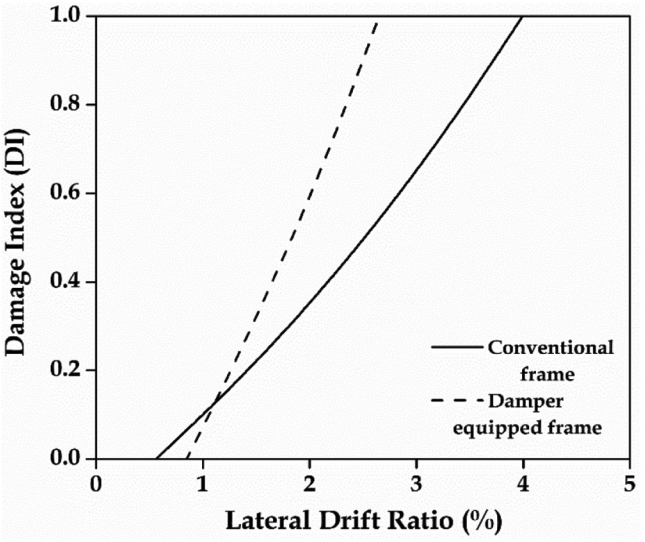

Fig. 22—DI comparison in tested model frames.

AUTHOR BIOS

ACI member **Naveen Kumar Kothapalli** *is a Research Scholar in the Department of Earthquake Engineering, Indian Institute of Technology (IIT) Roorkee, Roorkee, Uttarakhand, India. He received his BTech from Acharya Nagarjuna University, Guntur, Andhra Pradesh, India, in 2012, and his MTech from IIT Roorkee in 2015. His research interests include repair, retrofitting, and rehabilitation of reinforced concrete structures.*

R. Siva Chidambaram *is a Senior Scientist at the Central Building Research Institute (CSIR-CBRI), Roorkee, India. He received his BE and ME from Anna University, Chennai, Tamil Nadu, India, in 2007 and 2010, respectively, and his PhD from IIT Roorkee in 2016. His research interests include shear strengthening of beam-column joints with high-performance materials in precast and reinforced concrete structures.*

Pankaj Agarwal *is a Professor in the Department of Earthquake Engineering, IIT Roorkee. He received his BTech from G.B. Pant University of Agriculture & Technology, Pantnagar, Uttarakhand, India, in 1989, and his ME and PhD from the University of Roorkee, Roorkee, Uttarakhand, India, in 1994 and 2000, respectively. His research interests include earthquake-resistant design of structures, repair and retrofitting of masonry, and reinforced concrete buildings.*

ACKNOWLEDGMENTS

The authors acknowledge the research funding from PEHEL Foundation, a wholly owned Section 8 company of PNB Housing Finance Ltd. (PNBHFL), New Delhi, India (PHF-1710-EQD).

REFERENCES

ANSI/AISC-16 341, 2016, "Seismic Provisions for Structural Steel Buildings," American Institute of Steel Construction, Chicago, IL.

FEMA 461, 2007, "Interim Testing Protocols for Determining the Seismic Performance Characteristics of Structural and Nonstructural Components," Federal Emergency Management Agency, Washington, DC.

Goyal, A., and Agarwal, P., 2017, "Use of Co-Polymer of Styrene Butadiene Rubber-A Seismically Innovative Approach Towards Energy Dissipation," *Procedia Engineering*, V. 173, pp. 1800-1807. doi: 10.1016/j.proeng.2016.12.222

Hosseini Hashemi, B., and Moaddab, E., 2017, "Experimental Study of a Hybrid Structural Damper for Multi-Seismic Levels," *Proceedings of the Institution of Civil Engineers, Structures and Buildings*, V. 170, No. 10, pp. 722-734. doi: 10.1680/jstbu.15.00122

IS 1893:2016, 2016, "Criteria for Earthquake Resistant Design of Structures – Part 1, General Provisions and Buildings (Sixth Revision)," Bureau of Indian Standards, New Delhi, India.

IS 13920:2016, 2016, "Ductile Design and Detailing of Reinforced Concrete Structures Subjected to Seismic Forces – Code of Practice (First Revision)," Bureau of Indian Standards, New Delhi, India.

Kothapalli, N. K.; Chidambaram, R. S.; and Agarwal, P., 2022, "Cyclic Evaluation of Severely Damaged RC Frames Repaired and Strengthened Through FRP-Wrapped Coupler-Box Confinement," *Journal of Composites for Construction*, ASCE, V. 26, No. 3, p. 04022016. doi: 10.1061/(ASCE)CC.1943-5614.0001205

Kotulka, B. A., 2007, "Analysis for a Design Guide on Gusset Plates Used in Special Concentrically Braced Frames," doctoral dissertation, University of Washington, Seattle, WA.

Lee, C. H.; Ju, Y. K.; Min, J. K.; Lho, S. H.; and Kim, S. D., 2015, "Non-Uniform Steel Strip Dampers Subjected to Cyclic Loadings," *Engineering Structures*, V. 99, pp. 192-204. doi: 10.1016/j.engstruct.2015.04.052

Lee, J., and Kim, J., 2017, "Development of Box-Shaped Steel Slit Dampers for Seismic Retrofit of Building Structures," *Engineering Structures*, V. 150, pp. 934-946. doi: 10.1016/j.engstruct.2017.07.082

Lee, M.; Lee, J.; and Kim, J., 2017, "Seismic Retrofit of Structures Using Steel Honeycomb Dampers," *International Journal of Steel Structures*, V. 17, No. 1, pp. 215-229. doi: 10.1007/s13296-015-0101-5

Li, H. N., and Li, G., 2007, "Experimental Study of Structure with 'Dual Function' Metallic Dampers," *Engineering Structures*, V. 29, No. 8, pp. 1917-1928. doi: 10.1016/j.engstruct.2006.10.007

Li, Z.; Shu, G.; and Huang, Z., 2019, "Development and Cyclic Testing of an Innovative Shear-Bending Combined Metallic Damper," *Journal of Constructional Steel Research*, V. 158, pp. 28-40. doi: 10.1016/j.jcsr.2019.03.008

Maleki, S., and Bagheri, S., 2010, "Pipe Damper, Part I: Experimental and Analytical Study," *Journal of Constructional Steel Research*, V. 66, No. 8-9, pp. 1088-1095. doi: 10.1016/j.jcsr.2010.03.010

Maleki, S., and Mahjoubi, S., 2013, "Dual-Pipe Damper," *Journal of Constructional Steel Research*, V. 85, pp. 81-91. doi: 10.1016/j.jcsr.2013.03.004

Maleki, S., and Mahjoubi, S., 2014, "Infilled-Pipe Damper," *Journal of Constructional Steel Research*, V. 98, pp. 45-58. doi: 10.1016/j.jcsr.2014.02.015

Nakazono, T., and Matsumoto, A., 2011, "Mechanical Aging Behavior of Styrene-Butadiene Rubbers Evaluated by Abrasion Test," *Journal of Applied Polymer Science*, V. 120, No. 1, pp. 379-389. doi: 10.1002/app.33150

Oinam, R. M., and Sahoo, D. R., 2019, "Using Metallic Dampers to Improve Seismic Performance of Soft-Story RC Frames: Experimental and Numerical Study," *Journal of Performance of Constructed Facilities*, ASCE, V. 33, No. 1, p. 04018108. doi: 10.1061/(ASCE)CF.1943-5509.0001254

Park, Y. J., and Ang, A. H. S., 1985, "Mechanistic Seismic Damage Model for Reinforced 18 Concrete," *Journal of Structural Engineering*, ASCE, V. 111, No. 4, pp. 722-739. doi: 10.1061/(ASCE)0733-9445(1985)111:4(722)

Sahoo, D. R., and Rai, D. C., 2009, "A Novel Technique of Seismic Strengthening of Nonductile RC Frame Using Steel Caging and Aluminum Shear Yielding Damper," *Earthquake Spectra*, V. 25, No. 2, pp. 415-437. doi: 10.1193/1.3111173

Sahoo, D. R.; Singhal, T.; Taraithia, S. S.; and Saini, A., 2015, "Cyclic Behavior of Shear-and-Flexural Yielding Metallic Dampers," *Journal of Constructional Steel Research*, V. 114, pp. 247-257. doi: 10.1016/j.jcsr.2015.08.006

TahamouliRoudsari, M.; Eslamimanesh, M. B.; Entezari, A. R.; Noori, O.; and Torkaman, M., 2018, "Experimental Assessment of Retrofitting RC Moment Resisting Frames with ADAS and TADAS Yielding Dampers," *Structures*, V. 14, pp. 75-87.

Zhang, C.; Aoki, T.; Zhang, Q.; and Wu, M., 2013, "Experimental Investigation on the Low-Yield-Strength Steel Shear Panel Damper Under Different Loading," *Journal of Constructional Steel Research*, V. 84, pp. 105-113. doi: 10.1016/j.jcsr.2013.01.014

ACI STRUCTURAL JOURNAL TECHNICAL PAPER

Title No. 120-S97

Modeling of Shear Strength for Squat Reinforced Concrete Walls with Boundary Elements

by Ju-Hyung Kim, Yail J. Kim, and Hong-Gun Park

This paper presents mechanics-based modeling methodologies to predict the shear strength of squat walls incorporating boundary elements. Developed with the intention of surmounting the limitations of empirical models that are prevalent in the structural engineering community, these approaches are composed of an iterative analytical method and simplified design equations. Conforming to experimental observations, a failure criterion is established to determine the web crushing and shear compression of each wall component. Upon validating the methodologies against 123 test data compiled from the literature, detailed responses of the wall system are examined to comprehend the behavior of the web and the compression and tension boundary elements subjected to lateral loading. Model outcomes indicate that the overall strength of the squat walls is distributed to the web and the boundary elements by 58% and 42%, respectively, signifying that the contribution of the boundary elements should not be ignored, unlike the case of most customary models. In contrast to the provision of published design specifications, both horizontal and vertical reinforcing bars affect the shear strength of the web concrete. The growth of compressive principal strains, which dominate the failure of the members, is a function of the reinforcement ratio. According to statistical evaluations, the proposed models outperform existing models in terms of capacity prediction. The effects of major parameters are articulated from a practical standpoint.

Keywords: boundary elements; capacity prediction; modeling; seismic design; shear strength; squat walls.

INTRODUCTION

Reinforced concrete squat walls are prevalent in the seismic design of medium-rise buildings owing to their favorable stiffness and strength, as compared with those of other members.[1] Per the classification of ACI 318-19,[2] vertical load-bearing elements with a height-to-length ratio of less than 1.5 are categorized into squat walls. Contrary to ordinary structural walls that are tied to flexure,[3] shear is deemed crucial for the behavior of squat walls, which dominates failure mechanisms and energy dissipation, depending on the amount of reinforcement.[4,5] Shear-induced inelastic deformation is particularly noteworthy because such stubby walls undergo rapid damage, insufficient ductility, and large diagonal cracking.[6,7] To intensify resistance, supplementary reinforcing bars may be arranged near the ends of a shear wall in the longitudinal direction, and the zones are frequently called boundary elements. Technically speaking, the necessity of boundary elements is contingent upon the geometry and lateral displacement of shear walls.[2] Holistic discussions on the functional use of boundary elements are available elsewhere.[8]

A plethora of experimental programs have been conducted to elucidate the underlying principles of how boundary elements influence the behavior of squat walls in shear.[5,9-12] The studies clarified that boundary elements were instrumental in figuring out the capacity of the walls, whereas current practices are heavily reliant upon approximate methods without explicitly accommodating the presence of flanges and bases that support columns.[2] Regarding shear strength models for squat walls, several equations were proposed (Table 1). Some types hypothesized that 100% of vertical reinforcing bars were effectual and ruled out horizontal reinforcing bars,[13-16] while others allowed for the placement of horizontal reinforcing bars.[2,17,18] Among the eight models shown in Table 1, the fitting equation of Gulec and Whittaker[19] was the only one that encompassed the contribution of boundary elements to the strength of squat walls. Across the board, there are inevitable discrepancies in the state of the art concerning the shear strength modeling of squat walls, especially with boundary elements.

The present study suggests mechanics-based methodologies to predict the shear strength of squat walls entailing boundary elements. Based on the Modified Compression Field Theory,[20] analytical equations are derived in light of cracking patterns, failure modes, and stress distributions in a wall system. After validation with test data gleaned from the literature, design recommendations are provided to facilitate the shear design of squat walls.

RESEARCH SIGNIFICANCE

In the shear design of squat walls, unified agreement is not yet available because most expressions were developed empirically, and hence their applicability is restricted on many occasions. Conventional approaches, such as strut-and-tie and multiple-spring models and finite element analysis, are limitedly used in the industry,[4] so practice-oriented solutions are essential. Furthermore, ACI 318-19[2] does not give full consideration to the reinforcing scheme of squat walls by neglecting the resistance of vertical reinforcing bars and does not separately appraise the implications of constituting elements by adding up all cross-sectional areas of concrete segments and treating them as a single gross area. The effectiveness of these simplifications should, however,

ACI Structural Journal, V. 120, No. 6, November 2023.

MS No. S-2022-271.R1, doi: 10.14359/51739090, received June 1, 2023, and reviewed under Institute publication policies.

Table 1—Design variables of existing shear strength models for squat walls

Shear strength model	Wall geometry as modeling parameter					Reinforcement ratio as modeling parameter				Material strength		Axial load
						Web		Boundary element				
	Wall height h_w	Wall length l_w	Web thickness t_w	Width of B.E. b_{be}	Thickness of B.E. t_{be}	Horizontal ρ_h	Vertical ρ_v	Horizontal ρ_{hbe}	Vertical ρ_{vbe}	f_c'	f_y	
ACI 318-19[2]	✓	✓	✓	N/A	N/A	✓	N/A	N/A	N/A	✓	✓	N/A
ASCE/SEI 43-05[15]	✓	✓	✓	N/A	N/A	✓	✓	N/A	N/A	✓	✓	✓
Barda et al.[13]	✓	✓	✓	N/A	N/A	N/A	✓	N/A	N/A	✓	✓	✓
Wood[14]	N/A	✓	✓	N/A	N/A	N/A	✓	N/A	N/A	✓	✓	N/A
Gulec and Whittaker[19]	✓	✓	✓	✓	✓	N/A	✓	N/A	✓	✓	✓	✓
Kassem[17]	✓	✓	✓	N/A	N/A	✓	✓	N/A	N/A	✓	✓	N/A
Moehle[16]	N/A	✓	✓	N/A	N/A	N/A	✓	N/A	N/A	✓	✓	✓
Luna and Whittaker[18]	✓	✓	✓	N/A	N/A	✓	✓	N/A	N/A	✓	✓	✓
Proposed model	✓	✓	✓	✓	✓	✓	✓	✓	N/A	✓	✓	N/A

Note: N/A is not applicable; B.E. is boundary element.

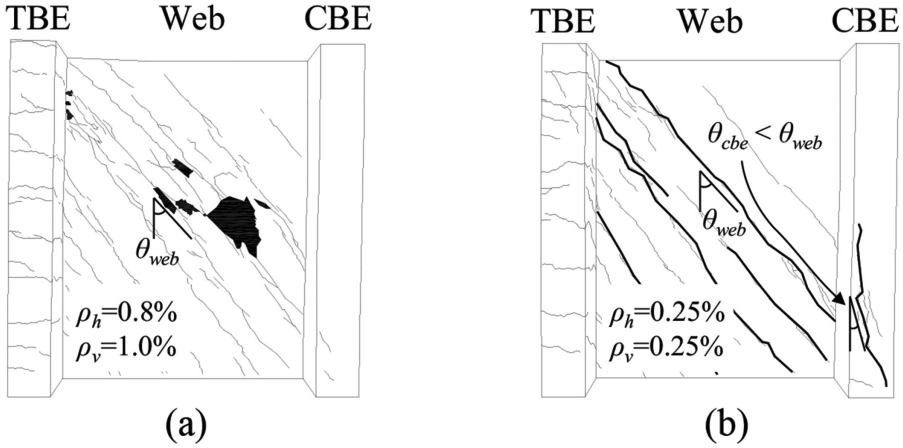

Fig. 1—Cracking patterns of squat walls with boundary elements failed in shear (TBE is tension boundary element and CBE is compression boundary element): (a) web crushing; and (b) diagonal tension of web with shear compression of compression boundary element.

be revisited for walls that experience substantial damage with large crack openings. Acknowledging the needs of the building community, mechanics-based models are formulated to account for the intricate relationships between assorted parameters and the shear strength of squat walls incorporating boundary elements. The research aims to overcome the limitations of current practices and to render implementable recommendations that can update specification articles.

FAILURE MODES OF FLANGED SQUAT WALLS IN SHEAR

Previous studies examined the failure mechanisms and cracking patterns of flanged squat walls under shear loading.[5,12] As illustrated in Fig. 1, two types of failure modes were identified: web crushing and diagonal tension. When the web of the specimens possessed horizontal and vertical reinforcement ratios (ρ_h and ρ_v, respectively) higher than 1.5 times those specified in ACI 318-19,[2] web crushing occurred (Fig. 1(a)). Due to the large amount of steel in the web (ρ_h = 0.8% and ρ_v = 1.0%), the reinforcing bars did not yield, and marginal damage was observed in the compression boundary element. As the reinforcement ratio of the web was decreased to ρ_h = 0.25% and ρ_v = 0.25% in line with the minimum ratio of ACI 318-19,[2] the failure of the wall was controlled by diagonal tension (Fig. 1(b)). The reinforcing bars in the web yielded, and thus a significant portion of the applied load was transferred to the boundary elements, causing shear compression with steep diagonal cracks in the compression flange—that is, the crack angle of the web (θ_{web}) was greater than that of the compression boundary element (θ_{cbe}). Regardless of failure mode, the boundary elements accounted for up to approximately 50% of the total shear strength of the wall system, which reaffirms the significance of contemplating the contribution of those elements in calculating the wall capacity.

ANALYTICAL MODEL

Aligning with the preceding discussions pertaining to Table 1, the majority of existing models have been developed

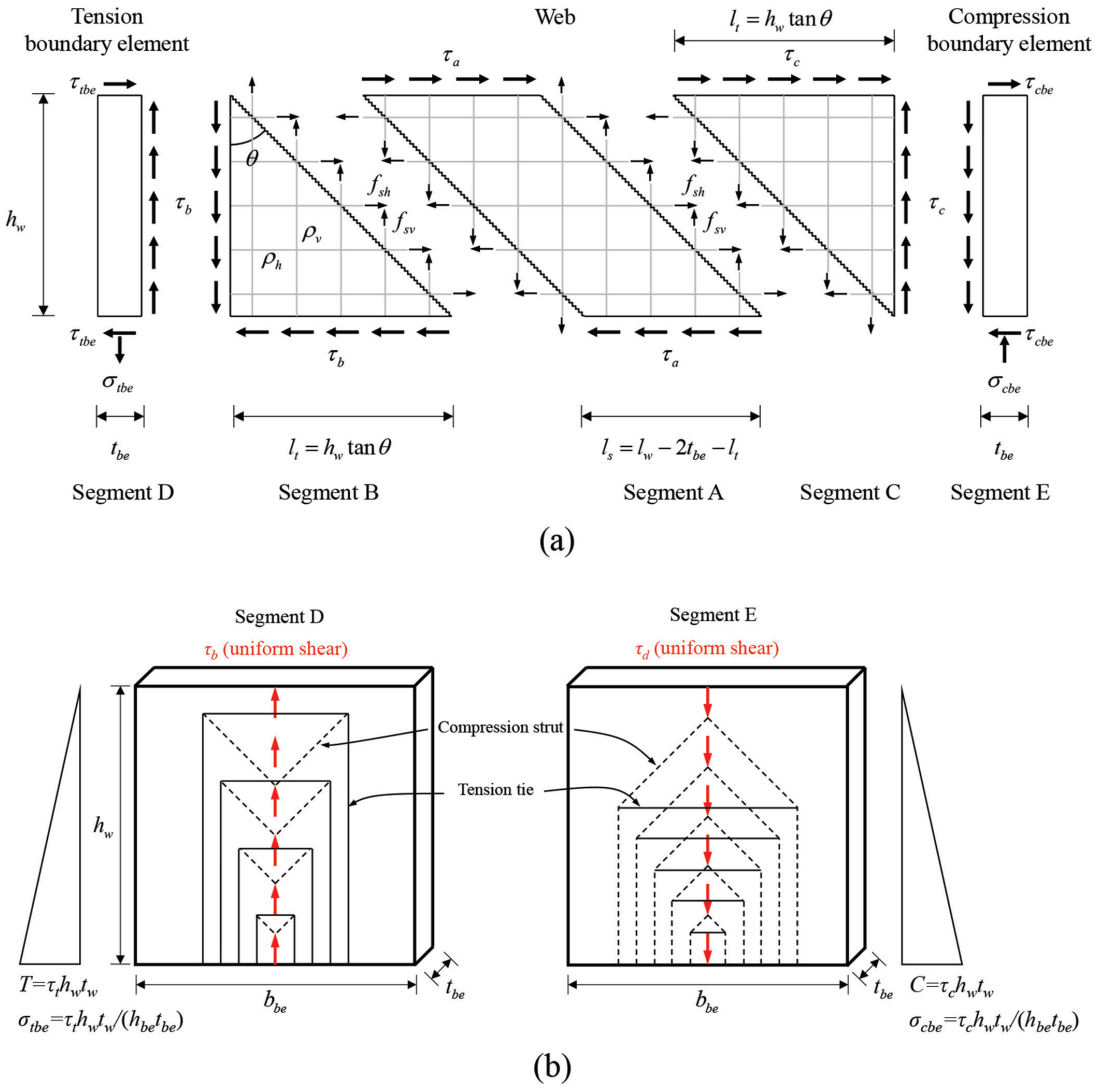

Fig. 2—Analytical model for squat wall with boundary elements: (a) stress components and force equilibrium; and (b) stress distribution of boundary elements.

empirically for shear strength calculations. The rationale of these models is legitimate because force equilibrium is in part accomplished alongside the stress states of structural configurations; however, none of them have considered the evolution of displacements and compatibility requirements. In an effort to address the limitations of the state of the art, a strain-based model is proposed together with specific shear stress distributions in a squat wall system that is composed of a web and boundary elements. The Modified Compression Field Theory[20] forms the backbone of the model to obtain the stress and strain components of each constituent. Below is a detailed description of technical approaches handling fundamental mechanics, shear capacities, failure modes, and a solution algorithm. An experimental database is constructed using published papers to assess the validity of the systematized model.

Shear strength

Figure 2(a) shows a free-body diagram of a squat wall with boundary elements. For modeling purposes, the wall was divided into five segments: Segments A, B, and C indicate the web portion subjected to diagonal cracking, and Segments D and E represent the tension and compression flanges, respectively. Conforming to the aforementioned laboratory testing,[5] lateral loading was applied to generate a uniform shear stress in the longitudinal direction of the wall. The following describes the distribution of stresses and forces in the individual segments.

Segment A—Force equilibrium may be established by

$$\rho_h f_{sh} = \tau_a \tan\theta \quad (1)$$

$$\rho_v f_{sv} = \tau_a \cot\theta \quad (2)$$

where f_{sh} and f_{sv} are the stresses of the horizontal and vertical reinforcing bars, respectively, along the inclined boundary of the segment; τ_a is the shear stress that brings about the segment's deformation; and θ is a representative crack angle. Given that the base resistance of Segment A needs to be the same as the applied shear stress (τ), Eq. (3) becomes valid

$$\tau = \tau_a \quad (3)$$

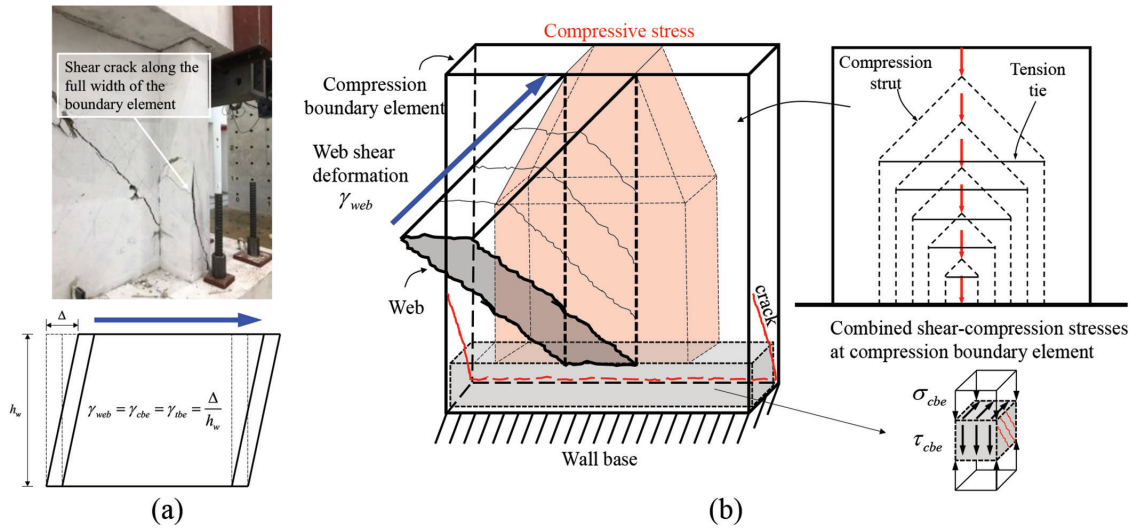

Fig. 3—Deformation of compression boundary element: (a) failure and compatibility condition; and (b) combined shear-compression stresses in compression boundary element.

When design information is provided, such as wall geometries and reinforcing details in tandem with the magnitude of τ, the f_{sh} and f_{sv} terms are determined as per the Cracked Membrane Model[21] dealing with reinforcing bar stresses on the surface of cracks (to be discussed). It should be noted that aggregate interlock was not included in Segment A owing to the rotating crack assumption of the Cracked Membrane Model.

Segments B and C—By employing the reinforcing bar stresses along the crack surface (f_{sh} and f_{sv}) between Segments A and B or Segments A and C, shear stresses in Segments B (τ_b) and C (τ_c) are calculated

$$\tau_b = \rho_h f_{sh} \cot\theta = \tau_a = \tau \tag{4}$$

$$\tau_c = \rho_v f_{sv} \tan\theta = \tau_a = \tau \tag{5}$$

Combining Segments A, B, and C under the uniform shear stress τ, a lateral force exerted on the web (V_{web}) is attained

$$V_{web} = \tau(l_w - 2t_{be})t_w \tag{6}$$

where l_w is the length of the wall; t_{be} is the thickness of the boundary elements; and t_w is the thickness of the web.

Segments D and E—To satisfy force equilibrium, the shear stress of Segment B (τ_b) is transferred to Segment D. On account of the geometric integrity between the web and the tension flange, the shear stress τ_b induces a variable stress state that can be approximated by compression struts and tension ties in Segment D (Fig. 2(b)). These force distributions vary linearly,[22] and the tensile stress at the bottom of Segment D (σ_{tbe}) is calculated using

$$\sigma_{tbe} = \frac{\tau_b h_w t_w}{b_{be} t_{be}} = \frac{\tau h_w t_w}{b_{be} t_{be}} \tag{7}$$

where h_w is the height of the wall; and b_{be} is the width of the boundary element. Likewise, the stress at the bottom of the compression flange (σ_{cbe} of Segment E in Fig. 2(b)) is expressed as

$$\sigma_{cbe} = \frac{\tau_c h_w t_w}{b_{be} t_{be}} = \frac{\tau h_w t_w}{b_{be} t_{be}} \tag{8}$$

Integration of all segments—The nominal shear strength of the squat wall (V_n) is hence written as the summation of the respective components

$$V_n = V_{web} + V_{tbe} + V_{cbe} = \tau_{web}(l_w - 2t_{be})t_w + (\tau_{tbe} + \tau_{cbe})b_{be}t_{be} \tag{9}$$

where V_{tbe} and V_{cbe} are the shear forces resisted by the tension and compression boundary elements, respectively; and τ_{tbe} and τ_{cbe} are the shear stresses of Segments D and E, respectively.

Shear deformation

Figure 3(a) exhibits the shear deformation of the web and the boundary elements. For displacement compatibility, the shear strain of the web (γ_{web}) was equated with those of the boundary elements

$$\gamma_{web} = \gamma_{cbe} = \gamma_{tbe} \tag{10}$$

where γ_{cbe} and γ_{tbe} are the shear strains of the compression and tension boundary elements, respectively. From a mechanics standpoint, the experimentally observed damage pattern of the compression flange (Fig. 3(a)) was attributed to the combined shear and compression stresses (Fig. 3(b)), which hindered the propagation of diagonal cracks along the flange ($\theta_{cbe} < \theta_{web}$ in Fig. 1(b)). Specifically, the direction of the principal compressive strain in the compression boundary element was closer to the vertical direction than that in the web under a pure shear state.

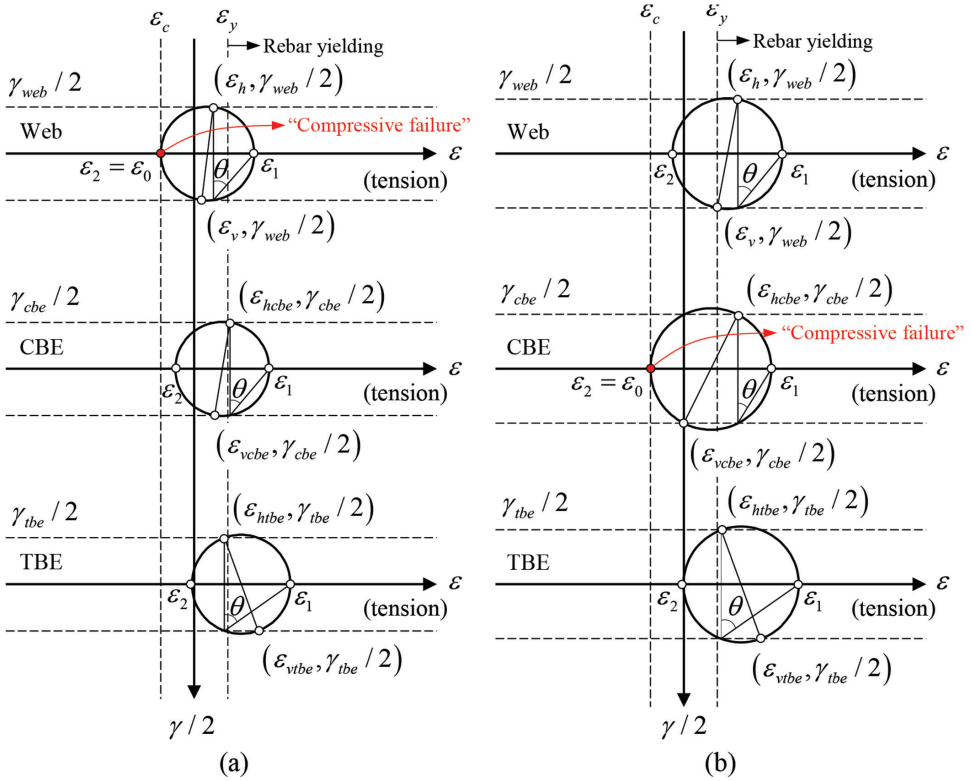

Fig. 4—Determination of failure modes (CBE is compression boundary element and TBE is tension boundary element): (a) web crushing; and (b) shear compression.

Determination of failure modes

A failure criterion for the squat wall is defined in Fig. 4, where Mohr's circles are used to relate the normal and shear strains of the web and boundary elements within a domain that was encircled by principal tensile (ε_1) and compressive (ε_2) strains (equivalent stress notations are f_1 and f_2, respectively). When the principal compressive strain (ε_2) reaches the strain corresponding to the maximum compressive stress (ε_0), web crushing takes place (Fig. 4(a)). The characteristic strain of ordinary concrete is usually assigned to be $\varepsilon_0 = 0.002$.[23] In this failure mode, the strains of the web reinforcing bars remain elastic ($\varepsilon_h < \varepsilon_y$ and $\varepsilon_v < \varepsilon_y$), and the principal strains (ε_2) of the compression and tension boundary elements (CBE and TBE in Fig. 4(a), respectively) are less than ε_0. As demonstrated in Fig. 4(b), the foregoing condition of $\varepsilon_2 = \varepsilon_0$ also controls the failure of the compression boundary element. Although the tension boundary element extensively cracks due to lateral loading (Fig. 1), it does not precipitate the failure of the wall system (TBE in the Mohr's circles in Fig. 4).

Solution algorithm

The mechanics-based modeling approach was solved through an iterative procedure (Fig. 5). For the calculation of shear capacities in each segment, the Cracked Membrane Model[21] was adopted in conjunction with compression softening and tension stiffening. On the compression-softening part, the stress (f_2) that matches the principal compressive strain (ε_2) is acquired by[20]

$$f_2 = \frac{f_c'}{0.8 + 170\varepsilon_1}\left(2\frac{\varepsilon_2}{\varepsilon_0} - \left(\frac{\varepsilon_2}{\varepsilon_0}\right)^2\right) \quad (11)$$

where f_c' is the compressive strength of the concrete. As far as the tension stiffening is concerned, the stress of the reinforcing bar on a crack surface (f_s) was refined with bond[21]

$$f_s = E_s\varepsilon_s + \frac{\tau_{b0}s_r}{D} \left(f_s \le f_y\right) \quad (12a)$$

$$f_s = f_y + 2\frac{\frac{\tau_{b0}s_r}{D} - \sqrt{(f_y - E_s\varepsilon_s)\frac{\tau_{b1}s_r}{D}\left(\frac{\tau_{b0}}{\tau_{b1}} - \frac{E_s}{E_{sp}}\right) + \frac{E_s}{E_{sp}}\tau_{b0}\tau_{b1}\frac{{s_r}^2}{D^2}}}{\frac{\tau_{b0}}{\tau_{b1}} - \frac{E_s}{E_{sp}}} \left(f_{s,min} \le f_y < f_s\right) \quad (12b)$$

$$f_s = f_y + E_{sp}\left(\varepsilon_s - \frac{f_y}{E_s}\right) + \frac{\tau_{b1}s_r}{D} \left(f_y < f_{s,min}\right) \quad (12c)$$

where f_y, E_s, E_{sp}, ε_s, and D are the yield stress, elastic modulus, post-yield stiffness, strain, and diameter of the reinforcing bar, respectively; τ_{b0} and τ_{b1} are the bond stresses between the concrete and reinforcing bar before and after yielding ($\tau_{b0} = 0.6(f_c')^{2/3}$ and $\tau_{b1} = 0.5\tau_{b0}$), respectively; $f_{s,min}$ is the minimum stress of the steel reinforcement between two adjacent cracks; and s_r is the crack spacing ($s_r = \lambda 0.3(f_c')^{2/3}/(2\rho\tau_{b0})$, in which λ and ρ are the characteristic constant [$\lambda = 0.5$] and reinforcement ratio, respectively).

For the implementation of the analytical model, various parameters are necessary: the height and length of the wall (h_w and l_w, respectively), the thickness of the web (t_w), the

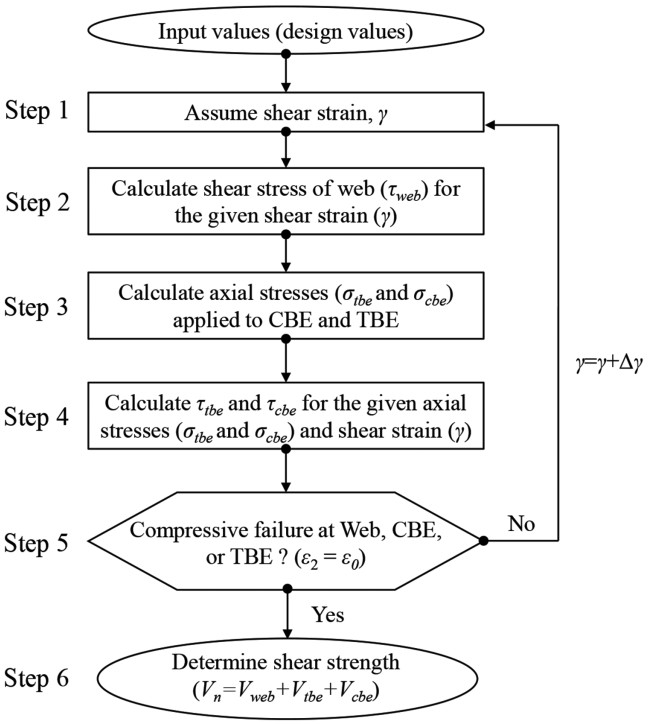

Fig. 5—Flowchart of mechanics-based modeling.

width and thickness of the boundary elements (b_{be} and t_{be}, respectively), and the horizontal and vertical reinforcement ratios of the web (ρ_h and ρ_v, respectively) and boundary elements (ρ_{hbe} and ρ_{vbe}, respectively). Additionally, the constitutive relationships of the concrete and reinforcing bars are in demand along with the compression-softening and tension-stiffening attributes. It is worth noting that: 1) the full width of the boundary element (b_{be}) is taken to properly reflect the interactions between the web and the flanges (Fig. 3(a)); and 2) the horizontal reinforcement ratio of the boundary elements (ρ_{hbe}) denotes a fraction of the reinforcing area (A_s) against the area of the boundary element ($h_w b_{be}$). A step-by-step solution process is delineated as follows:

- **Step 1:** A value of the shear strain (γ) is initially assumed and, at every iteration, the principal strain (ε_2) is updated with an increment of $0.01\varepsilon_0$ to increase the shear strain (Eq. (13)) until the web and the compression boundary element fail by web crushing and shear compression, respectively.
- **Step 2:** Given the initial shear strain in Step 1, the strain (ε_v, ε_h, ε_1, and ε_2, where $\varepsilon_1 = \varepsilon_2 + \varepsilon_v + \varepsilon_h$) and shear stress ($\tau_{web} = \tau$) components of the web are found through trial and error using Eq. (11) and (12) until displacement compatibility and force equilibrium in the vertical and horizontal directions are achieved by varying the strains of the vertical and horizontal reinforcing bars (ε_v and ε_h, respectively)

$$\gamma = \sqrt{(\varepsilon_h + \varepsilon_2)(\varepsilon_v + \varepsilon_2)} \quad (13)$$

- **Step 3:** Upon gaining the web shear stress (τ_{web}), the axial stresses applied to the tension and compression boundary elements (σ_{tbe} and σ_{cbe} in Eq. (7) and (8), respectively) are calculated.

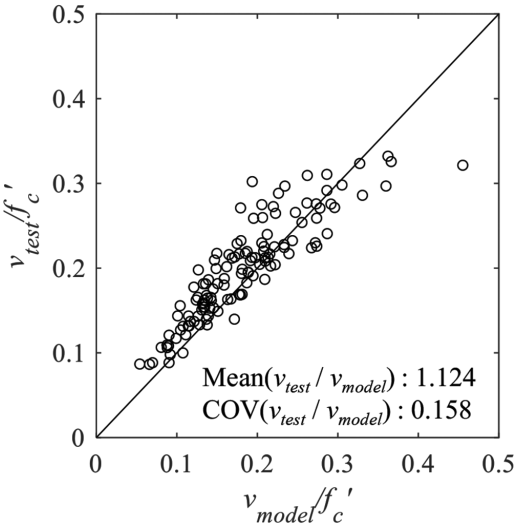

Fig. 6—Comparison of predicted and tested shear strengths of squat walls with boundary elements.

- **Step 4:** The shear stress of the boundary elements (τ_{tbe} and τ_{cbe}, respectively) are obtained by the axial stresses (σ_{tbe} and σ_{cbe}) and Eq. (10).
- **Step 5:** Referring to the strains of the web and the boundary elements solved in Steps 2 and 4, a failure mode is identified (Fig. 4). If the failure of these constituents is not predicted ($\varepsilon_2 < \varepsilon_0$), go back to Step 1 and repeat the procedure with a new value of the shear strain (γ). If the failure condition is satisfied ($\varepsilon_2 = \varepsilon_0$), the numerical procedure is terminated, and Step 6 is pursued.
- **Step 6:** The nominal shear strength of the squat wall (V_n) is determined by Eq. (9).

Validation

To validate the proposed approach, a total of 123 test specimens were collected from the literature.[5,11-13,24-48] These data sets contained 24 rectangular walls involving boundary regions with concentrated horizontal and vertical reinforcing bars, and 99 walls with either flanges or columns. Table 2 enumerates the range of geometric and material properties for the sampled specimens, including a web reinforcement ratio greater than 0.25% and a minimum wall thickness of 70 mm (2.75 in.). For consistency with the analytical model, the aspect ratio of these walls (h_w/l_w) was less than 1.5. The ultimate shear stresses of the squat walls predicted by the model ($v_{model} = V_{model}/(l_w t_w)$, where $V_{model} = V_n$ in Eq. (9)) are compared with their experimental counterparts ($v_{test} = V_{test}/(l_w t_w)$) in Fig. 6. Because all test programs had different concrete strengths (f_c'), the shear stresses were normalized to be v/f_c'. Complying with ACI 318-19,[2] the cross-sectional area of the concrete was calculated by the section length (l_w) and web thickness (t_w) of the wall. The average ratio between the test and model was $v_{test}/v_{model} = 1.124$ with a coefficient of variation of COV = 0.158. Referring to a recent reliability study that reported the variation in COV from 0.10 to 0.44 in shear walls,[49] the degree of scatter shown in Fig. 6 is acceptable.

Figure 7 assesses the adequacy of the model (v_{test}/v_{model}) with respect to significant design parameters: aspect ratios (h_w/l_w, Fig. 7(a)), normalized vertical and horizontal reinforcement ratios in the web ($\psi_v = \rho_v f_{yv}/f_c'$ and $\psi_h = \rho_h f_{yh}/f_c'$, Fig. 7(b) and (c), respectively, where f_{yv} and f_{yh} are the yield strength of the vertical and horizontal reinforcing bars, respectively), normalized reinforcement ratios in the boundary elements ($\psi_{vbe} = \rho_{vbe} f_{yvbe}/f_c'$, Fig. 7(d)), axial force ratios ($N/(A_g f_c')$, Fig. 7(e)), and cross-sectional-area ratios of the boundary elements (A_{be}/A_g, Fig. 7(f)), in which ρ_{vbe}, f_{yvbe}, and A_{be} are the vertical reinforcement ratio, yield strength of the vertical reinforcing bars, and cross-sectional area of the boundary elements, respectively; N is the axial load applied to the wall; and A_g is the gross sectional area of the wall. All in all, the predicted shear stresses were congruous with the experimental ones; however, the former tended to underestimate the stresses. This is ascribed to the fact that the compression-softening model[20] did not allow for the strain localization of the yielded reinforcing bars between the adjacent cracks, which affected the progression of the principal strain ε_1.

Table 2—Property range of squat wall tests

Design variables	Minimum	Maximum
Wall thickness t_w, mm	70	203
Wall length l_w, mm	800	3960
Wall height h_w, mm	401	2619
Aspect ratio h_w/l_w	0.21	1.38
Thickness of boundary element t_{be}, mm	75	360
Width of boundary element, h_{be} (mm)	79	1500
Concrete compressive strength f_c', MPa	13.7	110.7
Reinforcing bar yield strength f_y, MPa	272.3	754.2
Horizontal reinforcement ratio of web ρ_h, %	0.25	2.80
Vertical reinforcement ratio of web ρ_v, %	0.26	2.80
Boundary element horizontal reinforcement ratio ρ_{hbe}, %	0.05	4.93
Boundary element vertical reinforcement ratio ρ_{vbe}, %	0.48	14.35
Axial load ratio $N/(A_g f_c')$, %	0	27

Note: Minimum and maximum indicate minimum and maximum properties of 123 test specimens; 1 kN = 0.225 kip; 1 mm = 0.0394 in.

Fraction of shear resistance

The verified model was executed to particularize the contribution of each component, which was essential for comprehending the role of the boundary elements in the shear strength of the squat wall system. Figure 8 displays the fractionated resistance of the 123 experimental data versus the ratio of the boundary element area (A_{be}) to the gross cross-sectional area of the wall ($A_{web} + A_{be}$). As the quantity of the area ratio rose, the shear resistance of the web diminished (V_{web} in Fig. 8(a)); by contrast, an increasing propensity was noted for the V_{cbe} and V_{tbe} terms with the ratio (Fig. 8(b) and (c), respectively). In opposition to the clustered data of the compression boundary element (Fig. 8(b)), dispersion was observed for the tension boundary element (Fig. 8(c)) owing to the formation of irregular cracks that disturbed the steady growth of the shear stress, as depicted in Fig. 1. The average resistance of V_{web}, V_{cbe}, and V_{tbe} was 58%, 29%, and 13%, respectively. In other words, the boundary elements accounted for 42% of the total strength of the wall; for this

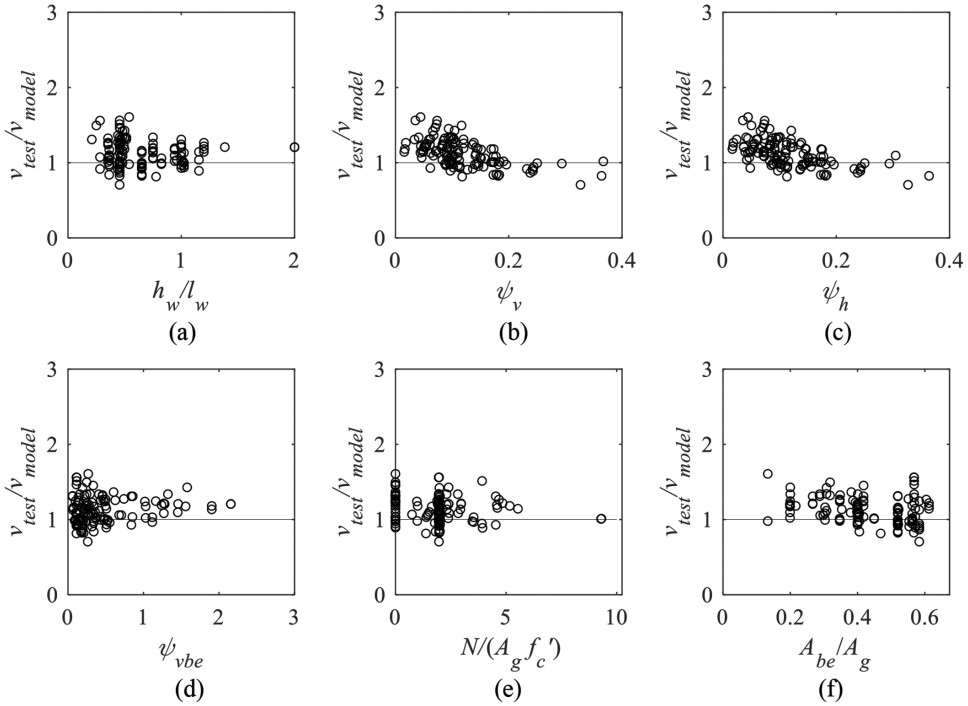

Fig. 7—Parametric investigation: (a) aspect ratio; (b) normalized vertical reinforcement ratio; (c) normalized horizontal reinforcement ratio; (d) normalized vertical reinforcement ratio of boundary elements; (e) axial load ratio; and (f) area ratio of boundary elements to gross section.

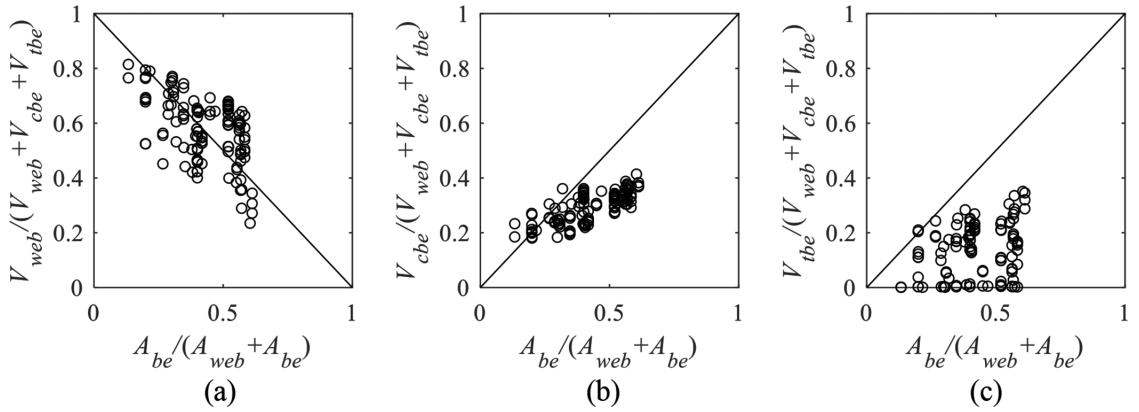

Fig. 8—Fraction of shear strength in squat walls with boundary elements: (a) web; (b) compression boundary element; and (c) tension boundary element.

reason, these elements should not be ignored in practice unless otherwise justified.

SIMPLIFIED DESIGN EQUATION

For the convenience of structural design, a simplified approach is suggested. Because the contribution of tension boundary elements to the entire shear resistance of squat walls is at most 13% in the test database, these elements can reasonably be disregarded. Therefore, when deriving the shear strength of the wall system (v_{web} and v_{cbe}), Eq. (14) may be used in accordance with the free-body diagram given in Fig. 2

$$v_{web} = (f_1 + \rho_h f_{sh})\cot\theta \tag{14a}$$

$$v_{cbe} = (f_1 + f_2)/(\tan\theta + \cot\theta) \tag{14b}$$

Shear strength of web

At the maximum capacity of the squat wall, the strain components of the web (ε_1, ε_2, ε_v, and ε_h) may be obtained from two extreme conditions of $\psi_h = 0$ and $\psi_h = 0.25$. The lower bound of the solution represents the absence of the horizontal reinforcement ($\psi_h = 0$), while the upper bound points out that the principal compressive concrete strain (ε_2) reaches ε_0 and the horizontal reinforcing bars yield ($\varepsilon_h = \varepsilon_y = 0.002$) simultaneously.[50] Accordingly, these strains are restated as

$$\varepsilon_2 = \frac{0.002}{0.25}\psi_h \le 0.002 \tag{15}$$

$$\varepsilon_h = \frac{0.002 \cdot 0.25}{\psi_h} = \frac{0.0005}{\psi_h} \tag{16}$$

In the same fashion, the tensile strain of the vertical reinforcing bars (ε_v) is abridged to be

$$\varepsilon_v = \frac{0.0005}{\psi_v} \tag{17}$$

In compliance with ACI 318-19,[2] the shear strength of the web (v_{web}) is constituted with those of the concrete and reinforcing bars (v_c and v_s, respectively). Rearranging Eq. (14a) with the tension-stiffening model[20]

$$\begin{aligned} v_{web} &= v_c + v_s = (f_1 + \rho_h f_{sh})\cot\theta \\ &= \left(\frac{0.33\sqrt{f_c'}}{1+\sqrt{500\varepsilon_1}} + \rho_h E_s \varepsilon_h\right)\cot\theta \end{aligned} \tag{18}$$

The crack angle term of $\cot\theta$, approximated with ψ_h and ψ_v, is replaced by the relative reinforcement (R_{vh})

$$\cot\theta = \sqrt{\frac{\varepsilon_h + \varepsilon_2}{\varepsilon_v + \varepsilon_2}} \approx \sqrt{\frac{\psi_v}{\psi_h}} = R_{vh} \tag{19}$$

Because ε_2 was merely 15% of ε_h and ε_v in the 123 test data, on average, the ε_2 term was omitted in Eq. (19). Substituting Eq. (15) to (17) and (19) into Eq. (18) yields

$$v_{web} = v_c + v_s \tag{20a}$$

$$v_c = \frac{0.33\sqrt{f_c'}}{1 + 0.5\sqrt{\frac{1}{\psi_v} + \frac{1}{\psi_h}}} R_{vh} \ (\psi_v > 0 \text{ and } \psi_h > 0) \tag{20b}$$

$$v_s = \rho_h E_s \frac{0.0005}{\psi_h} R_{vh} \le \rho_h f_{yh} R_{vh} \ (\psi_v > 0 \text{ and } \psi_h > 0) \tag{20c}$$

Because the model has stemmed from the orthogonally reinforced wall (Fig. 2), Eq. (20) is applicable to any squat walls having horizontal and vertical reinforcing bars ($\psi_h > 0$ and $\psi_v > 0$). Incorporating the preset boundary condition of $\psi_h = 0.25$, the maximum strength of the web ($v_{web,max}$) becomes

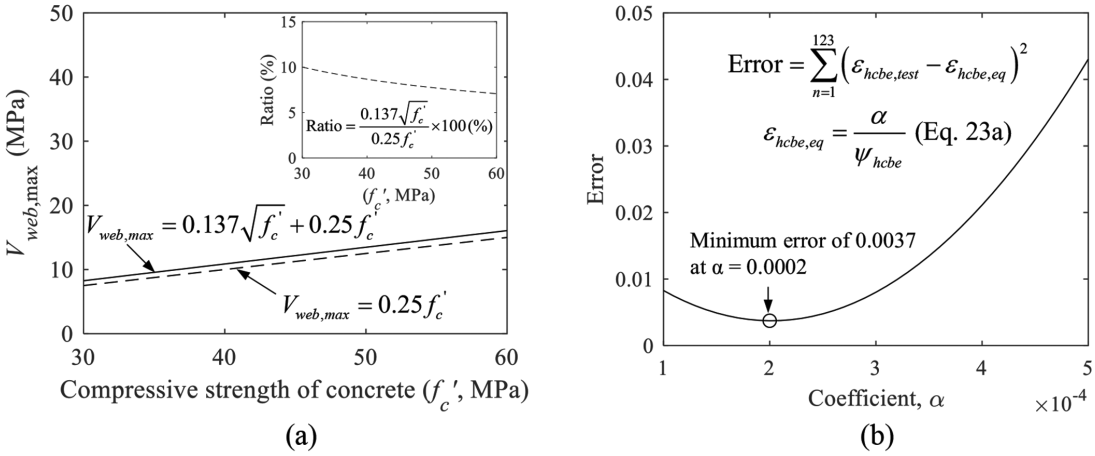

Fig. 9—Response of wall components: (a) maximum shear resistance of web; and (b) margin of error in horizontal reinforcing bars of compression boundary element.

$$v_{web,max} = \left(0.33\sqrt{f_c'}\left\{\frac{\sqrt{\psi_v}}{\sqrt{\psi_v}+\sqrt{\psi_v+0.25}}\right\} + 0.25f_c'\right)R_{vh} \tag{21}$$

With reference to ACI 318-19,[2] ψ_h can be equal to ψ_h (scilicet, $\psi_h = \psi_h = 0.25$); then, Eq. (21) is shortened to be

$$v_{web,max} = 0.137\sqrt{f_c'} + 0.25f_c' \approx 0.25f_c' \tag{22}$$

The fact that $0.137(f_c')^{0.5}$ is less than 10% of $0.25f_c'$ for a concrete strength ranging between f_c' = 30 and 60 MPa (4350 and 8700 psi) leads to the concise form of $v_{web,max} = 0.25f_c'$ (Fig. 9(a)).

Shear strength of compression boundary element

The strains of the horizontal and vertical reinforcing bars in the compression boundary element (ε_{hcbe} and ε_{vcbe}, respectively) may be estimated by

$$\varepsilon_{hcbe} = \frac{0.0002}{\psi_{hcbe}} \tag{23a}$$

$$\varepsilon_{vcbe} = 0 \tag{23b}$$

where ψ_{hcbe} is the normalized horizontal reinforcement ratio of the compression boundary element in the direction of the lateral loading. Compared with the test data compiled from the 123 specimens, the expression of ε_{hcbe} (Eq. (23a)) revealed the smallest margin of error (Fig. 9(b)), and the magnitude of ε_{vcbe} was practically negligible ($\varepsilon_{vcbe} = 0.13\varepsilon_y$, on average). Manipulating Eq. (11) and (14b) with the fact that the principal tensile stress plays an insignificant role in the compression boundary element ($f_1 \approx 0$)

$$v_{cbe} = (f_1 + f_2)/(\tan\theta + \cot\theta) = f_2/(\tan\theta + \cot\theta) = \frac{f_c'}{0.8 + 170\varepsilon_1}/(\tan\theta + \cot\theta) \tag{24}$$

The crack angle term of cotθ in Eq. (24) is rearranged using Eq. (19) and (23), accompanied by the failure condition of $\varepsilon_2 = \varepsilon_0$ (for consistency with the general expression of cotθ in Eq. (19), ε_h and ε_v are visible in Eq. (25), which, respectively, mean ε_{hcbe} and ε_{vcbe} for the compression boundary element)

$$\cot\theta = \sqrt{\frac{\varepsilon_h + \varepsilon_2}{\varepsilon_v + \varepsilon_2}} = \sqrt{\frac{0.0002/\psi_{hcbe} + 0.002}{0.002}} = \sqrt{0.1/\psi_{hcbe} + 1} \tag{25}$$

By combining Eq. (24) and (25), in which $\varepsilon_1 = \varepsilon_2 + \varepsilon_v + \varepsilon_h$, the shear strength of the compression boundary element is provided as

$$v_{cbe} = \frac{f_c'}{0.8 + 170\varepsilon_1}/(\tan\theta + \cot\theta) = \frac{f_c'}{1.14 + 0.034/\psi_{hcbe}}\frac{\sqrt{1 + 0.1/\psi_{hcbe}}}{2 + 0.1/\psi_{hcbe}} \tag{26}$$

Implementation

Web components—Using the analytical model, Fig. 10(a) to (c) plot the primary strains of the web against those extracted from the 123 test results. Despite a couple of outliers, Eq. (15) adequately represented the principal strains of the measured values (ε_2 in Fig. 10(a)). Similarly, the predicted horizontal (ε_h, Eq. (16)) and vertical (ε_v, Eq. (17)) strains of the web agreed with the strains of the experimental data (Fig. 10(b) and (c), respectively). As mentioned earlier, the horizontal strain of the compression boundary element demonstrating the lowest margin of error (ε_{hcbe}, Eq. (23a)) traced the trend of the collated values (Fig. 10(d)). Graphed in Fig. 11 is the variation in shear strength in the concrete and steel components (Eq. (20b) and (20c), respectively) and their amalgamated resistance (Eq. (20a)). To investigate the representative response of squat walls cast with ordinary concrete versus the normalized vertical and horizontal reinforcement ratios in the web (ψ_v and ψ_h, respectively), a typical concrete strength of f_c' = 30 MPa (4350 psi) was

taken. With an increase in the normalized horizontal reinforcement ratio (ψ_h), the concrete strength (v_c) dwindled (Fig. 11(a)), and such a tendency was pronounced as the normalized vertical reinforcement ratio went up from ψ_v = 0.02 to 0.4. The circles connected by a solid line signify the ramifications of archetypal reinforcing schemes in practice ($\psi_v = \psi_h$). These observations substantiated that the horizontal and vertical reinforcing bars interacted with the web concrete. Figure 11(b) confirms the dependency of the steel strength (v_s) on the ψ_v and ψ_h ratios. In relation to the previous occasion (v_c), the coverage of v_s was much wider up to the limit of $0.25f_c'$ (Eq. (22)). The integrated strength of the web ($v_c + v_s$) is shown in Fig. 11(c). Notwithstanding the descending contours of v_c with the increased ψ_h (Fig. 11(a)), the development of the web resistance was governed by the ascending nature of v_s (Fig. 11(b)). The gradually elevating $v_c + v_s$ values under the condition of $\psi_v = \psi_h$ (Fig. 11(c)) reemphasize the importance of the orthogonally placed reinforcing bars in the web; consequently, the provision of ACI 318-19[2] that does not involve the contribution of vertical reinforcement is recommended to be rectified.

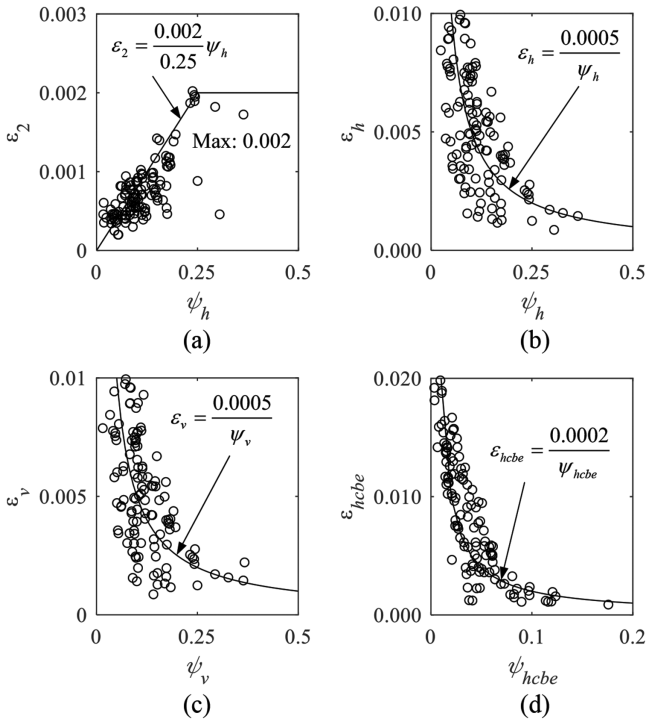

Fig. 10—Strains at ultimate strength of walls: (a) compressive principal strain of web concrete (ε_2); (b) horizontal reinforcing bar strain of web (ε_h); (c) vertical reinforcing bar strain of web (ε_v); and (d) horizontal reinforcing bar strain of compression boundary element (ε_{hcbe}).

Appraisal of simplified design equations—The adoptability of the proposed design equations (v_{web} and v_{cbe}) is examined in Fig. 12 using their equivalent resistances garnered from a combination of the test data and the iterative analytical model. The prediction of Eq. (20) and (21) concerning the web component (v_{web}) was compatible with the experimental outcomes at a coefficient of determination of R^2 = 0.94 (Fig. 12(a)). The design limit of $v_{web,max}$ (Eq. (22)) is demarcated in an appropriate manner. On the compression boundary element (Fig. 12(b)), Eq. (26) enveloped the collected data at R^2 = 0.90. The response slope of v_{cbe}/f_c' (Fig. 12(b)) was stiffer than that of v_{web}/f_c' (Fig. 12(a)) because the former was related to the shear-compression state of the compression boundary element, which was explained in Fig. 3, where the combined stress state was described.

Proposal

As elaborated previously, the shear strength of the squat wall can be adduced with the exclusion of the tension boundary element (Eq. (20), (22), and (26))

$$\begin{aligned} V_{proposed} &= v_{web}A_{web} + v_{cbe}A_{cbe} \\ &= (v_c + v_s)A_{web} + v_{cbe}A_{cbe} \\ &= (v_c + v_s)(l_w - 2t_{be})t_w + v_{cbe}b_{be}t_{be} \end{aligned} \quad (27)$$

where $V_{proposed}$ is the overall shear strength of the wall; and A_{cbe} is the cross-sectional area of the compression boundary element. A comprehensive comparison between the proposed shear strength ($v_{prop.} = V_{proposed}/(l_w t_w)$) and the test results ($v_{test} = V_{test}/(l_w t_w)$) is made in Fig. 13. Table 3 lists statistical properties associated with the iterative analytical model and the proposed design equation. Relative to the case

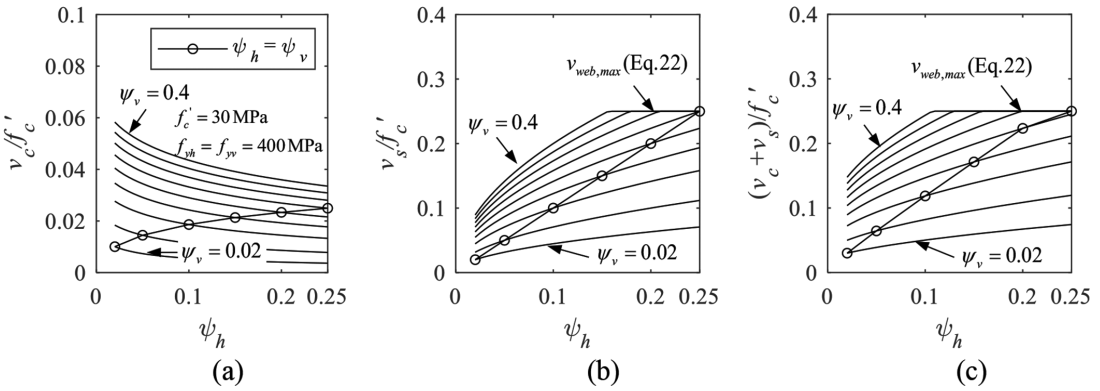

Fig. 11—Shear strength of web components: (a) concrete (v_c); (b) reinforcing bar (v_s); and (c) combined resistance of concrete and reinforcing bar ($v_c + v_s$).

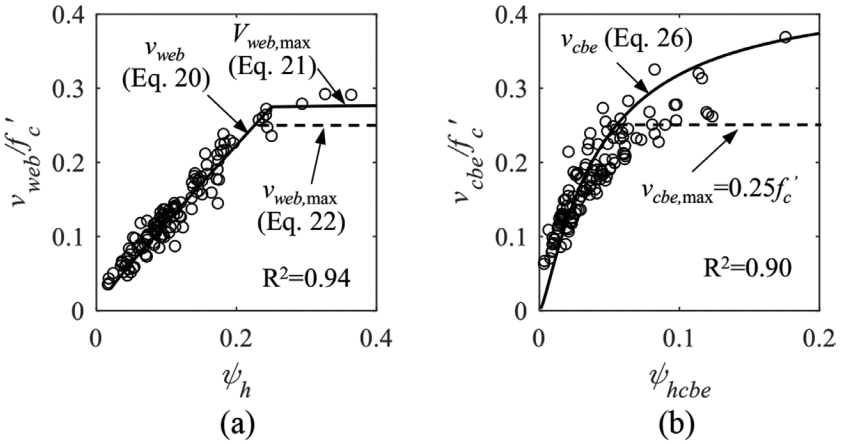

Fig. 12—Comparison of shear strength between analytical model and simplified design equation: (a) web; and (b) compression boundary element.

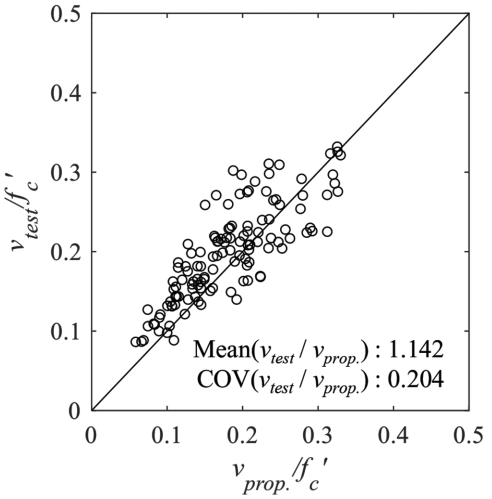

Fig. 13—Assessment of proposed shear strength expression ($v_{prop.}$) against test data (v_{test}).

of the simplified expression, the mean value and COV of the analytical model were lower by 1.6% and 29.9%, respectively. The discrepancy of the COV is attributable to the decomplicated processes engaged with Eq. (15) to (17) and Eq. (23) to (25).

Figure 14 evaluates the predictability of the existing models (Table 1) and the proposed ones through the experimental shear strength of the 123 squat walls. The upper and lower edges of the box plots indicate the 75th and 25th percentiles of the prediction ratio ($v_{test}/v_{pred.}$). Also shown are the borderlines for the maximum and minimum ratios as well as the mean and COV values. The (a) and (c) models recorded remarkable discrepancies with a mean ratio of 2.13 and 2.32, respectively, while the proposed (i) and (j) models exhibited low deviations of 1.12 and 1.14, respectively. The ratios of the ACI 318-19 and ASCE/SEI 43-05 approaches ((d) and (f), respectively) were 1.78 and 1.44, implying that Eq. (27) is recommended to be taken into account when the specifications are updated for a revision.

Parametric investigation

The effects of various geometric and material parameters on the shear strength of a benchmark squat wall are given

Table 3—Shear strength prediction

Prediction method	Analytical model (v_{test}/v_{model})	Proposed equation ($v_{test}/v_{prop.}$)
Mean	1.124	1.142
Standard deviation	0.177	0.233
COV	0.157	0.204
Minimum	0.706	0.721
Maximum	1.607	1.722

Note: COV is coefficient of variation.

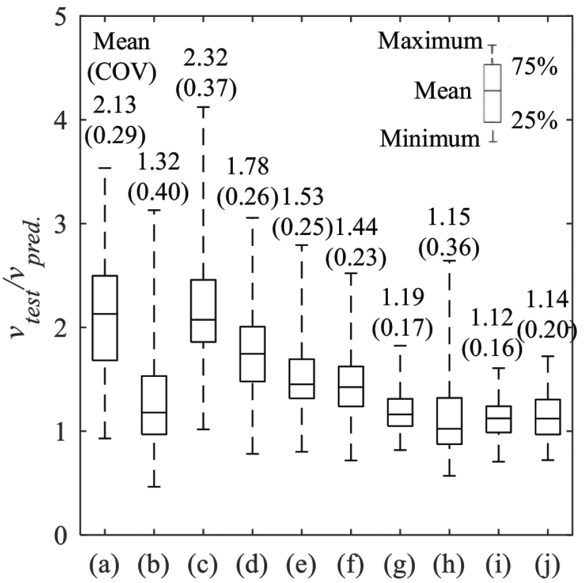

Fig. 14—Comparison between tested (v_{test}) to predicted ($v_{pred.}$) shear strengths: (a) Wood[14]; (b) Moehle[16]; (c) Luna and Whittaker[18]; (d) ACI 318-19[2]; (e) Barda et al.[13]; (f) ASCE/SEI 43-05[15]; (g) Gulec and Whittaker[19]; (h) Kassem[17]; (i) iterative analytical model; and (j) simplified design equation (Eq. (27)).

in Fig. 15. The default properties of the wall system were taken from Kim and Park[5] and, as enunciated, the independent variable in the abscissa spanned from ψ_h = 0 to 0.25. The strength of the wall was proportional to the size of the boundary elements (Fig. 15(a)), verifying the rationale for

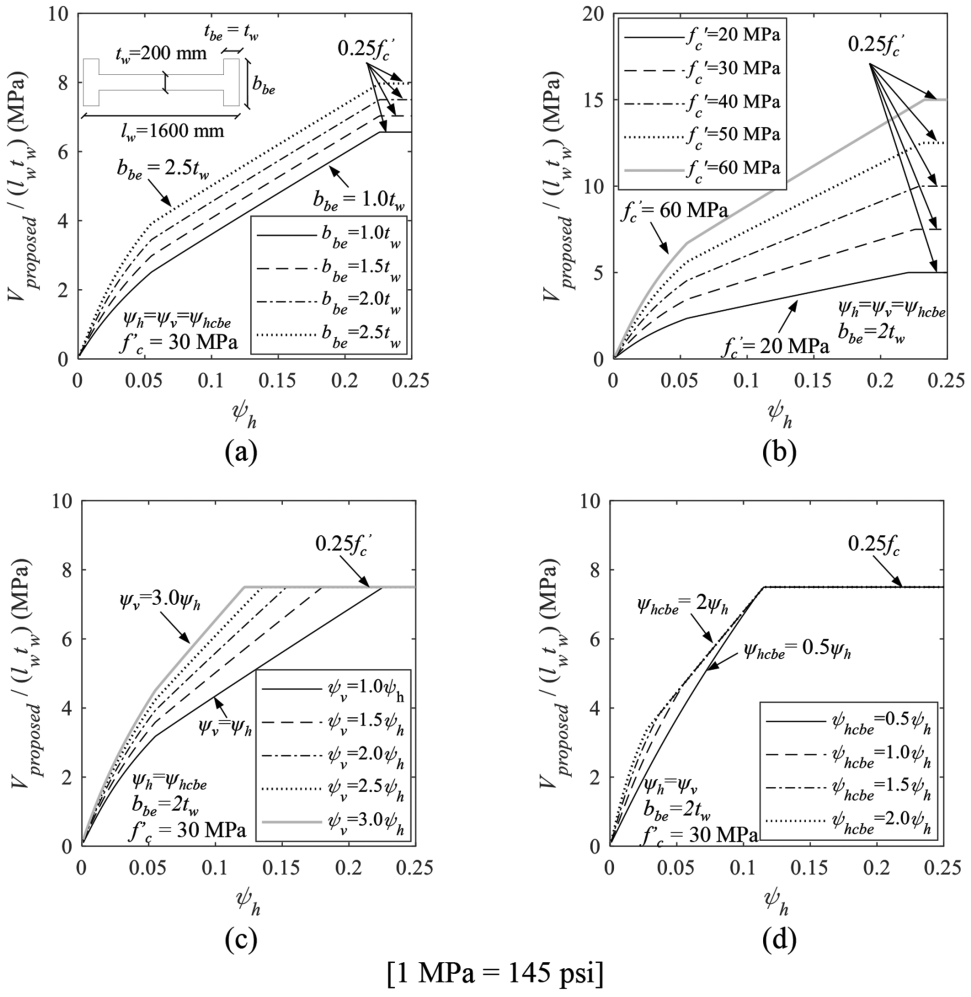

Fig. 15—Parametric study: (a) size of boundary elements; (b) compressive strength of concrete; (c) normalized reinforcement ratio in web; and (d) normalized horizontal reinforcement ratio in web and compression boundary element.

counting in the compression boundary element. The trilinear curves in the ordinate were correlated with design strength; namely, the stipulated limits of $0.25f_c'$ in the wall components restricted the development of shear resistance, which does not necessarily mean the physical failure of the structure (this explanation is applicable to all others in Fig. 15). The compressive strength of the concrete markedly shifted the capacities of the wall up to 15 MPa (Fig. 15(b)). The incremented amount of the vertical reinforcing bars was beneficial within the specified limit (Fig. 15(c)), and the reduced intervals between the graphs toward the direction of $\psi_v = 3.0\psi_h$ are due to the influence of the R_{vh} term in Eq. (19) and (20): the degree of the crack angle declined when the difference between the normalized vertical and horizontal reinforcement ratios was enlarged. The repercussions of the normalized horizontal reinforcement ratio in the compression boundary element (ψ_{hcbe}) with respect to the ratio in the web (ψ_h) are minimal (Fig. 15(d)). On that account, the potential inconsistency of placing horizontal reinforcing bars in the web and the boundary elements may not raise any practical concern.

SUMMARY AND CONCLUSIONS

This paper developed a mechanics-based model to predict the shear strength of squat walls built with boundary elements. The proposed methods, comprising an iterative analytical approach and simplified design equations, were intended to explain the specific behavioral aspects of a web as well as of compression and tension boundary elements, which were not available in empirically calibrated models. Corroborated by previously reported research, a failure criterion was established in reliance on the magnitude of principal strains, leading to web crushing and shear compression. Subsequent to a validation phase employing 123 experimental specimens excerpted from the literature, the refined analytical model generated a variety of strains and stresses that were indispensable to understanding the contribution of the individual components to the overall shear strength of the wall system. The suitability of the design equations was explored against the test data coupled with the analytical model. The credible performance of the published and suggested models was assessed and ranked through statistical properties. The following conclusions are drawn:

- In view of the fact that the total shear strength of the sampled squat walls was allocated to the web and the boundary elements by 58% and 42%, respectively, attention should be paid to the boundary elements so as not to overlook their significance in resisting lateral load. Nonetheless, the tension boundary element may be neglected for design convenience.

- As the horizontal reinforcement ratio rose, the shear strength of the web concrete abated, and this trend became prominent with the increased vertical reinforcing bar ratio. It is thus ascertained that both horizontal and vertical reinforcing bars altered the behavior of the concrete. In consequence, the provision of ACI 318-19[2] that ignores the portion of vertical reinforcement is recommended to be revised.
- The increased horizontal reinforcement ratio escalated the compressive principal strains of the web; accordingly, the failure of the member was accelerated. The response of the compression boundary element was stiffer than that of the web, prompting the precipitous growth of diagonal cracks in the vertical direction of the wall system.
- The shear capacities of the 123 squat wall specimens predicted by the analytical model and the simplified design equations were comparable, with a mean difference of 1.6%, whereas the former revealed a lower coefficient of variation (COV) of 29.9%. The discrepancy between the measured capacities and those calculated using the existing models ($v_{test}/v_{pred.}$) varied from 1.15 to 2.32. The proposed methods improved the effectiveness of modeling by reducing the ratio to 1.12 (analytical) and 1.14 (simplified equations).
- The impact of the compressive concrete strength was notable on the capacity of the wall system, and the extended disparity between the normalized vertical and horizontal reinforcement ratios lowered the propagation angle of the cracks. Irregular placement of horizontal reinforcing bars in the web (ψ_h) and the compression boundary element (ψ_{hcbe}) would not cause strength issues within a range of ψ_{hcbe}/ψ_h = 0.5 to 2.0.

AUTHOR BIOS

Ju-Hyung Kim *is a Postdoctoral Researcher in the Department of Civil Engineering at the University of Colorado Denver, Denver, CO. He received his BE, MS, and PhD from the Department of Architecture and Architectural Engineering at Seoul National University, Seoul, South Korea. His research interests include seismic design, performance evaluation, and statistical analysis of reinforced concrete structures.*

Yail J. Kim, *FACI, is President of the Bridge Engineering Institute, An International Technical Society, and a Professor in the Department of Civil Engineering at the University of Colorado Denver. He is Chair of ACI Subcommittee 440-I, FRP-Prestressed Concrete, past Chair of ACI Committee 345, Bridge Construction and Preservation, and a member of ACI Committees 342, Evaluation of Concrete Bridges and Bridge Elements; 377, Performance-Based Structural Integrity & Resilience of Concrete Structures; and 440, Fiber-Reinforced Polymer Reinforcement; and Joint ACI-ASCE Committee 343, Concrete Bridge Design. He received the ACI Chester Paul Siess Award for Excellence in Structural Research in 2019. His research interests include advanced composite materials for rehabilitation; structural informatics; complex systems; and science-based structural engineering, including statistical, interfacial, and quantum physics.*

Hong-Gun Park, *FACI, is a Professor in the Department of Architecture and Architectural Engineering at Seoul National University. He received his BE and MS in architectural engineering from Seoul National University, and his PhD in civil engineering from The University of Texas at Austin, Austin, TX. His research interests include numerical analysis, earthquake design of reinforced concrete, and composite structures.*

ACKNOWLEDGMENTS

This work was supported by the Korea Institute of Energy Technology Evaluation and Planning (KETEP) and the Ministry of Trade, Industry and Energy (MOTIE) of the Republic of Korea (No. 20201510100020).

REFERENCES

1. Zhang, X.; Shan, W.; Zhang, Z.; and Li, B., "AE Monitoring of Reinforced Concrete Squat Wall Subjected to Cyclic Loading with Information Entropy-Based Analysis," *Engineering Structures*, V. 165, June 2018, pp. 359-367. doi: 10.1016/j.engstruct.2018.03.059

2. ACI Committee 318, "Building Code Requirements for Structural Concrete (ACI 318-19) and Commentary (ACI 318R-19) (Reapproved 2022)," American Concrete Institute, Farmington Hills, MI, 2019, 624 pp.

3. Sánchez-Alejandre, A., and Alcocer, S. M., "Shear Strength of Squat Reinforced Concrete Walls Subjected to Earthquake Loading – Trends and Models," *Engineering Structures*, V. 32, No. 8, Aug. 2010, pp. 2466-2476. doi: 10.1016/j.engstruct.2010.04.022

4. Terzioglu, T.; Orakcal, K.; and Massone, L. M., "Cyclic Lateral Load Behavior of Squat Reinforced Concrete Walls," *Engineering Structures*, V. 160, Apr. 2018, pp. 147-160. doi: 10.1016/j.engstruct.2018.01.024

5. Kim, J.-H., and Park, H.-G., "Shear Strength of Flanged Squat Walls with 690 MPa Reinforcing Bars," *ACI Structural Journal*, V. 119, No. 2, Mar. 2022, pp. 209-220.

6. Paulay, T., "Seismic Design in Reinforced Concrete: The State of the Art in New Zealand," *Bulletin of the New Zealand Society for Earthquake Engineering*, V. 21, No. 3, Sept. 1988, pp. 208-232. doi: 10.5459/bnzsee.21.3.208-232

7. Zhou, Y.; Zheng, S.; Chen, L.; Long, L.; and Wang, B., "Experimental Investigation into the Seismic Behavior of Squat Reinforced Concrete Walls Subjected to Acid Rain Erosion," *Journal of Building Engineering*, V. 44, Dec. 2021, Article No. 102899. doi: 10.1016/j.jobe.2021.102899

8. Rosso, A.; Almeida, J. P.; and Beyer, K., "Stability of Thin Reinforced Concrete Walls under Cyclic Loads: State-of-the-Art and New Experimental Findings," *Bulletin of Earthquake Engineering*, V. 14, No. 2, Feb. 2016, pp. 455-484. doi: 10.1007/s10518-015-9827-x

9. Brueggen, B. L., "Performance of T-Shaped Reinforced Concrete Structural Walls under Multi-Dimensional Loading," PhD dissertation, University of Minnesota, Minneapolis, MN, 2009, pp. 259-267.

10. Liu, X.; Burgueño, R.; Egleston, E.; and Hines, E. M., "Inelastic Web Crushing Performance Limits of High-Strength-Concrete Structural Wall – Single Wall Test Program," Report No. CEE-RR-2009/03, Michigan State University, East Lansing, MI, 2009, 281 pp.

11. Teng, S., and Chandra, J., "Cyclic Shear Behavior of High-Strength Concrete Structural Walls," *ACI Structural Journal*, V. 113, No. 6, Nov.-Dec. 2016, pp. 1335-1345. doi: 10.14359/51689158

12. Kim, J.-H., and Park, H.-G., "Shear and Shear-Friction Strengths of Squat Walls with Flanges," *ACI Structural Journal*, V. 117, No. 6, Nov. 2020, pp. 269-280. doi: 10.14359/51728075

13. Barda, F.; Hanson, J. M.; and Corley, W. G., "Shear Strength of Low-Rise Walls with Boundary Elements," *Reinforced Concrete Structures in Seismic Zones*, SP-53, American Concrete Institute, Farmington Hills, MI, 1977, pp. 149-202.

14. Wood, S. L., "Shear Strength of Low-Rise Reinforced Concrete Walls," *ACI Structural Journal*, V. 87, No. 1, Jan.-Feb. 1990, pp. 99-107.

15. ASCE/SEI 43-05, "Seismic Design Criteria for Structures, Systems, and Components in Nuclear Facilities," American Society of Civil Engineers, Reston, VA, 2005.

16. Moehle, J., *Seismic Design of Reinforced Concrete Buildings*, McGraw-Hill Education, New York, 2015, 760 pp.

17. Kassem, W., "Shear Strength of Squat Walls: A Strut-and-Tie Model and Closed-Form Design Formula," *Engineering Structures*, V. 84, Feb. 2015, pp. 430-438. doi: 10.1016/j.engstruct.2014.11.027

18. Luna, B. N., and Whittaker, A. S., "Peak Strength of Shear-Critical Reinforced Concrete Walls," *ACI Structural Journal*, V. 116, No. 2, Mar. 2019, pp. 257-266. doi: 10.14359/51712280

19. Gulec, C. K., and Whittaker, A. S., "Empirical Equations for Peak Shear Strength of Low Aspect Ratio Reinforced Concrete Walls," *ACI Structural Journal*, V. 108, No. 1, Jan.-Feb. 2011, pp. 80-89.

20. Vecchio, F. J., and Collins, M. P., "The Modified Compression-Field Theory for Reinforced Concrete Elements Subjected to Shear," *ACI Journal Proceedings*, V. 83, No. 2, Mar.-Apr. 1986, pp. 219-231.

21. Kaufmann, W., and Marti, P., "Structural Concrete: Cracked Membrane Model," *Journal of Structural Engineering*, ASCE, V. 124, No. 12, Dec. 1998, pp. 1467-1475. doi: 10.1061/(ASCE)0733-9445(1998)124:12(1467)

22. Muttoni, A.; Schwartz, J.; and Thürlimann, B., "Stress Fields for Simple Structures," *Design of Concrete Structures with Stress Fields*, Springer Science & Business Media, Berlin, Germany, 1996, pp. 46-50.

23. Nawy, E. G., *Reinforced Concrete: A Fundamental Approach*, Pearson, Upper Saddle River, NJ, 2009.

24. Antebi, J.; Utku, S.; and Hansen, R. J., "The Response of Shear Walls to Dynamic Loads," Department of Civil and Sanitary Engineering, Massachusetts Institute of Technology, Cambridge, MA, 1960.

25. Hirosawa, M., "Past Experimental Results on Reinforced Concrete Shear Walls and Analysis on Them," Building Research Institute, Ministry of Construction, Tokyo, Japan, 1975, 277 pp. (in Japanese)

26. Synge, A. J., "Ductility of Squat Shear Walls," Report No. 80-8. Department of Civil Engineering, University of Canterbury, Christchurch, New Zealand, 1980, 142 pp.

27. Ogata, K., and Kabeyasawa, T., "Experimental Study on the Hysteretic Behavior of Reinforced Concrete Shear Walls under the Loading of Different Moment-to-Shear Ratios," *Transactions of the Japan Concrete Institute*, V. 6, 1984, pp. 717-724.

28. AIJ, "Load-Deflection Characteristics of Nuclear Reactor Building Structures: Parts 8-9-10," Summaries of Technical Papers, Structural Division, Architectural Institute of Japan, Tokyo, Japan, 1985, 58 pp. (in Japanese)

29. AIJ, "Load-Deflection Characteristics of Nuclear Reactor Building Structures: Parts 37-38-39-40," Summaries of Technical Papers of Annual Meeting B, Structures I, Architectural Institute of Japan, Tokyo, Japan, 1985. (in Japanese)

30. Maier, J., and Thürlimann, B., "Bruchversuche an Stahlbetonscheiben," Institut für Baustatik und Konstruktion, Eidgenössische Technische Hochschule (ETH) Zürich, Zürich, Switzerland, 1985, 130 pp. (in German)

31. Wiradinata, S., "Behavior of Squat Walls Subjected to Load Reversals," MS thesis, Department of Civil Engineering, University of Toronto, Toronto, ON, Canada, 1985, 171 pp.

32. Kabeyasawa, T., and Somaki, T., "Reinforcement Details for Reinforced Concrete Shear Walls with Thick Panel," *Transactions of the Japan Concrete Institute*, V. 7, 1985, pp. 369-372. (in Japanese)

33. AIJ, "Load-Deflection Characteristics of Nuclear Reactor Building Structures: Parts 21-22," Summaries of Technical Papers, Structural Division, Architectural Institute of Japan, Tokyo, Japan, 1986, 59 pp. (in Japanese)

34. AIJ, "Load-Deflection Characteristics of Nuclear Reactor Building Structures: Parts 59-60-61," Summaries of Technical Papers of Annual Meeting B, Structures I, Architectural Institute of Japan, Tokyo, Japan, 1986. (in Japanese)

35. AIJ, "Load-Deflection Characteristics of Nuclear Reactor Building Structures: Parts 62-63," Summaries of Technical Papers of Annual Meeting B, Structures I, Architectural Institute of Japan, Tokyo, Japan, 1986. (in Japanese)

36. Pilette, C. F., "Behavior of Earthquake Resistant Squat Shear Walls," MS thesis, Department of Civil Engineering, University of Ottawa, Ottawa, ON, Canada, 1987, 177 pp.

37. Saito, H.; Kikuchi, R.; Kanechika, M.; and Okamoto, K., "Experimental Study of the Effect of Concrete Strength on Shear Wall Behavior," *Proceedings*, Tenth International Conference on Structural Mechanics in Reactor Technology (SMiRT 10), Anaheim, CA, 1989, pp. 227-232.

38. Sato, S.; Ogata, Y.; Yoshizaki, S.; Kanata, K.; Yamaguchi, T.; Nakayama, T.; Inada, Y.; and Kadoriku, J., "Behavior of Shear Wall Using Various Yield Strength of Rebar, Part 1: An Experimental Study," *Proceedings*, Tenth International Conference on Structural Mechanics in Reactor Technology (SMiRT 10), Anaheim, CA, 1989, pp. 233-238.

39. Rothe, D., "Untersuchugen zum Nichtlinearen Verhalten von Stahlbeton Wandschieben unter Erdebenbeanspruchung," PhD dissertation, Fachbereich Konstruktiver Ingenieurbau der Technischen Hochschule Darmstadt, Darmstadt, Germany, 1992, 161 pp. (in German)

40. Mohammadi-Doostdar, H., "Behaviour and Design of Earthquake Resistant Low-Rise Shear Walls," PhD thesis, University of Ottawa, Ottawa, ON, Canada, 1994, 234 pp.

41. Seki, M.; Kobayashi, J.; Shibata, A.; Kubo, T.; Taira, T.; and Akino, K., "Restoring Force Verification Test on RC Shear Wall," *Proceedings*, Thirteenth International Conference on Structural Mechanics in Reactor Technology (SMiRT 13), Porto Alegre, RS, Brazil, 1995, pp. 39-44.

42. Mo, Y. L., and Chan, J., "Behavior of Reinforced-Concrete-Framed Shear Walls," *Nuclear Engineering and Design*, V. 166, No. 1, Oct. 1996, pp. 55-68. doi: 10.1016/0029-5493(96)01244-7

43. Hidalgo, P. A.; Jordan, R. M.; and Martinez, M. P., "An Analytical Model to Predict the Inelastic Seismic Behavior of Shear-Wall, Reinforced Concrete Structures," *Engineering Structures*, V. 24, No. 1, Jan. 2002, pp. 85-98. doi: 10.1016/S0141-0296(01)00061-X

44. Salonikios, T. N.; Kappos, A. J.; Tegos, I. A.; and Penelis, G. G., "Cyclic Load Behavior of Low-Slenderness Reinforced Concrete Walls: Design Basis and Test Results," *ACI Structural Journal*, V. 96, No. 4, July-Aug. 1999, pp. 649-661.

45. Gao, X., "Framed Shear Walls under Cyclic Loading," PhD dissertation, University of Houston, Houston, TX, 1999, 285 pp.

46. Bouchon, M.; Orbovic, N.; and Foure, B., "Tests on Reinforced Concrete Low-Rise Shear Walls under Static Cyclic Loading," *Proceedings*, Thirteenth World Conference on Earthquake Engineering (13 WCEE), Vancouver, BC, Canada, 2004, Paper No. 257, 10 pp.

47. Park, H.-G.; Baek, J.-W.; Lee, J.-H.; and Shin, H.-M., "Cyclic Loading Tests for Shear Strength of Low-Rise Reinforced Concrete Walls with Grade 550 MPa Bars," *ACI Structural Journal*, V. 112, No. 3, May-June 2015, pp. 299-310. doi: 10.14359/51687406

48. Luna, B. N.; Rivera, J. P.; and Whittaker, A. S., "Seismic Behavior of Low-Aspect-Ratio Reinforced Concrete Shear Walls," *ACI Structural Journal*, V. 112, No. 5, Sept.-Oct. 2015, pp. 593-604. doi: 10.14359/51687709

49. Kim, S., and Wallace, J. W., "Reliability of Structural Wall Shear Design for Tall Reinforced-Concrete Core Wall Buildings," *Engineering Structures*, V. 252, Feb. 2022, Article No. 113492. doi: 10.1016/j.engstruct.2021.113492

50. Bentz, E. C.; Vecchio, F. J.; and Collins, M. P., "Simplified Modified Compression Field Theory for Calculating Shear Strength of Reinforced Concrete Elements," *ACI Structural Journal*, V. 103, No. 4, July-Aug. 2006, pp. 614-624.

ACI STRUCTURAL JOURNAL TECHNICAL PAPER

Title No. 120-S98

Aggregate Size on Punching Shear Behavior of Interior Slab-Column Connections

by Marnie B. Giduquio, Min-Yuan Cheng, and Shang-Wei Lin

Coarse aggregate size has been considered as one of the critical parameters affecting the shear resistance of reinforced concrete elements. However, existing research discussing its effects on punching shear is limited. In this study, 12 large-scale interior slab-column subassemblages were tested to investigate the influence of coarse aggregate size on the punching shear behavior of interior slab-column connections subjected to monotonically increased concentric load. Three aggregate sizes were selected: one with a nominal maximum coarse aggregate size, d_{agg}*, of 3/16 in. (4.75 mm), another with* d_{agg} *of 3/4 in. (19 mm), and the last with* d_{agg} *of 1 in. (25 mm). The experimental evidence indicated that all specimens failed in punching shear. In general, the increase in* d_{agg} *improved the punching shear response, with an increase in either the normalized maximum shear or the corresponding deformation, or both. The effects of the* d_{agg} *were more consistent and apparent in specimens with slab tensile flexural reinforcement ratios of 0.80 and 1.28%, where both the normalized maximum shear and the corresponding deformation increased as the* d_{agg} *increased. For the specimens with (low) slab tensile flexural reinforcement ratios of 0.40 and 0.53%, the increase in coarse aggregate size led to an increase in the normalized maximum shear and the corresponding deformation when the* d_{agg} *was increased from 3/16 to 3/4 in. (4.75 to 19 mm) due to better bond strength. As the* d_{agg} *was further increased from 3/4 to 1 in. (19 to 25.4 mm), the effects of the* d_{agg} *on the normalized maximum shear and the corresponding deformation were not apparent in the specimens with slab tensile reinforcement ratios of 0.40 and 0.53%.*

Keywords: aggregate size; flexural reinforcement; punching shear.

INTRODUCTION

According to ACI 318-19 (ACI Committee 318 2019), the punching shear capacity of an interior reinforced concrete (RC) slab-column connection (with normalweight concrete) is estimated using the strength model presented in the second row of Table 1. This model, however, has long been criticized for its overly simplified form without considering the influences of other key variables (Mitchell et al. 2005; Dilger et al. 2005; Muttoni 2008; Guandalini et al. 2009; Gardner 2011; Giduquio et al. 2019; among others). With respect to the earlier version, a couple of modifications were made in ACI 318-19. First, the effect of the slab size on the punching shear capacity was considered in Section 22.6.5 by the factor λ_s. Second, a minimum area of tensile flexural reinforcement, as per Section 8.6.1.2, is required within the effective slab width when the shear stress demand, v_{uv}, is greater than $\phi 2\lambda_s\sqrt{f_c'}$, where ϕ is the strength reduction factor taken as 0.75, and f_c' is the specified concrete strength. This required minimum area of slab tensile flexural reinforcement, $A_{s,min}$, was intended to prevent flexure-driven punching shear failure (Dam et al. 2017; Hawkins and Ospina 2017). To show the design parameters considered in different building codes, the punching shear strength models adopted in Eurocode 2 (EN 1992-1-1:2004 2004), and the *fib* Model Code 2010 (*fib* 2013) are summarized in Table 1.

As presented in Table 1, the coarse aggregate size in the concrete material appears to be another variable that has an influence on punching shear capacity. Aggregate interlock is one of the key mechanisms in shear resistance (Fenwick 1966; Joint ASCE-ACI Committee 426 1973). Previous research has shown that one-way shear capacity increases as the coarse aggregate size increases (Sherwood et al. 2007; Deng et al. 2017). For two-way shear (punching shear), however, test results are relatively limited. Concerns were raised about the effectiveness of the aggregate interlock as the crack width increases, particularly for slabs in which the tensile flexural reinforcement ratio is typically low. Sherif and Dilger (1996) indicated that most slab designs have a reinforcement ratio of less than 1%. Several structural drawings of flat-plate structures located in the western United States revealed a slab flexural reinforcement ratio of approximately 0.5% in the column strip (Widianto 2006).

The issues discussed previously motivated this study to investigate the influence of coarse aggregate size on punching shear strength. A test program consisting of 12 large-scale interior RC slab-column subassemblages was conducted. All specimens were tested under monotonically increased concentric loading. Considering that the crack width of RC members is closely associated with the tensile flexural reinforcement ratio, which may influence the aggregate interlock mechanism, the primary test parameters investigated in this study included both the coarse aggregate size and the slab tensile flexural reinforcement ratio.

RESEARCH SIGNIFICANCE

Aggregate interlock has long been recognized as one of the key mechanisms in shear resistance. However, its effectiveness decreases as the crack width increases. Research on the influence of coarse aggregate size on punching shear strength is limited. Through a systematic test program

ACI Structural Journal, V. 120, No. 6, November 2023.
MS No. S-2022-304.R1, doi: 10.14359/51739091, received March 25, 2023, and reviewed under Institute publication policies.

Table 1—Punching shear strength models from different building codes

Building code	U.S. customary units	SI units
ACI 318-19	Least of (a), (b), and (c): (a) $V_{ACI} = 4\lambda_s\sqrt{f_c'\,[\text{psi}]}\,b_o d$ (b) $V_{ACI} = \left(2+\frac{4}{\beta}\right)\lambda_s\sqrt{f_c'\,[\text{psi}]}\,b_o d$ (c) $V_{ACI} = \left(2+\frac{\alpha_s d}{b_o}\right)\lambda_s\sqrt{f_c'\,[\text{psi}]}\,b_o d$ where $\lambda_s = \sqrt{\frac{2}{1+\frac{d\,[\text{in.}]}{10}}} \le 1$	Least of (a), (b), and (c): (a) $V_{ACI} = \frac{1}{3}\lambda_s\sqrt{f_c'\,[\text{MPa}]}\,b_o d$ (b) $V_{ACI} = \frac{1}{6}\left(1+\frac{2}{\beta}\right)\lambda_s\sqrt{f_c'\,[\text{MPa}]}\,b_o d$ (c) $V_{ACI} = \frac{1}{12}\left(2+\frac{\alpha_s d}{b_o}\right)\lambda_s\sqrt{f_c'\,[\text{MPa}]}\,b_o d$ where $\lambda_s = \sqrt{\frac{2}{1+\frac{d\,[\text{mm}]}{250}}} \le 1$
Eurocode 2	$V_{EC2} = 5k(100\rho_l f_c'\,[\text{psi}])^{1/3} b_o d$ where $k = 1+\sqrt{\frac{8}{d\,[\text{in.}]}} \le 2$ $\rho_l = \sqrt{\rho_x \rho_y} \le 0.02$	$V_{EC2} = 0.18k(100\rho_l f_c'\,[\text{MPa}])^{1/3} b_o d$ where $k = 1+\sqrt{\frac{200}{d\,[\text{mm}]}} \le 2$ $\rho_l = \sqrt{\rho_x \rho_y} \le 0.02$
fib Model Code	$V_{fib} = k_\psi\sqrt{f_c'\,[\text{psi}]}\,b_o d$ where $k_\psi = \frac{8}{1+16k_{dg}\psi d} \le 0.6$ $\psi = 1.5\frac{r_s}{d}\frac{f_y}{E_s}\left(\frac{m_{Ed}}{m_{Rd}}\right)^{1.5}$ (Level II approximation) For $d_{agg} \ge 5/8$ in.: $k_{dg} = 1.0$ For $d_{agg} < 5/8$ in.: $k_{dg} = \frac{1.25}{\frac{5}{8}+d_{agg}\,[\text{in.}]} \ge 0.75$	$V_{fib} = k_\psi\sqrt{f_c'\,[\text{MPa}]}\,b_o d$ where $k_\psi = \frac{1}{1.5+0.9k_{dg}\psi d} \le 0.6$ $\psi = 1.5\frac{r_s}{d}\frac{f_y}{E_s}\left(\frac{m_{Ed}}{m_{Rd}}\right)^{1.5}$ (Level II approximation) For $d_{agg} \ge 16$ mm: $k_{dg} = 1.0$ For $d_{agg} < 16$ mm: $k_{dg} = \frac{32}{16+d_{agg}\,[\text{mm}]} \ge 0.75$

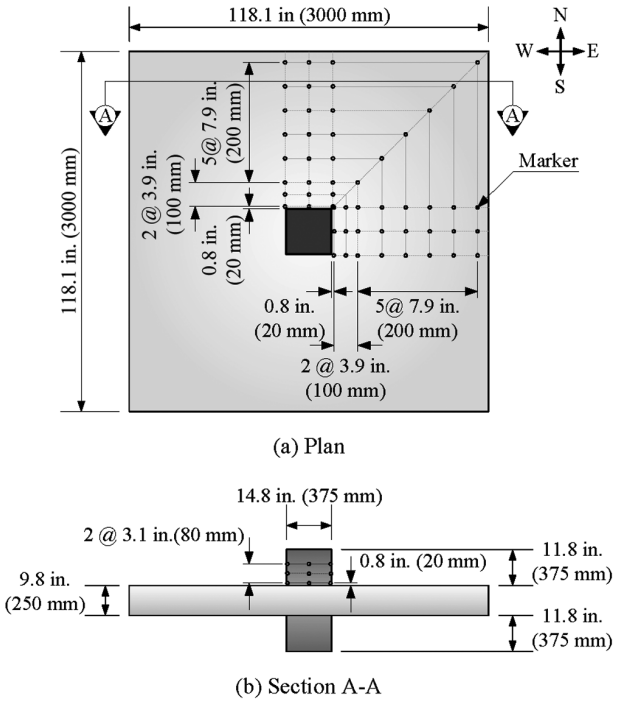

Fig. 1—Specimen geometry and marker layout.

consisting of 12 large-scale interior RC slab-column subassemblages, this research intends to shed some light on this subject.

EXPERIMENTAL PROGRAM

Test specimens

The experimental program consisted of 12 interior RC slab-column subassemblages. All specimens had the same geometry, with a 118.1 x 118.1 x 9.8 in. (3000 x 3000 x 250 mm) slab and a 14.8 x 14.8 in. (375 x 375 mm) central column stub that protruded 11.8 in. (300 mm) from the top and bottom faces of the slab, as shown in Fig. 1. The slab thickness was chosen to satisfy the minimum thickness requirement of $\ell_n/33$ per ACI 318-19 for a typical flat-plate framing system with a span of approximately 23 ft (7000 mm). The slab plan dimensions were designed to include vertical supports that were uniformly placed along the contraflexure line, located at a distance of 0.22 times the span length (23 ft [7000 mm]) from the column center.

The key design parameters of all the test specimens are summarized in Table 2. All slabs were reinforced with tensile flexural reinforcement only. Specimens with labels starting with R2.5, R4, R6, and R8 had slab tensile flexural

Table 2—Specimen design parameters

Specimen	s, in. (mm)	ρ, %	d_{agg}*, in. (mm)
R8S	7.9 (200)	0.40	3/16 (4.75)
R8M	7.9 (200)	0.40	3/4 (19)
R8L	7.9 (200)	0.40	1 (25)
R6S	5.9 (150)	0.53	3/16 (4.75)
R6M	5.9 (150)	0.53	3/4 (19)
R6L	5.9 (150)	0.53	1 (25)
R4S	3.9 (100)	0.80	3/16 (4.75)
R4M	3.9 (100)	0.80	3/4 (19)
R4L	3.9 (100)	0.80	1 (25)
R2.5S	2.5 (63)	1.28	3/16 (4.75)
R2.5M	2.5 (63)	1.28	3/4 (19)
R2.5L	2.5 (63)	1.28	1 (25)

*Nominal maximum coarse aggregate size based on ASTM C33/C33M-18.

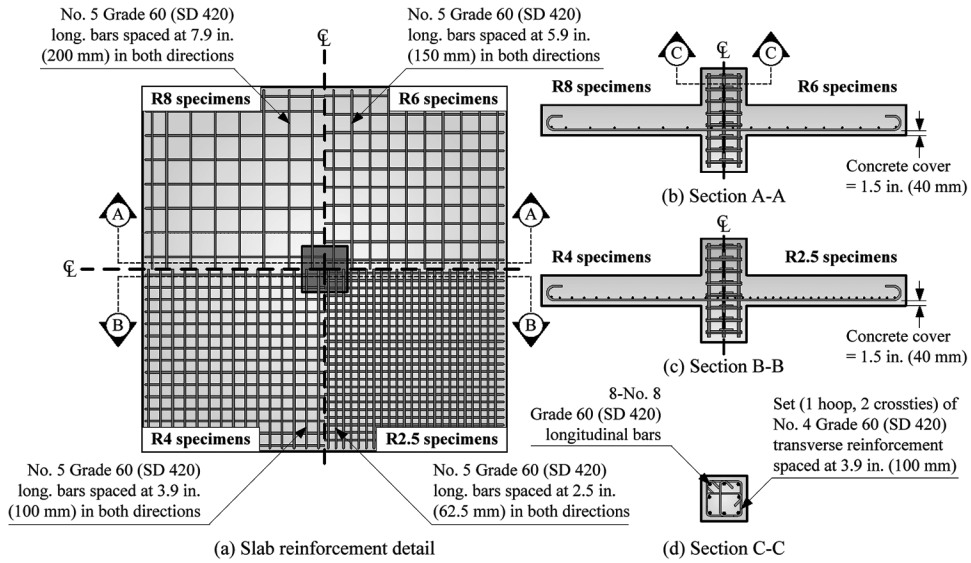

Fig. 2—Reinforcement details.

Table 3—Particle-size distribution of aggregates

Sieve size	Percentage passing, %		
	R8S, R6S, R4S, and R2.5S	R8M, R6M, R4M, and R2.5M	R8L, R6L, R4L, and R2.5L
1 in. (25 mm)	—	100	100
3/4 in. (19 mm)	—	100	0.00
1/2 in. (12.5 mm)	—	52.9	—
3/8 in. (9.5 mm)	100	22.0	—
No. 4 (4.75 mm)	98.6	7.00	—
No. 8 (2.36 mm)	83.3	3.50	—
No. 16 (1.18 mm)	57.9	—	—
No. 30 (0.60 mm)	41.7	—	—
No. 50 (0.30 mm)	27.7	—	—
No. 100 (0.15 mm)	9.30	—	—
No. 200 (0.075 mm)	4.20	0.80	—

reinforcement spaced at 2.5 in. (62.5 mm) (ρ = 1.28%), 3.9 in. (100 mm) (ρ = 0.80%), 5.9 in. (150 mm) (ρ = 0.53%), and 7.9 in. (200 mm) (ρ = 0.40%), respectively. In this study, the slab flexural reinforcement ratio, ρ, was determined as the area of longitudinal reinforcement (No. 5) divided by the spacing of flexural reinforcement and slab thickness. The reinforcement layouts of the test specimens are presented in Fig. 2. The mixture proportions of the three concrete materials, each consisting of a different coarse aggregate size, were developed through several trial batches with an aim to have a strength close to 5000 psi (34.5 MPa) at 28 days, an identical water-binder ratio (*w*/*b*) of 0.47, and similar binder proportions (cement, slag, and fly ash). Specimens with labels ending in "S," "M," and "L" used concrete materials with coarse aggregate sizes smaller than 3/8 in. (9.5 mm), primarily between 3/8 and 3/4 in. (9.5 and 19 mm), and between 3/4 and 1 in. (19 and 25 mm), respectively. The aggregate size distributions and concrete mixture proportions of the three concrete materials are summarized

Table 4—Concrete mixture proportions

Constituent material	Relative density	R8S, R6S, R4S, R2.5S, lb/ft^3 (kg/m^3)	R8M, R6M, R4M, R2.5M, lb/ft^3 (kg/m^3)	R8L, R6L, R4L, R2.5L, lb/ft^3 (kg/m^3)
Cement	3.15	13.3 (212.5)	13.3 (212.5)	13.3 (212.5)
Slag	2.87	6.64 (106.3)	6.64 (106.3)	6.64 (106.3)
Fly ash	2.21	6.64 (106.3)	6.64 (106.3)	6.64 (106.3)
Admixture	1.06	0.220 (3.60)	0.220 (3.60)	0.110 (1.70)
Fine aggregates	2.61	111 (1780)	55.7 (892)	46.7 (1020)
Coarse aggregates	2.64	—	54.8 (878)	63.6 (748)
w/*b*	—	0.471	0.471	0.471

in Tables 3 and 4, respectively. According to the definition of ASTM C33/C33M (2018), the nominal maximum coarse aggregate size, d_{agg}, for each specimen is presented in the last column of Table 2.

Experimental setup and instrumentation

The experimental setup is presented in Fig. 3. Specimens were tested upside down; thus, the slab tensile flexural reinforcement was at the bottom of the slab. The slab was supported by eight vertical steel supports, spaced evenly around the center of the slab on a circle with a diameter of 118.1 in. (3000 mm), as shown in Fig. 3(b). The load was monotonically applied through a 660 kip (3000 kN) hydraulic jack placed on top of the column stub. A strong steel frame provided reactions for the hydraulic jack. The test was displacement-controlled with a loading rate of 0.001 in./s (0.03 mm/s).

A load cell was placed between the hydraulic jack and the reaction frame to monitor the applied load. Three linear variable differential transducers (LVDTs) were installed to

monitor the vertical displacement of the top and bottom column stubs. Two more LVDTs were attached to two opposite vertical steel supports to monitor the vertical displacement of the supports. Several strain gauges were attached to the slab flexural reinforcement to monitor the extent of yielding at several locations. An infrared-based optical system that tracked the position of "markers" was employed to measure the exterior deformation of the slab top surface. The locations of the markers are illustrated in Fig. 1.

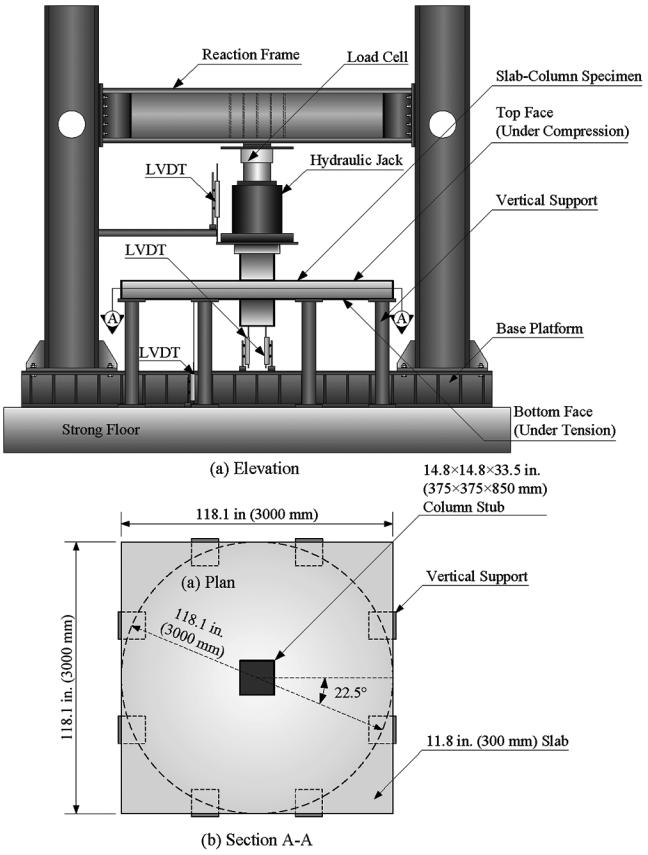

Fig. 3—Test setup.

EXPERIMENTAL RESULTS

Materials

All concrete materials were supplied by a local ready mixed concrete company. Specimens with the same maximum aggregate size were cast together to ensure consistency between the materials used. The concrete strengths of the specimens labeled with "M" and "L" were obtained as the average compressive strengths of four 4 x 8 in. (100 x 200 mm) concrete cylinder samples per ASTM C39/C39M (2014). The concrete strengths of the specimens labeled with "S" were determined based on the average compressive strengths of four 2 in. (50 mm) cube specimens per ASTM C109/C109M (2020). Compression tests of the concrete cylinder/cube specimens were conducted within 24 hours after the test of the corresponding slab-column specimens. The tested concrete strengths, f_{cm}, of all specimens are summarized in Table 5. All specimens used steel reinforcement from the same batch. The tensile properties of the steel reinforcement were determined using a direct tensile test according to ASTM A370 (2020). Based on the results from three steel coupon samples, the average yield stress of the slab flexural reinforcement was 70.0 ksi (482.6 MPa).

Crack pattern

Each specimen was tested until the applied force dropped by more than 50% from the maximum value. All specimens experienced a sudden drop in applied force, accompanied by a loud banging sound.

Table 5—Summary of test results

Specimen	f_{cm}, psi (MPa)	V_{max}, kip (kN)	d_{max}*, in. (mm)	V_{ACI}, kip (kN)	V_{EC2}, kip (kN)	V_{fib}, kip (kN)	V_{flex}, kip (kN)	$V_{max}/b_o d\sqrt{f'_c}$, psi (MPa)	V_{max}/V_{ACI}	V_{max}/V_{EC2}	V_{max}/V_{fib}	V_{max}/V_{flex}
R8S	4680 (32.3)	153 (680)	0.72 (18.3)	NA†	158 (701)	61.1 (272)	151 (673)	3.26 (0.270)	NA†	0.97	2.50	1.01
R8M	4620 (31.8)	185 (825)	1.17 (29.6)	NA†	157 (698)	68.2 (303)	151 (672)	3.98 (0.330)	NA†	1.18	2.72	1.23
R8L	6410 (44.2)	196 (870)	1.11 (28.3)	NA†	175 (778)	76.5 (340)	153 (681)	3.57 (0.300)	NA†	1.12	2.56	1.28
R6S	4890 (33.7)	184 (819)	0.590 (15.1)	192 (852)	176 (783)	69.6 (310)	199 (885)	3.85 (0.320)	0.96	1.05	2.65	0.93
R6M	4710 (32.5)	203 (901)	0.725 (18.4)	188 (836)	174 (773)	85.4 (380)	199 (883)	4.31 (0.360)	1.08	1.17	2.37	1.02
R6L	6250 (43.1)	224 (998)	0.846 (21.5)	217 (964)	191 (850)	89.2 (397)	202 (897)	4.14 (0.340)	1.04	1.17	2.51	1.11
R4S	5060 (34.9)	221 (983)	0.506 (12.8)	195 (867)	204 (907)	89.0 (396)	290 (1290)	4.53 (0.380)	1.13	1.08	2.48	0.76
R4M	4520 (31.2)	247 (1100)	0.581 (14.8)	184 (820)	196 (873)	101 (449)	287 (1280)	5.37 (0.450)	1.34	1.26	2.45	0.86
R4L	5680 (39.1)	283 (1260)	0.705 (17.9)	206 (918)	212 (942)	99.8 (444)	293 (1300)	5.49 (0.460)	1.37	1.34	2.84	0.97
R2.5S	5370 (37.0)	250 (1110)	0.427 (10.8)	201 (893)	243 (1080)	126 (561)	442 (1970)	4.97 (0.410)	1.24	1.03	1.98	0.56
R2.5M	4820 (33.2)	289 (1290)	0.518 (13.2)	190 (846)	235 (1040)	135 (599)	435 (1940)	6.08 (0.510)	1.52	1.23	2.15	0.66
R2.5L	5630 (38.8)	356 (1580)	0.584 (14.8)	205 (914)	247 (1100)	122 (541)	445 (1980)	6.93 (0.580)	1.73	1.44	2.93	0.80
								Mean	1.27‡	1.17	2.51	—
								Standard deviation	0.25‡	0.13	0.27	—

*Corresponding to V_{max}.

†Flexural reinforcement not satisfying $A_{s,min}$ per ACI 318-19.

‡Considering R6, R4, and R2.5 specimens only.

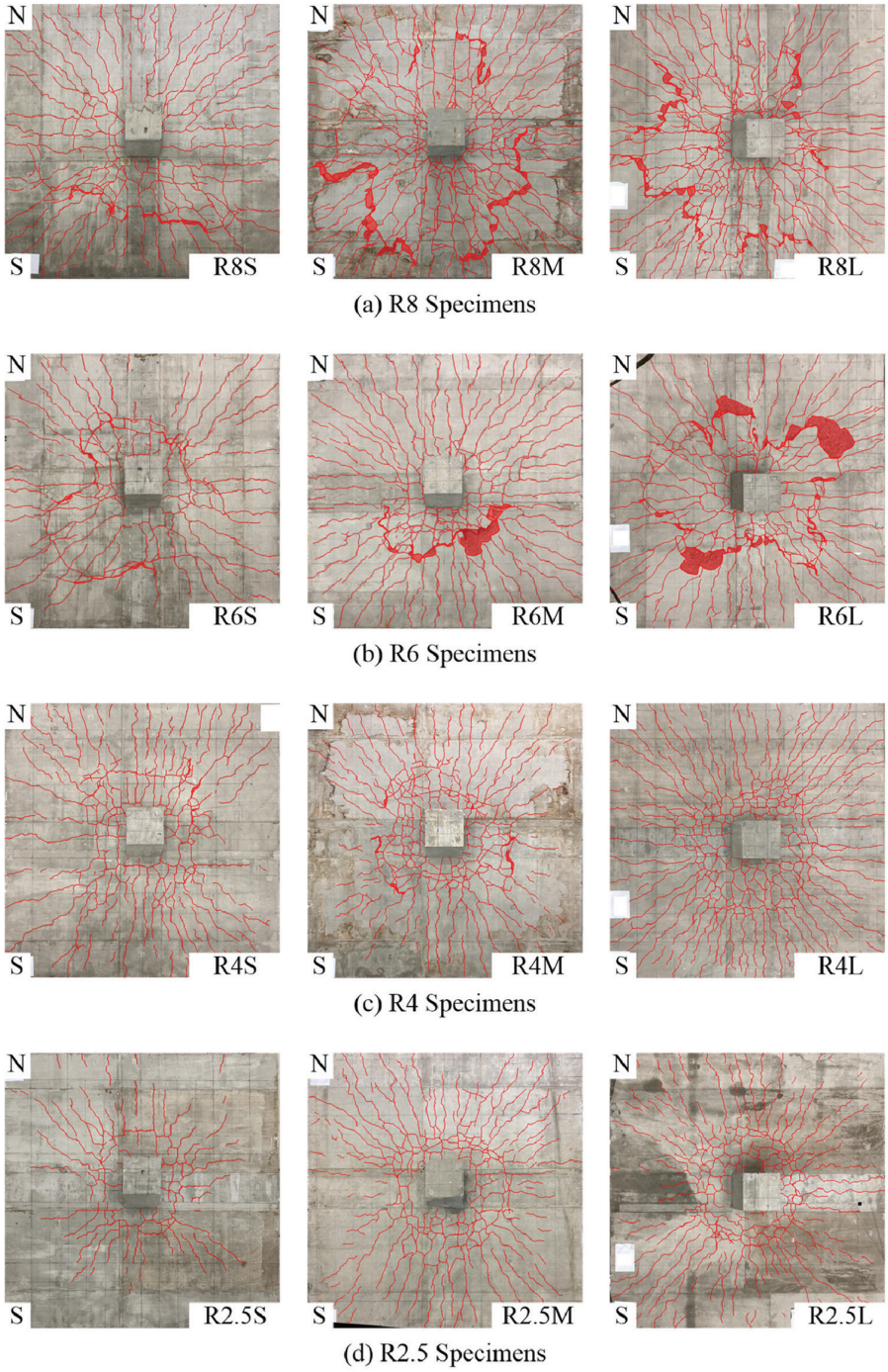

Fig. 4—Crack patterns on slab tension face.

After the test, the crack pattern was marked on the tension side of the slab, as shown in Fig. 4. Generally, all specimens had extensive radial cracks propagating from the center region toward the slab edges and multiple circumferential cracks around the column. The major circumferential crack resulting from the extension of the punching cone failure surface was more obvious on the tension face of the slab in the specimens with slab tensile flexural reinforcement ratios of 0.53 and 0.4%.

To further investigate the extent of the punching cone near the connection, the slab was saw-cut at a distance of approximately 2.8 in. (70 mm) from the column face (east side), as shown in Fig. 5. The inclined cracks resulting from the development of the punching cone failure surface were observed in all test specimens. In the specimens with relatively low tensile flexural reinforcement of 0.40 and 0.53%, the punching cone extended across the slab thickness. However, in the specimens with higher reinforcement ratios of 0.80 and 1.28%, after the inclined cracks reached the layer of tensile flexural reinforcement, the cracks tended to extend horizontally along the tensile flexural reinforcement. It was also noted that the inclined crack plane was considerably rougher for the specimens with larger aggregate sizes. Based on the evidence from the sudden drop in applied force and crack patterns, it can be concluded that all specimens failed in punching shear.

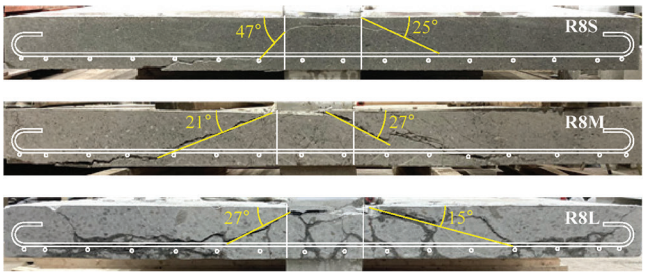

(a) R8 Specimens

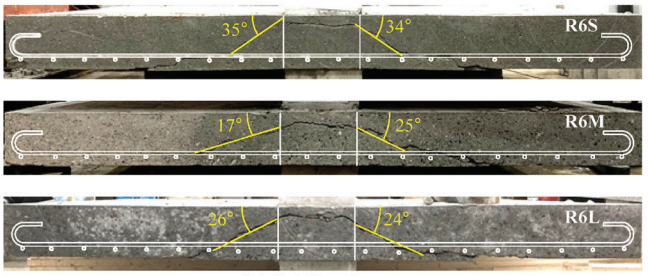

(b) R6 Specimens

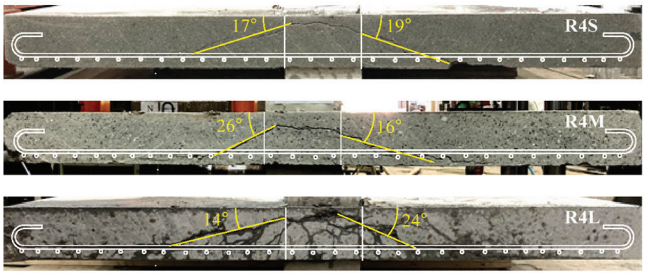

(c) R4 Specimens

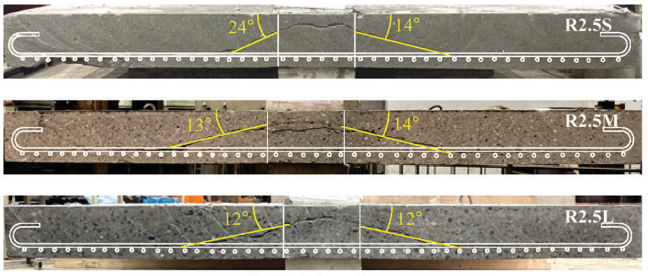

(d) R2.5 Specimens

Fig. 5—Saw-cut section.

Load-displacement response

The connection shear versus column vertical displacement responses of all the specimens are presented in Fig. 6. In this figure, the vertical axis is the normalized shear at the critical section, determined as the applied force divided by the perimeter of the critical section, b_o, according to ACI 318-19; the slab's effective depth, d (7.6 in. [194 mm]); and the square root of the tested concrete strength, f_{cm}. The applied force consisted of the force applied from the hydraulic jack, the specimen self-weight within the critical section assuming a concrete unit weight of 150 lb/ft^3 (23.6 kN/m^3), and the hydraulic jack self-weight. The horizontal axis in Fig. 6 represents the measurement from the average readings of the two LVDTs under the bottom column stub (Fig. 3). The combined deformation of the vertical steel supports and sliding along the slab-column interface at the maximum applied load was found to be smaller than 0.1 in. (2.5 mm), and thus, negligible. The maximum shear, V_{max}, and the corresponding deformation, d_{max}, of all the test specimens are summarized in Table 5. In general, the results in Fig. 6 indicate that the increase in maximum coarse aggregate size improved the punching shear response, with an increase in either the normalized V_{max} or d_{max}, or both.

In Fig. 7, the effects of the nominal maximum coarse aggregate size, d_{agg}, on the normalized maximum shear, V_{max}, and the corresponding deformation, d_{max}, are presented. As can be seen, the influence of d_{agg} on the punching shear response was quite consistent for the specimens with slab tensile reinforcement ratios of 0.80 and 1.28% where both V_{max} and d_{max} appeared to be governed by shear based on their limited inelastic response and apparent crack patterns (Fig. 5 and 6). In these specimens, the increase in d_{agg} led to an increase in both the normalized V_{max} and d_{max}.

For the specimens with slab tensile reinforcement ratios of 0.40 and 0.53%, where V_{max} was likely governed by local flexural yielding (Dam et al. 2017) due to the apparent inelastic response (Fig. 6) and d_{max} was limited by shear (Fig. 5), both the normalized V_{max} and d_{max} increased when d_{agg} was increased from 3/16 to 3/4 in. (4.75 to 19 mm). The readings of the two strain gauges shown in Fig. 8 indicated that the bond strengths around the connection of R8M and R6M were better than those of R8S and R6S, respectively. Furthermore, in Fig. 4, the number of circumferential and radial cracks in the specimens with the label "S" appeared to be consistently lower than that in the specimens with the labels "M" or "L." Therefore, it appeared that the enhanced normalized V_{max} and, consequently, d_{max}, from R8S to R8M or from R6S to R6M were primarily attributed to the better bond strength due to the existence of the larger coarse aggregate size. As d_{agg} was further increased from 3/4 to 1 in. (19 to 25.4 mm), both V_{max} and d_{max} were similar in the specimens with slab tensile reinforcement ratios of 0.40 and 0.53%. As can be seen in Fig. 8, the bond strengths in R8L and R6L were similar to those in R8M and R6M, respectively.

Strength model comparison

The punching shear capacity was estimated using the strength models considered in Table 1. The analytical results are summarized in Table 5. It should be noted that the ACI 318-19 strength model was applicable to specimens with ρ of 0.53, 0.80, and 1.28% only because of the required $A_{s,min}$, which resulted in a minimum slab tensile flexural reinforcement ratio of approximately 0.46% using the tested material properties (f_{cm} in Table 5] and f_y = 70.0 ksi [482.6 MPa]), v_{uv} of $4\sqrt{f_{cm}[\text{psi}]}$ ($0.33\sqrt{f_{cm}[\text{MPa}]}$), and ϕ taken as 1.0.

The results in Table 5 indicate that the strength model according to Eurocode 2 provided the closest experimental-to-predicted-strength ratio. Without including the coarse aggregate size effect, the experimental-to-predicted-strength ratio based on Eurocode 2 typically increased as the coarse aggregate size increased. The results from the *fib* Model Code, which considers both the slab tensile reinforcement and the coarse aggregate effects, were the most conservative, with a mean experimental-to-predicted-strength ratio of approximately 2.5. The strength model of ACI 318-19, without considering both the coarse aggregate and the slab

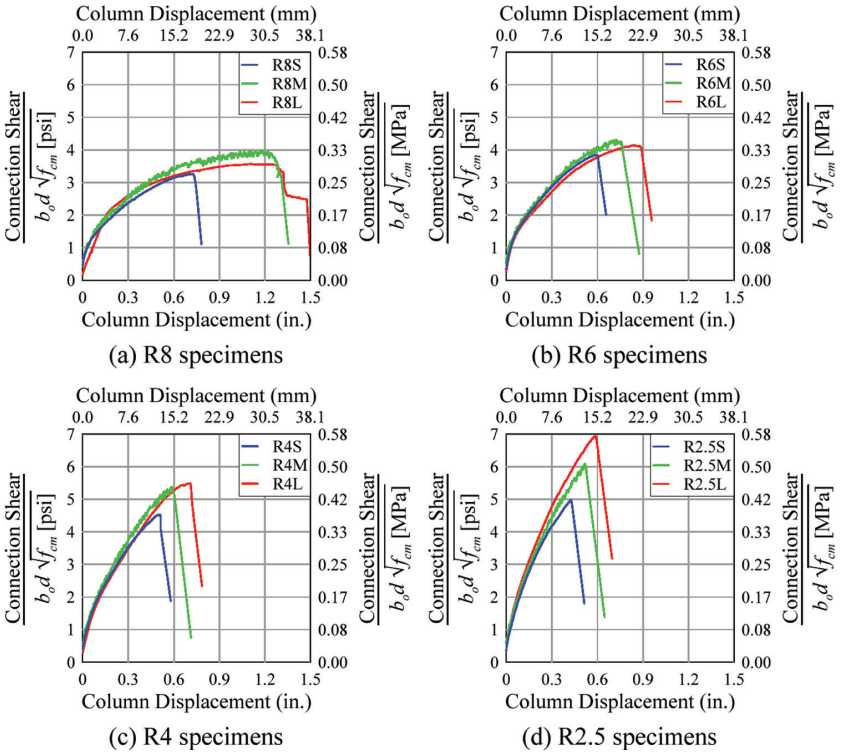

Fig. 6—Punching shear versus column displacement.

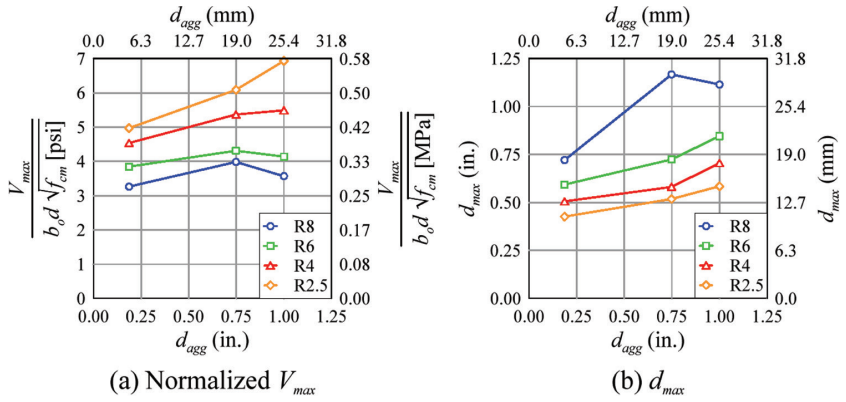

Fig. 7—Aggregate size effect.

tensile flexural reinforcement ratio, resulted in an increase in the experimental-to-predicted-strength ratio as either the coarse aggregate size or the specimen slab tensile flexural reinforcement increased.

The results of the V_{max}/V_{ACI} indicated that the strength model of ACI 318-19 was conservative for the applicable specimens. However, providing larger amounts of slab tensile flexural reinforcement inevitably reduced the connection deformation capacity. For the specimens with a nominal maximum coarse aggregate size of 3/4 in. (19 mm), the connection drift capacity determined using d_{max} divided by the shear span of approximately 51.1 in. (1300 mm) decreased from approximately 2.3 to 1.0% as the specimen slab tensile reinforcement ratio increased from 0.40 to 1.28%.

As discussed previously, the maximum shear of the specimens with slab tensile reinforcement ratios of 0.40 and 0.53% appeared to be limited by local flexural yielding. An attempt was made to estimate the V_{max} of these specimens using Eq. (1), proposed by Dam et al. (2017). In Eq. (1), the V_{flex} developed based on the yield line analysis represents the gravity-type (vertical) load on the column stub required to achieve local flexural yielding at the connection; h_c is the column dimension; ℓ is the distance between opposite vertical supports; and m is the flexural capacity per unit width. The analytical results suggested that V_{max} could be acceptably estimated by V_{flex} for the specimens with nominal maximum coarse aggregate sizes of 3/4 in. (19 mm) or larger.

$$V_{flex} = \frac{4\sqrt{2}}{\cos\left(\frac{\pi}{8}\right) - \frac{h_c\sqrt{2}}{\ell}} m \quad (1)$$

Slab deformation profile

The slab vertical deformation profile at V_{max} is presented in Fig. 9, where the vertical deformation for each point was

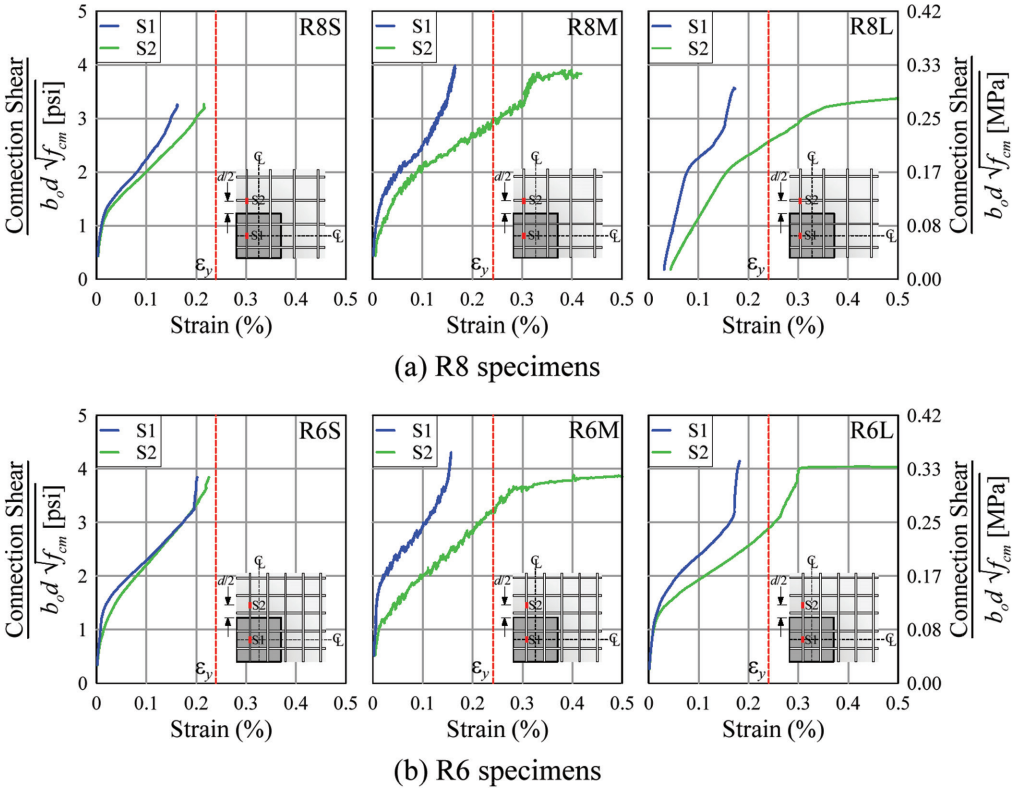

Fig. 8—Reinforcement strain.

estimated using the average result of six markers attached on the slab with nominally the same distance from the column face in the east-west and north-south directions (refer to Fig. 1).

As shown in Fig. 9, an apparent kink was observed at 8.7 in. (220 mm) distance from the column face, and the deformation profile became approximately linear afterward. This suggested that the specimen vertical deformation was primarily attributed to the slab rotation within roughly one effective depth, d, distance from a column face, and with significant rotation concentrated within a very limited length between the column face and the first row of markers (0.8 in. [20 mm]). The slab section more than d distance away from the column face behaved approximately as a rigid body.

CONCLUSIONS

Twelve large-scale interior slab-column subassemblages were tested under monotonically increased gravity-type loading to investigate the effect of the tensile flexural reinforcement ratio and maximum coarse aggregate size on the punching shear behavior of the interior slab-column connection. Based on the findings of this study, the following conclusions were drawn:

1. Test results indicated that all specimens failed in punching shear, regardless of the coarse aggregate size and slab tensile reinforcement ratio.

2. For the specimens with high slab tensile flexural reinforcement ratios (0.80 or 1.28%) where the load-deflection response was primarily governed by the punching shear, the increase in the nominal maximum aggregate size led to an apparent increase in both the normalized maximum shear and the corresponding deformation.

3. For the specimens with low slab tensile flexural reinforcement ratios (0.40 and 0.53%) where the load-deflection response was governed by flexure-driven punching shear, the increase in coarse aggregate size led to an increase in the normalized maximum shear and the corresponding deformation when the d_{agg} was increased from 3/16 to 3/4 in. (4.75 to 19 mm) due to better bond strength. As the d_{agg} was further increased from 3/4 to 1 in. (19 to 25.4 mm), the effects of the d_{agg} on the normalized maximum shear and the corresponding deformation were not apparent.

4. Based on the test results, the strength model based on Eurocode 2 provides a more consistent experimental-to-predicted-strength ratio. The ACI 318-19 strength model is conservative for specimens with reinforcement ratios larger than $A_{s,min}$, and d_{agg} of at least 3/4 in. (19 mm). Providing $A_{s,min}$, however, may significantly reduce the connection deformation capacity.

5. The specimen vertical deformation was primarily attributed to the slab rotation within roughly one effective depth, d, distance from a column face, and with significant rotation concentrated within a very limited length between the column face and the first row of markers (0.8 in. [20 mm]).

AUTHOR BIOS

ACI member **Marnie B. Giduquio** *is a Project Assistant Professor in the Department of Civil and Construction Engineering at National Taiwan University of Science and Technology, Taipei, Taiwan. He received his BS in civil engineering from the University of San Carlos, Cebu City, Philippines, and his MS and PhD in civil and construction engineering from National Taiwan University of Science and Technology.*

ACI member **Min-Yuan Cheng** *is a Professor in the Department of Civil and Construction Engineering at National Taiwan University of Science*

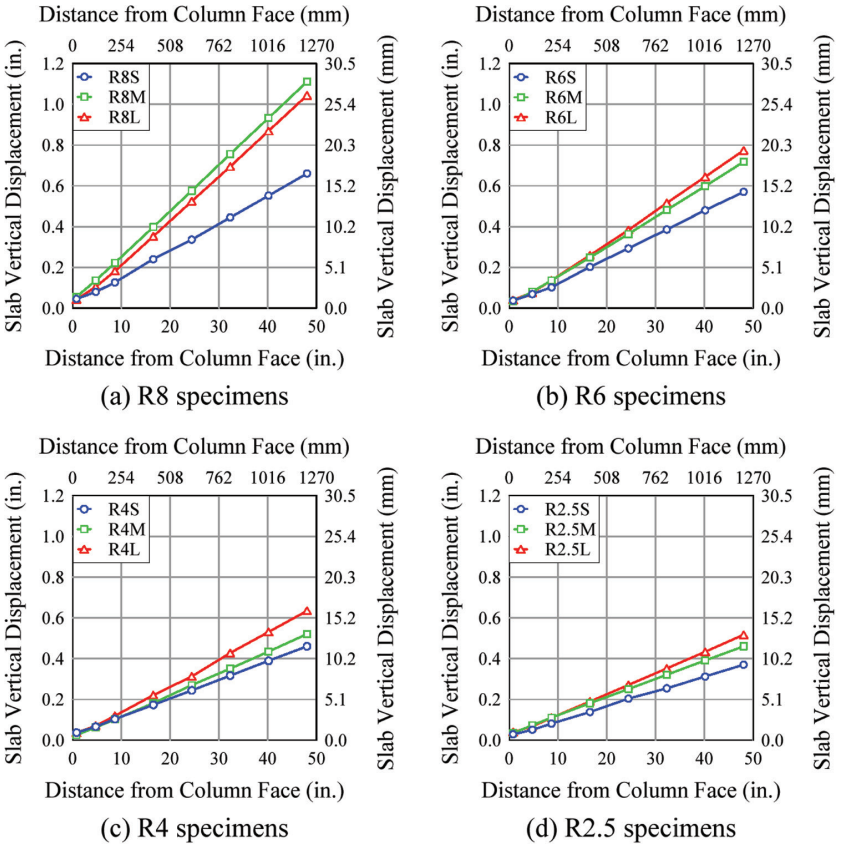

Fig. 9—Slab vertical displacement profile.

and Technology. He is a member of ACI Subcommittee 318-J, Joints and Connections, and Joint ACI-ASCE Committee 352, Joints and Connections in Monolithic Concrete Structures.

Shang-Wei Lin *is a Design Engineer at TH Tsai and Associates, Taipei, Taiwan. He received his BS in civil engineering from National Chung Hsing University, Taichung, Taiwan, and his MS in civil and construction engineering from National Taiwan University of Science and Technology.*

NOTATION

$A_{s,min}$ = minimum slab tensile flexural reinforcement area for two-way shear per ACI 318-19
b_o = perimeter of critical section
d = average slab effective depth
d_{agg} = nominal maximum coarse aggregate size
d_{max} = vertical displacement of column stub corresponding to V_{max}
E_s = modulus of elasticity of steel
f_c' = specified concrete compressive strength
f_{cm} = measured average concrete compressive strength
f_y = yield stress of longitudinal reinforcement
h_c = column dimension
k = size effect factor per Eurocode 2
k_{dg} = coefficient related to maximum aggregate per *fib* Model Code 2010
k_ψ = coefficient related to slab rotation per *fib* Model Code 2010
ℓ = diameter of support circle, 118.1 in. (3000 mm)
ℓ_n = two-way slab clear span
m = flexural capacity per unit length
m_{Ed} = average bending moment per unit length acting in support strip per *fib* Model Code 2010
m_{Rd} = design average flexural capacity per unit length per *fib* Model Code 2010
r_s = location of zero moment per *fib* Model Code 2010, approximately 0.22 times span
s = spacing of slab tensile flexural reinforcement
V_{ACI} = two-way shear strength per ACI 318-19
V_{EC2} = two-way shear strength per Eurocode 2
V_{fib} = two-way shear strength per *fib* Model Code 2010
V_{flex} = two-way shear strength associated with flexure-driven punching shear failure
V_{max} = specimen maximum two-way shear
v_{uv} = factored two-way shear stress on slab critical section as per ACI 318-19
α_s = constant to determine V_{ACI}, taken as 40 for interior connection
β = ratio of long to short dimensions of supporting column
ε_y = yield strain of longitudinal reinforcement
ϕ = strength reduction factor for shear
λ_s = size effect factor per ACI 318-19
ρ = slab tensile flexural reinforcement ratio, estimated as area of slab tensile flexural reinforcement divided by its spacing and slab thickness
ρ_l = equivalent tensile flexural reinforcement ratio per Eurocode 2
ρ_x, ρ_y = tensile flexural reinforcement ratio in x- and y-directions, respectively, per Eurocode 2, estimated as area of slab tensile flexural reinforcement divided by its spacing and average effective depth
ψ = slab rotation per *fib* Model Code 2010

REFERENCES

ACI Committee 318, 2019, "Building Code Requirements for Structural Concrete (ACI 318-19) and Commentary (ACI 318R-19) (Reapproved 2022)," American Concrete Institute, Farmington Hills, MI, 624 pp.

ASTM A370-20, 2020, "Standard Test Methods and Definitions for Mechanical Testing of Steel Products," ASTM International, West Conshohocken, PA, 50 pp.

ASTM C33/C33M-18, 2018, "Standard Specification for Concrete Aggregates," ASTM International, West Conshohocken, PA, 8 pp.

ASTM C39/C39M-14, 2014, "Standard Test Method for Compressive Strength of Cylindrical Concrete Specimens," ASTM International, West Conshohocken, PA, 7 pp.

ASTM C109/C109M-20, 2020, "Standard Test Method for Compressive Strength of Hydraulic Cement Mortars (Using 2-in. or [50-mm] Cube Specimens)," ASTM International, West Conshohocken, PA, 11 pp.

Dam, T. X.; Wight, J. K.; and Parra-Montesinos, G. J., 2017, "Behavior of Monotonically Loaded Slab-Column Connections Reinforced with Shear Studs," *ACI Structural Journal*, V. 114, No. 1, Jan.-Feb., pp. 221-232.

Deng, Q.; Yi, W.-J.; and Tang, F.-J., 2017, "Effect of Coarse Aggregate Size on Shear Behavior of Beams without Shear Reinforcement," *ACI Structural Journal*, V. 114, No. 5, Sept.-Oct., pp. 1131-1142.

Dilger, W.; Birkle, G.; and Mitchell, D., 2005, "Effect of Flexural Reinforcement on Punching Shear Resistance," *Punching Shear in Reinforced Concrete Slabs*, SP-232, M. A. Polak, ed., American Concrete Institute, Farmington Hills, MI, pp. 57-74.

EN 1992-1-1:2004, 2004, "Eurocode 2: Design of Concrete Structures – Part 1-1: General Rules and Rules for Buildings," European Committee for Standardization, Brussels, Belgium, 225 pp.

Fenwick, R. C., 1966, "The Shear Strength of Reinforced Concrete Beams," PhD thesis, University of Canterbury, Christchurch, New Zealand, 358 pp.

fib, 2013, "*fib* Model Code for Concrete Structures 2010," International Federation for Structural Concrete, Lausanne, Switzerland, 434 pp.

Gardner, N. J., 2011, "Verification of Punching Shear Provisions for Reinforced Concrete Flat Slabs," *ACI Structural Journal*, V. 108, No. 5, Sept.-Oct., pp. 572-580.

Giduquio, M. B.; Cheng, M.-Y.; and Dlamini, L. S., 2019, "Reexamination of Strength and Deformation of Corner Slab-Column Connection with Varied Slab Reinforcement Ratio," *ACI Structural Journal*, V. 116, No. 2, Mar., pp. 53-63. doi: 10.14359/51712276

Guandalini, S.; Burdet, O. L.; and Muttoni, A., 2009, "Punching Tests of Slabs with Low Reinforcement Ratios," *ACI Structural Journal*, V. 106, No. 1, Jan.-Feb., pp. 87-95.

Hawkins, N. M., and Ospina, C. E., 2017, "Effect of Slab Flexural Reinforcement and Depth on Punching Strength," *ACI*-fib *International Symposium on Punching Shear of Structural Concrete Slabs: Honoring Neil M. Hawkins*, SP-315, C. E. Ospina, D. Mitchell, and A. Muttoni, eds., American Concrete Institute, Farmington Hills, MI, pp. 117-140.

Joint ASCE-ACI Committee 426. 1973, "The Shear Strength of Reinforced Concrete Members," *Journal of the Structural Division*, V. 99, No. 6, June, pp. 1091-1187. doi: 10.1061/JSDEAG.0003532

Mitchell, D.; Cook, W. D.; and Dilger, W., 2005, "Effects of Size, Geometry and Material Properties on Punching Shear Resistance," *Punching Shear in Reinforced Concrete Slabs*, SP-232, M. A. Polak, ed., American Concrete Institute, Farmington Hills, MI, pp. 39-56.

Muttoni, A., 2008, "Punching Shear Strength of Reinforced Concrete Slabs without Transverse Reinforcement," *ACI Structural Journal*, V. 105, No. 4, July-Aug., pp. 440-450.

Sherif, A. G., and Dilger, W. H., 1996, "Critical Review of the CSA A23.3-94 Punching Shear Strength Provisions for Interior Columns," *Canadian Journal of Civil Engineering*, V. 23, No. 5, Oct., pp. 998-1011. doi: 10.1139/l96-907

Sherwood, E. G.; Bentz, E. C.; and Collins, M. P., 2007, "Effect of Aggregate Size on Beam-Shear Strength of Thick Slabs," *ACI Structural Journal*, V. 104, No. 2, Mar.-Apr., pp. 180-190.

Widianto, 2006, "Rehabilitation of Reinforced Concrete Slab-Column Connections for Two-Way Shear," PhD dissertation, The University of Texas at Austin, Austin, TX, 374 pp.

ACI STRUCTURAL JOURNAL TECHNICAL PAPER

Title No. 120-S99

Behavior of Large Pile Caps Subjected to Column Uplift

by Yasmeen Al-Sakin, Christopher Higgins, James Newell, and Kent Yu

The structural performance of four reinforced concrete pile cap specimens anchored by widely used proprietary high-strength threaded bars (HSTBs) and subjected to column uplift loads is investigated. The specimens were full-scale replicas of in-service foundations in terms of geometry, material properties, reinforcement details, and loading conditions. The study also included isolated pullout tests of HSTB anchorages. Two of the specimens were modified by increasing the embedment depth of the column anchor plate to assess effectiveness as a possible retrofit approach. Failure of all specimens was brittle without yielding of embedded reinforcing steel. Moreover, the ultimate pullout capacity of the anchors was not achieved in any of the specimens. ACI 318-19 provisions underestimated the concrete breakout capacity of all specimens and were unable to incorporate the beneficial effects of the column anchor plate modification as it only considered the anchor embedment length and edge distance as critical parameters for calculating strength.

Keywords: anchor; breakout strength; experimental test; failure; high-strength threaded bars (HSTBs); pile caps; uplift.

INTRODUCTION

Buildings loads are commonly transferred from columns to deep pile foundations through pile caps. Typically, pile caps resist compression loads but can be subjected to high uplift demands due to wind or seismic loading. While new designs of pile caps make use of recent advances in strut-and-tie modeling, as well as improved detailing, past designs used sectional methods and generally contained only top and bottom mats of reinforcing steel with straight-bar terminations. These older details may produce inadequate performance that could lead to failures during earthquakes. Evaluation, retrofitting, and rehabilitation of in-service structures has been the focus of an immense body of research to enhance seismic performance. However, almost no prior work has addressed large-sized pile caps subjected to column uplift due to physical limitations in laboratory facilities and capabilities. Thus, there is a critical lack of data on structural performance and failure mechanisms of pile caps, despite their critical contribution to overall building performance.

Background

Understanding pile cap performance under column uplift is crucial to ensuring safety and performance of structures with deep foundations during earthquakes. In most previous work, piles were considered to be the critical elements, and their performance under uplift and/or lateral loading was the subject of prior studies carried out by Gotman,[1] Dash and Pise,[2] Karthigeyan et al.,[3] Shanker et al.,[4] and Madhusudan Reddy and Ayothiraman.[5] Other researchers aimed at providing a better understanding of the connection between the pile and the pile cap. Shama et al.[6] studied the seismic performance of steel pile-to-pile cap connections commonly used in the eastern United States. They examined the response of the existing short pile embedment depth inside the cap beam by testing two specimens under cyclic lateral loading. Then they tested one specimen retrofitted according to a proposed theoretical model that assumed linear stress distribution through the embedment length. Finite element models corroborated their experimental findings. Xiao et al.[7] tested five full-scale H-shaped steel pile-to-pile-cap connections that replicate a typical bridge foundation to evaluate seismic performance. Two specimens were tested under vertical cyclic load, and two others under vertical load combined with cyclic lateral force. A fifth specimen was loaded by proportionally varying horizontal and vertical forces. The specimens showed brittle failure around the connections while supporting a significant amount of moment through the connections. Also, connections using two V-shaped anchorages were shown to develop full tensile capacity. The connection between the pile and pile caps was the focus of a large study by Iekel et al.[8] The authors addressed the lack of literature on the pile-to-pile cap connection and aimed at defining an effective and economical anchorage detail for the pile-to-cap connection subjected to uplift forces. They contributed new experimental data from 21 full-scale steel H-pile specimens with and without anchorages, and with different pile embedment depths under tension. High connection capacity was found to be related to extending the embedment length above the lower reinforcement mat, while concrete cracking caused loss of bond in the connections.

The study of vintage pile caps that incorporate realistic details and properties is imperative to accurately assess their structural performance, identify deficiencies, and develop retrofit strategies for remediation. However, this remains unexplored, and no studies of pile cap tests under column uplift are found in the literature to date. Further, there is limited design guidance available in U.S. normative documents including the *Design Guide for Pile Caps* from CRSI[9] and ACI 318-19.[10] Therefore, this work presents a completely new set of experimental data using full-scale and realistically proportioned pile caps subjected to column uplift, to elucidate structural behavior, enable comparisons with available design recommendations, and allow the development of new analysis and remediation designs.

ACI Structural Journal, V. 120, No. 6, November 2023.

MS No. S-2022-323.R1, doi: 10.14359/51739088, received December 25, 2022, and reviewed under Institute publication policies.

RESEARCH SIGNIFICANCE

This study provides the engineering community with the first set of experimental data on the behavior of full-scale pile caps subjected to column uplift. Four specimens were constructed, instrumented, and tested to failure. The pile cap specimens replicated an existing foundation in terms of geometrical aspects, material properties, reinforcement details, loading conditions, and support configurations. A retrofitting strategy was investigated using two of the specimens. The concrete breakout strength of the steel anchors that connect the pile to the cap was evaluated according to ACI 318-19 provisions and discussed in comparison to the obtained tests results.

EXPERIMENTAL INVESTIGATION

This study consists of three pile-to-pile cap anchorage specimens and four reinforced concrete pile cap specimens subjected to uplift loading to evaluate their structural performance. All specimens were full-scale replicas that represent the geometry, reinforcing details, materials properties, and the number and layout of piles of an in-service deep foundation for a nine-story steel-braced frame hospital located in a high-seismic zone in Portland, OR. The hospital was designed according to the seismic design standards for an essential facility in 1982. The pile caps were designed to withstand uplift loads using widely used proprietary high-strength threaded bar (HSTB) rock anchors attached to anchor plates within the caps. Some uplift resistance could also be provided by four No. 4 (13 mm) reinforcing bar anchors welded directly to the pipe piles and embedded into the cap, though these were designed to resist column compression. The naming convention of the pile cap specimens is based on the number of steel pipe piles as the first indicator and the number of tension rock anchors as the second indicator. Two specimens were modified by moving the column anchor plate to the bottom of the specimen and under the lower reinforcement mat to model a possible retrofit approach. These specimens were denoted with the letter "R". The specimens, identified as PC6-2, PC8-4, PC8-4R, and PC12-10R, had two, four, four, and 10 rock anchors, respectively. The specimens were rectangular-shaped pile caps reinforced by ASTM A615/A615M-18e1[11] Grade 60 (420 MPa) upper and lower reinforcing steel mats that consisted of uniformly distributed straight steel reinforcing bars in both longitudinal and transverse directions. The assembly of each rock anchor consisted of a 1-3/8 in. (35 mm) diameter ASTM A722/A722M-15[12] Grade 150 (1034 MPa) HSTB, connected to 1 x 7 x 7 in. (25.4 x 178 x 178 mm) ASTM A36/A36M-19[13] steel anchor plate with a standard hex nut. The anchor plate was positioned at 24 in. (610 mm) from the bottom of the pile cap and held in place by a 0.5 in. (12.7 mm) tall HSTB coupler nut, cut from a full-sized coupler. The HSTB was placed inside a 10 in. (254 mm) diameter Schedule 40 polyvinyl chloride (PVC) pipe and built-up plywood plate to simulate the steel pipe pile and steel bearing plate of the original design, as they do not contribute structurally during uplift.

In these experiments, the steel wide flange column was not modeled as it only transfers uplift forces to the pile cap (no shear or moment) through threaded anchor rods attached to the column base plate. The threaded rods were connected in the pile cap with a 1.75 in. (44.5 mm) thick ASTM A36[13] steel embedment plate. The threaded rods were 1.5 in. (38 mm) diameter and extended above the surface of the pile cap. The threaded rod was connected to a loading beam that when engauged, produces tension in the rods, as though loaded through the column base plate. In Specimen PC6-2, the anchor plate was embedded at 25.5 in. (648 mm) and connected to four ASTM A449-14[14] steel threaded anchor rods. In Specimen PC8-4, the anchor plate was embedded at 29.5 in. (749 mm) and connected to eight ASTM A449 steel threaded anchor rods. In the retrofitted Specimens PC8-4R and PC12-10R, the anchor plate was placed at the bottom of the pile cap and connected to eight and 12 ASTM A193/A193M-17 Grade B7[15] steel threaded anchor rods, respectively, because higher capacities were expected that could have resulted in yielding of the lower-grade A449 threaded rod.

For pullout tests, six specimens were constructed in a 36 x 120 x 300 in. (914 x 3048 x 7620 mm) concrete footing, cast in an excavation with native soil at the bottom and side edges of the footing, to realistically reflect in-place conditions. The concrete edge and cover dimensions were the same as those used in the pile caps and the individual specimens were spaced to prevent overlap of potential failure surfaces. The aforementioned rock anchor assembly was used in an inverted orientation for three specimens: A, B, and C. Specimen A was loaded monotonically, while Specimens B and C were loaded cyclically. The other three specimens were pipe pile specimens reinforced with ASTM A615[11] Grade 40 (280 MPa) No. 4 (13 mm) steel reinforcing bars that were also subjected to pullout forces. These were originally designed to carry gravity loads and were found to provide little uplift resistance. The full details and results of pipe pile pullout tests are not included in this paper due to space limitations. The concrete footing was reinforced with ASTM A615[11] Grade 60 (420 MPa) No. 7 (22 mm) straight reinforcing steel rebars uniformly distributed at 6 in. (152 mm) on the center in both directions. Details of the tested specimens and the HSTB rock anchor are listed in Table 1 and illustrated in Fig. 1 and 2, respectively.

Material properties

The in-place foundations replicated in the present study have been in service for over three decades. Consequently, their concrete compressive strength has increased significantly above the specified design value. To accurately represent the strength gained over time, concrete cores from in-place pile caps were taken and tested as part of a previous study.[16] Based on the core results, a new mixture was designed to gain the high concrete strengths in less than 28 days while maintaining the same aggregate size, types, and distribution as the in-place materials. The concrete was provided by a local ready-mix supplier for all specimens. Concrete cylinders were made according to ASTM C31/C31M-18b[17] and tested in accordance with ASTM C39/39M-18[18] and ASTM C496/496M-17[19] to obtain the compressive and split tensile strength on the day of the test.

Material properties of reinforcing steel, HSTBs, and threaded anchor rods were established by conducting

Table 1—Specimens details

Specimen ID	No. of pipe piles	No. of rock anchors	Specimen dimensions H x W x L, in. (mm)	Column embedment plate dimensions H x W x L, in. (mm)	Column embedment plate location*, in. (mm)	Column embedment plate threaded rods†
PC6-2	6	2	40 x 72 x 114 (1016 x 1829 x 2896)	1.75 x 12 x 14 (44.5 x 305 x 356)	25.5 (648)	Four ASTM A449 steel
PC8-4	8	4	44 x 102 x 114 (1118 x 2591 x 2896)	1.75 x 14 x 29.5 (44.5 x 356 x 749)	29.5 (749)	Eight ASTM A449 steel
PC8-4R	8	4	44 x 102 x 114 (1118 x 2591 x 2896)	1.75 x 14 x 29.5 (44.5 x 356 x 749)	41.75 (1509)	Eight ASTM A193-B7 steel
PC12-10R	12	10	56 x 114 x 156 (1422 x 2896 x 3962)	1.75 x 25 x 28 (44.5 x 635 x 711)	53.75 (1365)	12 ASTM A193-B7 steel

*From top of pile cap.

†1.5 in. (38 mm) diameter.

tensile tests according to ASTM E8/E8M-16a[20] and ASTM A370-17a[21] using 2 in. (51 mm) gauge lengths. Full-diameter samples were used for No. 6, 7, and 8 (19, 22, and 25 mm) reinforcing bars, while HSTBs, threaded anchor rods, and No. 9 and 11 (28.6 and 35.8 mm) reinforcing bars were machined into the 505 specimen size. The measured mechanical properties of concrete on the test day, reinforcing steel, HSTBs, and threaded anchor rods are summarized in Table 2.

Specimen construction and instrumentation

All specimens were constructed and tested at Oregon State University's Structural Engineering Research Laboratory. Steel reinforcement, HSTB anchors, and column anchor plates were placed in the formwork of pile cap specimens before concrete casting. The formwork used 3/8 in. (9.5 mm) diameter fiber-reinforced polymer (FRP) rods to resist the hydrostatic force induced by the placement of the fresh concrete. Those rods were inserted inside polypropylene tubes to prevent bonding to the concrete. Due to the excessive size of Specimen PC12-10R, a grid of smooth 1/2 x 1/4 (12.7 x 6.35 mm) ASTM A36[13] steel bars was used to maintain the geometry of the HSTBs during concrete placement. The bars were tack welded to anchor plates and cut flush at the formwork surface. The steel bars were located above the potential concrete failure planes and did not contribute to the specimen strength. After curing, the FRP rods were removed where possible, and the specimens were positioned onto a steel reaction frame to conduct the test.

For the pullout tests, the reinforcement mat and three rock anchor assemblies were placed inside the excavated footing, and concrete was placed and consolidated around them. After curing, the test setup was built around each specimen to apply the tension force. For pullout tests, three displacement sensors were placed on the concrete surfaces around the anchors, and two displacement sensors were attached to opposite sides of the flat portion of the HSTB to measure the axial elongation and remove bending effects. Load cells attached to the hydraulic loading jacks directly measured the applied force.

Pile cap specimens were instrumented with 14 to 65 sensors to measure the motion and strain of the HSTBs, reinforcement strain, the motion of concrete surfaces, and the applied load. Each HSTB was instrumented by two displacement sensors placed oppositely at the lower end and one sensor connected to the embedded end through a PVC pipe that had been connected to the bar before the placement of concrete. This sensor was attached using a rare earth magnet that was placed on the embedded HSTB using a brass wire which allowed the monitoring of the bar's motion throughout the test. Strains in each HSTB and various locations on the lower and upper reinforcing steel mat were measured with strain gauges. The concrete motion was also monitored using one displacement sensor placed near each HSTB on the upper and lower surfaces, as well as under the column in each specimen.

The fully detailed instrumentation plans for pullout and pile cap specimens can be found in Higgins.[22-26] Data from the sensors were captured and recorded using a commercially available data acquisition system. Visible cracks and evident changes were monitored and documented throughout the test.

Test setup and methodology

The experimental testing setups for the pile cap specimens are illustrated in Fig. 3. After curing, pile cap Specimens PC6-2, PC8-4, and PC8-4R were placed on two parallel W27x258 beams, while Specimen PC12-10R was placed on four parallel W27x258 beams. The W27x258 reaction beams were attached to the embedded HSTB rock anchors with four 1.25 in. (31.8 mm) diameter ASTM A193-B7 threaded rods, using a 2 x 12 x 12 in. (51 x 305 x 305 mm) ASTM A36 steel plate and a 1.5 x 7 x 7.5 in. (38 x 178 x 191 mm) ASTM A36 steel spherical nut plate to develop the full strength of each HSTB. To apply the column uplift load, specimens PC6-2, PC8-4, and PC8-4R were connected to a W33x291 steel loading beam by 1.5 in. (39 mm) diameter ASTM A193-B7 threaded rods that were attached to column anchor rods using heavy hex coupler nuts. The load was applied using two hydraulic cylinders of 800 kip (3559 kN) nominal capacity, placed under the loading beam, and reacted against a W30x261 spreader beam, which distributed the load to W27x258 reaction beams.

In Specimen PC12-10R, the 1.5 in. (38 mm) diameter ASTM A193-B7 threaded rods were used to connect the column anchor rods to twin W33x291 steel loading beams

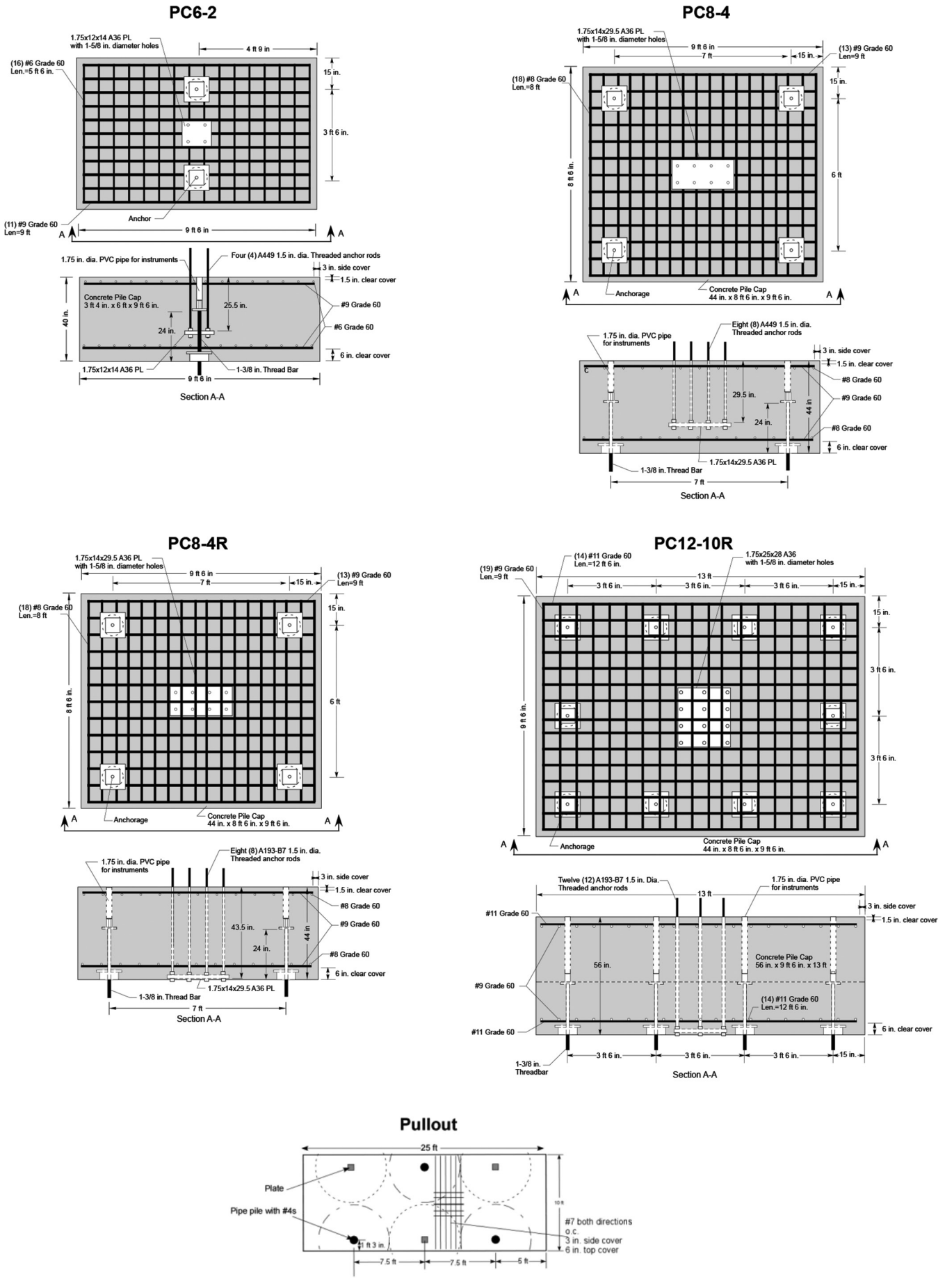

Fig. 1—Specimen details. (Note: 1 in. = 25.4 mm.)

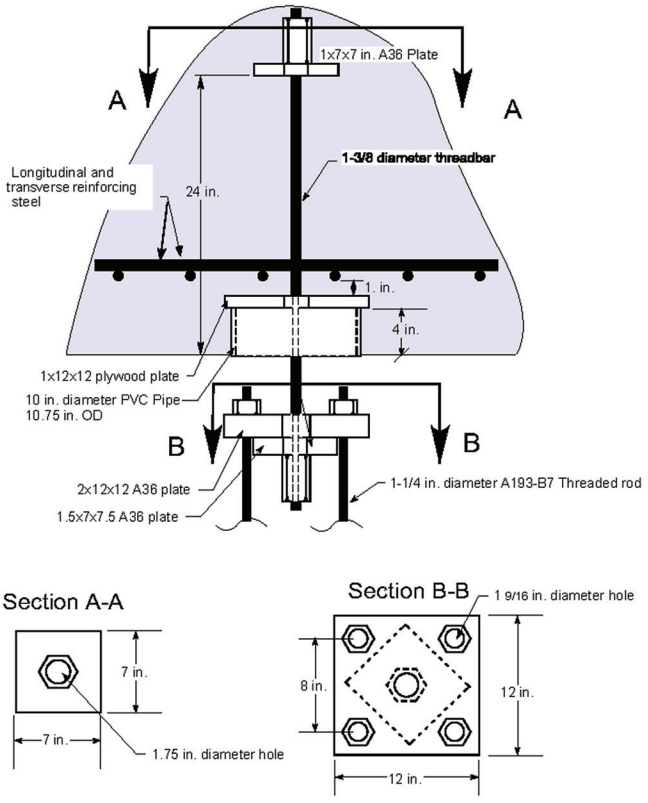

Fig. 2—HSTB tension anchor details. (Note: 1 in. = 25.4 mm.)

using heavy hex nuts. A column section of W14x156 was placed under the twin loading beams to transfer the hydraulic cylinder forces to the reaction members. The 800 kip (3559 kN) nominal capacity hydraulic cylinders were reacted against W30x261 spreader beams and W12x120 transfer beams, which distributed the loads to W27x258 reaction beams. The location of the end reactions for the W27x258 beams on the simple span W12x120 transfer beams was intended to produce reaction forces in the underlying W27x258 beams such that the East and West W27x258 beams, which were attached to three HSTB tension anchors each, would each carry three-tenths of the total upward force, while the center W27x258 beams, which were connected to two HSTB tension anchors each, would each carry two-tenths of the total upward force, based on a rigid pile cap assumption of the indeterminate system. The hydraulic cylinder force was measured directly by 1000 kip (4448 kN) capacity load cells.

The test setup for the pullout test was built around the HSTB specimens that were embedded in the concrete footing. The HSTB was connected to a W33x291 loading beam using four 1.5 in. (38 mm) diameter ASTM A193-B7 threaded rods that were connected to 1.5 in. (38 mm) thick ASTM A36 steel loading plate with spherical nut and matching washer plate. The uplift load was applied using two 800 kip (3559 kN) capacity hydraulic cylinders and measured using two 150 kip (667 kN) capacity load cells. The forces were transmitted to the concrete surface by reacting against two W12x120 steel beams that were placed 7.5 ft (2286 mm) from the center of the anchors to permit a free-field formation of the breakout surface.

All specimens were controlled manually to create the applied uplift force. Pile cap Specimens PC6-2, PC8-4, and PC8-4R were subjected to 150 kip (667 kN) increment cycles of loading and unloading until failure. Specimen PC12-10R was subjected to three stages of loading; the first stage was with 150 kip (667 kN) increment of loading and unloading cycles until a force level of 600 kip (2669 kN). In the second stage, the increment was increased to 300 kip (1334 kN), and the specimen was loaded to 900 kip (4003 kN). In the third and final stage, the specimen was unloaded and loaded to failure.

For the pullout tests, Specimen A was tested using three loading and unloading cycles to balance the deformation between the two hydraulic cylinders. The other two specimens were tested cyclically, without full reversal, with 100, 30, and 10 cycles of loading and unloading at force levels corresponding to 0.25, 0.375, and 0.5 times the ultimate load obtained from Specimen A, respectively. After completing the cyclic loading, Specimen B and Specimen C were loaded monotonically until failure.

EXPERIMENTAL RESULTS

Three HSTB anchors and four pile cap specimens were subjected to uplift loading. The observed cracking load, ultimate load, vertical displacement of the concrete top surface, yielding of the reinforcement, and failure mode are reported in Table 3 and the results are discussed as follows.

Pullout specimens

Pullout tests were carried out to examine the performance of three HSTB anchors under isolated loading conditions and in realistic configurations representative of existing pile caps including edge distance to the soil interface. Cyclic loading did not affect the strength nor the behavior of Specimens B and C compared to Specimen A, which was tested almost monotonically. The three HSTBs exhibited linear response until approximately 190 kip (845 kN) when nonlinear behavior initiated and continued until specimen fracture. The ultimate strength was 244.4, 248.2, and 250 kip (1087, 1104, and 1112 kN) for Specimens A, B, and C, respectively, with an average of 247 kip (1099 kN) and a coefficient of variation of 1.2%. The average concrete surface displacement was 0.035 in. (0.89 mm) at failure with narrow coalescence of shrinkage cracks and without the formation of a concrete pullout prism. The applied tension load versus the average displacement of the HSTBs are shown in Fig 4. For Specimens B and C, only the monotonic tests to failure are presented herein; further details could be found in Higgins.[22-26] In addition to the load cell measurement, the force in the individual HSTBs was also computed based on strain gauge measurements. For each bar, the strains from two strain gauges, placed on opposite sides of the flat faces of the bar at the same location along the length, were averaged and used to estimate the uniaxial force in the elastic range according to Hook's law by taking the modulus of elasticity as 29,000 ksi (200 GPa) and nominal bar area as 1.58 in.^{2} (1019 mm^2). The HSTB force measured by the load cells was in good agreement with the force calculated from the strain gauges, which indicates the efficiency of using the

Table 2—Material properties

Specimen ID	Concrete		Reinforcement steel				HSTBs*			Column embedment plate threaded rods		
	f_c', psi (MPa)	f_t, psi (MPa)	Reinforcing bar No.	f_y, ksi (MPa)	f_u, ksi (MPa)	%	f_y, ksi (MPa)	f_u, ksi (MPa)	%	f_y, ksi (MPa)	f_u, ksi (MPa)	%
PC6-2	6153 (42.4)	443	6	61.8 (426)	95.1 (656)	31	135.8 (936)	160.3 (1105)	14.5	88.1† (607)	120.3† (829)	21
		(3.1)	9	68.3 (471)	108.6 (749)	22						
PC8-4	6259 (43.2)	509 (3.5)	8	69.8 (481.3)	101.3 (698)	36				88.1† (607)	120.3† (829)	21
			9	68.3 (471)	108.6 (749)	22						
PC8-4R	6516 (45)	472 (3.3)	8	62.6 (432)	91.9 (634)	37				‡		
			9	68.3 (471)	108.6 (749)	22						
PC12-10R	5954 (41)	417 (2.9)	9	71.1 (490)	109.8 (757)	22				‡		
			11	73.4 (506)	107.3 (740)	24						
Pullout	6146 (42.4)	474 (3.3)	7	68.6 (473)	99.7 (687)	34				NA		

*1-3/8 in. (35 mm) diameter.

†1.5 in. (38 mm) diameter ASTM A449 steel.

‡1.5 in. (38 mm) diameter ASTM A193-B7 steel.

strain gauge deployment to predict the HSTB forces in the pile cap test specimens. Accordingly, strain gauges measurements were used for the subsequent pile cap tests to characterize the force distribution in the rock anchors.

Pile cap specimens

The four pile cap specimens were subjected to column uplift loading through the column embedment plate until failure. Plots of applied load and the corresponding vertical displacement of the concrete top surface are shown in Fig. 4. Schematic and photographic illustrations of the cracks are shown in Fig. 5. The first two specimens, PC6-2 with two tension anchors and PC8-4 with four tension anchors, exhibited an initial linear elastic response with slight nonlinearity preceding failure. The ultimate load was 391 kip (1739 kN) for Specimen PC6-2 and 696 kip (3096 kN) for Specimen PC8-4. Failure was brittle and controlled by the breakout of the column embedment plate that was embedded at approximately 65% of the specimens' heights. At failure, the top surface was displaced 0.32 in. (8.1 mm) for PC6-2 and 0.21 in. (5.3 mm) for PC8-4. No significant cracking or visible deformation was observed during both tests until the moment of failure. After failure, the top portion of the two specimens was completely separated from the bottom portion, forming a truncated pyramidal surface that initiated at the column embedment plate and propagated toward the plates, as can be seen in Fig. 5.

As part of this study, a possible retrofitting approach would be to excavate under the pile cap and anchor the column with a new embedment plate under the lower reinforcing mat using longer rods. This was experimentally investigated by increasing the embedment length of the column embedment plate to include the full height of Specimens PC8-4R and PC12-10R. Thus, Specimen PC8-4R was identical to Specimen PC8-4 and only differed in two aspects; placing the column embedment plate at the bottom of the pile cap, and replacing the ASTM A449 threaded anchor rods with ASTM A193-B7 threaded rods, as mentioned earlier.

Specimen PC8-4R also showed initial linear elastic behavior followed by nonlinear response at approximately 764 kip (3398 kN). The ultimate capacity of Specimen PC8-4R was higher than the similar unretrofitted Specimen PC8-4 by 30% with a total load of 909 kip (4043 kN) and 0.32 in. (8.1 mm) displacement of the concrete top surface at failure. The specimen did not show visible cracks prior to failure, except for coalescence of shrinkage cracks that appeared on the sides and propagated from the top surface to the bottom at 700 kip (3113 kN). The failure was initiated at the southeast HSTB anchor and advanced to the northeast anchor, marking the failure of the specimen by the tension breakout of those two anchors.

In the three specimens, PC6-2, PC8-4, and PC8-4R, the HSTB anchors were equally distanced from the column in the center and therefore equally loaded. That was observed from the strain gauge measurements on each anchor, which showed similar force among the anchors through the elastic phase. Moreover, displacement measurements at the top and bottom of each HSTB also showed similar responses among the locations of the HSTBs.

For Specimen PC12-10R, the column embedment anchor plate was at the bottom and under the reinforcement lower mat, as in Specimen PC8-4R. With 10 HSTB anchors

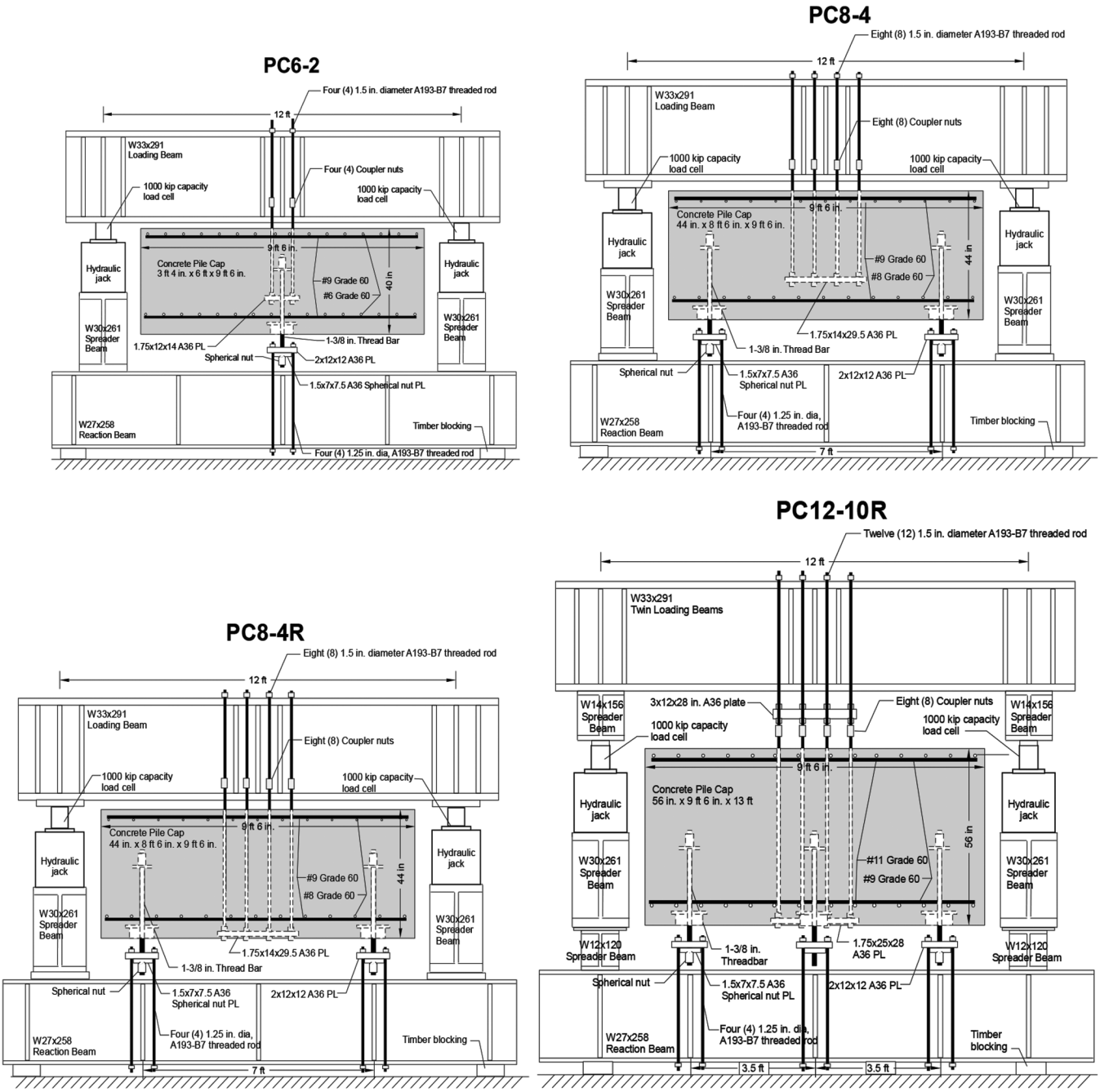

Fig. 3—Elevation view of experimental setups. (Note: 1 in. = 25.4 mm; 1 kip = 4.448 kN.)

distributed around the perimeter, Specimen PC12-10R was the largest and most complex specimen, weighing over 40 tons (36,287 kg). Though the test setup was designed to produce equal reactions of one-tenth the applied force to each anchor, the actual distribution was nonuniform and varied among the anchors, with the corner anchors carrying the highest loads due to the flexibility of the heavy steel reaction beams. The load percentage carried by each anchor with respect to the applied uplift load is shown at each anchor location in Fig. 6. As seen herein, the Northeast anchor (NE) carried the highest percentage of the column load until the maximum load level was achieved when concrete breakout failure of the corner anchor was observed. The force in the anchor dropped momentarily and was picked up by the adjacent two Eastside HSTBs (ECL and SE) simultaneously, which, in turn, unloaded as the concrete around them failed, resulting in one-way diagonal tension failure of the concrete along the east side of the specimen engaging all three HSTBs. The initial behavior was elastic with the formation of the first crack approximately 1400 kip (6228 kN) on the north face. The specimen reached the nominal capacity of the test setup at approximately 1600 kip (7117 kN) with no pronounced cracks or visible physical deformation. The load was being held to start the unloading sequence when the failure occurred abruptly at a load of 1576 kip (7010 kN) and a top concrete surface displacement of 0.23 in. (5.8 mm).

Yielding of reinforcing steel

Strains in the instrumented steel reinforcing bars were low, and yielding was not observed in any of the specimens.

Table 3—Experimental results

Specimen ID		Experimental cracking load, kip (kN)	Experimental ultimate load, kip (kN)		Displacement, in. (mm)		Reinforcement yielding (Yes/No)	Failure mode
Pullout	A	Not observed	244.4 (1087)	Avg: 247 (1099)	0.036 (0.9)	Avg: 0.035 (0.89)	NA	Fracture of HSTB
	B	Not observed	248.2 (1104)		0.057 (1.4)		NA	
	C	Not observed	250 (1112)		0.013 (0.3)		NA	
PC6-2		Not observed	391 (1739)		0.32 (8.1)		No	Breakout of column embedment plate
PC8-4		Not observed	696 (3096)		0.21 (5.3)		No	Breakout of column embedment plate
PC8-4R		700 (3114)	909 (4043)		0.32 (8.1)		No	Breakout of two anchors
PC12-10R		1400 (6228)	1576 (7010)		0.23 (5.8)		No	One way diagonal-tension

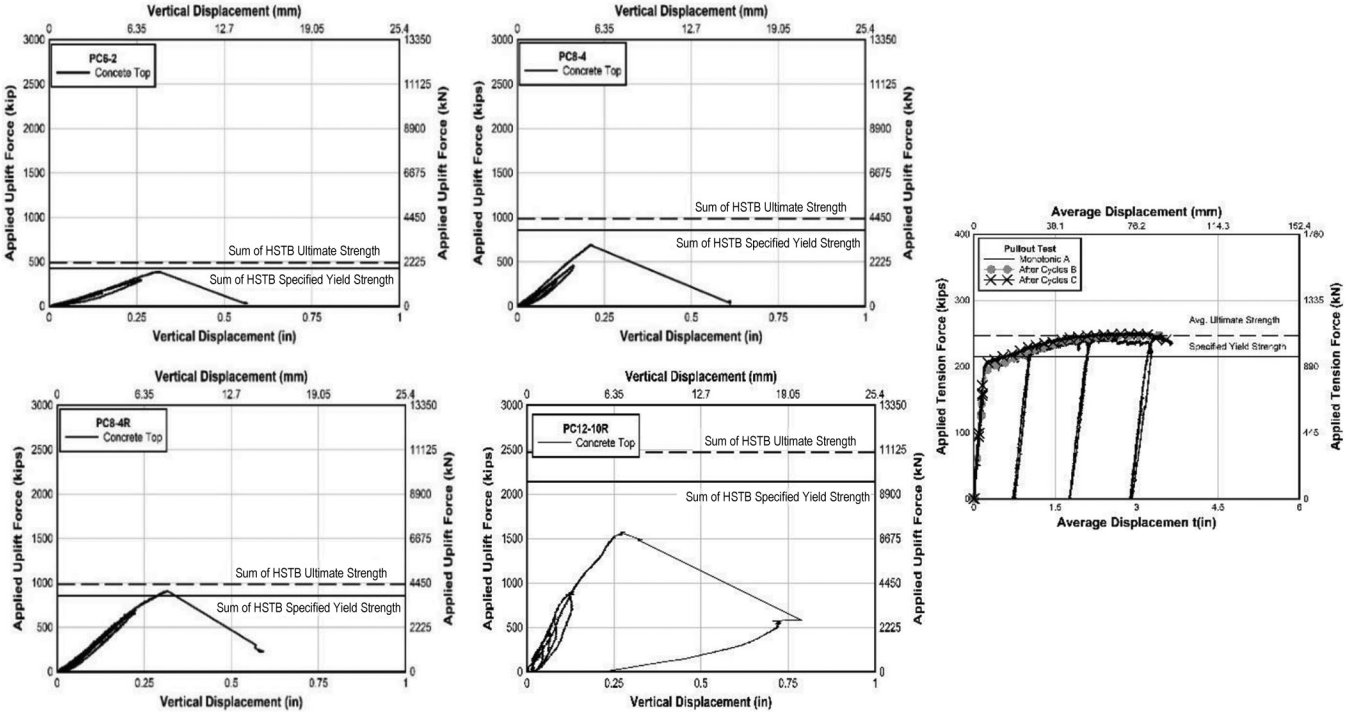

Fig. 4—Load-displacement responses for all specimens.

The reinforcing steel bars with the highest stresses relative to the yield stresses are shown in Fig. 7. Specimen PC6-2 reinforcing steel stresses on the bottom mat were very low until the peak load. In Specimen PC8-4, the instrumented reinforcing bars were at the upper mat and showed low stress until approximately peak load, where the stress reached half the yielding stress in bar No. 9 (28.65 mm). In the retrofitted specimen, PC4-8R, both reinforcement mats were instrumented. Low stress dominated the bottom mat, while the stress in the top mat increased at 450 kip (2002 kN) in bar No. 9 (28.65 mm), followed by bar No. 8 (25.4 mm) at a load level of 550 kip (2447 kN). At 700 kip (3114 kN), a rapid increase in stress was recorded in both reinforcing bars as a result of the observed macrocracking. Similar to the other specimens, the stresses were also very low in the bottom mat of Specimen PC12-10R. However, the stress of bar No. 11 (35.8 mm) on the top mat increased at approximately 815 kip (3625 kN). This growth in stress was not accompanied by any observable macrocracking on the concrete surface, which indicates that some microcracking had already taken place in the specimen before the visible appearance of the cracks at a load of 1400 kip (6228 kN).

COMPARISON WITH PREDICTED STRENGTHS

To evaluate the experimental results, pile cap strength was predicted using two approaches: the HSTB anchor strength that was observed in the pullout tests ($P_{u,Dy}$), and the concrete breakout strength for anchors under tension according to the ACI 318-19[10] provisions ($P_{B,Anchor}$). The predicted strengths were compared to the experiment's ultimate load ($P_{u,EXP}$) and the results are summarized in Table 4. The HSTB's observed

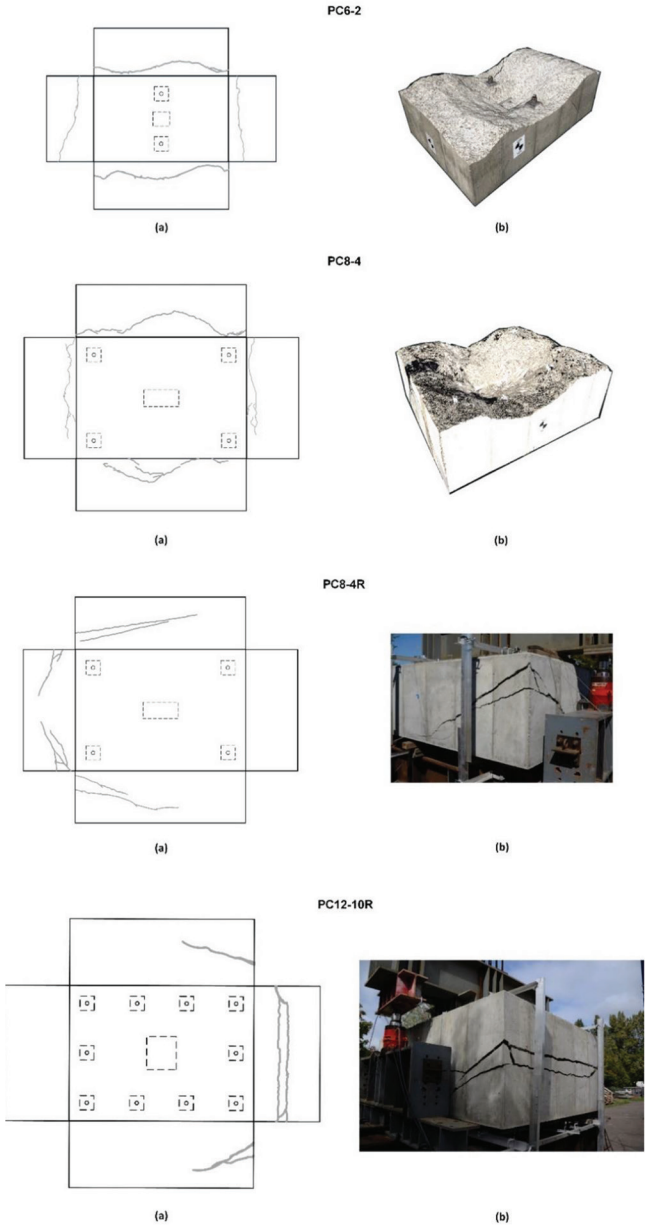

Fig. 5—(a) Schematic crack patterns; and (b) specimens after failure.

yield strength ($P_{y,Dy}$) and the concrete breakout strength for the column ($P_{B,Column}$) are also reported in Table 4.

The HSTB anchors were assumed to reach the average of the measured individual pullout test capacities of 247 kip (1099 kN). Hence, based on the number of anchors used in each pile cap specimen, the predicted strength was computed by summing the full capacities of two, four, four, and 10 anchors for Specimens PC6-2, PC8-4, PC8-4R, and PC12-10R, respectively. However, none of the tested four pile caps reached the capacity of the HSTB anchors, and thus, the value would be an expected upper bound if controlled by the HSTBs.

Based on ACI 318-19,[10] concrete breakout failure for cast-in steel anchors under tension is assumed to occur in the form of prism spreading from the anchor at 35 degrees, once tensile stress on the concrete surrounding the anchor is sufficiently high to cause the fracture.[27] The basic tensile concrete breakout strength of a single anchor N_b with effective embedment length h_{ef} ranging between 11 and 25 in. (279 and 635 mm) is calculated as follows

$$N_b = 16\lambda_a\sqrt{f_c'}(h_{ef})^{5/3} \quad (1)$$

where λ_a is the lightweight concrete modification factor, taken as 1 for the normalweight concrete used herein. Because the failure angle of the breakout concrete prism is 35 degrees, the failure surface extends to $1.5h_{ef}$ from the center of the anchor, resulting in a projected failure area for a single anchor A_{Nco} of $9h_{ef}^2$. However, if the anchor is at a distance less than $1.5h_{ef}$ from an edge, the capacity of the anchor is reduced as there is not enough edge distance for the failure prism to be fully mobilized. In this study, each anchor was positioned at less than $1.5h_{ef}$ away from at least one edge of the specimen. To account for this, the basic tensile concrete breakout strength of a single anchor N_b is multiplied by the ratio of the available projected breakout area of a group of anchors A_{NC} to the assumed projected area of a single anchor A_{Nco}, as

$$N_{cb} = \frac{A_{Nc}}{A_{Nco}}\psi_{ed}\psi_{c,N}\psi_{cp,N}N_b \quad (2)$$

where $\psi_{c,N}$ is the crack modification factor and is unity for cracked concrete; $\psi_{cp,N}$ is the pullout modification factor and is also taken as unity for cracked concrete; and ψ_{ed} is the modification factor for an anchor near one or more edges. If the minimum distance from the center of the anchor to the edge of concrete $c_{a,min}$ is less than $1.5h_{ef}$, then ψ_{ed} is calculated according to Eq. (3) as

$$\psi_{ed} = 0.7 + 0.3\frac{h_{ef}}{1.5} \quad (3)$$

In addition to the concrete breakout capacity for the HSTB anchors, the concrete breakout capacity of the column embedment plate was calculated, assuming it acted as one large anchor. Although the column embedment length is outside the range prescribed for Eq. (1), Eq. (1) was applied nonetheless to examine how it might predict strength. Generally, the ACI 318-19 provisions for concrete breakout strength of the anchors underestimated the strength of all specimens, as shown in Table 4.

The strength of the individual HSTB anchors reached in the pullout test was higher than the predicted concrete breakout strength by 70%. The anchors in the pullout test were near one edge, which resulted in the application of the edge distance reduction factor from Eq. (3) to the calculated concrete breakout strength. In pile cap Specimen PC6-2, each anchor was near only one edge and each was able to reach the yield strength at approximately 80% of ultimate capacity before the breakout of the column embedment plate. Reaching the yielding threshold corresponded in the observed response nonlinearity prior to specimen failure. The experimental capacity was higher than the predicted concrete breakout capacity for the summation of two anchors by 33% and also higher than the predicted column

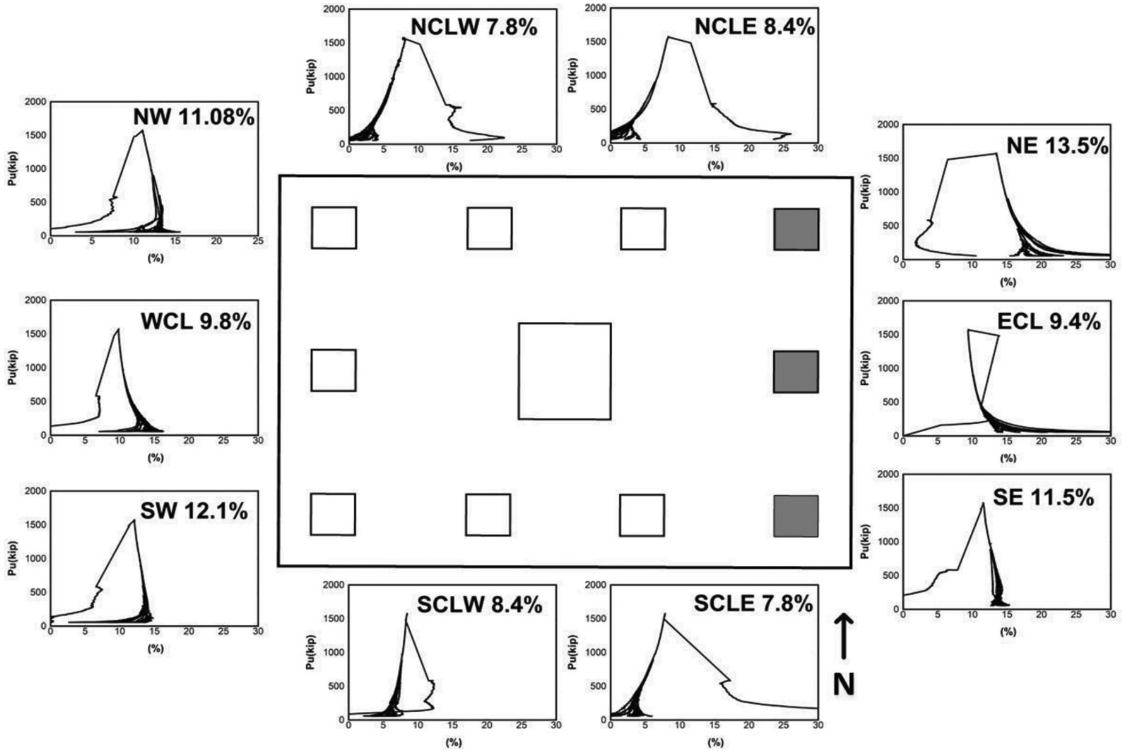

Fig. 6—Load distribution for Specimen PC12-10R (shaded areas indicate failed sections).

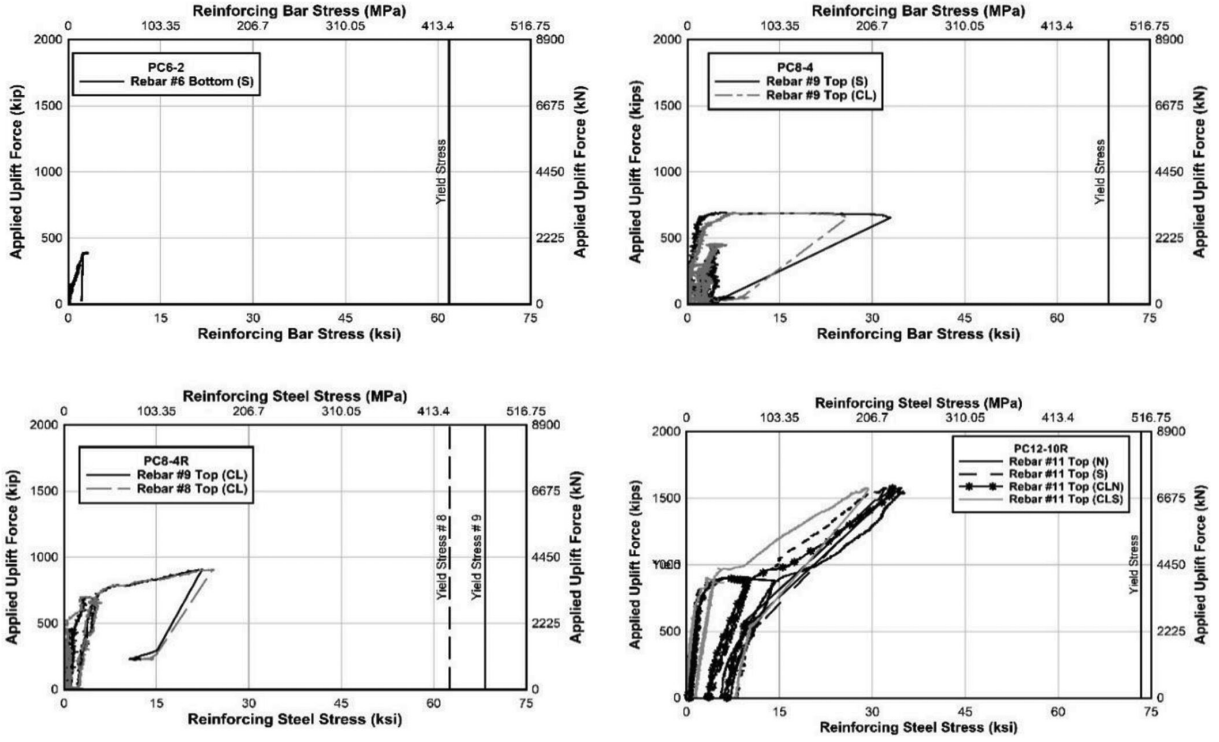

Fig. 7—Reinforcing steel stresses measured in pile cap specimens.

embedment plate breakout capacity by 53%. Anchors in Specimen PC8-4 were located at the corners; thus, the breakout occurred at only 70% of their ultimate capacity and 92% of their yield strength during the test. The experimental capacity was higher than the summation of the anchor concrete breakouts and column embedment plate breakout by 66% and 95%, respectively. In Specimen PC8-4R, increasing the column embedment length allowed development of direct compression struts in the concrete between the column embedment plate and anchor plates, which are well confined and allowed the specimen to achieve yield and approximately 92% of the summation of the ultimate capacity of the HSTBs. This noticeable positive effect of the retrofitting technique is not accounted for in the ACI 318-19

Table 4—Predicted strengths

Specimen ID	Experimente ultimate load $P_{u,EXP}$, kip	Sum of HSTB observed ultimate strength $P_{u,Dy}$, kip	$P_{u,EXP}/P_{u,Dy}$	Sum of HSTB observed yield strength $P_{y,Dy}$, kip	$P_{u,EXP}/P_{y,Dy}$	Concrete breakout for anchors $P_{B,Anchor}$, kip	$P_{u,EXP}/P_{B,Anchor}$	Concrete breakout for column embedment plate $P_{B,Column}$, kip	$P_{u,EXP}/P_{B,Column}$
Pullout	247	247	1.0	190	1.3	146	1.7	NA	NA
PC6-2	391	494	0.8	380	1.02	293	1.3	256	1.53
PC8-4	696	988	0.7	760	0.92	419	1.66	357	1.95
PC8-4R	909	988	0.92	760	1.2	427	2.13	454	2
PC12-10R	1576	Assumed uniform load distribution*						590	2.7
		2470	0.64	1900	0.83	1020	1.5		
		Measured load distribution†							
		1830	0.86	1407	1.1	756	2.1		

*10% of total applied load carried by each HSTB.

†Amount of applied load varies among HSTBs (refer to Fig. (6)).

Note: 1 kip = 4.448 kN.

approach for determining concrete breakout strength as it is a function of anchor embedment depth and edge distance. Therefore, the predicted concrete breakout capacity for anchors was overly conservative at approximately 47% of the experimental strength. The change in the embedment length of the column was considered in the calculation of the concrete breakout capacity of the column embedment plate; however, it was also very conservative as the experimental capacity exceeded the prediction by approximately 100%.

Specimen PC12-10R had one anchor at each corner and six anchors near the edges. The concrete breakout capacity for anchors near the corner was the controlling value for the other anchors as they have the lowest strength and once achieved the forces cannot be redistributed to the adjacent anchors. As mentioned earlier, the column uplift force was designed to be uniformly distributed to each of the 10 HSTB anchors. Each was expected to carry 10% of the applied force. Applying this idealized assumption, all anchors developed 64% of their capacity, limited by the breakout of the corner anchors, and none reached yield. The experimentally observed strength was 50% higher than the predicted strength based on the assumption of uniform force distribution. The forces in each of the HSTBs were measured by strain gauges and the force distribution was observed to be nonuniform and with the distribution shown in Fig. 6. According to the experimentally observed distribution, anchor NE was more highly stressed than the others, as it carried approximately 13.5% of the applied load. Based on the measured anchor force distribution, the highest loaded anchor was able to develop 86% of the ultimate capacity and reached yield, as can be seen in Table 4. However, due to strain hardening, the force increased in the anchor until corner concrete breakout was observed, leading to almost immediate failure of adjacent anchors on that side of the specimen. Considering the measured anchor load distribution, the unique percentage in each anchor was compared to the computed anchor breakout capacities and added together to predict failure. The experimental strength for PC12-10R was higher than the computed breakout strength using the measured anchor force distribution by more than 100%. Moreover, the concrete breakout capacity for the column embedment plate was highly underestimated at approximately only 37% of the experimental outcome. Comparisons between the experimentally observed and predicted strength are shown in Fig. 8.

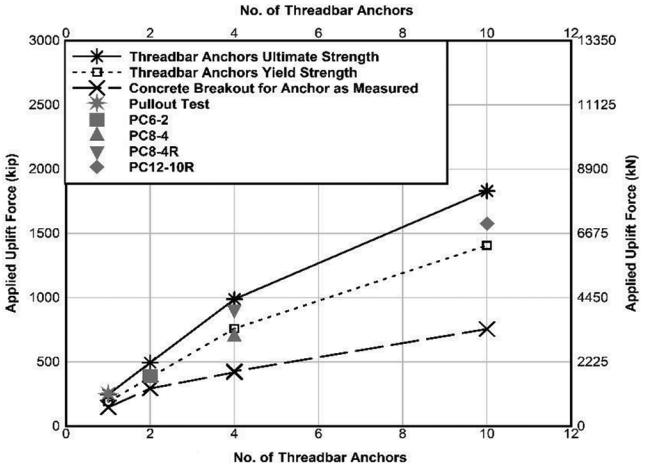

Fig. 8—Strength predictions for pile cap specimens.

Using the ACI 318-19[10] approach to estimate the uplift capacity of large pile caps specimens based on concrete breakout capacity for anchors in tension resulted in conservative predictions. This was strongly influenced by the location of anchorages close to the concrete edges. Evidently, this approach was unable to capture the positive effects of the retrofitting technique, which resulted in highly conservative predictions of strength for the retrofitted specimens. On the other hand, using the ultimate capacity of the HSTBs to predict the strength of the pile caps gave nonconservative results for all pile cap specimens as all failures were controlled by breakout. This disparity in strength predictions for pile caps under tension demonstrates a need for additional data to develop reliable and consistent analysis methods and improve designs. These methods are needed to consider large-sized, three-dimensional, deep reinforced

concrete elements subjected to indirect loads that produce disturbed strain fields with a response dominated by the tensile properties of the concrete to better predict strength.

CONCLUSIONS

The performance of four full-scale pile cap specimens representative of existing foundations was investigated. The specimens were supported by widely used proprietary high-strength threaded bar (HSTB) anchors and subjected to column uplift loading simulating a condition expected during seismic or wind events. The study also evaluated the tensile capacity of the individual anchors by conducting pullout tests of three HSTB anchor specimens. Additionally, a retrofitting concept consisting of increasing the column embedment plate depth was examined using two pile cap specimens. The experimental results were compared to the normative predicted concrete breakout strength of anchors and column embedment plates in tension. Conclusions based on the results of this study are made and summarized as:

- This is the first study to provide experimental results on the behavior of full-size reinforced concrete pile caps subject to column uplift.
- Failure of the four tested pile cap specimens was sudden and without any major cracking or visual distress. Specimens PC6-2 and PC8-4 failed by a breakout of the column anchor plate, PC8-4R failed by a breakout of two anchors located on one side of the specimen, while PC12-10R failed due to concrete rupture at a corner that propagated into one-way diagonal failure along one side of the specimen involving three adjacent anchors.
- The lack of observable damage, neither surface cracks nor concrete crushing, at the top surface of the failed pile cap specimens indicates that visual inspections of pile caps after a major earthquake may not be able to identify failed foundations. The broken-out column embedment plate, or anchor plates, may only be resting back into the socket from which they ruptured. Performance in the unknown failed state may be of significant concern for aftershock or future earthquake response of the building. It is possible that such conditions exist today in similar pile caps for buildings subjected to past strong shaking.
- Brittle failure was the dominant failure mode because yielding of reinforcement steel was not observed in any of the tested specimens, and steel stress in the reinforcement steel was overall low. The tensile properties of the concrete dominate the overall pile cap behavior and strength.
- The ultimate tensile capacity of the individual anchors observed in the pullout tests was not achieved in any of the pile cap specimens, as pile cap failures occurred at approximately 80%, 70%, and 92% of the anchor's ultimate capacity for Specimens PC6-2, PC8-4, and PC8-4R, respectively
- For Specimen PC12-10R, load distribution varied among the anchors, with the corner anchors carrying the highest proportion of the applied load. The specimen reached approximately 86% of the ultimate capacity of one of the corner anchors at failure, with that same anchor experiencing yielding prior to failure.
- Increasing the embedment depth of the column embedment plate as retrofitting strategy enhanced the capacity of Specimen PC8-4R by 30% compared to the similar unretrofitted Specimen PC8-4.
- The predicted concrete breakout strength for anchors in tension was excessively conservative and inconsistent among the tested specimens. That is because the provisions emphasize embedment length and edge distance and do not consider the potential beneficial effects of direct compression force transfer within the pile cap.
- Improved detailing should be considered for new designs that includes the addition of vertical bars (closed stirrups) through the pile cap to improve strength and ductility and to reduce reliance on the concrete tensile properties.
- There is an absence of experimental data for large pile caps subjected to column uplift. Additional work is required to better predict behavior and develop improved analysis and design methods.

AUTHOR BIOS

ACI member **Yasmeen Al-Sakin** *is a Faculty Member in the College of Engineering at Al-Mustansiriyah University, Baghdad, Iraq. She received her BS and MS from Al-Mustansiriyah University, and her PhD from Oregon State University, Corvallis, OR. Her research interests include experimental investigation and nonlinear finite element modeling of structures.*

ACI member **Christopher Higgins** *is the Cecil and Sally Drinkward Professor of Structural Engineering in the School of Civil and Construction Engineering at Oregon State University. He received his BS from Marquette University, Milwaukee, WI; his MS from The University of Texas at Austin, Austin, TX; and his PhD from Lehigh University, Bethlehem, PA. His research interests include the evaluation and rehabilitation of structures.*

James Newell *is a Project Manager with SEFT Consulting Group, Beaverton, OR. He received his BS from Clarkson University, Potsdam, NY; his MS from Oregon State University; and his PhD from the University of California, San Diego, La Jolla, CA. His interests include seismic retrofit and functional recovery planning for critical buildings and lifeline infrastructure systems.*

ACI member **Kent Yu** *is a Principal with SEFT Consulting Group. He received his PhD from the University of California, San Diego. His interests include development of solutions that enhance the resilience of the built environment through practical research, advanced analysis, large-scale testing, and resilience planning.*

NOTATION

A_{Nc} = projected breakout area of group of anchors
A_{Nco} = assumed projected area of single anchor
$c_{a,min}$ = minimum distance from center of anchor to edge of concrete
f_c' = cylinder compressive strength of concrete
f_t = cylinder tensile strength of concrete
f_u = ultimate strength of reinforcement steel
f_y = yield strength of reinforcement steel
H = height of pile cap
h_{ef} = effective embedment length
L = length of pile cap
N_b = basic tensile concrete breakout strength of single anchor
$P_{B,Anchor}$ = concrete breakout strength for anchors
$P_{B,Column}$ = concrete breakout strength for column
$P_{u,Dy}$ = HSTB's observed ultimate strength
$P_{u,EXP}$ = experimental ultimate load
$P_{y,Dy}$ = HSTB's observed yield strength
W = width of pile cap
λ_a = lightweight concrete modification factor
$\psi_{c,N}$ = crack modification factor
$\psi_{cp,N}$ = pullout modification factor

ψ_{ed} = modification factor for anchor near one or more edges

REFERENCES

1. Gotman, A. L., "Finite-Element Analysis of Tapered Piles under Combined Vertical and Horizontal Loadings," *Soil Mechanics and Foundation Engineering*, V. 37, No. 1, 2000, pp. 5-12. doi: 10.1007/BF0248431910.1007/BF02484319

2. Dash, B. K., and Pise, P. J., "Effect of Compressive Load on Uplift Capacity of Model Piles," *Journal of Geotechnical and Geoenvironmental Engineering*, ASCE, V. 129, No. 11, 2003, pp. 987-992. doi:10.1061/(ASCE)1090-0241(2003)129:11(987)

3. Karthigeyan, S.; Ramakrishna, V.; and Rajagopal, K., "Numerical Investigation of the Effect of Vertical Load on the Lateral Response of Piles," *Journal of Geotechnical and Geoenvironmental Engineering*, ASCE, V. 133, No. 5, 2007, pp. 512-521. doi:10.1061/(ASCE)1090-0241(2007)133:5(512)

4. Shanker, K.; Basudhar, P. K.; and Patra, N. R., "Uplift Capacity of Single Piles: Predictions and Performance," *Geotechnical and Geological Engineering*, V. 25, No. 2, 2007, pp. 151-161. doi: 10.1007/s10706-006-9000-z

5. Madhusudan Reddy, K., and Ayothiraman, R., "Experimental Studies on Behavior of Single Pile under Combined Uplift and Lateral Loading," *Journal of Geotechnical and Geoenvironmental Engineering*, ASCE, V. 141, No. 7, 2015, p. 04015030. doi: 10.1061/(ASCE)GT.1943-5606.0001314

6. Shama, A. A.; Mander, J. B.; and Aref, A. J., "Seismic Performance and Retrofit of Steel Pile to Concrete Cap Connections," *ACI Structural Journal*, V. 99, No. 1, Jan.-Feb. 2002, pp. 51-61.

7. Xiao, Y.; Wu, H.; Yaprak, T. T.; Martin, G. R.; and Mander, J. B., "Experimental Studies on Seismic Behavior of Steel Pile-to-Pile-Cap Connections," *Journal of Bridge Engineering*, ASCE, V. 11, No. 2, 2006, pp. 151-159. doi: 10.1061/(ASCE)1084-0702(2006)11:2(151)

8. Iekel, P. P.; Phares, B.; and Nop, M., "Performance Investigation and Design of Pile-to-Pile Cap Connections Subject to Uplift," *Transportation Research Record: Journal of the Transportation Research Board*, V. 2672, No. 52, 2018, pp. 278-290. doi: 10.1177/0361198118796733

9. CRSI, "Design Guide for Pile Caps – CRSI Resource Materials," first edition, Concrete Reinforcing Steel Institute, Schaumberg, IL, 2015, 152 pp.

10. ACI Committee 318, "Building Code Requirements for Structural Concrete (ACI 318-19) and Commentary (ACI 318R-19) (Reapproved 2022)," American Concrete Institute, Farmington Hills, MI, 2019, 623 pp.

11. ASTM A615/A615M-18e1, "Standard Specification for Deformed and Plain Carbon-Steel Bars for Concrete Reinforcement," ASTM International, West Conshohocken, PA, 2018, 8 pp.

12. ASTM A722/722M-15, "Standard Specification for High-Strength Steel Bars for Prestressed Concrete," ASTM International, West Conshohocken, PA, 2015, 5 pp.

13. ASTM A36/A36M-19, "Standard Specification for Carbon Structural Steel," ASTM International, West Conshohocken, PA, 2019, 3 pp.

14. ASTM A449-14, "Standard Specification for Hex Cap Screws, Bolts and Studs, Steel, Heat Treated, 120/105/90 ksi Minimum Tensile Strength, General Use," ASTM International, West Conshohocken, PA, 2014, 7 pp.

15. ASTM A193/A193M-17, "Standard Specification for Alloy-Steel and Stainless Steel Bolting for High Temperature or High Pressure Service and Other Special Purpose Applications," ASTM International, West Conshohocken, PA, 2017, 13 pp.

16. Higgins, C., and Sorentino, A., "Report: VA Hospital Pile Cap Testing," Oregon State University, Corvallis, OR, 2011, 98 pp.

17. ASTM C31/C31M-18b, "Standard Practice for Making and Curing Concrete Test Specimens in the Field," ASTM International, West Conshohocken, PA, 2018, 7 pp.

18. ASTM C39/C39M-18, "Standard Test Method for Compressive Strength of Cylindrical Concrete Specimens," ASTM International, West Conshohocken, PA, 2018, 8 pp.

19. ASTM C496/C496M-17, "Standard Test Method for Splitting Tensile Strength of Cylindrical Concrete Specimens," ASTM International, West Conshohocken, PA, 2017, 5 pp.

20. ASTM E8/E8M-16a, "Standard Test Methods for Tension Testing of Metallic Materials," ASTM International, West Conshohocken, PA, 2016, 7 pp.

21. ASTM A370-17a, "Standard Test Methods and Definitions for Mechanical Testing of Steel Products," ASTM International, West Conshohocken, PA, 2017, 50 pp.

22. Higgins, C., "Structural Engineering Report 19-09: VA Hospital Pullout Tests of Existing Pile Cap Components," Oregon State University, Corvallis, OR, 2019, 23 pp.

23. Higgins, C., "Structural Engineering Report 19-10: VA Hospital Pile Cap Test of Specimen PC6-2," Oregon State University, Corvallis, OR, 2019, 22 pp.

24. Higgins, C., "Structural Engineering Report 19-11: VA Hospital Pile Cap Test of Specimen PC8-4," Oregon State University, Corvallis, OR, 2019, 25 pp.

25. Higgins, C., "Structural Engineering Report 19-12: VA Hospital Pile Cap Test of Specimen PC8-4R (Retrofit)," Oregon State University, Corvallis, OR, 2019, 26 pp.

26. Higgins, C., "Structural Engineering Report 19-12: VA Hospital Pile Cap Test of Specimen PC12-10R (Retrofit)," Oregon State University, Corvallis, OR, 2019, 30 pp.

27. Darwin, D.; Dolan, C. W.; and Nilson, A. H., *Design of Concrete Structures*, 15th edition, McGraw-Hill Education, 2016, New York, NY, 786 pp.

aci in Your Classroom

Integrate aci into your classroom!

To support future leaders, ACI has launched several initiatives to engage students in the Institute's activities and programs – select programs that may be of interest to Educators are:

- **Free student membership –** encourage students to sign up
- **Special student discounts on *ACI 318 Building Code Requirements for Structural Concrete*, *ACI 530 Building Code Requirements and Specification for Masonry Structure*, & *Formwork for Concrete* manual.**
- **Access to *Concrete International* –** free to all ACI student members
- **Access to *ACI Structural Journal* and *ACI Materials Journal* –** free to all ACI student members
- **Free sustainability resources –** free copies of Sustainable Concrete Guides provided to universities for use in the classroom
- **Student competitions –** participate in ACI's written and/or team-based competitions
- **Scholarships and fellowships –** students who win awards are provided up to $15,000 and may be offered internships and paid travel to attend ACI's conventions
- **ACI Award for University Student Activities –** receive local and international recognition for your University's participation in concrete-related activities
- **Free access to the *ACI Collection of Concrete Codes, Specifications, and Practices* –** in conjunction with ACI's chapters, students are provided free access to the online ACI Collection
- **ACI online recorded web sessions and continuing education programs –** online learning tools ideal for use as quizzes or in-class study material

https://www.concrete.org/educatorsandresearchers/aciinyourclassroom.aspx

ACI STRUCTURAL JOURNAL TECHNICAL PAPER

Title No. 120-S100

Chord Rotation Capacity and Strength of Diagonally Reinforced Concrete Coupling Beams

by A. Lepage, R. D. Lequesne, A. S. Weber-Kamin, S. Ameen, and M.-Y. Cheng

A database of results from 27 tests of diagonally reinforced concrete coupling beams was analyzed to develop improved force-deformation envelopes (backbone curves) for modeling and analysis of coupling beams. The database, which was selected from a larger set of 60 test results, comprises specimens that generally satisfy ACI 318-19 requirements. The analyses show that the chord rotation capacity of diagonally reinforced concrete coupling beams compliant with ACI 318-19 is closely correlated with beam clear span-to-overall depth ratio and, to a lesser extent, the ratio of hoop spacing to diagonal bar diameter. A simple expression is proposed for estimating beam chord rotation capacity. Coupling beam strength was shown to be more accurately estimated from flexural strength calculations at beam ends than other methods. Recommendations are made for obtaining more accurate backbone curves in terms of chord rotation capacity, strength, and stiffness.

Keywords: backbone curve; beam aspect ratio; confining reinforcement; database; deformation capacity; force-deformation envelope; hoop spacing; reinforcement grade; shear stress.

INTRODUCTION

Coupled structural walls are a common lateral force-resisting system in buildings designed for earthquakes. Studies of the behavior of coupling beams subjected to displacement reversals have shown that beams reinforced with diagonally oriented reinforcing bars exhibit large strength and deformation capacity.[1,2] Since ACI 318-99,[3] which first required diagonal reinforcement in short and highly stressed coupling beams, diagonally reinforced coupling beams have become common in practice.

Nonlinear response history analysis of buildings is permitted by ASCE/SEI 7-16[4] as part of the design of any structure. This type of analysis is common in the design and assessment of high-rise buildings with coupled walls. Appendix A in ACI 318-19[5] complements ASCE/SEI 7-16[4] with additional analysis and modeling requirements for the design of new reinforced concrete structures. For evaluation and retrofit of existing buildings, ASCE/SEI 41-17[6] and ACI CODE-369.1-22[7] provide the generalized force-deformation relationship shown in Fig. 1. ASCE/SEI 41-17[6] defines the envelope in Fig. 1 using the parameters in Table 1, which are also permitted by Appendix A in ACI 318-19.[5] The data in Fig. 1 and Table 1 will be referred to as the ASCE/SEI 41-17[6] envelope.

Figure 1 and Table 1 suggest that well-detailed diagonally reinforced coupling beams exhibit their peak strength at or beyond a chord rotation of 0.03 rad and retain 80% of their strength Q_y to a chord rotation of at least 0.05 rad. These deformation parameters underestimate the chord rotation capacity of well-detailed slender coupling beams ($\ell_n/h >$ 3). Naish et al.[2,9] reported that coupling beams with ℓ_n/h = 3.3 exhibit peak strengths at chord rotations exceeding 0.05 rad and can retain strengths of $0.8V_m$ to chord rotations exceeding 0.08 rad. Recent test results[10,11] furthermore suggest that chord rotation capacity is related to ℓ_n/h, with beams retaining residual strengths of $0.8V_m$ to 0.05 rad when ℓ_n/h = 1.5 and approaching 0.07 rad for ℓ_n/h = 3.5. Test data therefore suggest that deformation capacity parameters in Table 1 should account for ℓ_n/h. Effects of other parameters including bar grade, concrete strength, shear stress, transverse reinforcement detailing, axial restraint, and other variables should be investigated.

Parameters in Table 1 for coupling beam strength are a function of Eq. (1), which is based on the ACI 318-19[5] provisions for diagonally reinforced coupling beams. This equation attributes the entire beam strength to the diagonal reinforcement, neglecting the shear strength attributable to hoops and the flexural strength resulting from any non-diagonal reinforcement developed into the walls. The ASCE/SEI 41-17[6] envelope uses Eq. (1) (with expected material properties instead of specified values) to define the strength Q_y at point B. The peak strength Q_C is $1.25Q_y$, and the residual strength is $0.8Q_y$. Studies have shown this approach can substantially underestimate beam strength,[10-14] with reported measured strengths that were 30 to 100% larger than Q_y when all non-diagonal bars terminated near the beam end (and 40 to over 200% more than Q_y when non-diagonal bars extended into the supports). It is not necessarily conservative to underestimate expected beam strength because beam shear strengths contribute to force demands in wall piers and foundations.[15,16] Research shows that the shear corresponding to the beam developing its nominal flexural strength at both ends $(M_n^+ + M_n^-)/\ell_n$ provides a considerably more accurate estimate of beam strength than Eq. (1).[10-14] Determining beam shear based on M_n also allows accounting for the effects of slabs and axial restraint.

$$\begin{aligned} V_{n,\text{Eq.(1)}} &= 2A_{vd}f_y\sin\alpha \le 10\sqrt{f_c'}b_w h \quad \text{(in.-lb)} \\ V_{n,\text{Eq.(1)}} &= 2A_{vd}f_y\sin\alpha \le 0.83\sqrt{f_c'}b_w h \quad \text{(metric)} \end{aligned} \tag{1}$$

ACI Structural Journal, V. 120, No. 6, November 2023.

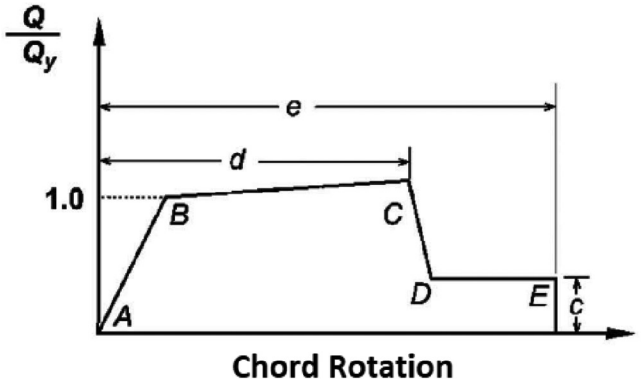

Fig. 1—Generalized force-deformation relationship defined in ASCE/SEI 41-17 Fig. 10-1(b),[6] similar to ACI CODE-369.1-22 Fig. 3.1.2.2.3(b).[7]

Table 1 shows that the ASCE/SEI 41-17[6] envelope defines coupling beam stiffness based on an effective moment of inertia of $0.3I_g$, even though coupling beam specimens often exhibit stiffnesses closer to $0.15I_g$.[9] TBI[8] recommends Eq. (2), which closely approximates the effective stiffness of coupling beams reinforced with Grade 60 (420) bars. When multiplied by $60/f_y$, ksi ($420/f_y$, MPa), the resulting equation (Eq. (3)) works well for coupling beams with Grade 60 to 120 (420 to 830) bars.[17]

$$I_{eff}/I_g = 0.07(\ell_n/h) \tag{2}$$

$$\begin{aligned} I_{eff}/I_g &= 0.07(\ell_n/h)(60/f_y)\ \text{(in.-lb)} \\ I_{eff}/I_g &= 0.07(\ell_n/h)(420/f_y)\ \text{(metric)} \end{aligned} \tag{3}$$

Although the simplicity of the parameters in Table 1 is desirable, improvements to the parameters for chord rotation capacity, strength, and stiffness are possible. This paper reports analyses of a database of diagonally reinforced coupling beam specimens tested under reversed cyclic loads. The two main motivations were to: 1) identify the variables that most affect coupling beam deformation capacity and propose a simple equation that represents the deformation capacity of coupling beam specimens; and 2) assess the accuracy of Eq. (1) and alternative methods for calculating the expected strength of diagonally reinforced concrete coupling beams.

RESEARCH SIGNIFICANCE

This paper reports analyses of a database of results from tests of diagonally reinforced coupling beams. The analyses support revising the force-deformation envelope (backbone curves) recommended in ASCE/SEI 41-17[6] and ACI CODE-369.1-22[7] for modeling and analysis of coupling beams. Specific recommendations are made, and the resulting backbone curves are compared against sample test results. These recommendations aim to improve the state of engineering practice in the analysis and design of buildings with structural walls and coupling beams.

COUPLING BEAM DATABASE

A database of results from tests of 60 diagonally reinforced coupling beams was assembled.[18] From this database, a smaller "analysis" database was selected,[19] comprising 27 specimens. Refer to Table 2 for the data summary and the Notation section for definitions. The following describes how specimens were selected from the literature and the criteria used to select specimens for the analysis database. The contents of the analysis database are briefly reported; more details, including reasons for excluding individual specimens from the analysis database, are available in References 11 and 19.

Table 1—Force-deformation envelope for nonlinear procedures

Parameters*		Envelope from ASCE/SEI 41-17[6]
Deformation capacity	d	0.03
	e	0.05
Strength	Q_y	$V_{n,\text{Eq.(1)}}$†
	Q_C	V_{pr}‡
	c	0.8
Stiffness	I_{eff}/I_g	0.3§

*Refer to Notation.

†Equation (1) using expected yield stress, $f_{y,e}$.

‡Equation (1) using $1.25f_{y,e}$.

§Based on Table 10-5 of ASCE/SEI 41-17. Reference 8 recommends 0.07 (ℓ_n/h) instead of 0.3.

Database description

The 60 specimens in the full database[18] satisfy the following criteria: 1) enough information was available describing the specimens to support the analyses described herein; 2) the beam was reinforced with straight (not bent) diagonal bars throughout the beam clear span that were continuously bonded to the concrete; 3) the beam contained no fiber reinforcement or structural steel sections; 4) the concrete was confined with rectilinear hoops enclosing either the diagonal bar groups or the full beam section; 5) the beam was subjected to reversed cyclic displacements and double curvature; 6) the failure mode did not include twisting due to inadequate out-of-plane bracing; and 7) the beam was prismatic and without penetrations or notches.

Table 2 contains the subset of 27 specimens selected to form an analysis database.[19] In addition to the conditions listed previously, the specimens in Table 2 also meet the following criteria: 1) diagonal bar confinement spacing was nominally consistent throughout the span; 2) the ratio of transverse reinforcement spacing to diagonal bar diameter (s/d_b) was less than or equal to 6; 3) the average of the maximum axial forces imposed in each loading direction was measured, reported, and not larger than $0.15A_gf_{cm}$; 4) a systematic loading protocol consisting of fully reversed cyclic displacements with increasing amplitude was used, and testing was continued until beam strength diminished to less than 80% of the peak strength; 5) beams had a rectangular cross section (that is, not integral with a slab); and 6) the least cross-sectional dimension was not less than 5 in. (125 mm). These limits were imposed so specimens in the analysis database would generally represent beams conforming to requirements of ACI 318-19.[5] The

Table 2—Database of diagonally reinforced coupling beams included in derivation of equation for chord rotation capacity

Specimen number			1	2	3	4	5	6	7	8	9	10	11	12	13
Reference			Naish et al.[2]			Lim et al.[20]		Lim et al.[21]		Cheng et al.[10]					
Specimen ID			CB24D	CB24F	CB33F	CB30-DA	CB30-DB	CB10-1	CB20-1	D1.5_H	D1.5_H2	D1.5_L	D2.5_H	D2.5_L	D3.5_L
Beam properties	b_w	in.	12.0	12.0	12.0	11.8	11.8	9.84	11.8	11.0	11.0	11.0	11.0	11.0	11.0
	h	in.	15.0	15.0	18.0	19.7	19.7	19.7	19.7	19.0	19.0	19.0	19.0	19.0	19.0
	Confinement*		Diag.	Full	Full	Diag.	Full	Full	Full	Full	Full	Full	Full	Full	Full
	$b_c \perp b_w$	in.	8.125	9.50	9.50	5.98	10.2	8.27	10.2	9.00	9.00	9.00	9.00	9.00	9.00
	$b_c \perp h$	in.	4.00	13.5	16.5	5.20	16.5	16.5	16.5	17.0	17.0	17.0	17.0	17.0	17.0
	ℓ_n	in.	36.0	36.0	60.0	59.1	59.1	19.7	39.4	28.0	28.0	28.0	47.0	47.0	67.0
	ℓ_n/h		2.40	2.40	3.33	3.00	3.00	1.00	2.00	1.47	1.47	1.47	2.47	2.47	3.53
	f_{cm}	psi	6850	6850	6850	5750	5550	5000	7550	6600	7000	4400	5100	4700	6800
Diagonal reinforcement	Quantity	ea. diag.	6	6	6	4	4	4	4	8	4	4	6	4	4
	α	degrees	15.7	15.7	12.3	8.80	8.80	26.0	16.0	20.9	18.5	20.9	12.5	9.00	8.90
	d_b	in.	0.875	0.875	0.875	1.27	1.27	1.00	1.13	0.750	1.13	0.750	1.13	1.13	1.13
	f_{ym}	ksi	70.0	70.0	70.0	67.4	67.4	70.4	67.6	66.2	66.8	69.5	70.8	70.8	66.8
Parallel reinforcement	Quantity	total	10	10	12	4	10	10	10	6	6	6	6	6	6
	d_{bp}	in.	0.250	0.375	0.375	0.500	0.375	0.375	0.500	0.500	0.500	0.500	0.500	0.500	0.500
	f_{ym}	ksi	70.0	70.0	70.0	64.0	68.9	68.9	72.8	61.9	61.9	64.1	64.1	64.1	61.9
	Condition†		Cut	Cut	Cut	Devel.	Devel.	Devel.	Devel.	Cut	Cut	Cut	Cut	Cut	Cut
Transverse reinforcement	d_{bt}	in.	0.375	0.375	0.375	0.375	0.375	0.500	0.500	0.500	0.500	0.500	0.500	0.500	0.500
	f_{ytm}	ksi	70.0	70.0	70.0	68.9	68.9	67.9	72.8	120	120	125	125	125	120
	s	in.	2.50	3.00	3.00	5.91	3.94	3.94	3.94	4.33	4.33	4.33	4.50	4.50	4.33
	s/d_b		2.86	3.43	3.43	4.65	3.10	3.94	3.49	5.78	3.84	5.78	3.99	3.99	3.84
	$(s/d_b)\sqrt{f_{ym}/60\ \text{ksi}}$		3.09	3.70	3.70	4.93	3.29	4.27	3.71	6.07	4.05	6.22	4.33	4.33	4.05
	$\frac{A_{sh,provided}}{sb_c} \perp b_w$‡, %		1.62	1.16	1.16	0.62	0.82	1.01	0.82	1.03	1.03	1.03	0.99	0.99	1.03
	$\frac{A_{sh,provided}}{sb_c} \perp h$‡, %		2.20	1.09	1.11	0.72	0.68	0.68	0.68	0.81	0.81	0.81	0.78	0.78	0.81
	$\frac{A_{sh,provided}}{A_{sh,required}} \perp b_w$‡		1.84	1.31	1.31	0.83	1.13	1.53	0.88	2.07	1.95	3.24	2.69	2.92	2.01
	$\frac{A_{sh,provided}}{A_{sh,required}} \perp h$‡		2.50	1.23	1.26	0.95	0.93	1.02	0.72	1.65	1.55	2.57	2.14	2.32	1.60
V_m	–	kip	155	171	109	154	156	315	241	347	378	209	237	173	166
	+	kip	159	150	124	151	164	325	234	356	401	221	238	178	163
v_{max}	$\frac{v_{max}}{b_w h\sqrt{f_{cm}, \text{psi}}}$		10.7	11.5	6.9	8.7	9.5	23.7	11.9	21.0	22.9	15.9	15.9	12.4	9.6
$CR_{cap,m}$	–	%	8.50	9.00	8.00	7.40	8.40	5.80	7.70	5.40	5.10	4.70	5.90	6.70	6.30
	+	%	8.80	10.0	8.10	7.00	7.50	6.20	8.20	5.70	5.40	5.30	6.90	6.00	7.10
	Avg.	%	8.65	9.50	8.05	7.20	7.95	6.00	7.95	5.55	5.25	5.00	6.40	6.35	6.70
Axial restraint			No	No	No	No	No	No	No	Yes	Yes	Yes	Yes	Yes	Yes

*Diag. is confinement of each diagonal bar group; Full is confinement of entire beam cross section (except concrete cover).

†Cut is secondary longitudinal bars cut off near support face; Devel. is secondary longitudinal bars developed into supports.

‡$\perp b_w$ is transverse reinforcement perpendicular to beam width; $\perp h$ is transverse reinforcement perpendicular to beam depth.

Note: 1 in. = 25.4 mm; 1 ksi = 1000 psi = 6.89 MPa; 1 kip = 4.45 kN.

small number of specimens with slabs were omitted from the analysis database to remove a variable that could not be easily evaluated due to the limited data. The specimens with axial forces larger than $0.15A_g f_{cm}$, or with axial restraint and an unknown magnitude axial force, were also excluded due to the limited data available. The effects of slabs and axial forces on chord rotation capacity are addressed later.

Table 2, cont.—Database of diagonally reinforced coupling beams included in derivation of equation for chord rotation capacity

Specimen number			14	15	16	17	18	19	20	21	22	23	24	25	26	27
Reference			Ameen et al.[17]					Weber-Kamin et al.[11]								
Specimen ID			CB1	CB2	CB2AD	CB2D	CB3D	D80-1.5	D80-2.5	D80-3.5	D100-1.5	D100-2.5	D100-3.5	D120-1.5	D120-2.5	D120-3.5
Beam properties	b_w	in.	10.0	10.0	10.0	10.0	10.0	12.0	12.0	12.0	12.0	12.0	12.0	12.0	12.0	12.0
	h	in.	18.0	18.0	18.0	18.0	18.0	18.0	18.0	18.0	18.0	18.0	18.0	18.0	18.0	18.0
	Confinement*		Full	Full	Full	Full	Full	Full	Full	Full	Full	Full	Full	Full	Full	Full
	$b_c \perp b_w$	in.	8.50	8.50	8.50	8.50	8.50	10.5	10.5	10.5	10.5	10.5	10.5	10.5	10.5	10.5
	$b_c \perp h$	in.	16.5	16.5	16.5	16.5	16.5	16.5	16.5	16.5	16.5	16.5	16.5	16.5	16.5	16.5
	ℓ_n	in.	34.0	34.0	34.0	34.0	34.0	27.0	45.0	63.0	27.0	45.0	63.0	27.0	45.0	63.0
	ℓ_n/h		1.89	1.89	1.89	1.89	1.89	1.50	2.50	3.50	1.50	2.50	3.50	1.50	2.50	3.50
	f_{cm}	psi	6000	7200	5650	6300	6200	7600	8400	7800	8200	8000	7900	7600	7800	8200
Diagonal reinforcement	Quantity	ea. diag.	6	4	4	4	6	6	9	9	5	7	9	4	6	8
	α	degrees	18.0	18.0	18.0	18.0	18.0	22.7	14.2	10.0	22.7	14.2	10.3	22.7	14.2	10.3
	d_b	in.	0.875	0.750	0.750	0.750	0.750	0.750	0.750	0.875	0.750	0.750	0.750	0.750	0.750	0.750
	f_{ym}	ksi	63.0	128	128	128	128	83.0	83.0	84.0	108	108	108	116	116	116
Parallel reinforcement	Quantity	total	8	8	8	8	8	10	10	10	10	10	10	10	10	10
	d_{bp}	in.	0.375	0.375	0.375	0.375	0.375	0.375	0.375	0.375	0.375	0.375	0.375	0.375	0.375	0.375
	f_{ym}	ksi	69	69	69	69	69	89.0	89.0	89.0	89.0	89.0	89.0	89.0	133	89.0
	Condition†		Cut	Cut	Devel.	Devel.	Devel.	Cut	Cut	Cut	Cut	Cut	Cut	Cut	Devel.	Cut
Transverse reinforcement	d_{bt}	in.	0.375	0.375	0.375	0.375	0.375	0.375	0.375	0.375	0.375	0.375	0.375	0.375	0.375	0.375
	f_{ytm}	ksi	68.0	68.0	68.0	68.0	68.0	89.0	89.0	89.0	89.0	89.0	89.0	89.0	133	89.0
	s	in.	3.00	3.00	3.00	3.00	3.00	3.00	3.00	3.00	3.00	3.00	3.00	3.00	3.00	3.00
	s/d_b		3.43	4.00	4.00	4.00	4.00	4.00	4.00	3.43	4.00	4.00	4.00	4.00	4.00	4.00
	$(s/d_b)\sqrt{f_{ym}/60\text{ ksi}}$		3.51	5.84	5.84	5.84	5.84	4.70	4.70	4.06	5.37	5.37	5.37	5.56	5.56	5.56
	$\frac{A_{sh,provided}}{sb_c} \perp b_w$‡, %		0.86	0.86	0.86	0.86	0.86	1.05	1.05	1.05	1.05	1.05	1.05	1.05	1.05	1.05
	$\frac{A_{sh,provided}}{sb_c} \perp h$‡, %		0.89	0.89	0.89	0.89	0.89	0.89	0.89	0.89	0.89	0.89	0.89	0.89	0.89	0.89
	$\frac{A_{sh,provided}}{A_{sh,required}} \perp b_w$‡		1.09	0.91	1.15	1.03	1.05	1.36	1.23	1.33	1.26	1.29	1.31	1.36	1.98	1.26
	$\frac{A_{sh,provided}}{A_{sh,required}} \perp h$‡		1.12	0.93	1.19	1.07	1.08	1.16	1.05	1.13	1.07	1.10	1.11	1.16	1.68	1.07
V_m	–	kip	184	192	234	194	268	239	220	218	257	220	192	262	283	216
	+	kip	182	207	228	204	275	254	218	219	252	214	196	264	286	212
v_{max}	$\frac{v_{max}}{b_w h\sqrt{f_{cm},\text{psi}}}$		13.2	13.6	17.3	14.3	19.4	13.5	11.1	11.5	13.1	11.4	10.2	14.0	15.0	11.0
$CR_{cap,m}$	–	%	7.00	4.60	5.50	5.40	5.20	6.40	6.90	8.40	4.70	5.30	6.90	5.40	6.70	6.60
	+	%	8.00	5.60	5.30	5.40	6.50	7.30	8.30	8.80	5.80	6.60	6.70	5.00	7.00	6.80
	Avg.	%	7.50	5.10	5.40	5.40	5.85	6.85	7.60	8.60	5.25	5.95	6.80	5.20	6.85	6.70
Axial restraint			No	No	Yes	No	No	No	No	No	No	No	No	No	No	No

*Diag. is confinement of each diagonal bar group; Full is confinement of entire beam cross section (except concrete cover).

†Cut is secondary longitudinal bars cut off near support face; Devel. is secondary longitudinal bars developed into supports.

‡$\perp b_w$ is transverse reinforcement perpendicular to beam width; $\perp h$ is transverse reinforcement perpendicular to beam depth.

Note: 1 in. = 25.4 mm; 1 ksi = 1000 psi = 6.89 MPa; 1 kip = 4.45 kN.

Table 2 reports the main variables (refer to Notation) that define geometry, material properties, reinforcement details, measured strength, and chord rotation capacity for the specimens in the analysis database. Table 3 and Fig. 2 show the range, mean, and distribution of several important variables within the database. The variables include beam width, b_w; beam overall depth, h; aspect ratio, ℓ_n/h; measured concrete compressive strength, f_{cm}; measured yield stress of the

Table 3—Range of values for main variables in analysis database for diagonally reinforced coupling beams

	b_w, in. (mm)	h, in. (mm)	ℓ_n/h	f_{cm}, psi (MPa)	f_{ym}, ksi (MPa)	s/d_b	$\frac{s}{d_b}\sqrt{\frac{f_{ym}}{60\text{ ksi}}}$	$\frac{v_{max}}{\sqrt{f_{cm}\text{ psi}}}$* (MPa)	$CR_{cap,m}$, %
Min.	9.8 (250)	15 (381)	1.0	4400 (30.3)	63.0 (434)	2.9	3.1	6.9 (0.58)	5.0
Mean	11.3 (287)	18.2 (464)	2.3	6740 (46.4)	88.6 (611)	4.0	4.8	13.7 (1.14)	6.7
Max.	12 (305)	19.7 (500)	3.5	8400 (57.9)	128 (883)	5.8	6.2	23.7 (1.97)	9.5

*Ratios of $2A_{vd}f_{ym}\sin\alpha$ to $\sqrt{f_{cm}\text{ (psi)}}b_w d$ ranged between 4.8 and 14.8 with a mean of 8.8.

Note: 1 ksi = 6.89 MPa.

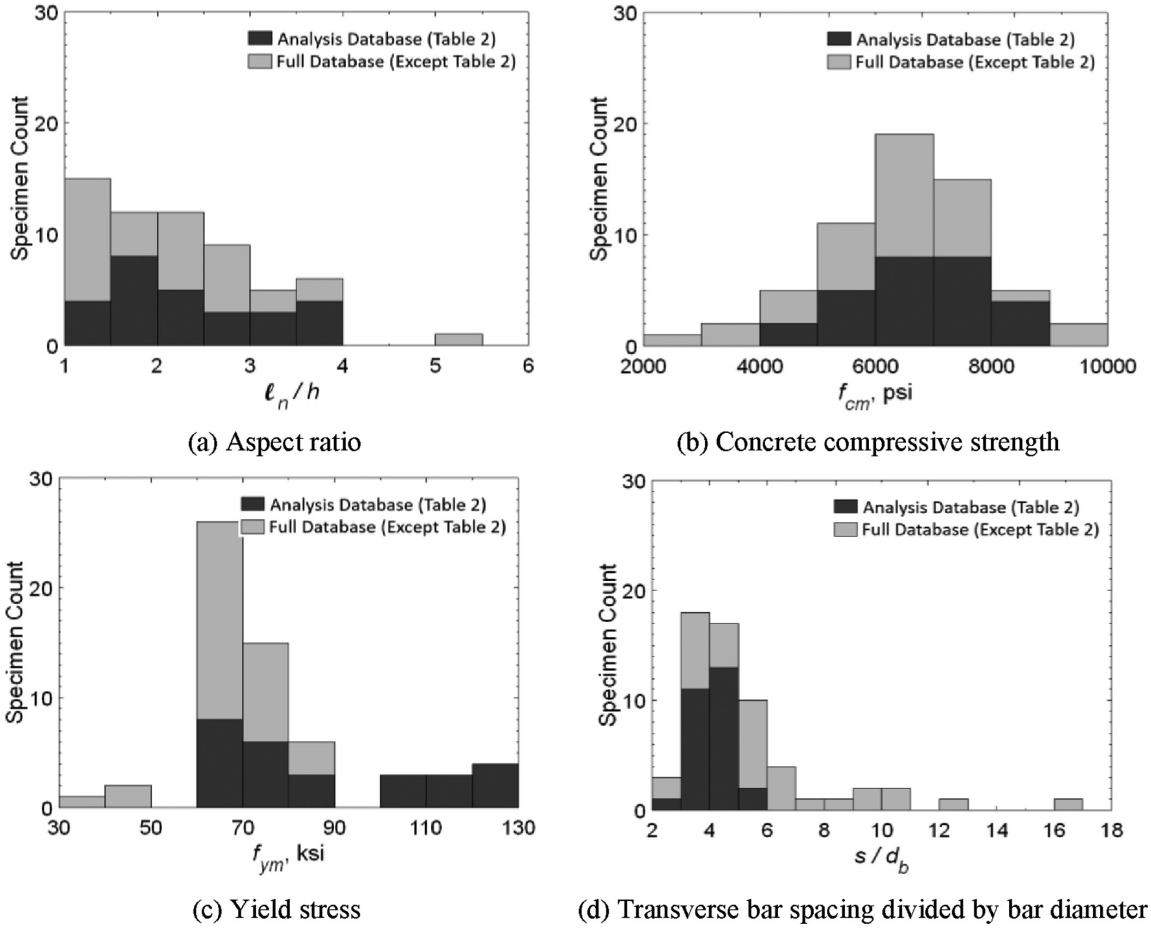

(a) Aspect ratio

(b) Concrete compressive strength

(c) Yield stress

(d) Transverse bar spacing divided by bar diameter

Fig. 2—Histograms of variables within database. (Note: 1 ksi = 1000 psi = 6.89 MPa.)

diagonal reinforcement, f_{ym}; hoop spacing-to-bar diameter ratio, s/d_b; normalized hoop spacing-to-bar diameter ratio, $\overline{s/d_b} = (s/d_b)(\sqrt{f_{ym}/60\text{ ksi}})$ [$(s/d_b)(\sqrt{f_{ym}/420\text{ MPa}})$]; normalized shear stress, $v_{max}/\sqrt{f_{cm}}$; and chord rotation capacity, $CR_{cap,m}$. (Note that s/d_b was normalized by the square root of f_{ym}/60 ksi [f_{ym}/420 MPa] because the Euler buckling equation indicates buckling stress is inversely proportional to the square of the slenderness ratio, assumed proportional to s/d_b, where d_b and f_{ym} refer to the diagonal bar and s refers to the hoop spacing. This was done for simplicity, although it is acknowledged that the Euler equation represents elastic buckling, while buckling of a diagonal bar is an inelastic phenomenon.) The range and distribution of values shown in Table 3 and Fig. 2 generally show that the analysis database represents ACI 318-19[5]-compliant coupling beams, except specimens with higher strength reinforcement and higher shear stresses are also included.

COUPLING BEAM CHORD ROTATION CAPACITY

Correlations between chord rotation capacity and design variables

Chord rotation capacity was defined for each specimen as the average of the chord rotations in each loading direction where the envelope of the post-peak shear versus chord rotation data (formed by connecting the maximum chord rotation of the first cycle of each loading step) intersected a line at 80% of the maximum applied shear in each loading direction. This definition of chord rotation capacity, which is based on an envelope drawn according to ASCE/SEI 41-17,[6] is less sensitive to the drift increment of the loading protocol than some other definitions because the shear-chord rotation

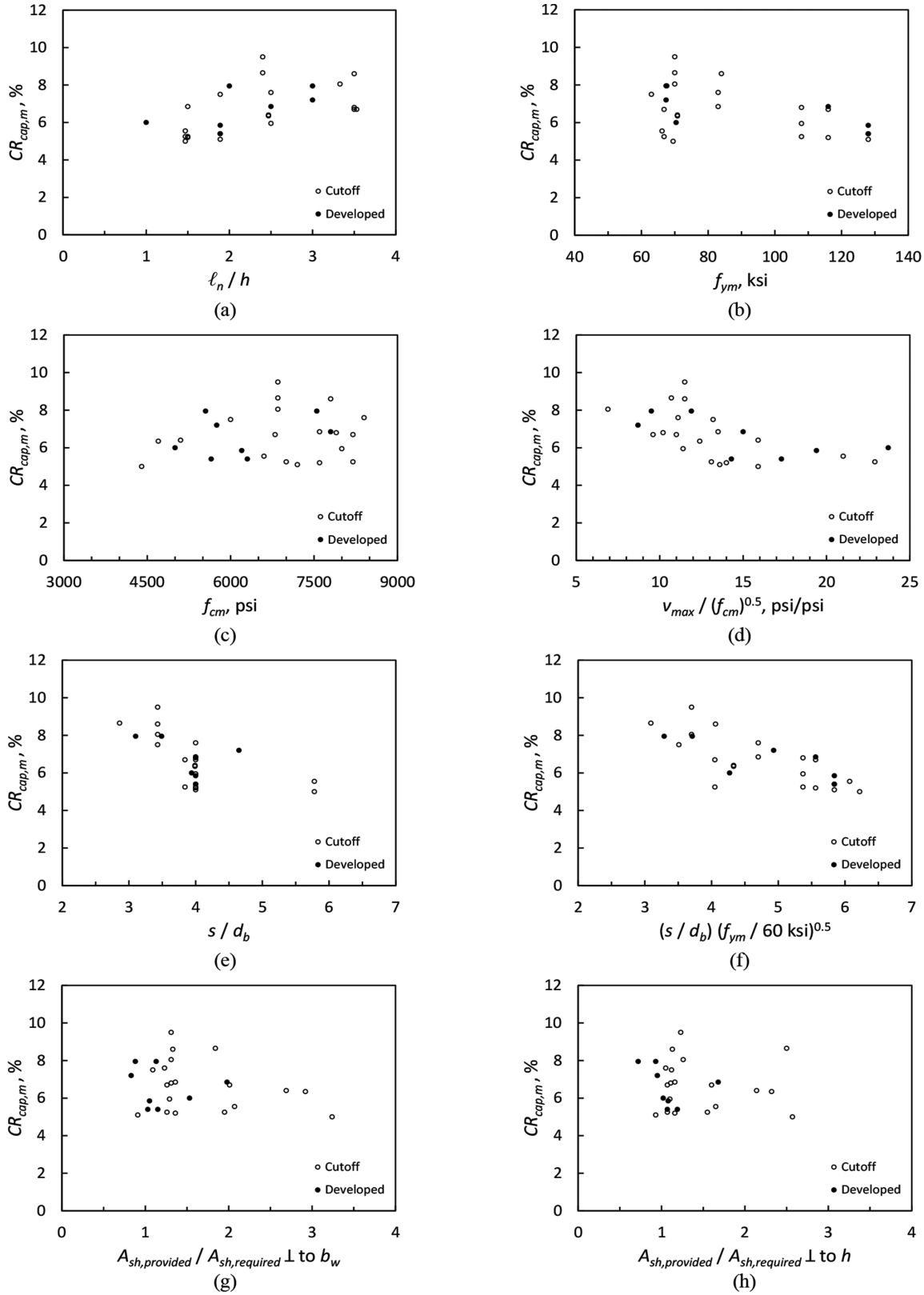

Fig. 3—Chord rotation capacity versus design variables. (Note: 1 ksi = 1000 psi = 6.895 MPa.)

relationship is represented by linear interpolations between measured values.

In Fig. 3, the measured chord rotation capacity ($CR_{cap,m}$) for specimens in the analysis database (Table 2) is plotted against ℓ_n/h, f_{ym}, f_{cm}, $v_{max}/\sqrt{f_{cm}}$, s/d_b, $\overline{s/d_b}$, and $A_{sh,provided}/A_{sh,required}$ (both perpendicular to b_w and h). Beams with cutoff longitudinal bars (not developed into the supports) and beams with developed longitudinal bars are identified with open and solid circles, respectively. Qualitatively, it can be observed that $CR_{cap,m}$ is positively correlated with ℓ_n/h and negatively correlated with s/d_b and $\overline{s/d_b}$. It also appears that $CR_{cap,m}$ is negatively correlated with f_{ym}, but further

Table 4—Summary data for single-variable linear regression of chord rotation capacity versus selected parameters based on Eq. (4)

	ℓ_n/h	f_{ym}	f_{cm}	$\frac{v_{max}}{\sqrt{f_{cm}}\ \text{psi}}$	s/d_b	$\frac{s}{d_b}\sqrt{\frac{f_{ym}}{60\ \text{ksi}}}$	$\frac{A_{sh,provided}^*}{A_{sh,required}}$	
							⊥ to b_w	⊥ to h
c_0†	4.53	8.79	5.39	9.02	11.37	11.37	7.35	6.92
c_1†	0.92	–0.024	0.19/1000	–0.17	–1.19	–0.99	–0.46	–0.20
r^2	0.31	0.22	0.03	0.34	0.37	0.57	0.05	0.01

*⊥ to b_w is transverse reinforcement perpendicular to beam width; ⊥ to h is transverse reinforcement perpendicular to beam depth.

†c_0 and c_1 are constants in Eq. (4), where chord rotation is in percentage units.

Note: 1 ksi = 6.89 MPa.

investigation is needed because the 10 specimens with f_{ym} > 100 ksi (690 MPa) all had $\overline{s/d_b}$ > 5, so the apparent correlations with f_{ym} and $\overline{s/d_b}$ are not independent. Likewise, the apparent negative correlation between $CR_{cap,m}$ and $v_{max}/\sqrt{f_{cm}}$ requires further investigation because the apparent correlations with ℓ_n/h and $v_{max}/\sqrt{f_{cm}}$ are not independent (12 of the 14 beams with $v_{max}/\sqrt{f_{cm}}$ > 13 psi [1.08 MPa] also had ℓ_n/h < 2). These interdependencies are addressed later.

Chord rotation capacity does not appear sensitive to $A_{sh,provided}/A_{sh,required}$. Providing $A_{sh,provided}/A_{sh,required} \geq 1$ is important, but Fig. 3 suggests that $CR_{cap,m}$ is not sensitive to $A_{sh,provided}$ in diagonally reinforced beams that satisfy ACI 318-19[5] confinement requirements. This observation should be considered with some caution, as evidence from strain gauges on hoops have shown that transverse reinforcement yielding can be expected under some conditions. For example, coupling beams with developed longitudinal (non-diagonal) bars tend to exhibit less concentrated rotations at the beam ends but more shear distress within the span, which causes larger hoop strain demands.[13,17] It may be advantageous to provide additional transverse reinforcement when all longitudinal bars are developed.

In general, Fig. 3 shows no clear difference between the trends for beams with cutoff longitudinal reinforcement and beams with developed longitudinal reinforcement. This suggests that this detail has little effect on the deformation capacity of well-detailed diagonally reinforced coupling beams, consistent with prior findings.[17]

Using data from Table 2, a simple linear regression was done to quantify the strength of the correlations between $CR_{cap,m}$ and parameters X_i, which were taken as ℓ_n/h, f_{ym}, f_{cm}, $v_{max}/\sqrt{f_{cm}}$, s/d_b, $\overline{s/d_b}$, and $A_{sh,provided}/A_{sh,required}$. An equation with the form of Eq. (4) was fit to each of the eight plots in Fig. 3.

$$CR_{cap,\text{Eq.(4)}} = c_0 + c_1 X_i \tag{4}$$

Table 4 shows the coefficients c_0 and c_1, as well as the coefficient of determination r^2, for each of the resulting eight equations. The coefficients c_0 and c_1 informed initial values for later multivariate regression analyses. Larger values of r^2 suggest stronger correlations between the selected variables and $CR_{cap,m}$.

Table 4 shows that $CR_{cap,m}$ was most strongly correlated with $\overline{s/d_b}$, having $r^2 = 0.57$. The correlations between $CR_{cap,m}$ and ℓ_n/h, $v_{max}/\sqrt{f_{cm}}$, and s/d_b were similar in terms of r^2, with values of 0.31, 0.34, and 0.37, respectively. Table 4 shows that $CR_{cap,m}$ was more weakly correlated with f_{ym}, having $r^2 = 0.22$, and not correlated with f_{cm} and $A_{sh,provided}/A_{sh,required}$, with $r^2 \leq 0.05$.

It was observed previously that f_{ym} and $\overline{s/d_b}$ are not independent within the analysis database because the 10 specimens with f_{ym} > 100 ksi (690 MPa) all had $\overline{s/d_b}$ > 5. A trend line for f_{ym} versus $\overline{s/d_b}$ has r^2 = 0.50, indicating a relatively strong correlation between these variables within the database. To separate these variables, specimens with f_{ym} > 100 ksi (690 MPa) were removed to produce a subset of 17 specimens with f_{ym} between 63 and 84 ksi (434 and 579 MPa) that have no correlation between f_{ym} and $\overline{s/d_b}$ (r^2 = 0.01). When compared against this smaller data set, $CR_{cap,m}$ and $\overline{s/d_b}$ are still relatively strongly correlated (r^2 = 0.47), whereas $CR_{cap,m}$ and f_{ym} are not (r^2 = 0.05). On this basis, it will be assumed for subsequent analyses that $CR_{cap,m}$ is more strongly dependent on $\overline{s/d_b}$ than f_{ym}.

It was also previously observed that ℓ_n/h and $v_{max}/\sqrt{f_{cm}}$ are not independent within the analysis database because 12 of the 14 beams with $v_{max}/\sqrt{f_{cm}}$ > 13 psi (1.08 MPa) also had ℓ_n/h < 2. A trend line for ℓ_n/h versus $v_{max}/\sqrt{f_{cm}}$ has r^2 = 0.55, indicating a relatively strong correlation between these variables within the database. It is therefore not clear from the data in Table 4 whether $CR_{cap,m}$ is correlated with ℓ_n/h, $v_{max}/\sqrt{f_{cm}}$, or both. Studies[10,17] have shown that well-detailed diagonally reinforced coupling beams with the same aspect ratio and different shear stress demands exhibit similar chord rotation capacities. On this basis, the following analyses include ℓ_n/h and not $v_{max}/\sqrt{f_{cm}}$.

Equation for chord rotation capacity

Multiple regression analysis was done using the analysis database (Table 2) to develop an equation for chord rotation capacity (Eq. (5)). Based on the r^2 values in Table 4 and the preceding discussion, ℓ_n/h and $\overline{s/d_b}$ were selected as the primary variables. Both f_{ym} and $v_{max}/\sqrt{f_{cm}}$ were omitted from Eq. (5) for reasons described previously. Although s/d_b was also somewhat correlated with $CR_{cap,m}$, it is omitted from Eq. (5) to avoid redundancy with $\overline{s/d_b}$.

$$CR_{cap,\text{Eq.(5)}} = (9.3 + 0.62\ell_n/h - 0.85\overline{s/d_b})/100 \tag{5}$$

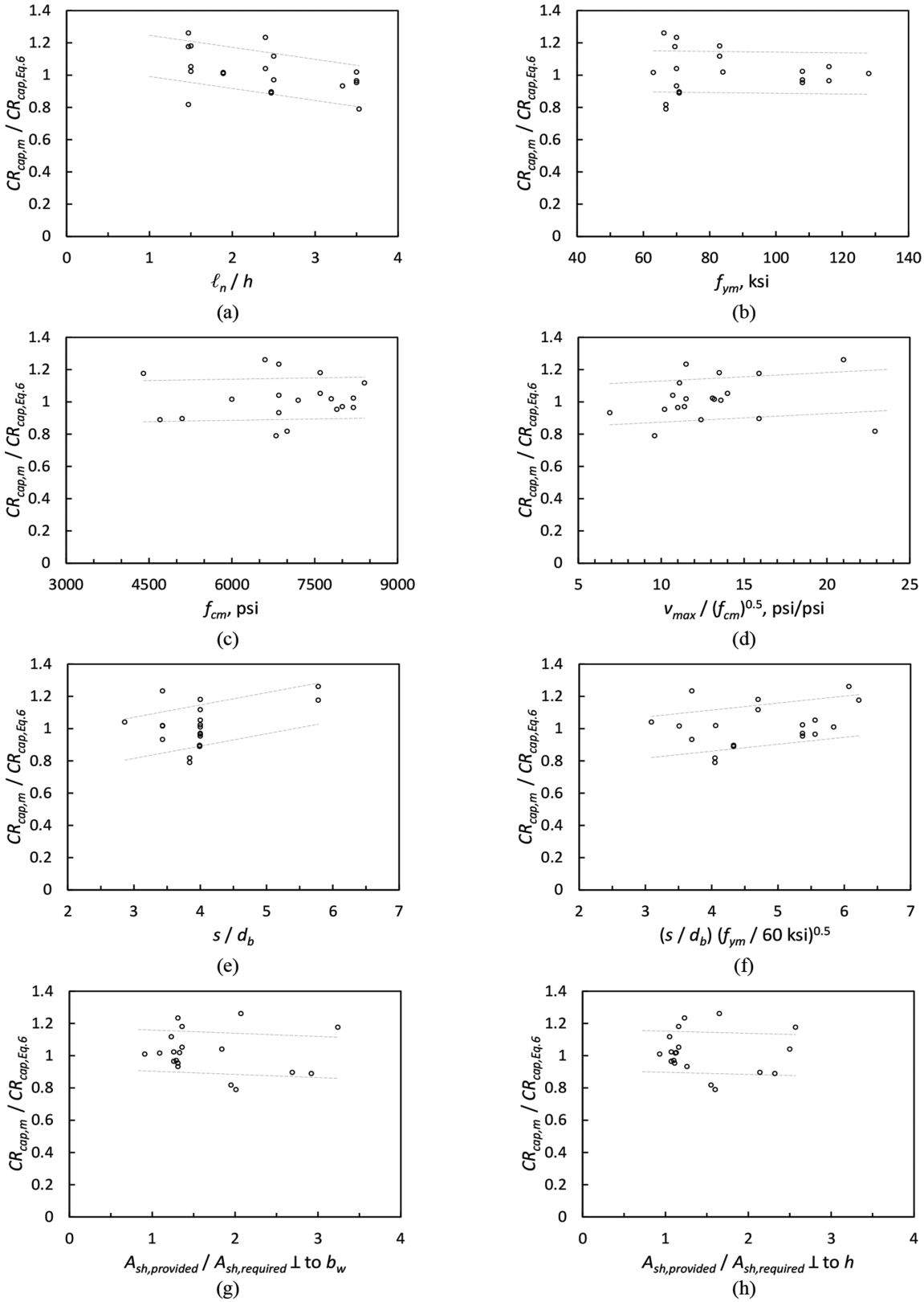

Fig. 4—Measured chord rotation capacity divided by chord rotation capacity calculated with Eq. (6) versus design variables. (Note: 1 ksi = 1000 psi = 6.895 MPa.)

Equation (5) relates $CR_{cap,\text{Eq.(5)}}$ with ℓ_n/h and $\overline{s/d_b}$ for diagonally reinforced coupling beams like those in the analysis database, which included coupling beams with approximately $1 \le \ell_n/h < 4$, $3 \le \overline{s/d_b} \le 6$, $60 \le f_{ym} \le 130$ ksi [$420 \le f_{ym} \le 900$ MPa], and transverse reinforcement satisfying the minimum area required in ACI 318-19 Section 18.10.7.4.[5] Equation (5) was simplified to Eq. (6), an approximation that is appropriate because the analysis database contains only 27 specimens and the design variables are not independently distributed within the database.

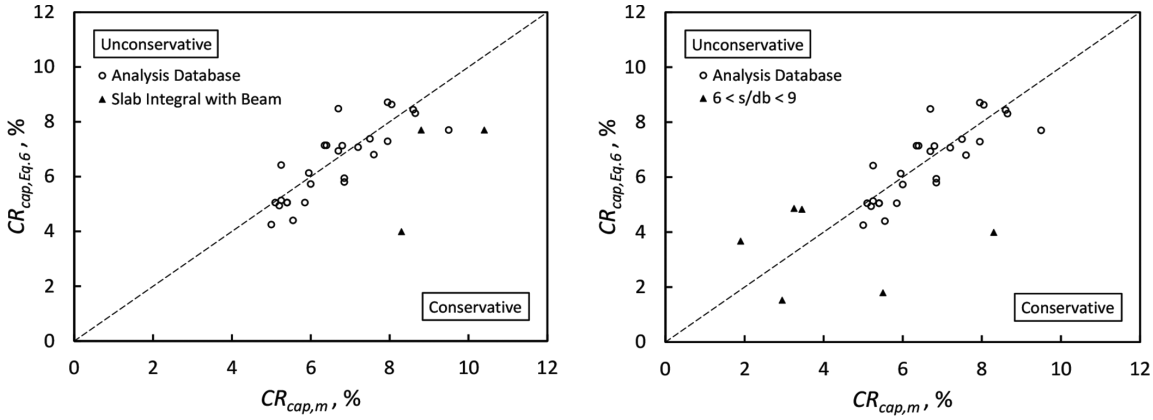

(a) Analysis database and specimens with slabs

(b) Analysis database and specimens with $6 < s/d_b < 9$

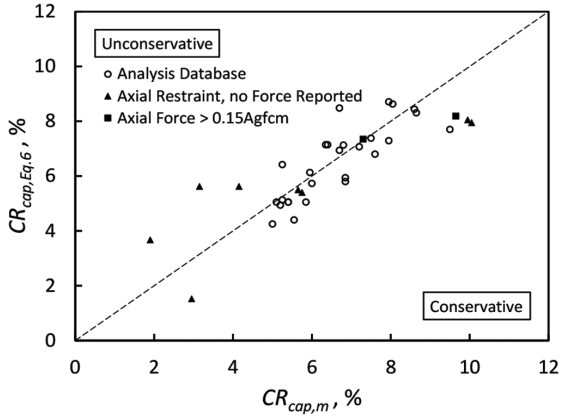

(c) Analysis database and specimens with axial restraint and no reported axial force or axial forces > $0.15A_g f_{cm}$ (specimens with $s/d_b \geq 9$ omitted)

Fig. 5—Chord rotation capacity calculated with Eq. (6) versus measured chord rotation capacity for analysis database and selected specimens excluded from analysis database.

$$CR_{cap,\text{Eq.(6)}} = (9 + \ell_n/h - \overline{s/d_b})/100 \quad (6)$$

Further simplification is possible (Eq. (7)) by setting $\overline{s/d_b} = 6$ and therefore neglecting the beneficial effects of having $\overline{s/d_b} < 6$.

$$CR_{cap,\text{Eq.(7)}} = (3 + \ell_n/h)/100 \quad (7)$$

Figure 4 shows $CR_{cap,m}$ divided by $CR_{cap,\text{Eq.(6)}}$ for the specimens in Table 2, plotted versus the same variables considered in Fig. 3. The dotted lines in Fig. 4 represent a linear best-fit line offset by ±σ. The mean and *CV* of $CR_{cap,m}/CR_{cap,\text{Eq.(6)}}$ are 1.03 and 0.11, indicating that Eq. (6) provides a reasonably close estimate of chord rotation capacity. For comparison, the mean and *CV* of the ratio of measured to calculated CR_{cap} are 1.00 and 0.10 for Eq. (5) and 1.26 and 0.16 for Eq. (7). This shows that the loss of either accuracy or precision was negligible when simplifying Eq. (5) to obtain Eq. (6). Equation (7) is less accurate and precise, but also simpler. If a version of these equations were used as a basis for design or evaluation of structures, they should be modified to produce an appropriate level of conservatism.

Effects of variables omitted from analysis database

Some of the specimens omitted from the analysis database represent design conditions that will be found in practice, and it is important to examine how the chord rotation capacities of those specimens compare against the values calculated with Eq. (6). In particular, the effects of slabs built integrally with a coupling beam, hoops with $s/d_b > 6$, and axial restraint are worth assessing even though the available data are limited.

Figure 5 shows $CR_{cap,\text{Eq.(6)}}$ plotted versus measured $CR_{cap,m}$. Specimens in the analysis database are represented with open circles, and relevant specimens from the full database[18] that were omitted from the analysis database are represented with solid triangles and squares. Specimens omitted from the analysis database for reasons unrelated to slabs, hoop spacing, or axial restraint are not included in Fig. 5.

Figure 5(a) shows that the three specimens in the full database[18] that had slabs built integrally with the coupling beam (obtained from Naish et al.[2]) exhibited $CR_{cap,m}$ that were similar to or larger than $CR_{cap,\text{Eq.(6)}}$. This is consistent with the discussion of slab effects in Naish et al.,[2] which noted no detrimental effects of slabs on chord rotation capacity.

Figure 5(b) has solid triangles representing the six specimens from the full database[18] that had $6 < s/d_b < 9$ (obtained

from References 1, 2, and 22 to 24). Two of the six specimens also had axial restraint with no reported axial forces; another had a post-tensioned slab built integrally with the beam. Figure 5(b) shows that $CR_{cap,\text{Eq.(6)}}$ is conservative for half of the specimens with $6 < s/d_b < 9$, but the scatter is also larger for these specimens than specimens within the analysis database. Four of the six specimens with $6 < s/d_b < 9$ also had $CR_{cap,m} < 5\%$, which is less than any of the specimens in the analysis database. The two beams with axial restraint, $6 < s/d_b < 9$, and without slabs had $CR_{cap,m} < 3\%$. Hoop spacings wider than permitted in ACI 318-19[5] therefore appear to have a detrimental effect on chord rotation capacity. This is unsurprising because the deformation capacity of diagonally reinforced coupling beams is often limited by fracture of diagonal bars after buckling in prior loading cycles.

Figure 5(c) has solid triangles representing eight specimens from the full database[18] that had axial restraint, but where the induced axial forces were not reported (obtained from References 22 and 25 to 27), and two solid squares representing the specimens from the full database with peak axial forces larger than $0.15A_gf_{cm}$ (obtained from Poudel et al.[14] and Gonzalez[28]). Figure 5(c) shows that four axially restrained specimens had $CR_{cap,m} < 5\%$, but two of these also had $6 < s/d_b < 9$, so the effects of axial restraint are difficult to isolate (the two specimens with axial restraint and $6 < s/d_b < 9$ had $CR_{cap,m} < 3\%$). The six other axially restrained specimens in Fig. 5(c) had $CR_{cap,m}$ values that were similar to or slightly larger than $CR_{cap,\text{Eq.(6)}}$. Without more data from tests with axial restraint and reported axial forces, it is difficult to draw conclusions about effects of axial restraint on $CR_{cap,m}$ in an aggregated way. Based on a targeted study with four specimens, Poudel et al.[14] observed an approximately 10% reduction of $CR_{cap,m}$ when axial restraint induced axial forces of approximately $0.2A_gf_{cm}$, and negligible effects on $CR_{cap,m}$ when induced axial forces were approximately $0.1A_gf_{cm}$.

COUPLING BEAM STRENGTH

Equation (1), from ACI 318-19 Section 18.10.7.4,[5] gives estimates of coupling beam strength that can be substantially conservative.[10-14] The beam shear corresponding to beam-end moments based on calculated flexural strength is a more accurate estimate of beam strength and allows the engineer to account for effects on strength of developed non-diagonal longitudinal reinforcement, a slab built integrally with the coupling beam, and axial forces.

These prior findings are supported by the results in Table 5, which shows V_m for the 27 specimens in the analysis database and ratios of measured to calculated beam strength based on three calculation methods. Method 1 is the nominal shear strength from Eq. (1), Method 2 is the shear force corresponding to development of M_n at both beam ends, and Method 3 is the shear force corresponding to development of M_{pr} at both beam ends. No strength reduction factors were used to produce Table 5. To calculate $V_{n,\text{Eq.(1)}}$ and M_n, measured material properties (f_{cm} and f_{ym}) were used, which are analogous to the expected material properties recommended in ASCE/SEI 41-17.[6] To calculate M_n, beams were considered doubly reinforced, and the longitudinal component of the diagonal bar areas was used. Concrete compression zone stresses were represented with an equivalent rectangular stress block, and reinforcing bars were assumed to be elastoplastic. The presence of non-diagonal longitudinal reinforcement was neglected in specimens where this reinforcement was cut off near the face of the wall (a detail recommended in Section R18.10.7 of ACI 318-19[5]). Axial forces were considered. The same assumptions were used to calculate M_{pr}, except that $1.1f_{ym}$ was used in place of f_{ym}. If f_{ym} is assumed to be $1.1f_y$, then $1.1f_{ym}$ is similar to the $1.25f_y$ recommended in ACI 318-19[5] for calculating probable flexural strength ($1.1f_{ym} = 1.21f_y \approx 1.25f_y$).

Table 5 shows that Method 1 systematically underestimates beam strength, with a mean measured-to-calculated strength ratio of 1.59 and values as high as 2.46. This is likely too conservative when used to model a coupled wall system, where neglecting beam overstrength can produce unintended and negative effects on wall and foundation behavior.[15,16] Method 2 provides conservative but considerably more accurate and precise estimates of beam strength, with a mean measured-to-calculated ratio of 1.20 and a range of 1.01 to 1.57. Method 3 produces a mean measured-to-calculated ratio of 1.12 and a range of 0.94 to 1.48, indicating it also gives an accurate and generally conservative estimate of expected beam strength. To produce a backbone curve (Fig. 1) with more accurate expected strengths, Methods 2 and 3 are recommended for calculating Q_y and Q_C, respectively.

COUPLING BEAM ENVELOPE RECOMMENDATIONS

Table 6 lists recommendations for a revised force-deformation envelope with parameters corresponding to Fig. 1. Equation (6) is recommended for calculating e, which is the total chord rotation at E. Consistent with ASCE/SEI 41-17[6] recommendations, the total chord rotation at peak strength, d, is taken as 0.02 rad less than e. It is recommended that the coupling beam shear Q_y at B be calculated from M_n at each end of the coupling beam based on expected material properties and that the strength Q_C be calculated from M_{pr} based on expected concrete compressive strength and $1.1f_{y,e}$. No change is recommended to the post-peak residual strength, which is still defined in Table 6 with $c = 0.8$, producing a post-peak strength of $0.8Q_y$. Lastly, Eq. (3) is recommended for calculating I_{eff}/I_g. The recommended envelope is intended to provide an estimate of mean response and has no built-in conservatism. Some modification may be appropriate to produce an acceptable level of conservatism.

Table 6 produces the envelopes plotted in Fig. 6, which includes the measured force-chord rotation data of six specimens from the database. In general, the proposed envelope provides better approximations of beam stiffness than the ASCE/SEI 41-17[6] envelope. The proposed envelope also gives a more realistic estimate of chord rotation capacity, particularly for slender coupling beams ($\ell_n/h > 3$), which consistently exhibit more deformation capacity than the ASCE/SEI 41-17[6] envelope suggests. For the specimens in Fig. 6, both envelopes provide similar estimates of beam strength. It is expected that the recommended strength

Table 5—Coupling beam measured and calculated strengths

Specimen number	Reference	Specimen ID	Measured	Ratio of measured to calculated strength		
			V_m, kip	Method 1* $V_m/V_{n,\text{Eq.(1)}}$	Method 2* $V_m/(2M_n/\ell_n)$	Method 3† $V_m/(2M_{pr}/\ell_n)$
1	Naish et al.[2]	CB24D	157	1.15	1.08	1.00
2		CB24F	161	1.18	1.14	1.05
3		CB33F	117	1.09	1.06	0.98
4	Lim et al.[20]	CB30-DA‡	153	1.46	1.03	0.95
5		CB30-DB‡	160	1.53	1.06	0.99
6	Lim et al.[21]	CB10-1‡	320	1.64	1.05	0.98
7		CB20-1‡	238	1.59	1.01	0.94
8	Cheng et al.[10]	D1.5_H§	352	2.11	1.51	1.40
9		D1.5_H2§	390	2.30	1.49	1.39
10		D1.5_L§	215	2.46	1.57	1.48
11		D2.5_H§	238	1.29	1.03	0.95
12		D2.5_L§	176	1.98	1.17	1.13
13		D3.5_L§	165	1.99	1.44	1.34
14	Ameen et al.[17]	CB1	183	1.31	1.07	0.99
15		CB2‖	200	1.43	1.19	1.11
16		CB2AD‡,§,‖	231	1.66	1.20	1.18
17		CB2D‡,‖	199	1.43	1.07	1.03
18		CB3D‡,‖	272	1.30	1.15	1.10
19	Weber-Kamin et al.[11]	D80-1.5	247	1.46	1.19	1.10
20		D80-2.5	219	1.36	1.16	1.07
21		D80-3.5	219	1.39	1.23	1.14
22		D100-1.5	255	1.39	1.14	1.05
23		D100-2.5	217	1.33	1.15	1.06
24		D100-3.5	194	1.27	1.14	1.09
25		D120-1.5‖	263	1.67	1.34	1.24
26		D120-2.5‡,‖	285	1.89	1.36	1.28
27		D120-3.5‖	214	1.47	1.31	1.25
			Minimum	1.09	1.01	0.94
			Maximum	2.46	1.57	1.48
			Mean	1.59	1.20	1.12
			CV	0.23	0.13	0.13

*Based on f_{cm} and f_{ym}.

†M_{pr} based on f_{cm} and $1.1f_{ym}$.

‡Specimen with non-diagonal longitudinal reinforcement developed into supports.

§Specimen with axial restraint and peak axial force < $0.15A_g f_{cm}$.

‖Specimen with bars exhibiting a so-called "roundhouse" stress-strain curve with no yield plateau.

Note: 1 kip = 4.45 kN.

calculations will be advantageous when there is a slab, axial force, or developed non-diagonal reinforcement, given that the strength calculations do not exclusively depend on the area of the diagonal bars.

Limitations of proposed envelope

The recommendations in Table 6 are intended for diagonally reinforced concrete coupling beams compliant with ACI 318-19.[5] The approach taken in this study was to propose an envelope that represents the expected response, and thus there is little inherent conservatism incorporated in the factors in Table 6. It would likely be appropriate to incorporate some conservatism in estimates of chord rotation capacity. Effects of axial restraint are also not considered in the proposal.

Table 6—Force-deformation envelopes for coupling beams compliant with ACI 318-19[5]

Parameters*		Envelope from ASCE/SEI 41-17[6]	Recommended envelope
Deformation capacity	d	0.03	$(7 + \ell_n/h - \overline{s/d_b})/100$†
	e	0.05	$(9 + \ell_n/h - \overline{s/d_b})/100$†
Strength	Q_y	$V_{n,\text{Eq.(1)}}$‡	$(M_n^+ + M_n^-)/\ell_n$§
	Q_C	V_{pr}‖	$(M_{pr}^+ + M_{pr}^-)/\ell_n$#
	c	0.8	0.8
Stiffness	I_{eff}/I_g	0.3**	0.07 (ℓ_n/h) (60 ksi/f_y)††

*Refer to Notation.

†$\overline{s/d_b}$ may be taken as 6 for coupling beams compliant with ACI 318-19.

‡Equation (1) using $f_{y,e}$.

§M_n based on expected material properties.

‖Equation (1) using a bar stress of $1.25f_{y,e}$.

#M_{pr} based on expected concrete compressive strength and $1.1f_{y,e}$.

**Based on Table 10-5 of ASCE/SEI 41-17.[6]

††From Reference 8, modified as recommended in Reference 17.

Note: 1 ksi = 6.89 MPa.

SUMMARY AND CONCLUSIONS

A database of results from 27 tests of diagonally reinforced concrete coupling beams was analyzed to develop improved force-deformation envelopes for modeling and analysis of coupling beams. The database (Table 2), which was selected from a larger set of 60 test results,[18] comprises specimens that generally satisfy ACI 318-19[5] requirements, except specimens with high-strength reinforcement and shear stresses (based on measured forces) greater than $10\sqrt{f_{cm}}$ psi ($0.83\sqrt{f_{cm}}$ MPa) were also included. The following conclusions were drawn:

1. Within the database, coupling beam chord rotation capacity was correlated with ℓ_n/h and $\overline{s/d_b} = (s/d_b)(\sqrt{f_{ym}/60\text{ ksi}})$ $[(s/d_b)(\sqrt{f_{ym}/420\text{ MPa}})]$.

2. After accounting for correlations with ℓ_n/h and $\overline{s/d_b}$, coupling beam chord rotation capacity was not strongly correlated with $v_{max}/\sqrt{f_{cm}}$, f_{ym}, f_{cm}, or the quantity of transverse reinforcement, as long as the quantity of transverse reinforcement exceeded that required in ACI 318-19.[5]

3. The chord rotation capacity of coupling beams such as those in the analysis database can be estimated with Eq. (6) (reproduced as Eq. (8)). The equation gives mean and CV values of 1.03 and 0.11 for measured-to-calculated ratios. The equation is based on a database of diagonally reinforced concrete coupling beams with approximately $1 \le \ell_n/h \le 4$, $3 \le \overline{s/d_b} \le 6$, $60 \le f_{ym} \le 130$ ksi (420 and 900 MPa), and $4 \le 2A_{vd}f_{ym}\sin\alpha/(b_w h\sqrt{f_{cm}\text{ (psi)}}) \le 15$ $(0.33 \le 2A_{vd}f_{ym}\sin\alpha/(b_w h\sqrt{f_{cm}\text{ (MPa)}})) \le 1.25)$.

$$CR_{cap,\text{Eq.(6)}} = (9 + \ell_n/h - \overline{s/d_b})/100 \quad (8)$$

4. The limited data support prior observations[9] that slabs built integrally with a coupling beam do not reduce $CR_{cap,m}$.

5. Beams with $6 < s/d_b < 9$ tend to exhibit reduced $CR_{cap,m}$. Four of the six specimens with $6 < s/d_b < 9$ had $CR_{cap,m} < 5\%$, which is less than any of the coupling beams in the analysis database.

6. It is difficult to draw conclusions about the effects of axial restraint on $CR_{cap,m}$ in an aggregated way without more data from tests with axial restraint and reported axial forces. Prior work[14] found a negative effect on $CR_{cap,m}$ for axial forces of approximately $0.2A_gf_{cm}$.

7. Analyses support prior findings that coupling beam strength is more accurately estimated using the nominal flexural strength at beam ends than the nominal shear strength (Eq. (1)). Strengths based on $(M_n^+ + M_n^-)/\ell_n$ and $(M_{pr}^+ + M_{pr}^-)/\ell_n$ had mean ratios of measured-to-calculated strengths of 1.2 and 1.1, respectively, both with a CV of 0.13. Strengths based on Eq. (1) had a mean measured-to-calculated strength ratio of 1.6 with a CV of 0.23.

AUTHOR BIOS

Andrés Lepage, *FACI, is a Professor at The University of Kansas, Lawrence, KS. He is a member of ACI Committees 318, Structural Concrete Building Code; 374, Performance-Based Seismic Design of Concrete Buildings; and 375, Performance-Based Design of Concrete Buildings for Wind Loads; and Joint ACI-ASCE Committee 335, Composite and Hybrid Structures.*

ACI member **Rémy D. Lequesne** *is the Stanley T. and Phyllis W. Rolfe Chair's Council Associate Professor at The University of Kansas. He is Chair of Joint ACI-ASCE Committee 408, Bond and Development of Steel Reinforcement, and a member of ACI Committee 133, Disaster Reconnaissance; ACI Subcommittee 318-J, Joints and Connections; and Joint ACI-ASCE Committee 352, Joints and Connections in Monolithic Concrete Structures.*

Alexander S. Weber-Kamin *is a Research and Design Engineer in the Structural Engineering Department and the Caltrans Seismic Response Modification Device Test Facility at the University of California, San Diego, La Jolla, CA. They received their BS from The University of Oklahoma, Norman, OK, and their PhD from The University of Kansas.*

Shahedreen Ameen *is a Project Consultant at Simpson Gumpertz & Heger Inc., New York, NY. She received her BS from Bangladesh University of Engineering and Technology, Dhaka, Bangladesh, and her PhD from The University of Kansas.*

ACI member **Min-Yuan Cheng** *is a Professor in the Department of Civil and Construction Engineering at National Taiwan University of Science and Technology, Taipei, Taiwan. He is a member of ACI Subcommittee 318-J, Joints and Connections, and Joint ACI-ASCE Committee 352, Joints and Connections in Monolithic Concrete Structures.*

ACKNOWLEDGMENTS

Financial support from the following sources is gratefully acknowledged: The University of Kansas Department of Civil, Environmental & Architectural Engineering; the Charles Pankow Foundation; the ACI Foundation's Concrete Research Council; and the Concrete Reinforcing Steel Institute.

NOTATION

A_g = gross area of concrete section, in.^{2} (mm^2)
$A_{sh,provided}$ = cross-sectional area of transverse reinforcement provided within s, in.^{2} (mm^2)
$A_{sh,required}$ = cross-sectional area of transverse reinforcement within s required in ACI 318-19, Section 18.10.7.4,[5] $=0.09sb_cf_{cm}/f_{ytm}$, in.^{2} (mm^2)
A_{vd} = total area of reinforcement in each group of diagonal bars, in.^{2} (mm^2)
b_c = cross-sectional dimension measured to outside edges of hoops, in. (mm)
b_w = beam width, in. (mm)
$CR_{cap,\text{Eq.(X)}}$ = chord rotation capacity calculated with Eq. (X), rad
$CR_{cap,m}$ = average of maximum chord rotations in each loading direction where envelope of shear versus chord rotation curve (formed by connecting maximum chord rotation of first

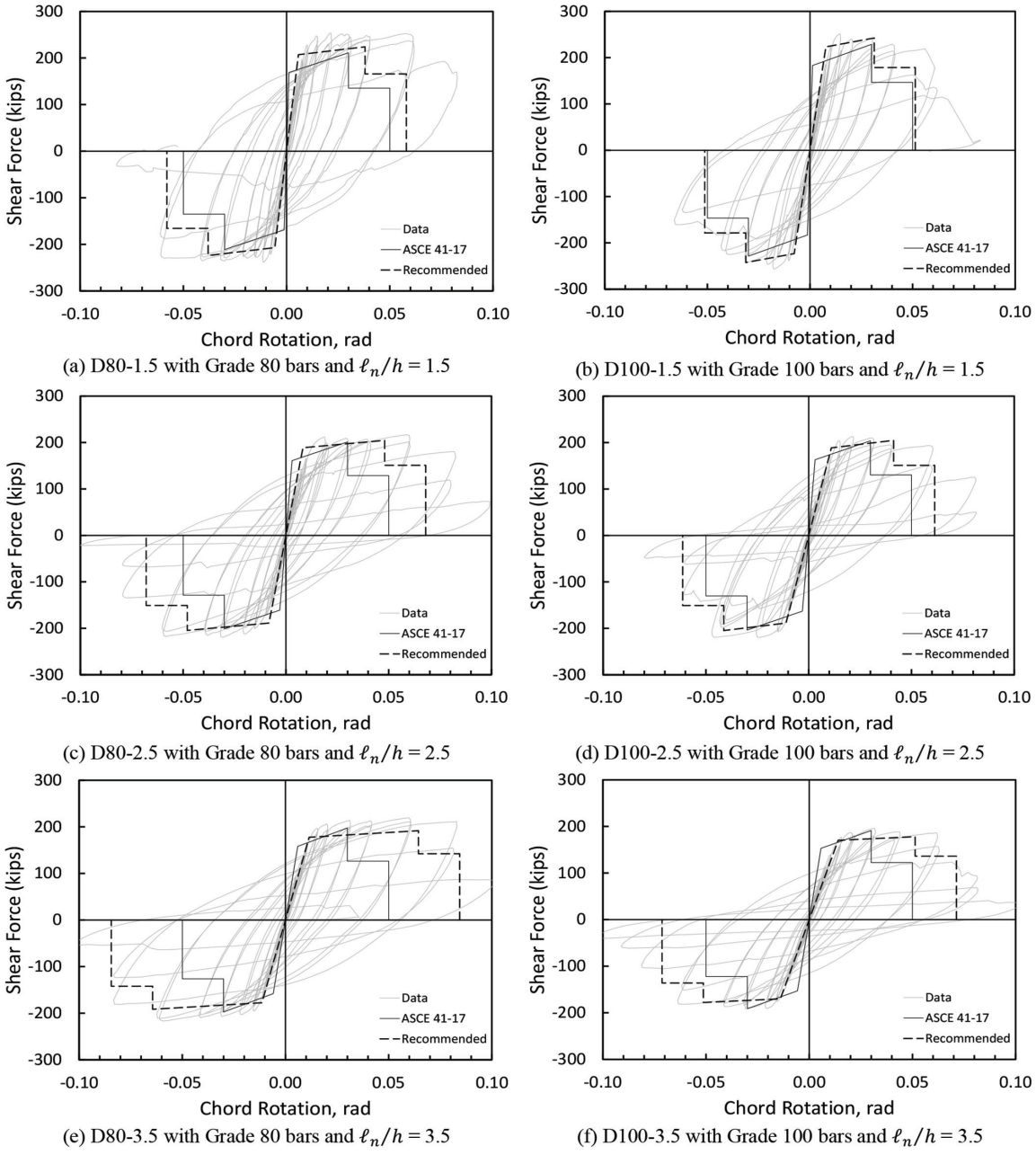

Fig. 6—Results from tests of diagonally reinforced concrete coupling beams compliant with ACI 318-19[5] from Weber-Kamin et al.[11] and envelopes from Table 6. (Note: 1 kip = 4.45 kN.)

cycle of each loading step) intersects 80% of maximum applied shear, rad

CV = coefficient of variation, ratio of standard deviation to mean
c = parameter used to quantify residual strength (Fig. 1)
c_0, c_1 = intercept and slope of best-fit line defined by Eq. (4)
d = parameter used to quantify total deformation to capping point C (Fig. 1)
d_b = diameter of diagonal bar, in. (mm)
d_{bp} = diameter of parallel bar, in. (mm)
d_{bt} = diameter of transverse bar, in. (mm)
e = parameter used to quantify total deformation to point E (Fig. 1)
f_c' = specified concrete compressive strength, psi (MPa)
f_{cm} = measured concrete compressive strength, psi (MPa)
f_y = specified yield stress, ksi (MPa)
$f_{y,e}$ = expected yield stress; refer to ASCE/SEI 41-17,[6] ksi (MPa)
f_{ym}, f_{ytm} = measured yield stress of diagonal and transverse reinforcement, ksi (MPa)
h = overall depth of beam, in. (mm)
I_{eff} = effective moment of inertia about centroidal axis, in.^{4} (mm^4)
I_g = moment of inertia of gross concrete section about centroidal axis, neglecting reinforcement, in.^{4} (mm^4)
ℓ_n = beam clear span length, in. (mm)
M_n = calculated nominal flexural strength corresponding to stress of $1.0f_y$, $1.0f_{ym}$, or $1.0f_{y,e}$ in diagonal reinforcement, kip·in. (kN·m) (+/− identify loading direction)
M_{pr} = calculated probable flexural strength corresponding to stress of $1.25f_y$, $1.1f_{ym}$, or $1.1f_{y,e}$ in diagonal reinforcement, kip·in. (kN·m) (+/− identify loading direction)
Q = force (Fig. 1), kip (kN)
Q_C = force at capping point C (Fig. 1), kip (kN)
Q_y = force at point B (Fig. 1), kip (kN)
r^2 = coefficient of determination
s = transverse reinforcement spacing, in. (mm)
s/d_b = normalized hoop spacing-to-bar diameter ratio = $(s/d_b)(\sqrt{f_{ym}/60\text{ ksi}})[(s/d_b)(\sqrt{f_{ym}/420\text{ MPa}})]$
V_m = maximum measured shear force, kip (kN)
$V_{n,\text{Eq.(1)}}$ = nominal shear strength per Eq. (1), kip (kN)
V_{pr} = probable shear strength per Eq. (1) using bar stress of $1.25f_y$, $1.1f_{ym}$, or $1.1f_{ye}$, kip (kN)

v_{max} = maximum shear stress $V_m/(b_w h)$, psi (MPa)
X_i = variable in Eq. (4) to evaluate correlation with $CR_{cap,m}$
α = inclination of diagonal bars relative to beam longitudinal axis, degrees
σ = standard deviation

REFERENCES

1. Paulay, T., and Binney, J. R., "Diagonally Reinforced Coupling Beams of Shear Walls," *Shear in Reinforced Concrete*, SP-42, American Concrete Institute, Farmington Hills, MI, 1974, pp. 579-598.

2. Naish, D.; Fry, A.; Klemencic, R.; and Wallace, J., "Reinforced Concrete Coupling Beams—Part 1: Testing," *ACI Structural Journal*, V. 110, No. 6, Nov.-Dec. 2013, pp. 1057-1066.

3. ACI Committee 318, "Building Code Requirements for Structural Concrete (ACI 318-99) and Commentary (ACI 318R-99)," American Concrete Institute, Farmington Hills, MI, 1999, 369 pp.

4. ASCE/SEI 7-16, "Minimum Design Loads and Associated Criteria for Buildings and Other Structures," American Society of Civil Engineers, Reston, VA, 2017, 822 pp.

5. ACI Committee 318, "Building Code Requirements for Structural Concrete (ACI 318-19) and Commentary (ACI 318R-19) (Reapproved 2022)," American Concrete Institute, Farmington Hills, MI, 2019, 624 pp.

6. ASCE/SEI 41-17, "Seismic Evaluation and Retrofit of Existing Buildings," American Society of Civil Engineers, Reston, VA, 2017, 576 pp.

7. ACI Committee 369, "Seismic Evaluation and Retrofit of Existing Concrete Buildings—Code and Commentary (ACI CODE-369.1-22)," American Concrete Institute, Farmington Hills, MI, 2022, 125 pp.

8. TBI, "Guidelines for Performance-Based Seismic Design of Tall Buildings (Tall Buildings Initiative)," Report No. 2017/06, Pacific Earthquake Engineering Research Center, University of California, Berkeley, Berkeley, CA, 2017, 145 pp.

9. Naish, D.; Fry, A.; Klemencic, R.; and Wallace, J., "Reinforced Concrete Coupling Beams—Part II: Modeling," *ACI Structural Journal*, V. 110, No. 6, Nov.-Dec. 2013, pp. 1067-1076.

10. Cheng, M.-Y.; Gitomarsono, J.; and Zeng, H.-Y., "Cyclic Test of Diagonally Reinforced Concrete Coupling Beam with Different Shear Demand," *ACI Structural Journal*, V. 116, No. 6, Nov. 2019, pp. 241-250. doi: 10.14359/51718010

11. Weber-Kamin, A. S.; Lequesne, R. D.; and Lepage, A., "Reinforced Concrete Coupling Beams with High-Strength Steel Bars," SM Report No. 143, The University of Kansas Center for Research, Inc., Lawrence, KS, 2020, 598 pp.

12. Lequesne, R. D., "Behavior and Design of High-Performance Fiber-Reinforced Concrete Coupling Beams and Coupled-Wall Systems," PhD dissertation, University of Michigan, Ann Arbor, MI, 2011, 277 pp.

13. Ameen, S.; Lequesne, R. D.; and Lepage, A., "Diagonally-Reinforced Concrete Coupling Beams with High-Strength Steel Bars," SM Report No. 138, The University of Kansas Center for Research, Inc., Lawrence, KS, 2020, 346 pp.

14. Poudel, A.; Ameen, S.; Lequesne, R. D.; and Lepage, A., "Diagonally Reinforced Concrete Coupling Beams: Effects of Axial Restraint," *ACI Structural Journal*, V. 118, No. 6, Nov. 2021, pp. 293-303.

15. Malcolm, R. C.; Bull, D. K.; Henry, R. S.; and Ingham, J. M., "The Effects of Axial Restraint in Reinforced Concrete Coupling Beams," *Proceedings of the New Zealand Concrete Industry Conference*, Taupō, New Zealand, 2014, pp. 150-159.

16. Cheng, M.-Y.; Fikri, R.; and Chen, C.-C., "Experimental Study of Reinforced Concrete and Hybrid Coupled Shear Wall Systems," *Engineering Structures*, V. 82, 2015, pp. 214-225. doi: 10.1016/j.engstruct.2014.10.039

17. Ameen, S.; Lequesne, R. D.; and Lepage, A., "Diagonally Reinforced Concrete Coupling Beams with Grade 120 (830) High-Strength Steel Bars," *ACI Structural Journal*, V. 117, No. 6, Nov. 2020, pp. 199-210.

18. Weber-Kamin, A. S.; Ameen, S.; Lequesne, R. D.; and Lepage, A., "PRJ-3053 - Database of Diagonally-Reinforced Concrete Coupling Beams," Designsafe-ci.org, 2021. doi: 10.17603/ds2-46wc-n185

19. Lepage, A.; Lequesne, R. D.; Weber-Kamin, A. S.; and Ameen, S., "Chord Rotation Capacity of Diagonally-Reinforced Concrete Coupling Beams," *12th National Conference on Earthquake Engineering*, Salt Lake City, UT, 2022, Paper No. 10806.

20. Lim, E.; Hwang, S.-J.; Cheng, C.-H.; and Lin, P.-Y., "Cyclic Tests of Reinforced Concrete Coupling Beam with Intermediate Span-Depth Ratio," *ACI Structural Journal*, V. 113, No. 3, May-June 2016, pp. 515-524. doi: 10.14359/51688473

21. Lim, E.; Hwang, S.-J.; Wang, T.-W.; and Chang, Y.-H., "An Investigation on the Seismic Behavior of Deep Reinforced Concrete Coupling Beams," *ACI Structural Journal*, V. 113, No. 2, Mar.-Apr. 2016, pp. 217-226.

22. Howard, B., "Seismic Response of Diagonally Reinforced Coupling Beams with Varied Hoop Spacings," MS thesis, McGill University, Montreal, QC, Canada, 2017, 99 pp.

23. Kwan, A. K. H., and Zhao, Z.-Z., "Cyclic Behaviour of Deep Reinforced Concrete Coupling Beams," *Proceedings of the Institution of Civil Engineers - Structures and Buildings*, V. 152, No. 3, 2002, pp. 283-293. doi: 10.1680/stbu.2002.152.3.283

24. Shimazaki, K., "De-Bonded Diagonally Reinforced Beam for Good Repairability," *Proceedings of the 13th World Conference on Earthquake Engineering*, Vancouver, BC, Canada, 2004, Paper No. 3173.

25. Han, S. W.; Kang, J.-W.; Jee, H.-W.; Shin, M.; and Lee, K., "Cyclic Behavior of HPFRCC Coupling Beams with Bundled Diagonal Bars," *International Journal of Concrete Structures and Materials*, V. 12, No. 1, 2018, Article No. 42. doi: 10.1186/s40069-018-0271-6

26. Han, S. W.; Lee, C. S.; Shin, M.; and Lee, K., "Cyclic Performance of Precast Coupling Beams with Bundled Diagonal Reinforcement," *Engineering Structures*, V. 93, 2015, pp. 142-151. doi: 10.1016/j.engstruct.2015.03.034

27. Park, W.-S.; Kang, T. H.-K.; Kim, S.; and Yun, H.-D., "Seismic Performance of Moderately Short Concrete Coupling Beams with Various Reinforcements," *ACI Structural Journal*, V. 117, No. 3, May 2020, pp. 141-154.

28. Gonzalez, E., "Seismic Response of Diagonally Reinforced Slender Coupling Beams," MS thesis, The University of British Columbia, Vancouver, BC, Canada, 2001, 164 pp.

ACI STRUCTURAL JOURNAL TECHNICAL PAPER

Title No. 120-S101

Redistribution of Internal Forces in Reinforced Concrete Beams Subjected to Combined Load

by Jung-Yoon Lee, Na-Yeong Kim, DongIk Shin, Kil-Hee Kim, and Muhammad Haroon

In an actual structure, torsion seldom acts alone; rather, a complex load combination acts together. Members subjected to a complex loading condition—that is, shear, bending, torsion, and so on—show lower strength compared to the members under torsion only. However, when structural members exhibit ductile behavior, the force-deformation correlation of shear force, bending, and torsional moment may change due to the redistribution of internal forces. In this study, the interaction of bending and torsional moments was evaluated by analyzing the test results of 123 reinforced concrete (RC) members subjected to combined loading. Additionally, 13 RC beams subjected to combined actions of bending and torsional moments were tested to investigate the effect of force redistribution. The results indicate that the post-yielding behavior of actual members subjected to combined loading significantly differs from the theoretically predicted one. This is because the theoretically induced bending and torsional moment interaction curves are based on strengths corresponding to the yield point of reinforcement. However, the experimental results show that the force redistribution mechanism develops after the first reinforcement yielding. Consequently, the torsional strength does not decrease as sharply as theoretically assumed, even when the bending moment increases.

Keywords: bending moment; combined load; force redistribution; torsional strength.

INTRODUCTION

With the recent increasing architectural trend of developing atypical structures, the need for more research on torsional design has increased, in particular the torsional behavior in the presence of other loads. Considering the complexities associated with the torsional behavior of reinforced concrete (RC) members in the presence of other actions, a majority of existing studies focused on investigating the members subjected to pure torsion, to achieve a better understanding by reducing complexity. A noticeable number of studies on torsional strength evaluation were conducted by Hsu,[1] McMullen and Rangan,[2] Mitchell and Collins,[3] MacGregor and Ghoneim,[4] Rahal and Collins,[5] and Lee and Kim,[6] which mainly focused on experimental evaluation of the behavior of members subjected to pure torsion. The torsional strength of members with high-strength concrete was studied by Rasmussen and Baker,[7] Koutchoukali and Belarbi,[8] and Fang and Shiau.[9] In recent years, Kim et al.[10] and Lee et al.[11] investigated the applicability of high-strength torsion reinforcing bars and pointed out the difference between high-strength shear and torsion reinforcing bars.

On the other hand, studies on members subjected to combined loads—such as bending moment and torsion or bending moment, shear, and torsion—were mainly conducted in the 1960s and 1970s. Gesund and Boston,[12] Collins et al.,[13] and Pandit and Warwaruk[14] evaluated the correlation of bending and torsional moments by testing the RC members subjected to combined bending and torsion. Gesund and Boston[12] observed that the torsional strength decreases as the bending moment increases. Collins et al.[13] showed that when the amount of flexural tensile reinforcement was greater than that of compression reinforcement, the rate of decrease in torsional strength was noticeably reduced. Pandit and Warwaruk[14] reported changes in the maximum torsional strength with variations in the amount of flexural tensile and compression reinforcement. Pritchard,[15] Badawy et al.,[16] and Ewida and McMullen[17] pointed out that the torsional strength decreases as the shear force increases. Elfren et al.,[18] Klus,[19] McMullen and Warwaruk,[20] and Osburn et al.[21] evaluated the behavior of members subjected to three loads: bending, shear, and torsion. Klus[19] developed the interaction relationship between torsional and bending shear capacities through tests of rectangular RC members. McMullen and Warwaruk[20] evaluated the correlation between failure mode and strength through experiments with the ratio of torsion to bending moment, considering the transverse shear force as the principal variable. Meanwhile, Rahal and Collins[5] evaluated the correlation of combined loads based on a truss analogy. Li[22] experimentally evaluated the torsional behavior of RC bridge columns subjected to cyclic combined loading and reported that the pinching effect of flexural hysteresis was magnified by combined actions, along with increasing torsional-to-bending-moment ratios (T/M). Consequently, the flexural energy-dissipation capacity of columns was reduced. Greene and Belarbi[23] developed a model capable of predicting the load-deformation response up to the ultimate capacity of RC members subjected to torsion combined with bending and shear. Ju[24] and Ju and Lee[25] developed a torsional behavior model of RC members subjected to combined loads based on a nonlinear analysis method and used a database of experimental results to verify the proposed model.

Based on the research thus far, the torsional design guidelines in design codes such as ACI 318-19[26] and Eurocode 2[27] present a correlation curve for the internal forces of members subjected to shear and torsion. This correlation curve has

ACI Structural Journal, V. 120, No. 6, November 2023.
MS No. S-2022-396.R1, doi: 10.14359/51739093, received May 22, 2023, and reviewed under Institute publication policies.

a circular shape, where the torsional strength decreases as the shear force increases. On the other hand, the correlation between bending and torsional strength proposed in previous studies[28] is affected by either the cross-sectional shape or failure mode. Various other correlations such as linear, circular, trilinear, and square have also been proposed.[28] Because most of the members in structures are subjected to combined loads, the amount of reinforcement required may vary depending on the correlation used for these loads. From a theoretical point of view, the correlation between bending moment and torsional moment is circular, but analysis of the existing data shows that this correlation is close to trilinear or square in shape. If the correlation between moment and torsional strength is not linear or circular, but trilinear or square, members may be over-reinforced when overlapping the bending and torsional reinforcement. In this study, a scheme of experimental tests was carried out under combined loading actions to investigate the effect of the force redistribution mechanism developed after the first yielding of reinforcement. The correlation of bending and torsional moments was evaluated by conducting experiments on 13 RC members subjected to combined loading. A detailed analysis of existing experimental test data of 123 specimens was also conducted to comprehend the important experimental observations reported in this study.

RESEARCH SIGNIFICANCE

In current design codes—that is, ACI 318-19,[26] CSA A23.3:19,[29] and Eurocode 2[27]—the longitudinal flexural and torsional reinforcement are superimposed. Although designed separately, both reinforcements will resist bending and torsional forces at the same time in an actual structure. Under different loading conditions, the longitudinal torsional reinforcement may act as flexural reinforcement, and vice versa. Therefore, depending on the role of reinforcing bars and the state of stress (whether yielded or not yielded), the behavior of structures subjected to combined loads may be different. In this study, the effect of the redistribution of forces in correlation with bending and torsional moments was evaluated by conducting experiments on 13 members subjected to combined loading and the detailed analysis of existing experimental tests of 123 specimens. When the correlation between bending and torsional moment is clearly understood, the design of members subjected to complex loading conditions can be improved, and excessive reinforcement can be prevented.

SHEAR FORCE, BENDING, AND TORSIONAL MOMENT INTERACTION

When shear force (V), bending (M), and torsional moment (T) act simultaneously on a structural member, these forces cause different effects on parts of the cross section. For example, when the summation of the shear stresses caused by shear force and torsional moment ($v_s + v_t$) acts on the left or right side of the section, the difference between the two values ($v_s - v_t$) acts on the opposite side. Bending and torsional moments generate axial forces N_t and N_b in the upper and lower reinforcement, respectively. The correlation between shear, torsion, and bending moments can be obtained by using the equilibrium of forces with respect to the reinforcing bar and the forces acting on each face of the section[30]

$$\frac{M}{M_o} + \left(\frac{V}{V_o}\right)^2 R + \left(\frac{T}{T_o}\right)^2 R = 1 \quad (1)$$

where M_o, V_o, and T_o are pure bending moment, shear, and torsional moment, respectively; and R is the ratio of the axial forces induced by the upper and lower longitudinal reinforcement (N_t and N_b).

The correlation between shear force and torsion (V-T) without bending moment becomes Eq. (2), and the correlation between bending moment and torsion (M-T) without shear force becomes Eq. (3).

$$\frac{V}{V_o} + \frac{T}{T_o} = 1 \quad (2)$$

$$\frac{M}{M_o} + \left(\frac{T}{T_o}\right)^2 R = 1 \quad (3)$$

In Eq. (1) and (3), when $R = 1$, the shear force and bending moment have a circular relationship, and when R is less than 1, it becomes a curve having a discontinuity point.[30]

The point to be noted here is that Eq. (2) and (3) are derived based on the assumption that the member failure is governed by the material properties. For illustration, the V, M, and T in Eq. (2) and (3) are determined by either the yield strength of the reinforcing bar (f_y), the compressive strength of concrete (f_c'), or even the effective compressive strength of concrete ($\xi f_c'$). At the moment when either the reinforcement or concrete reaches any of the aforementioned limits (f_y, f_c', or $\xi f_c'$), it is assumed that the member reaches its failure point while ignoring the effect of force redistribution on the correlation of strengths. In previous studies[28] on the correlation between bending moment and torsional moment, the interaction curve was found to be affected by several factors, such as the presence or absence of reinforcement, the shape of the section, and the failure mode. Based on these studies, linear, circular, trilinear, and square correlation curves were proposed.

Figure 1 presents the theoretical lines for the V-T and M-T interactions compared with the test results of 123 RC members subjected to combined loading, collected from the literature (Klus,[19] Collins et al.,[13] McMullen and Warwaruk,[31] Badawy et al.,[16] Rahal and Collins,[5] Gesund and Boston,[12] Pritchard,[15] Pandit and Warwaruk,[14] Osburn et al.,[21] and Onsongo[32]). The basic criteria for specimen selection were the type of loads—that is, shear, torsion, and bending moment. The specimens in the test database had a wide range of design parameters. The compressive strength of concrete (f_c') ranged from 15.5 to 53.9 MPa (2195 to 7632 psi), the depth of the section (h) ranged from 203.2 to 640 mm (8 to 25.2 in.), the amount of longitudinal reinforcement (ρ_w) ranged from 0.0081 to 0.0397, and the minimum and maximum amount of transverse reinforcement (ρ_v) were 0.0047 to 0.0203. Details of the specimens are listed in Table 1.

Table 1—123 specimens in literature

Author	Number of specimens	Description
Klus[19]	8	A series of rectangular RC beams with normal percentages of both longitudinal and transverse steel was tested, and variables are moment-torsion ratio (M/T) and shear-torsion ratio (V/T).
Collins et al.[13]	15	Rectangular RC beams with R = 0.25 and 1 were tested with the moment-torsion ratio (M/T) as a variable.
McMullen and Warwaruk[31]	34	To investigate the behavior of RC beams subjected to combined loading, 34 specimens subjected to bending, shear, and torsion were tested. The specimens were designed to have R = 0.14, 0.25, 0.36, and 1.
Badawy et al.[16]	5	Straight RC beams were tested under different combinations of bending, torsion, and shear.
Rahal and Collins[5]	5	Seven large RC beams with R = 1 were tested at different shear-torsion ratios and relatively low bending.
Gesund and Boston[12]	12	RC beams with various concrete strengths, amounts of reinforcement, and moment-torsion ratios (M/T) were tested under combined bending and torsional loads.
Pritchard[15]	4	Torsion and shear interaction of RC beams were investigated through the experiment of RC beams with shear-torsion ratio (V/T) as a variable.
Pandit and Warwaruk[14]	14	Rectangular RC beams with R = 0.36, 0.57, 0.69, and 1 under combined bending and torsional loads were tested.
Osburn et al.[21]	14	Conducted combined torsion, shear, and bending tests with the total reinforcement ratio ($\rho_l + \rho_t$) as a variable.
Onsongo[32]	12	For large rectangular RC beams with R = 0.11, tests under combined bending and torsional loads were conducted.

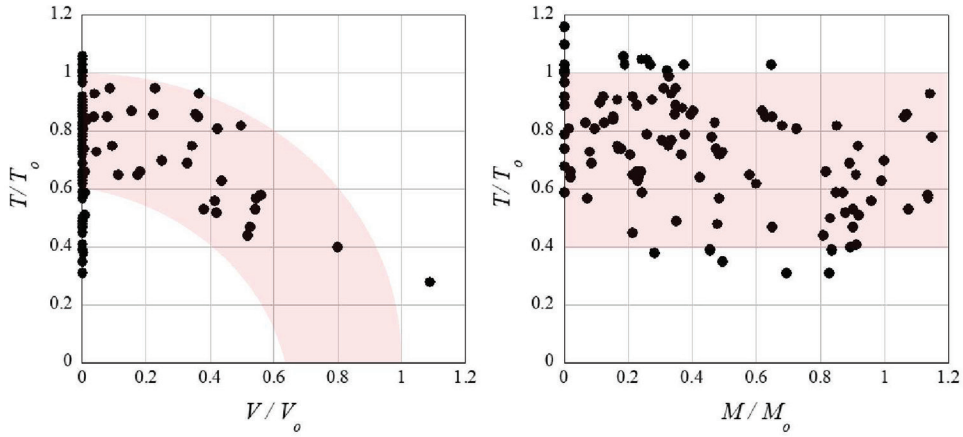

(a) *V-T* interaction (b) *M-T* interaction

Fig. 1—(a) V-T*; and (b)* M-T *interactions of 123 RC members subjected to combined load.*

Figure 1(a) shows that the distribution of experimental *V-T* interaction data closely matches the circular-shaped theoretical interaction line. However, the *M-T* correlation of Fig. 1(b) has data points distributed over a nearly rectangular-shaped band, which is different from the results obtained by Eq. (3). This is because the *M-T* correlation is expected to be affected by the redistribution of internal forces, which the theoretical model presented in Eq. (3) does not account for. The members failing in flexural tension failure mode exhibit more ductile behavior because of the redistribution of forces than the members failing in shear. Figure 2 shows the relationship between the bending moment and the drift angle of three RC members under bending moment and shear force without torsion, selected from the literature.[33] The cross section, material conditions, reinforcing bar ratio, and compressive strength of concrete of all three members were the same, while only the axial force ratio ($n = P_o/A_g f_c'$) was different, where P_o is the axial force, A_g is the gross area of the cross section, and f_c' is the compressive strength of concrete. All three members failed in flexural tension failure mode. As is widely known, when the axial force ratio (n) increases, the bending moment increases, but the ductility decreases rapidly. In the case of a member without axial force (n = O), the ductility was increased even after the bending reinforcements yielded at a point up to a maximum drift ratio of more than 12%. In members subjected to a pure bending moment, there is no significant difference between the flexural yielding moment (M_y) at Point A and the flexural strength (M_u) at Point B. Therefore, in the *M-T* correlation curve in Fig. 1, even if M_o is set as the moment value of Point A or Point B, no significant change occurs. Also, even when the drift angle increases, the failure area is limited only to the plastic hinge region. However, in the case of members subjected to combined action, such as bending moment and torsion, the loads may be redistributed while maintaining the moment after flexural yielding up to Point B, and the failure region may also be transferred from the plastic hinge region to other parts.

Considering these discrepancies in the experimental observations and the theoretical assumptions, and for a

Table 2—Properties of specimens

Specimens		f_c', MPa	Longitudinal reinforcement			Transverse reinforcement				R	Force	
			A_l, mm^2	f_{yl}, MPa	ρ_l, %	A_t, mm^2	s, mm	f_{yt}, MPa	ρ_t, %		T, %	M/M_o, %
Group A	A1	35.0	2678	446 (Two D25) 440 (Two D16) 418.7 (10 D13)	1.12	71.3	72.5	440	0.672	0.5	Max.	0
	A2										Max.	64
	A3										Max.	85
	A4										Max.	96
	A5										Max.	106
Group B	B1	35.0	2534	446 (Four D25) 418.7 (Four D13)	1.06	71.3	72.5	440	0.672	0.25	Max.	0
	B2										Max.	40
	B3										Max.	60
	B4										Max.	80
	B5										Max.	90
Group C	C1	32.3	2740	446 (Four D25) 442 (10 D10)	1.14	71.3	67.0	442	0.727	1.0	Max.	0
	C2		2740		1.14					1.14	Max.	100
Group D	D1	32.3	2740		1.14	71.3	67.0	442	0.727	1.0	69	Max.

Note: Sectional areas of D10, D16, and D25 are 71.3, 198.6, and 506.7 mm^2 (0.11, 0.31, and 0.79 in.^{2}), respectively; 1 mm = 0.039 in.; 1 mm^2 = 0.00155 in.^{2}; 1 MPa = 145 psi.

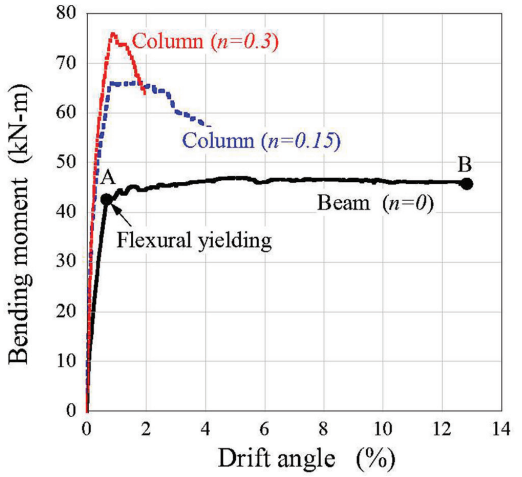

Fig. 2—Bending moment versus drift angle curves (Lee et al.[33]). (Note: 1 kN·m = 0.74 kip·ft.)

better understanding of the force redistribution mechanism and its effects on *M-T* correlation, an experimental testing program was carried out on 13 RC members subjected to combined loads. The subsequent section explains the details of the test program and its main findings.

TEST PROGRAM AND MEASUREMENTS

Specimens

A total of 13 RC beams were tested under combined bending, shear, and torsional moment. The main variable of the test specimens was the moment-torsion ratio (M/T). The specimens were tested under a sequential loading protocol, in which the bending moment (or torsional moment) was applied first, and then the torsional moment (or bending moment) was applied. The test specimens were divided into four groups (A to D). The specimens in Group A were designed to have R = 0.5, where R is the ratio of the axial force induced by upper and lower longitudinal reinforcement and calculated as the ratio of upper and lower longitudinal reinforcement. The five specimens in this group were first subject to the bending moments ratios M/M_o = 0%, 64%, 85%, 96%, and 106%, respectively, where M_o is equal to the flexural yield strength (M_y). In the next step, while maintaining the bending moment, a torsional moment was applied to the specimens until failure. In Table 2, specimen A1 with M/M_o = 0% means that the specimen was subjected to only pure torsion without bending moment. In addition, specimen A5 with M/M_o = 106% means that the bending moment was applied to the specimen until the strain of longitudinal tensile reinforcement reached 1.06 times the yield strain (ε_y).

Five specimens in Group B were designed to have R = 0.25, and bending moments of M/M_o = 0, 40, 60, 80, and 90% were applied first. Later, the torsional moment was applied to the specimen until failure. Specimens C1 and C2 in Group C had R = 1.0 and 1.14, respectively. The bending moment was first applied to Specimens C1 and C2 in the same manner as the specimens of Groups A and B, and then the torsional moment was applied. The M/M_o of C1 and C2 were 0% (pure torsion) and 100%, respectively. Unlike the other specimens, Specimen D1 in Group D was initially subjected to a torsional moment of $0.69T_n$; then, while maintaining the torsional moment, bending moment was applied to the specimen until failure. The torsional strength (T_n) and flexural yield strength (M_y) of specimens in Table 2 were calculated according to ACI 318-19.

As shown in Fig. 3, the specimen has a total length of 2500 mm (98.4 in.), with 500 mm and 700 mm (19.7 and 27.6 in.) long stubs on the left and right, respectively. The length of the test region was 1300 mm (51.2 in.) in the center (between the support and loading regions). The size of the cross section was 400 x 600 mm (15.7 x 23.6 in.), and the spacing between the centers of the closed stirrup was 310 x 510 mm (12.2 x 20.1 in.). The thickness of the cover concrete of all specimens was 40 mm (1.6 in.). In Groups A, C, and D, the longitudinal torsional reinforcing bars were evenly

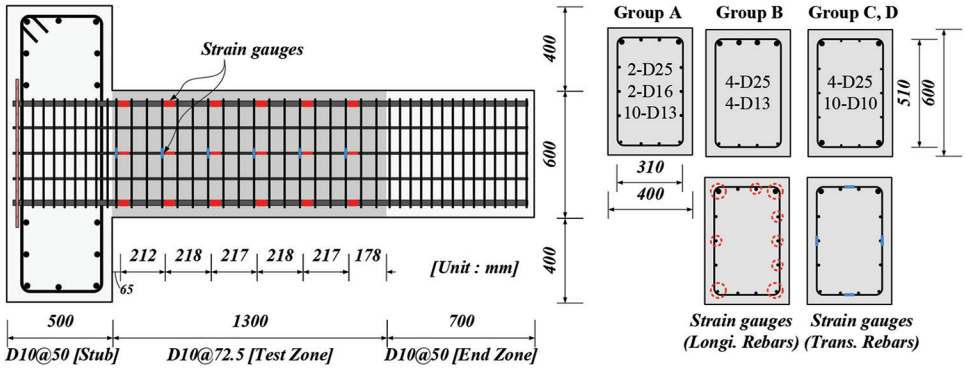

Fig. 3—Test specimens. (Note: Units in mm; 1 mm = 0.0394 in.)

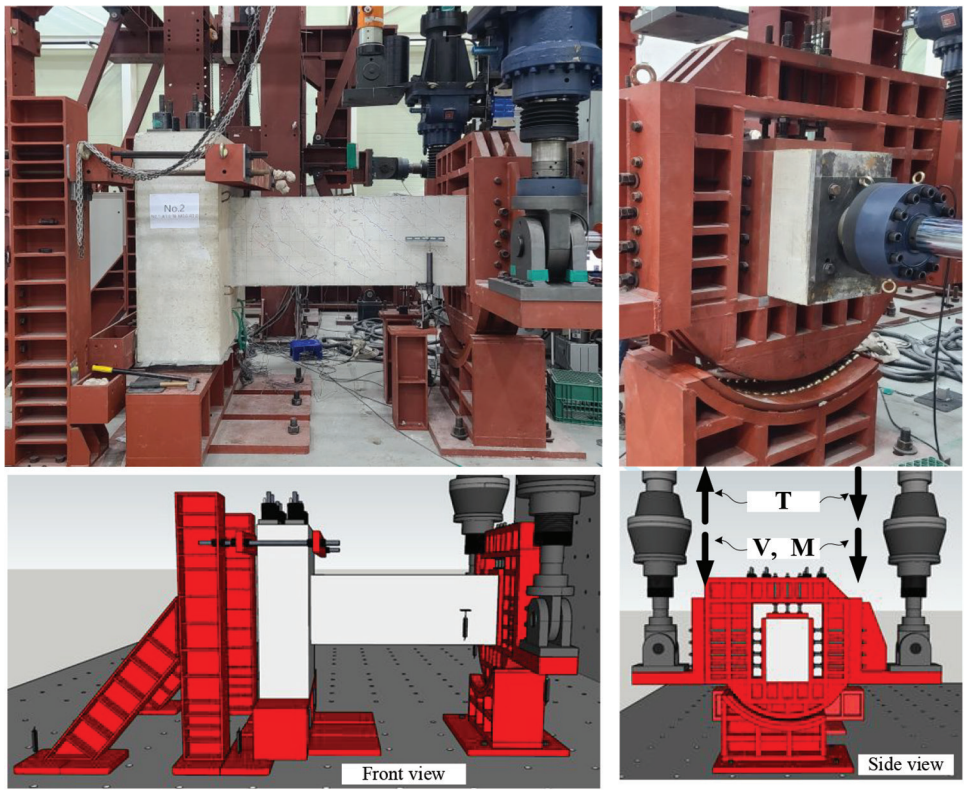

Fig. 4—Loading system.

distributed on all four sides. On the other hand, in Group B, the longitudinal reinforcing bars were concentrated on the top and bottom sides of the section, without any reinforcement on the left and right sides of the section, to evaluate the effect of reinforcement direction on the torsional behavior. The stub on the left end was fixed to a strong floor using a hydraulic jack, and the stub on the right end of the test specimen was connected to the load-bearing frame. Strain gauges were attached to the transverse and longitudinal torsional reinforcement to monitor the torsional strain. Four linear variable differential transducers (LVDTs) were used to record the angle of twist. Figure 3 shows the location of the strain gauges of the specimens to monitor the strain of longitudinal and torsional reinforcement.

Using two actuators connected to the left end of the specimen, bending and torsional moments were applied to the specimen, as shown in Fig. 4. The two actuators were operated in the same downward direction to apply the bending moment to the specimen, and in the opposite directions to apply the torsional moment. The difference in the bending and torsion was controlled by the difference in the load applied by the two actuators. A ball-shaped hinge was designed and installed under the torsional loading frame to prevent longitudinal deformation.

TEST RESULTS

Overview of test results

All the test specimens showed either a torsional or flexural failure. Figure 5 shows the crack pattern of the front or rear side of the test specimen at the maximum load. To understand the cracking behavior more clearly, Fig. 5 shows the crack pattern in members of Group A on the left side, along with the actual crack pictures of specimens in Groups B, C, and D on the right side. In the case of Specimens A1, B1, and C1 subjected only to torsion, diagonal web cracks with almost a constant angle occurred, and finally, the concrete crushed

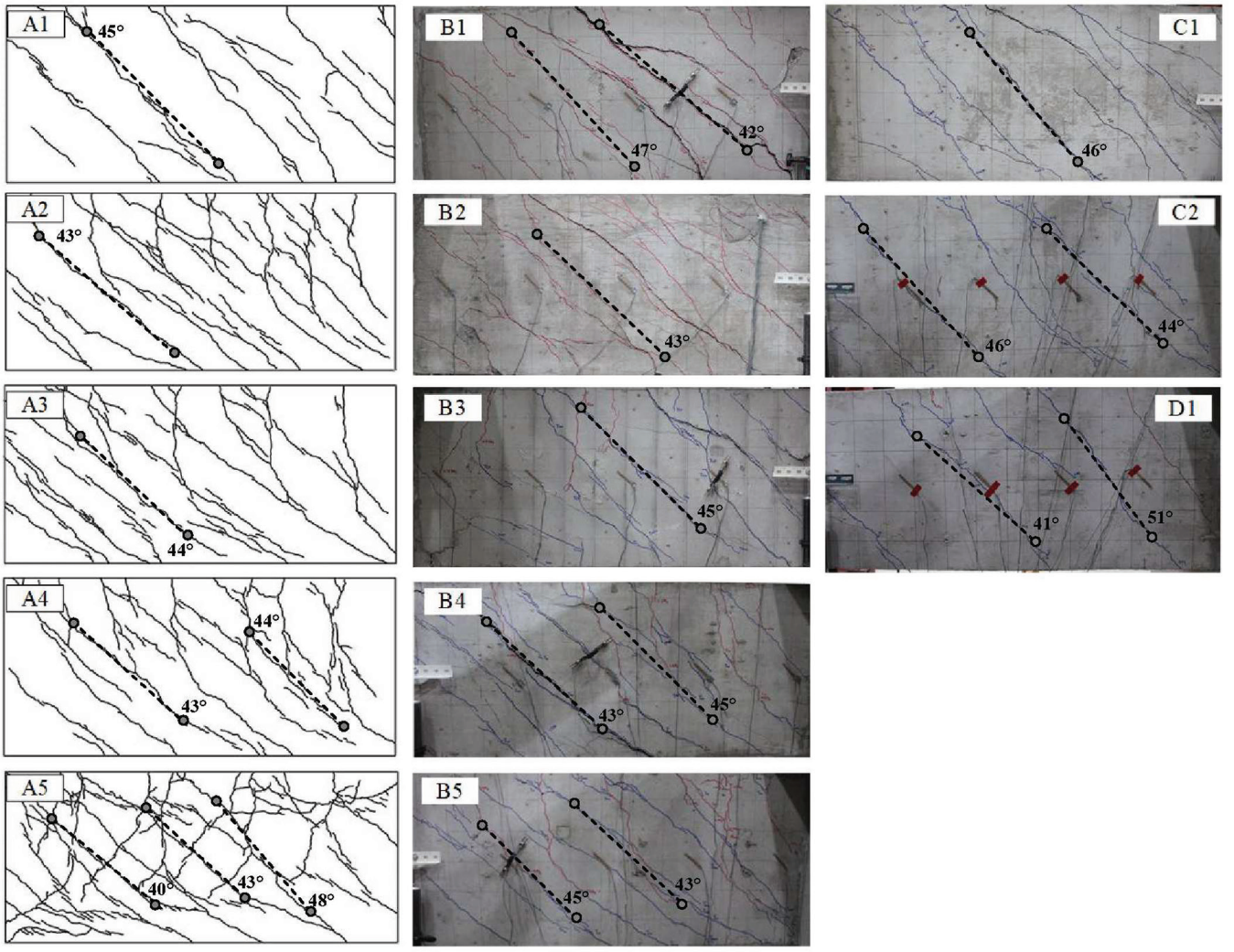

Fig. 5—Crack patterns of test specimens at peak load.

in the web region or corner of the member. On the other hand, in members subjected to both bending and torsional moments, after flexural cracking in the direction perpendicular to the member axis, the crack direction was changed to an angle of nearly 45 degrees to the member axis. The length of the flexural crack increased with increasing M/M_o.

Relationship between torsion and angle of twist

Figure 6 shows the relationship between the torsional moment and rotation angles of 13 specimens in four groups. Specimen D1 has a very small torsional rotation angle because it was designed to fail due to bending moment. In this specimen, while maintaining the torsional moment of 100 kN·m (571 lb·in.), bending moment was applied to the specimen until failure. As shown in Fig. 6, the torsional rigidity of members subjected to pure torsion was greater than that of the other specimens. This is because the cracks due to bending, which was applied first, lowered the stiffness when the torsional moment was applied. The torsional behavior of members was affected by both the M/M_o and the ratio of the forces induced by the upper and lower longitudinal bars (R). However, the effect was insignificant due to R. Figures 7(a) and (b) show the diagonal cracking and maximum torsional strengths with respect to the bending moment ratio, M/M_o. As shown in the figure, the cracking strength decreases as M/M_o increases. This is because of the reduction in the torsional stiffness due to prior flexural cracking. In the case of specimens subjected to a combined loading, the maximum torsional strength remained almost unchanged, or reduced slightly, which was insignificant when the bending moment ratio (M/M_o) was increased. Table 3 shows the crack strength, torsional strength, and torsion angle of specimens.

DISCUSSION

The torsional moment ratio (T/T_o) calculated by Eq. (1) results in a curve with discontinuity points[30] because this equation is affected by the ratio of the longitudinal tensile and compression reinforcement ratios (R). While using this equation, when M/M_o is greater than 1.0, T/T_o becomes zero (0). However, experimental results show that even when M/M_o is greater than 1.0, T/T_o still maintains a value close to 1.0. There is a significant difference between the experimental and the theoretically calculated results. Also, the torsional moment calculated by Eq. (1) depicts a point of discontinuity because of R, but there was no such discontinuity in the test results, which can be confirmed in Fig. 1(b), based on the analysis of the test results of 123 RC members

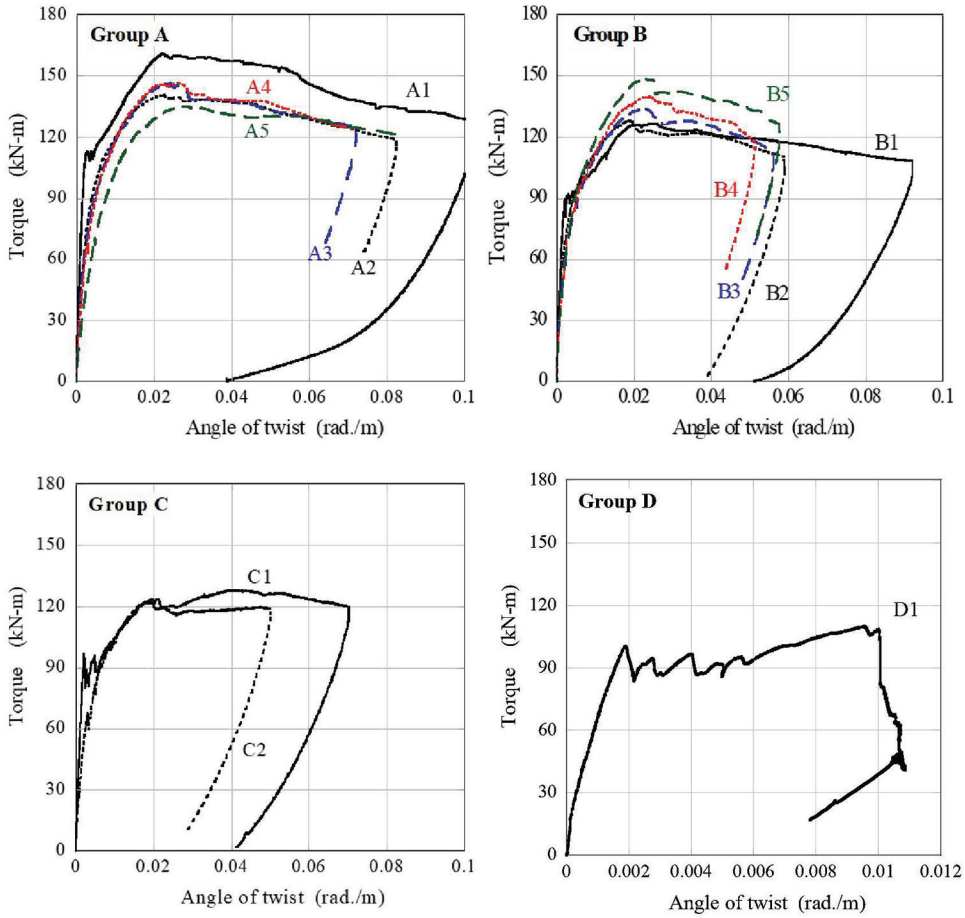

Fig. 6—Torque versus twist angle curves of specimens. (Note: 1 kN·m = 0.74 kip·ft.)

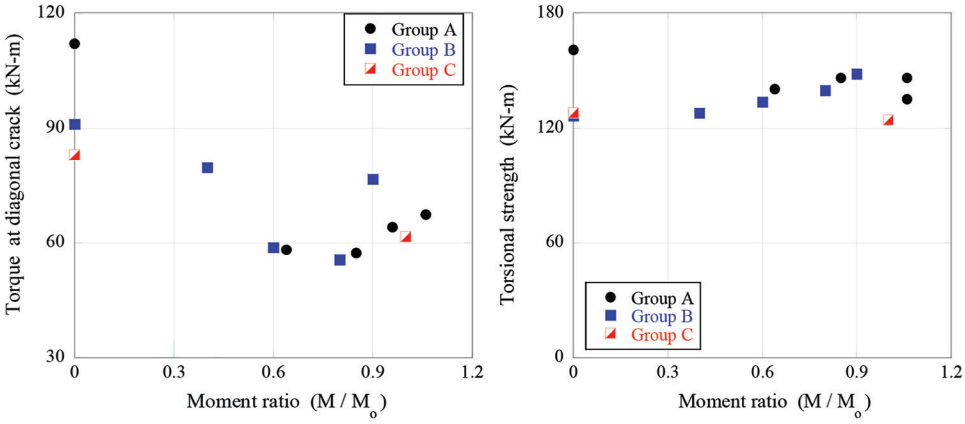

Fig. 7—(a) Crack strength; and (b) torsional strength of specimens. (Note: 1 kN·m = 0.74 kip·ft.)

subjected to combined loads. The main reasons for this significant contrast between experimental observations and theoretical predictions can be associated with the following important points.

Failure criteria

As shown in Fig. 8, when shear force, bending moment, and torsion act simultaneously on the RC members, the effect of these forces on the sectional area is different at different points. The sum ($v_s + v_t$) of the shear stresses induced by shear force and torsional moment acts on the right side (or left side) of the section, whereas the difference ($v_s - v_t$) of shear stresses acts on the left side (or right side). As a result, the shear stress acting on one side of the section becomes much greater than the stress acting on the other side.[30] In this paper, the right side on which the sum of shear stresses ($v_s + v_t$) acts is denoted as the "weak side" of the section, while the left side where the difference of shear stresses ($v_s - v_t$) acts is called the "strong side." The right (weak) side of the section is more prone to failure. The deformation of the

Table 3—Test results of specimens

Specimen		Cracking		Ultimate				Failure mode
		T_{cr}, kN·m	θ_{cr}, rad/m	T_n, kN·m	θ_n, rad/m	V_d, kN	M_d, kN·m	
Group A	A1	112.06	0.0027	161.03	0.0222	000.00	—	TT
	A2	58.25	0.0018	140.47	0.0226	123.89	207.51	TT
	A3	57.43	0.0018	146.39	0.0242	163.30	273.52	TT
	A4	64.12	0.0025	146.38	0.0258	170.70	285.93	TT
	A5	67.42	0.0045	135.19	0.0285	167.91	281.25	TT
Group B	B1	91.12	0.0030	126.57	0.0249	—	—	TT
	B2	79.83	0.0032	128.01	0.0187	105.64	176.94	TT
	B3	58.81	0.0023	133.82	0.0229	122.87	205.80	TT
	B4	55.59	0.0020	139.82	0.0242	166.33	278.61	TT
	B5	76.69	0.0035	148.41	0.0233	197.33	330.52	TT
Group C	C1	82.98	0.0024	128.23	0.0392	—	—	TT
	C2	61.57	0.0031	124.29	0.0200	87.55	146.64	TT
Group D	D1	—	—	110.05	0.0096	—	—	F

Note: TT is torsional tension failure; F is flexural failure; 1 kN·m = 0.74 kip·ft; 1 kN = 0.225 kip; 1 kN = 0.225 kip.

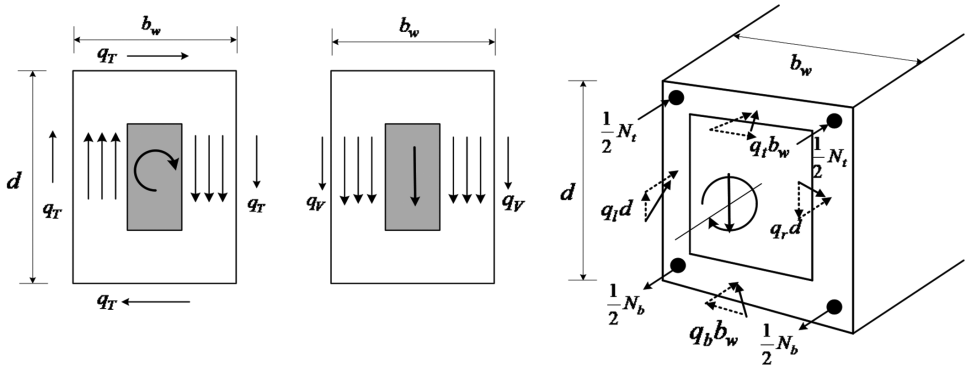

Fig. 8—RC beam subjected to shear and torsion.

reinforcing bar and concrete on this side will be greater than that on the left side. Therefore, the stress of each longitudinal bar may vary according to the direction of bending and torsional moments. To experimentally measure the stress and deformation variation in the longitudinal reinforcement, nearly 100 strain gauges were attached to the longitudinal steel bars and stirrups of each specimen tested in this study. Figure 9 shows the strain distribution of longitudinal steel bars of Specimens A1 and A2.

Specimen A1 is subjected to torsional moment only, while A2 is subjected to combined loads. The strain distribution of A2 shows the typical strain distribution of the other specimens subjected to combined loads. The strains corresponding to the four loading levels (40, 60, 80, and 100% of T_{max}) are shown in Fig. 9. In the case of A1 subjected to pure torsion, the strain was distributed almost uniformly over the four sides of the section. The two reinforcing bars on the left and bottom sides reached the yield strain almost simultaneously. On the other hand, for specimen A2 subjected to combined loading, the strain of the upper and right sides was much greater than that of the left and lower sides due to the effects of bending moment and shear force. None of the specimens subjected to combined loads failed at the moment when the steel bar yielded. Even after the longitudinal bar yielded, the strains of the other bars continued to increase, and the member continued to resist the loads.

Figures 10(a) and (b) show the strain distribution of the stirrups on the four sides of the section of specimen A1. As shown, the strain distributions on the four sides were nearly similar for A1 under pure torsion. At the maximum load, the strains on the four sides reached the strain corresponding to yield strain, whereas, in specimen A2 under combined loads, the strain on the right side (weak side) of the section was much greater than that on the left side (strong side) of the section. The strain on the upper and lower sides was smaller than that on the right side (weak side). The strain on the left side, where the directions of shear force and torsional moment are opposite, was the smallest. The stirrups on the three sides (right, upper, and lower sides) reached the yield strain, but the strain on the left side did not reach the yield strain. In addition, the load continued to increase even after the reinforcing bars on the right side (weak side) yielded, which is identical behavior to that of the specimens subjected to bending moment in Fig. 2.

As explained earlier, in the moment, shear, and torsion (*M*-*V*-*T*) relationships in Eq. (1) to (3), it is assumed that the

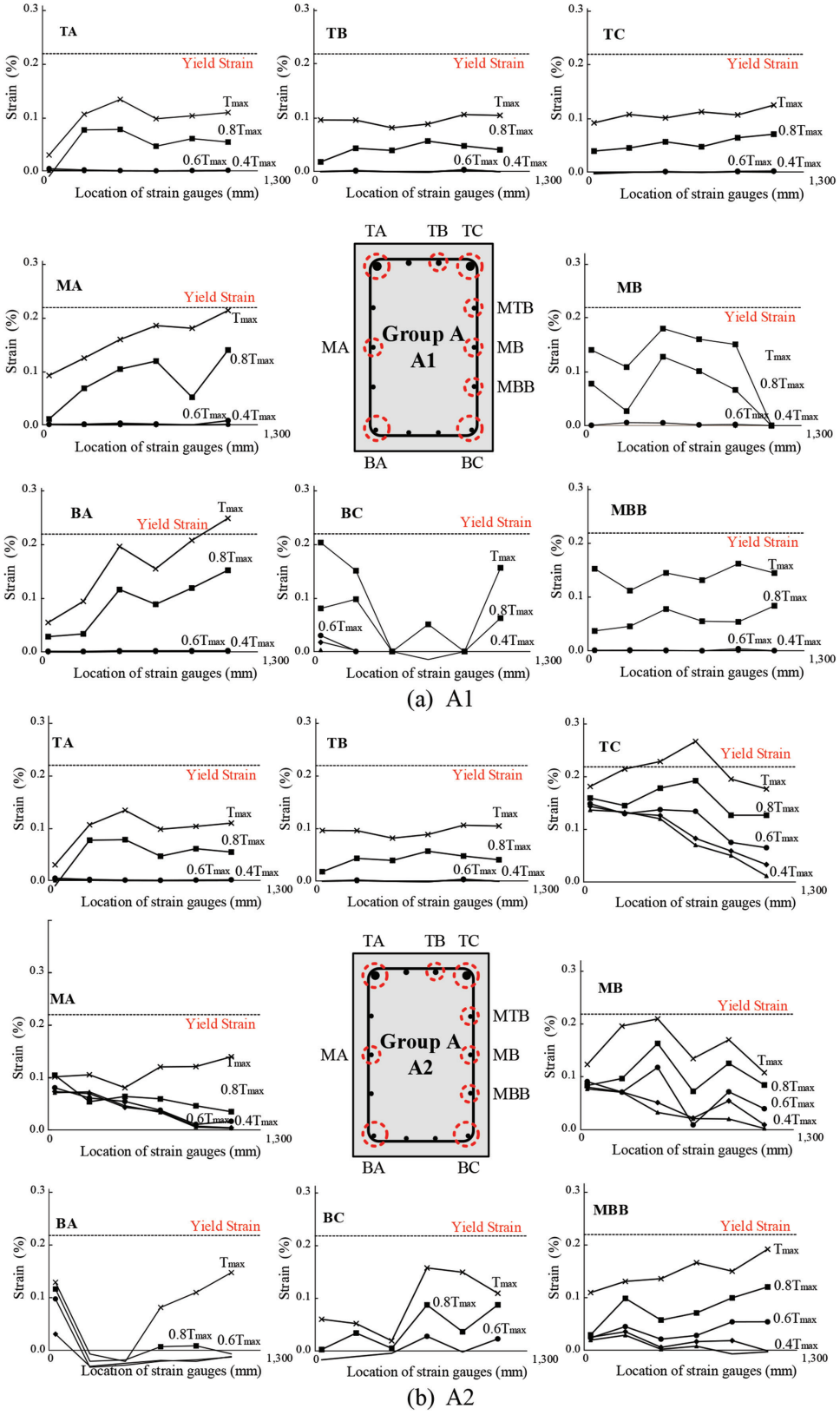

Fig. 9—Strain distribution of longitudinal steel bars of: (a) A1; and (b) A2. (Note: 1 mm = 0.0394 in.)

failure is controlled by the material properties, such as when reinforcement reaches the yield strength (f_y) or concrete reaches its crushing compressive strength (f_c').[28] Therefore, if it is theoretically assumed that the member reaches the maximum load at the moment when the steel bars yield or the concrete reaches the compressive strength, the resulting correlation curve by using Eq. (1) to (3) becomes almost circular. In the case of a concrete member without reinforcement or a member subjected to a high axial force (as shown in Fig. 2), where failure is governed by concrete crushing before the reinforcement yields, the *M-V-T* correlation curve can be circular, as drawn through Eq. (1) to (3),

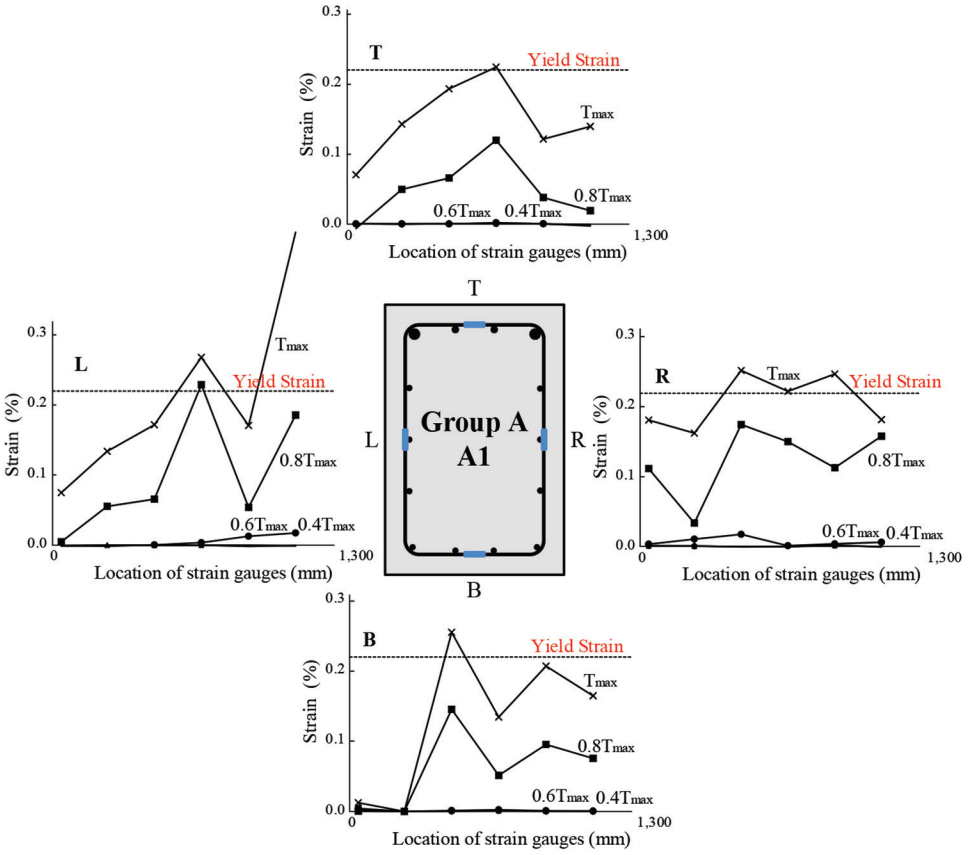

(a) A1

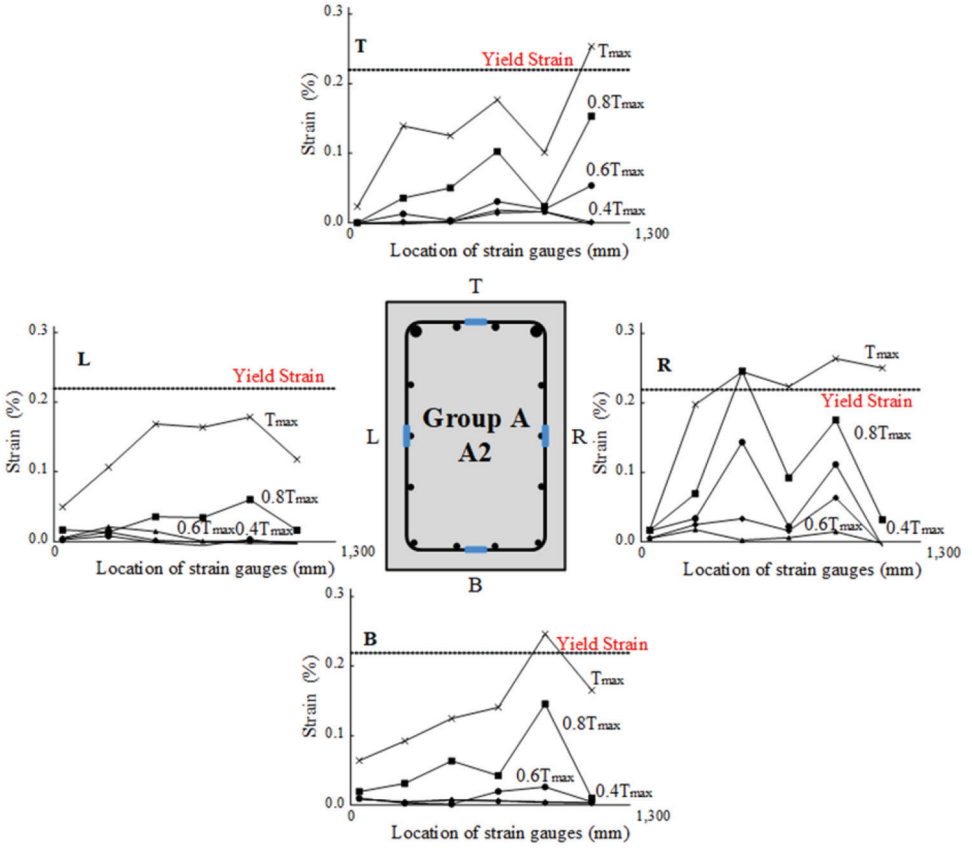

(b) A2

Fig. 10—Strain distribution of transverse steel bars of: (a) A1; and (b) A2. (Note: 1 mm = 0.0394 in.)

because these members fail immediately after one material reaches its maximum capacity. However, for the RC members that fall after the reinforcement yields, the *M-V-T* correlation curve may not be circular. This is because even after the reinforcing bar yields, the deformation increases and force redistribution occurs, as mentioned in Fig. 8. In this study, an *M-T* correlation curve was drawn by using the torsional moment when the measured strain of the steel bar first reached the yield strain. Figure 11 shows an *M-T* correlation curve developed based on the torsional moment corresponding to the reinforcing bar yielding. As shown in Fig. 11, similar to the circular curve[28] drawn using Eq. (1) to (3), the torsional moment decreases when M/M_o increases and becomes 0 when M/M_o is 1.0. Therefore, if the *M-T* correlation curve is drawn by using the torsional strength at reinforcing bar yielding, the theoretical and experimental *M-T* curves are quite similar. However, if this curve is drawn using the ultimate strength after force redistribution, the experimental *M-T* curve may not be the same as the theoretical one because the strength of the member increases, even after the reinforcing bar yields.

Force redistribution

The mechanism of force redistribution affects the deformability of RC members. To understand the force redistribution phenomena more clearly in RC members subjected to combined loading conditions, the stress (f_s) of the stirrup was calculated inversely by using the measured strains on the four sides of the section, which was later substituted in Eq. (4a) and (4b) to calculate the torsional moment[34]

$$T_{n1} = T_{n3} = \frac{A_t f_{ts} y_o}{s} \cot\theta \times \frac{x_o}{2} \quad (4a)$$

$$T_{n2} = T_{n4} = \frac{A_t f_{ts} x_o}{s} \cot\theta \times \frac{y_o}{2} \quad (4b)$$

where x_o is the length between the centers of the shorter sides of the closed stirrup; and y_o is the length between the centers of the longer sides of the closed stirrup. The torsional moment (T_{ns}) was calculated with the following assumptions:

1. The crack angle remains constant regardless of T_{ns}, which can be calculated as $\cot^2\theta = \rho_l f_{yl}/(\rho_t f_{yt})$.[30] This is because the crack angle calculated by substituting the yield strength (f_{yt} and f_{yl}), and the crack angle calculated by substituting the steel stresses (f_{ts} and f_{ls}) measured in the test did not significantly differ.
2. The effective area of concrete (A_o) was assumed to be equal to the area enclosed by the outermost transverse reinforcement (A_{oh}) because the spalling of corner concrete occurs after torsional moment decreased in the post-peak loading range.

Figure 12 compares the calculated torsional moments for the four sides of the section. In the case of Specimen B1, the calculated results of the torsional moment were jagged as some values of the strain increased rapidly in the initial stage of the experiment. Point A in the figure shows the moment at which one of the stirrup legs on the four sides of the section first reached the yield strain. For specimens A1, B1, and C1

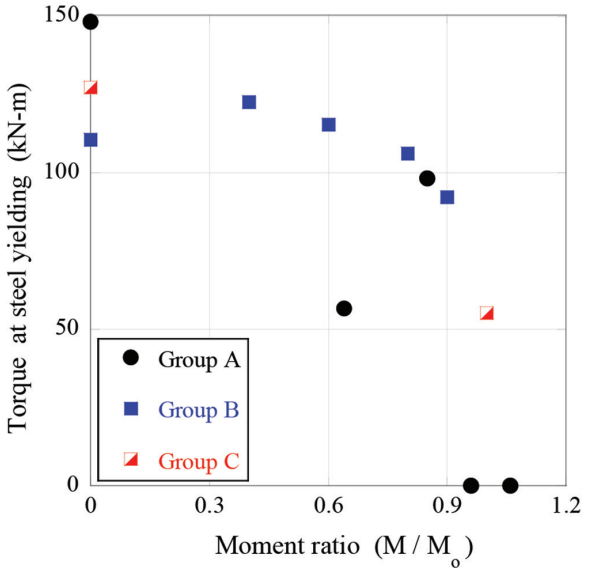

Fig. 11—Interaction of bending moment and torsional strength of specimens based on steel yielding. (Note: 1 kN·m = 0.74 kip·ft.)

subjected to pure torsion, the torsional moments on all four sides of the section were almost the same. However, for the specimens subjected to combined loads, the torsional moment on the right side (weak side), where shear and torsion acts in the same direction, was the largest. The torsional moment on the left side (strong side), where the two forces act in the opposite directions and cancel each other out, was the smallest. Even in the case of combined loads, the members did not fail at the moment when the stirrup on the weak side yielded. While the stirrup on the weak side first reached the maximum load and continued to support the load, the strain of the stirrup on the strong side continued to increase, and the torsional moment also increased. The strain rate of the stirrup on the strong side increased more rapidly after the stirrup on the weak side yielded. This indicates that if one side of the section fails, the other side of the section takes the loads over, and the member continues to resist the external forces. The total torsional moment can be calculated by taking a summation of the four torsional moments calculated by Eq. (4a) and (4b).

$$T_{ns} = T_{n1} + T_{n2} + T_{n3} + T_{n4} \quad (5)$$

Figure 13 compares the experimentally measured torsional moments with the calculated torsional moment, which is taken as the summation of the torsional moments of the four sides of the section, calculated using the measured stirrup strain. As shown in the figure, the calculated torsional moment (T_{ns}) of Eq. (5) is very similar to the measured one. Before cracking, the calculated torsional moment (T_{ns}) is lower than the measured one, because Eq. (5) does not include the concrete contribution to the torsional strength. After cracking, the difference between the calculated and measured torsional moments becomes smaller. The torsional moment continues to increase even after the first yielding of the stirrup on one of the four sides, as denoted by Point A.

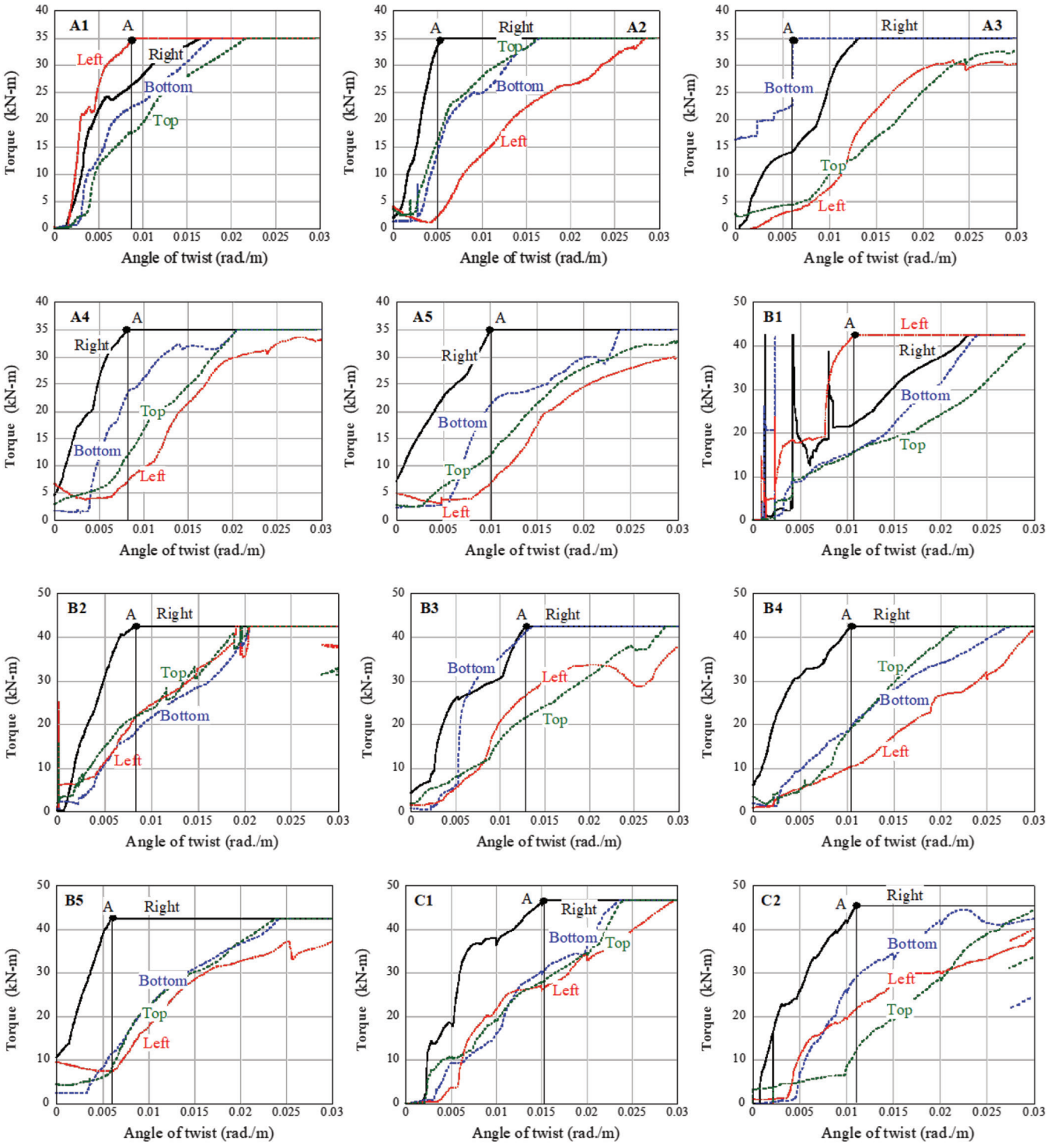

Fig. 12—Torsional moment calculated using measured stirrup stains on four sides of section. (Note: 1 kN·m = 0.74 kip·ft.)

Figure 14 shows the calculated torsional moment corresponding to the first stirrup yielding (Point A) in a similar way as it was done in the theoretically drawn *M-V-T* correlation curve using Eq. (1) to (3). Compared to the results shown in Fig. 11 based on the yield point of longitudinal bars, the torsional moment reduction ratio of Fig. 14 was slightly lower than that of Fig. 11. However, both the figures show a matching trend of decreasing torsional moment with increasing M/M_o.[28] The comparisons of torsional strengths presented in Fig. 7(b), 11, and 14 show that the torsional moments increase due to the redistribution of forces even after the reinforcement yields.

ACI 318-19[26] requires an under-reinforced design of RC members to have more desired ductile behavior through the redistribution of internal forces after the first yielding of reinforcement. In this study, the failure modes of 123 specimens collected in the literature were investigated to see if these members failed in ductile failure mode. Because these specimens were subjected to both bending and torsional moments, the failure mode must also be classified in accordance with each load. Figures 15(a) and (b) classify the failure modes

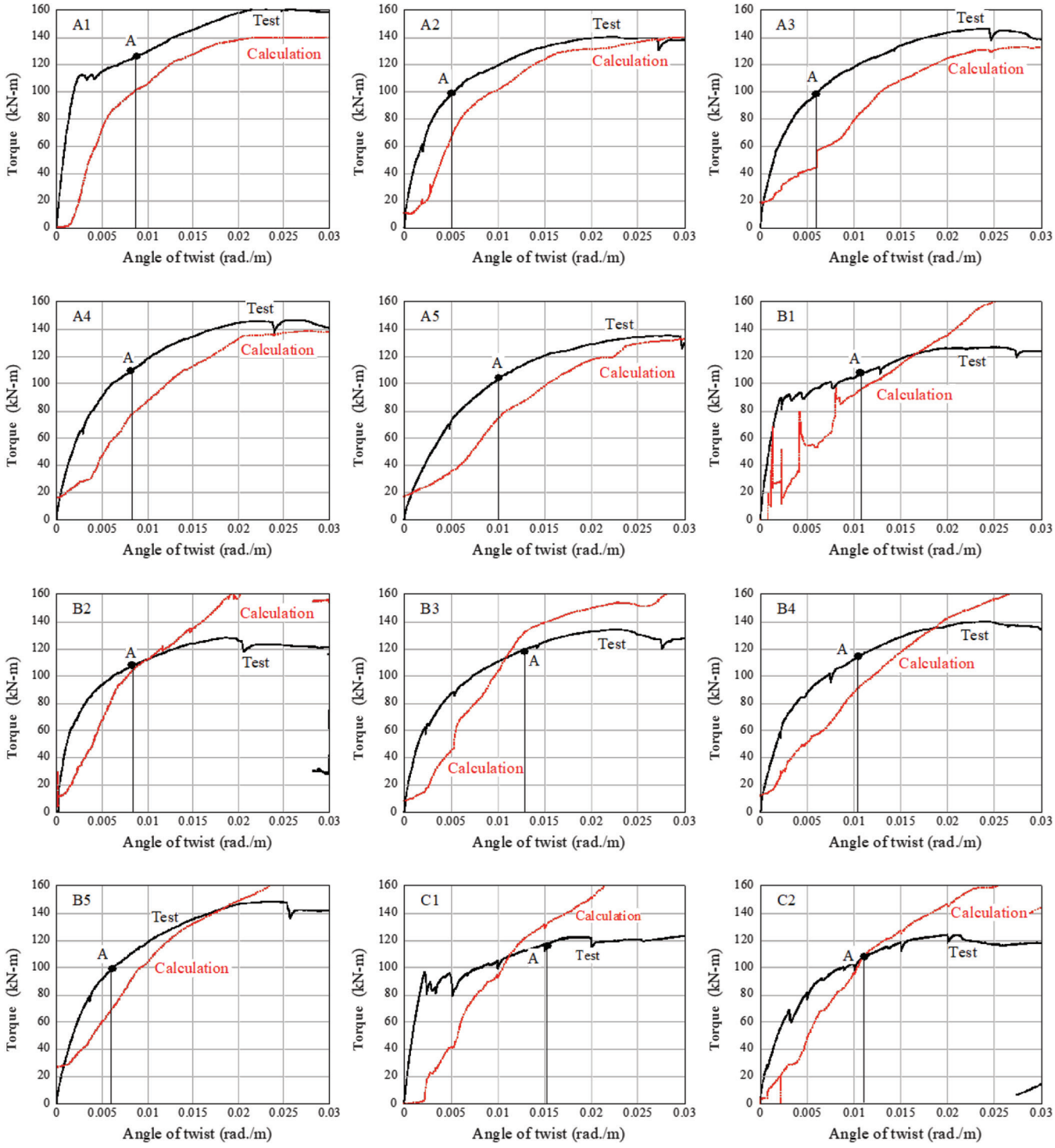

Fig. 13—Predicted torsional moment using measured stirrup stress. (Note: 1 kN·m = 0.74 kip·ft.)

of 123 specimens based on bending moment (Section 22.2 in ACI 318-19[26]) and torsional moment (Eq. (22.7.7.1a) and (22.7.7.1b) in ACI 318-19[26]), respectively. The figures show that most of the test specimens available in the existing literature failed in an over-reinforced failure mode with either flexural compression or torsional compression failure. In Fig. 15(a) and (b), when M/M_o increased, the torsional moment of over-reinforced specimens decreased sharply because the failure was governed by concrete crushing, and the redistribution of forces was negligible. However, for members failing in under-reinforced failure mode, the torsional strength reduction was slight because of the redistribution of the internal forces. As ACI 318-19[26] allows only under-reinforced failure mode for RC beams, the torsional moment may decrease slightly or remain constant with the increase of M/M_o.

CONCLUSIONS

The members in reinforced concrete (RC) structures are always subjected to complex loading conditions. The interaction of these combined loads is an important design consideration. Theoretically, the bending and torsional

moments are known to have a circular relationship, but the experimental data show a trilinear or square-shaped correlation. In this study, the correlation between the torsional and bending moments was evaluated through 13 RC beam tests subjected to combined loads. In addition, the test data of 123 RC beams collected from the literature were also analyzed. Based on this study, the following conclusion can be made:

1. The experimental moment-torsion (*M-T*) interaction curve drawn using the measured yield strength of reinforcement was almost identical to the theoretical *M-T* curve. However, the experimental *M-T* curve drawn using the ultimate strength was significantly different from the theoretical one.

2. The test results showed that for members under combined loading, while maintaining the moment after flexural yielding, the internal force is redistributed and members continue to resist loads. This force redistribution mechanism may transfer the failure regions from the weak region to other parts.

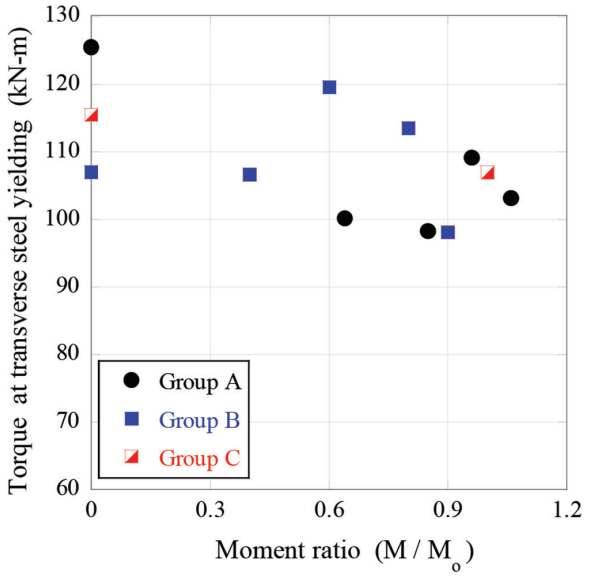

Fig. 14—Interaction of bending moment and torsional strength of specimens based on transverse steel yielding.

3. The detailed analysis of experimental data from 123 specimens from the previous literature showed that in over-reinforced sections, the failure is generally governed by concrete crushing. Therefore, the internal force redistribution was negligible, and the torsional moment sharply decreased. However, for members failing in under-reinforced failure mode, the torsional strength reduction was slight because of the redistribution of the internal forces.

AUTHOR BIOS

ACI member **Jung-Yoon Lee** *is a Professor in the School of Civil, Architectural Engineering and Landscape Architecture at Sungkyunkwan University, Seoul, South Korea. His research interests include the shear behavior and seismic design of reinforced and prestressed concrete structures.*

Na-Yeong Kim *is a Structural Engineer at Yunwoo. Her research interests include the torsional behavior of reinforced concrete beams under combined load.*

DongIk Shin *is a Postdoctoral Researcher at Sungkyunkwan University. His research interests include the shear and torsion behavior of reinforced concrete structures.*

ACI member **Kil-Hee Kim** *is a Professor at Kongju National University, Gongju, South Korea. His research interests include the seismic design of reinforced concrete structures.*

Muhammad Haroon *is an Assistant Professor in the Department of Civil Engineering at Balochistan University of Engineering and Technology (BUET), Khuzdar, Balochistan, Pakistan. His research interests include the shear behavior, seismic analysis, and design of concrete structures.*

ACKNOWLEDGMENTS

This research was supported by the Basic Science Research Program through the National Research Foundation of Korea (NRF) funded by the Ministry of Education (2022R1A2C2091144).

NOTATION

A_g = gross area of cross section, mm^2 (in.^{2})
A_o = gross area enclosed by torsional shear flow path, mm^2 (in.^{2})
A_{oh} = area enclosed by centerline of outermost closed transverse torsional reinforcement, mm^2 (in.^{2})
f_c' = compressive strength of concrete, MPa (psi)
f_y = yield strength of reinforcing bar, MPa (psi)
f_{yl} = yield strength of longitudinal reinforcement, MPa (psi)
f_{yt} = yield strength of transverse reinforcement, MPa (psi)
M_o = pure bending moment strength, kN·m (lb·in.)
M_y = flexural yielding moment strength, kN·m (lb·in.)
N_b = axial force provided by lower longitudinal reinforcement, kN (lb)
N_t = axial force provided by upper longitudinal reinforcement, kN (lb)
P_o = axial force, kN (lb)

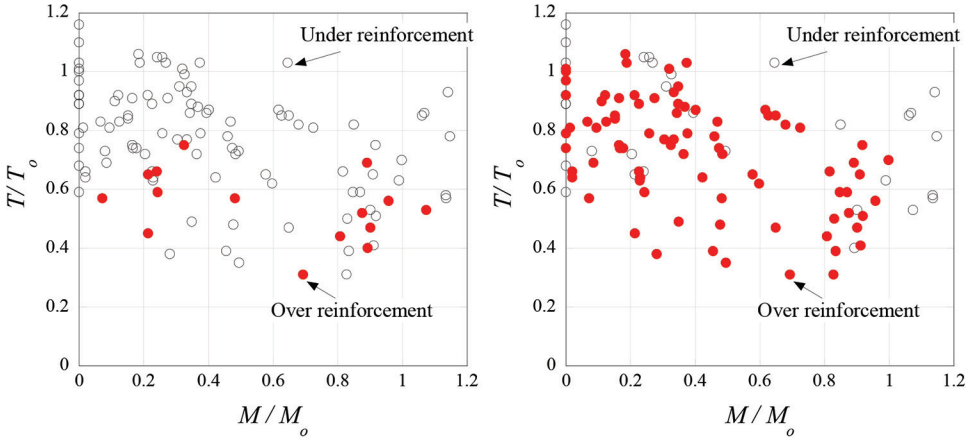

*Fig. 15—*M-T *interaction of 123 RC members based on failure mode: (a) flexural failure mode; and (b) torsional failure mode.*

R = ratio of axial force induced by upper and lower longitudinal reinforcement
T_n = nominal torsional moment strength, kN·m (lb·in.)
T_o = pure torsional moment strength, kN·m (lb·in.)
V_o = pure shear strength, kN (lb)
v_s = shear stress induced by shear force, MPa (psi)
v_t = shear stress induced by torsional moment, MPa (psi)
x_o = length between centers of shorter sides of closed stirrup, mm (in.)
y_o = length between centers of longer sides of closed stirrup, mm (in.)
ε_y = yield strain
θ = crack angle
ρ_l = ratio of area of distributed longitudinal reinforcement to gross concrete area perpendicular to that reinforcement
ρ_t = ratio of area of distributed transverse reinforcement to gross concrete area perpendicular to that reinforcement
ρ_v = transverse reinforcement ratio
ρ_w = longitudinal reinforcement ratio
ξ = effective strength coefficient of concrete

REFERENCES

1. Hsu, T. T. C., "Torsion of Structural Concrete—Behavior of Reinforced Concrete Rectangular Members," *Torsion of Structural Concrete*, SP-18, American Concrete Institute, Farmington Hills, MI, 1968, pp. 261-306.

2. McMullen, A. E., and Rangan, B. V., "Pure Torsion in Rectangular Sections—A Re-Examination," *ACI Journal Proceedings*, V. 75, No. 10, Oct. 1978, pp. 511-519.

3. Mitchell, D., and Collins, M. P., "The Behaviour of Structural Concrete Beams in Pure Torsion," Publication 74-06, Department of Civil Engineering, University of Toronto, Toronto, ON, Canada, 1974, 88 pp.

4. MacGregor, J. G., and Ghoneim, M. G., "Design for Torsion," *ACI Structural Journal*, V. 92, No. 2, Mar.-Apr. 1995, pp. 211-218.

5. Rahal, K. N., and Collins, M. P., "Effect of Thickness of Concrete Cover on Shear-Torsion Interaction—An Experimental Investigation," *ACI Structural Journal*, V. 92, No. 3, May-June 1995, pp. 334-342.

6. Lee, J.-Y., and Kim, S.-W., "Torsional Strength of RC Beams Considering Tension Stiffening Effect," *Journal of Structural Engineering*, ASCE, V. 136, No. 11, Nov. 2010, pp. 1367-1378. doi: 10.1061/(ASCE)ST.1943-541X.0000237

7. Rasmussen, L. J., and Baker, G., "Torsion in Reinforced Normal and High-Strength Concrete Beams—Part 1: Experimental Test Series," *ACI Structural Journal*, V. 92, No. 1, Jan.-Feb. 1995, pp. 56-62.

8. Koutchoukali, N.-E., and Belarbi, A., "Torsion of High-Strength Reinforced Concrete Beams and Minimum Reinforcement Requirement," *ACI Structural Journal*, V. 98, No. 4, July-Aug. 2001, pp. 462-469.

9. Fang, I.-K., and Shiau, J.-K., "Torsional Behavior of Normal- and High-Strength Concrete Beams," *ACI Structural Journal*, V. 101, No. 3, May-June 2004, pp. 304-313.

10. Kim, C.; Kim, S.; Kim, K.-H.; Shin, D.; Haroon, M.; and Lee, J.-Y., "Torsional Behavior of Reinforced Concrete Beams with High-Strength Steel Bars," *ACI Structural Journal*, V. 116, No. 6, Nov. 2019, pp. 251-263. doi: 10.14359/51718014

11. Lee, J.-Y.; Haroon, M.; Shin, D.; and Kim, S.-W., "Shear and Torsional Design of Reinforced Concrete Members with High-Strength Reinforcement," *Journal of Structural Engineering*, ASCE, V. 147, No. 2, Feb. 2021, p. 04020327. doi: 10.1061/(ASCE)ST.1943-541X.0002887

12. Gesund, H., and Boston, L. A., "Ultimate Strength in Combined Bending and Torsion of Concrete Beams Containing Only Longitudinal Reinforcement," *ACI Journal Proceedings*, V. 61, No. 11, Nov. 1964, pp. 1453-1472.

13. Collins, M. P.; Walsh, P. F.; Archer, F. E.; and Hall, A. S., "Ultimate Strength of Reinforced Concrete Beams Subjected to Combined Torsion and Bending," *Torsion of Structural Concrete*, SP-18, American Concrete Institute, Farmington Hills, MI, 1968, pp. 379-402.

14. Pandit, G. S., and Warwaruk, J., "Reinforced Concrete Beams in Combined Bending and Torsion," *Torsion of Structural Concrete*, SP-18, American Concrete Institute, Farmington Hills, MI, 1968, pp. 133-163.

15. Pritchard, R. G., "Torsion Shear Interaction of Reinforced Concrete Beams," master's thesis, University of Calgary, Calgary, AB, Canada, 1970, 146 pp.

16. Badawy, H. E. I.; McMullen, A. E.; and Jordaan, I. J., "Experimental Investigation of the Collapse of Reinforced Concrete Curved Beams," *Magazine of Concrete Research*, V. 29, No. 99, June 1977, pp. 59-69. doi: 10.1680/macr.1977.29.99.59

17. Ewida, A. A., and McMullen, A. E., "Concrete Members Under Combined Torsion and Shear," *Journal of the Structural Division*, ASCE, V. 108, No. 4, Apr. 1982, pp. 911-928. doi: 10.1061/JSDEAG.0005932

18. Elfren, L.; Karlsson, I.; and Losberg, A., "Torsion-Bending-Shear Interaction for Concrete Beams," *Journal of the Structural Division*, ASCE, V. 100, No. 8, Aug. 1974, pp. 1657-1676. doi: 10.1061/JSDEAG.0003843

19. Klus, J. P., "Ultimate Strength of Reinforced Concrete Beams in Combined Torsion and Shear," *ACI Journal Proceedings*, V. 65, No. 3, Mar. 1968, pp. 210-216.

20. McMullen, A., and Warwaruk, J., "Concrete Beams in Bending, Torsion and Shear," *Journal of the Structural Division*, ASCE, V. 96, No. 5, May 1970, pp. 885-903. doi: 10.1061/JSDEAG.0002577

21. Osburn, D. L.; Mayoglou, B.; and Mattock, A. H., "Strength of Reinforced Concrete Beams with Web Reinforcement in Combined Torsion, Shear, and Bending," *ACI Journal Proceedings*, V. 66, No. 1, Jan. 1969, pp. 31-41.

22. Li, Q., "Performance of RC Bridge Columns under Cyclic Combined Loading Including Torsion," PhD dissertation, University of Houston, Houston, TX, 2012, 346 pp.

23. Greene, G. Jr., and Belarbi, A., "Model for Reinforced Concrete Members under Torsion, Bending, and Shear. I: Theory," *Journal of Engineering Mechanics*, ASCE, V. 135, No. 9, Sept. 2009, pp. 961-969. doi: 10.1061/(ASCE)0733-9399(2009)135:9(961)

24. Ju, H., "Multi-Potential Capacity Model for Torsion in Reinforced Concrete Members Subjected to Combined Loads," PhD thesis, University of Seoul, Seoul, South Korea, 2017, 321 pp.

25. Ju, H., and Lee, D., "Nonlinear Analysis of Reinforced Concrete Members Subjected to Combined Torsion and Bending Moment," *ACI Structural Journal*, V. 118, No. 4, July 2021, pp. 55-70.

26. ACI Committee 318, "Building Code Requirements for Structural Concrete (ACI 318-19) and Commentary (ACI 318R-19) (Reapproved 2022)," American Concrete Institute, Farmington Hills, MI, 2019, 624 pp.

27. EN 1992, "Eurocode 2: Design of Concrete Structures," European Committee for Standardization, Brussels, Belgium, 1992.

28. Joint ACI-ASCE Committee 445, "Report on Torsion in Structural Concrete (ACI 445.1R-12) (Reapproved 2021)," American Concrete Institute, Farmington Hills, MI, 2013, 92 pp.

29. CSA A23.3:19, "Design of Concrete Structures," CSA Group, Toronto, ON, Canada, 2019, 301 pp.

30. Hsu, T. T. C., and Mo, Y.-L., *Unified Theory of Concrete Structures*, John Wiley & Sons, Ltd., Chichester, UK, 2010, 520 pp.

31. McMullen, A. E., and Warwaruk, J., "The Torsional Strength of Rectangular Reinforced Concrete Beams Subjected to Combined Loading," Structural Engineering Report No. 2, Department of Civil Engineering, University of Alberta, Edmonton, AB, Canada, 1967, 258 pp.

32. Onsongo, W. M., "The Diagonal Compression Field Theory for Reinforced Concrete Beams Subjected to Combined Torsion, Flexure and Axial Load," PhD thesis, Department of Civil Engineering, University of Toronto, Toronto, ON, Canada, 1978, 261 pp.

33. Lee, J.-Y.; Haroon, M.; Park, J.; and Kim, C., "Longitudinal Axial Strain in Plastic Hinge Regions of Reinforced-Concrete Columns," *Magazine of Concrete Research*, V. 71, No. 20, Oct. 2019, pp. 1043-1069. doi: 10.1680/jmacr.17.00438

34. Lampert, P., "Bruchwiderstand von Stahlbetonbalken unter Torsion und Biegung," Institut für Baustatik, ETH Zürich, Zürich, Switzerland, 1970, 189 pp. (in German)

CALL FOR ACTION

ACI Invites You To...

Share your expertise

Do you have EXPERTISE in any of these areas?

- BIM
- Chimneys
- Circular Concrete Structures Prestressed by Wrapping with Wire and Strand
- Circular Concrete Structures Prestressed with Circumferential Tendons
- Concrete Properties
- Demolition
- Deterioration of Concrete in Hydraulic Structures
- Electronic Data Exchange
- Insulating Concrete Forms, Design, and Construction
- Nuclear Reactors, Concrete Components
- Pedestal Water Towers
- Pipe, Cast-in-Place
- Strengthening of Concrete Members
- Sustainability

Become a Reviewer for the ACI Journals

Then become a REVIEWER for the *ACI Structural Journal* or the *ACI Materials Journal*.

How to become a Reviewer:

1. Go to: **http://mc.manuscriptcentral.com/aci**;
2. Click on "Create Account" in the upper right-hand corner; and
3. Enter your E-mail/Name, Address, User ID and Password, and Area(s) of Expertise.

Update your Manuscript Central user account information

Did you know that the database for MANUSCRIPT CENTRAL, our manuscript submission program, is separate from the ACI membership database?

How to update your user account:

1. Go to **http://mc.manuscriptcentral.com/aci**;
2. Log in with your current User ID & Password; and
3. Update your E-mail/Name, Address, User ID and Password, and Area(s) of Expertise.

QUESTIONS?

E-mail any questions to Journals.Manuscripts@concrete.org.

American Concrete Institute

Always advancing

ACI STRUCTURAL JOURNAL TECHNICAL PAPER

Title No. 120-S102

Assessment of Deflection Prediction Models for Cracked Prestressed Concrete Beams

by Wassim Nasreddine, Adi Obeidah, Peter H. Bischoff, and Hani Nassif

Variability of deflection prediction models is assessed for cracked prestressed concrete flexural members with bonded steel tendons. Current models for computing deflection are based on an effective moment of inertia (with or without an offset moment for the cracked section response) or a bilinear moment-deflection response using the moment of inertia of the uncracked section before cracking and moment of inertia of the cracked section after cracking. The accuracy of the approaches provided in ACI 318-19, the PCI Design Handbook, and elsewhere are examined for computing immediate deflection using a large database of 180 fully prestressed as well as partially prestressed beams. Parameters considered in the analysis include the effect of tension-stiffening, reinforcement ratio, prestressing type (fully or partially prestressed), cracking moment, concrete elastic modulus, modulus of rupture, and the use of transformed or gross section properties. Results highlight the need for a rational model that can be universally applied to reinforced as well as prestressed concrete flexural members.

Keywords: deflection; effective moment of inertia; partially prestressed; prestressed concrete.

INTRODUCTION

Discrepancies between predicted and observed deflection values of prestressed concrete members can increase construction problems significantly (Branson et al. 1970). In the design of prestressed concrete structures, the predicted deflection at service loads can be a governing criterion in determining the required member size and amount of prestress. Deflection is typically computed using the gross (uncracked) section properties for Class U members defined by ACI 318 (ACI Committee 318 2019) as being uncracked at service loads. Computing the deflection of Class T and C members which are cracked under service load is more problematic and not as well understood. Adoption of a new expression in ACI 318-19 for the effective moment of inertia I_e used to compute deflection of reinforced (nonprestressed) concrete has led to interest in extending this approach for computing immediate deflection of cracked prestressed concrete flexural members (Bischoff et al. 2018).

The focus of this paper is to help clarify and better predict deflection of cracked prestressed concrete members. Factors contributing to short-term deformation are investigated with the aim of helping a competent designer to make a reasonable estimate of deflection considering that some factors and properties can cause a high variability in deflection. A detailed analysis is presented for the calculation process following ACI 318-19, the PCI Design Handbook (PCI 2017), and others that include Bischoff et al. (2018) and Bischoff (2022).

RESEARCH SIGNIFICANCE

This study examines the accuracy of established and proposed approaches for predicting the immediate deflection of prestressed concrete flexural members cracked under service load. An evaluation is carried out using a total of 180 beams taken from numerous studies for simply supported beams prestressed with bonded steel tendons (with or without nonprestressed reinforcement) and subjected to two-point loading. The aim is to provide engineers and researchers with the variability and level of accuracy for each approach considered. Several factors are taken into consideration, including the modulus of elasticity and modulus of rupture of concrete, use of transformed or gross section properties, cracking moment, and reinforcement ratio that dictates the level of prestressing.

DEFLECTION PREDICTION MODELS

Cracking of concrete occurs when the extreme fiber of a member section reaches the modulus of rupture, defined by ACI 318-19 as $f_r = 7.5\sqrt{f_c'}$ in psi ($0.62\sqrt{f_c'}$ in MPa). Prior to cracking, the deflection of a prestressed concrete member equals the sum of the camber due to prestressing plus the deflection from dead and live loads. Linear elastic behavior is assumed for an uncracked member and deflection is calculated using elastic deflection equations appropriate for the prestressing profile and amount of prestress, type of loading, and support conditions. The moment of inertia of the uncracked transformed section I_{tr} is often approximated with the gross moment of inertia I_g.

Cracked prestressed member response

For a cracked prestressed concrete member, deflections are typically calculated using an effective member response E_cI_e that lies between the two extremes of an uncracked E_cI_{tr} (or gross E_cI_g) response and a cracked E_cI_{cr} response. The cracked E_cI_{cr} response can be shifted upwards relative to the uncracked response as shown in Fig. 1(a) for the different prediction models examined in this study. In other words, the effective moment of inertia I_e represents a weighted average of the I_{tr} (usually approximated with I_g) and I_{cr} values that depends on the assumed shift in the cracked member response and level of cracking. The general moment-deflection response in Fig. 1(b) corresponds to an arbitrary value

ACI Structural Journal, V. 120, No. 6, November 2023.

MS No. S-2022-410.R1, doi: 10.14359/51739094, received May 9, 2023, and reviewed under Institute publication policies.

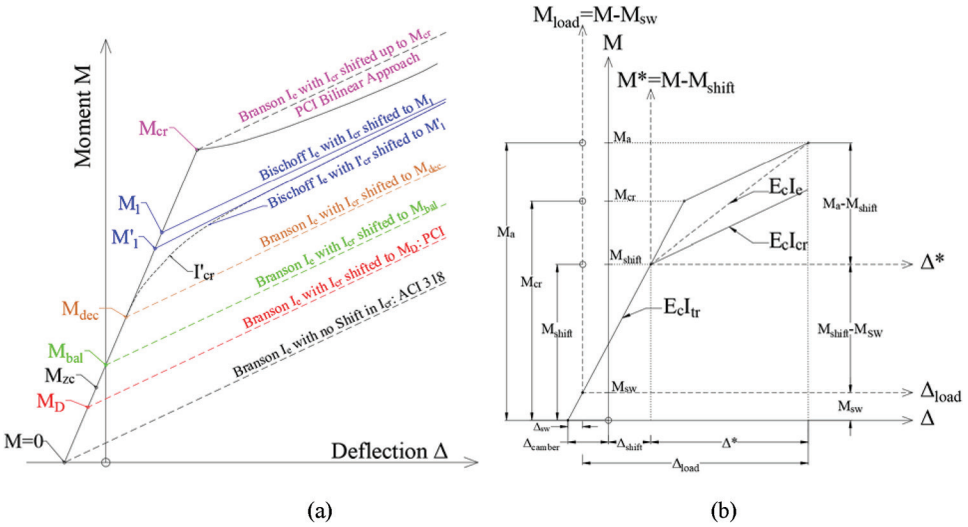

Fig. 1—Prestressed concrete member response.

Table 1—Summary of deflection prediction approaches and relevant equations

Effective moment of inertia	Branson's modified Eq. (2)			$I_e = I_{cr}$	Bischoff's Eq. (4a) or (4b)	Bischoff's Eq. (5b)
Approach	ACI 318-19	PCI	—	PCI bilinear	Bischoff et al. (2018)	Bischoff (2022)
Offset moment (M_{Shift})	0	M_D	M_{dec}	M_{cr}	M_1 or M_1'	M_1
Moment of inertia of cracked transformed section (I_{cr} or I_{cr}')	I_{cr}	I_{cr}	I_{cr}	I_{cr}	I_{cr} for $M_1 \le M_{cr}$ I_{cr}' for $M_1 > M_{cr}$	I_{cr}
	Rectangular section: $I_{cr} = \frac{b(c_{cr})^3}{3} + n_p A_{ps}(d_p - c_{cr})^2 + n_s A_s(d_s - c_{cr})^2$ where neutral axis location c_{cr} is equal to centroid of cross section and is determined using conventional approaches for a nonprestressed section. $I_{cr}' = \frac{b(c_{cr}')^3}{12} + bc_{cr}'\left(\bar{y}_{cr}' - \frac{c_{cr}'}{2}\right)^2 + n_p A_{ps}(d_p - \bar{y}_{cr}')^2 + n_s A_s(d_s - \bar{y}_{cr}')^2$ or $I_{cr}' = \frac{[M_a - P_o\,(d_p - \bar{y}_{cr}')]\,c_{cr}'}{E_c \varepsilon_c}$ and $\bar{y}_{cr}' = \frac{\frac{b(c_{cr}')^2}{2} + n_p A_{ps} d_p + n_s A_s\ d_s}{b\,c_{cr}' + n_p A_{ps} + n_s A_s}$ where neutral axis c_{cr}' is determined from equilibrium of section forces and compatibility of strains (Naaman 1982; Mast 1998; Bischoff et al. 2018).					

For partially prestressed member, cracking moment $M_{cr} = \frac{(f_r + f_{pe})I_{tr}}{y_t}$ is replaced by M_{cr}' to account for shrinkage restraint stresses from reinforcing steel, where $M_{cr}' = M_{cr}\left(\frac{2}{3} + \frac{1}{3}\frac{\rho_p}{\rho_p + \rho_s}\right)$. This gives $M_{cr}' = 2/3 M_{cr}$ for a reinforced (nonprestressed) section and $M_{cr}' = M_{cr}$ for a fully prestressed section.

M_{dec} is also replaced by $M_{dec}' = M_{dec}\left(\frac{2}{3} + \frac{1}{3}\frac{\rho_p}{\rho_p + \rho_s}\right)$ for partially prestressed section.

$f_{pe} = \frac{P_e}{A_c} + \frac{P_e e_c y_{t,c}}{I_c}$ and $y_{t,c} = h - \bar{y}_c$ for prestressing steel only (fully prestressed)

$f_{pe} = \frac{P_e}{A_{tr,s}} + \frac{P_e e_{tr,s} y_{t,s}}{I_{tr,s}}$ and $y_{t,s} = h - \bar{y}_{tr,s}$ for prestressing and reinforcing steel (partially prestressed)

$P_o = P_e + A_{ps}E_p\,\varepsilon_{c,p}$ with $\varepsilon_{c,p} = \frac{P_e}{A_c E_c}\left(1 + \frac{e_c^2}{r_c^2}\right)$ and $r_c^2 = \frac{I_c}{A_c}$ for prestressing steel only

$\varepsilon_{c,p} = \frac{P_e}{A_{tr,s}E_c}\left(1 + \frac{e_{tr,s}^2}{r_{tr,s}^2}\right)$ and $r_{tr,s}^2 = \frac{I_{tr,s}}{A_{tr,s}}$ for prestressing and reinforcing steel (partially prestressed)

$M_{zc} = P_o e_{tr}$ and $M_{dec} = P_o\left(e_{tr} + \frac{I_{tr}}{A_{tr} y_{t,tr}}\right)$ or $\frac{f_{pe} I_{tr}}{y_{t,tr}}$ with $y_{t,tr} = h - \bar{y}_{tr}$

$M_1 = \frac{\left(M_o - M_{zc}\frac{I_{cr}}{I_{tr}}\right)}{\left(1 - \frac{I_{cr}}{I_{tr}}\right)}$ with $M_o = P_o e_{cr}$ and $M_1' = \frac{\left(M_o' - M_{zc}\frac{I_{cr}'}{I_{tr}}\right)}{\left(1 - \frac{I_{cr}'}{I_{tr}}\right)}$ with $M_o' = P_o e_{cr}'$

Note: Concrete section properties (denoted by subscript *c*) are approximately equal to gross section properties (denoted by subscript *g*); uncracked transformed section properties (denoted by subscript *tr*) are often approximated with gross section properties (denoted by subscript *g*); compression steel A_s' is accounted for when present; T and I shapes are accounted for in section analysis when neutral axis extends into web.

for the shifted moment M_{shift}. When using this approach, the deflection value computed using I_e is relative to the deflection value corresponding to the shifted moment, which must be included to obtain the total deflection. An alternative approach that considers deformation using an effective eccentricity of the prestress force (Tadros et al. 1985) or effective curvature from the prestress force (Bischoff 2022) is not addressed in this paper. Table 1 provides a summary of the deflection prediction approaches evaluated along with

relevant equations needed to compute deflection of a cracked prestressed concrete member.

Branson's modified approach—Branson's (1965) expression for the effective moment of inertia has been used to compute deflection of reinforced (nonprestressed) concrete flexural members since the early 1970s

$$I_e = \left(\frac{M_{cr}}{M_a}\right)^3 I_g + \left[1 - \left(\frac{M_{cr}}{M_a}\right)^3\right] I_{cr} \le I_g \quad (1)$$

and was subsequently modified by Branson (1977) and others to compute deflection of a cracked prestressed concrete member with

$$I_e = \left(\frac{M_{cr} - M_{shift}}{M_a - M_{shift}}\right)^3 I_g + \left[1 - \left(\frac{M_{cr} - M_{shift}}{M_a - M_{shift}}\right)^3\right] I_{cr} \le I_g \quad (2)$$

where I_g (an approximation for I_{tr}) and I_{cr} are used to compute I_e for the service load moment M_a at the critical section of the member. Equation (2) incorporates an offset moment M_{shift} to account for the upwards shift in the cracked section response of a prestressed member (Fig. 1).

Branson (1977) adopted the dead load moment M_D as the offset moment so that deflection computed with I_e gives the live load deflection directly without the need to compute the deflection value at the shifted origin (corresponding to deflection from the dead load). PCI (2017) uses Branson's Eq. (1) with an expression for (M_{cr}/M_a) set equal to $[1-(f_{tot}-f_r)/f_L]$ that is equivalent to using $M_{shift} = M_D$ in Eq. (2). Other work by Branson and Trost (1982a,b) sets M_{shift} equal to the balanced moment M_{bal} corresponding to zero deformation (in this case, deflection), as this gives the total value of deflection directly.

Setting the offset moment equal to the decompression moment M_{dec} is presumed to have a more rational basis (Tadros 1982) as this value corresponds to zero stress at the precompressed face of the critical section, which is thought to be equivalent to a reinforced (nonprestressed) section. This decompression moment does not, however, correspond to decompression of the entire section (Nilson 1976). Others also have based the effective moment of inertia on $M_{shift} = M_{dec}$ (Chen 1973; Naaman 1982; Krishna Mohan Rao and Dilger 1992; Kassian 2016).

Naaman (1982) uses Branson's modified Eq. (2) for I_e with $M_{shift} = M_{dec}$ but with an effective camber from prestressing computed using I_e (not I_{tr} or I_g) and an eccentricity of the prestressing force relative to the gross (uncracked) section, which provides an incremental value of deflection relative to the balanced moment M_{bal} (and not M_{dec} as assumed in this paper). Chen (1973) also uses I_e based on $M_{shift} = M_{dec}$, but the secant value of the I_e response originates at M_{dec} to give an incremental value of deflection relative to M_{dec} as defined in Fig. 1. Krishna Mohan Rao and Dilger (1992) compute the total deflection using the service load moment M_a with I_e based on $M_{shift} = M_{dec}$. Deflection from live load is then obtained by subtracting the deflection caused by the dead load and effective prestress from the total service load deflection. In summary, all three approaches use the same expression for I_e to compute deflection, but not for the same origin. This inconsistency in past work highlights the need to identify an appropriate starting point or origin for computing the incremental value of deflection when using a secant I_e value.

Naaman (1982) also suggested using the moment of inertia I_{cr}' of the partially cracked transformed section instead of I_{cr} in Eq. (2) to compute I_e, but using M_{dec} for the offset moment instead of the M_1' offset value corresponding to I_{cr}' as shown in Fig. 1(a). The cracked section E_cI_{cr}' response begins at M_{dec} and is initially nonlinear because of the axial compressive force from the prestress, but the cracked section response does eventually converge to an asymptotic slope of the E_cI_{cr} response that lies above M_{dec} and is defined by $M_{shift} = M_1$ as shown (Fig. 1(a)). Hence, the decompression moment M_{dec} underestimates the upwards shift in the E_cI_{cr} response with the correct offset moment $M_1 > M_{dec}$ and dependent on the level of prestress.

PCI (2017) additionally recommends a bilinear moment-deflection relationship equivalent to setting the offset moment in Eq. (2) equal to the cracking moment M_{cr} to give $I_e = I_{cr}$. With this approach, deflection before cracking is computed using the gross moment of inertia and additional deflection after cracking is computed using the cracked moment of inertia I_{cr}. ACI 318-19 is at the other extreme, with the offset moment set equal to zero as for reinforced concrete—hence the wide range in values assumed for the offset moment used to compute the effective moment of inertia I_e with Branson's modified expression, ranging anywhere from 0 up to M_{cr}.

Bischoff's approach—Branson's (1965) approach underestimates deflection for reinforced concrete members with low reinforcement ratios such as slabs and does not consider the effect of shrinkage restraint or loading of concrete at an early age (Bischoff and Scanlon 2007)—hence the reason ACI 318-19 adopted Bischoff's (2005, 2020) expression for I_e in lieu of Branson's (1965) expression for computing deflection of reinforced (nonprestressed) concrete. The new expression for I_e given by

$$I_e = \frac{I_{cr}}{1 - \left(\frac{2/3\ M_{cr}}{M_a}\right)^2 \left(1 - \frac{I_{cr}}{I_g}\right)} \quad (3)$$

for $M_a > 2/3M_{cr}$ is applicable over a wide range of reinforcement ratios. For $M_a \le 2/3M_{cr}$, $I_e = I_g$. Once again, I_g is an approximation for I_{tr}. The reduced cracking moment of $2/3M_{cr}$ accounts for early-age loading and the tensile stresses that develop in the concrete from restraint to shrinkage by the internal steel reinforcement (Scanlon and Bischoff 2008). For computing deflection of prestressed concrete, ACI 318-19 continues to use Branson's Eq. (1), equivalent to Eq. (2) with $M_{shift} = 0$, as described earlier.

Bischoff et al. (2018) broadened the formulation of Eq. (3) to compute the effective moment of inertia for prestressed concrete, expressed as

$$I_e = \frac{I_{cr}}{1 - \left(\frac{M_{cr} - M_1}{M_a - M_1}\right)^2 \left(1 - \frac{I_{cr}}{I_{tr}}\right)} \quad (4a)$$

for $M_a > M_{cr}$ and when $M_1 \le M_{cr}$. Equation (4a) uses an offset moment set equal to M_1 as illustrated in Fig. 1(a), with the stipulation that M_1 does not exceed the cracking moment M_{cr}. I_{cr}' and M_1' are used in lieu of I_{cr} and M_1 when $M_1 > M_{cr}$, provided that $M_1' \le M_{cr}$. In this case

$$I_e = \frac{I_{cr}'}{1 - \left(\frac{M_{cr} - M_1'}{M_a - M_1'}\right)^2 \left(1 - \frac{I_{cr}'}{I_{tr}}\right)} \quad (4b)$$

for $M_1 > M_{cr}$ and $M_1' \le M_{cr}$. Otherwise, $I_e \approx I_{cr}'$ for $M_1' > M_{cr}$. The cracking moment in Eq. (4a) and (4b) is computed using $M_{cr} = (f_r + f_{pe})I_{tr}/y_t$, where I_{tr} is typically approximated with I_g for design purposes (ACI 318-19). The values M_1 and M_1' are derived from the moment-curvature relationship and are approximate when used with the load-deflection response. Equations for M_1, M_1', I_{cr}, I_{cr}', and other related expressions are provided in Table 1 with a full explanation given by Bischoff (2022).

For a fully prestressed member (with prestressing steel only), M_{cr} is not reduced when the value of f_{pe} is used to compute M_{cr}, as this includes an allowance for prestress loss from shrinkage that accounts for shrinkage restraint. Comparison of the computed and experimental values of M_{cr} for the beams taken from the database used in this paper substantiates this observation, whereas the computed value of M_{cr} for partially prestressed beams is notably greater than the experimentally observed value because of shrinkage restraint from the nonprestressed steel. Hence, for partially prestressed concrete (with reinforcing and prestressing steel), the cracking moment in Eq. (4a) and (4b) is replaced with $M_{cr}' = \left[\left(\frac{2}{3}\right) + \left(\frac{1}{3}\right)\frac{\rho_p}{\rho_p + \rho_s}\right] M_{cr}$. This gives $M_{cr}' = M_{cr}$ for fully prestressed concrete when $\rho_s = 0$, and $M_{cr}' = (2/3)\,M_{cr}$ for reinforced concrete when $\rho_p = 0$. The decompression moment is also replaced with

$$M_{dec}' = \left[\left(\frac{2}{3}\right) + \left(\frac{1}{3}\right)\frac{\rho_p}{\rho_p + \rho_s}\right] M_{dec}$$

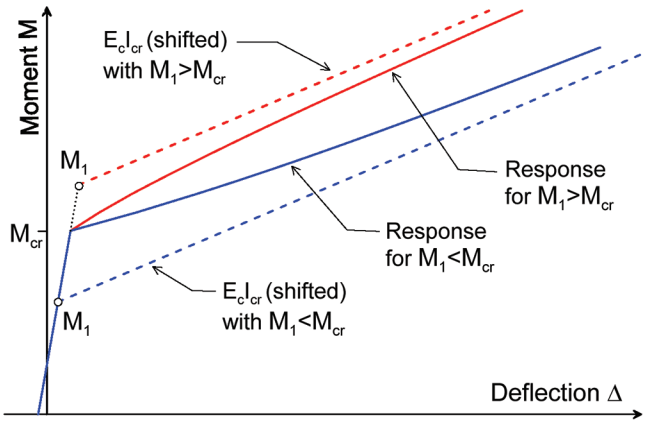

Fig. 2—Prestressed response with $M_1 \le M_{cr}$ *and* $M_1 > M_{cr}$.

for a partially prestressed concrete member.

Bischoff (2022) extended the approach used to develop an I_e expression for reinforced concrete to formulate a general I_e equation for prestressed concrete that includes a tension-stiffening component defined partly by a tension-stiffening factor β_{ts}.

$$I_e = \frac{I_{cr}}{1 - \beta_{ts}\left(\frac{M_{cr} - M_1}{M_a - M_1}\right)\left(1 - \frac{I_{cr}}{I_{tr}}\right)} \quad (5a)$$

for $M_a > M_{cr}$, where the term $\left(\frac{M_{cr} - M_1}{M_a - M_1}\right)$ in Eq. (5a) accounts for the upwards shift in I_{cr} shown in Fig. 1(a). Setting the tension-stiffening factor $\beta_{ts} = \left(\frac{M_{cr} - M_1}{M_a - M_1}\right)$ gives Eq. (4a) but limits the applicability of this equation to prestressed concrete with $M_1 \le M_{cr}$. Otherwise, the terms M_1' and I_{cr}' can be substituted for M_1 and I_{cr} as explained earlier, but this requires more detailed calculations involving a partially cracked section.

A more rational and realistic approach for I_e sets $\beta_{ts} = \left(\frac{M_{cr} - M_{dec}}{M_a - M_{dec}}\right)$ to give

$$I_e = \frac{I_{cr}}{1 - \left(\frac{M_{cr} - M_{dec}}{M_a - M_{dec}}\right)\left(\frac{M_{cr} - M_1}{M_a - M_1}\right)\left(1 - \frac{I_{cr}}{I_{tr}}\right)} \quad (5b)$$

for $M_a > M_{cr}$, which is applicable for both cases of $M_1 \le M_{cr}$ and $M_1 > M_{cr}$. While values of I_e vary between I_{tr} and I_{cr} when $M_1 \le M_{cr}$, values of I_e can vary anywhere between $-\infty$ and $+\infty$ for cases when $M_1 > M_{cr}$ (Bischoff 2022). Figure 2 shows the response of a prestressed member for the two scenarios where $M_1 \le M_{cr}$ and $M_1 > M_{cr}$. Assessment of the test beams from the database described later indicates that M_1 is likely to exceed M_{cr} when the average effective compressive stress in concrete f_{pc} (from the effective prestress force) exceeds 400 psi (2.75 MPa). When using the reduced cracking moment M_{cr}' for a partially prestressed member, M_1 is likely to exceed M_{cr}' for f_{pc} greater than 300 psi (2 MPa). Close to 35% of the prestressed beams from this database (both partially and fully prestressed) have $M_1 > M_{cr}$ and this increases to approximately half the beams assessed when the cracking moment is replaced with M_{cr}' (with 80% of the partially prestressed beams now having $M_1 > M_{cr}'$).

Prestressed section response

Figure 3 illustrates section details for an uncracked, partially cracked, and fully cracked transformed section reinforced with both reinforcing steel A_s and prestressing steel A_{ps}. The presence of compression steel A_s' is easily taken into account. The moment of inertia I_{tr} of the uncracked transformed section is often approximated with the gross moment of inertia I_g ignoring the reinforcement as shown. The moment of inertia I_{cr}' of a partially cracked section starts off with a value equal to I_{tr} when the moment M_a equals the decompression moment M_{dec} (assuming the member is cracked), and then decreases as cracking progresses under an increasing moment with $M_a > M_{dec}$ until the value of I_{cr}'

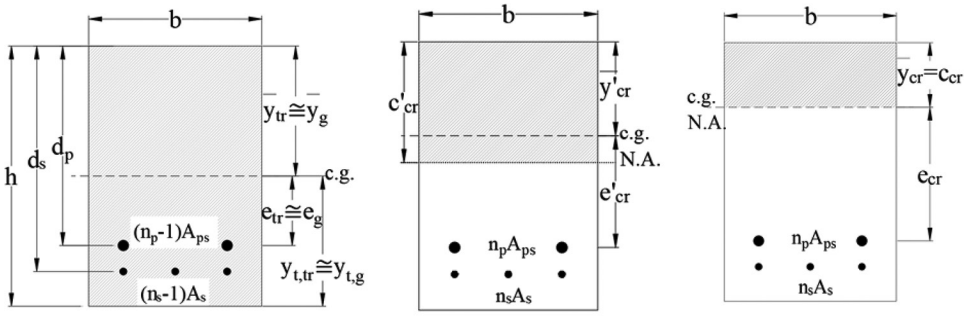

(a): Uncracked (gross) transformed section (I_{tr} or I_g for $M_a \le M_{cr}$)

(b): Partially cracked transformed section (I'_{cr} for $M_a > M_{dec}$)

(c): Fully cracked transformed section (I_{cr} for $M_a/P_o d_p \to \infty$)

Fig. 3—Section details for uncracked and cracked prestressed concrete member.

converges to I_{cr} for a fully cracked section corresponding to the value computed for a nonprestressed section with the same reinforcement details. Hence, $I_{cr} \le I_{cr}' \le I_{tr}$ with I_{cr} being a lower limit for I_{cr}'.

The neutral axis of a partially cracked section determined from equilibrium of forces and compatibility of strains is iterative in nature, as the solution depends on the prestressing force and applied moment (Mast 1998; Bischoff et al. 2018). I_{cr}' is computed relative to the centroidal axis, which is not coincident with the neutral axis. For a fully cracked section where $P_o d_p/M_a \to 0$, the neutral axis coincides with the centroidal axis, and computation of the neutral axis location and I_{cr} is relatively straightforward.

PCI (2017) provides an often-used empirical expression to compute I_{cr} for a fully prestressed member (with ρ_p only) that is extended to include partially prestressed members with ρ_p and ρ_s (ACI Committee 435 2000).

$$I_{cr} = \left(n_p A_{ps} d_p^2 + n_s A_s d_s^2\right)\left(1 - 1.6\sqrt{n_p \rho_p + n_s \rho_s}\right) \quad (6)$$

where A_{ps} is the prestressing reinforcement area; and A_s is the nonprestressed tension reinforcement area. This approximate formulation for I_{cr} does not require the location of the neutral axis and is intended for use in lieu of a more exact analysis for a cracked section, ignoring the effect of the axial prestress force (PCI Committee on Allowable Stresses in Prestressed Concrete Design 1970). In other words, Eq. (6) is an approximation for a fully cracked section that represents a lower bound for a cracked transformed section.

The validity of the PCI formula given by Eq. (6) for estimating I_{cr} is assessed by comparing this value with the exact value of I_{cr} for a fully cracked section. The percentage difference between the PCI approximate value and the exact value is plotted in Fig. 4 as a function of reinforcement ratio for beams taken from the database used in this paper to evaluate deflection (described in subsequent sections). Theoretical comparison is also made for a fully prestressed rectangular section with a typical modular ratio n between 6 and 8. The results demonstrate that the PCI expression for I_{cr} defined by Eq. (6) provides a good approximation of I_{cr} for members with a low reinforcement ratio ρ up to approximately 0.4

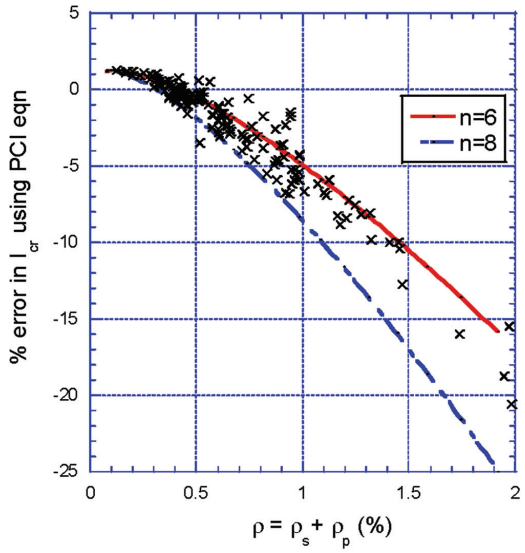

Fig. 4—Percent difference between PCI approximation for I_{cr} and exact I_{cr} for fully cracked section.

to 0.5% (depending on the modular ratio), but can underestimate the value of I_{cr} considerably at higher reinforcement ratios. For this reason, the exact value of I_{cr} for a fully cracked section is used in this study instead of the PCI empirical formulation for I_{cr}.

Deflection calculations

The accuracy of deflection prediction models is assessed by comparing the calculated value of deflection to the measured deflection. At any given load, the measured or experimental deflection Δ_{exp} is given by

$$\Delta_{exp} = \Delta_{load} + \Delta_{sw} - \Delta_{camber} \quad (7a)$$

where Δ_{load} is the deflection (at midspan) measured from the loads applied during testing. Δ_{sw} and Δ_{camber} are the deflections (both taken as positive) due to the member self-weight and camber, respectively, and are estimated using the equations given as follows

$$\Delta_{sw} = \frac{5 w_{sw} L^4}{384 E_c I_{tr}} \quad \text{and} \quad \Delta_{camber} = \frac{P_e e_{tr,s} L^2}{8 E_c I_{tr,s}} \quad (7b)$$

The equation for Δ_{sw} is based on a uniformly distributed load w_{sw} from the member self-weight acting on a simply supported span, while Δ_{camber} is for a simply supported prestressed beam with a straight tendon profile of constant eccentricity. Figure 1(b) provides a graphical representation of the different deflection components.

Predicted values of deflection Δ_{calc} are based on a shifted E_cI_{cr} response defined by the offset moment M_{shift} as shown in Fig. 1(b), where

$$\Delta_{calc} = \Delta^* + \Delta_{shift} \tag{8a}$$

$$\Delta^* = \frac{(M_a - M_{shift})}{24E_cI_e}(3L^2 - 4a^2) \tag{8b}$$

for a simply supported beam under two-point loading with a shear span of length a. M_a represents the total moment at midspan defined by $M_a = M_{sw} + Fa/2$ and $M_{sw} = w_{sw}L^2/8$. F is the applied force from a two-point loading test.

$$\Delta_{shift} = \frac{(M_{shift} - M_{sw})}{24E_cI_{tr}}(3L^2 - 4a^2) - [\Delta_{camber} - \Delta_{sw}] \tag{8c}$$

where M_{sw} is the moment at midspan from the member self-weight as defined previously. For $M_{shift} = 0$ (because $M_{shift} < M_{sw}$), $\Delta_{shift} = -\Delta_{camber}$ and $\Delta^* = 5w_{sw}L^4/(384E_cI_e) + (M_a - M_{sw})(3L^2 - 4a^2)/(24E_cI_e)$. Table 1 provides a summary of the deflection calculation approaches.

DATABASE DESCRIPTION

A database of 180 beams prestressed with bonded steel tendons (with or without nonprestressed steel) has been collected from the literature and is used to validate the different deflection approaches considered. One-hundred thirty-nine of the beams are pretensioned and 41 are post-tensioned bonded. Beams with center-point loading ($a/L = 0.5$) or $a/L < 0.2$, $f_c' < 4$ ksi (27.5 MPa), or $f_{se}/f_{pu} < 0.4$ are excluded. Beam height h ranged from 8 to 18 in. (200 to 450 mm), and L/h ratios ranged from 6.4 to 24. Table 2 provides details of the beam tests evaluated and Fig. 5 plots the distribution of shear span-to-total span ratio a/L, concrete strength f_c', prestressed reinforcement ratio ρ_p, and effective prestress ratio after losses f_{se}/f_{pu}. The average

Table 2—Beam properties from database

Reference	No. of beams	Cross section*	f_c', ksi	f_{se}/f_{pu}	f_{pc}, ksi	a/L
Zwoyer (1953)	6	R	4.7 to 8.0	0.43 to 0.58	0.46 to 0.74	0.333
Billet (1953)	16	R	4.1 to 8.3	0.44 to 0.63	0.18 to 0.91	0.333
Janney et al. (1956)	6	R	4.9 to 6.1	0.47 to 0.52	0.26 to 0.78	0.333
Warwaruk (1957)	3	R	5.0 to 6.1	0.42 to 0.44	0.15 to 0.55	0.333
Hernandez (1958)	4	I	4.3 to 5.4	0.46 to 0.47	0.54 to 0.63	0.333
Warwaruk et al. (1962)	14	R	4.2 to 8.1	0.44 to 0.63	0.18 to 0.90	0.333
	2	R	4.1 to 5.7	0.42 to 0.43	0.32 to 0.55	0.333
Hanson and Hulsbos (1963)	17	I	6.6 to 7.8	0.53 to 0.58	0.85 to 0.95	0.2 to 0.4
Hanson (1964)	18	I	5.8 to 7.4	0.44 to 0.53	0.77 to 0.93	0.25 to 0.476
Slepetz (1968)	4	R	5.8	0.45 to 0.49	0.39 to 0.99	0.36
Shaikh and Branson (1970)	12	R	5.4 to 6.6	0.46 to 0.65	0.39 to 0.64	0.367
Huang (1975)	16	T	4.1 to 4.9	0.51 to 0.56	0.34 to 0.9	0.389
Alkokani (1982)	5	R	5.5 to 6.8	0.59 to 0.6	0.25 to 0.78	0.35
	4	T	5.3 to 6.5	0.59 to 0.6	0.30 to 0.96	0.35
Harajli and Naaman (1984)	9	R	5.3 to 6.8	0.48 to 0.64	0.22 to 0.86	0.333
Elzanaty et al. (1986)	11	I	5.8 to 10.7	0.41 to 0.58	1.05 to 1.6	0.363 to 0.375
Founas (1989)	5	T	4.5 to 6.7	0.5 to 0.51	0.16 to 0.75	0.333
Abdelrahman (1995)	2	R	9.7	0.42	0.34 to 0.48	0.414
Gowripalan and Zou (1999)	2	R	8.0 to 10.9	0.51	0.26	0.333
Shi (2003)	2	R	5.5	0.48 to 0.55	0.32 to 0.43	0.333
Zou (2003)	2	R	5.2 to 11.9	0.62 to 0.72	0.22 to 0.25	0.333
Oukaili and Khattab (2018)	4	R	5.8	0.59 to 0.65	0.51 to 0.57	0.333
Jiang et al. (2021)	12	R	7.0 to 8.9	0.64	0.54 to 0.82	0.333
Obeidah and Nassif (2022)	3	T	11.2 to 14.0	0.51 to 0.62	0.13 to 0.45	0.333
Nasreddine (2022)	1	T	12.3	0.49	0.24	0.333

*R is rectangular section; T is T-shaped section; and I is I-shaped section.

Note: 1 ksi = 6.89 MPa.

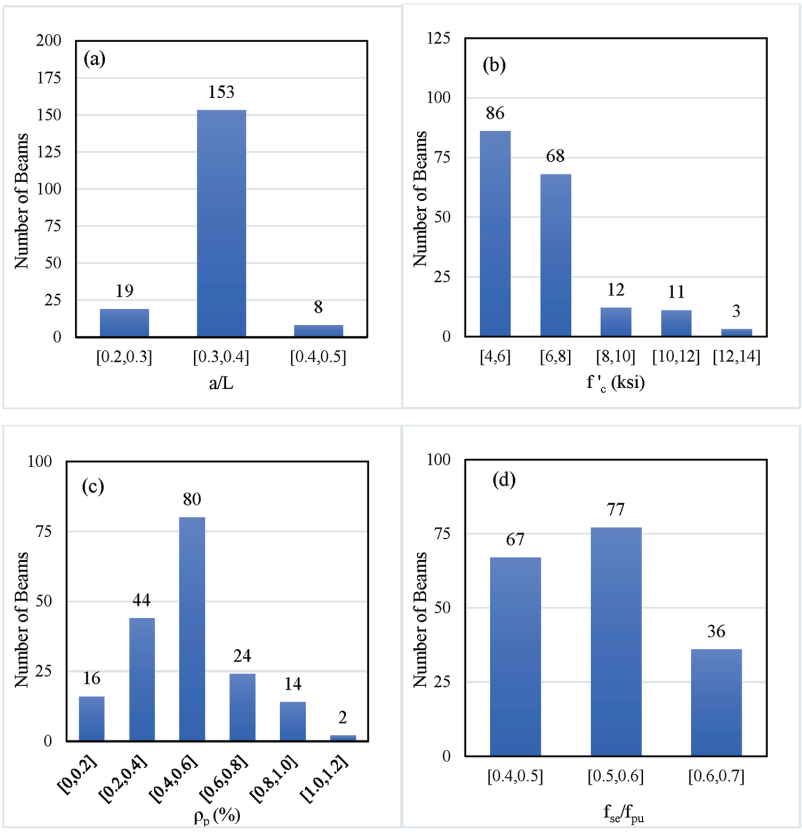

Fig. 5—Distribution of beams in database for: (a) shear span-to-total span ratio a/L; (b) concrete strength f_c'; (c) prestressing reinforcement ratio ρ_p; and (d) effective prestress ratio f_{se}/f_{pu}. (Note: 1 ksi = 6.89 MPa.)

effective compressive stress in concrete f_{pc} is a better indicator of prestress for partially prestressed members and ranges between 130 and 1600 psi (0.9 and 11 MPa) for both the partially and fully prestressed members. Three points are taken from the load-deflection response of each beam, between cracking and yielding of the nonprestressed reinforcement for the partially prestressed beams, and between cracking and tendon yielding for the fully prestressed beams. The points are roughly equidistant and correspond to moments of approximately $1.2M_{cr}$, $1.4M_{cr}$, and $1.6M_{cr}$.

RESULTS AND DISCUSSION

Calculated versus experimental deflections

Figure 6 plots a comparison between the calculated Δ_{calc} and experimental Δ_{exp} deflections for all beams using the six approaches presented in Table 1. Plots show lines for perfect prediction and ±30% deviation. Statistical values of the deflection ratio $\Delta_{calc}/\Delta_{exp}$ are provided in Table 3 for the mean μ, standard deviation, coefficient of variation (COV), and other parameters. The transformed moment of inertia I_{tr} for the uncracked section is used instead of I_g for all calculations and deflection is calculated using computed values of f_r and E_c, with E_c defined by ACI 318 as $E_c = w_c^{1.5}33\sqrt{f_c'}$ in psi ($w_c^{1.5}0.0423\sqrt{f_c'}$ in MPa) for concrete with a unit weight w_c between 90 and 160 lb/ft^3 (1440 and 2560 kg/m^3) and $f_c' \leq$ 8000 psi (55 MPa). For concrete with $f_c' >$ 8000 psi (55 MPa), E_c is taken as $\left(40,000\sqrt{f_c'} + 1,000,000\right)\left(\frac{w_c}{145}\right)^{1.5}$ in psi or $\left(3300\sqrt{f_c'} + 6900\right)\left(\frac{w_c}{2300}\right)^{1.5}$ in MPa (Martinez et al. 1984).

Computed results of deflection are presented for the full cracking moment, except for the PCI Bilinear approach and Bischoff's two approaches (Eq. (4) and (5b)), which also include the effect of using a reduced cracking moment M_{cr}' to account for shrinkage restraint in the partially prestressed members. All plots show considerable scatter of results as expected when computing deflection (ACI Committee 435 2000), with a coefficient of variation ranging between 32 and 37% depending on the approach used.

The ACI 318 approach (Branson's equation with M_{shift} = 0) and PCI approach (Branson's equation with $M_{shift} = M_D$) both underestimate deflection by 13% on average, indicating the offset moment of M_D has little effect on the overall accuracy of the calculated deflection compared to the ACI 318 approach of setting the offset moment to zero. The dead load moment comes from the beam self-weight only, however, and would typically be greater when used to support slabs or decks. Using Branson's modified Eq. (2) with $M_{shift} = M_{dec}$ improves the estimate of deflection considerably to give a slight overestimation with an average deflection prediction ratio of 1.04. Keeping $M_{shift} = M_{dec}$ but replacing I_{cr} with the partially cracked moment of inertia I_{cr}' as suggested by Naaman (1982) results in a slightly lower average deflection ratio of 1.01, so has little influence on the accuracy of computed deflections.

The PCI bilinear approach (Branson's equation with $M_{shift} = M_{cr}$) overestimates deflection by 5% on average, while the approaches based on Bischoff's formulation using Eq. (4) or (5b) overestimate the deflection on average by 8% and 5%, respectively. Reducing the cracking moment to account

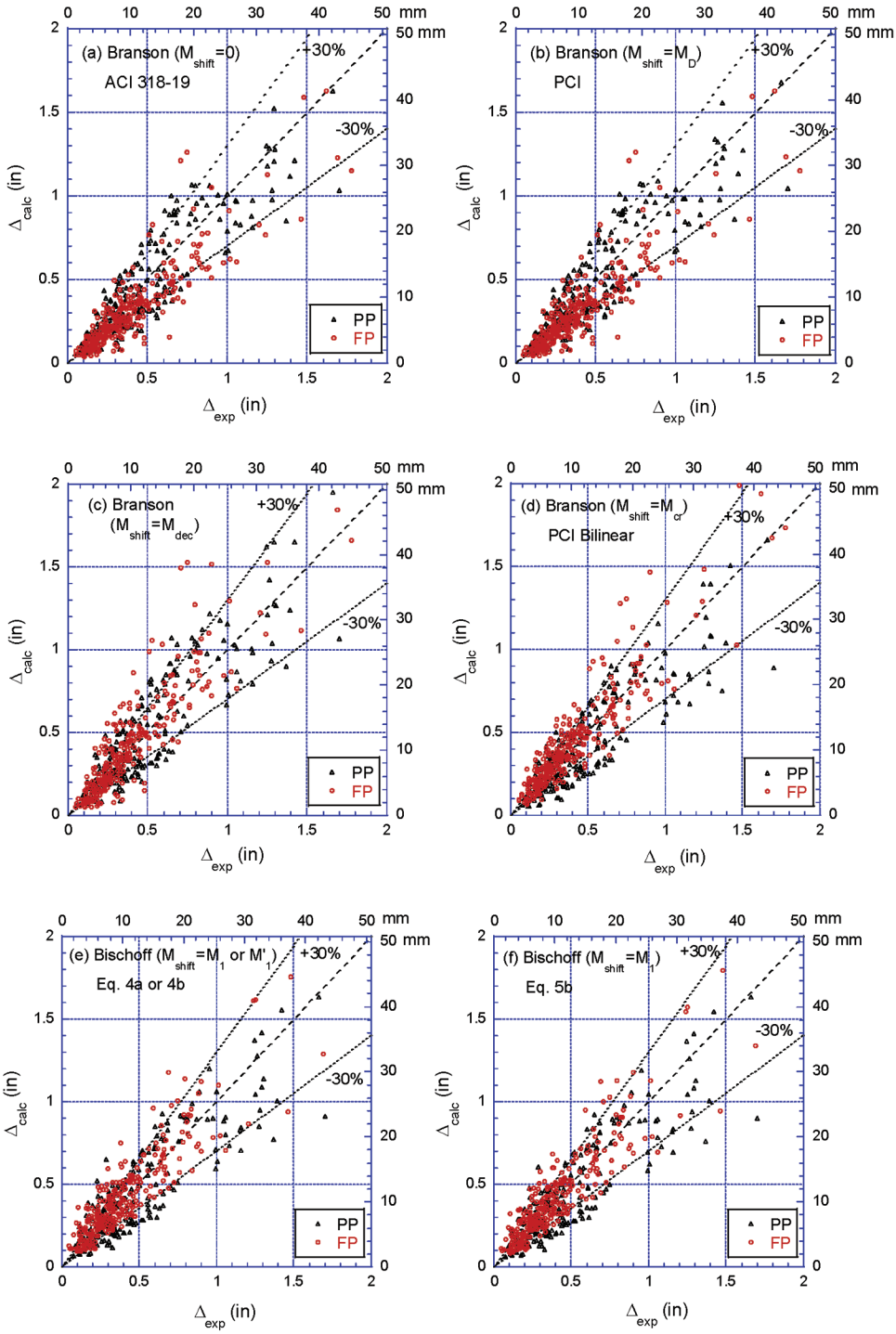

Fig. 6—Calculated versus experimental deflections (using M_{cr}*).*

for shrinkage restraint in the partially prestressed members with the use of M_{cr}' gives a somewhat greater overall prediction of deflection as expected, such that the PCI bilinear approach overestimates deflection by 15% on average, while Bischoff's two equations (Eq. (4) and (5b)) overestimate deflection by 11% and 9% on average.

Effect of nonprestressed reinforcement and cracking moment on deflection

The effect of nonprestressed reinforcement on the calculated deflection is evaluated through categorizing the beams into fully prestressed (ρ_p only) and partially prestressed (ρ_p and ρ_s). Out of the 180 beams considered, 104 are fully prestressed and 76 are partially prestressed. Results are presented in Table 3.

The ACI 318 and PCI approaches (Branson's equation with M_{shift} equal to 0 and M_D, respectively) show a greater deflection prediction ratio for the partially prestressed (PP) beams compared to the fully prestressed (FP) beams contrary to what would be expected (0.96 for the PP beams versus 0.80 for the FP beams). The deflection ratio of the PP beams should be less (not more) than that of the FP beams when no account is taken of the reduced cracking moment. Branson's equation with $M_{shift} = M_{dec}$ gives a deflection ratio

Table 3—Statistical parameters for ratio of calculated to experimental deflections ($\Delta_{calc}/\Delta_{exp}$)

Effective moment of inertia I_e		Branson's Modified Eq. (2)				Eq. (4a) or (4b)	Eq. (5b)
M_{shift}		0	M_D	M_{dec}	M_{cr}	M_1 with I_{cr} M_1' with I_{cr}'	M_1 with I_{cr}
Approach		ACI 318	PCI	—	PCI bilinear	Bischoff et al. (2018)	Bischoff (2022)
Database	Parameter	$\Delta_{calc}/\Delta_{exp}$					
All beams (FP + PP)	Mean μ	0.86	0.87	1.04	1.05 (1.15*)	1.08 (1.11*)	1.05 (1.09*)
	Standard deviation	0.29	0.30	0.36	0.34 (0.37*)	0.38 (0.41*)	0.35 (0.38*)
	COV, %	34	34	34	33 (32*)	36 (37*)	34 (35*)
	% points < 1	74	72	50	47 (40*)	44 (42*)	48 (44*)
	% points within ± 30%	59	59	62	66 (63*)	66 (65*)	67 (66*)
FP beams (104 beams)	Mean μ	0.79	0.80	1.05	1.14	1.14	1.10
PP beams (76 beams)	Mean μ	0.95	0.96	1.02	0.93 (1.16*)	1.00 (1.07*)	0.97 (1.08*)

*Δ_{calc} is computed using M_{cr}' and M_{dec}' for partially prestressed (PP) members.

of 1.05 for the FP beams, which is close to the value of 1.02 for the PP beams.

Both the PCI bilinear approach and Bischoff's approaches give a somewhat greater deflection ratio for the FP beams compared to the PP beams when using the full cracking moment M_{cr}. The deflection ratio for the PP beams increases with the reduced cracking moment M_{cr}' (to account for shrinkage restraint) to give a value comparable to the FP beams, with the effect being greater with the PCI bilinear approach. For the PCI bilinear approach, the mean deflection ratio for the PP beams increases from 0.93 to 1.16 and is comparable to the value of 1.14 for the FP beams.

With Bischoff's approach, the mean deflection ratio for the PP beams (using the reduced cracking moment) increases from approximately 1.0 to 1.07, which is somewhat comparable to the FP beams (with a value of either 1.14 using Eq. (4) or 1.10 using Eq. (5b)). Mean values of the deflection ratio for the entire dataset equal 1.15 for the PCI bilinear approach, 1.11 using Bischoff's Eq. (4), and 1.09 using Bischoff's Eq. (5b). Approximating the fictitious decompression force P_o (which affects the offset moment M_1) with P_e increases the mean deflection ratio by approximately another 5%. Overprediction of deflection is expected with either of Bischoff's approaches when the effective moment of inertia is taken at the critical section where the stiffness is lowest. Integration of curvature takes account of the stiffer regions in the member span and is expected to reduce these deflection estimates. It is worthwhile noting that Branson's approach tends to give less deflection than Bischoff's approach for prestressed beams with low reinforcement ratios, but more deflection at high reinforcement ratios.

Effect of f_r and E_c on deflection

The modulus of rupture f_r and modulus of elasticity of concrete E_c can influence computed values of deflection (Bischoff 2022). For this study, E_c was measured for 77 out of the 180 beams under investigation, while either f_r or the split-cylinder strength f_{sp} was measured for 110 of the beams. No distinction is made between the measured values of f_r and f_{sp}, as there was not more than a 2% difference in the average of these two values when both were measured.

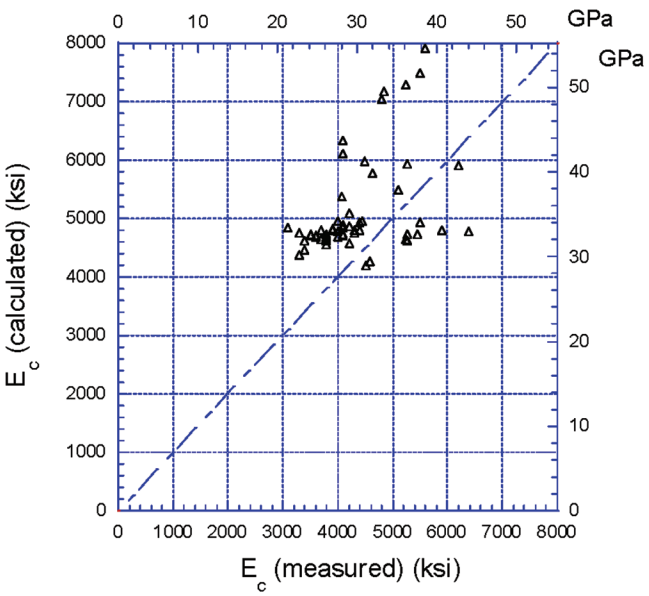

Fig. 7—E_c *(calculated) versus* E_c *(measured) from reduced database.*

ACI 318 calculated values of f_r (which partly controls the cracking moment) were 3% less on average than measured values, while the mean deflection ratio (for deflection computed with M_{cr} based on the calculated value of f_r) is approximately 4% greater than the mean when deflection is computed with M_{cr} using the measured values of f_r. The assumed value of effective stress in the prestressed reinforcement is also likely to influence the computed value of deflection (Bischoff 2022).

Calculated values of E_c from the reduced database are mostly greater than the measured values (by approximately 14% on average) as shown in Fig. 7 and leads to deflection being underestimated with the calculated value of E_c as indicated by the comparison of deflection prediction ratios in Table 4. Computed values of deflection using the calculated value of E_c give a mean deflection ratio between 6 and 14% less than deflection computed with measured values of E_c, depending on the approach used and offset moment for I_e.

Table 4—Effect of E_c (calculated versus measured) on deflection prediction ratio $\Delta_{calc}/\Delta_{exp}$

77 beams (reduced database)	Mean $\mu(\Delta_{calc}/\Delta_{exp})$		
	$E_{c,meas}$	$E_{c,calc}$	% change
Branson: $M_{shift} = 0$ (ACI 318)	1.03	0.89	–14%
Branson: $M_{shift} = M_D$ (PCI)	1.03	0.90	–13%
Branson: $M_{shift} = M_{dec}$	1.22	1.09	–11%
Branson: $M_{shift} = M_{cr}$ (PCI bilinear)	1.21	1.10	–9%
Bischoff: Eq. (4a) or (4b)	1.18	1.11	–6%
Bischoff: Eq. (5b)	1.16	1.08	–7%

Table 5—Effect of I_g versus I_{tr} on deflection prediction ratio $\Delta_{calc}/\Delta_{exp}$

180 beams	Mean $\mu(\Delta_{calc}/\Delta_{exp})$		
	I_{tr}	I_g	% change
Branson: $M_{shift} = 0$ (ACI 318)	0.86	0.98	+ 14%
Branson: $M_{shift} = M_D$ (PCI)	0.87	0.99	+14%
Branson: $M_{shift} = M_{dec}$	1.04	1.18	+13%
Branson: $M_{shift} = M_{cr}$ (PCI bilinear)	1.05 (1.15*)	1.16 (1.25*)	+10% (+9%*)
Bischoff: Eq. (4a) or (4b)	1.08 (1.11*)	1.12 (1.14*)	+4% (+3%*)
Bischoff: Eq. (5b)	1.05 (1.09*)	1.11 (1.14*)	+6% (+5%*)

*Δ_{calc} computed using M_{cr}' and M_{dec}' for partially prestressed (PP) members.

Effect of I_g versus I_{tr} on deflection

Prediction of deflection is assessed using I_e based on the moment of inertia I_{tr} of the uncracked section in all deflection calculations. Approximating I_{tr} with the gross moment of inertia I_g decreases M_{cr} by approximately 5%, which results in an amplified decrease in I_e that leads to an increase in computed values of deflection by between 4 and 14% on average depending on the approach used (as indicated by the deflection ratios summarized in Table 5). The mean prediction ratio ($\Delta_{calc}/\Delta_{exp}$) increases from 0.86 to 0.98 using Branson's equation with M_{shift} equal to either 0 or M_D, while the mean prediction ratio for the other approaches evaluated increases to values between 1.11 and 1.18 for comparisons made using the full cracking moment M_{cr}. The ACI 318 approach using Branson's equation with I_g appears to provide a reasonable estimate of deflection overall but is inconsistent, as deflection is underestimated by 12% for the FP beams and overestimated by 11% for the PP beams.

CONCLUSIONS

Approaches commonly used for computing post-cracking deflection of concrete beams prestressed with bonded steel tendons are reviewed and assessed. Each approach evaluated is based on an upwards shift in the cracked section response relative to the uncracked response as defined by an offset moment M_{shift}. Deflection is calculated using the moment of inertia of an uncracked section up to the value of the shifted or offset moment (which includes the camber from prestressing), plus the deflection beyond this point computed with an effective moment of inertia I_e.

The PCI approximation for computing I_{cr} of a fully cracked section is shown to be valid up to a reinforcement ratio of approximately 0.4% and underestimates I_{cr} beyond this limit with the error becoming greater as the reinforcement ratio increases. Hence, the exact value of I_{cr} along with the moment of inertia of the uncracked transformed section I_{tr} are used in deflection calculations (together with the ACI 318 equations for computing values for f_r and E_c). The effect of approximating I_{tr} with the gross moment of inertia I_g is also evaluated. The following conclusions are drawn:

- The I_e method computes incremental deflection relative to a reference point that is not always identified. This reference point often, but not always, corresponds to the shifted moment used in the formulation for I_e (such as Branson's modified Eq. (2)) and has led to inconsistencies and confusion in computing deflection depending on the approach adopted.
- The ACI 318 approach (Branson's equation with $M_{shift} = 0$) and the PCI approach (using Branson's equation with $M_{shift} = M_D$) underestimate deflection by an average of 13%.
- Branson's approach with $M_{shift} = M_{dec}$ provides a good approximation of deflection for both the FP and PP beams, overestimating deflection by 4% on average. Using I_{cr}' instead of I_{cr} has little effect on the computed value of deflection.
- The PCI bilinear approach (equivalent to using Branson's equation with $M_{shift} = M_{cr}$) provides a quick and simple method for deflection calculations. This approach overestimates deflection by an average of 5%, with deflection being overestimated for the FP beams (+14%) and underestimated for the PP beams (–7%). Deflection of both the FP and PP beams is overestimated by between 14 and 16% when using a reduced cracking moment $M_{cr}' = M_{cr}\left(\frac{2}{3} + \frac{1}{3}\frac{\rho_p}{\rho_p + \rho_s}\right)$ to account for shrinkage restraint in the PP beams.
- Approximating the uncracked transformed section properties with the gross section properties can increase computed values of deflection by up to 14%. The effect is not as significant with Bischoff's approach, with increases between 3 and 6%.
- Values of the rupture modulus f_r and elastic modulus E_c can affect computed values of deflection. Calculated values of E_c were greater than measured values, leading to deflection being underestimated by up to 14% compared to deflection computed with the measured value of E_c (with the amount depending on the approach used). Differences between the measured and computed values of f_r are not more than 3% on average and led to a 4% increase in deflection using calculated values of f_r compared to measured values for computing M_{cr}.
- When using the full cracking moment M_{cr}, the Bischoff et al. (2018) approach overestimates deflection by an average of 8%, while using Bischoff (2022) overestimates deflection by 5%. In both cases, deflection of the FP beams is overestimated more than the PP beams,

which have a deflection prediction ratio close to 1.0. Deflection estimates of the PP beams increase when using the reduced cracking moment M_{cr}' and are more comparable to the FP beams, giving a mean deflection ratio for all beams combined that is overestimated by 11% for Bischoff et al. (2018) and 9% for Bischoff (2022). Using I_g instead of I_{tr} increases deflection as expected, with deflection overestimated by approximately 12% on average when computed with the full M_{cr} and by 14% when using M_{cr}'. Deflection is expected to be overestimated when I_e is based on the value at the critical section where the member stiffness is lowest. Calculated values of deflection will decrease with integration of curvature and is a topic for further work.

- Comparison of the applicability and variability of the aforementioned models, particularly with the advent of nonmetallic reinforcement and different types of prestressing (such as unbonded and hybrid tendons), underscores the need for a rational approach such as that proposed by Bischoff (2022) to ensure uniformity of design outcomes and adherence to serviceability limit states. While some empirical models offer simplicity (with less accuracy), they are not necessarily practical or conducive to a unified application for both reinforced and prestressed concrete members.

AUTHOR BIOS

ACI member **Wassim Nasreddine** *is a Research Associate at Rutgers, The State University of New Jersey, New Brunswick, NJ. His research interests include prestressed concrete member behavior, innovative concrete materials, and strengthening and retrofitting of concrete structures.*

ACI member **Adi Obeidah** *is a Research Associate at Rutgers. He received his BS and MS from American University of Sharjah, Sharjah, United Arab Emirates, and his PhD from Rutgers. His research interests include prestressed fiber-reinforced concrete and ultra-high-performance concrete (UHPC) behavior with nonmetallic reinforcement, strengthening, and retrofitting of concrete elements.*

Peter H. Bischoff, *FACI, is an Honorary Research Professor in the Civil Engineering Department at the University of New Brunswick, Fredericton, NB, Canada. He is a member of ACI Committees 224, Cracking; 360, Design of Slabs on Ground; 435, Deflection of Concrete Building Structures; and 440, Fiber-Reinforced Polymer Reinforcement; and Joint ACI-ASCE Committee 408, Bond and Development of Steel Reinforcement. He received the ACI Design Award in 2014. His research interests include the serviceability behavior of concrete structures.*

Hani Nassif, *FACI, is Professor of structural engineering at Rutgers. He is past Chair of ACI Committees 348, Structural Reliability and Safety, and 444, Structural Health Monitoring; and is a past member of ACI's Technical Activities Committee (TAC). He is a member of ACI Committees 209, Creep and Shrinkage in Concrete, and 435, Deflection of Concrete Building Structures, and Joint ACI-ASCE Committee 343, Concrete Bridge Design. His research interests include structural concrete and the use of advanced cementitious and composite materials.*

ACKNOWLEDGMENTS

Support received in part from the Connected Cities for Smart Mobility toward Accessible and Resilient Transportation (C2SMART) Tier I University Transportation Center at New York University and the New Jersey Department of Transportation (NJDOT) through the Bridge Resource Program (BRP) is gratefully appreciated. The contents of this paper do not reflect the official views or policies of the supporting agencies. The accuracy and facts of the data presented herein are the responsibility of the authors.

NOTATION

A_c	=	concrete cross-sectional area, not including area of reinforcement ($\cong A_g$)
A_g	=	gross area of concrete section
A_{ps}	=	area of prestressed longitudinal tension reinforcement
A_s	=	area of nonprestressed longitudinal tension reinforcement
A_s'	=	area of nonprestressed longitudinal compression reinforcement
A_{tr}	=	area of uncracked transformed section (including A_{ps} and A_s if present)
$A_{tr,s}$	=	area of uncracked transformed section without A_{ps} (including A_s if present)
a	=	shear span for symmetric two-point loading
b	=	width of compression face of member
c	=	neutral axis depth
c_{cr}	=	distance from compression face to neutral axis of fully cracked cross section
c_{cr}'	=	distance from compression face to neutral axis of partially cracked cross section
d_p	=	effective depth of prestressed reinforcement
d_s	=	effective depth of nonprestressed tension reinforcement
E_c	=	elastic modulus of concrete
E_p	=	elastic modulus of prestressed reinforcement
E_s	=	elastic modulus of nonprestressed reinforcement
e_c	=	eccentricity of prestressed reinforcement relative to centroid of concrete section ($\cong e_g$)
e_{cr}	=	eccentricity of prestressed reinforcement relative to centroid of fully cracked section ($=d_p - \bar{y}_{cr}$ with $\bar{y}_{cr} = c_{cr}$)
e_{cr}'	=	eccentricity of prestressed reinforcement relative to centroid of partially cracked section ($=d_p - \bar{y}_{cr}'$)
e_g	=	eccentricity of prestressed reinforcement relative to centroid of gross concrete section ($=d_p - \bar{y}_g$)
e_{tr}	=	eccentricity of prestressed reinforcement relative to centroid of uncracked transformed section (including A_{ps} and A_s if present) ($=d_p - \bar{y}_{tr}$)
$e_{tr,s}$	=	eccentricity of prestressed reinforcement relative to centroid of uncracked transformed section without A_{ps} (including A_s if present) ($=d_p - \bar{y}_{tr,s}$)
F	=	total applied force on test beam
f_c'	=	compressive strength of concrete
f_L	=	live load stress at tensile face (assuming section is uncracked)
f_{pc}	=	average effective compressive stress in concrete from effective prestress force (acting on concrete section, including transformed area of nonprestressed steel A_s if present)
f_{pe}	=	compressive stress in concrete from effective prestress force at precompressed tensile face
f_{pu}	=	tensile strength of prestressing reinforcement
f_r	=	modulus of rupture of concrete
f_{se}	=	effective stress in prestressed reinforcement after allowance for all prestress losses
f_{sp}	=	split-cylinder tensile strength of concrete
f_{tot}	=	total stress at tensile face (assuming section is uncracked) from prestress force plus dead and live load
h	=	overall height of member
I_c	=	moment of inertia of (uncracked) concrete section ($\cong I_g$)
I_{cr}	=	moment of inertia of fully cracked transformed section (equivalent to cracked section ignoring effect of axial prestressing force)
I_{cr}'	=	moment of inertia of partially cracked transformed section
I_e	=	effective moment of inertia
I_g	=	moment of inertia of gross (uncracked) section
I_{tr}	=	moment of inertia of uncracked transformed section (including A_{ps} and A_s if present)
$I_{tr,s}$	=	moment of inertia of uncracked transformed section without A_{ps} (including A_s if present)
L	=	member span
M	=	external moment applied to member
M^*	=	moment corresponding to shifted coordinate system defined by $M - M_{shift}$
M_1	=	intercept of shifted I_{cr} response with uncracked response
M_1'	=	intercept of shifted I_{cr}' response with uncracked response
M_a	=	service load moment at critical section
M_{bal}	=	balanced moment corresponding to zero deflection
M_{cr}	=	moment applied to nonprestressed or prestressed section that results in flexural cracking
M_{cr}'	=	reduced cracking moment (to account for shrinkage restraint stresses from nonprestressed reinforcement)
M_D	=	dead load moment

M_{dec} = decompression moment corresponding to zero stress at tension face of prestressed member
M_{dec}' = reduced decompression moment
M_{load} = moment at critical section (usually midspan) from applied test force F
M_o = product of P_o and e_{cr}
M_o' = product of P_o and e_{cr}'
M_{shift} = offset moment to account for shift in I_{cr} response
M_{sw} = moment at critical section (usually midspan) from member self-weight
M_{zc} = zero curvature moment (corresponding to product of P_o and e_{tr})
n = ratio of reinforcement elastic modulus to elastic modulus of concrete
n_p = ratio of E_p to E_c
n_s = ratio of E_s to E_c
P_e = effective prestress force
P_o = fictitious decompression force
r_c = radius of gyration of concrete section ($\cong r_g$)
r_g = radius of gyration of gross section
$r_{tr,s}$ = radius of gyration of uncracked transformed section without A_{ps} (including A_s if present)
w_c = unit weight of concrete
w_{sw} = distributed dead load from member self-weight
$\bar{y}_c$ = centroid location of uncracked concrete section (not including area of reinforcement) relative to compression face ($\cong \bar{y}_g$)
$\bar{y}_{cr}$ = centroid location of fully cracked transformed section relative to compression face
$\bar{y}_{cr}'$ = centroid location of partially cracked transformed section relative to compression face
$\bar{y}_g$ = centroid location of gross (uncracked) section relative to compression face
$\bar{y}_{tr}$ = centroid location of uncracked transformed section (including A_{ps} and A_s if present) relative to compression face
$\bar{y}_{tr,s}$ = centroid location of uncracked transformed section without A_{ps} (including A_s if present) relative to compression face
y_t = distance from centroid of uncracked section to tension face
$y_{t,c}$ = distance from centroid of concrete section to tension face ($=h-\bar{y}_c$), also ($\cong y_{t,g}$)
$y_{t,g}$ = distance from centroid of gross (uncracked) section to tension face ($=h-\bar{y}_g$)
$y_{t,s}$ = distance from centroid of uncracked transformed section without A_{ps} (and including A_s if present) to tension face ($=h-\bar{y}_{tr,s}$)
$y_{t,tr}$ = distance from centroid of uncracked transformed section (with A_{ps} and including A_s if present) to tension face ($=h-\bar{y}_{tr}$)
β_{ts} = tension-stiffening factor
Δ = deflection
Δ^* = member deflection relative to shifted coordinate system defined by $M-M_{shift}$
Δ_{calc} = calculated or predicted member deflection
$\Delta_{calc}/\Delta_{exp}$ = deflection prediction ratio
Δ_{camber} = deflection from prestressing only
Δ_{exp} = experimental deflection (including deflection from camber, member self-weight, and applied test force)
Δ_{load} = deflection from applied test force F
Δ_{shift} = uncracked member deflection corresponding to offset moment M_{shift}
Δ_{sw} = deflection from member self-weight
ε_c = concrete strain at compression face
$\varepsilon_{c,p}$ = concrete strain at level of prestressed reinforcement
ρ = sum of ρ_s and ρ_p
ρ_p = ratio of A_{ps} to bd_p
ρ_s = ratio of A_s to bd_s

REFERENCES

Abdelrahman, A. A., 1995, "Serviceability of Concrete Beams Prestressed by Fiber Reinforced Plastic Tendons," PhD thesis, University of Manitoba, Winnipeg, MB, Canada.

ACI Committee 318, 2019, "Building Code Requirements for Structural Concrete (ACI 318-19) and Commentary (ACI 318R-19)," American Concrete Institute, Farmington Hills, MI, 624 pp.

ACI Committee 435, 2000, "Control of Deflection in Concrete Structures (ACI 435R-95) (Reapproved 2000), American Concrete Institute, Farmington Hills, MI, 77 pp.

Alkokani, A. F., 1982, "Behavior and Design of Partially Prestressed Concrete Beams," PhD thesis, The Pennsylvania State University, University Park, PA.

Billet, D. F., 1953, "Study of Prestressed Concrete Beams Failing in Flexure," MS thesis, University of Illinois, Engineering Experiment Station, Urbana, IL.

Bischoff, P. H., 2005, "Reevaluation of Deflection Prediction for Concrete Beams Reinforced with Steel and Fiber Reinforced Polymer Bars," *Journal of Structural Engineering*, ASCE, V. 131, No. 5, May, pp. 752-767. doi: 10.1061/(ASCE)0733-9445(2005)131:5(752)

Bischoff, P. H., 2020, "Comparison of Existing Approaches for Computing Deflection of Reinforced Concrete," *ACI Structural Journal*, V. 117, No. 1, Jan., pp. 231-240. doi: 10.14359/51718072

Bischoff, P. H., 2022, "Deformation Model for Reinforced and Cracked Prestressed Concrete," *ACI Structural Journal*, V. 119, No. 1, Jan., pp. 243-254. doi: 10.14359/51733138

Bischoff, P. H.; Naito, C. J.; and Ingaglio, J. P., 2018, "Immediate Deflection of Partially Prestressed Concrete Flexural Members," *ACI Structural Journal*, V. 115, No. 6, Nov., pp. 1683-1693. doi: 10.14359/51702381

Bischoff, P. H., and Scanlon, A., 2007, "Effective Moment of Inertia for Calculating Deflections of Concrete Members Containing Steel Reinforcement and Fiber-Reinforced Polymer Reinforcement," *ACI Structural Journal*, V. 104, No. 1, Jan.-Feb., pp. 68-75.

Branson, D. E., 1965, "Instantaneous and Time-Dependent Deflections of Simple and Continuous Reinforced Concrete Beams," *HPR Report* No. 7, Part 1, Alabama Highway Department, Bureau of Public Roads, Montgomery, AL, 78 pp.

Branson, D. E., 1977, *Deformation of Concrete Structures*, McGraw-Hill, New York, NY, 546 pp.

Branson, D. E.; Meyers, B. L.; and Kripanarayanan, K. M., 1970, "Loss of Prestress, Camber, and Deflection of Noncomposite and Composite Structures Using Different Weight Concretes," *Report* No. 70-6, Department of Civil Engineering, University of Iowa, Iowa City, IA.

Branson, D. E., and Trost, H., 1982a, "Unified Procedures for Predicting the Deflection and Centroidal Axis Location of Partially Cracked Non-Prestressed and Prestressed Concrete Members," *ACI Journal Proceedings*, V. 79, No. 2, Mar.-Apr., pp. 119-130.

Branson, D. E., and Trost, H., 1982b, "Application of the I-Effective Method in Calculating Deflections of Partially Prestressed Members," *PCI Journal*, V. 27, No. 5, Sept.-Oct., pp. 62-77. doi: 10.15554/pcij.09011982.62.77

Chen, C. I., 1973, "Integrated Procedures for Predicting the Initial and Time-Dependent Deformation of 'Reinforced' Concrete Structures," PhD thesis, University of Iowa, Iowa City, IA.

Elzanaty, A. H.; Nilson, A. H.; and Slate, F. O., 1986, "Shear Capacity of Prestressed Concrete Beams Using High-Strength Concrete," *ACI Journal Proceedings*, V. 83, No. 3, May-June, pp. 359-368.

Founas, M., 1989, "Deformations and Deflections of Partially Prestressed Concrete T-Beams under Static and Random Amplitude Fatigue Loading," PhD thesis, University of Michigan, Ann Arbor, MI.

Gowripalan, N., and Zou, X. W., 1999, "Flexural Behavior and Ductility of Prestressed Beams with High-Strength Concrete," *High Performance Concrete—Proceedings: ACI International Conference, Malaysia, 1997*, SP-172, V. M. Malhotra, ed., American Concrete Institute, Farmington Hills, MI, pp. 573-600.

Hanson, J. M., 1964, "Ultimate Shear Strength of Prestressed Concrete Beams with Web Reinforcement," PhD thesis, Lehigh University, Bethlehem, PA.

Hanson, J. M., and Hulsbos, C. L., 1963, "Overload Behavior of Prestressed Concrete Beams with Web Reinforcement," Fritz Engineering Laboratory *Report* No. 223.25, Lehigh University, Bethlehem, PA.

Harajli, M., and Naaman, A. E., 1984, "Deformation and Cracking of Partially Prestressed Concrete Beams under Static and Cyclic Fatigue Loading," *Report* No. UMEE 84R1, Department of Civil Engineering, University of Michigan, Ann Arbor, MI.

Hernandez, G., 1958, "Strength of Prestressed Concrete Beams with Web Reinforcement," PhD thesis, University of Illinois, Engineering Experiment Station, Urbana, IL.

Huang, P. T., 1975, "Serviceability Behavior and Crack Control in Pretensioned Prestressed Concrete I- and T-Beams," PhD thesis, Rutgers, the State University of New Jersey, New Brunswick–Piscataway, NJ.

Janney, J. R.; Hognestad, E.; and McHenry, D., 1956, "Ultimate Flexural Strength of Prestressed and Conventionally Reinforced Concrete Beams," *ACI Journal Proceedings*, V. 52, No. 2, Feb., pp. 601-620.

Jiang, Q.; Wang, H.; Chong, X.; Feng, Y.; and Ye, X., 2021, "Flexural Behavior of High-Strength, Steel Reinforced and Prestressed Concrete Beams," *Frontiers of Structural and Civil Engineering*, V. 15, No. 1, pp. 227-243. doi: 10.1007/s11709-020-0687-3

Kassian, W., 2016, *Prestressed Concrete*, *Concrete Design Handbook*, fourth edition, Cement Association of Canada, Ottawa, ON, Canada, pp. 10-1 – 10-78.

Krishna Mohan Rao, S. V., and Dilger, W. H., 1992, "Evaluation of Short-Term Deflections of Partially Prestressed Concrete Members," *ACI Structural Journal*, V. 89, No. 1, Jan.-Feb., pp. 71-78.

Martinez, S.; Nilson, A. H.; and Slate, F. O., 1984, "Spirally Reinforced High-Strength Concrete Columns," *ACI Journal Proceedings*, V. 81, No. 5, May, pp. 431-442.

Mast, R. F., 1998, "Analysis of Cracked Prestressed Concrete Sections: A Practical Approach," *PCI Journal*, V. 43, No. 4, July-Aug., pp. 80-91. doi: 10.15554/pcij.07011998.80.91

Naaman, A. E., 1982, *Prestressed Concrete Analysis and Design: Fundamentals*, McGraw-Hill Book Company, New York, 670 pp.

Nasreddine, W., 2022, "Flexural Behavior of Continuous and Simply Supported Beams Prestressed with Hybrid (CFRP and Steel) Tendons," PhD thesis, Rutgers, the State University of New Jersey, New Brunswick–Piscataway, NJ.

Nilson, A. H., 1976, "Flexural Stresses after Cracking in Partially Prestressed Beams," *PCI Journal*, V. 21, No. 4, July-Aug., pp. 72-81. doi: 10.15554/pcij.07011976.72.81

Obeidah, A., and Nassif, H., 2022, "Serviceability of Beams Prestressed with Hybrid (Steel/Carbon Fiber-Reinforced Polymer) Tendons," *ACI Structural Journal*, V. 119, No. 3, May, pp. 179-190. doi:10.14359/51734437

Oukaili, N. K. A., and Khattab, M. M., 2018, "Strength and Serviceability of Partially Prestressed Concrete Beams Exposed to Limited Repeated Loading," *Proceedings*, *5th International* fib *Congress*, Oct. 7-11, 2018, Melbourne, Australia.

PCI Committee on Allowable Stresses in Prestressed Concrete Design, 1970, "Allowable Tensile Stresses for Prestressed Concrete," *PCI Journal*, V. 15, No. 1, Feb., pp. 37-42.

Precast/Prestressed Concrete Institute (PCI), 2017, *PCI Design Handbook: Precast and Prestressed Concrete (MNL-120-17)*, eighth edition, PCI, Chicago, IL.

Scanlon, A., and Bischoff, P. H., 2008, "Shrinkage Restraint and Loading History Effects on Deflections of Flexural Members," *ACI Structural Journal*, V. 105, No. 4, July-Aug., pp. 498-506.

Shaikh, A. F., and Branson, D. E., 1970, "Non-Tensioned Steel in Prestressed Concrete Beams," *PCI Journal*, V. 15, No. 1, Feb., pp. 14-36. doi: 10.15554/pcij.02011970.14.36

Shi, C., 2003, "Static and Fatigue Behaviour of Prestressed Concrete Beams Strengthened with Prestressed CFRP Sheets," PhD thesis, Queens University, Kingston, ON, Canada.

Slepetz, J. M., 1968, "Behavior of Rectangular Prestressed Concrete Beams Subjected to Heavy Repeated Loads," PhD thesis, Department of Civil Engineering, Duke University, Durham, NC.

Tadros, M. K., 1982, "Expedient Service Load Analysis of Cracked Prestressed Concrete Sections," *PCI Journal*, V. 27, No. 6, Nov.-Dec., pp. 86-111. See also Reader Comment, *PCI Journal*, V. 28, No. 6, pp. 137-158.

Tadros, M. K.; Ghali, A.; and Meyer, A. W., 1985, "Prestressed Loss and Deflection of Precast Concrete Members," *PCI Journal*, V. 30, No. 1, Jan.-Feb., pp. 114-141. doi: 10.15554/pcij.01011985.114.141

Warwaruk, J., 1957, "Strength in Flexure of Bonded and Unbonded Prestressed Concrete Beams," MS thesis, University of Illinois, Engineering Experiment Station, Urbana, IL.

Warwaruk, J.; Sozen, M. A.; and Siess, C. P., 1962, "Strength and Behavior in Flexure of Prestressed Concrete Beams," Investigation of Prestressed Reinforced Concrete for Highway Bridges, Part III, University of Illinois, Engineering Experiment Station, Urbana, IL.

Zou, P. X. W., 2003, "Flexural Behavior and Deformability of Fiber Reinforced Polymer Prestressed Concrete Beams," *Journal of Composites for Construction*, ASCE, V. 7, No. 4, Nov., pp. 275-284. doi: 10.1061/(ASCE)1090-0268(2003)7:4(275)

Zwoyer, E. M., 1953, "Shear Strength of Simply Supported Prestressed Concrete Beams," PhD thesis, University of Illinois, Engineering Experiment Station, Urbana, IL.

ARE YOU A RESEARCHER?

SIGN UP FOR ORCID TODAY!

ORCID provides a persistent digital identifier that distinguishes you from every other researcher and, through integration in key research workflows such as manuscript and grant submission, supports automated linkages between you and your professional activities, ensuring that your work is recognized.

Individuals may use ORCID services freely and it's as easy as **1-2-3**:

1. REGISTER
2. ADD YOUR INFO
3. USE YOUR ORCID ID

For more information and to register, visit:

WWW.ORCID.ORG

ACI STRUCTURAL JOURNAL TECHNICAL PAPER

Title No. 120-S103

Evaluating Behavior of Shear-Critical Glass Fiber-Reinforced Polymer-Reinforced Concrete Beams

by Jahanzaib and Shamim A. Sheikh

Two shear-critical beams completely reinforced with glass fiber-reinforced polymer (GFRP) bars were constructed and tested in the current study. One beam was tested at room temperature and the second beam was subjected to accelerated thermal conditioning to simulate long-term behavior of GFRP-reinforced concrete (RC) beams, considering the recent climate challenges leading to increasing temperatures across the world. Conditioning of the beam was carried out at 50°C (122°F) for 4 months under 60% relative humidity while subjected to sustained load throughout the conditioning period. No significant change in behavior was observed because of the conditioning. Additionally, available models including code provisions (CSA S806, CSA S6, and ACI 440.1R) to estimate the shear strength of shear-critical beams were critically evaluated and discussed. It was noticed that the inclusion of a second-order equation to predict the shear contribution from concrete (V_c) seemed to improve the accuracy of the predictions.

Keywords: code provisions; glass fiber-reinforced polymer (GFRP); shear capacity; thermal conditioning.

INTRODUCTION

Recently, there has been a significant research focus towards understanding the behavior of fiber-reinforced polymer (FRP) bars in reinforced concrete (RC) members. Several design codes and standards have now allowed the use of glass fiber-reinforced polymer (GFRP) bars for flexural, compression, and shear resistance. ACI 440.1R-15 (2015) allows the use of GFRP straight bars in flexural members and bent bars in shear members; however, it ignores the strength of GFRP bars in compression. Likewise, CSA S806-12 (2012) provides design guidelines to use FRP bars in members subjected to flexure and shear but ignores the strength of FRP bars in compression. CSA S6, by contrast, recently allowed the use of FRP bars in compression in columns (CSA S6-19).

Although most design codes and guides have allowed the use of bent bars as transverse reinforcement, strength at the bend location has been a persistent design concern. The bending of fibers in GFRP bent bars causes a significant reduction in the bend strength in comparison to the straight portion strength (Vint and Sheikh 2015; Johal 2016). Most of the researchers conducted laboratory testing on bare stirrups to evaluate the performance of bent bars. Earlier research found that the bend strength was between 30 and 80% of the straight portion strength (Nagasaka et al. 1993). Jeremic and Sheikh (2021) tested 24 stirrups in the standardized testing procedure (CSA S806-12 Annex D) and found that the bend strength of GFRP stirrups varied from 35 to 55% of the straight portion strength.

Due to the uncertainty in the bend strength, design guidelines put a limit on the usable strain of GFRP stirrups. ACI 440.1R and CSA S6 limit the strain to 0.004 mm/mm, and CSA S806 standard increases this limit to 0.005 mm/mm. To design the shear members, CSA A23.3-19 (2019) provides a general design model of shear behavior for steel-reinforced concrete members. The model was developed based on the Modified Compression Field Theory (MCFT) (Vecchio and Collins 1986) and considers the member size and strain effect on the shear strength. In previous years, different modifications have been made into these steel-based design provisions to predict the shear strength of GFRP RC members (CSA S806-12; CSA S6-19; Bentz et al. 2010; Johnson and Sheikh 2014). A comprehensive investigation is needed to evaluate the accuracy of existing models in predicting the shear strength of the RC members reinforced with GFRP stirrups.

Another important aspect of GFRP bent bars that requires further investigation is their long-term durability under increased surface temperatures resulting from recent climate changes. Park et al. (2014) studied the long-term flexural behavior of GFRP-RC beams by conditioning them inside a chamber at an average temperature of 47°C (117°F) and an average relative humidity of 80% for 300 days. A maximum reduction of approximately 9% was observed in the moment capacity. However, no such test results are available in the literature that investigate the long-term durability of shear critical beams reinforced with GFRP stirrups. ACI 440.1R-15 highlights that the effects of elevated temperature exposure on the shear capacity of FRP-reinforced members are not well known, and additional research is warranted in this area.

The conditioning protocol adopted in this study serves two main purposes. The first is to evaluate the material and structural behavior using accelerated laboratory testing primarily driven by increased temperature that can be used to predict degradation in real-world scenarios using empirical models dependent on the geographic locations and mean annual temperatures. The second purpose is simulation of the effects of extreme temperatures resulting from

ACI Structural Journal, V. 120, No. 6, November 2023.
MS No. S-2022-412.R1, doi: 10.14359/51739095, received May 31, 2023, and reviewed under Institute publication policies.

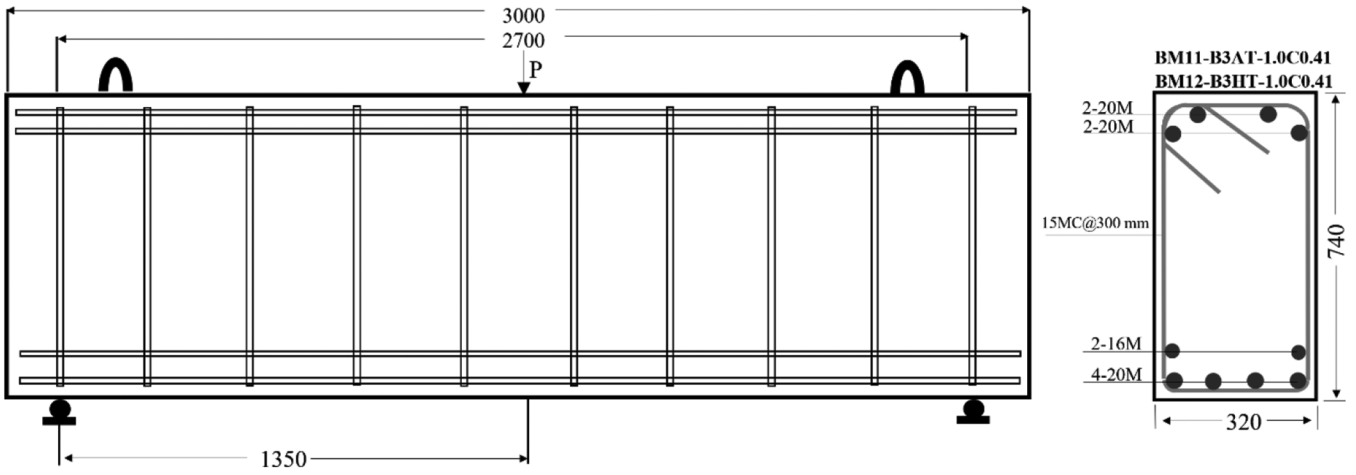

Fig. 1—Design of two deep beams. (Note: 1 mm = 0.0394 in.)

Table 1—Summary of specimen's details

Nomenclature	Beam No.	h, mm	b, mm	Longitudinal reinforcement	Spacing of ties, mm	ρ_L, %	d, mm	ρ_T, %	Test temperature, °C
Beam 1	11	740	320	4-20M + 2-15M	300	0.78	670	0.41%	Ambient
Beam 2	12	740	320	4-20M + 2-15M	300	0.78	670	0.41%	50

Note: 1 mm = 0.0394 in.; °F = (°C × 1.8) + 32.

Table 2—Concrete cylinders test result at time of testing

Group name	Test age, days	f_c', MPa	E_c, MPa	ϵ_c', mm/mm
AS	163	46.7	30,518	0.00215
CS	163	42.2	23,645	0.00229

Note: 1 MPa = 0.145 ksi.

recent climate changes that have led to a continuous rise in surface temperatures worldwide. For example, on June 29, 2021, in Lytton, BC, Canda, the temperature recorded was the highest ever in Canada at 49.6°C (121°F), approximately 15°C (27°F) higher than normal.

It is worth noting that numerous locations, especially in the Middle East and Asia, are already experiencing surface temperatures near 50°C (122°F). Thus, the outcomes of the current study provide an understanding of the behavior of FRP-RC members under these challenging weather conditions.

RESEARCH SIGNIFICANCE

The work presented in this paper investigates the shear behavior of RC beams completely reinforced with GFRP bars. Experimentally determined rupture strains of the stirrups due to shear failure of the beam are discussed. The work presented herein further provides an insight into the shear behavior of the beam after accelerated laboratory conditioning for 4 months at 50°C (122°F) and 60% relative humidity while subjected to sustained load. The conditioned beam was tested at the specified temperature. Additionally, a comprehensive review of existing design models—including the one developed from previous research at the University of Toronto (Johnson and Sheikh 2014)—to predict the shear strength is conducted in the current study.

EXPERIMENTAL PROGRAM

The experimental program of the current study consisted of several concrete beams, bond specimens, and material specimens. Results from two shear-critical beams (320 x 740 x 3000 mm [12.6 x 29.1 x 118.1 in.]) reinforced with GFRP straight and bent bars are reported in this paper. GFRP stirrups were anchored into the concrete core with 135-degree hooks at the corner. Reinforcement details and the geometry of the specimens are shown in Fig. 1 and Table 1.

Material properties

Concrete—Concrete was provided by a local supplier. The two beams were cast in the same batch, along with several 100 x 200 mm (3.94 x 7.87 in.) cylinders. Strength at the time of testing of the beams is listed in Table 2. Values in the table represent the average of at least three cylinder specimens. Group-AS in Table 2 represents the test results of the cylinders cured beside the control beam at ambient temperature, and group-CS cylinders were cured under the studied thermal exposure beside the conditioned beams and were tested at 50°C (122°F).

The development of the concrete compressive strength with time under two exposures—ambient conditions and 50°C (122°F) thermal exposure—from the results of 24 cylinders tested under compression is plotted in Fig. 2. It was found that the concrete cured under ambient conditions

Table 3—Mechanical properties of GFRP bars

Material properties	15M	20M	15M stirrup
Nominal core diameter, mm	16	19	16
Nominal area, mm^2	199	285	199
Actual area, mm^2	214	314	202
Ultimate tensile strength, MPa	1338	1336	1153
Modulus of elasticity, GPa	57.7	55.7	53.1
Elongation at failure, %	2.32	2.40	2.17
Bend radius, mm	—	—	56[†]
Bend average failure strain, με	—	—	14,700[†]
Glass transition temperature, °C[*]	114	125	109
Fiber content by weight, %	82.2	82.9	71.0

[*]Properties specified by manufacturer.

[†]Properties reported by Jeremic and Sheikh (2021).

Note: 1 mm = 0.0394 in.; 1 mm^2 = 0.00155 in.^{2}; 1 MPa = 0.145 ksi; 1 GPa = 145 ksi; °F = (°C × 1.8) + 32.

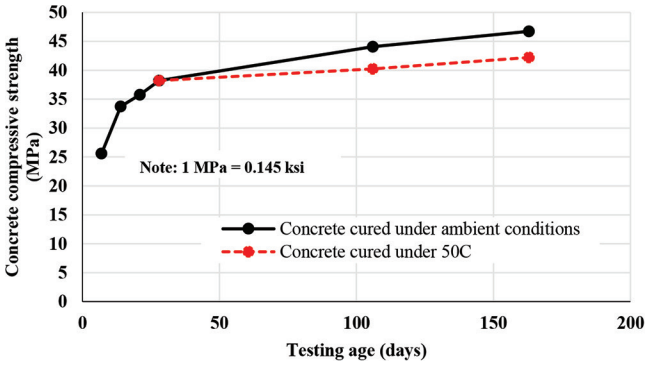

Fig. 2—Development of concrete compressive strength for Batch 3 concrete.

gained slightly higher strength over time than the concrete cured at a higher temperature of 50°C (122°F).

GFRP mechanical properties—The mechanical properties of all GFRP bars are listed in Table 3. Tensile properties of GFRP straight bars were determined through lab testing in accordance with the test procedure in ASTM D7205, as recommended in CSA S807-19. Actual cross-sectional areas were used for the calculation of the mechanical properties of straight bars. The properties of GFRP stirrups were determined in a parallel study conducted at the University of Toronto (Jeremic and Sheikh 2021) and are also provided in Table 3.

Instrumentation

Overall instrumentation plan consisted of both internal and external measurement tools. Internally, several electrical resistance strain gauges of 5 mm (0.2 in.) gauge length were installed on both the longitudinal and transverse reinforcing bars. Locations of strain gauges mounted on the straight bars and stirrups are shown in Fig. 3.

Externally, vertical displacements along the length of the beams were measured using linear variable displacement transformers (LVDTs). In total, five LVDTs were used during the testing in each beam. Two of them were located at the supports (one on each end of the beam) to measure support movements. In addition to the previously-mentioned instrumentation, a three-dimensional (3-D) light-emiting diode (LED) targeting system was used to measure the surface strains. The grid size for the shear critical control beam was chosen as 225 x 225 mm (8.86 x 8.86 in.). Complete external instrumentation is summarized in Fig. 4. It is to be noted that one additional LED target was mounted on the left support to measure the support settlement.

Test setup

Test setup for control beam—The Control Shear beam was tested under three-point bending. Testing was conducted in a monotonic displacement-controlled manner with the loading rate varying from 0.008 to 0.025 mm/s (0.000315 to 0.000984 in./s). The loading setup is shown in Fig. 5.

Test setup for conditioned beam—Conditioned beam was exposed to a temperature of 50°C (122°F) for 4 months under 60% relative humidity. In addition to the temperature exposure, the beam was also subjected to sustained load throughout the conditioning duration to replicate service loads. The load was applied to the beam with the help of threaded steel rods and load cells, and the complete loading protocol is explained in parallel tests published elsewhere (Jahanzaib and Sheikh 2022). The sustained load was applied with the help of a point load as the test setup shown in Fig. 5. Load level applied to this shear critical beam was 190 kN (4.27 kip, 19% of ultimate failure load), and the maximum average stain recorded in the bottom layer of the longitudinal reinforcement was 1500 με.

The sustained load levels applied in the current study induced strain in GFRP longitudinal bars of approximately 1500 με, which is approximately 8 to 9% of the ultimate failure strain of GFRP bar. Current code guidelines ignore the creep effect if the stress level in GFRP bars is below 20 to 25%. Therefore, it may be assumed that the sustained load level in the current study would create minimal creep effects that were ignored.

After conditioning, the beam was tested at 50°C (122°F). To ensure the temperature of GFRP bars embedded in concrete at the time of testing was equal to that in the conditioning

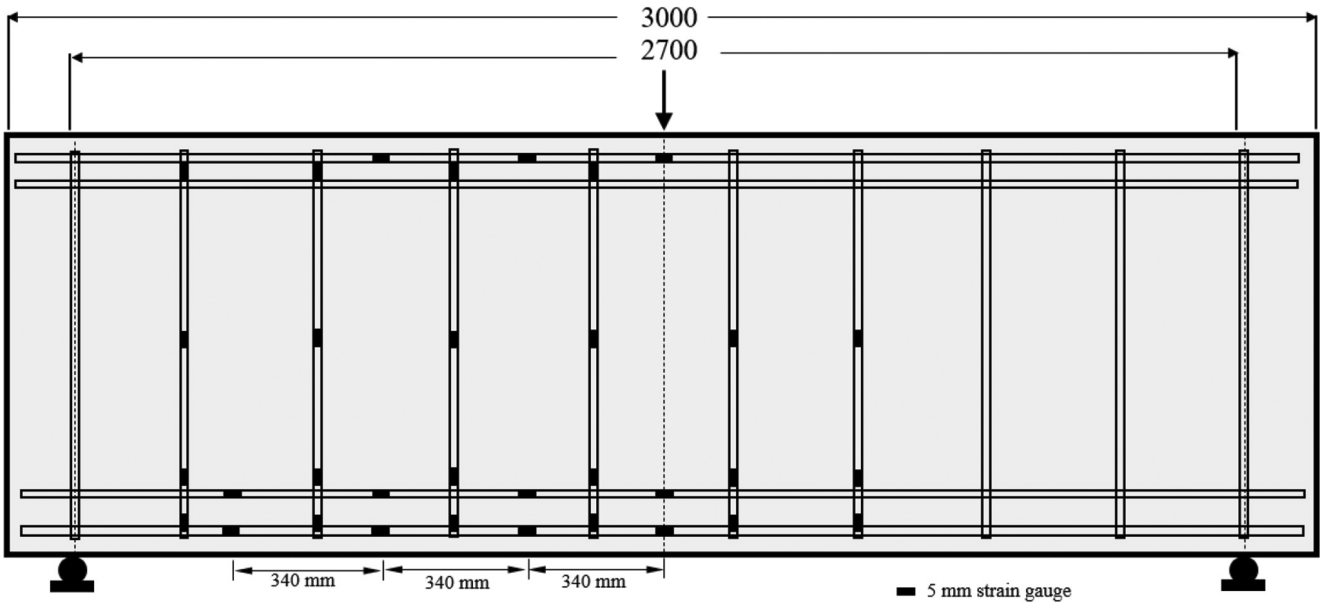

Fig. 3—Internal instrumentation of two shear-critical beams. (Note: 1 mm = 0.0394 in.)

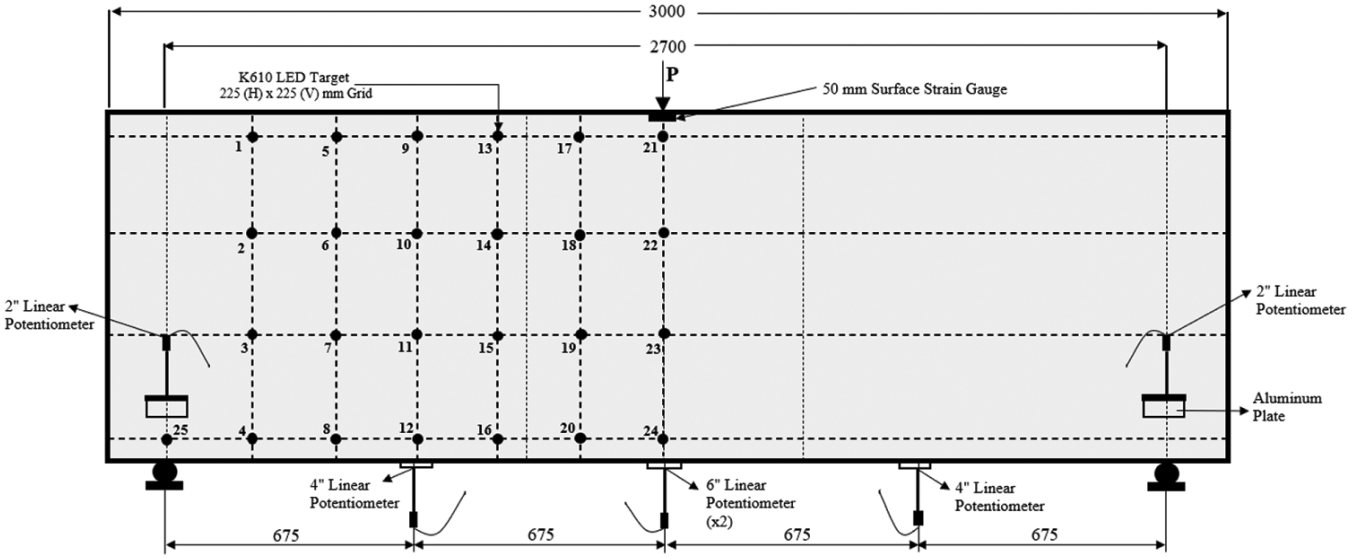

Fig. 4—External instrumentation for shear-critical control beam. (Note: 1 mm = 0.0394 in.)

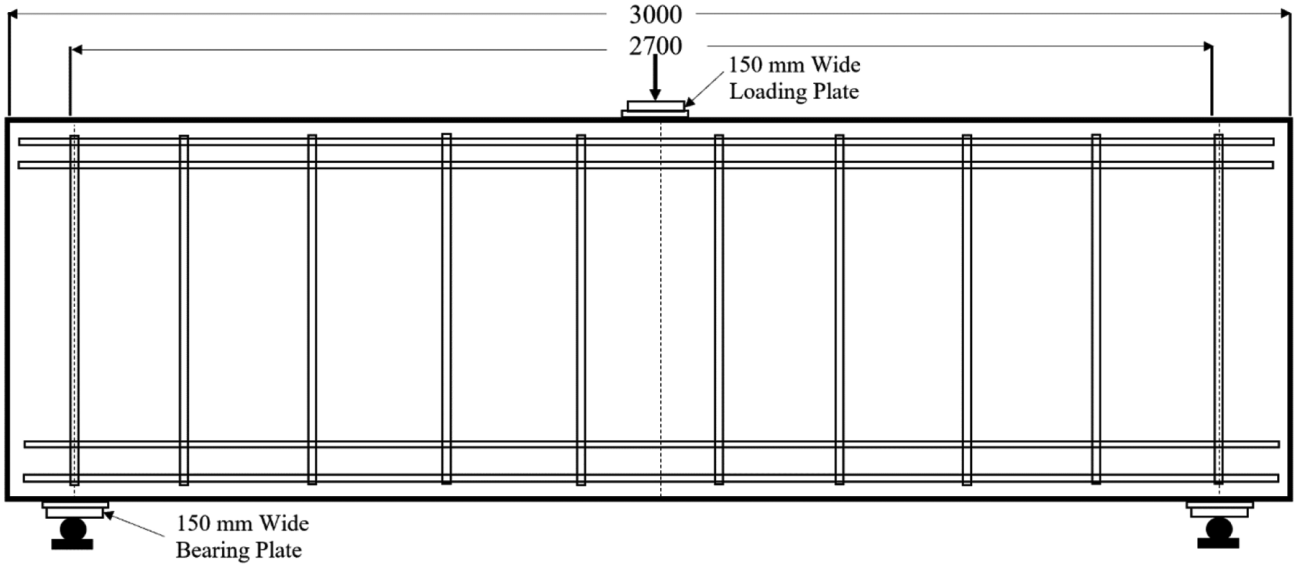

Fig. 5—Three-point bending test of deep beam. (Note: 1 mm = 0.0394 in.)

chamber, the beam was installed in the machine 24 hours prior to testing and was wrapped with heating blankets, as shown in Fig. 6. On the day of the test, the blankets were removed just before commencing the load.

TEST RESULTS AND DISCUSSION

As expected, both the beams failed in pure shear failure due to the rupture of GFRP stirrups. Beams were internally instrumented with several strain gauges and assigned a particular name based on their location as shown in Fig. 7.

The location of strain gauges attached to the stirrups is defined according to the following convention: SXY; S stands for stirrup; X refers to the stirrup's number which varies from 1 to 7 and represents the location of the stirrup along the length of the beam; and the letter Y denotes the location of strain gauge on the stirrup (T for top, M for midheight, B for the bottom corner, and B′ for the location where transitioning of the stirrup from the straight portion to the bent portion occurs).

Test result of control beam

The control Beam failed in shear with a shear crack running diagonally from the loading plate towards the left span crossing three instrumented stirrups. The ultimate failure occurred on the instrumented side and hence, recorded stirrups' strains from strain gauges provided a clear picture of the actual failure. Cracking at the tension face of the beam was first noticed at 187.6 kN (42.2 kip) followed by a slight drop in the load and a noticeable reduction in the stiffness. Further increase in the load resulted in the formation of shear cracks in both of the shear spans. At higher load levels, the width of the major shear crack started increasing significantly, and the failure occurred at a load of 958.7 kN (215.5 kip) with 28.92 mm (1.14 in.) midspan deflection. The failure happened due to the rupture of the stirrup located at 450 mm (17.7 in.) (strain gauge location: S4B′) from the midspan. It was noticed after the test that the stirrup ruptured at the transitioning point from the straight portion to the bent portion starts.

Fig. 6—Power-blankets wrapped on shear beam for heating before start of test.

The load-deflection behavior of the beam is shown in Fig. 8 and the failure crack is shown in Fig. 9. Beam failure and the rupture of the stirrup are shown in Fig. 10.

Recorded strain in stirrups—Most of the strain gauges functioned adequately during the test. Only a few of them failed before the peak load due to either saturation or a crack passing through the gauge causing the damage. As shown in Fig. 9, the failure crack crossed stirrup number 3 and 4 below the middepth. Therefore, recorded strains with the increasing load for the gauges S3T, S3M, S3B, S3B′, S4T, S4M, S4B, and S4B′ are shown in Fig. 11. Close to the failure point, strain values at the transitioning point (B′) in two of the stirrups (S3B′ and S4B′) were found to be the highest with maximum recorded strains of 14,410 and 12,830 με, respectively.

It is important to note that the strains at the beginning of the bend increased at a faster rate with an increasing load than the strains at the bent location (corner), and the stirrup ruptured at the beginning of the bend instead of the critical corner location. Therefore, the rupture stirrup strain in this beam test was defined as the maximum strain recorded at the beginning of bends before failure, as shown in Fig. 11, and was found to be 14,410 and 12,830 με for stirrup numbers 3 and 4, respectively, with an average value of 13,620 με. Material tests on the same stirrups conducted in a parallel

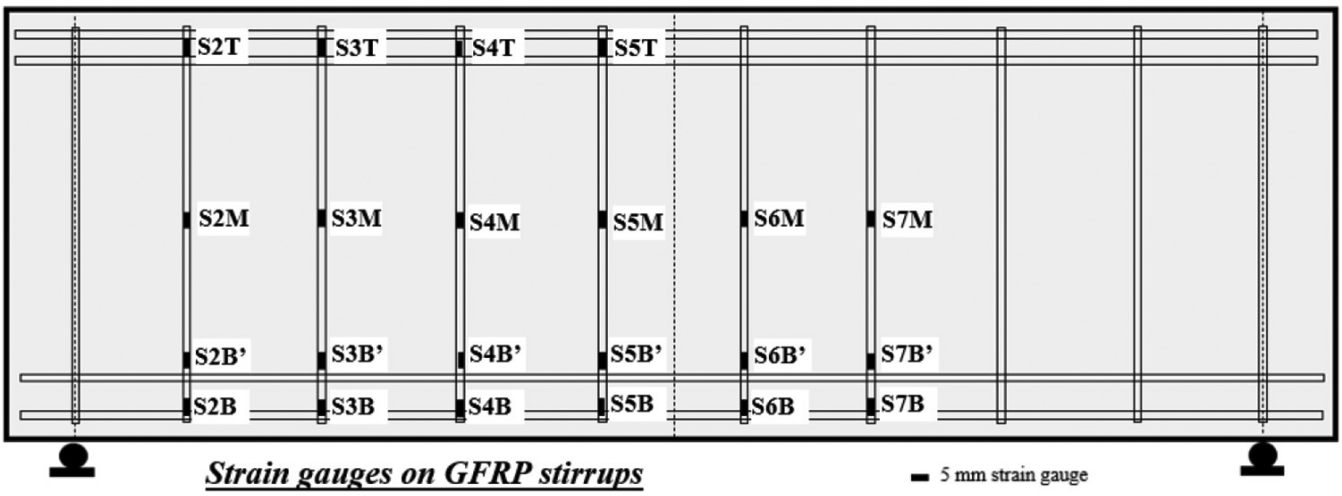

Fig. 7—Locations and nomenclatures of strain gauges.

study by Jeremic and Sheikh (2021) reported an average rupture strain of 14,700 με, which was considered to be reasonably close to the experimentally determined strain of 13,620 με from the current beam test. It should be noted that the actual strain may likely be higher than recorded.

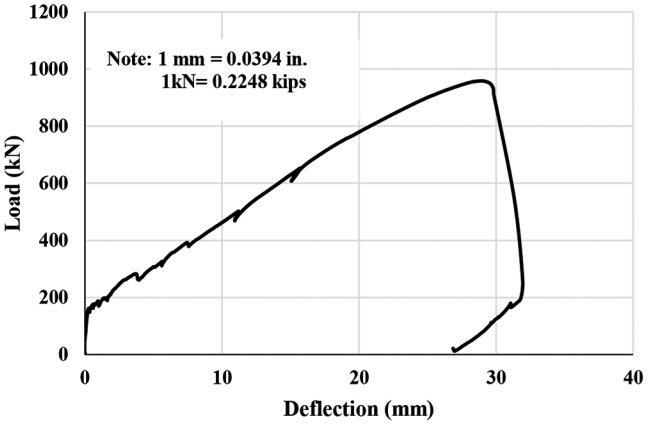

Fig. 8—Load deflection curve of control beam (Beam 1).

The reason behind the rupture of the stirrup at the transitioning point (B′) instead of the bottom corner (B, precisely where the weak point is located due to the bending of fibers) can perhaps be attributed to the presence of multiple layers of longitudinal bars. Bentz et al. (2010) found that with only one layer of longitudinal bars, the highest shear stress demand is predicted near the bottom of the stirrup (weak corner location); however, with multiple layers of longitudinal bars, the shear stress demand reduces in a more gradual fashion at the bottom. Therefore, the stirrup rupture in the beam with multiple layers did not occur at the critical corner location. To experimentally determine this gradual reduction, strain gauges were attached at both of the locations (B: bottom corner; and B′: above longitudinal layers) in the current study. As expected, strain gauge values showed a decrease in the recorded strains going from the beginning

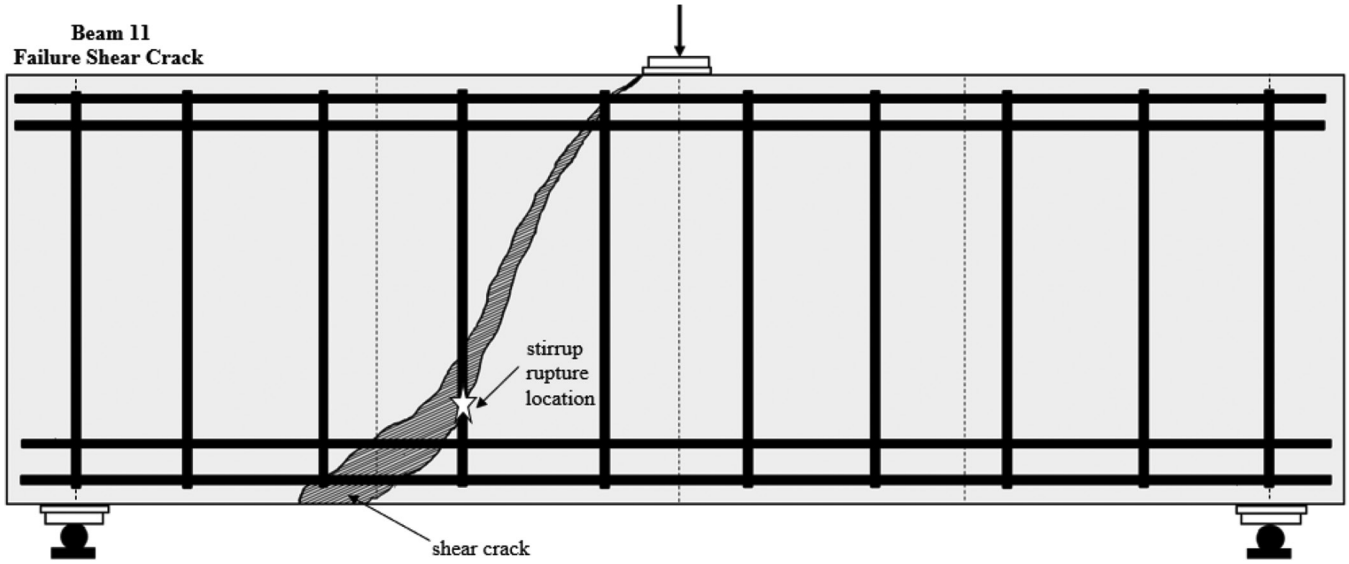

Fig. 9—Failure crack of Beam 1 (east side of beam failed which was instrumented).

Fig. 10—Control beam failure and stirrup rupture (north face of beam).

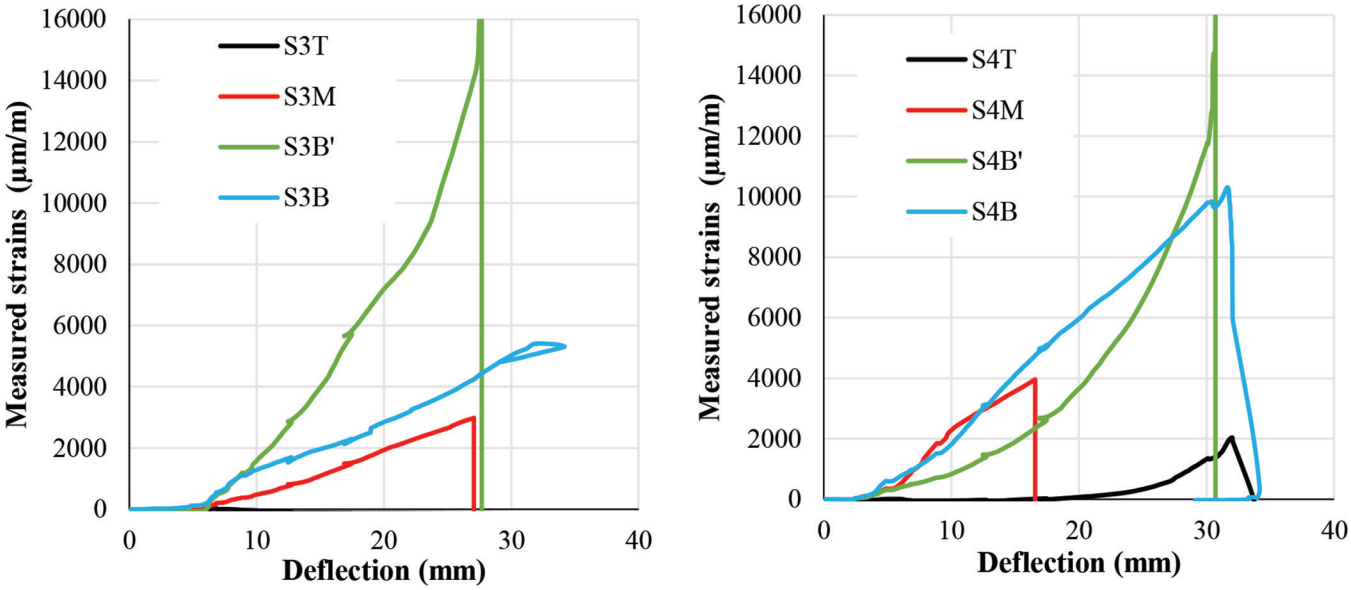

Fig. 11—Recorded strains in stirrups (Control Beam). (Note: 1 mm = 0.0394 in.)

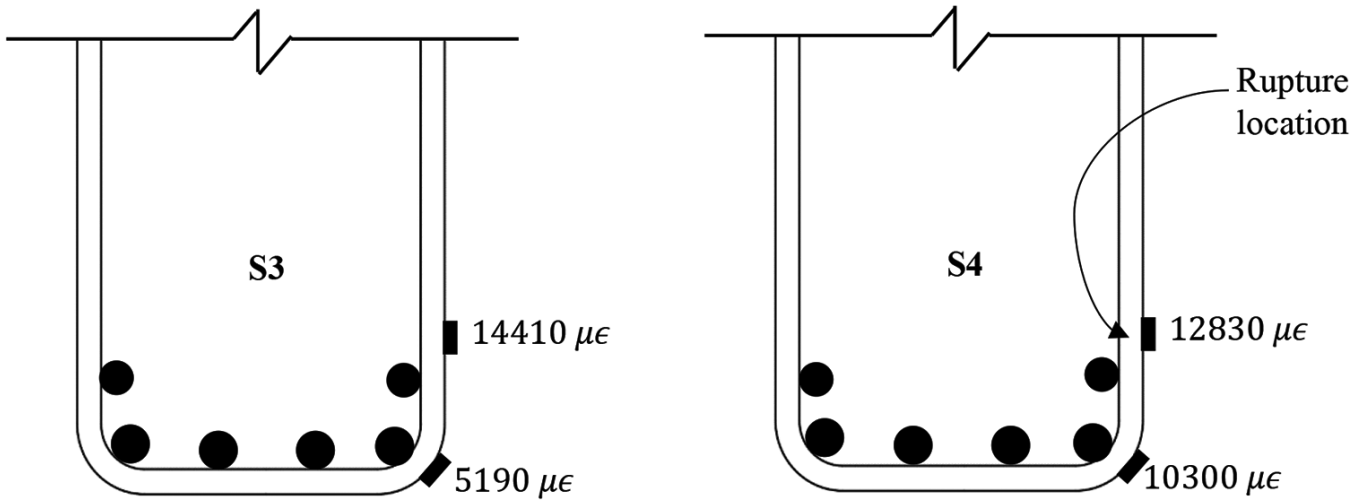

Fig. 12—Maximum recorded strains in stirrups S3 and S4 at bottom (Beam 1).

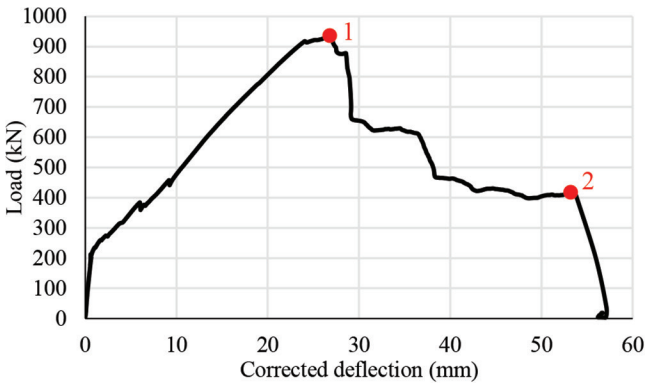

Fig. 13—Load versus midspan deflection curve of conditioned beam (Beam 2). (Note: 1 kN = 0.2248 kip; 1 mm = 0.0394 in.)

of bend location to the corner location, as shown in Fig. 12. This interesting finding can be helpful to protect weaker corner location in GFRP stirrups and allow the stirrup failure to happen away from the bend by providing multiple layers of longitudinal bars.

Test results of conditioned beam

As detailed previously, Beam 2 was conditioned for 4 months at 50°C (122°F) and tested at 50°C (122°F). The load-deflection behavior of Beam 2 is shown in Fig. 13. The beam failed in pure shear with a peak load of 936.2 kN (210.5 kip) and midspan deflection of 27 mm (1.06 in.). Failure at the peak load was initiated because of the rupture of the GFRP stirrup on the top bend location just beside the loading plate (marked as location 1 in Fig. 14). Peak load was accompanied by a significant drop in the load, but the beam did not fail. This drop in the load was followed by a significant increase in the midspan deflection, and the opening of the major shear crack. Finally, ultimate failure occurred because of the rupture of GFRP stirrups at the bottom corners (marked as location 2 on Fig. 13 and 14). Failure pictures from the Beam 2 test are shown in Fig. 15.

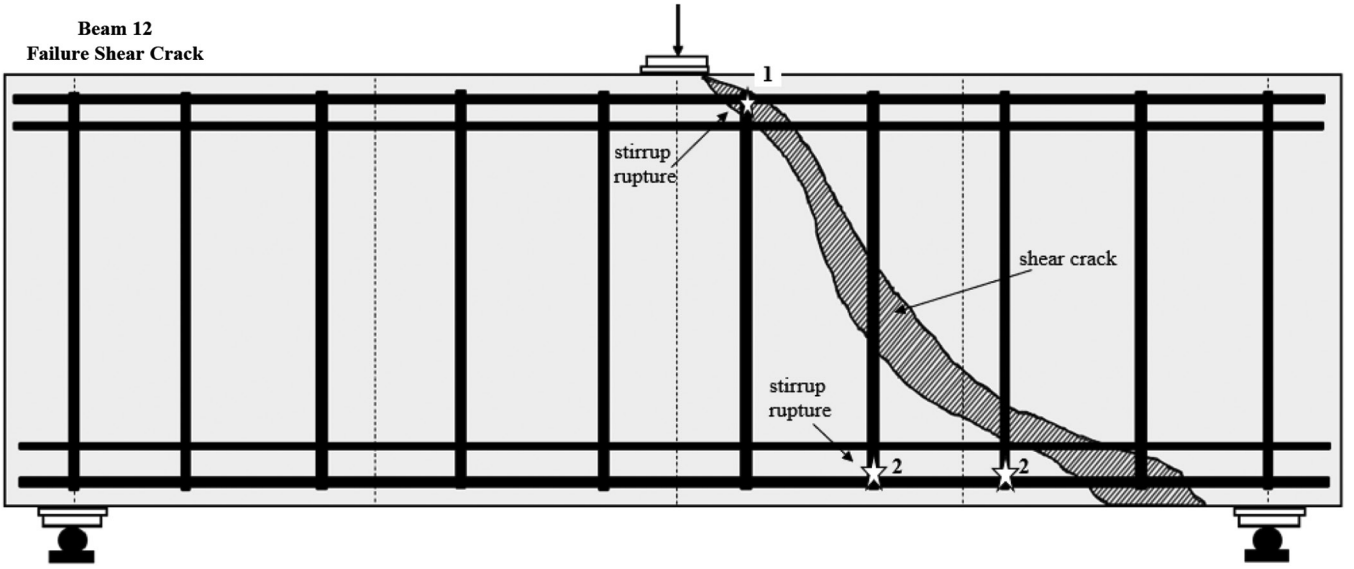

Fig. 14—Failure crack of conditioned beam (Beam 2) (north face of beam).

Fig. 15—Failure of Beam 2 (shear-critical conditioned beam)-south face of beam.

This beam failed in un-instrumented shear span and therefore, exact strain information for the failed span could not be determined.

Effect of thermal conditioning on shear behavior

Comparison between load deflection curves of the control and the conditioned shear-critical beams (Beams 1 and 2) is shown in Fig. 16. A slight reduction in the peak load was observed in the thermally conditioned beam. Beam 1 failed at 958.7 kN (215.5 kip), and Beam 2 at 936.2 kN (210.5 kip), showing only 1% reduction in the peak load. This can be due to the normal scatter in the experimental data. It can be concluded that the beam shear behavior was not affected much because of the long-term thermal conditioning. Failure modes of the stirrups were different in the two beams. Stirrups in the control beam failed due to rupture at the beginning of the bend (B′ location). However, stirrups in the conditioned beam failed at the corner locations of the stirrups. This variation in the failure mode may be attributed to the fact that thermal conditioning induced relatively more damage to the bent locations (corners) of the stirrups than the straight portion, and consequently, stirrups prematurely failed, showing a drop in the peak load.

PREDICTING SHEAR CAPACITY OF BEAM

Current code provisions and available models in literature

The accuracy of the predicted shear strengths using different models is evaluated against the test data from the beam tests. Provisions of the three design codes—ACI 440.1R, CSA S806, and CSA S6—are used to predict shear strength. Additionally, predictions using the equations

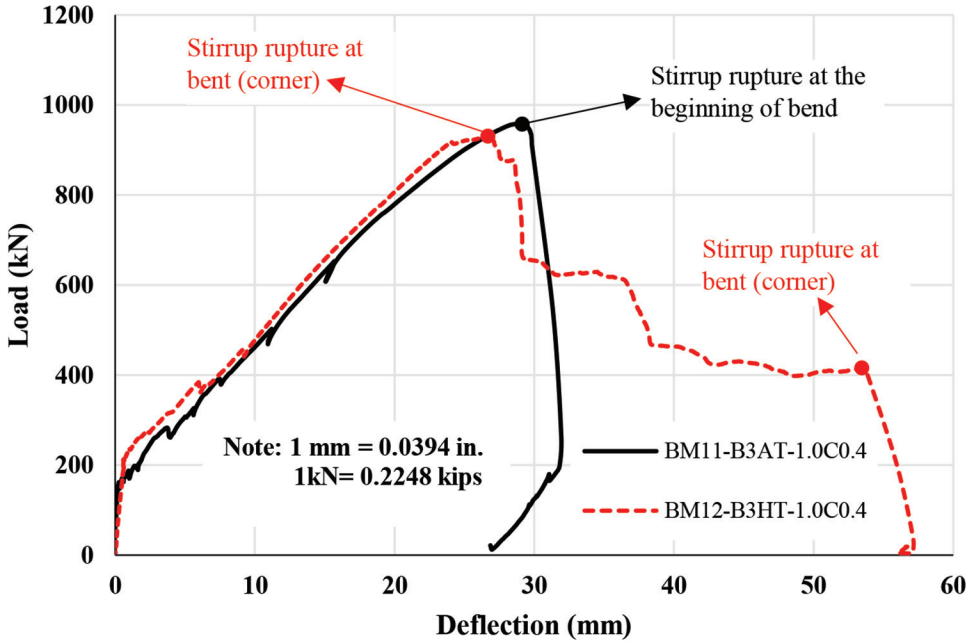

Fig. 16—Load deflection of shear critical control and conditioned beams (Beams 1 and 2).

proposed by Bentz et al. (2010) and Johnson and Sheikh (2014) are also critically evaluated and discussed. It is to be noted that different codes used different notations for the parameters involved in the equations. However, consistent notation is used in this paper and explained at the end of the paper.

A detailed summary of these current provisions is provided in Table 4. ACI 440.1R code uses a 45-degree fixed crack model with a strain limit applied to the ultimate strength. Both Canadian codes (CSA S806 and CSA S6) consider the effects of member size and middepth strain effect when determining shear capacity. Equations to find the angle of the principal compression strut in the CSA codes vary depending on the longitudinal strain at middepth.

It is to be noted that the accuracy of predictions from these equations mainly depends on two main parameters: 1) β-factor, which is the function of middepth strain and crack spacing; and 2) θ, which is the angle of principal compressive stresses and is a function of middepth strain. CSA S6 defines these parameters as recommended in the CSA A23.3 code for steel-reinforced members. Current equations to determine β and θ parameters in CSA S6 code are listed in Eq. (1) and (2), respectively.

$$\beta = \left(\frac{0.4}{1 + 1500\epsilon_x}\right)\left(\frac{1300}{1000 + s_{xe}}\right) \quad (1)$$

$$\theta = (29^\circ + 7000\epsilon_x)\left(0.88 + \frac{s_{xe}}{2500}\right) \quad (2)$$

To predict the shear strength of members with high longitudinal strains at shear failure as can occur with FRP reinforcement, Bentz et al. (2010) used the second-order expression (Eq. (3)) derived by Hoult et al. (2008) for the determination of β-factor.

$$\beta = \left(\frac{0.30}{0.5 + (1000\epsilon_x + 0.15)^{0.7}}\right)\left(\frac{1300}{1000 + s_{xe}}\right) \quad (3)$$

In a comprehensive study conducted by Johnson and Sheikh (2014) at the University of Toronto, experimental and analytical investigations were carried out to predict the shear strength of FRP reinforced beams. It was observed from the predictions that the CSA S6 equations are found to be more conservative. To accurately predict the shear capacity of the beam, relation between ϵ_x and θ (Eq. (2)) was reevaluated for high values of ϵ_x to result in less rotation of the strut at higher longitudinal strains. The modification in relation between ϵ_x and θ was made based on the experimental data of shear critical beams reinforced with different types of FRP transverse reinforcements. The following relations were suggested to determine the angle of principal compressive stresses

$$\text{for } \epsilon_x \le 9.0 \times 10^{-3};\ \theta =$$

$$(29^\circ + 7000\epsilon_x - 400{,}000\epsilon(2/x))(0.88 + s_{xe}/2500) \quad (4)$$

$$\text{for } \epsilon_x > 9.0 \times 10^{-3};\ \theta = 60(0.88 + s_{xe}/2500) \quad (5)$$

θ need not be taken greater than 75 degrees.

Predicted capacities

As highlighted previously, Beam 1 failed in pure shear with one major shear crack, and the peak load occurred at 958.7 kN (215.5 kip) (shear of 488 kN [109.5 kip] including the self-weight) and 28.92 mm (1.14 in.) midspan deflection. The failure happened due to the rupture of the stirrup at a location where transitioning of the bar from the straight portion to the bent portion starts at the lower end of the stirrup. The average recorded strain of the two stirrups ruptured at the failure was found to be 13,620 με. This average strain yields the bent strength of 723.2 MPa (104.9 ksi), assuming the same modulus of elasticity as observed in the straight portion. The crack angle from visual observation was found

Table 4—Provisions to predict shear capacity of GFRP RC members

Description	Equations
ACI 440.1R-15 (ACI 2015) code provisions	
Shear strength by concrete	$V_c = \frac{2}{5}\sqrt{f_c'}\ b_w k d\ k = \sqrt{(2\rho_f n_f + (\rho_f n_f)^2} - \rho_f n_f$; $\rho_f = A_f/b_d$; $n_f = E_f/E_c$
Shear strength by FRP stirrups	$V_s = \frac{A_{fv} f_{fv} d}{s}$
Limit on FRP stirrup strain	$f_{fv} = 0.004E_f \le f_{fb} f_{fb} = \left(0.05.\frac{r_b}{d_b} + 0.3\right) f_{fu} \le f_{fu}$
CSA S806-12 (CSA 2012) code provisions	
Shear strength by concrete	$V_c = 0.05\lambda k_m k_r k_s (f_c')^{1/3} b_w d\ k_m = \sqrt{\left(\frac{V_f d}{M_f}\right)} \le 1.0\ \ k_r = 1 + (E_f\rho_f)^{1/3}\ k_s = 750/450 + d \le 1.0$ for members with $d > 300$ mm
Shear strength by FRP stirrups	$V_s = \frac{0.4 A_{fv} f_{fv} d_v}{s}\cot(\theta)\ \theta = 30° + 7000\epsilon_x \le 60°\ \epsilon_x = \frac{\left(\frac{M_f}{d_v}\right) + V_f}{2E_f A_f}$
Limit on FRP stirrup strain	$f_v = 0.005E_f$
CSA S6 (CSA 2019) code provisions	
Shear strength by concrete	$V_c = 2.5 f_{cr}\beta b_w d_v\ \beta = \left(\frac{0.4}{1 + 1500\epsilon_x}\right)\left(\frac{1300}{1000 + s_{xe}}\right)\ \epsilon_x = \frac{\left(\frac{M_f}{d_v}\right) + V_f}{2E_f A_f}$ as d_v $\le 0.003\ \ s_{xe} = 35s_x/15 + a_g$; where s_x shall be taken
Shear strength by FRP stirrups	$V_s = \frac{A_{fv} f_{fv} d_v}{s}\cot(\theta)\ \theta = (29° + 7000\epsilon_x)(0.88 + s_{xe}/2500)$
Limit on FRP stirrup strain	$f_{fv} =$ Lesser of $0.004E_f$ or $\frac{\left(0.05\frac{r_b}{d_b} + 0.3\right) f_{fu}}{1.5}$
Bentz et al. (2010)	
Shear strength by concrete	$V_c = \beta\sqrt{f_c'} b_w d_v\ \beta = \left(\frac{0.30}{0.5 + (1000\epsilon_x + 0.15)^{0.7}}\right)\left(\frac{1300}{1000 + s_{xe}}\right)\ \epsilon_x = \frac{\left(\frac{M_f}{d_v}\right) + V_f}{2E_f A_f}\ \ s_{xe} = 31.5d/16 + a_g$
Shear strength by FRP stirrups	$V_s = \frac{A_{fv} f_{fv} d_v}{s}\cot(\theta)\ \theta = (29° + 7000\epsilon_x)(0.88 + s_{xe}/2500)$
Limit on FRP stirrup strain	$f_{fv} = f_{fu}$ or $\frac{\left(0.05\frac{r_b}{d_b} + 0.3\right) f_{fu}}{1.5}$
Johnson and Sheikh (2014) equations	
Shear strength by concrete	$V_c = \beta b_w d_v\sqrt{f_c}\ \beta = \left(\frac{0.3}{0.5 + (1500\epsilon_x + 0.15)^{0.7}}\right)\left(\frac{1300}{1000 + s_{xe}}\right)\ \epsilon_x = \frac{\left(\frac{M_f}{d_v}\right) + V_f}{2E_f A_f}$
Shear strength by FRP stirrups	$V_s = \frac{A_{fv} f_{fv} d_v}{s}\cot(\theta)$ for $\epsilon_x \le 9.0 \times 10^{-3}$; $\theta = (29° + 7000\epsilon_x - 400{,}000\epsilon\ 2/x)(0.88 + s_{xe}/2500)$ for $\epsilon_x > 9.0 \times 10^{-3}$; $\theta = 60(0.88 + s_{xe}/2500)$; θ need not to be taken greater than 75°
Limit on FRP stirrup strain	$f_{fv} = 0.004E_f$

Table 5—Comparison of predictions made by different models

Models	Using observed bend strength of 723.2 MPa					
	V_c, kN	θ	V_s, kN	V_r, kN	V_r/V_{exp} (Beam 1)	V_r/V_{exp} (Beam 2)
ACI 440.1R-15	91.6	45.0	652.5	744.2	1.53	1.56
CSA S806-12	290.1	60	135.6	425.6	0.87	0.89
CSA S6-19	96.0	50.0	492.7	588.7	1.21	1.24
Bentz et al. (2010)	110.5	63.0	299.1	411.5	0.84	0.86
Johnson (2014)	98.9	56.2	395.1	493.4	1.01	1.03

Note: 1 kN = 0.2248 kip.

to be 54 degrees. As discussed earlier, thermal conditioning did not induce significant degradation in the Beam 2 failure load; therefore, predictions are compared against the failure loads of both beams in Table 5. Experimentally, Beam 2 failed at 936.2 kN (210.5 kip) (shear of 476 kN [107 kip] including the self-weight).

Equations summarized in Table 4 were used to predict the shear strength of this beam. Predictions were made using the observed bend strength of 723.2 MPa (104.9 ksi) from the current beam experiment (rupture strength observed in Beam 1). A summary of the predictions using the observed bend strength is provided in Table 5.

Of the five predictions, it can be seen in Table 5 that ACI 440.1R and CSA S6 resulted in un-conservative estimates when using the actual bend strength. The 45-degree truss model opted by ACI 440.1R in combination with the static estimate of concrete contribution is responsible for the higher strength prediction. In reality, larger angles of principle compression have been observed because of the larger FRP strains. Likewise, in the CSA S6 equations, the middepth strain limit of 0.003 in the code limits the angle of principle compression to 50 degrees, and hence the equations resulted in unsafe predictions. On the other hand, the CSA S806 equations resulted in lower predictions. This lower prediction can be attributed to the 0.4 factor for the FRP stress limit in equations, which significantly reduces the shear contribution from the FRP stirrups.

Equations proposed by Bentz et al. (2010) slightly underestimated the shear strength with predicted to experimental ratio of 0.85 to 0.86. Bentz et al. (2010) modified the CSA S6 equations to predict the shear strength of FRP members. Overall, it was observed that using the second-order expression (Eq. (3)) to predict the shear contribution of concrete and removing the 0.003 middepth strain limit greatly improved the accuracy of predicted strength.

Finally, the model developed by Johnson and Sheikh (2014) proved to be the most accurate among all other models. Predicted to experimental shear strength ratio was found to be 1.02 to 1.03. This can be attributed to the changes made in this model. First, Johnson and Sheikh (2014) implemented the second-order V_c equation for concrete shear contribution proposed by Hoult et al. (2008). Secondly, the relation between ϵ_x and θ was reevaluated for higher values of ϵ_x to account for lower rotation of the strut at higher longitudinal strains. These two changes enhanced the accuracy of the prediction.

CONCLUSIONS

Based on the results of this experimental and analytical investigation, the following concluding remarks can be made:

1. The conditioned shear critical beam exhibited a mere 1% reduction in the ultimate shear capacity, which falls within the expected range of variability in the experimental data. Test results of these two beams suggest that long-term thermal exposure to elevated temperatures in the range of 50°C (122°F) did not cause any significant deterioration in the shear behavior. It is advisable to conduct additional tests under similar conditions to corroborate these results and expand the database.

2. Strain values recorded around the bent location showed that the presence of multiple layers of the longitudinal bar appear to protect the weak corner location of the bend due to the gradual reduction in the strain values.

3. It was also observed that the second-order V_c equation, developed to capture the higher middepth strain values in glass fiber-reinforced polymer (GFRP)-reinforced concrete members, provided more accurate predictions. Therefore, it is recommended to modify the current code provisions by analytically incorporating the behavior of FRP bars.

AUTHOR BIOS

ACI member **Jahanzaib** *is a Postdoctoral Fellow in the Department of Civil and Mineral Engineering at the University of Toronto, Toranto, ON, Canada. He received his BSc in civil engineering from the University of Engineering and Technology, Lahore, Pakistan. His research interests include the effect of climate change on glass fiber-reinforced polymer (GFRP)-reinforced concrete structures.*

Shamim A. Sheikh, *FACI, is a Professor of civil and mineral engineering at the University of Toronto. He is a member and past Chair of Joint ACI-ASCE Committee 441, Reinforced Concrete Columns, and a member of ACI Committee 374, Performance-Based Seismic Design of Concrete Buildings. His research interests include earthquake resistance and seismic upgrade of concrete structures, confinement of concrete, and the use of fiber-reinforced polymer (FRP) in concrete structures.*

ACKNOWLEDGMENTS

The authors would like to acknowledge funding received from the National Research Council of Canada (NRC) for their financial and technical support for this study. Financial and material support from the University of Toronto, Fiberline, and Pultrall Inc. is also appreciated. Assistance provided by the technical staff at the University of Toronto Structural Laboratories is gratefully acknowledged.

NOTATIONS

A_f	=	area of longitudinal FRP reinforcement
A_{fv}	=	area of FRP shear reinforcement
a_g	=	maximum aggregate size
b_w	=	beam width
d	=	effective depth of beam cross section
d_v	=	effective shear depth, larger of $0.9d$ or $0.72h$
E_f	=	elastic modulus of longitudinal FRP straight bar reinforcement
f_c'	=	concrete compressive strength
f_{cr}	=	concrete cracking strength
f_{fu}	=	ultimate strength of FRP straight bars
f_{fv}	=	usable stress for FRP stirrups
h	=	beam overall depth
k	=	ratio of depth of neutral axis to effective depth
M_f	=	factored moment at critical shear section
n_f	=	modular ratio
r	=	bend radius
s	=	spacing of stirrups
s_{xe}	=	crack spacing
V_c	=	shear strength provided by concrete
V_f	=	factored shear at critical shear section
V_r	=	shear capacity of GFRP RC beam
V_s	=	shear strength provided by FRP shear reinforcement
θ	=	angle of compression
ϵ_x	=	middepth strain
ρ_f	=	reinforcement ratio

REFERENCES

ACI Committee 440, 2015, "Guide Test Methods for Fiber-Reinforces Polymers (FRPs) for Reinforcing or Strengthening Concrete Structures (ACI 440.1R-15)," American Concrete Institute, Farmington Hills, MI, 88 pp.

Bentz, E. C.; Massam, L.; and Collins, M. P., 2010, "Shear Strength of Large Concrete Members with FRP Reinforcement," *Journal of Composites*

for Construction, ASCE, V. 14, No. 6, pp. 637-646. doi: 10.1061/(ASCE)CC.1943-5614.0000108

CAN/CSA-A23.3, 2019, "Design of Concrete Structures," CSA Group, Toronto, ON, Canada.

CSA S6, 2019, "Canadian Highway Bridge Design Code," CSA Group, Toronto, ON, Canada.

CSA S806, 2012, "Specification for Fiber-Reinforced Polymers," Canadian Standard Association, Mississauga, ON, Canada.

Hoult, N. A.; Sherwood, E. G.; Bentz, E. C.; and Collins, M. P., 2008, "Does the Use of FRP Reinforcement Change the One-Way Shear Behavior of Reinforced Concrete Slabs?" *Journal of Composites for Construction*, V. 12, No. 2, pp. 125-133.

Jahanzaib, and Sheikh, S. A., 2022, "Effect of Long-term Thermal Conditioning on GFRP-RC Beams," *ACI Structural Journal*, V. 119, No. 5, Sept., pp. 311-324.

Jeremic, N., and Sheikh, S. A., 2021, "Performance of Glass Fiber-Reinforced Polymer Bent Bars," *ACI Structural Journal*, V. 118, No. 2, Mar., pp. 273-285.

Johal, K. S., 2016, "Investigation of Creep Rupture Phenomenon in Glass Fibre Reinforced Polymer (GFRP) Stirrups," MASc thesis, Department of Civil Engineering, University of Toronto, Toronto, ON, Canada.

Johnson, D. T., 2014, "Investigation of Glass Fiber Reinforced Polymer (GFRP) Bars as Internal Reinforcement for Concrete Structures," PhD thesis, Department of Civil and Mineral Engineering, University of Toronto, Toronto, ON, Canada.

Johnson, D. T., and Sheikh, S. A., 2014, "Investigation of Glass Fiber Reinforced Polymer (GFRP) Bars as Internal Reinforcement for Concrete Structures," *Research Report JS-14-1*, Department of Civil and Mineral Engineering, University of Toronto, Toronto, ON, Canada.

Nagasaka, T.; Fukuyama, H.; and Tanigaki, M., 1993, "Shear Performance of Concrete Beams Reinforced with FRP Stirrups," *Fiber-Reinforced-Plastic Reinforcement for Concrete Structures − International Symposium,* SP-138, American Concrete Institute, Farmington Hills, MI, pp. 789-811.

Park, Y.; Kim, Y. H.; and Lee, S. H., 2014, "Long-Term Flexural Behavior of GFRP Reinforced Concrete Beams Exposed to Accelerated Aging Exposure Conditions," *Polymers*, V. 6, No. 6, pp. 1773-1793. doi: 10.3390/polym6061773

Vecchio, F. J., and Collins, M. P., 1986, "The Modified Compression Field Theory for Reinforced Concrete Elements Subject to Shear," *ACI Structural Journal*, V. 83, No. 2, Mar.-Apr., pp. 219-231.

Vint, L., and Sheikh, S. A., 2015, "Investigation of Bond Properties of Alternate Anchorage Schemes for Glass Fiber-Reinforced Polymer Bars," *ACI Structural Journal*, V. 112, No. 1, Jan.-Feb., pp. 59-68.

ACI STRUCTURAL JOURNAL TECHNICAL PAPER

Title No. 120-S104

Stochastic Finite Element Approach to Assess Reliability of Fiber-Reinforced Polymer-Strengthened Concrete Beams

by Connor Petrie and Fadi Oudah

This paper presents a novel framework to assess the reliability of externally bonded (EB) fiber-reinforced polymer (FRP)-strengthened steel-reinforced concrete (RC) beams by considering the spatial variation of concrete and concrete-FRP bond interface properties. The spatial variation is considered by developing resistance models using nonlinear stochastic finite element (FE) simulation, where the concrete properties are represented using three-dimensional (3-D) random fields and the concrete-FRP bond strengths are represented using two-dimensional (2-D) random fields. The framework was developed, automated, and applied to select configurations of RC beams strengthened using carbon FRP. A parametric analysis consisting of 3000 nonlinear stochastic FE models was performed to assess the effect of spatial variability on the reliability index of members designed using CSA S806, CSA S6, and ACI 440.2R. Analysis results verified the developed framework and indicated the sensitivity of analysis results to variations in the spatial properties of the considered beams.

Keywords: fiber-reinforced polymer; random fields; reinforced concrete; reliability analysis; spatial variability; stochastic finite element.

INTRODUCTION

The use of externally bonded (EB) fiber-reinforced polymer (FRP) to strengthen a reinforced concrete (RC) beam in flexure has been shown to be an alternative way to strengthen existing beams. Several studies have assessed the reliability of EB FRP-strengthened RC members in flexure to optimize the FRP design and calibrate material resistance factors and member reduction factors for code adaptation.[1-7] Most existing reliability-related research considered resistance models (distribution type, coefficient of variation [COV], and bias) based on controlled laboratory experiments, where the concrete strength and bond quality may not necessarily be representative of real-life conditions of existing RC members.[8] The concrete strength parameters (compressive strength, tensile strength, and modulus) in existing structures vary spatially across the member dimensions as evident in experimental tests and engineering practice.[9,10] This spatial variation contributes to the uncertainty in predicting the flexural resistance of tension-controlled and compression-controlled EB FRP-strengthened RC members. For tension-controlled members, the spatial variation in the concrete strength impacts the bond strength at the concrete-FRP interface which would, in turn, impact the onset of intermediate flexural cracks (IFC) and the flexural resistance.[11] For compression-controlled members, the spatial variation within the compression zone of the maximum moment region also impacts the flexural resistance.

Design provisions of EB FRP-strengthened RC beams for the ultimate limit state (ULS) in codes and standards including ACI 440.2R,[12] CSA S806,[13] and CSA S6[14] were not calibrated nor assessed using rigorous analysis for the effect of spatial variability in the reliability assessment of code-compliant designs. To further optimize the design of EB FRP and to promote FRP as a reliable alternative material for strengthening, work is needed to assess the safety of EB FRP-strengthened RC members by considering the effect of the spatial variation of the concrete properties on the reliability of beams designed according to established codes.

A method of accounting for the spatial variation in a member is with nonlinear stochastic finite element (SFE) analysis. SFE uses mathematical expressions to describe the randomness in the material properties over select domains in nonlinear FE models, where the mathematical expressions are referred to as random fields.[15] Multiple SFE simulations are required to develop a resistance model to be used to assess the reliability of the considered structure using available reliability estimation techniques such as Monte Carlo Simulation (MCS), First-order Reliability Method (FORM), Importance Sampling (IS), or using surrogated aided methods. A breadth of literature regarding the use of SFE in estimating the reliability of systems exists in the geotechnical field where the spatial variability in the soil response is significant,[16-19] while its use for concrete reliability assessment is limited although concrete properties (strength and stiffness) change spatially as established in practice and literature.[10,20]

The objective of this research is to develop a framework for assessing the reliability of EB FRP-strengthened RC flexural members using SFE-MCS analysis and apply it to assess the effect of the spatial variability of concrete and bond properties on beams designed as per ACI 440.2R,[12] CSA S806,[13] and CSA S6.[14] The non-linear FE software LS-DYNA has been chosen for developing the SFE models. An LS-DYNA-Python-MATLAB interface has been developed to automate the generation of the random fields,

ACI Structural Journal, V. 120, No. 6, November 2023.

MS No. S-2022-416.R1, doi: 10.14359/51739096, received June 2, 2023, and reviewed under Institute publication policies.

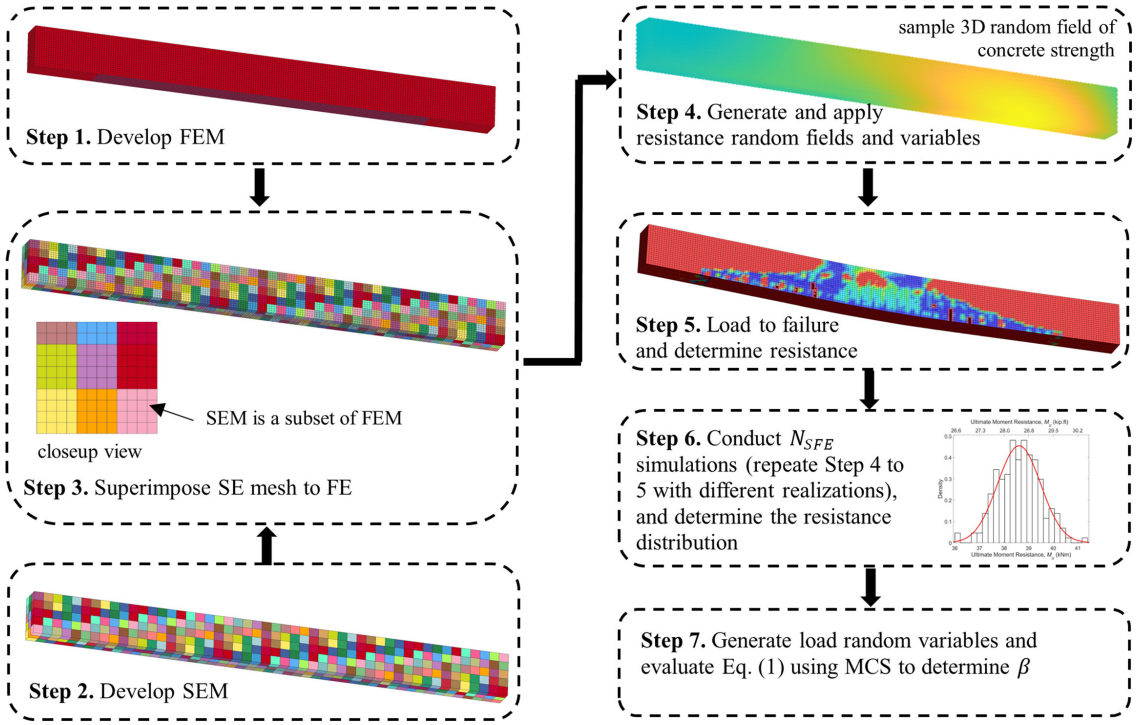

Fig. 1—Schematic illustration of SFE-MCS framework. (Note: Full-color PDF of this paper can be accessed at www.concrete.org.)

discretize the FE model for stochastic analysis, parallelize the SFE simulation, and conduct MCS analysis. The framework is described first, followed by applying it to conduct a parametric analysis of select beam configurations.

RESEARCH SIGNIFICANCE

The present study is the first to develop and apply a framework of analysis to examine the effect of concrete and bond spatial variability on the reliability of EB FRP-strengthened RC beams using nonlinear SFE and MCS. The framework addresses a major gap in existing literature relating to quantifying the effect of spatial variation of material properties on the reliability of EB FRP-strengthened RC members. The framework is adaptive and can be applied to assess the reliability of project-specific conditions (situations where the spatial variability is quantified) or for design code calibration.

SFE-MCS FRAMEWORK DEVELOPMENT

Overview

The general framework for assessing the reliability of EB FRP strengthened RC beams using SFE-MCS at ULS is schematically illustrated in Fig. 1 for a select flexural member. In this illustration, the concrete strength properties (strength and stiffness), and the bond strength at the concrete-FRP interface (normal and shear) are considered as random fields, while the FRP tensile strength, FRP modulus, and the reinforcing steel are considered as random variables. The first step consists of developing a nonlinear FE model of the assessed flexural element using commercial FE software (LS-DYNA is used in this research) by determining the appropriate material constitutive models and an appropriate finite element mesh (FEM) based on a sensitivity analysis. The second step consists of discretizing the concrete volume and the concrete-interface to form a stochastic element mesh (SEM), where the SEM is a subset of the FEM and the mesh size ratio, SEM/FEM, should be determined using a sensitivity analysis. The two meshes (FEM and SEM) are superimposed in Step 4 and the randomly generated random variables and fields are applied to form the SFE model. The three-dimensional (3-D) random field realizations of the concrete properties and the two-dimensional (2-D) random realizations of the concrete-FRP interface bond are generated at the centroids of the stochastic element and are assigned to all finite elements contained within the stochastic element (discussed in the next section).

The realization at each stochastic element is correlated in 3-D with all elements within the SEM for the concrete volume and in 2-D for the concrete-FRP bond strength. The degree of correlation is determined based on the input random field properties (correlation function and length as discussed in the following section). A sample contour of the spatial variation of the concrete compressive strength is shown in Step 4 of Fig. 1. The SFE model is loaded to ultimate (displacement- or load-controlled), and the ultimate moment of resistance is determined based on load-deflection curve in the fifth step. An N_{SFE} number of SFE models are generated and loaded to failure each with a different set of realizations of the random fields and variables. The ultimate moment of resistance, M_u, for the N_{SFE} simulations are extracted, and the distribution of the resistance model is obtained where the distribution type, bias, and standard deviations are quantified in the sixth step. MCS is then performed to assess the reliability index, β, of the considered performance function, $G(X)$, in the seventh step as expressed in Eq. (1), where $R(X)$ is the resistance model determined using SFE and $L(X)$ is the

load model. Model error can be included in $R(X)$ to account for uncertainty in SFE model versus experimental tests. The procedure for generating the random fields is described in the following section.

$$G(X) = R(X) - L(X) \tag{1}$$

Discretization of random fields

Several methods of generating random fields have been proposed in literature.[21,22] These techniques include methods to discretize the field based on point discretization techniques, such as the midpoint (MP), the shape function (SF), and optimal linear estimator (OLE) methods; based on average discretization techniques, such as the spatial average (SA) and weighted integral methods; or based on series expansion techniques, such as the Karhunen-Louve expansion, and the expanded optimal linear expansion (EOLE) method. The EOLE method is a spectral presentation of the OLE method and has been shown to have low error with fewer terms in the truncation when generating the field.[21] The EOLE method was used for discretization in this study.

The first step in discretization of the SEM is the selection of a stochastic mesh density for representng the geometry of the member as a 3-D mesh (Step 2 in Fig. 1). Let M_{SEM} represent an array containing all SEM vectors at a given mesh density, $M_{SEM} = \{SEM^{(1)}, SEM^{(2)}, SEM^{(3)},\ldots, SEM(N_{mesh})\}$, where N_{mesh} is the number of discretized stochastic elements, and $SEM^{(i)}$ is the i-th element in M_{SEM} and is represented by its 3-D coordinates in space, $SEM^{(i)} = (X_{SEM,i},Y_{SEM,i},Z_{SEM,i})$. The first two moments (that is, the mean and standard deviation) are found for each point in the mesh. To do this, the mean value of the lognormal field is evaluated at the centroid of each SEM, while the standard deviation of each SEM is evaluated as the mean multiplied by the coefficient of variation of the field. Next, the lognormal covariance matrix must be established using a chosen correlation function. The equation for the covariance matrix, C_{YY}' is given in Eq. (2). A squared exponential correlation function was used as expressed in Eq. (3)

$$C_{YY}' = C_{Y_iY_j}(i,j) = \sigma_i\sigma_j\rho_{ij} \tag{2}$$

$$\rho_{ij} = \prod_{k=1}^{\eta}\exp\left(-\frac{Y_k^{(i)} - Y_k^{(j)2}}{a_k^2}\right) \tag{3}$$

where σ is the standard deviation of i-th and j-th point considered, and ρ_{ij} is the correlation function between the set of two points.

The term $Y_k^{(i)}$ represents the i-th point in the field for the k-th iteration, and similarly, $Y_k^{(j)}$ represents the j-th point for the k-th iteration. The term a represents the autocorrelation length (also referred to as the correlation length). It is a measure of how correlated two points are in any given direction. Expanding Eq. (3) for a 3-D problem will give Eq. (4), where each of the two points considered is represented by a 3-D vector of coordinates. A Nataf transformation can be applied to the lognormal covariance matrix to convert it to be in gaussian space using Eq. (5)[22]

$$\rho_{ij} = \rho_{YY'}(i,j) = \prod_{k=1}^{\eta}\exp\left(-\frac{\left(Y_x^{(i)} - Y_x^{(j)}\right)^2}{a_x^2} - \frac{\left(Y_y^{(i)} - Y_y^{(j)}\right)^2}{a_y^2} - \frac{\left(Y_z^{(i)} - Y_z^{(j)}\right)^2}{a_z^2}\right) \tag{4}$$

$$\rho_{ij}' = s\rho_{ij} = \frac{\ln\left(1 + \rho_{ij}\,v_i\,v_j\right)}{\rho_{ij}\sqrt{\ln\left(1 + v_i^2\right)\ln\left(1 + v_j^2\right)}} \tag{5}$$

where ρ_{ij}' is the correlation for the standard normal field between two points $Y^{(i)}$ and $Y^{(j)}$; and s is a conversion factor converting the lognormal field. The terms v_i and v_j are the coefficient of variation of the mesh points $Y^{(i)}$ and $Y^{(j)}$, respectively.

Once in standard normal space, eigenvalues and eigenvectors can be obtained and ranked so that the r largest (r out of N_{SEM}, where N_{SEM} refers to the number of elements within the SEM) participating eigenmodes can be retained for field generation. Realizations of the gaussian field can be calculated using Eq. (6) by generating r random standard normal variables, $\xi(\theta)$

$$\hat{H}(Y,\theta) = \mu_{lny} + \sigma_{lny}\sum_{i=1}^{r}\frac{\xi_i(\theta)}{\sqrt{a_i}}\psi_i^T C_{Y,Y_i} \tag{6}$$

where

$$\sigma_{lny} = \sqrt{\ln\left(1 + \frac{\sigma_y^2}{\mu_y^2}\right)} \tag{7}$$

$$\mu_{lny} = \ln(\mu_y) - \frac{1}{2}\sigma_{lny}^2 \tag{8}$$

$\hat{H}(Y,\theta)$ is the gaussian field, made of two parts: i) the points within the discretized mesh Y; and ii) the random component of generated standard normal random variables, θ; σ_{lny} is the lognormal standard deviation of H, calculated using Eq. (7); and μ_{lny} is the lognormal mean of H, calculated using Eq. (8). The i-th standard normal random variable is represented by $\xi_i(\theta)$. The variable a_i is the i-th eigenvalue, while ψ_i^T is the i-th eigenvector matrix. Finally, C_{YYi} is the i-th vector of the correlation matrix. The generated field values from Eq. (6) can be converted to be lognormal through Eq. (9).

$$\hat{H}_{ln}(Y,\theta) = \exp\left\{\hat{H}(Y,\theta)\right\} \tag{9}$$

A measure of the representation quality of the generated field needs to be assessed based on the truncation value, r. Two measures in literature have been used; one based on the variance of the field,[21] shown in Eq. (10), and another based on the participation of retained eigenmodes used in field generation,[23] expressed in in Eq. (11), where $H(Y)$ and $\hat{H}(Y)$ are the exact and randomly realized value, respectively, of the stochastic field realization for point Y. Note the terms in Eq. (10) are the same as Eq. (6). The term Q in Eq. (11) is named the representation quality and it is equal the sum of the eigenvalues divided by the trace of the covariance matrix. The value of r (that is, the number of eigenvalues and eigenvectors included in field generation) will need to be increased with decreasing correlation length to maintain adequate representation quality

using either measure. Equation (11) was used in this research to determine r based on a target Q. The steps of random field generation are summarized in Fig. 2.

$$Var[H(Y) - \hat{H}(Y)] = \sigma_{lny}^2 \left[1 - \sum_{i=1}^{r} \frac{1}{a_i} (\psi_i^T C_{Y,Y_i})^2\right] \quad (10)$$

$$Q = \frac{\sum_{i=1}^{r} C_{Y,Y_i}}{tr(C_{YY})} \quad (11)$$

Automation of SFE-MCS analysis and computer code development

A computer interface was developed to automate the SFE-MCS analysis using MATALB, LS-DYNA, and Python. It consists of two parts: the SFE analysis part, and the MCS analysis part, as shown in Fig. 3. In the SFE analysis part, inputs for the random variable statistics, beam geometry, material properties, and stochastic parameters are taken by MATLAB and passed to Python and MATLAB subscripts. The MATLAB subscript generates the random values for the design random variables and generates the random fields for the concrete and bond. The Python subscript generates the discretization command file and applies it to generate the SFE model. The generated random field values in MATLAB are linked to the SFE model through Python. This process is repeated for N_{SFE} the number of times needed to build the resistance distribution histogram. In the MCS analysis part, a Python script has been used to extract the ultimate moment from the saved simulation data and calculate the resistance statistics (mean and standard deviation) for each sample population of beams generated in the SFE analysis part.[24] Using the load and resistance statistics, MCS is conducted considering these variables as random inputs in the performance function to calculate the probability of failure, p_f, and reliability index, β, by considering the performance function as normally distributed. The automated computer script is adaptive and can be applied to assess the reliability of various RC configurations under different limit states.

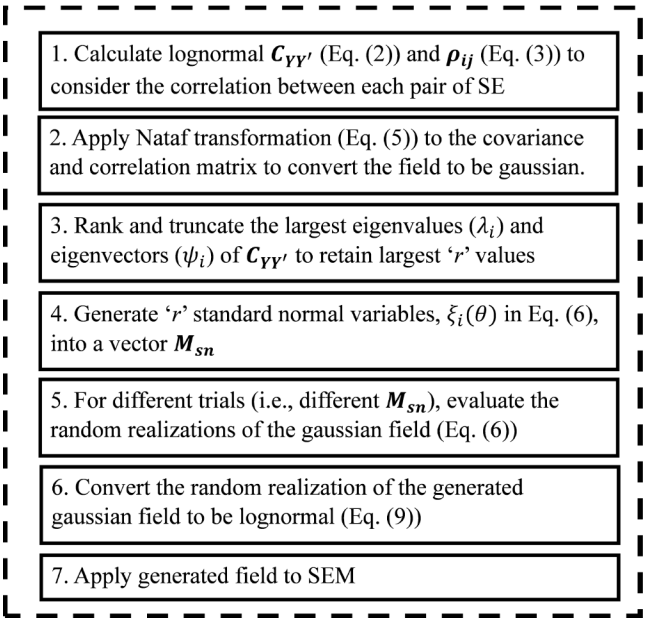

Fig. 2—Steps of discretization/generation of SFE model using EOLE.

SFE-MCS FRAMEWORK APPLICATION

Evaluation matrix and performance function

The developed SFE-MCS framework is applied to examine the effect of the spatial variability in the concrete and bond strength properties on the reliability of EB FRP strengthened RC beams designed according to ACI 440.2R,[12] CSA S806,[13] and CSA S6.[14] A parametric analysis using eight beams was performed, where the member design type (compression-controlled and tension-controlled), the specified concrete compressive strength (25 and 45 MPa [3626 and 6527 psi]), and the COV of the concrete compressive strength (0.1 and 0.3) are varied as shown in Table 1, and the corresponding beam details are shown in Fig. 4. Each strengthened beam has a unique ID label to denote it,

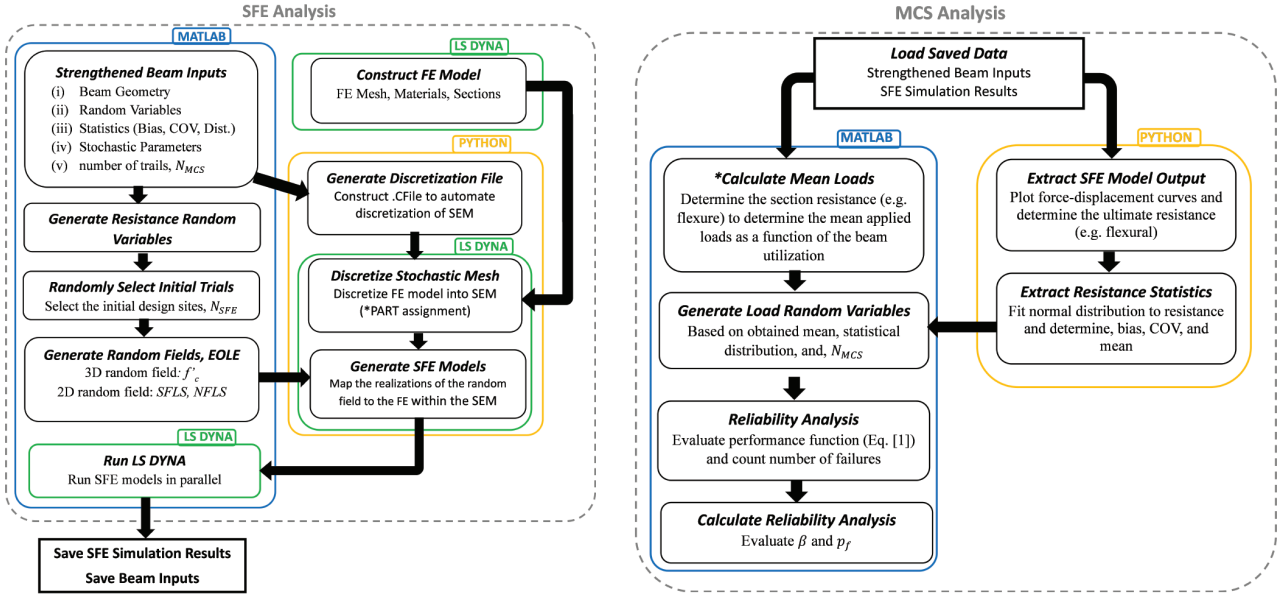

Fig. 3—Structure of developed automated computer interface for SFE-MCS analysis.

Table 1—Summary of strengthened beam configurations for parametric analysis

Beam ID	Design failure mode	f_c', MPa (psi)	$COV_{f_c'}$	Code M_r, kN·m (kip·ft)		
				CSA S806:17	CSA S6:19	ACI 440.2R:17
TF25C01	Tension	25 (3626)	0.1	21.5 (15.9)	21.9 (16.2)	25.1 (18.5)
TF25C03	Tension	25 (3626)	0.3	21.5 (15.9)	21.9 (16.2)	25.1 (18.5)
TF45C01	Tension	45 (6527)	0.1	22.0 (16.2)	22.4 (16.5)	25.9 (19.1)
TF45C03	Tension	45 (6527)	0.3	22.0 (16.2)	22.4 (16.5)	25.9 (19.1)
CF25C01	Compression	25 (3626)	0.1	42.7 (31.5)	48.1 (35.5)	38.6 (28.5)
CF25C03	Compression	25 (3626)	0.3	42.7 (31.5)	48.1 (35.5)	38.6 (28.5)
CF45C01	Compression	45 (6527)	0.1	55.3 (40.8)	59.7 (44.0)	46.1 (34.0)
CF45C03	Compression	45 (6527)	0.3	55.3 (40.8)	59.7 (44.0)	46.1 (34.0)

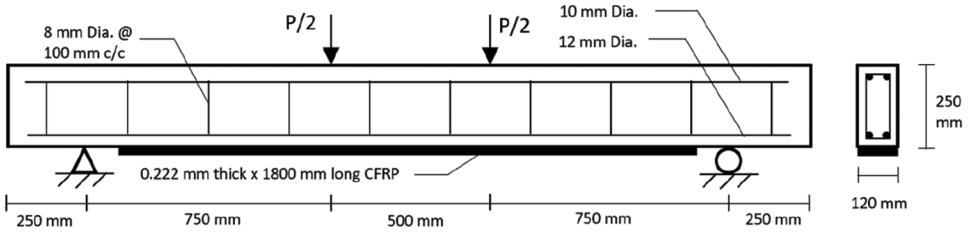

Fig. 4—Schematic illustration of beam details. (Note: 1 mm = 0.039 in.)

where the first letter denotes the failure modes of tension (T) and compression (C). The second letter and following two-character number denote the concrete strength of the beam in MPa (that is, F25 denotes $f_c' = 25$ MPa [3626 psi]). The last letter-numeric combination gives the COV value (that is, C01 denotes COV = 0.1). The factored moments of resistance, M_r, as per the considered design codes, are provided in Table 1.

The rationale for the choice of the varying parameters is as follows. For the COV range, it reflects different concrete production qualities where a variation in the concrete compressive strength for poor-quality concrete (that is, COV = 0.3) is likely to be higher than a good-quality concrete (that is, COV = 0.1). The range of COV is consistent with field observations.[25] For the design type, tension-controlled members are sensitive to variations in the concrete strength along the CFRP interface, while compression-controlled members are sensitive to variations in the concrete strength in the compression block of the constant moment region in four-point bending. For the specified f_c', the range of values covers a practical range used in practice.

All beams have a length (L), width (b), height (h), and depth to tensile reinforcing bar (d) equal to 2500, 120, 250, and 225 mm (98.4, 4.7, 9.8, and 8.9 in.), respectively, as shown in Fig. 4. The longitudinal reinforcement consists of four reinforcing steel bars made up of two compression and two tensile bars with a bar diameter, d_b, equal to 12 and 10 mm (0.47 and 0.39 in.), respectively, while the stirrups are 8 mm (0.31 in.) diameter bars spaced at 100 mm (3.9 in.) center-to-center. The EB FRP used for strengthening is a carbon FRP (CFRP) laminate that has a dual-layer thickness t_{frp} equal to 0.222 mm (0.009 in.), a width w_{frp} equal to 120 mm (4.72 in.), and has been attached to the tension face of the concrete with a length L_{frp} equal to 1800 mm (70.9 in.). The specified CFRP tensile strength, f_{frpu}, and CFRP modulus of elasticity, E_{frp}, are 3350 MPa and 235 GPa (486 and 34,075 ksi), respectively. The specified steel tensile yield strength, f_y, and modulus of elasticity, E_s, are 335 MPa and 200 GPa (48.6 and 29,000 ksi), respectively. Beam TF25C01 corresponds to the experimentally tested Beam 20A in Zhang et al.[26]

The performance function $G(X)$ is evaluated as per Eq. (1), where $L(X)$ and $R(X)$ are expressed in Eq. (12) and (13), respectively, where a negative value for $G(X)$ implies a failure. $L(X)$ consists of three random variables representing the dead load moment (DL), live load moment (LL), and transformation of live load to load effect ($T2L$) (for Canadian codes only). The statistical parameters of the load random variables are included in Table 2 and are based on the references that were largely used in calibrating the load and resistance factors of the respective design standard (ACI 440.2R,[12] CSA S806,[13] and CSA S6[14]). The load combination for each considered design standard is shown in the table.

The resistance model $R(X)$ is the product of the SFE flexural resistance random variable, $R_{SFE}(X)$, and a model error random variable, ϵ_{SFE}. $R_{SFE}(X)$ is determined based on SFE as per Fig. 1 (Steps 1 to 6) by considering three random variables and five random fields. The random variables include f_y, f_{frpu}, and E_{frp}. The random fields include f_c', concrete tensile strength f_t', concrete bulk modulus K, the normal bond strength at the concrete-CFRP interface $NFLS$, and shear bond strength at the concrete-CFRP interface $SFLS$. The f_t', K, $NFLS$, and $SFLS$ random fields are fully correlated to f_c'—that is, their realizations are described as a function of f_c' as detailed in the following section. The statistical parameters of the resistance random variables and fields are included in Table 3. The statistics of the resistance model are based on recommended values in literature.

Table 2—Statistics of load random variables for reliability analysis

	CSA S806-17			CSA S6-19			ACI 440.2R-17		
Variable	*DL*	*LL*	*T2L*	*DL*	*LL*	*T2L*	*DL*	*LL*	*T2L*
Dist.	Normal	Gumbel	Normal	Normal	Normal	Normal	Normal	Normal	N/A
Bias	1.050	0.900	1.000	1.040	1.168	1.020	1.050	1.000	—
COV	0.100	0.170	0.206	0.036	0.069	0.090	0.100	0.180	—
Reference	Bartlett et al.[27]			CSA S6.1-19[28]			Szerszen and Nowak[29]		

$$L(X) = DL(X) + LL(X) \times T2L(X) \quad (12)$$

$$R(X) = R_{SFE}(X) \times \epsilon_{SFE} \quad (13)$$

Overview of SFE model development

The SFE models are developed as per Steps 1 to 4 in Fig. 1 using the developed computer code described in Fig. 3 (SFE analysis part). First, the FE models of the considered beams are developed and validated against experimental tests (Step 1 in Fig. 1). Next, recommendations regarding the SEM and random field correlation lengths are made by performing a sensitivity analysis in two subsequent steps, where an optimum SEM density is determined through a sensitivity analysis, followed by using the optimum SEM density to perform a second sensitivity analysis to recommend the correlation length of the random fields (Steps 2 and 4 in Fig. 1). The FE development and validation, sensitivity of SEM, and sensitivity of the correlation length are described in the following sections.

FE model development and validation

Three-dimensional non-linear FE models of the beams were developed in LS-DYNA. The concrete volume was modeled using the Karagozian & Case (K&C) concrete model (*MAT 072R3 – Concrete Damage REL3 in LS-DYNA).[32,33] A Poisson's ratio and density of 0.2 and 2350 kg/m^3 were used, respectively. The material model parameters are generated solely by defining f_c', where f_t' in K&C is based on CEB-FIP Model Code 1990[34] as expressed in Eq. (14), and the bulk modulus is calculated using the equation of state (both are considered as fully correlated random fields defined by f_c').

$$f_t' = 1.58\left(\frac{f_c'^2}{145}\right)^{1/3} \quad (14)$$

The steel reinforcing bar was modeled using *MAT 003 – Plastic Kinematic, with a Poisson's ratio, density, and tangent modulus of 0.2, 7700 kg/m^3 (12,980 lb/yd^3), and 463 MPa (67 ksi), respectively. The CFRP layers were modeled using *MAT 054 – Enhanced Composite Damage, with a density of 1740 kg/m^3 and the CFRP properties described in the Evaluation Matrix section. A Lagrange constraint was used to model the bond between the steel reinforcing bar and the concrete volume. A penalty-based tiebreak contact with automatic surface to surface definition was used to simulate the FRP-concrete bond. All surfaces initially in contact are tied until failure of the bond strength is reached, meaning the FRP material is no longer able to carry tensile or shear stresses after the peak response is achieved. Post-peak softening of the bond stress at the interface is not considered.

The failure criterion is based on the normal surface stress, σ_n, and the shear surface stress, σ_s, of the contact interface, as expressed in Eq. (15).[35,36] *NFLS* and *SFLS* (both are considered as fully correlated random fields defined by f_c') were based on the work by Neale et al.,[37] as expressed in Eq. (16) and (17), respectively. *NFLS* and *SFLS* stresses were found to be 3.67 and 6.35 MPa (532 and 921 psi), respectively. The stress limits were validated for FE simulation in literature.[38,39] In the SFE models, the values of f_c' used to generate *NFLS* and *SFLS* refer to the values assigned to the FE concrete elements bonded to the CFRP material

$$\left(\frac{|\sigma_n|}{NFLS}\right)^2 + \left(\frac{|\sigma_s|}{SFLS}\right)^2 \geq 1.0 \quad (15)$$

$$NFLS = 0.62\sqrt{f_c'} \quad (16)$$

$$SFLS = 1.5\beta_w NFLS \quad (17)$$

$$\beta_w = \sqrt{\frac{2.25 - \frac{b_f}{b_c}}{1.25 + \frac{b_f}{b_c}}} \quad (18)$$

where b_f and b_c refer to the width of the CFRP sheet and concrete beam, respectively.

Fully integrated shell element formulation and fully integrated solid with accurate formulation were used for modeling the FRP and the concrete elements, respectively. A mesh density consisting of 47,700 concrete elements, 792 steel elements, and 1728 FRP elements was used. The element formulation and mesh density were determined based on a detailed sensitivity analysis. The loading protocol consisted of applying vertical displacement boundary conditions in implicit analysis to yield a four-point bending, where the translational degrees of freedom at the end supports were restrained accordingly to simulate a pin and a roller. The details of the FE model are illustrated in Fig. 5(a).

The force versus displacement curves of the experimentally tested and FE modeled Beam TF25C01 in Table 1, which corresponds to the experimentally tested Beam A20 in Zhang et al.,[26] are shown in Fig. 5(b). The FE model is validated for the ultimate capacity prediction, which is used in the reliability analysis, since the ratio of the ultimate capacity of the experimentally tested beam to the FE model was 0.94. The failure mode was yielding of the internal reinforcing bar followed by IFC debonding as observed in the experiment. The cracking of the beam at ultimate and a plan view of the FRP debonding pattern represented using the

Table 3—Statistic of resistance random variables for reliability analysis

Random variable	Distribution	Bias	COV	Reference
f_{frpu}	Lognormal	1.15	0.1	Huang et al.[5]
E_{frp}	Normal	1.0	0.04	Huang et al.[5]
f_y	Normal	1.145	0.05	Nowak and Szerszen[30]
f_c'	Lognormal random field	1.0	[0.1, 0.3]	This study
ϵ_{SFE}	Normal	1.10	0.12	Castaldo et al.[31]

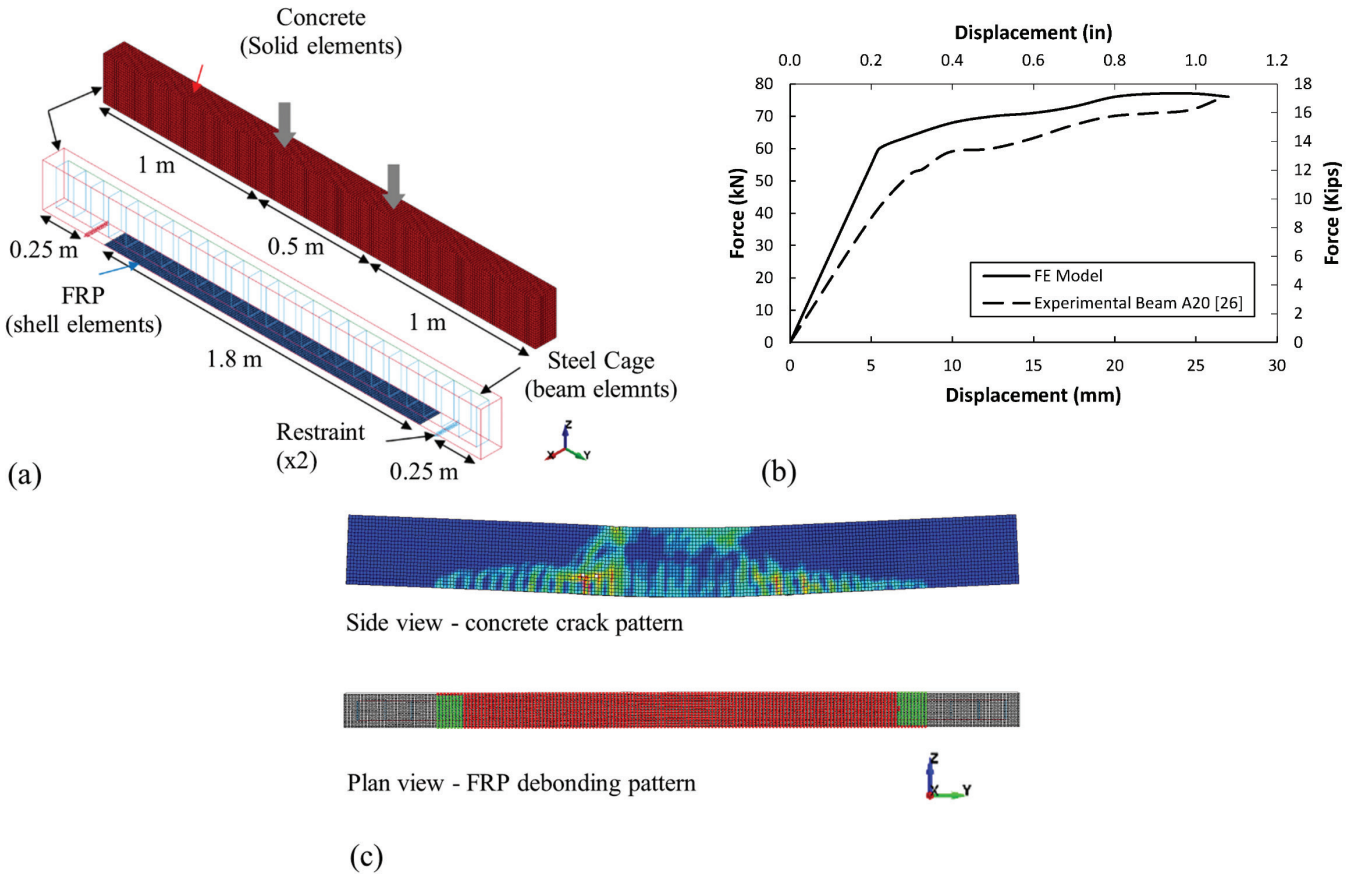

Fig. 5—View of FE model: (a) details of developed model; (b) crack and debonding pattern of validated model; and (c) force-displacement curve; FE and Exp.[26] (Note: 1 m = 3.28 ft; full-color PDF of this paper can be accessed at www.concrete.org.)

nodes of the FRP-concrete bond (bonded shown in green; de-bonded shown in red) are shown in Fig. 5(c). The flexural cracking that has reached the tension face has caused the FRP to debond from the center outward.

Stochastic element mesh (SEM) analysis

The mesh size ratio (*SEM*/*FEM*) is varied to investigate the effect on the distribution of the ultimate moment, M_u, at ULS and the computational time. Three SEM densities were considered: 320 SEM (SEM320), 750 SEM (SEM750), and 6000 SEM (SEM6000). Table 4 summarizes the input parameters for the sensitivity analysis including the total number of stochastic elements (SE), size of each SE, size of each finite element (FE), mesh size ratio, and N_{SFE} per analysis for the three considered SEM densities. The FEM size was kept constant at 10 x 12.5 x 12.5 mm (0.39 x 0.5 x 0.5 in.) (*x*,*y*,*z*) in all LS-DYNA models, while 200 SFE runs were conducted (N_{SFE}) per mesh configuration to obtain distributions of M_u. The participation of retained eigenmodes used in field generation (Q in Eq. (11)) was set to 0.80 and the required number of eigenmodes (r in Eq. (6)) was found to be 26 for all analyses.

The SEM density of the considered runs and a sample realization of the 3-D f_c' random field are shown in Fig. 6(a) and (b), respectively. The realizations of the f_c' random field are obtained at the geometric centroid of the SEM and then applied to all FE contained within the corresponding SE (SEM is a subset of FEM; refer to Step 3 in Fig. 1). The size of $C_{Y,Yi}$ in Eq. (6) equals the square of the total number of SEM, which implies that varying the SEM density yields a different set of ψ_i and θ_i, (eigenvalues and vectors). Consequently, the realizations of the random fields for the three select SEM densities are different, as shown in Fig. 6(b), although the three sample realizations are generated using the same set of standard normal variables $\xi_i(\theta)$. SEM320 and SEM750 were unable to capture the peak values of the

random fields as compared with the SEM6000, as observed based on the contours shown in Fig. 6(b). The histograms of M_u of the considered 200 runs per SEM density were obtained as shown in Fig. 6(c), while data are fitted using a normal distribution. M_u was found by plotting the force-displacement curves of the 600 SFE models, extracting the peak force, and calculating the applied moment given the moment arm. The statistical parameters of the fitted normal distributions, including the mean μ_{Mu}, standard deviation σ_{Mu}, COV, and the average run time per SFE model (200 models per considered SEM density) t_r, are also shown in Fig. 6(c). To examine the sensitivity of the *SEM*/*FEM*, the size of the FEM has been kept constant. Both the size of the FEM and the ratio of the *SEM*/*FEM* are important. Sensitivity should be done on both parameters to find the correct inputs when building the SFE model. In some cases, depending on the application and gradient of the random field, an *SEM*/*FEM* of unity may be advantageous.

Analysis results of the statistical properties of the normal fit indicate a marginal variation in the properties as function of the SEM density. The average run time was found to increase with finer SEM density (that is, larger number of stochastic elements). The SEM6000 (2 x 2 x 2 *SEM*/*FEM*) discretization was able to achieve the debonding failure mode more consistently (that is, numerical convergence as opposed to early termination due to divergence) than the courser SEM mesh densities of the SFE models, showing debonding of the FRP in almost all 200 models whereas the other mesh densities showed a variation in debonding failure and early termination (termination due to convergence issues). SEM6000 was used in the subsequent sensitivity analysis.

Random field correlation length analysis

The correlation length of f_c' random field is varied (a_x, a_y, and a_z in Eq. (3)) to investigate the effect on the distribution of M_u at ULS. The ratio of stochastic field length to correlation length, L_{SEM}/a, is used to determine the size of the discretization based on correlation length. A range of $L_{SEM} = a/5$ to $a/10$ is recommended to ensure a sufficiently refined mesh.[15] In this work, a range of $L_{SEM}/a = 1/2$ to $1/13$ is chosen, with L_{SEM} taken as the average of the field length in the three dimensions. The number of terms needed to be kept in the truncation of the expansion, r, when generating the field has been varied in each trial to meet the recommended eigenmode participation ratio greater than 0.80. As the correlation length decreases, the variation in the field realizations increases spatially. Four configurations of correlation length were investigated by generating 200 SFE models for each configuration. Table 5 summarizes the correlations lengths in the x, y, and z dimensions, the number of required eigenvalues (r in Eq. (6)), and the achieved eigenmode

Table 4—SEM parametric analysis: considered configurations of SEM density

Case ID	Total SE	FE size, mm	SE size, mm	*SEM*/*FEM* (x,y,z)	N_{SFE}
SEM320	320	12.5 x 12.5 x 10	60 x 62.5 x 62.5	6 x 5 x 5	200
SEM750	750	12.5 x 12.5 x 10	40 x 50 x 50	4 x 4 x 4	200
SEM6000	6000	12.5 x 12.5 x 10	25 x 25 x 20	2 x 2 x 2	200

Note: 1 mm = 0.039 in.

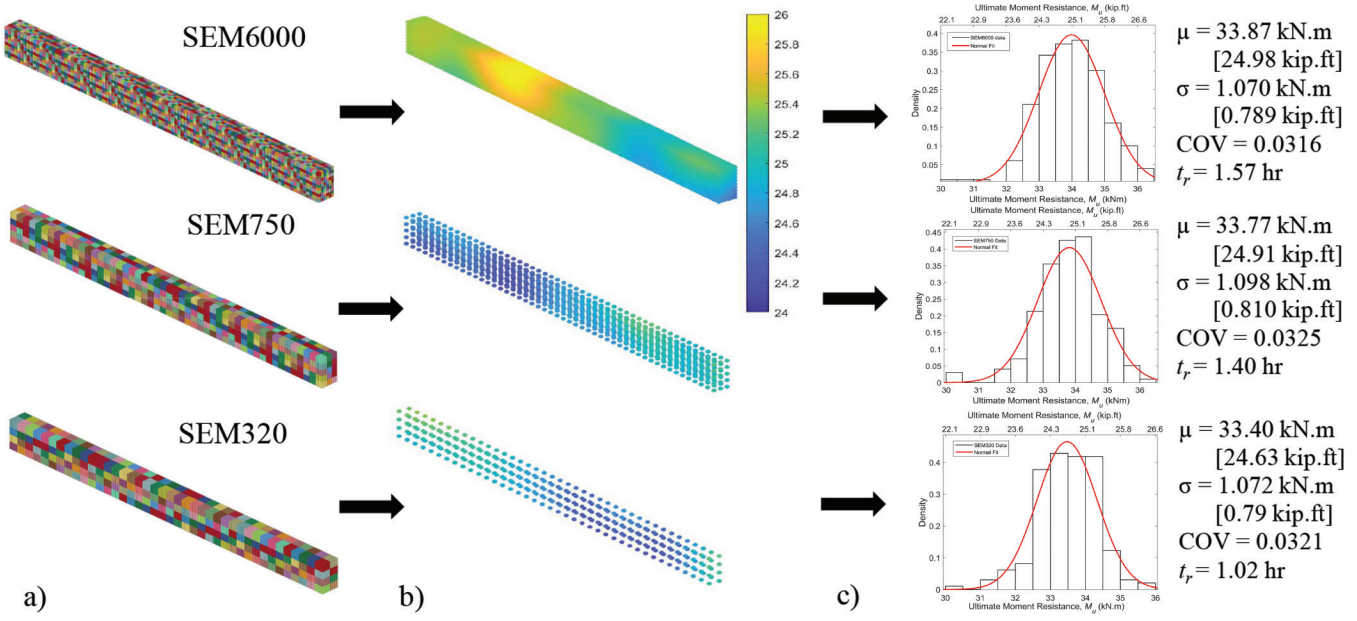

Fig. 6—Discretization and resistance distribution results of stochastic element mesh sensitivity analysis: (a) discretization of stochastic FE model; (b) sample realization of concrete compressive strength random field at centroid of stochastic elements; and (c) fitted distribution of M_u *based on conducting 200 SFE analysis. (Note: Full-color PDF of this paper can be accessed at www.concrete.org.)*

participation ratio for the considered configurations (Q in Eq. (11)).

Figure 7(a) shows the SEM density and corresponding correlation length considered (SEM6000 of the SEM sensitivity analysis). Figure 7(b) shows sample realizations of the 3-D field of f_c' for the considered correlation lengths, where the random fields were generated using the same set of standard normal variables used for the SEM sensitivity analysis. As expected, the spatial variation along the beam dimension is minimal for high correlation lengths. Figure 7(c) shows the histograms, fitted normal distributions, and the statistical parameters of the considered cases where 200 SFE models were used to generate each distribution. Results show that the mean is similar in all cases, which indicates the insensitivity of the member mean flexural capacity to variations in the correlation length of the concrete and bond random fields. The difference in results can be seen in the variation of COV, where increased COV is reported for the sample data when the correlation length is decreased.

Results and discussion of parametric analysis

The computer code presented in Fig. 3 was used to assess the reliability of the eight beams included in Table 1 based on the recommended SEM density and correlation length derived in the previous sections (case SEM6000 in Fig. 6 and CL150 in Fig. 7). Figure 8 presents the histograms of M_u of the considered beams, where 200 nonlinear SFE models were generated per each considered beam. The mean, COV, and σ of the $R_{SFE}(X)$ random variable in Eq. (13) were determined by fitting a normal distribution using the generated histograms in Fig. 8. The mean is divided by the respective code predicted nominal strength to obtain the bias of $R_{SFE}(X)$, where material resistance factors or member reduction factors are set to unity. The reliability index, β, was computed as per Eq. (1), (12), and (13) considering a fully

Table 5—CL parametric analysis: considered configurations of correlation length

Case ID	l/a^*	a_x	a_y	a_z	r	Q	N_{SFE}
CL75	1/13	75	75	75	3	0.821	200
CL150	1/6	150	150	150	26	0.817	200
CL600	1/2	600	600	600	150	0.827	200
CLVar	1/4	75	600	150	22	0.819	200

*Average in x,y,z.

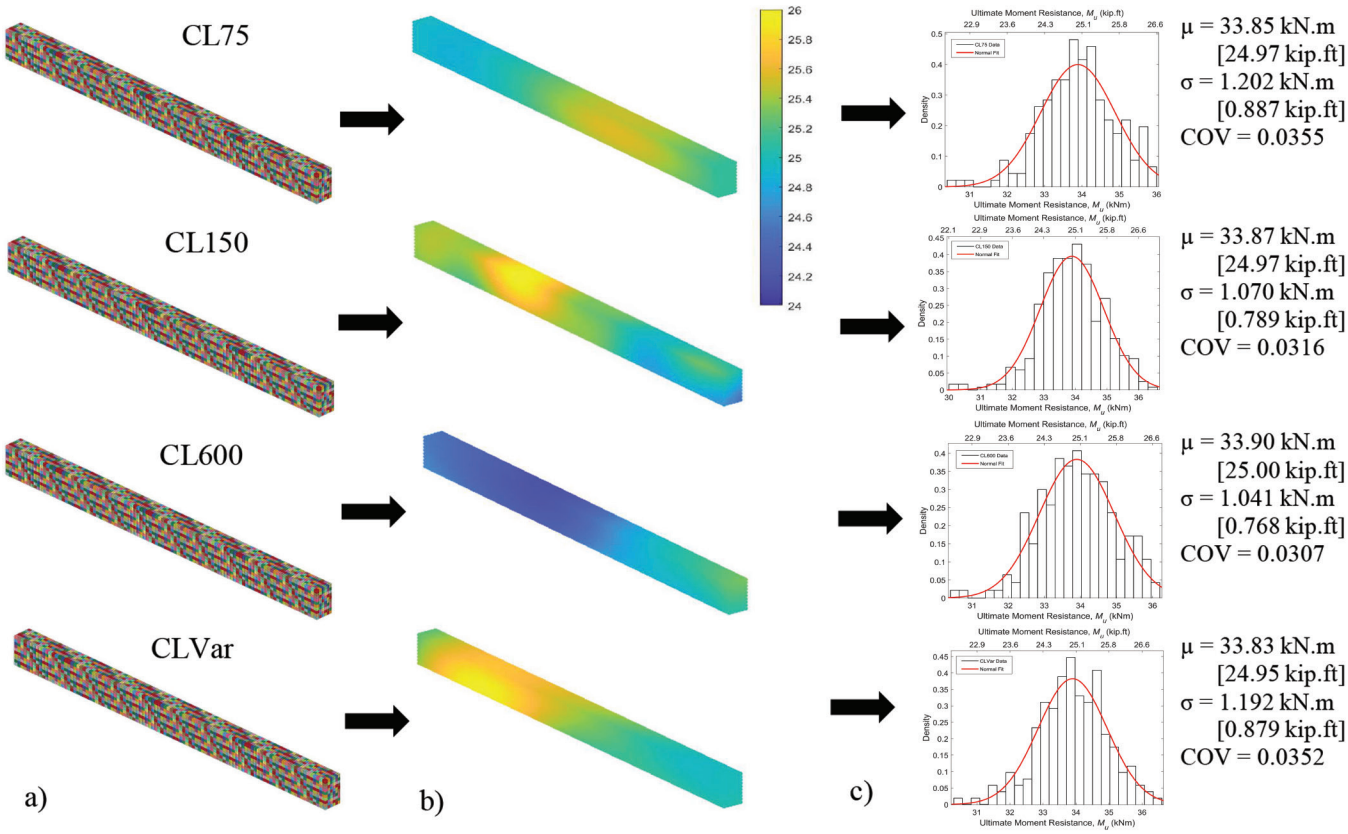

Fig. 7—Discretization and resistance distribution results of correlation length sensitivity analysis: (a) discretization of stochastic FE model; (b) sample realization of concrete compressive strength random field at centroid of stochastic elements; and (c) fitted distribution of M_u *based on conducting 200 SFE analysis. (Note: Full-color PDF of this paper can be accessed at www.concrete.org.)*

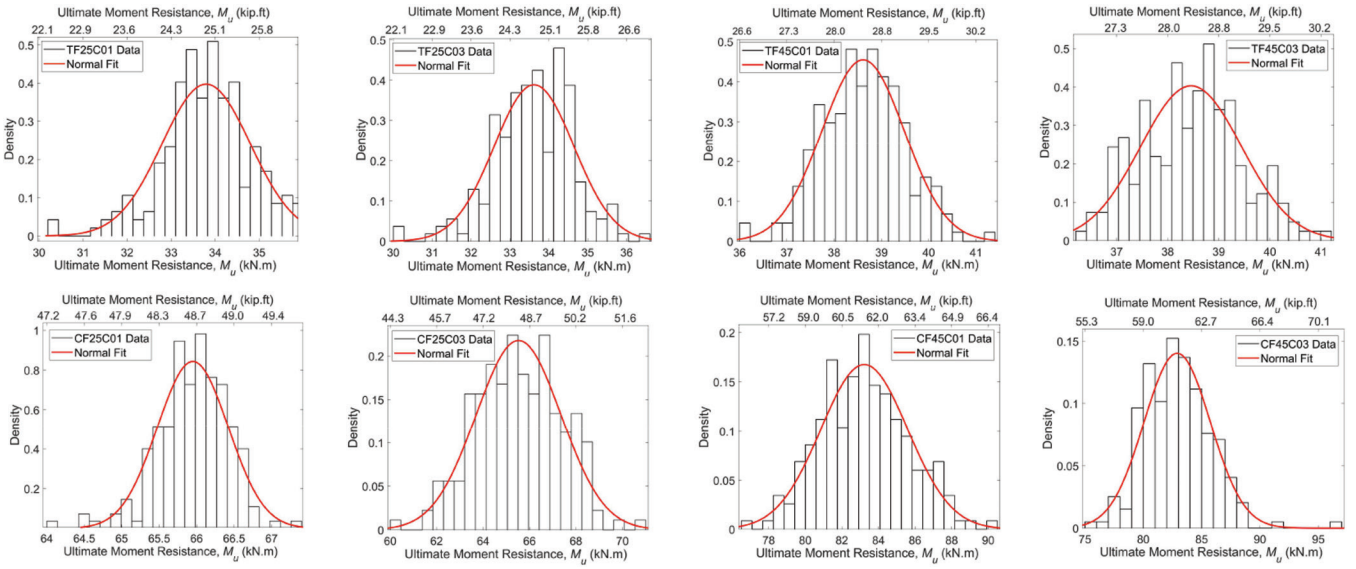

Fig. 8—Histograms of M_u *with fitted normal distributions for beams considered in parametric study.*

Table 6—Parametric reliability analysis results

Beam ID	Statistical parameters of R_{SFE}						Reliability index β		
	μ, kN·m (kip·ft)	σ, kN·m (kip·ft)	COV	Bias (μ/code M_n)					
				CSA S806-17	CSA S6-19	ACI 440.2R-17	CSA S806-17	CSA S6-19	ACI 440.2R-17
TF25C01	33.87 (24.98)	1.07 (0.789)	0.0316	1.58	1.55	1.35	4.91	4.79	4.17
TF25C03	33.59 (24.77)	1.07 (0.789)	0.0319	1.56	1.53	1.34	4.83	4.72	4.11
TF45C01	38.59 (24.77)	0.91 (0.671)	0.0236	1.75	1.72	1.49	5.37	5.20	4.62
TF45C03	38.47 (28.37)	0.99 (0.730)	0.0257	1.75	1.71	1.49	5.42	5.24	4.62
CF25C01	65.95 (48.64)	0.47 (0.346)	0.0072	1.54	1.37	1.71	5.06	4.29	5.24
CF25C03	65.43 (48.25)	2.07 (1.526)	0.0316	1.53	1.36	1.69	4.95	4.20	5.27
CF45C01	83.18 (61.35)	2.46 (1.814)	0.0296	1.50	1.39	1.81	4.85	4.32	5.29
CF45C03	82.90 (61.14)	2.84 (2.094)	0.0343	1.50	1.39	1.80	4.83	4.30	5.61

utilized section (factored demand to factored capacity ratio equal unity). The statistical parameters of R_{SFE} and analysis results of the computed β using 100 million trials for MCS are included in Table 6.

The reliability of the beams range between 4.1 to 5.6, which is greater than the conventional target range of β (3.0 to 4.0) used in the calibration of the respective design standards (ACI 440.2R,[12] CSA S806,[13] CSA S6,[14] and ISO 13822[40]). This is attributed to the relatively high bias factors computed for R_{SFE} which range from 1.34 to 1.75 for tension-controlled sections and from 1.39 to 1.80 for the compression-controlled sections. These biases are generally greater than reported in literature for conventional RC beams tested for the calibration of the ACI 318 code.[29] The reliability of the three codes decreases with the increase in f_c' for the tension-controlled beams because the mean of R_{SFE} increased with the increase in the concrete strength while the code nominal moment did not change (that is, increased bias for higher f_c'). This implies that the enhanced reliability of tension-controlled sections with higher f_c' due to an improved concrete-FRP bond strength is not captured in the nominal capacity prediction of the respective codes. For the compression-controlled beams, an opposite trend was observed whereby the reliability drops with the increase in f_c' for the considered codes (that is, reduced bias for higher f_c'). For the tension-controlled sections, the increase of COV of f_c' (0.1 to 0.3) has marginally increased the COV of R_{SFE}, while it considerably increased the COV of R_{SFE} of the compression-controlled sections because M_u of the latter is controlled by crushing of the concrete.

The reliability of tension-controlled sections is greater than the reliability of the compression-controlled sections for the CSA S806 and CSA S6 standards, while an opposite trend is observed for ACI 440.2R.[12] This is indicative that the FRP strain limits in CSA standards are conservative for the considered sections (0.007 and 0.006 for CSA S806[13] and CSA S6,[14] respectively). For ACI 440.2R,[12] the lower reliability of the tension-controlled sections is attributed to the lower member reduction factor as compared with compression-controlled sections. The lower the member reduction factor, the higher is the bias of R_{SFE}.

FUTURE STUDIES

The developed SFE-MCS framework is generic and can be applied to assess the safety of reinforced concrete elements strengthened using various techniques and different existing

conditions pertaining to the spatial variability of concrete properties. The application of the proposed framework to assess the safety of in-service concrete elements subjected to various levels of deterioration (concrete cracking and steel corrosion) should be considered in future studies by modeling the degradation process as spatial-temporal fields. Also, a robust field calibration process for the correlation length parameter of existing concrete members should be considered in future research. The use of surrogate aided reliability methods should be investigated to reduce the number of SFE models required to compute the reliability of the structure of interest.

CONCLUSIONS

A novel framework of analysis was developed to assess the reliability of externally bonded (EB) fiber-reinforced polymer (FRP)-strengthened steel reinforced concrete (RC) beams in flexure by considering the concrete properties (compressive strength, tensile strength, and bulk modulus) as spatially varying in three dimensions (3-D) within the concrete volume, and the bond strength (normal strength and shear strength) as spatially varying in two dimensions (2-D) along the concrete-FRP interface. Only the concrete compressive strength random field needs to be generated using the expanded optimal linear expansion (EOLE) method, while the remaining four spatially varying parameters are correlated based on the realizations of the concrete compressive strength random field. The realizations of the random fields are assigned to stochastic elements (SE) which are a subset of the conventional finite elements (FE). Stochastic finite element (SFE) analysis is then performed to determine the distribution of the resistance model, while Monte Carlo Simulation (MCS) is used to assess the reliability based on a select load model. An LS-DYNA-Python-MATLAB computer interface was developed to perform a parametric analysis, where 3000 nonlinear SFE models were analyzed to assess the effect of varying design parameters (section type, concrete compressive strength, and coefficient of variation) on the reliability of EB FRP strengthened RC flexural beams designed as per ACI 440.2R,[12] CSA S806,[13] and CSA S6.[14] The research conclusions are as follows:

- A sensitivity analysis is recommended to optimize the stochastic element mesh (SEM) density. Analysis results indicated that the use of a coarse SEM may result in missing the peak realizations of the field as compared with finer SEM generated using the same set of standard normal variables. The analysis results recommend sizing the dimensions of the SE as twice the dimension of the FE. That is, each SE contains a set of eight elements in a 3-D analysis (2 x 2 x 2). The recommendation is limited to concrete volumes modeled using uniform FE mesh densities.
- In the absence of field input data regarding the correlation length used to generate the concrete compressive strength random field, a sensitivity analysis is recommended to determine the values required for the SFE simulation. The higher number of participating modes for a small correlation length yields a higher number of required standard normal variables in the reliability analysis. Depending on the reliability method used for analysis, this can represent a computational burden to perform the analysis. The use of surrogate predictors to predict the performance function, such as active learning Kriging MCS (AK-MCS), can be used to reduce the computational burden.[41] If active learning techniques are used to assess the reliability, the standard normal variables can be used in training the predictor in active learning.[19] Research is required to recommend project-specific values for the correlation length, and to examine varying the random fields only within the critical region of the structure to improve efficiency.[42]
- The parametric analysis results showed that the reliability index of all considered compression- and tension-controlled beams are greater than the target reliability indexes used by the considered codes. It also showed that the reliability of the tension-controlled sections increases with the increase in the specified concrete compressive strength. This action is not recognized by the considered design standards. It is attributed to the improved bond strength at the FRP-concrete interface when the spatial variability is considered.

AUTHOR BIOS

ACI member **Connor Petrie** *is a Junior Structural Engineer at Norlander Oudah Engineering Ltd. in Calgary, AB, Canada. He received his BA in engineering and MA in applied science from Dalhousie University, Halifax, NS, Canada, in 2020 and 2022, respectively. His research interests include stochastic finite element analysis of fiber-reinforced polymer (FRP)-strengthened reinforced concrete beams and computational optimization of reliability-based assessment using active-learning techniques.*

ACI member **Fadi Oudah** *is an Associate Professor in the Department of Civil and Resource Engineering at Dalhousie University. He is a member of ACI Committee 251, Fatigue of Concrete, and ACI Subcommittee 440-J, FRP Stay-in-Place Forms. His research interests include assessment and retrofit of buildings and bridges using structural reliability, advanced composites, and smart materials.*

ACKNOWLEDGMENTS

The authors wish to acknowledge the financial contributions of Dalhousie University, the Mathematics of Information Technology and Complex Systems (MITACS) program, and Norlander Oudah Engineering Limited (NOEL).

REFERENCES

1. Okeil, A. M.; El-Tawil, S.; and Shahawy, M., "Flexural Reliability of Reinforced Concrete Bridge Girders Strengthened With Carbon Fiber-Reinforced Polymer Laminates," *Journal of Bridge Engineering*, ASCE, V. 7, No. 5, 2002, pp. 290-299. doi: 10.1061/(ASCE)1084-0702(2002)7:5(290)

2. Wang, N.; Ellingwood, B. R.; and Zureick, A., "Reliability-Based Evaluation of Flexural Members Strengthened with Externally Bonded Fiber-Reinforced Polymer Composites," *Journal of Structural Engineering*, ASCE, V. 136, No. 9, 2010, pp. 1151-1160. doi: 10.1061/(ASCE)ST.1943-541X.0000199

3. Wang, N., and Ellingwood, B. R., "Limit State Design Criteria for FRP Strengthening of RC Bridge Components," *Structural Safety*, V. 56, 2015, pp. 1-8. doi: 10.1016/j.strusafe.2015.03.004

4. Shi, J.; Wu, Z.; Wang, X.; and Noori, M., "Reliability Analysis of Intermediate Crack-Induced Debonding Failure in FRP-Strengthened Concrete Members," *Structure and Infrastructure Engineering*, V. 11, No. 12, 2015, pp. 1651-1671. doi: 10.1080/15732479.2014.987302

5. Huang, X.; Sui, L.; Xing, F.; Zhou, Y.; and Wu, Y., "Reliability Assessment for Flexural FRP-Strengthened Reinforced Concrete Beams Based on Importance Sampling," *Composites. Part B, Engineering*, V. 156, 2019, pp. 378-398. doi: 10.1016/j.compositesb.2018.09.002

6. Huang, X., Zhou, Y., Xing, F., Wu, Y., Sui, L., and Han, N., "Reliability-Based Design of FRP Flexural Strengthened Reinforced Concrete

Beams: Guidelines Assessment and Calibration," *Engineering Structures*, V. 209, 2020, p. 109953. doi: 10.1016/j.engstruct.2019.109953

7. Petrie, C., and Oudah, F., "Examining the Effects of Load Type and History Using Reliability on Optimizing the Design of FRP Strengthened RC Members in Flexure," *8th International Conference on Advanced Composite Materials in Bridges and Structures*, 2021.

8. Wieghaus, K. T., and Atadero, R. A., "Effect of Existing Structure and FRP Uncertainties on the Reliability Of FRP-Based Repair," *Journal of Composites for Construction*, ASCE, V. 15, No. 4, 2011, pp. 635-643. doi: 10.1061/(ASCE)CC.1943-5614.0000197

9. Liu, M., "Spatial Variation of Concrete Strength in Safety Evaluation of Existing Structures," *Dennis Mertz Symposium on Design and Evaluation of Concrete Bridges*, SP-340, American Concrete Institute, Farmington Hills, MI, 2020, pp. 197-209.

10. Nguyen, N. T.; Sbartaï, Z. M.; Lataste, J. F.; Breysse, D.; and Bos, F., "Assessing the Spatial Variability of Concrete Structures Using NDT Techniques - Laboratory Tests and Case Study," *Construction and Building Materials*, V. 49, 2013, pp. 240-250. doi: 10.1016/j.conbuildmat.2013.08.011

11. Petrie, C., "Reliability Analysis of Externally Bonded FRP Strengthened Beams Considering Existing Conditions: Application Of Stochastic FE and Conditional Probability," Master's of Applied Science Thesis, Dalhousie University, Halifax, NS, Canada, 2022.

12. ACI Committee 440, "Guide for the Design and Construction of Structural Concrete Reinforced with Fiber-Reinforced Polymer (FRP) Bars (ACI 440.2R-17)," American Concrete Institute, Farmington Hills, MI, 2017, 112 pp.

13. CSA S806-12, "Design and Construction of Building Structures With Fiber-Reinforced Polymers (Reapproved 2017)," Canadian Standards Association, Mississauga, ON, Canada, 2012.

14. CSA S6-19, Canadian Highway Bridge Design Code, Canadian Standards Association, Mississauga, ON, Canada, 2019.

15. Sudret, B., and Der-Kiureghian, A., *Stochastic Finite Elements and Reliability - A State-of-the-Art Report*, Department of Civil Engineering, University of California, Berkeley, Berkeley, CA, 2000.

16. El Haj, A. K., and Soubra, A. H., "Efficient Estimation of the Failure Probability of a Monopile Foundation Using a Kriging-Based Approach With Multi-Point Enrichment," *Computers and Geotechnics*, V. 121, 2020, p. 103451. doi: 10.1016/j.compgeo.2020.103451

17. Li, Y.; Liu, K.; Zhang, B.; and Xu, N., "Reliability of Shape Factors for Bearing Capacity of Square Footings on Spatially Varying Cohesive Soils," *International Journal of Geomechanics*, ASCE, V. 20, No. 3, 2020, pp. 1-13. doi: 10.1061/(ASCE)GM.1943-5622.0001614

18. Xhang, X.-L.; Jiao, B.-H.; Han, Y.; Chen, S.-L.; and Li, X.-Y., "Random Field Model of Soil Parameters and the Application in Reliability Analysis of Laterally Loaded Pile," *Soil Dynamics and Earthquake Engineering*, V. 147, 2021, p. 106821. doi: 10.1016/j.soildyn.2021.106821

19. Khorramian, K.; Alhashmi, A.; and Oudah, F., "Optimized Active Learning Kriging Reliability Based Assessment of Laterally Loaded Pile Groups Modeled Using Random Finite Element Analysis," *Computers and Geotechnics*, V. 154, 2023, p. 105135 doi: 10.1016/j.compgeo.2022.105135

20. Oudah, F., and Alhashmi, A., "Time-Dependent Reliability Analysis of Degrading Structural Elements Using Stochastic FE and LSTM Learning," *CSCE 2022 Annual Conference*, Whistler, BC, Canada, 2022.

21. Li, C., and Der-Kiureghian, A., "Optimal Discretization of Random Fields," *Journal of Engineering Mechanics*, ASCE, V. 119, No. 6, 1993, pp. 1136-1154. doi: 10.1061/(ASCE)0733-9399(1993)119:6(1136)

22. Nataf, A., "Determination des Distribution Dont les Marges Sont Donnees," *Comptes Rendus de l'Academie des Sciences*, V. 225, 1962, pp. 42-43.

23. Most, T., and Bucher, C., "Stochastic Simulation of Cracking in Concrete Structures Using Multiparameter Random Fields," *International Journal of Reliability and Safety*, V. 1, No. 1/2, 2006, pp. 168-187. doi: 10.1504/IJRS.2006.010696

24. Diez, C., "Build your own LD-DYNA Tools Quickly in Python," In the proceedings of the *15th International LS-DYNA User Conference,* 2018.

25. Bartlett, F. M., and MacGregor, J. G., "Variation of In-Place Concrete Strength in Structures," *ACI Materials Journal*, V. 96, No. 2, Mar.-Apr. 1999, pp. 261-270.

26. Zhang, A. H.; Jin, W. L.; and Li, G. B., "Behavior of Preloaded RC Beams Strengthened with CFRP Laminates," *Journal of Zhejiang University. Science*, V. 7, No. 3, 2006, pp. 436-444. doi: 10.1631/jzus.2006.A0436

27. Bartlett, F. M.; Hong, H. P.; and Zhou, W., "Load Factor Calibration for the Proposed 2005 Edition of the National Building Code of Canada: Statistics of Loads and Load Effects," *Canadian Journal of Civil Engineering*, V. 30, No. 2, 2003, pp. 429-439. doi: 10.1139/l02-087

28. CSA S6.1-19, "Commentary on CSA S6-19, Canadian Highway Bridge Design Code (CSA S6.1-19)," CSA Group, Toronto, ON, Canada, 2019.

29. Szerszen, M. M., and Nowak, A. S., "Calibration of Design Code for Buildings (ACI 318): Part 2 – Reliability Analysis and Resistance Factors," *ACI Structural Journal*, V. 100, No. 3, May-June 2003, pp. 383-391.

30. Nowak, A. S., and Szerszen, M. M., "Calibration of Design Code for Buildings (ACI 318): Part 1 - Statistical Models for Resistance," *ACI Structural Journal*, V. 100, No. 3, May-June 2003, pp. 377-382.

31. Castaldo, P.; Gino, D.; and Mancini, G., "Safety Formats for Non-Linear Finite Element Analysis of Reinforced Concrete Structures: Discussion, Comparison and Proposals," *Engineering Structures*, V. 193, 2019, pp. 136-153. doi: 10.1016/j.engstruct.2019.05.029

32. Livermore Software Technology Corporation (LSTC), LS-DYNA Keyword User Manual - Material Models (Nonlinear Dynamic Analysis of Structures in Three Dimensions), V. 2, Version 971, Livermore, CA, 2007.

33. Magallanes, J. M.; Wu, Y.; Malvar, L. J.; and Crawford, J. E., "Recent Improvements to Release III of the K&C Concrete Model," *11th International LS-DYNA User Conference*, 2010.

34. CEB-FIP, Model Code 1990: Design Code, Thomas Telford, London, UK, 1993.

35. Chen, J. F., and Teng, J. G., "Anchorage Strength Models for FRP and Steel Plates Bonded to Concrete," *Journal of Structural Engineering*, ASCE, V. 127, No. 7, 2001, pp. 784-791. doi: 10.1061/(ASCE)0733-9445(2001)127:7(784)

36. Lu, X. Z.; Teng, J. G.; Ye, L. P.; and Jiang, J. J., "Bond-Slip Models for FRP Sheets/Plates Bonded to Concrete," *Engineering Structures*, V. 27, No. 6, 2005, pp. 920-937. doi: 10.1016/j.engstruct.2005.01.014

37. Neale, K. W.; Ebead, U.; Abdel Baky, H.; Elsayed, W.; and Godat, A., "Modelling of Debonding Phenomena in FRP-Strengthened Concrete Beams and Slabs," *Proceedings of the International Symposium on Bond Behaviour of FRP in Structures (BBFS 2005)*, 2005.

38. Almusallam, T. H.; Elsanadedy, H. M.; and Al-Salloum, Y. A., "Effect of Longitudinal Steel Ratio on Behavior of RC Beams Strengthened with FRP Composites: Experimental and FE Study," *Journal of Composites for Construction*, ASCE, V. 19, No. 1, 2015, p. 04014028. doi: 10.1061/(ASCE)CC.1943-5614.0000486

39. Elsanadedy, H. M.; Almusallam, T. H.; Alsayed, S. H.; and Al-Salloum, Y. A., "Flexural Strengthening of RC Beams Using Textile Reinforced Mortar - Experimental and Numerical Study," *Composite Structures*, V. 97, 2013, pp. 40-55. doi: 10.1016/j.compstruct.2012.09.053

40. ISO 13822:2010, Bases for Design of Structures – Assessment of Existing Structures, International Organization for standardization, 2010.

41. Khorramian, K., and Oudah, F., "Active Learning Kriging-Based Reliability for Assessing the Safety of Structures: Theory and Application," In: *Leveraging Artificial intelligence into Engineering, Management, and Safety of Infrastructure*. s.l.:Taylor and Francis (CRC), 2022, pp. 184-231.

42. Khorramian, K.; Alhashmi, A. E.; and Oudah, F., "Efficient Representation of Random Fields for Training the Kriging Predictor in Adaptive Kriging Reliability Assessment of Civil Structures,"*Automation in Construction through Resilience: Robotics, Smart Materials & Intelligent Systems*, Taylor and Francis, 2023, pp. 485-502.

NEW Symposium Publications from ACI

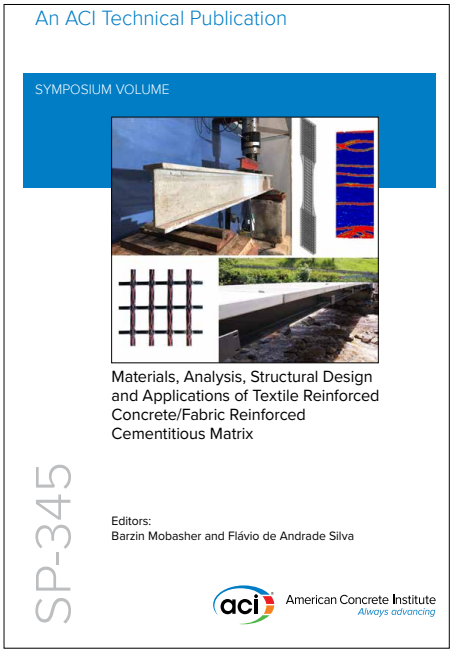

SP-345: Materials, Analysis, Structural Design and Applications of Textile Reinforced Concrete/Fabric Reinforced Cementitious Matrix

Several state-of-the-art sessions on textile-reinforced concrete/fabric-reinforced cementitious matrix (TRC/FRCM) were organized by ACI Committee 549 in collaboration with RILEM TC MCC during the ACI Fall 2019 Convention in Cincinnati, OH, and the ACI Virtual Technical Presentations in June 2020. The forum provided a unique opportunity to collect information and present knowledge in the field of TRC and FRCM as sustainable construction materials.

Available in PDF format: $69.50
(FREE to ACI members)

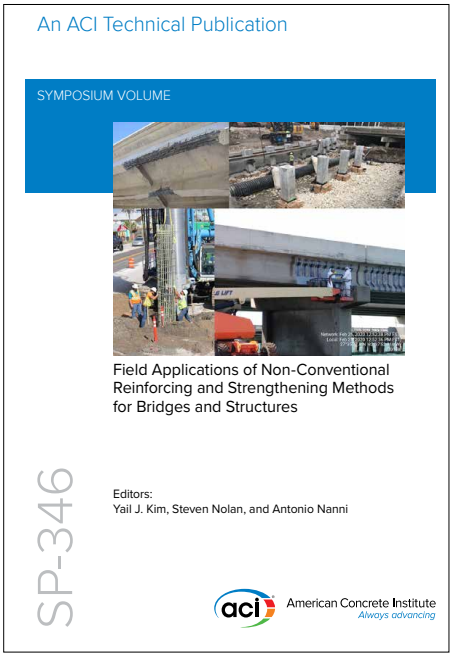

SP-346: Field Applications of Non-Conventional Reinforcing and Strengthening Methods for Bridges and Structures

A sustainable built environment requires a comprehensive process from material selection through to reliable management. Although traditional materials and methods still dominate the design and construction of our civil infrastructure, nonconventional reinforcing and strengthening methods for concrete bridges and structures can address the functional and economic challenges facing modern society.

Available in PDF format: $69.50
(FREE to ACI members)

American Concrete Institute
+1.248.848.3700 • www.concrete.org

NEW Symposium Publications from ACI

SP-347: Recent Developments in High Strain Rate Mechanics and Impact Behavior of Concrete

This Symposium Volume reports on the latest developments in the field of high-strain-rate mechanics and behavior of concrete subject to impact loads. This effort supports the mission of ACI Committee 370, Blast and Impact Load Effects, to develop and disseminate information on the design of concrete structures subjected to impact, as well as blast and other short-duration dynamic loads.

Available in PDF format: $69.50
(ACI members: $39.00) ($30.50 savings)

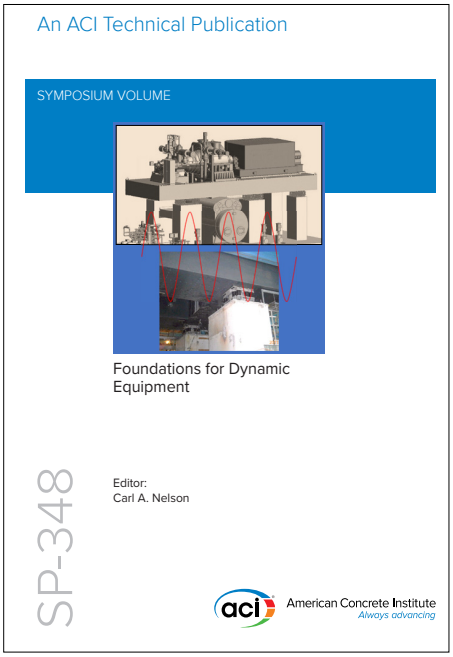

SP-348: Foundations for Dynamic Equipment

This special publication grew out of the Technical Session titled “Application of ACI 351-C Report on Dynamic Foundations,” held at the ACI Spring 2019 Convention in Québec City, Québec. Following this event, ACI Committee 351 decided to undertake a special publication with contributions from those session participants willing to develop their presentations into full-length papers. Three papers included in the current publication were contributed by these presenters and their coauthors, with six additional papers provided by others.

Available in PDF format: $69.50
(ACI members: $39.00) ($30.50 savings)

American Concrete Institute
+1.248.848.3700 • www.concrete.org

ACI STRUCTURAL JOURNAL

The American Concrete Institute (ACI) is a leading authority and resource worldwide for the development and distribution of consensus-based standards and technical resources, educational programs, and certifications for individuals and organizations involved in concrete design, construction, and materials, who share a commitment to pursuing the best use of concrete.

Individuals interested in the activities of ACI are encouraged to explore the ACI website for membership opportunities, committee activities, and a wide variety of concrete resources. As a volunteer member-driven organization, ACI invites partnerships and welcomes all concrete professionals who wish to be part of a respected, connected, social group that provides an opportunity for professional growth, networking, and enjoyment.

American Concrete Institute